
Novel Approaches for Direct Force Measurements: From Single Molecules to Giant Hydrogel Beads

Dissertation

zur Erlangung des akademischen Grades
eines Doktors der Naturwissenschaften (Dr. rer. nat.)
im Fach Chemie der Fakultät für Biologie, Chemie
und Geowissenschaften der Universität Bayreuth.

vorgelegt von

Nicolas Helfricht

geboren in Coburg, Deutschland

Bayreuth, 2017

Die vorliegende Arbeit wurde in der Zeit von Januar 2012 bis Mai 2017 in Bayreuth am Lehrstuhl Physikalische Chemie II / Physik der Polymere der Universität Bayreuth unter Betreuung von Herrn Professor Dr. Georg Papastavrou angefertigt.

Vollständiger Abdruck der von der Fakultät für Biologie, Chemie und Geowissenschaften der Universität Bayreuth genehmigten Dissertation zur Erlangung des akademischen Grades eines Doktors der Naturwissenschaften (Dr. rer. nat.).

Dissertation eingereicht am: 24.05.2017

Zulassung durch die Promotionskommission: 31.05.2017

Wissenschaftliches Kolloquium: 20.09.2017

Amtierender Dekan: Prof. Dr. Stefan Schuster

Prüfungsaussuss:

Prof. Dr. Georg Papastavrou (Erstgutachter)

JProf. Dr. Markus Retsch (Zweitgutachter)

Prof. Dr. Mukundan Thelakkat (Vorsitz)

Prof. Dr. Thomas Scheibel

*"It is necessary to look at
the results of observation objectively,
because you, the experimenter,
might like one result better than another."*

Richard P. Feynman

meiner Familie
Lena & Lukas

Contents

Zusammenfassung	iii
Summary	v
List of Publications	vii
1 Introduction	1
2 Theory / Status of the field	9
2.1 Scanning Probe Microscopy	9
2.2 Interaction Forces between Surfaces	20
3 Synopsis	39
3.1 Outline	39
3.2 Content of the Individual Publications	39
3.3 Individual Contributions to Joint Publications	59
Scientific Publications	69
4 A Direct Biocombinatorial Strategy towards Next Generation, Mussel-Glue Inspired Saltwater Adhesives	69
5 Surface Properties of Spider Silk Particles in Solution	97
6 Colloidal Properties of Recombinant Spider Silk Protein Particles	117
7 Extending the Limits of Direct Force Measurements: Colloidal Probes from Sub-Micron Particles	151

Contents

8 Writing with Fluid: Structuring Hydrogels with Micrometer Precision by AFM in Combination with Nanofluidics	185
9 Long-range interaction forces between 1,3,5-cyclohexanetrissamide fibers in crossed-cylinder geometry	213
10 Probing the Adhesion Properties of Alginate Hydrogels: A New Approach towards the Preparation of Soft Colloidal Probes for Direct Force Measurements	237
11 Appendix	277
Danksagung	339
(Eidesstattliche) Versicherungen und Erklärungen	343

Zusammenfassung

Die Rasterkraftmikroskopie (AFM) erlaubt das Messen von Wechselwirkungskräften zwischen Oberflächen mit hoher Auflösung. Hierbei stellt die Sonde, die sich am Ende des sogenannten *Cantilevers* befindet, den wichtigsten Bestandteil dar. Die Möglichkeit der individuellen Herstellung erlaubt direkt Wechselwirkungen zwischen molekularen und kolloidalen Bausteinen übergeordneter, mesoskopischer Strukturen zu messen. Das Ziel dieser Arbeit war die Entwicklung neuartiger kolloidaler AFM Sonden. Hierbei sollte das Spektrum an kolloidalen Sonden bezüglich verwendbarer Materialien sowie der zugrunde liegenden Längenskalen signifikant erweitert werden.

Im ersten Teil dieser Arbeit wurden bereits etablierte und damit 'klassische' AFM Sonden zur direkten Kraftmessung verwendet. Zunächst wurde das Adhäsionsverhalten von synthetischen Muschel-Fuß-Peptiden auf anorganischen Oxidoberflächen mittels Einzelmolekülkraftspektroskopie untersucht. Diese Messungen bestätigten, dass die Aminosäure L-Dopa maßgeblich für die bemerkenswerten Adhäsionseigenschaften von Muschel-Fuß-Proteinen verantwortlich ist. Darüber hinaus wurden kolloidale Sonden aus Silika-Partikeln hergestellt, um die Oberflächeneigenschaften von Spinnenseidenproteinpartikeln zu charakterisieren. Eine Kombination aus direkten Kraftmessungen in der Kugel-Kugel-Geometrie mit elektrokinetischen Untersuchungen zeigte, dass die Partikeloberfläche weich und permeabel ist.

Im zweiten Teil der Arbeit wurde eine Kombination aus AFM mit kontrollierter Nanofluidik, der sogenannten FluidFM-Technologie verwendet. Das zentrale Element dieser Methode sind spezielle, hohle AFM-*Cantilever* mit einer Öffnung. Durch Anlegen eines Unterdrucks an diesen Mikrokanal können kolloidale Partikel reversibel immobilisiert und somit schnell ausgetauscht werden. Mit Hilfe dieser Methode wurden Silika-Partikel aspiriert, um verschieden geladene Spinnenseidenproteinpartikel zu charakterisieren. Diese Kraftmessungen wurden mit elektrokinetischen Messungen sowie

0 Zusammenfassung

theoretischen Modellierungen für weiche und permeable Partikel begleitet, um das zuvor eingeführte Model zu verbessern. Cantileveröffnungen im sub- μm Bereich ermöglichen zum ersten Mal das Messen von kolloidalen Wechselwirkungen von Nanopartikeln. Hierzu wurden Silika-Partikel als Model-System gewählt. Diese Messungen wurden mit klassischen μm -großen kolloidalen Sonden sowohl in der Kugel-Kugel- als auch in der Kugel-Platten-Geometrie verglichen. Des Weiteren wurde die FluidFM-Technologie zur Strukturierung von weichen Hydrogelfilmen verwendet. Hierbei konnten elektrogelierte Filme des pH-responsiven Hydrogels durch Injektion einer basischen Lösung lokal aufgelöst werden. Somit konnte eine neuartige Methode zur subtraktiven Strukturierung von Hydrogelfilmen entwickelt werden.

Im letzten Teil wurden neuartige kolloidale Sonden hergestellt, um Kräfte in speziellen Wechselwirkungsgeometrien zu messen. Neben sphärischen Partikeln konnten auch Fasersegmente von elektroschmelzgesponnenen Cyclohexantrisamiden am *Cantilever* immobilisiert werden, um deren Oberflächenladung in gekreuzter Zylinder-Geometrie zu ermitteln. Des Weiteren wurde eine neue Methode zur *in-situ*-Herstellung von kolloidalen Hydrogel-Sonden entwickelt. Diese Methode basiert auf mikrobiologischen Techniken und ermöglicht eine vollständige Herstellung der Sonden in Flüssigkeit. Direkte Kraftmessungen zeigten, dass sich das Adhäsionsverhalten signifikant von dem klassischer, harter Partikel unterscheidet.

Summary

Atomic force microscopy (AFM) allows to determine interaction forces between surfaces with superior resolution. Thereby, the probe at the end of an AFM cantilever plays an important role. Using special preparation techniques, it is possible to measure the interaction forces between different building blocks of mesoscopic systems. The objective of the thesis was the development of novel AFM probes in order to broaden the spectrum of both available materials and underlying length scales.

Previously established, therefore 'classical' AFM methods were used in the first part of the thesis. Firstly, the adhesion behaviour of synthesized mussel-foot-peptides to inorganic oxide surfaces was studied by means of single molecule force spectroscopy. These measurements confirmed that the amino acid L-dopa is responsible for the outstanding adhesive properties of the selected peptides, as for natural marine mussels. Secondly, colloidal probes from silica particles were prepared to characterize spider silk protein particles. By combining direct force measurements in the sphere-sphere-geometry with electrokinetic measurements enabled the determination of a soft and porous interface of the particles.

In the second part, a combination of AFM with controlled nanofluidics, often referred to as FluidFM-technology has been utilized. The pivotal elements of this method are special hollow AFM-cantilevers with an aperture allowing for a reversible immobilization of the colloidal particle by means of an applied underpressure, and thus enabling a fast exchange of the probe. Silica particles were temporarily immobilized in order to investigate oppositely charged spider silk protein particles in the sphere-sphere-geometry. These experiments were again combined with electrokinetic measurements and theoretical modelling for soft and permeable particles allowing for the improvement of the presented model. The availability of sub- μm -sized apertures allows for the first time for a controlled measurement of interaction forces with nanoparticles. In this case,

0 Summary

silica particles have been used as a model system. The measurements were compared to μm -sized silica colloidal probes in both the sphere-sphere-geometry and the sphere-plane-geometry, respectively. Beside these force measurements, the FluidFM could be additionally used to structure soft hydrogel films. The reversible formation of electrogelated hydrogels is pH-dependent, whereby the injection of a basic solution leads to the local dissolution, representing a novel approach to structure hydrogel films.

In the last part, novel types of colloidal probes were used in special interaction geometries. The colloidal probe technique is not limited to spherical particles, hence also fiber segments of various electromeltspun cyclohexanetrismides have been immobilized onto AFM cantilevers in order to determine their surface potentials in the crossed-cylinder-geometry. Moreover, a novel method for the *in situ* preparation for soft hydrogel probes has been developed, which is based on techniques used in microbiology and allows for the complete manipulation in liquid. Direct force measurements revealed that the adhesion behaviour of hydrogels is quite different from the one observed for solid particles.

List of Publications

1. **Extending the Limits of Direct Force Measurements: Colloidal Probes from Sub-Micron Particles**

Nicolas Helfricht, Andreas Mark, Livie Dorwling-Carter, Tomaso Zambelli, Georg Papastavrou

Nanoscale, **2017**, 9, 9491-9501.

2. **Writing with Fluid: Structuring Hydrogels with Micrometer Precision by AFM in Combination with Nanofluidics**

Nicolas Helfricht, Andreas Mark, Marina Behr, Andreas Bernet, Hans-Werner Schmidt, Georg Papastavrou

Small, **2017**, 13(31), 1700962.

3. **Probing the Adhesion of Alginate Hydrogel: A New Approach towards the Preparation of Soft Colloidal Probes for Direct Force Measurements**

Nicolas Helfricht, Elena Doblhofer, Vera Bieber, Petra Lommes, Volker Sieber, Thomas Scheibel, Georg Papastavrou

Soft Matter, **2017**, 13, 578-589.

4. **Colloidal Properties of Recombinant Spider Silk Protein Particles**

Nicolas Helfricht, Elena Doblhofer, Jérôme F. L. Duval, Thomas Scheibel, Georg Papastavrou

Journal of Physical Chemistry C, **2016**, 120, 18015-18027.

0 List of Publications

5. **Long-Range Interaction Forces between Melt-Electrospun 1,3,5-Cyclohexane-trisamide Fibers in Crossed-Cylinder Geometry**

Benedikt R. Neugirg, Nicolas Helfricht, Steffen Czich, Hans-Werner Schmidt, Georg Papastavrou, Andreas Fery
Polymer, **2016**, 102, 363-371.

6. **A Direct Biocombinatorial Strategy towards Next Generation, Mussel-Glue Inspired Saltwater Adhesives**

Patrick Wilke, Nicolas Helfricht, Andreas Mark, Georg Papastavrou, Damien Faivre, Hans Börner
Journal of the American Chemical Society, **2014**, 136(36), 12667-12674.

7. **Surface Properties of Spider Silk Particles in Solution**

Nicolas Helfricht, Maria Klug, Andreas Mark, Volodymyr Kuznetsov, Claudia Blüm, Thomas Scheibel, Georg Papastavrou
Biomaterials Science, **2013**, 1, 1166-171.

CHAPTER 1

Introduction

Surface forces are ubiquitous on the colloidal and nanoscopic level and control many material properties on these length scales. [16, 17] But also on the macroscopic level, surface forces are responsible for many effects in our environment: The dry and reversible adhesion of gecko pads allows the gecko to climb up even smooth surfaces perpendicularly. [1, 2, 3] By contrast, mussels represent an important example for tough wet adhesion, as they adhere to inorganic surfaces even under harsh sea water conditions (*e.g.* hydrodynamic drag forces and high electrolyte concentrations). [3, 4] Materials scientists were inspired from these remarkable examples, especially in terms of surface forces, as they show the pathway for the development of novel materials with tunable properties. [5, 6, 7, 8, 9] Not only short-range adhesion forces are of great interest for the design of new materials but also long-range interactions such as electrostatic or steric repulsion.

Already at the beginning of the twentieth century, Derjaguin, Landau, Verwey and Overbeek presented with the so-called DLVO theory, a broad applicable framework for describing the stability of colloidal suspensions. The DLVO theory is based on the balance between attractive van der Waals and repulsive electrostatic interactions between two surfaces. [10, 11, 12, 13] The understanding and tuning of electrostatic interactions is fundamental for the development of formulations. A typical example are drug delivery systems, that ensure a controlled uptake and release of active substances into a porous matrix. [14, 15] Formulation provides a good example how the development of novel materials requires the understanding and the control over such surface forces, as well as their resulting microscopic and macroscopic properties. [16, 17] In this respect, techniques which allow for the determination of interaction forces, either on the molecular or on the colloidal level became very important. [18]

1 Introduction

The development of novel materials with defined properties is mostly based on the formation of hierarchical structures in mesoscopic systems, which represent the interface between the nanoscale and the macroscopic world. However, following the definition of Antonietti and Ozin, the mesoscale is not only limited to a defined length scale but is much more complex. [19] At the mesoscale, different effects such as cooperative interactions and interfaces are more dominating compared to effects at the nanoscale. Consequently, the characterization of local interaction forces between single building blocks is essential in order to further optimize the overall material properties. [19, 20, 18]

An instrumental technique, that is highly suitable to determine interaction forces on the level of mesoscopic systems is the atomic force microscopy (AFM), which became more and more a key technique for the characterization of various surface properties since its invention in 1986. [21, 22, 23] Starting with the pioneering work from Weisenhorn *et al.*, it was demonstrated that AFM allows to directly measure interaction forces between several materials as well as mesoscopic building blocks. From the very beginning it was clear, that direct force measurements can be conducted under defined environmental conditions (*e.g.* different liquids or gases), which is still one of the greatest advantages of the AFM technique. [24, 25] These preliminary studies generated already the basic concept of the fast growing discipline of the 'force spectroscopy' by AFM. A quantitative evaluation of interaction force measurements between colloidal particles became possible with the invention of the colloidal probe AFM technique, whereby the sharp tip is replaced by a spherical, colloidal particle. [26, 27, 22] Such AFM-based force measurements between individual pairs of μm -sized colloidal particles allowed for the first time the determination of inter-particle interactions. [22, 28, 29] Already, Weisenhorn *et al.* reported on the manipulation of single molecules by means of the AFM, representing a primary stage of the later single molecule force spectroscopy (SMFS). [25, 30] The latter allows for the measurement of rupture forces of single molecules from a solid surface. [31, 32, 30] Consequently, the AFM with its variety of sub-techniques represents the perfect tool to characterize interaction forces on different length scales: From single molecules to giant hydrogel beads ($\sim 100 \mu\text{m}$). [23, 33]

One of the primary limitation for colloidal probes is their size. In particular, the feasibility of the probe preparation is limited to particle diameters of several μm due to the

resolution limit of optical microscopy. Hence, the preparation of sub- μm -sized colloidal probes is currently not possible. However, direct measurement of interaction forces between individual nanoparticles would be important for their application in industrial formulations. In addition, classical preparation methods for colloidal probes require a drying step, which might lead to the alteration of surface properties, especially for soft (bio-)colloids such as hydrogels. Besides the 'multiple-particle colloidal probe technique' [29], these classical approaches for the preparation of colloidal probes are all based on the applicability of an UV-curable glue and consequently a permanent immobilization of the probe particle. [34, 22] To obtain statistically relevant data sets, several colloidal probes have to be prepared prior to the force measurements, which is time- and material-consuming, respectively. Furthermore, the application of glues might introduce contaminations during measurements under certain conditions. [22] Hence, a temporary immobilization without application of any glues is preferable.

The main objective of the present thesis is the development of novel approaches for the direct measurement of interaction forces to overcome the current limitations. By the utilization of purposely prepared probes for AFM, it became possible to determine surface forces between molecular and colloidal building blocks of mesoscopic structures.

In the first part, two by now 'classical' AFM techniques were used. The adhesive behaviour of artificial mussel foot peptides on inorganic surfaces was investigated by means of single molecule force spectroscopy. In contrast, the interfacial properties of soft recombinant spider silk protein particles were determined using a standard silica colloidal probe.

In the second part of the thesis, the recently developed fluidic force microscopy (FluidFM) was used to prepare exchangeable colloidal probes due to the unique combination of AFM with controlled nanofluidics. [35, 36] A temporary and reversible immobilization of probe particles is already known from the 'multi-particle colloidal probe' technique, [29] which has several advantages compared to permanently glued particles. The FluidFM is used to determine interaction forces between silica particles and recombinant spider silk protein particles with opposite surface charges. Moreover, this novel technique allows to broaden the range of available colloidal probes beyond current limits, even down to nanoparticles. Quantitative direct measurements of interaction forces with individual silica nanoparticles ($\leq 500\text{ nm}$) have been demonstrated. Beside these

1 Introduction

force measurements, the FluidFM technique is further applied to structure soft hydrogel films. For this purpose, a subtractive structuring method was developed based on pH-responsive hydrogels.

In the third part, direct force measurements are performed by means of 'novel' colloidal probes with special interaction geometries. The surface charge properties of electro-melt-spun fiber segments are determined in the crossed-cylinder geometry. An *in situ* preparation of soft hydrogel colloidal probes was developed in order to avoid any drying steps, which are inevitable for standard techniques. Such probes have been used to determine the specific adhesive behaviour of hydrogel materials.

In summary, a variety of novel approaches for the direct measurement of interaction forces by means of AFM have been developed over the course of this thesis. These novel approaches for probes illustrate the broad applicability of scanning probe based force measurements toward different materials and length scales: From single molecules to giant hydrogel beads.

References

- [1] K Autumn, Y A Liang, S T Hsieh, W Zesch, W P Chan, T W Kenny, R Fearing, and R J Full. Adhesive force of a single gecko foot-hair. *Nature*, 405(6787):681–685, 2000.
- [2] K Autumn, M Sitti, Y A Liang, A M Peattie, W R Hansen, S Sponberg, T W Kenny, R Fearing, J N Israelachvili, and R J Full. Evidence for van der Waals adhesion in gecko setae. *Proceedings of the National Academy of Sciences*, 99(19):12252–12256, 2002.
- [3] H Lee, B P Lee, and P B Messersmith. A reversible wet/dry adhesive inspired by mussels and geckos. *Nature*, 448:338–341, 2007.
- [4] B P Lee, P B Messersmith, J N Israelachvili, and J H Waite. Mussel-Inspired Adhesives and Coatings. *Annual Review of Materials Research*, 41(1):99–132, 2011.
- [5] A Mahdavi, L Ferreira, C Sundback, J W Nichol, E P Chan, D J D Carter, C J Bettinger, S Patanavanich, L Chignozha, E Ben-Joseph, A Galakatos, H Pryor, I Pomerantseva, P T Masiakos, W Faquin, A Zumbuehl, S Hong, J Borenstein, J Vacanti, R Langer, and J M Karp. A biodegradable and biocompatible gecko-inspired tissue adhesive. *Proceedings of the National Academy of Sciences*, 105(7):2307–2312, 2008.
- [6] L F Boesel, C Greiner, E Arzt, and A del Campo. Gecko-Inspired Surfaces: A Path to Strong and Reversible Dry Adhesives. *Advanced Materials*, 22(19):2125–2137, 2010.
- [7] H Yamamoto and T Hayakawa. Improved synthetic method and conformation studies of polymers and copolymers of l- β -3,4-dihydroxyphenyl- α -alanine with l-glutamic acid. *Polymer*, 19(10):1115 – 1117, 1978.
- [8] B P Lee, P B Messersmith, J N Israelachvili, and J H Waite. Mussel-Inspired Adhesives and Coatings. *Annual Review of Materials Research*, 41(1):99–132, 2011.
- [9] B K Ahn, S Das, R Linstadt, Y Kaufman, N R Martinez Rodriguez, R Mirshafian, E Kesselman, Y Talmon, B H Lipshutz, J N Israelachvili, and J H Waite. High-

1 Introduction

performance mussel-inspired adhesives of reduced complexity. *Nature Communications*, 6:1–7, 2015.

- [10] B A Derjaguin. Theory of Interaction of Particles in Presence of Electrical Double-Layers and the Stability of Lyophobic Colloids and disperse Systems. *Acta Physicochimica URSS*, 10:333–346, 1939.
- [11] B A Derjaguin and L D Landau. Theory of the Stability of Strongly Charged Lyophobic Sols and of the Adhesion of Strongly Charged Particles in Solutions of Electrolytes. *Acta Physicochimica URSS*, 14:633–662, 1941.
- [12] E L Verwey and J T G Overbeek. *Theory of Stability of Lyophobic Colloids*. Elsevier, 1948.
- [13] B V Derjaguin. Some results from 50 years' research on surface forces. *Progress in Surface Science*, 40(1-4):240–251, 1992.
- [14] T M Allen and P R Cullis. Drug delivery systems: entering the mainstream. *Science*, 303(5665):1818–1822, 2004.
- [15] E Doblhofer and T Scheibel. Engineering of recombinant spider silk proteins allows defined uptake and release of substances. *Journal of Pharmaceutical Sciences*, 104(3):988–994, 2015.
- [16] J N Israelachvili. *Intermolecular and Surface Forces*. Elsevier, 3rd edition, 2011.
- [17] H-J Butt, K Graf, and M Kappl. *Physics and Chemistry of Interfaces*. Wiley-VCH, 3rd edition, 2013.
- [18] Paul S Weiss. New Tools Lead to New Science. *ACS Nano*, 6(3):1877–1879, 2012.
- [19] M Antonietti and G A Ozin. Promises and Problems of Mesoscale Materials Chemistry or Why Meso? *Chemistry - A European Journal*, 10(1):28–41, 2004.
- [20] P S Weiss. Mesoscale Science: Lessons from and Opportunities for Nanoscience. *ACS Nano*, 8(11):11025–11026, 2014.
- [21] G Binnig, C F Quate, and C Gerber. Atomic force microscope. *Physical Review Letters*, 56(9):930–933, 1986.

References

- [22] H-J Butt, B Cappella, and M Kappl. Force Measurements with the Atomic Force Microscope: Technique, Interpretation and Applications. *Surface Science Reports*, 59(1-6):1–152, 2005.
- [23] H J Butt, R Berger, E Bonaccorso, Y Chen, and J Wang. Impact of atomic force microscopy on interface and colloid science. *Advances in Colloid and Interface Science*, 133(2):91–104, 2007.
- [24] A L Weisenhorn, P Maivald, H J Butt, and P K Hansma. Measuring adhesion, attraction, and repulsion between surfaces in liquids with an atomic-force microscope. *Physical Review B*, 45(19):11226–11232, 1992.
- [25] A L Weisenhorn, P K Hansma, T R Albrecht, and C F Quate. Forces in atomic force microscopy in air and water. *Applied Physics Letters*, 54(26):2651–2653, 1989.
- [26] H-J Butt. Measuring electrostatic, van der Waals, and hydration forces in electrolyte solutions with an atomic force microscope. *Biophysical Journal*, 60(6):1438–1444, 1991.
- [27] W A Ducker, T J Senden, and R M Pashlex. Direct Measurement of Colloidal Forces Using an Atomic Force Microscope. *Nature*, 353(6341):239–241, 1991.
- [28] M Kappl and H J Butt. The colloidal probe technique and its application to adhesion force measurements. *Particle & Particle Systems Characterization*, 19(3):129–143, 2002.
- [29] M Borkovec, I Szilagyi, I Popa, M Finessi, P Sinha, P Maroni, and G Papastavrou. Investigating forces between charged particles in the presence of oppositely charged polyelectrolytes with the multi-particle colloidal probe technique. *Advances in Colloid and Interface Science*, 179–182:85, 2012.
- [30] M I Giannotti and G J Vancso. Interrogation of Single Synthetic Polymer Chains and Polysaccharides by AFM-Based Force Spectroscopy. *The European Journal of Chemical Physics and Physical Chemistry*, 8(16):2290–2307, 2007.
- [31] E L Florin, V T Moy, and H E Gaub. Adhesion forces between individual ligand-receptor pairs. *Science*, 264(5157):415–417, 1994.
- [32] G U Lee, L A Chrisey, and R J Colton. Direct Measurement of the Forces Between Complementary Strands of DNA. *Science*, 266:711–773, 1994.

1 Introduction

- [33] N Helfricht, E Doblhofer, V Bieber, P Lommes, V Sieber, T Scheibel, and G Papatavrou. Probing the adhesion properties of alginate hydrogels: a new approach towards the preparation of soft colloidal probes for direct force measurements. *Soft Matter*, 13(3):578–589, 2017.
- [34] Y Gan. Invited Review Article: A review of techniques for attaching micro- and nanoparticles to a probe’s tip for surface force and near-field optical measurements. *Review of Scientific Instruments*, 78(8):081101–9, 2007.
- [35] A Meister, M Gabi, P Behr, P Studer, J Vörös, P Niedermann, J Bitterli, J Polesel-Maris, M Liley, H Heinzelmann, and T Zambelli. FluidFM: Combining Atomic Force Microscopy and Nanofluidics in a Universal Liquid Delivery System for Single Cell Applications and Beyond. *Nano Letters*, 9(6):2501–2507, 2009.
- [36] P Dörig, D Ossola, A M Truong, M Graf, F Stauffer, J Vörös, and T Zambelli. Exchangeable Colloidal AFM Probes for the Quantification of Irreversible and Long-Term Interactions. *Biophysical Journal*, 105(2):463–472, 2013.

CHAPTER 2

Theory / Status of the field

The measurement of interaction forces goes back to Derjaguin *et al.* [1, 2, 3] Originally, interaction forces have been measured by means of the surface force apparatus (SFA). [3, 4] However, by now most direct force measurements are carried out on base of the atomic force microscopy. Hence, this Chapter will concentrate on this technique and give a brief overview over surface forces.

2.1 Scanning Probe Microscopy

Scanning probe microscopy is based on a probe that can be approached and laterally scanned over a sample in order to obtain localized information about surface properties. The pioneer of the family of scanning probe microscopes (SPM) was the scanning tunnelling microscope (STM). It was possible for the first time to image the surface of electrically conductive materials with atomic resolution by the STM, which was invented by Binnig and Rohrer. [5] Its invention was granted in 1986 with the Nobel Prize in physics. [6, 7] The subsequent development of the atomic force microscope (AFM) allowed to study nonconductive materials under various environmental conditions, in particular different liquids or gases. [8, 9, 10, 11, 12, 13, 14] The AFM became instantaneously an interdisciplinary tool for the characterization of properties for various classes of materials, such as topography, elasticity or surface interactions. [11, 12, 14, 13, 15]

2.1.1 Components of an Atomic Force Microscope

In atomic force microscopy, interactions between a probe and the sample are used to determine the surface topography or to characterize other sample properties such as friction or adhesion. However, by determining the force acting on the probe as a function of separation distance in respect to the sample surface, one can also directly measure interaction force profiles. [11, 16, 3, 14, 12, 13, 17]

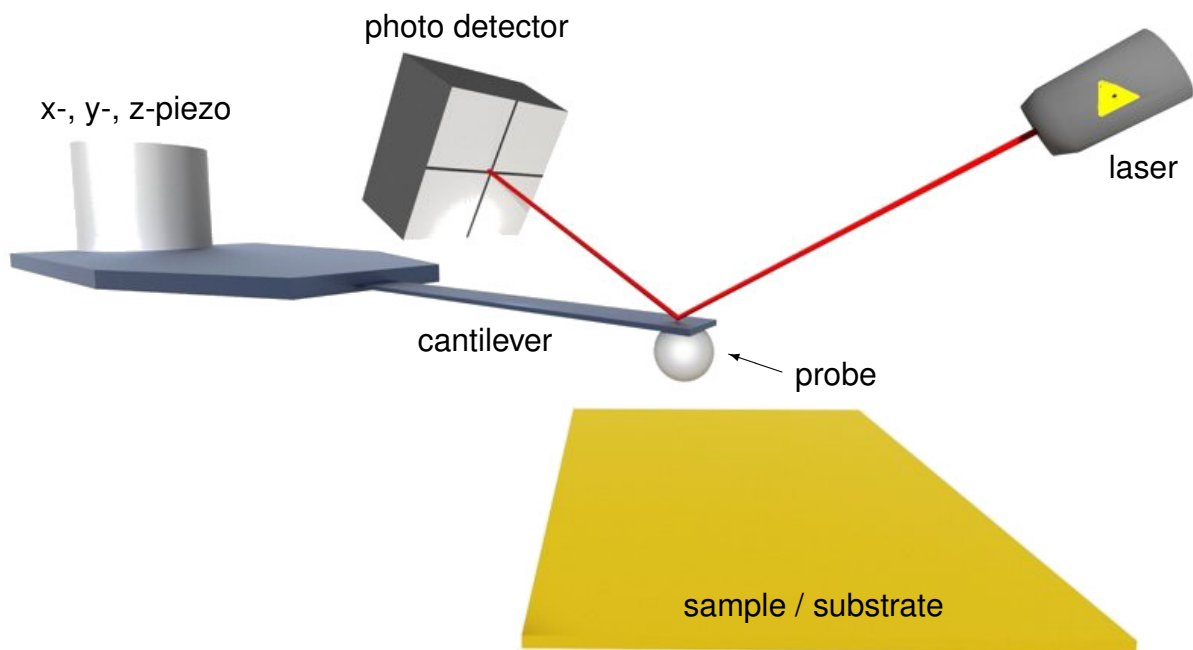


Figure 2.1: Schematic representation of the general setup of an atomic force microscope (AFM): A laser is focussed on the back of an AFM cantilever and its reflection is detected by a position-sensitive detector. Piezoelectric elements allow for a precise movement of the cantilever in x-, y- and z-direction.

Figure 2.1 shows in a schematic manner the general setup of an AFM. The pivotal element of an AFM is the force sensor, the so-called cantilever. The probe is either a sharp tip or a colloidal particle attached at its free end. The AFM cantilever bends due to forces acting between the probe and the sample surface. Its deflection is commonly detected by the so-called optical lever method. [18, 11] For this purpose, a laser beam is focussed onto the back of a cantilever and its reflection is monitored *via* a position-sensitive detector. Hence, a deflection of the cantilever leads to an intensity

shift between the upper and lower part of the photo detector, which allows to detect deflections < 1 nm. [11] Lateral and vertical movements of the sample and cantilever versus each other, are performed by piezoelectric translators. One major advantage of the atomic force microscopy is that experiments can be performed under various environmental conditions, such as gases, liquids, temperatures and humidity-controlled atmosphere. [11, 16, 19]

2.1.2 Direct Measurement of Interaction Forces

Interaction forces between the probe attached to an AFM cantilever and a surface in medium can be directly measured as a function of the separation distance by AFM. In static force *versus* separation measurements, the AFM cantilever is only moved in vertical direction up and down with a constant velocity, while the deflection of the cantilever is recorded. The ramping speed has to be low enough so that hydrodynamic forces acting on the cantilever can be neglected.[11]

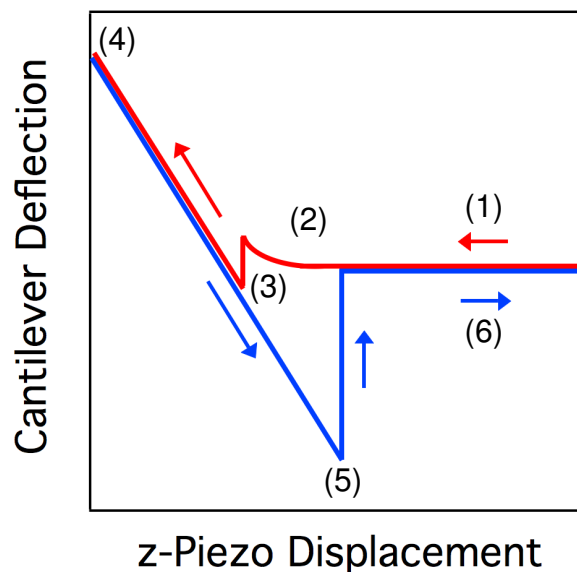


Figure 2.2: Schematic representation of a cantilever deflection vs. z-piezo displacement curve during approach (red) and retraction (blue) of the cantilever, respectively.

Figure 2.2 schematically illustrates a typical force vs. distance cycle, which can be subdivided into the approach (red) and the retraction (blue) part. Here, the raw data are shown: The cantilever deflection is plotted *versus* the z-piezo displacement. Far away

2 Theory / Status of the field

from the surface, the cantilever is in its undisturbed state (1), where no external interactions are acting on the probe. During approach, the cantilever starts to bend due to long-range interactions, which are indicated here to be repulsive (2). At a certain distance during the approach, attractive interaction forces (e.g. due to van der Waals forces) exceed the restoring force of the cantilever, which results in the jump-to contact (3). Henceforth, the z-piezo moves the cantilever further towards the surface until a pre-defined deflection set-point is reached (4), which corresponds to the maximum loading force exerted by the cantilever. This part of the force curves is called constant compliance region, from which information about mechanical deformations of the sample can be extracted. Upon retraction of the cantilever from the surface, a larger displacement of the z-piezo might be necessary to separate the cantilever, in particular the probe from the surface (5), in order to overcome adhesion forces. This second instability is called jump-off contact. The observed hysteresis between approach and retraction is caused due to adhesion phenomena. A further retraction leads again to the initial deflection of the cantilever (6), where no interactions are detectable anymore.

The raw data, as depicted in figure 2.2 have to be converted into a force F vs. distance D curve, whereby the separation distance D is simply the sum of cantilever deflection Z_c and the z-piezo position Z_p . For the data conversion, the optical lever sensitivity (OLS) has to be evaluated by performing force vs. distance cycles on a hard surface. The evaluation of the linear constant compliance region provides the relation between the photo detector signal [V] and the cantilever deflection [m]. Since the cantilever acts like a spring, the force F is obtained from Hooke's law ($F = k_c Z_c$), whereby k_c is the spring constant of the cantilever. [11, 20] Therefore, the accurate determination of the spring constant is essential for a quantitative data evaluation. [11]

Cantilever Calibration

The experimental determination of the cantilever's spring constant is indispensable for a quantitative data evaluation in direct force measurements. The spring constant of AFM cantilevers k_c can be estimated in an appropriate manner from material properties (cf. E , the Young's modulus) and beam theory of continuum mechanics:

$$k_c = \frac{Ewt^3}{4L^3} \quad (2.1)$$

where w is the width, t the thickness and L the length of the cantilever, respectively. Due to etching processes during the fabrication of AFM cantilevers, the thickness is

2.1 Scanning Probe Microscopy

the least controllable parameter. However, it contributes to the spring constant with the third power (*cf.* Equation 2.1). Furthermore, an additional reflective coating on the back influences the mechanical properties of the cantilever and thereby the spring constant, respectively. In consequence, k_c has to be experimentally measured for each cantilever. Several methods for the calibration of the spring constant have been developed and compared in a number of review articles [11, 21, 22] In the following a brief overview over several well-established methods, which have been used in this thesis, is given.

The most commonly used method is the so-called 'thermal noise method', which was first presented by Hutter and Bechhoefer. [23] The mean square deflection ($\langle \Delta Z_c^2 \rangle$) results from the Fourier transformed time series of the cantilever oscillations due to thermal fluctuations. The treatment of the AFM cantilever as an harmonic oscillator in combination with the equipartition theorem allows to calculate k_c from the power density spectrum (PSD): [23, 24]

$$\frac{1}{2}k_B T = \frac{1}{2}k_c \langle \Delta Z_c^2 \rangle \quad (2.2)$$

$$k_c = \frac{k_B T}{\langle \Delta Z_c^2 \rangle} \quad (2.3)$$

where k_B is the Boltzmann constant and T the temperature, representing the thermal energy of the system. For this method, the prior determination of the inverse optical lever sensitivity (*InvOLS*) is necessary.

Another method for the determination of k_c is based on the hydrodynamic properties of the surrounding environment and the top view dimensions of the cantilever (*cf.* width w and length L). This method was first described by Sader *et al.*. The resonance frequency ω_0 and the quality factor Q are obtained from the PSD, thus k_c is calculated according to: [25, 26]

$$k_c = 0.1906 \rho_f w^2 L Q \Gamma_i(Re) \omega_0^2 \quad (2.4)$$

where ρ_f being the density of the fluid and $\Gamma_i(Re)$ is the imaginary part of a 'hydrodynamic function', respectively. The latter is a function of the Reynolds number Re .

Cleveland *et al.* presented another method for the determination of the spring constant, which leads to very accurate results but is time consuming and is often called 'added

2 Theory / Status of the field

mass method'. This method is based on the reversible attachment of various masses to the cantilever. These additional mass leads to a shift in the resonance frequency. [27] The resonance frequency ω_0 is inversely proportional to the cantilever's mass m for a harmonic oscillator:

$$\omega_0 = \frac{1}{2\pi} \sqrt{\frac{k_c}{m}} \quad (2.5)$$

Spherical particles with a high density (e.g. gold or tungsten) [11] are picked up from a planar surface by means of capillary forces, and the resulting shift in the resonance frequency ω_0^* due to the additional mass M is monitored:

$$\omega_0^* = \frac{1}{2\pi} \sqrt{\frac{k_c}{m + M}} \quad (2.6)$$

Subsequently, the spring constant of the cantilever can be calculated as follows [27]:

$$k_c = \frac{4\pi^2 M}{1/\omega_0^{*2} - 1/\omega_0^2} \quad (2.7)$$

This expected shift in the resonance frequency due to an additive mass can be also used to 'weight' colloidal objects or cells attached to a previously calibrated AFM cantilever. [28, 29]

2.1.3 Colloidal Probe Technique

The colloidal probe technique has been independently developed by Butt [30] and Ducker *et al.* [31], who respectively glued glass and silica particles onto AFM cantilevers. The replacement of the sharp AFM tip by a spherical, colloidal particle (*cf.* Figure 2.3) was a major advancement for direct force measurements by AFM as a defined interaction geometry is essential for a quantitative evaluation of the obtained data. Due to the increased contact area, the interaction forces as recorded using a colloidal probe are much larger compared to the ones obtained by a sharp tip, thereby allowing for an increased force sensitivity. [11]

Commonly, colloidal probes are permanently immobilized onto AFM cantilevers. A small amount of glue is placed near the free end of the cantilever onto which a spherical colloidal particle is transferred by means of a thin wire and a micromanipulator. [32, 11] However, the use of any glue might introduce contaminations into the sys-

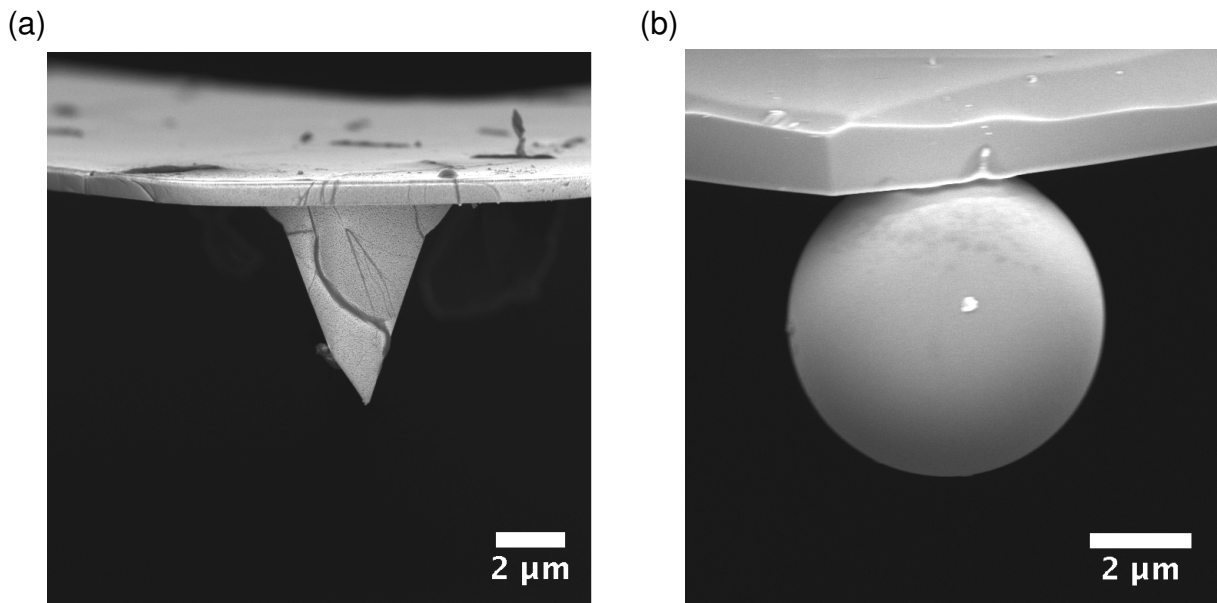


Figure 2.3: SEM images of AFM cantilevers with different interaction geometries: (a) a sharp tip and (b) a colloidal silica particle attached.

tem due to partial dissolution of the adhesives under certain environmental conditions. Alternatively, glass or silica particles can be sintered at high temperatures to the cantilever, thereby the risk of any cross-contaminations is avoided. [33, 34] The so-called 'multiple-particle colloidal probe' technique allows for a reversible attachment of the probe particle. For this purpose, the AFM cantilevers are chemically modified in order to pick up a spherical particle from the substrate. With this method, several probe particles can be used to determine interaction forces with one cantilever. [35, 36, 37] However, both methods, namely 'classical' glueing as well as the 'multi-particle colloidal probe' technique require the direct observation *via* optical microscopy. Therefore, the size of feasible colloidal probes is limited by the optical resolution of the microscope during cantilever manipulations. Nevertheless, several approaches are based on a simple pick up of nanoparticles without any control over the particle (*e.g.* size and shape) and its position on the cantilever. However, in this case a quantitative evaluation is not possible or requires post-analysis by *e.g.* electron microscopy. [38, 39]

The colloidal probe technique is a highly versatile technique due to a variety of attachable materials and geometries. This method is not only restricted to hard materials (*cf.* particles from glass, silica [40] or polystyrene latex [41, 42]), [11] but is also suitable for soft and deformable materials such as poly(dimethylsiloxane) [43, 44] or polyethylene [45]. Moreover, the colloidal probe technique allows for the attachment of various

2 Theory / Status of the field

fiber types such as aluminum [46, 47], hair [48, 49, 50] or polymers [51, 52]. Even force measurements between liquid droplets [53, 54, 55] and gas bubbles [56, 57] in aqueous environment can be performed by the colloidal probe technique.

2.1.4 FluidFM Technology

The FluidFM (*fluidic force microscopy*) technology combines the well-known force control of an AFM with a nanofluidic approach. [58, 59] Figure 2.4 schematically illustrates the experimental FluidFM setup, which is comparable to a conventional AFM (*cf.* figure 2.1) except for the use of special cantilevers. These cantilevers comprise a hollow micro-channel within the lever arm, ending in a μm -sized aperture at the free end of the cantilever. Even sub- μm apertures are available, which are located at the apex of a pyramidal tip. A liquid reservoir is located at the supported part of the cantilever, which is connected to a nanofluidic control system. This closed fluidic system enables the operation even in liquid environment, which has been previously not accomplishable with the fountain pen method. [60, 61]

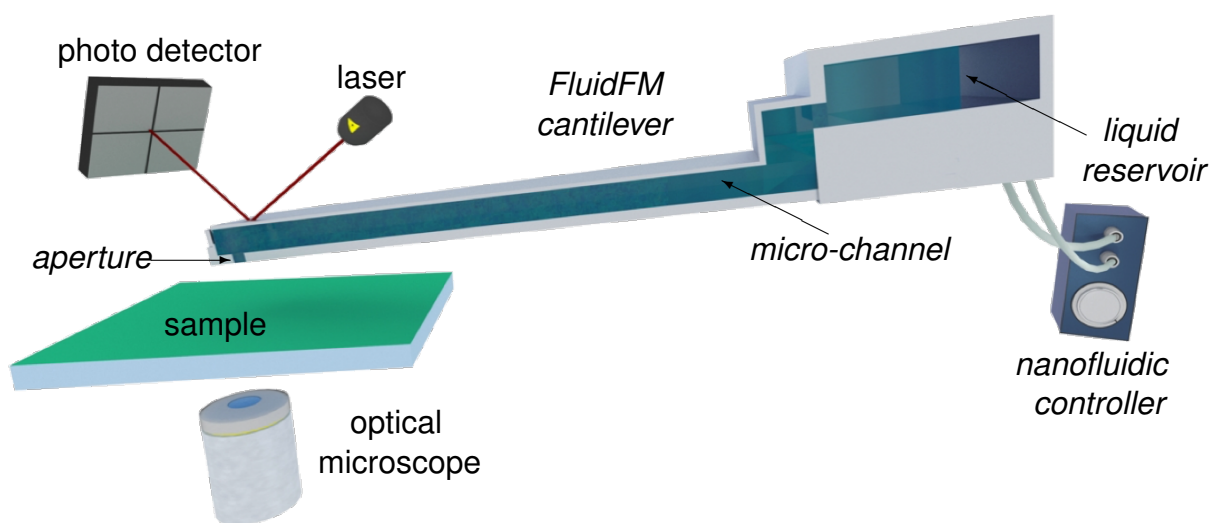


Figure 2.4: Schematic illustration of the experimental FluidFM setup. The pivotal element of this technique is the hollow, micro-channeled cantilever, which is connected to a nanofluidic controller.

The pivotal feature of the FluidFM technique are hollow cantilevers, which are manufactured from silicon nitride due its good chemical resistance, in a stepwise process: First, a layer of silicon nitride is deposited on a silicon wafer as solid support, whereby

2.1 Scanning Probe Microscopy

the later aperture is created by reactive ion etching (RIE) at the free end of the cantilever. Second, a patterned sacrificial layer of polysilicon is added forming the later micro-channel, which is encapsulated by deposition of another layer of silicon nitride. The final shape of the cantilever is again obtained by RIE. In the next step, the mechanical glass support is powder-blasted and anodically bound to the silicon substrate. Finally, the wafer containing the cantilevers is immersed in a silicon etchant in order to release the cantilevers and to remove the sacrificial material in the micro-channel. Further details about the preparation of FluidFM cantilevers are available in the literature [62, 63, 64]. Recently, novel micro-channeled cantilevers were developed based on the flexible photopolymer SU-8. [65, 66, 67]

The initial applications for the FluidFM technique were in the field of biology, such as the manipulation of single cells or bacteria. [64, 68, 69] The combination with the AFM allows here for a direct measurement of the underlying adhesion forces with the substrate. [70, 71, 72, 67, 73, 74] Furthermore, the force control of the AFM further enables the possibility to permeate a cell membrane in order to inject [75, 76], or even extract molecules from a cell. [77] Besides these basically biological applications, the FluidFM can be applied to deposit structures of nanoparticles [78, 79] or metals [80, 81].

However, the FluidFM can be used to determine interaction forces with aspirated colloidal particles, whereby the probe particle is reversibly immobilized to the aperture by means of an applied underpressure. Consequently, the probe particle can be exchanged after several force vs. distance cycles or in case of any contamination. [82, 83]

2.1.5 Single Molecule Force Spectroscopy

Already the first application of the AFM for force measurements by Weisenhorn *et al.* indicated the possibility to manipulate single molecules by means of the AFM. [10] The unraveling of ligand-receptor interactions of streptavidin-biotin complexes was the initial single molecule force spectroscopy (SMFS) studies. [84, 85] SMFS allows for the investigation of interaction forces of macromolecules (*e.g.* polymers or proteins) on the molecular level. [86, 87, 88, 89]

In order to investigate interaction forces on the level of single molecules, these macromolecules have to be attached covalently or adsorbed onto the tip of an AFM cantilever. The measurement of molecular interactions is quite similar compared to the static ex-

2 Theory / Status of the field

periments performed with a colloidal probe. The AFM cantilever is approached to a surface, remaining in contact with the surface for a predefined time interval in order to allow for the rearrangement of the polymeric chains and the interaction of individual binding sites. Upon retraction, the molecules are stretched as the distance is increased between the tip of the cantilever and the substrate until the rupture of bonds takes place. [89, 88]

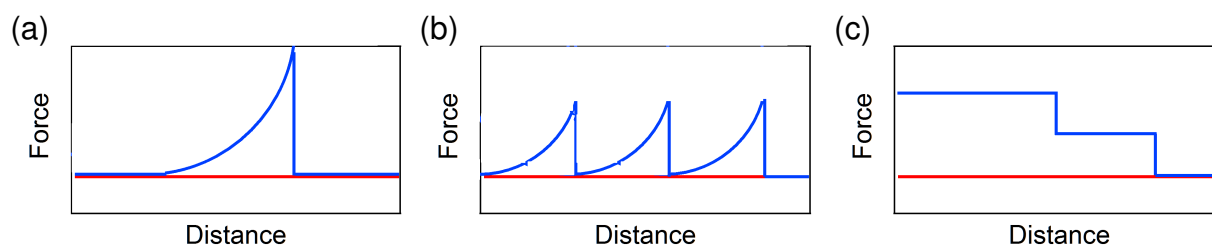


Figure 2.5: Schematic representation of possible rupture events as obtained by single molecule force spectroscopy measurements. (a) single rupture event, (b) saw-tooth pattern and (c) desorption plateaus.

Figure 2.5 illustrates in a schematic manner the different desorption patterns on the single molecule level, which can be observed in force vs. separation distance curves. Figure 2.5 a shows a single rupture peak, where first the macromolecule is stretched until the lowest bond ruptures. The desorption pattern as shown in figure 2.5 b includes several of these peaks, and is often referred to as saw-tooth pattern. Such patterns are indicative for the rupture of covalent bonds or specific interactions such as host-guest [90] or ligand-receptor complexes [85, 84]. Rupture force patterns allow further to identify the conformation of the adsorbed macromolecule on the surface. The rupture events can be also indicative for a loop- or tail-structure (*cf.* Figure 2.6) in the case of physisorbed polymer layers. [87, 88, 89] By contrast, the desorption plateaus are indicative for the 'unsnipping' of train-like adsorbed polymers (*cf.* Figure 2.6 c). This desorption behaviour has been observed for the detachment of polyelectrolytes [91, 92, 93].

The SMFS technique allows to determine the adsorption-desorption processes of a variety of molecules depending on the molecular architecture [94] such as dendronized polymers [95, 96, 97] and the influence of various surfaces [98, 99]. Interestingly, the surface roughness has less influence on the determined rupture forces of single molecules [99] as found for microscopic systems such as colloidal particles. [100, 101]

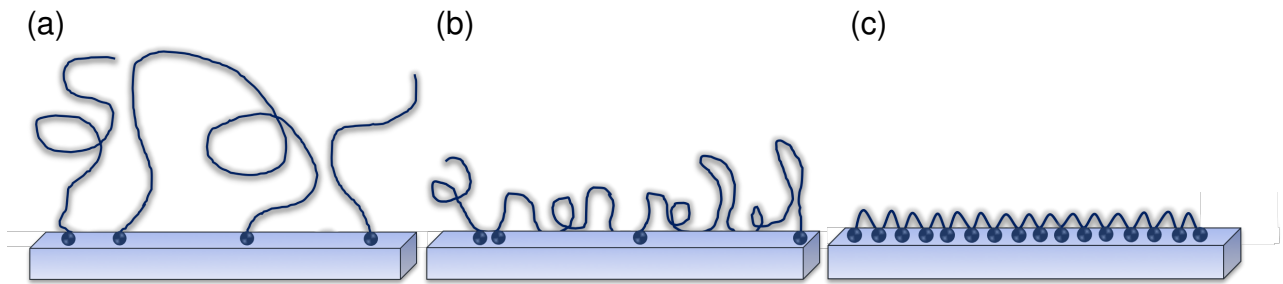


Figure 2.6: Schematic illustration of various conformations of polymers adsorbed onto a surface: (a) big loops and tails, (b) loop structure and (c) train-like structure.

Worm-like chain (WLC) or the freely jointed chain (FJC) models were applied to evaluate the elasticity of single molecule strands from the stretching behaviour upon extension. [102, 103, 89] The measurement of intramolecular effects such as conformational transitions of polysaccharides [104, 105] or the force controlled unfolding of proteins [106, 107] can be also measured by SMFS.

2.2 Interaction Forces between Surfaces

A brief overview over the various contributions of interaction forces, which can be measured by means of AFM techniques, is given in the following Chapter.

Derjaguin Approximation

The measured interaction forces depend strongly on the interaction geometry. The so-called Derjaguin approximation relates the acting forces $F(D)$ between two objects to the interaction energy per unit area $W(D)$ between two flat surfaces. Hence, it allows for the comparison between measurements as obtained from different techniques and to theoretical predictions [3, 108, 11]:

$$F(D) = 2\pi R_{eff}W(D) \quad (2.8)$$

where R_{eff} is the effective radius, which is determined by the geometry of two surfaces.

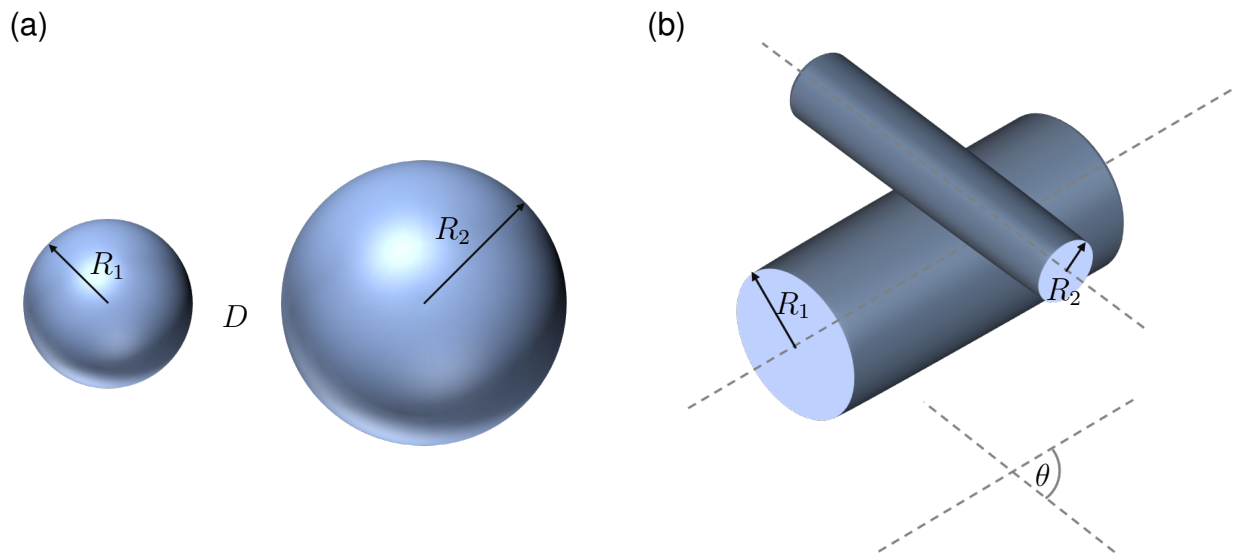


Figure 2.7: Schematic illustration of geometrical parameter for different interaction geometries within the Derjaguin approximation: (a) two spherical particles and (b) two crossed-cylinders

Figure 2.7 illustrates in a schematical manner the interaction geometries of two spherical particles and two crossed-cylinders for the Derjaguin approximation. R_{eff} for two spherical particles is given by:

2.2 Interaction Forces between Surfaces

$$\frac{1}{R_{eff}} = \frac{1}{R_1} + \frac{1}{R_2} \quad (2.9)$$

here R_1 and R_2 are the radii of curvature for the two spheres. R_{eff} for two interacting cylinders can be obtained from:

$$R_{eff} = \frac{\sqrt{R_1 R_2}}{\sin\theta} \quad (2.10)$$

where θ is the orientation angle of the two fibers.

The Derjaguin approximation is only valid if the range of the interaction forces is significantly small compared to the radius of curvature of the interacting bodies ($D \ll R_{eff}$), which is normally the case for colloidal objects. [3, 40, 108, 11]

2.2.1 Long-Range Interaction Forces

DLVO Theory

The colloidal stability of a particle suspension can be described over a wide range of colloids by the so-called DLVO theory, which has been developed by Derjaguin, Landau, Verwey and Overbeek. [1, 2, 109, 108, 3] The DLVO theory takes into account the superposition of repulsive diffuse layer overlap and attractive van der Waals interactions (*cf.* figure 2.8):

$$W(D) = W_{vdW}(D) + W_{edl}(D) \quad (2.11)$$

Figure 2.8 schematically illustrates that the attractive van der Waals $W_{vdW}(D)$ interactions dominate the overall interactions at rather short separation distances, whereby the electrostatic interactions $W_{edl}(D)$ are mainly present at larger separation distances.

Van der Waals forces are omnipresent and arise from fluctuating and rotating dipoles in molecules or even atoms. The strength of van der Waals interactions is described by the Hamaker constant H :

$$W_{vdW}(D) = -\frac{H}{12\pi D^2} \quad (2.12)$$

Surfaces in aqueous environment are charged due to the dissociation of surface func-

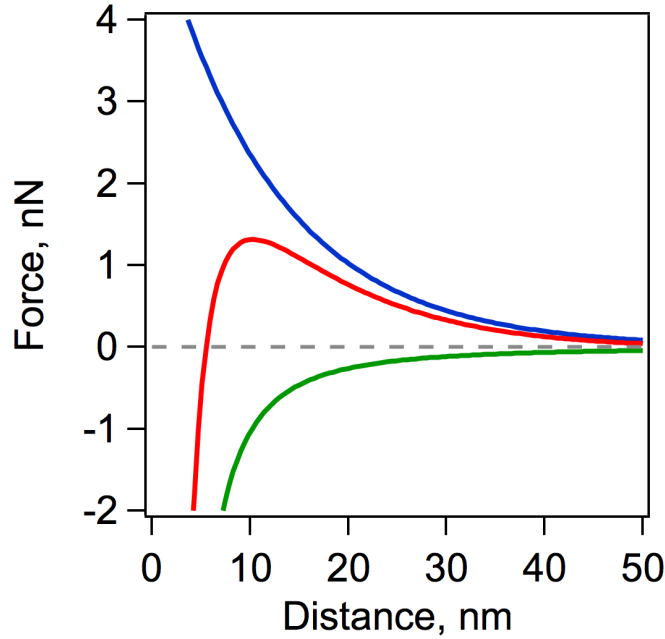


Figure 2.8: Schematic force *versus* distance curve including electrostatic interactions (blue), van der Waals contribution (green) and the combination of both within the DLVO theory (red).

tional groups or the adsorption of ions. [108] Dissociated counter- and co-ions are present around the surface and form the diffuse double layer. These electrical double layers can be described within the Poisson-Boltzmann (PB) theory. The latter is a combination of the Poisson equation, which describes the potential distribution Ψ in the vicinity of a charged surface and the Boltzmann statistics, which define the charge density ρ with respect to the thermal energy ($k_B T$):

$$\frac{d^2\Psi}{dD^2} = -\frac{\rho}{\epsilon_0\epsilon} \quad (2.13)$$

$$\rho = \sum_i z_i c_i e^{-\frac{z_i q \Psi}{k_B T}} \quad (2.14)$$

where ϵ_0 is the dielectric permittivity of vacuum, ϵ is the dielectric constant of water, z_i is the charge of ions of type i , c_i is the bulk concentration of the ions and q is the elementary charge. The Poisson-Boltzmann equation is a 2^{nd} order partial differential equation, which has to be solved numerically. However, for low potentials ($|\Psi| \leq 25$ mV), the Poisson-Boltzmann equation can be linearized: [108]

$$\Psi = \Psi_0 e^{-\kappa x} \quad (2.15)$$

2.2 Interaction Forces between Surfaces

with κ being the inverse Debye length. The Debye length for a 1:1 electrolyte is given by: [108]

$$\kappa^{-1} = \sqrt{\frac{\epsilon\epsilon_0 k_B T}{2c_0 q^2}} \simeq \frac{0.3 \text{ nm}}{\sqrt{I}} \quad (2.16)$$

For the full-solution of the Poisson-Boltzmann equation, the dimensionless potential $\gamma \equiv \frac{e\Psi}{k_B T}$ has to be considered:

$$e^{\frac{\gamma}{2}} = \frac{e^{\frac{\gamma_0}{2}} + 1 + (e^{\frac{\gamma_0}{2}} - 1)e^{-\frac{\kappa}{D}}}{e^{\frac{\gamma_0}{2}} + 1 - (e^{\frac{\gamma_0}{2}} - 1)e^{-\frac{\kappa}{D}}} \quad (2.17)$$

The Poisson-Boltzmann theory represents a mean-field approach, which neglects the finite size of the ions and image-charges. Moreover, the charge distributions and the solvents are treated as continuous. The model is only valid for smooth surfaces. Since, all these limitations cancel each other, the Poisson-Boltzmann equation still allows for a correct description of the overlap of electrical double layers. [108]

The linearized PB equation and the full-solutions coincide well for low potentials. However, for increased surface potentials, the full-solutions result in lower potentials due to a saturation effect. [108]

Figure 2.9 schematically illustrates the classical boundary conditions for solving the Poisson-Boltzmann equation. The 'classical' boundary conditions are the constant charge (CC) and the constant potential (CR). The former represents a limit and assumes that the surface charge upon approach of the two surfaces remains constant. The latter describes the situation where the surface potential remains constant. Both boundary conditions describe the overlap of two electrical double layers very well at large separation distances ($D > \kappa^{-1}$). However, at smaller separation distances, charge regulation (CR) approximation has to be taken into account, which includes the regulation of the electrical properties due to adsorption processes or environmental changes such as pH and ionic strength. [110, 111, 112, 113]

The surface potential Ψ can be directly related to the surface charge density by means of the Grahame equation: [108]

$$\sigma = \sqrt{8c_0\epsilon\epsilon_0(k_B T)} \sinh\left(\frac{e\Psi_0}{2(k_B T)}\right) \quad (2.18)$$

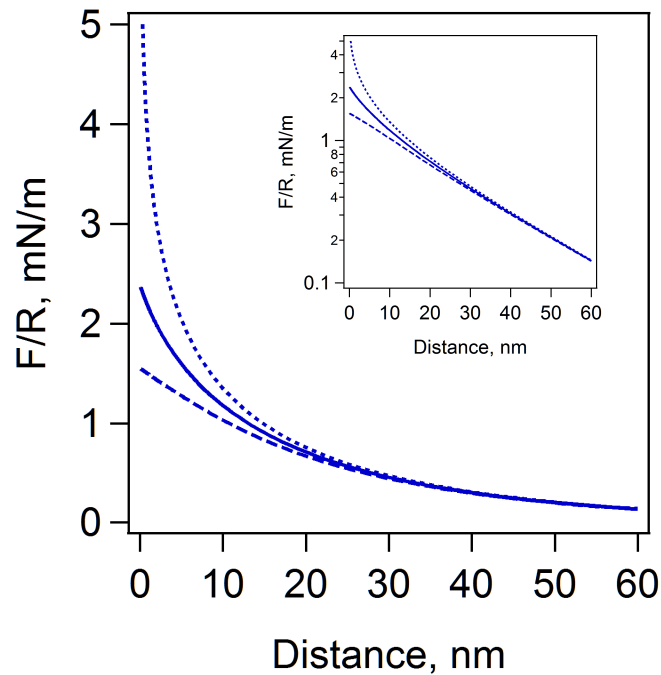


Figure 2.9: Schematic representation of the boundary conditions: constant charge (CC) (*cf.* dotted line), the constant potential (CP) (*cf.* dashed line) and the charge regulation (CR) (*cf.* solid line).

Besides direct force measurements by AFM, the surface charge of colloidal objects or planar surfaces can be further determined by various electrokinetic methods such as electrophoretic mobility (ζ -potential) or streaming potential measurements. [108, 3, 114, 115, 116, 117]

2.2.2 Contact Mechanics

Two bodies in contact deform under an externally applied force. The deformability of a material is described by its Young's modulus. Hence, this modulus can be determined on the colloidal level by means of AFM indentation experiments. If no hysteresis between the approach and the retraction curve is detectable, the deformation is called elastic. During the AFM experiment, the probe indents a defined distance into the sample, the so-called indentation depth δ (*cf.* Figure 2.10). After contact of two objects, this indentation depth goes back in its original state for the elastic case. If the indentation depth remains, a hysteresis is observable in the force vs. indentation curve, which indicates a plastic deformation of the sample. In the following, the general models for continuum contact mechanics are briefly introduced, which all neglect any plastic deformation. [118, 11]

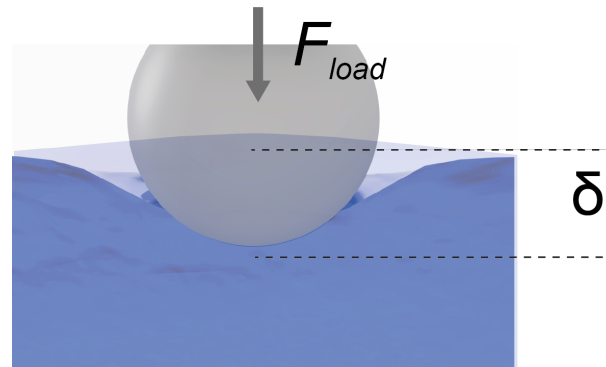


Figure 2.10: Schematic illustration of an elastic sample deformation. An external force F_{load} is exerted to a hard spherical particle, which results in the indentation of a depth δ into the sample. Adapted with permission from Helfricht *et al.*, *Soft Matter*, **2017**, 13, 578-589, © 2017 The Royal Society of Chemistry.

Hertz

The Hertz model assumes a system of two elastic bodies, where any surface forces are neglected. An externally applied loading force F leads to a deformation δ : [119, 11]

$$F(\delta) = \frac{4}{3} E_{red} \delta^{3/2} \sqrt{R_{eff}} \quad (2.19)$$

The Young's modulus E is the characteristic material property, which describes the stiffness of the material and is obtained from the reduced modulus E_{red} :

$$E_{red} = \frac{1 - \nu_1^2}{E_1} + \frac{1 - \nu_2^2}{E_2} \quad (2.20)$$

, where the ν are the Poisson's ratios of the surfaces, as indicated by the indices 1 and 2.

JKR & DMT Theory

The JKR model has been developed by Johnson, Kendall and Roberts and assumes surface forces only inside the contact area of two bodies into account. [120] Derjaguin, Muller and Toporov presented the so-called DMT-model, which also includes the interactions, however outside the contact area. [121] Both models are extreme cases of the Maugis-theory, which, however, cannot be solved analytically. The work of adhesion

2 Theory / Status of the field

W_{adh} can be calculated from the adhesion forces F_{adh} as determined from the jump-off contact within the JKR model: [11]

$$F_{adh} = -\frac{3}{2}\pi R_{eff}W_{adh} \quad (2.21)$$

and the DMT model, respectively: [11]

$$F_{adh} = -2\pi R_{eff}W_{adh} \quad (2.22)$$

References

- [1] B A Derjaguin. Theory of Interaction of Particles in Presence of Electrical Double-Layers and the Stability of Lyophobic Colloids and disperse Systems. *Acta Physicochimica URSS*, 10:333–346, 1939.
- [2] B A Derjaguin and L D Landau. Theory of the Stability of Strongly Charged Lyophobic Sols and of the Adhesion of Strongly Charged Particles in Solutions of Electrolytes. *Acta Physicochimica URSS*, 14:633–662, 1941.
- [3] J N Israelachvili. *Intermolecular and Surface Forces*. Elsevier, 3rd edition, 2011.
- [4] J N Israelachvili and G E Adams. Measurement of forces between two mica surfaces in aqueous electrolyte solutions in the range 0–100 nm. *Journal of the Chemical Society, Faraday Transactions 1: Physical Chemistry in Condensed Phases*, 74(0):975–1001, 1978.
- [5] G Binnig, H Rohrer, C Gerber, and E Weibel. Surface Studies by Scanning Tunneling Microscopy. *Physical Review Letters*, 49:57–61, 1982.
- [6] G Binnig, H Rohrer, C Gerber, and E Weibel. 7 x 7 Reconstruction on Si(111) resolved in Real Space. *Physical Review Letters*, 50:120–123, 1983.
- [7] G Binnig and H Rohrer. Nobel Lecture: Scanning Tunneling Microscopy - From Birth to Adolescence. *Reviews of Modern Physics*, 59:615–625, 1987.
- [8] G Binnig, C F Quate, and C Gerber. Atomic force microscope. *Physical Review Letters*, 56(9):930–933, 1986.
- [9] A L Weisenhorn, P Maivald, H J Butt, and P K Hansma. Measuring adhesion, attraction, and repulsion between surfaces in liquids with an atomic-force microscope. *Physical Review B*, 45(19):11226–11232, 1992.
- [10] A L Weisenhorn, P K Hansma, T R Albrecht, and C F Quate. Forces in atomic force microscopy in air and water. *Applied Physics Letters*, 54(26):2651–2653, 1989.
- [11] H-J Butt, B Cappella, and M Kappl. Force Measurements with the Atomic Force Microscope: Technique, Interpretation and Applications. *Surface Science Reports*, 59(1-6):1–152, 2005.

2 Theory / Status of the field

- [12] D G Yablon. *Scanning Probe Microscopy in Industrial Applications: Nanomechanical Characterization*, chapter Overview of Atomic Force Microscopy, pages 1–14. John Wiley & Sons, Inc, 1st edition, 2014.
- [13] G Haugsted. *Atomic Force Microscopy: Understanding Basic Modes and Advanced Applications*. John Wiley & Sons, Inc, 1st edition, 2012.
- [14] F J Giessibl. Advances in Atomic Force Microscopy. *Reviews of Modern Physics*, 75(3):949–983, 2003.
- [15] Paul S Weiss. New Tools Lead to New Science. *ACS Nano*, 6(3):1877–1879, 2012.
- [16] M Kappl and H J Butt. The colloidal probe technique and its application to adhesion force measurements. *Particle & Particle Systems Characterization*, 19(3):129–143, 2002.
- [17] H J Butt, R Berger, E Bonaccorso, Y Chen, and J Wang. Impact of atomic force microscopy on interface and colloid science. *Advances in Colloid and Interface Science*, 133(2):91–104, 2007.
- [18] S Alexander, L Helleman, O Marti, J Schneir, V Elings, P K Hansma, Matt Longmire, and John Gurley. An atomic-resolution atomic-force microscope implemented using an optical lever. *Journal of Applied Physics*, 65(1):164–167, 1989.
- [19] B Cappella and G Dietler. Force-distance curves by atomic force microscopy. *Surface Science Reports*, 34(1-3):1–104, 1999.
- [20] T J Senden. Force microscopy and surface interactions. *Current Opinion in Colloid & Interface Science*, 6(2):95–101, 2001.
- [21] N A Burnham, X Chen, C S Hodges, and G A Matei. Comparison of calibration methods for atomic-force microscopy cantilevers. *Nanotechnology*, 14(1):1–6, 2002.
- [22] J te Riet, A J Katan, C Rankl, S W Stahl, A M van Buul, I Y Phang, A Gomez-Casado, P Schön, J W Gerritsen, A Cambi, A E Rowan, G J Vancso, P Jonkheijm, J Huskens, T H Oosterkamp, H Gaub, P Hinterdorfer, C G Figdor, and S Speller. Interlaboratory round robin on cantilever calibration for AFM force spectroscopy. *Ultramicroscopy*, 111(12):1659–1669, 2011.

References

- [23] J L Hutter and J Bechhoefer. Calibration of atomic–force microscope tips. *Review of Scientific Instruments*, 64(7):1868–1873, 1993.
- [24] H J Butt and M Jaschke. Calculation of thermal noise in atomic force microscopy. *Nanotechnology*, 6(1):1–7, 1995.
- [25] J E Sader, I Larson, P Mulvaney, and L R White. Method for the calibration of atomic force microscope cantilevers. *Review of Scientific Instruments*, 66(7):3789–3798, 1995.
- [26] J E Sader, J W M Chon, and P Mulvaney. Calibration of rectangular atomic force microscope cantilevers. *Review of Scientific Instruments*, 70(10):3967–3969, 1999.
- [27] J P Cleveland, S Manne, D Bocek, and P K Hansma. A nondestructive method for determining the spring constant of cantilevers for scanning force microscopy. *Review of Scientific Instruments*, 64(2):403–405, 1993.
- [28] D Ossola, P Dörig, J Vörös, T Zambelli, and M Vassalli. Serial weighting of micro-objects with resonant microchanneled cantilevers. *Nanotechnology*, 27(41):415502, 2016.
- [29] M A Mahmoud. Validity and Accuracy of Resonance Shift Prediction Formulas for Microcantilevers: A Review and Comparative Study. *Critical Reviews in Solid State and Materials Sciences*, pages 1–44, 2016.
- [30] H-J Butt. Measuring electrostatic, van der Waals, and hydration forces in electrolyte solutions with an atomic force microscope. *Biophysical Journal*, 60(6):1438–1444, 1991.
- [31] W A Ducker, T J Senden, and R M Pashley. Direct Measurement of Colloidal Forces Using an Atomic Force Microscope. *Nature*, 353(6341):239–241, 1991.
- [32] Y Gan. Invited Review Article: A review of techniques for attaching micro- and nanoparticles to a probe’s tip for surface force and near-field optical measurements. *Review of Scientific Instruments*, 78(8):081101–9, 2007.
- [33] E Kokkoli and C F Zukoski. Interaction Forces between Hydrophobic and Hydrophilic Self-Assembled Monolayers. *Journal of Colloid and Interface Science*, 230(1):176–180, 2000.

2 Theory / Status of the field

- [34] V Kuznetsov and G Papastavrou. Note: Mechanically and chemically stable colloidal probes from silica particles for atomic force microscopy. *Review of Scientific Instruments*, 83(11):116103–116103, 2012.
- [35] M Borkovec, I Szilagyi, I Popa, M Finessi, P Sinha, P Maroni, and G Papastavrou. Investigating forces between charged particles in the presence of oppositely charged polyelectrolytes with the multi-particle colloidal probe technique. *Advances in Colloid and Interface Science*, 179–182:85, 2012.
- [36] F J Montes Ruiz-Cabello, G Trefalt, P Maroni, and M Borkovec. Electric double-layer potentials and surface regulation properties measured by colloidal-probe atomic force microscopy. *Physical Review E*, 90(1):012301–10, 2014.
- [37] I Popa, P Sinha, M Finessi, P Maroni, G Papastavrou, and M Borkovec. Importance of Charge Regulation in Attractive Double-Layer Forces between Dissimilar Surfaces. *Physical Review Letters*, 104(22):228301, 2010.
- [38] I U Vakarelski and K Higashitani. Single-Nanoparticle-Terminated Tips for Scanning Probe Microscopy. *Langmuir*, 22(7):2931–2934, 2006.
- [39] D J D'Sa, H-K Chan, and W Chrzanowski. Attachment of micro- and nanoparticles on tipless cantilevers for colloidal probe microscopy. *Journal of Colloid and Interface Science*, 426(C):190–198, 2014.
- [40] S Rentsch, R Pericet-Camara, G Papastavrou, and M Borkovec. Probing the validity of the Derjaguin approximation for heterogeneous colloidal particles. *Physical Chemistry Chemical Physics*, 8(21):2531, 2006.
- [41] M Finessi, P Sinha, I Szilagyi, I Popa, P Maroni, and M Borkovec. Charge Reversal of Sulfate Latex Particles by Adsorbed Linear Poly(ethylene imine) Probed by Multiparticle Colloidal Probe Technique. *The Journal of Physical Chemistry B*, 115(29):9098–9105, 2011.
- [42] I Popa, G Papastavrou, and M Borkovec. Effective Charge of Adsorbed Poly(amido amine) Dendrimers: Transition from Heterogeneous to Homogeneous Charge Distribution. *Macromolecules*, 43(2):1129–1136, 2010.
- [43] J Erath, S Schmidt, and A Fery. Characterization of adhesion phenomena and contact of surfaces by soft colloidal probe AFM. *Soft Matter*, 6(7):1432, 2010.

References

- [44] R Buzio, A Bosca, S Krol, D Marchetto, S Valeri, and U Valbusa. Deformation and Adhesion of Elastomer Poly(dimethylsiloxane) Colloidal AFM Probes. *Langmuir*, 23(18):9293–9302, 2007.
- [45] G W Tormoen and J Drelich. Deformation of soft colloidal probes during AFM pull-off force measurements: elimination of nano-roughness effects. *Journal of Adhesion Science and Technology*, 19(3-5):181–198, 2005.
- [46] L Meagher, G V Franks, M L Gee, and P J Scales. Interaction forces between α -alumina fibres in aqueous electrolyte measured with an atomic force microscope. *Colloids and Surfaces A: Physicochemical and Engineering Aspects*, 146(1–3):123 – 137, 1999.
- [47] I Muir, L Meagher, and M Gee. Interaction Forces between α -Alumina Fibers with Coadsorbed Polyelectrolyte and Surfactant. *Langmuir*, 17(16):4932–4939, 2001.
- [48] E Max, W Häfner, F W Bartels, A Sugiharto, C Wood, and A Fery. A novel AFM based method for force measurements between individual hair strands. *Ultramicroscopy*, 110(4):320–324, 2010.
- [49] H Mizuno, G S Luengo, and M W Rutland. Interactions between crossed hair fibers at the nanoscale. *Langmuir*, 26(24):18909–18915, 2010.
- [50] H Mizuno, G S Luengo, and M W Rutland. New insight on the friction of natural fibers. Effect of sliding angle and anisotropic surface topography. *Langmuir*, 29(19):5857–5862, 2013.
- [51] H Mizuno, N Kjellin, T Pettersson, V Wallqvist, M Fielden, and M W Rutland. Friction measurement between polyester fibres using the fibre probe SPM. *Australian Journal of Chemistry*, 59(6):390–393, 2006.
- [52] U Stachewicz, F Hang, and A H Barber. Adhesion Anisotropy between Contacting Electrospun Fibers. *Langmuir*, 30(23):6819–6825, 2014.
- [53] R R Dagastine, G W Stevens, D Y C Chan, and F Grieser. Forces between two oil drops in aqueous solution measured by AFM. *Journal of Colloid and Interface Science*, 273(1):339–342, 2004.

2 Theory / Status of the field

- [54] I U Vakarelski, E Q Li, and S T Thoroddsen. Soft colloidal probes for AFM force measurements between water droplets in oil. *Colloids and Surfaces A: Physicochemical and Engineering Aspects*, 462:259–263, 2014.
- [55] H J Lockie, R Manica, G W Stevens, F Grieser, D Y C Chan, and R R Dagastine. Precision AFM Measurements of Dynamic Interactions between Deformable Drops in Aqueous Surfactant and Surfactant-Free Solutions. *Langmuir*, 27(6):2676–2685, 2011.
- [56] C Browne, R F Tabor, F Grieser, and R R Dagastine. Direct AFM force measurements between air bubbles in aqueous polydisperse sodium poly(styrene sulfonate) solutions: Effect of collision speed, polyelectrolyte concentration and molar mass. *Journal of Colloid and Interface Science*, 449(C):236–245, 2015.
- [57] L Xie, C Shi, X Cui, and H Zeng. Surface Forces and Interaction Mechanisms of Emulsion Drops and Gas Bubbles in Complex Fluids. *Langmuir*, 2017. DOI: 10.1021/acs.langmuir.6b04669.
- [58] A Meister, M Gabi, P Behr, P Studer, J Vörös, P Niedermann, J Bitterli, J Polesel-Maris, M Liley, H Heinzelmann, and T Zambelli. FluidFM: Combining Atomic Force Microscopy and Nanofluidics in a Universal Liquid Delivery System for Single Cell Applications and Beyond. *Nano Letters*, 9(6):2501–2507, 2009.
- [59] O Guillaume-Gentil, E Potthoff, D Ossola, C M Franz, T Zambelli, and J A Vorholt. Force-controlled manipulation of single cells: from AFM to FluidFM. *Trends in biotechnology*, 32(7):381–388, 2014.
- [60] A Meister, M Gabi, P Behr, P Studer, J Vörös, P Niedermann, J Bitterli, J Polesel-Maris, M Liley, H Heinzelmann, and T Zambelli. FluidFM: Combining Atomic Force Microscopy and Nanofluidics in a Universal Liquid Delivery System for Single Cell Applications and Beyond. *Nano Letters*, 9(6):2501–2507, 2009.
- [61] K-H Kim, N Moldovan, and H D Espinosa. A Nanofountain Probe with Sub-100-nm Molecular Writing Resolution. *Small*, 1(6):632–635, 2005.
- [62] S Deladi, N R Tas, J W Berenschot, G J M Krijnen, M J de Boer, J H de Boer, M Peter, and M C Elwenspoek. Micromachined fountain pen for atomic force microscope-based nanopatterning. *Applied Physics Letters*, 85(22):5361–5363, 2004.

References

- [63] S Deladi, J W Berenschot, and N R Tas. Fabrication of micromachined fountain pen with in situ characterization possibility of nanoscale surface modification. *Journal of Micromechanics and Microengineering*, 15(3):528–534, 2005.
- [64] P Dörig, P Stiefel, P Behr, E Sarajlic, D Bijl, M Gabi, J Vörös, J A Vorholt, and T Zambelli. Force-controlled spatial manipulation of viable mammalian cells and micro-organisms by means of FluidFM technology. *Applied Physics Letters*, 97(2):023701–1–023701–3, 2010.
- [65] A Gaitas and R W Hower. SU-8 microcantilever with an aperture, fluidic channel, and sensing mechanisms for biological and other applications. *Journal of micro/nanolithography, MEMS, and MOEMS : JM3*, 13(3), 2014.
- [66] V Martinez, C Forró, S Weydert, M J Aebersold, H Dermutz, O Guillaume-Gentil, T Zambelli, J Vörös, and L Demkó. Controlled single-cell deposition and patterning by highly flexible hollow cantilevers. *Lab on a Chip*, 16(9):1663–1674, 2016.
- [67] V Martinez, P Behr, U Drechsler, J Polesel-Maris, E Potthoff, J Vörös, and T Zambelli. SU-8 hollow cantilevers for AFM cell adhesion studies. *Journal of Micromechanics and Microengineering*, 26(5):055006, 2016.
- [68] P Stiefel, T Zambelli, and J A Vorholt. Isolation of optically targeted single bacteria by application of fluidic force microscopy to aerobic anoxygenic phototrophs from the phyllosphere. *Applied and Environmental Microbiology*, 79(16):4895–4905, 2013.
- [69] O Guillaume-Gentil, T Zambelli, and J A Vorholt. Isolation of single mammalian cells from adherent cultures by fluidic force microscopy . *Lab on a Chip*, 14(2):402–414, 2014.
- [70] E Potthoff, O Guillaume-Gentil, D Ossola, J Polesel-Maris, S LeibundGut-Landmann, T Zambelli, and J A Vorholt. Rapid and Serial Quantification of Adhesion Forces of Yeast and Mammalian Cells. *PLoS ONE*, 7(12):e52712, December 2012.
- [71] E Potthoff, D Ossola, T Zambelli, and J A Vorholt. Bacterial adhesion force quantification by fluidic force microscopy. *Nanoscale*, 7(9):4070–4079, 2015.

2 Theory / Status of the field

- [72] L Jaatinen, E Young, J Hyttinen, J Vörös, T Zambelli, and L Demkó. Quantifying the effect of electric current on cell adhesion studied by single-cell force spectroscopy. *Biointerphases*, 11(1):011004–9, 2016.
- [73] J Eisenbeis, H Peisker, C S Backes, S Bur, S Hölter, N Thewes, M Greiner, C Junker, E C Schwarz, M Hoth, K Junker, K T Preissner, K Jacobs, M Herrmann, and M Bischoff. The extracellular adherence protein (Eap) of *Staphylococcus aureus* acts as a proliferation and migration repressing factor that alters the cell morphology of keratinocytes. *International Journal of Medical Microbiology*, 307:116–125, 2017.
- [74] A Sancho, I Vandersmissen, S Craps, A Luttun, and J Groll. A new strategy to measure intercellular adhesion forces in mature cell-cell contacts. *Nature Publishing Group*, 2017.
- [75] P Stiefel, F I Schmidt, P Dörig, P Behr, T Zambelli, J A Vorholt, and J Mercer. Cooperative vaccinia infection demonstrated at the single-cell level using FluidFM. *Nano Letters*, 12(8):4219–4227, 2012.
- [76] O Guillaume-Gentil, E Potthoff, D Ossola, P Dörig, T Zambelli, and J A Vorholt. Force-Controlled Fluidic Injection into Single Cell Nuclei. *Small*, 9(11):1904–1907, 2012.
- [77] O Guillaume-Gentil, R V Grindberg, R Kooger, L Dorwling-Carter, V Martinez, D Ossola, M Pilhofer, T Zambelli, and J A Vorholt. Tunable Single-Cell Extraction for Molecular Analyses. *Cell*, 166(2):506–516, 2016.
- [78] R R Grüter, J Vörös, and T Zambelli. FluidFM as a lithography tool in liquid: spatially controlled deposition of fluorescent nanoparticles. *Nanoscale*, 5(3):1097–1104, 2013.
- [79] R R Grüter, B Dielacher, L Hirt, J Vörös, and T Zambelli. Patterning gold nanoparticles in liquid environment with high ionic strength for local fabrication of up to 100 μm long metallic interconnections. *Nanotechnology*, 26(17):175301, 2015.
- [80] L Hirt, S Ihle, Z Pan, L Dorwling-Carter, A Reiser, J M Wheeler, R Spolenak, J Vörös, and T Zambelli. Template-Free 3D Microprinting of Metals Using a Force-Controlled Nanopipette for Layer-by-Layer Electrodeposition. *Advanced Materials*, 28(12):2311–2315, 2016.

- [81] L Hirt, A Reiser, R Spolenak, and T Zambelli. Additive Manufacturing of Metal Structures at the Micrometer Scale. *Advanced Materials*, 2017. DOI: 10.1002/adma.201604211.
- [82] P Dörig, D Ossola, A M Truong, M Graf, F Stauffer, J Vörös, and T Zambelli. Exchangeable Colloidal AFM Probes for the Quantification of Irreversible and Long-Term Interactions. *Biophysical Journal*, 105(2):463–472, 2013.
- [83] B R Simona, L Hirt, L Demkó, T Zambelli, J Vörös, M Ehrbar, and V Milleret. Density gradients at hydrogel interfaces for enhanced cell penetration. *Biomaterials Science*, 3(4):586–591, 2015.
- [84] E L Florin, V T Moy, and H E Gaub. Adhesion forces between individual ligand-receptor pairs. *Science*, 264(5157):415–417, 1994.
- [85] G U Lee, L A Chrisey, and R J Colton. Direct Measurement of the Forces Between Complementary Strands of DNA. *Science*, 266:711–773, 1994.
- [86] A Janshoff, M Neitzert, Y Oberdorfer, and H Fuchs. Force spectroscopy of molecular systems - Single molecule spectroscopy of polymers and biomolecules. *Angewandte Chemie Internationale Edition*, 39(18):3213–3237, 2000.
- [87] W Zhang and X Zhang. Single molecule mechanochemistry of macromolecules. *Progress in Polymer Science*, 28(8):1271–1295, 2003.
- [88] T Hugel and M Seitz. The study of molecular interactions by AFM force spectroscopy. *Macromolecular Rapid Communications*, 22(13):989–1016, 2001.
- [89] M I Giannotti and G J Vancso. Interrogation of Single Synthetic Polymer Chains and Polysaccharides by AFM-Based Force Spectroscopy. *The European Journal of Chemical Physics and Physical Chemistry*, 8(16):2290–2307, 2007.
- [90] Öznur Kaftan, S Tumbiolo, F Dubreuil, R Auzeily-Velty, A Fery, and G Papastavrou. Probing Multivalent Host-Guest Interactions between Modified Polymer Layers by Direct Force Measurement. *The Journal of Physical Chemistry B*, 115(24):7726–7735, 2011.
- [91] C Friedsam, A del Campo Becares, U Jonas, M Seitz, and H E Gaub. Adsorption of polyacrylic acid on self-assembled monolayers investigated by single-molecule force spectroscopy. *New Journal of Physics*, 6, 2004.

2 Theory / Status of the field

- [92] C Friedsam, M Seitz, and H E Gaub. Investigation of polyelectrolyte desorption by single molecule force spectroscopy. *Journal of Physics: Condensed Matter*, 16(26):S2369–S2382, 2004.
- [93] C Friedsam, A Del Campo Bécáres, U Jonas, H E Gaub, and M Seitz. Polymer Functionalized AFM tips for Long-Term Measurements in Single-Molecule Force Spectroscopy. *A European Journal of Chemical Physics and Physical Chemistry*, 5(3):388–393, 2004.
- [94] S Kienle, M Gallei, H Yu, B Zhang, S Krysiak, B N Balzer, M Rehahn, A D Schlüter, and T Hugel. Effect of Molecular Architecture on Single Polymer Adhesion. *Langmuir*, 30(15):4351–4357, 2014.
- [95] L Grebikova, P Maroni, B Zhang, A D Schlüter, and M Borkovec. Single-Molecule Force Measurements by Nano-Handling of Individual Dendronized Polymers. *ACS Nano*, 8(3):2237–2245, 2014.
- [96] I Popa, B Zhang, P Maroni, A D Schlüter, and M Borkovec. Large Mechanical Response of Single Dendronized Polymers Induced by Ionic Strength. *Angewandte Chemie International Edition*, 49(25):4250–4253, 2010.
- [97] L Grebikova, P Maroni, L Muresan, B Zhang, A D Schlüter, and M Borkovec. Interactions between Individual Charged Dendronized Polymers and Surfaces. *Macromolecules*, 46(9):3603–3610, 2013.
- [98] M Geisler, S Xiao, E M Puchner, F Gräter, and T Hugel. Controlling the Structure of Proteins at Surfaces. *Journal of the American Chemical Society*, 132(48):17277–17281, 2010.
- [99] M Geisler, D Horinek, and T Hugel. Single Molecule Adhesion Mechanics on Rough Surfaces. *Macromolecules*, 42(23):9338–9343, 2009.
- [100] Y I Rabinovich, J J Adler, A Ata, R K Singh, and B M Moudgil. Adhesion between Nanoscale Rough Surfaces. *Journal of Colloid and Interface Science*, 232(1):17–24, 2000.
- [101] V Kuznetsov and G Papastavrou. Adhesion of colloidal particles on modified electrodes. *Langmuir*, 28(48):16567–16579, 2012.
- [102] J E Bemis, B B Akhremitchev, and G C Walker. Single Polymer Chain Elongation by Atomic Force Microscopy. *Langmuir*, 15(8):2799–2805, 1999.

References

- [103] L J Kirwan, P Maroni, S H Behrens, G Papastavrou, and M Borkovec. Interaction and Structure of Surfaces Coated by Poly(vinyl amines) of Different Line Charge Densities. *The Journal of Physical Chemistry B*, 112(46):14609–14619, 2008.
- [104] H Li, M Rief, F Oesterhelt, H E Gaub, X Zhang, and J Shen. Single-molecule force spectroscopy on polysaccharides by AFM - nanomechanical fingerprint of α -(1,4)-linked polysaccharides . *Chemical Physics Letters*, 305(3-4):197 – 201, 1999.
- [105] M Rief, F Oesterhelt, B Heymann, and H E. Gaub. Single molecule force spectroscopy on polysaccharides by atomic force microscopy. *Science*, 275(5304):1295–1297, 1997.
- [106] E M Puchner, G Franzen, M Gautel, and H E Gaub. Comparing Proteins by Their Unfolding Pattern. *Biophysical Journal*, 95(1):426–434, 2008.
- [107] C A Bippes, H Janovjak, A Kedrov, and D J Muller. Digital force-feedback for protein unfolding experiments using atomic force microscopy. *Nanotechnology*, 18(4):044022, 2007.
- [108] H-J Butt, K Graf, and M Kappl. *Physics and Chemistry of Interfaces*. Wiley-VCH, 3rd edition, 2013.
- [109] E L Verwey and J T G Overbeek. *Theory of Stability of Lyophobic Colloids*. Elsevier, 1948.
- [110] I Popa, P Sinha, M Finessi, P Maroni, G Papastavrou, and M Borkovec. Importance of Charge Regulation in Attractive Double-Layer Forces between Dissimilar Surfaces. *Physical Review Letters*, 104:228301–1–228301–4, 2010.
- [111] G Trefalt, S H Behrens, and M Borkovec. Charge Regulation in the Electrical Double Layer: Ion Adsorption and Surface Interactions. *Langmuir*, 32(2):380–400, 2016.
- [112] F J Montes Ruiz-Cabello, G Trefalt, P Maroni, and M Borkovec. Electric double-layer potentials and surface regulation properties measured by colloidal-probe atomic force microscopy. *Physical Review E*, 90(1):012301–10, 2014.
- [113] M Borkovec and S H Behrens. Electrostatic Double Layer Forces in the Case of Extreme Charge Regulation. *The Journal of Physical Chemistry B*, 112(35):10795–10799, 2008.

2 Theory / Status of the field

- [114] A V Delgado, F Gonzalez-Caballero, R J Hunter, L K Koopal, and J Lyklema. Measurement and interpretation of electrokinetic phenomena. *Journal of Colloid and Interface Science*, 309(2):194 – 224, 2007.
- [115] J L Hunter. *Zeta-Potential in Colloid Science*. Academic Press, 1989.
- [116] R H Müller. *Zetapotential und Partikelladung in der Laborpraxis*. Wissenschaftliche Verlagsgesellschaft mbH, 1996.
- [117] P C Hiemenz. *Principles of Colloid and Surface Chemistry*. Marcek Dekker Inc., 1986.
- [118] M E McConney, S Singamaneni, and V V Tsukruk. Probing soft matter with the atomic force microscopies: imaging and force spectroscopy. *Polymer Reviews*, 50:235–286, 2010.
- [119] H Hertz. Über die Berührung fester elastischer Körper. *Journal für die reine und angewandte Mathematik*, 92, 1881.
- [120] K L Johnson, K Kendall, and A D Roberts. Surface Energy and Contact of Elastic Solids. *Proceedings of the Royal Society of London Series of a-Mathematical and Physical Sciences*, 324.1558:301, 1971.
- [121] B V Derjaguin, V M Muller, and Y P Toporov. Effect of Contact Deformations on Adhesion of Particles. *Journal of Colloid and Interface Science*, 53.2:314–326, 1975.

CHAPTER 3

Synopsis

3.1 Outline

The aim of this thesis is the development of novel AFM probes in order to study interface dominated systems by direct force measurements. The availability of suitable probes is the major prerequisite to extend the range of probes for direct force measurements, such as hydrogels and nanoparticles.

The results, obtained in the framework of this thesis are reported in seven scientific publications (*cf.* Chapters 4 through 10). In the following, the content of these individual publications is briefly summarized. The distinct contributions of all co-authors are specified at the end of this Chapter.

3.2 Content of the Individual Publications

The atomic force microscopy (AFM) provides an experimental technique, that allows to determine interaction forces with the colloidal probe technique or with single molecule force spectroscopy. Such probes can vary in materials and dimensions: Practically, from hydrogel particles with a diameter of several hundred μm down to single peptide molecules. [1, 2, 3]

In the first part of the thesis, two standard AFM techniques were used to determine interaction forces on the molecular level by means of single molecule force spectroscopy, where the outstanding adhesion behaviour of marine mussel inspired peptides could

3 Synopsis

be attributed to one specific amino acid (*cf.* Chapter 4). Moreover, the soft interface of recombinant spider silk protein particles was probed by 'classical' silica colloidal probes (several μm in diameter) (*cf.* Chapter 5).

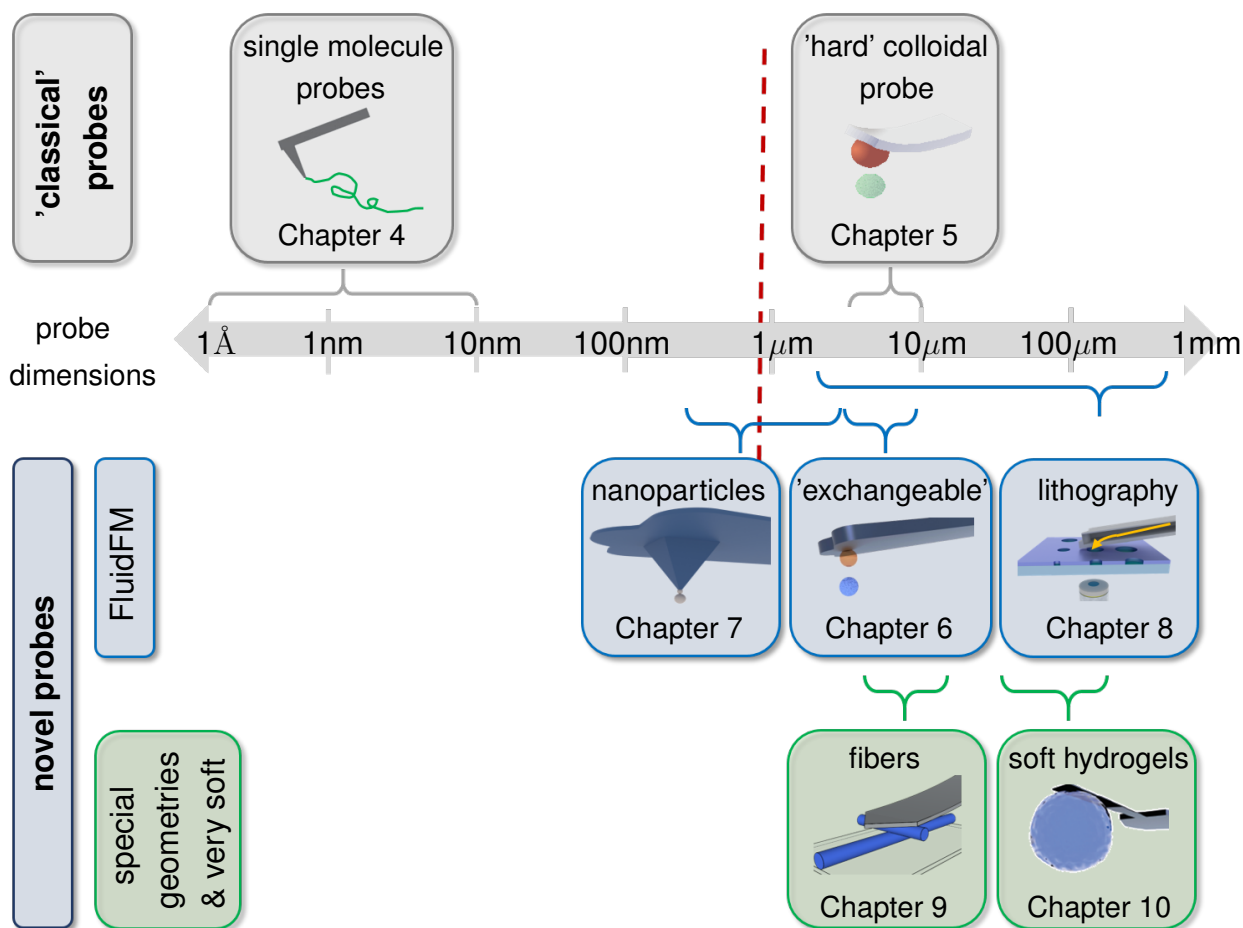


Figure 3.1: Schematic illustration of the variety of AFM probes, implemented in the present thesis in order to determine surface interactions such as surface charge properties and adhesion behaviour. The individual Chapters are subdivided in 'classical' probes, exchangeable probes using the FluidFM technique and novel probes, respectively. Furthermore, the length scale of the different probe dimensions is indicated.

In the second part, it is demonstrated that temporary colloidal probes were achievable with the recently developed FluidFM technique, due to the unique combination of AFM with nanofluidics. In Chapter 6, this FluidFM technology allowed for the preparation of exchangeable colloidal probes to study protein particles as described in Chapter 5. However, this time a single amino acid in the primary structure of the protein has been

3.2 Content of the Individual Publications

exchanged. The FluidFM technique further enables the possibility to push the size limitation of available colloidal probes down to the range of nanoparticles, which are used in industrial formulations (*cf.* Chapter 7). Another application of the FluidFM is the capability to structure even soft materials, such as hydrogel films, with μm precision, while preventing any damage of the surface due to the force control of the AFM during the subtractive process (*cf.* Chapter 8).

The final two Chapters of the thesis demonstrate how, the 'classical' colloidal probe technique could be extended toward non-standard interaction geometries or very soft, μm -sized probes. Fiber-fiber interactions were determined in the crossed-cylinder geometry known from the surface force apparatus (SFA) (*cf.* Chapter 9). In Chapter 10, a novel method for the *in situ* preparation of giant hydrogel colloidal probes ($\sim 100 \mu\text{m}$) was developed enabling all essential manipulation steps in liquid environment.

The various AFM probes presented in Chapters 4 through 10, cover the size range from single molecules up to giant hydrogel beads ($\geq 100 \mu\text{m}$) as schematically shown in Figure 3.1. In particular, the approach of temporary colloidal probes from nanoparticles extends the limit of accessible probe dimension down to a size regime, where direct inter-particle measurements were not possible until now. As in this case the size-limiting step, the control by optical microscopy during the glueing procedure of the probe particles, can be omitted.

3.2.1 'Classical' AFM Probes

Typically, two types of AFM probes are extensively used for direct force measurements: Hard colloidal particles such as glass or silica [1] as well as proteins attached to a sharp AFM tip by means of a polymer spacer [2]. Hence, these two types are referred in the following to as 'classical' AFM probes. In the first part of the present thesis, such 'classical' AFM probes were used to determine interactions on the molecular level of single mussel foot peptides to inorganic surfaces (*cf.* Chapter 4). Furthermore, the interaction forces between individual μm -sized colloidal protein particles were evaluated in terms of their soft interface (*cf.* Chapter 5).

3 Synopsis

A Direct Biocombinatorial Strategy towards Next Generation, Mussel-Glue Inspired Saltwater Adhesives

Mussel foot proteins are well-known for their outstanding adhesive properties even under very hostile conditions (*e.g.* high ionic strength and large mechanical shear forces) in aqueous environment. The design of novel wet-adhesives is inspired from these marine proteins containing the amino acid L-dopa, which is mainly responsible for these remarkable properties. [4, 5] The adhesion behaviour of synthetic mussel inspired polymer-peptide conjugates was investigated on the molecular level by single molecule force spectroscopy (SMFS), where the molecules were covalently coupled to a chemically modified AFM cantilever.

In this collaborative project, the group of Prof. Dr. Hans Börner implemented an additional step to extend the phage display biopanning with an enzymatic oxidation step. The untreated peptides exhibit no or only weak adhesion to aluminum oxide surfaces, while after enzymatic oxidation by mushroom tyrosinase, the adhesion is drastically increased. Several peptides were selected from the phage display biopanning for adsorption experiments and were investigated by quartz crystal microbalance (QCM). These measurements revealed a clear difference between the adsorption kinetics of the untreated and treated peptides: The not activated ones only bind weakly and the binding process on the aluminum surfaces is reversible. By contrast, the oxidized species adhere stronger and even resist rinsing with harsh electrolyte conditions, respectively.

The most promising peptide (Pep₃) was studied in terms of its adhesive properties onto aluminum oxide surfaces. For this purpose, Pep₃ and its oxidized counterpart (Pep₃^{*-synth.}) were both synthesized and were covalently coupled to chemically modified AFM cantilevers (*cf.* Figure 3.2 a). Since, the 12-mer peptides are quite short, a PEG-spacer of approximately 100 nm was introduced in order to reduce the influence of the cantilever's surface. This heterofunctional PEG-spacer possessed a NHS-group at one termini and a maleimide-group at the other termini, respectively. The peptides were coupled with a terminal cystein residue to a maleimide group in the PEG-spacer, and the polymer-peptide conjugates were attached *via* the NHS-activated end to amino-terminated AFM cantilevers.

Single molecule force spectroscopy experiments were performed with unoxidized and

3.2 Content of the Individual Publications

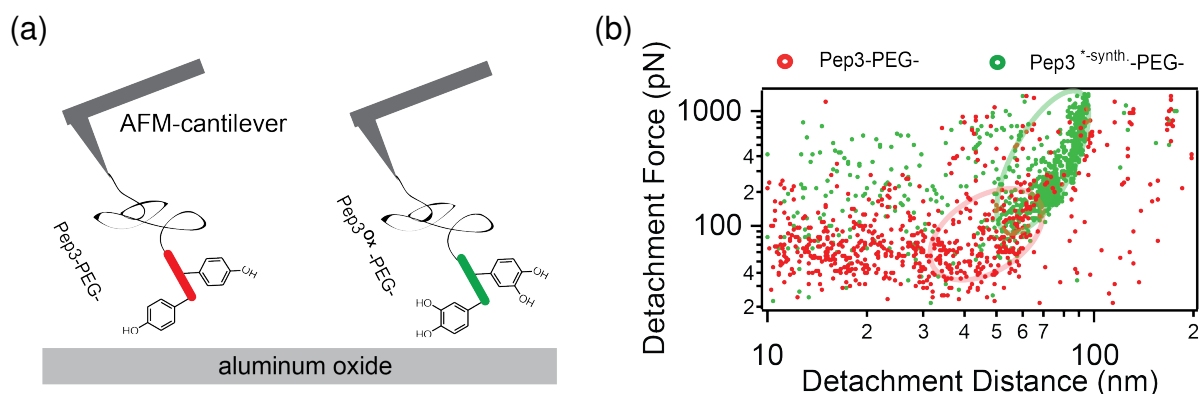


Figure 3.2: (a) Schematic illustration of covalently coupled polymer-peptide probes bearing either two L-tyrosine (red) or two L-dopa (green) residues, respectively. (b) The scatter plot of the determined detachment forces as a function of the separation distance reveals distinct differences in the molecular adhesive behaviour of these different polymer-peptide probes. Adapted with permission from Wilke *et al.*, *Journal of the American Chemical Society*, **2014**, 136(36), 12667-12674, © 2014 American Chemical Society.

oxidized polymer-peptide probes on aluminium oxide surfaces. The direct comparison of these measurements were in-line with QCM-experiments. For both oxidation states a bimodal distribution of the rupture forces has been observed, since both peptides comprise each two residues of the respective amino acids. The rupture forces for the oxidized peptide bearing two L-dopa residues were found to be around 640 pN, which is in the order of a very strong non-covalent bond. By contrast, the unbinding of the unoxidized peptide was found to take place at much smaller forces of around 55 pN. The rupture of the oxidized peptides take further place at larger separation distances due the longer extension of the polymer-peptide molecules (*cf.* Figure 3.2 b). The evaluated pull-off forces for the two different oxidation states (L-tyrosine and L-dopa) were in good agreement with the values reported by Messersmith *et al.* [6] and were recently confirmed by Hugel and co-workers. [7]

Surface Properties of Spider Silk Particles in Solution

Spider silk proteins can be assembled not only into the well-known fibers but also into several morphologies such as spherical particles. Due to their biocompatibility, such particles have applications for example as drug delivery systems. [8, 9] However, understanding and tuning the particle's properties is a prerequisite for their use in pharmaceutical formulations. Hence, the colloidal stability of the particle suspension is a

3 Synopsis

crucial parameter, in particular for high electrolyte concentrations, *e.g.* at physiological conditions. The colloidal stability is often directly related to the surface charge. Chapter 5 demonstrates how the latter is studied by means of two independent methods. Firstly, the electrophoretic mobility of the protein particles was determined as a function of pH and total ionic strength. Secondly, the inter-particle interaction forces were probed in the sphere-sphere geometry by direct force measurements using an AFM.

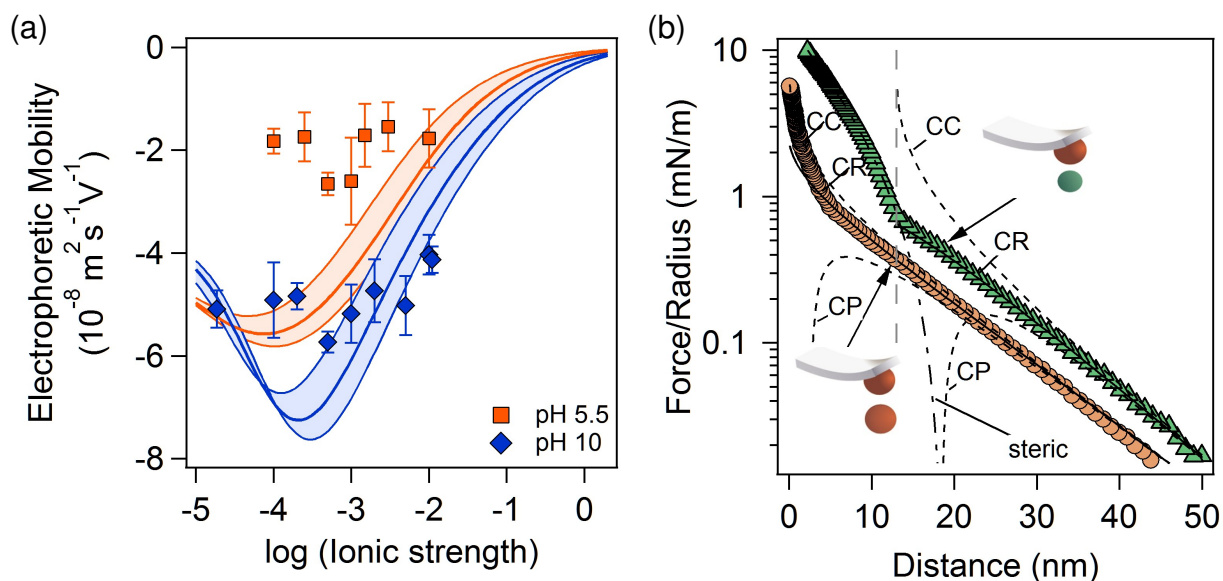


Figure 3.3: The surface charge properties of recombinant spider silk protein particles were determined by (a) electrophoretic mobility measurements and (b) direct force measurements by AFM. Adapted with permission from Helfrich *et al.*, *Biomaterials Science*, **2013**, 1, 1166, © 2013 The Royal Society of Chemistry.

The recombinant spider silk protein eADF4(C16) was assembled into spherical particles by a salting-out procedure. The particle's charge properties were determined by microelectrophoresis measurements. The measured electrophoretic mobility of the protein particles did not decrease monotonically with increased ionic strength (*cf.* Figure 3.3 a), as expected for standard electrokinetic theories. The presence of such a local minimum in the electrophoretic mobility as a function of the ionic strength is indicative for the O'Brien and White theory. [10] This theory can be applied to theoretically calculate the electrophoretic mobility based solely on the underlying amino acid sequence of the protein. However, these calculations overestimated the magnitude of the measured electrophoretic mobility. This discrepancy can be attributed to the fact, that the O'Brien and White theory is valid strictly for 'hard' particles. By contrast, the

3.2 Content of the Individual Publications

spider silk protein particles were obtained by a salting-out procedure leading to a soft and permeable interface of the protein particles and no distinct plane of charges could be assigned.

In order to validate the presence of such a diffuse interfacial layer, direct force measurements by AFM were performed between individual particles in the sphere-sphere interaction geometry. Firstly, hard silica colloidal probes were utilized as 'internal' standards. As expected, the force profiles between two silica colloidal particles were dominated by electrostatic interactions, which could be evaluated quantitatively by fits to full solutions of the Poisson-Boltzmann equation. The obtained diffuse layer potential of the silica particles was in good agreement with previously reported values under the investigated conditions. In the following, the asymmetric combination between silica colloidal probes and protein particles has been measured. In this case, the electrostatic decay was only observable at large separation distances $> 10\text{-}15\text{ nm}$ (*cf.* Figure 3.3 b). An additional force contribution at small separation distances could be revealed upon the approach of a silica colloidal probe and a protein particle. These additional forces were attributed to steric interactions, which could be approximated with the Alexander-deGennes model for polymer brushes with brush heights in the order of $30\text{-}50\text{ nm}$. Upon contact of the hard colloidal probe, the protein particles were deformed upon exertion of larger forces and the calculated internal stiffness was in good agreement with the reported Young's modulus for the same type of particles. [11]

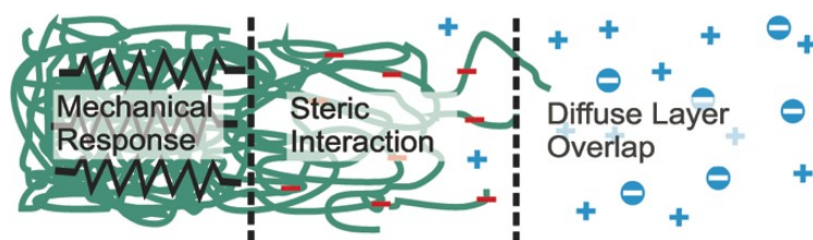


Figure 3.4: Schematic illustration of the internal structure of the investigated recombinant spider silk protein particles: Mechanically deformable particle core, which is surrounded by a brush-like protein layer bearing ionizable functional groups. Adapted with permission from Helfricht *et al.*, *Biomaterials Science*, **2013**, 1, 1166, © 2013 The Royal Society of Chemistry.

By combining the results of these two different methods, a simple model for the internal structure of recombinant spider silk protein particles was proposed (*cf.* Figure 3.4). The examined protein particles are only slightly charged and obtain no sharp surface

3 Synopsis

transition with a defined plane of charges. The presence of steric forces due to dangling protein chains in the solution provides an important contribution for the stability of the particles in suspension, especially at high ionic strength.

The suggested model is a good approximation for the complex structure of recombinant spider silk protein particles as prepared by salting-out procedure. In Chapter 6, the same recombinant spider silk protein was tuned on the molecular level by controlled exchange of one amino acid per module. However, the electrophoretic mobility has been described by a more sophisticated model for soft and permeable particles.

3.2.2 FluidFM Technology

In the second part of the thesis, the newly developed FluidFM technology was applied to determine interaction forces between soft particles (*cf.* Chapter 6) and between individual pairs of nanoparticles (*cf.* Chapter 7). The FluidFM combines the force control of an AFM with nanofluidic control of the fluid movement at an aperture located at the end of special AFM cantilevers bearing an internal channel. The FluidFM technology allows for direct force measurements with temporary and exchangeable colloidal probes. [12, 13] Moreover, it was demonstrated, that the FluidFM technology could also be used to structure soft materials, such as stimuli-responsive hydrogels (*cf.* Chapter 8).

Colloidal Properties of Recombinant Spider Silk Protein Particles

As already introduced in Chapter 5, one of the main requirements for the application of spider silk protein particles as drug delivery systems is the presentation of the direct relation between the amino acid sequence and the colloidal properties. The recombinant production pathway of the engineered spider silk fibroins enables the possibility to modify the proteins on the molecular level, without alteration of the assembly procedures. [14, 8] In Chapter 6, the amino acid sequence was tuned by exchanging one specific amino acid per repetitive module. The expected charge reversal of the protein particles at neutral pH was investigated using electrophoretic mobility measurements and is described by an electrokinetic model for soft particles. This model allows to obtain a more detailed understanding of the internal particle structure and its influence on the electrokinetic properties. Direct force measurements in sphere-sphere geome-

3.2 Content of the Individual Publications

try allow to identify steric force contributions in order to estimate the extension of the soft protein layer, which is an essential parameter in the electrokinetic modeling.

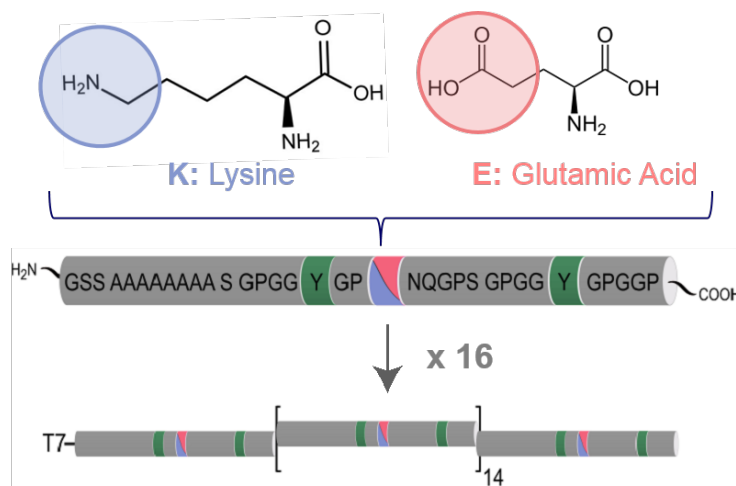


Figure 3.5: Schematic representation of the repetitive modules of the amino acid sequences of the used recombinant spider silk proteins eADF4(κ 16) and eADF4(C16) and the chemical structures of the charge determining amino acids, namely lysine in eADF4(κ 16) and glutamic acid in eADF4(C16), respectively. Adapted with permission from Helfricht *et al.*, *Journal of Physical Chemistry C*, **2016**, 130(32), 18015-18027, © 2016 American Chemical Society.

The recombinant production of spider silk proteins allows for an easy and desired modification of the underlying amino acid sequence. The anionic glutamic acid residues of the already established eADF4(C16) (*cf.* Chapter 5) were exchanged by cationic lysine residues, resulting in a reversal of the overall charge of eADF4(κ 16) at neutral pH (*cf.* Figure 3.5). Particles from both types of proteins were obtained by a salting-out procedure and their electrophoretic mobility was investigated as a function of pH and total ionic strength. The presence of a soft interface has been already demonstrated in Chapter 5. Moreover, it became obvious that these soft interfaces limit the application of the O'Brien and White theory [10] as developed for hard particles. In contrast to 'hard' particles, soft particles are permeable to ions and solvent. Therefore, the electrophoretic mobility shows a non-zero-mobility plateau at large ionic strength due to the intra-layer electroosmotic flow according to the electrokinetic theory presented by Ohshima. [15] Up to now, the Ohshima theory has never been applied to protein particles, which were prepared by a salting-out procedure. Here, this theory was used to determine a set of two characteristic parameters, namely the net charge density ρ_0

3 Synopsis

and the penetration length of the electroosmotic flow $1/\lambda_0$ within the particle (*cf.* Figure 3.6 a, b).

The electrophoretic mobility has been determined as a function of the pH. The resulting pI was in good agreement with the one calculated according to the amino acid sequences of both protein types. eADF4(κ 16) particles are only poorly charged and show therefore only a weak dependency of the electrophoretic mobility on the total ionic strength. In general, the electrophoretic mobility could be reproduced well with the presented model. However, at the lowest investigated ionic strength (0.1 mM) a smaller $1/\lambda_0$ has been found most likely due to the swelling of the particles. Since $1/\lambda_0$ is in the order of several tens of nm, it could be further demonstrated, that the electrophoretic mobility is independent of the particle's size (diameter $\sim 1\text{-}4\ \mu\text{m}$). The electrophoretic mobility for the eADF4(C16) particles has been also reconstructed by the analogous procedure, resulting in slightly larger $1/\lambda_0$ compared to the eADF4(κ 16) particles (*cf.* Figure 3.6 c).

The availability of two spider silk proteins with different overall surface charge allows for the building up multilayer structures. The electrophoretic mobility of such multilayered particles confirmed that only the outermost part of the layer is dominating the overall electrokinetic properties.

Direct force measurements by AFM confirm the soft behaviour of the protein particles, that does not allow for the identification of a sharp interface. Therefore, no distinct plane of charges could be attributed to the electrokinetic measurements. The FluidFM technique allowed to obtain temporary colloidal probes by aspiration of single silica particles to the aperture at the end of the micro-channeled cantilever. This temporary immobilization enables a better statistics over several probe particles. Furthermore, the probe particle can be quickly exchanged in case of any contamination, such as protein molecules in the solution. 'Hard' silica particles served again as internal standards to calibrate the diffuse layer properties of the probe particles. The direct force measurements were performed at pH 3, where the silica colloidal probes bear only a slight negative surface charge and both protein particle types are positively charged. Despite the opposite surface charges between silica probe particles and recombinant spider silk protein particles, only repulsive long-range interaction forces could be detected. These repulsive forces are attributed to steric interactions resulting from pro-

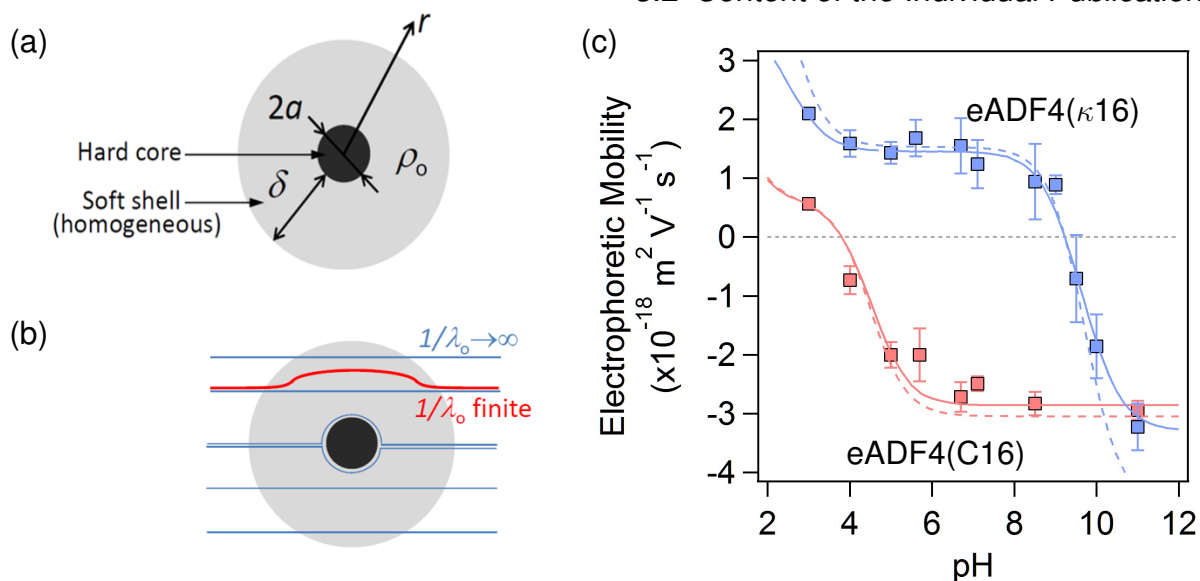


Figure 3.6: Schematic illustration of the characteristic parameters of the electrokinetic theory for soft and porous particles: (a) ρ_0 the net charge density of ionizable groups within the soft shell and (b) $1/\lambda_0$ the penetration length for the intra-layer electroosmotic flow. (c) Electrophoretic mobility as a function of pH for recombinant spider silk protein particles prepared from eADF4(C16) (red) and eADF4(κ 16) (blue). Adapted with permission from Helfricht *et al.*, *Journal of Physical Chemistry C*, **2016**, 130(32), 18015-18027, © 2016 American Chemical Society.

truding protein chains, which lead to a fuzzy interfacial layer around the particles. The quantitative evaluation by the asymmetric Alexander and de Gennes brush theory revealed a comparable average anchor density for both types of protein particles, but the brush lengths are significantly different. However, the brush thickness obtained from the direct force measurements were in-line with the values found for the electrohydrodynamic parameter $1/\lambda_0$ for the electrophoretic mobility.

Extending the Limits of Direct Force Measurements: Colloidal Probes from Sub-Micron Particles

The preparation of colloidal probes from small particles (*e.g.* particles with diameter $< 1 \mu\text{m}$) is still one of the major limitations during direct force measurements by AFM. Standard preparation procedures for colloidal probes are based on the manipulation of particles under an optical microscope. [16, 17, 1] Hence, the current benchmark for particle dimensions available for colloidal probes is $\geq 1 \mu\text{m}$, [18, 19] due to the practical resolution limits in optical microscopy. The second restriction of the colloidal probe

3 Synopsis

method is the permanent immobilization of particles onto AFM cantilevers. In this respect, the FluidFM technology allows for the possibility to immobilize a probe particle in a temporary manner to overcome this limitation, analogous to Chapter 6, albeit for much smaller particles.

Chapter 7 demonstrates for the first time, that the FluidFM can be used to probe the interaction forces with individual silica nanoparticles in the size range of ≤ 500 nm. Silica particles were chosen as model particles, since silica surfaces are one of the most investigated systems as well as by direct force measurements. [20, 21, 1] The interaction forces between silica particles were determined between two single particles in the sphere-sphere geometry and against the plane glass surface in the sphere-plane geometry, respectively. Three different diameters of silica particles were selected for the direct force measurements: (i) $\sim 4 \mu\text{m}$, which is the standard size regime for 'classical' colloidal probes, allowing for a direct comparison between the standard permanent immobilization and temporary FluidFM probes, respectively. (ii) $\leq 1 \mu\text{m}$, representing the current size limit of colloidal probes, and (iii) finally true nanoparticles of diameters ≤ 500 nm (*cf.* Figure 3.7 a).

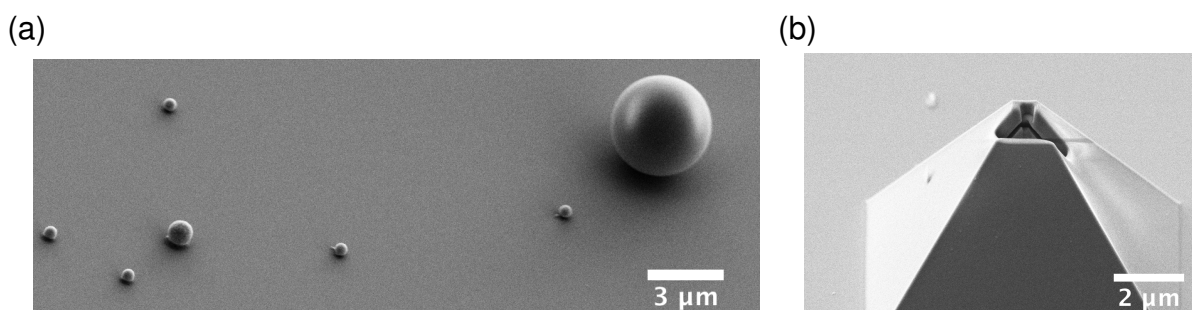


Figure 3.7: (a) SEM image of the used silica particles with varying dimensions. (b) SEM image of a cross-section through a pyramidal tip of a FluidFM cantilever with an aperture of ~ 300 nm. Adapted with permission from Helfricht *et al.*, *Nanoscale*, **2017**, 9, 9491-9501, © 2017 The Royal Society of Chemistry.

The large μm -sized particles (i), aspirated to a FluidFM cantilever, were used for a direct comparison to 'classical', permanently glued colloidal probes. For both types of colloidal probes, direct force measurements were performed in the sphere-sphere geometry between two silica particles as well as in the sphere-plane geometry against the plane glass surface, respectively. From these measurements, the diffuse layer

3.2 Content of the Individual Publications

properties of silica and glass surfaces were obtained from fits to full solutions of the Poisson-Boltzmann equation and constant charge regulation. The resulting diffuse layer potentials and regulation parameters were in good agreement with previously reported values for silica and glass surfaces. [22, 23, 24] The observed, slight deviations between the two data sets were attributed to optical interferences in the force profiles arising from the sandwich structure of the FluidFM cantilevers.

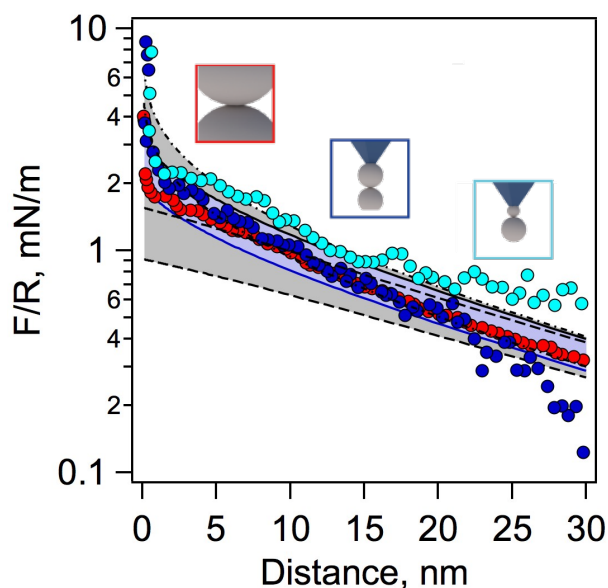


Figure 3.8: Normalized force vs. distance curves as obtained from direct force measurements in the sphere-sphere geometry between various combinations of silica particles of different diameters (*cf.* inset). Adapted with permission from Helfricht *et al.*, *Nanoscale*, **2017**, 9, 9491-9501, © 2017 The Royal Society of Chemistry.

While, the aspiration of μm -sized silica particles could be directly observed by optical microscopy, which is not feasible for particles $\leq 1 \mu\text{m}$ anymore. Consequently, an alternative approach for the aspiration of sub- μm particles had to be developed: The applied external pressure to the micro-channeled FluidFM cantilever leads to hydrodynamic forces if the cantilever was in the vicinity of a surface. An applied overpressure resulted in repulsive forces, similar to a 'garden hose effect'. By contrast, an applied underpressure leads to attractive interactions due to a suction effect. By recording continuous force *versus* distance cycles during the aspiration process with an applied underpressure, the state of the aperture (open / blocked) can be verified. The abrupt change from long-range attraction to rather short-ranged repulsion corresponds to a successful aspiration of a sub- μm particle and a subsequent blocking of the aperture.

3 Synopsis

Furthermore, the piezo-displacement is shifted to shorter distances by a value close to the diameter of a nanoparticle, providing another indication for a successful particle aspiration.

The interaction forces of sub- μm colloidal probes were determined in the sphere-sphere as well in the sphere-plane geometry, as for the μm -sized silica colloidal probes. However, for these smaller particles, the particle dimensions are not directly accessible during the measurements and the force profiles were normalized to the average particle diameters. Figure 3.8 shows normalized force vs. distance curves for several combinations of particle dimensions in the sphere-sphere geometry. All of these curves fall in the grey shaded area, which was calculated based on the diffuse layer properties as determined from 'classical' colloidal probe experiments for μm -sized silica particles.

Writing with Fluid: Structuring Hydrogels with Micrometer Precision by AFM in Combination with Nanofluidics

The applications of the FluidFM technology are by no means restricted to direct force measurements (*cf.* Chapters 6 and 7), but can be further used for deposition or removal of material on the nanoscale. It was recently demonstrated that this technique could also be applied to create structures of nanoparticles [25] or metals [26]. In Chapter 8, the FluidFM technology was used to locally structure soft materials such as pH responsive hydrogel films with μm precision, whereby the force control of the AFM allows for a controlled structuring process avoiding any damage of the surface. This novel subtractive approach is substantially different compared to recent additive manufacturing approaches by FluidFM. [25, 26, 27]

The carboxylated derivate of 1,3,5-benzene tricarboxamides (BTA) represents a low-molecular weight hydrogelator, which reversibly forms hydrogels upon pH change. [28] Its terminal carboxylate groups are protonated in acidic pH, whereby the water soluble BTA molecules assemble into supramolecular hydrogels. Hydrogel films are prepared by an electrogelation process directly onto an ITO working electrode, to which a potential is applied. This overpotential induces a local pH change due to the generation of H^+ -ions in the vicinity of the electrode. The film thickness is controlled by the applied potentials and time. The film thickness was determined by *in situ* Peak Force Tapping Mode AFM.

3.2 Content of the Individual Publications

The approach presented in this study makes use of the dissolution of BTA-hydrogels upon basic pH. This dissolution takes place for bulk hydrogels as well as for electro-gelated hydrogel films. The FluidFM is used to inject a basic solution precisely in a local manner in order to structure the hydrogel films (*cf.* Figure 3.9 a). This 'chemical writing' process is governed by several parameters such as applied pressure and time. The influence of these parameters was investigated by so-called 'ramp & write'-cycles, whereby the FluidFM cantilever is approached to the surface and a pressure pulse with defined parameters (pressure and time) was applied. Afterwards the cantilever was retracted and moved to an untreated position of the film and a new cycle was initiated using different parameters (*cf.* Figure 3.9). The evaluation of patterns from AFM and CLSM images demonstrated that the removed volume of the hydrogel increased linearly with the injected volume of the basic solution (*cf.* Figure 3.9 b). Similar experiments, where the FluidFM cantilever was loaded with pure water, proofed that the removal of the hydrogel is based solely on chemical reactions and do not emerge due to the applied overpressure. The smallest spot size achieved with the presented method was around $2\ \mu\text{m}$, which is in the range of the used aperture. The application of even smaller aperture dimensions should result in smaller structures.

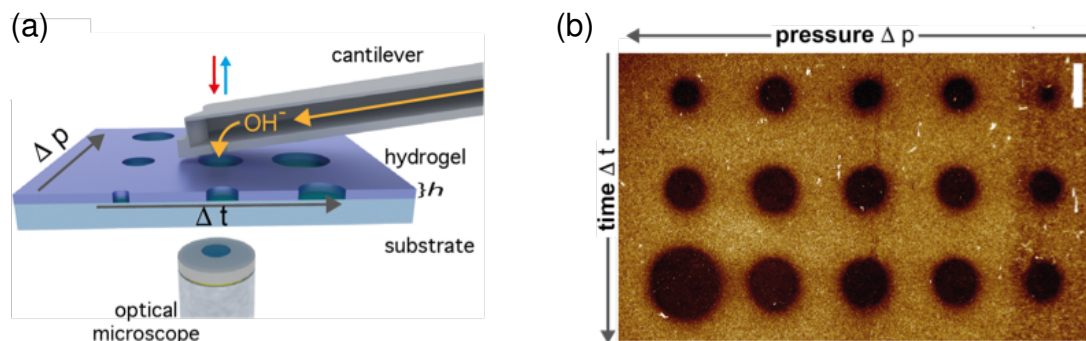


Figure 3.9: (a) Schematic illustration of the experimental FluidFM setup for the 'ramp & write'-cycles and (b) AFM topography image of several 'ramp & write'-cycles using different pressure pulses. The reduced film height of the dark areas corresponds to the removed parts of the hydrogel film. The white scale bar corresponds to $10\ \mu\text{m}$. Adapted with permission from Helfricht *et al.*, *Small*, **2017**, 13(31), 1700962, © 2017 WILEY-VCH Verlag & Co. KGaA, Weinheim.

Beside these static experiments, the FluidFM can be also moved over the surface during the structuring process. The obtained line width inversely depends on the velocity ($\Delta w \propto v^{-1}$). This finding is in good agreement with the deposition of nanoparticles us-

3 Synopsis

ing the FluidFM technique. [25] However, in contrast to solid surfaces no dependency on the loading force was found, which was attributed to the softness of the hydrogel films. In a first *proof-of-concept*, the controlled removal was achieved in terms of the film height as well. Therefore, the film thickness was increased by longer gelation times and a rectangular pattern was dissolved, in such a manner that the obtained cavity is not going down to the hard substrate. One application of such confinements would be substrates with compartments for single cell isolation, which require a soft surface.

The presented subtractive manufacturing technique by FluidFM is not limited to the used BTA hydrogel films and can be further extended to other stimuli-responsive hydrogels. Furthermore, the FluidFM technology can be applied in the future for a controlled deposition of active substances for trapped cells in the structured hydrogel films.

3.2.3 Novel and Specific AFM Probes

In the third part of the thesis, the motif of conventional colloidal probes (*e.g.* a colloidal particle glued to a cantilever) was developed in two different directions. The electrostatic interactions between two fiber fragments were determined in the special crossed-cylinder geometry (*cf.* Chapter 9). The *in situ* preparation of large and soft colloidal probes from hydrogel beads was used to determine their adhesion behaviour (*cf.* Chapter 10).

Long-Range Interaction Forces between Melt-Electrospun 1,3,5-Cyclohexane-trisamide Fibers in Crossed-Cylinder Geometry

The colloidal probe AFM technique is not limited to the attachment of spherical particles but can be further extended to cylindrical objects such as fibers. In Chapter 9 long-range interaction forces between individual fiber segments were investigated. The crossed-cylinder interaction geometry is well-known from the surface force apparatus [29, 30] and has been adapted for AFM in several studies. [31, 32, 33]

Fibers were prepared by a melt-electrospinning process using two different derivatives of 1,3,5-cyclohexanetrissamides (CTAs). These derivatives differ in their terminal functional groups of their periphery, namely alkyl- and fluorinated-groups, respectively. The obtained fibers had diameters in the range of around 5 μm and smooth surfaces with a roughness of several nanometers.

3.2 Content of the Individual Publications

Fragments of these fibers were permanently glued on tipless AFM cantilevers as well as on glass slides allowing for direct force measurements in the crossed-cylinder geometry. These measurements were only performed between symmetric combinations of CTA fiber types in order to determine their apparent diffuse layer properties. The attachment of fiber fragments led to a reduced lever arm. Therefore, an effective spring constant had to be considered. For a qualitative evaluation, the force profiles were normalised to the effective radius for two crossed-cylinders according to the Derjaguin approximation.

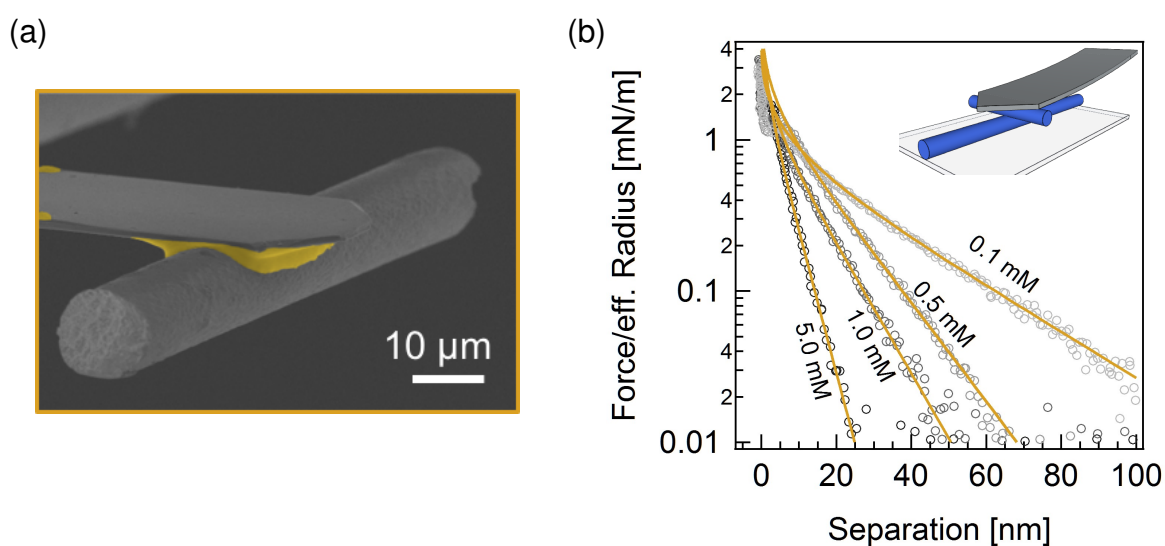


Figure 3.10: (a) SEM image of a CTA fiber segment glued onto an AFM cantilever. These fiber probes were used to determine the diffuse layer properties from direct force measurements (b) in the crossed-cylinder geometry (*cf.* inset). Adapted with permission from Neurgig *et al.*, *Polymer*, **2016**, 102, 363-371, © 2016 Elsevier Ltd.

The apparent diffuse layer potentials were evaluated from fits to full solutions of the Poisson-Boltzmann equation and constant charge approximation. The van der Waals interactions were neglected as surface roughness and the low Hamaker constants for alkyl- and fluorinated-surfaces would not lead to a significant contribution. As the direct force measurements for symmetric systems do not reveal the sign of the obtained diffuse layer potentials, the investigated fibers can be either negatively or positively charged, respectively. In order to validate the sign of the diffuse layer potentials, similar direct force measurements were performed using spherical silica colloidal probes. It is well-known from literature, that silica surfaces are negatively charged under the

3 Synopsis

investigated electrolyte conditions. Force profiles in the sphere-cylinder geometry revealed again pure repulsive interaction forces, indicating a negative sign of the apparent diffuse layer potential for both types of CTA fibers, which is in good agreement with previous studies. Since, these apparent charges arise from the asymmetric adsorption of water ions to hydrophobic surfaces. So far, this effect had been only observed for planar surfaces and not for such fibrillar systems. Furthermore, it was found that the fluorinated fibers beared a lower diffuse layer charge than the aliphatic ones, which was expected from several studies on planar surfaces examined with different techniques.

Probing the Adhesion of Alginate Hydrogel: A New Approach towards the Preparation of Soft Colloidal Probes for Direct Force Measurements

The standard preparation procedure for colloidal probes is carried out in air, whereby a thin wire is used to pick up and transfer a μm -sized particle onto a previously placed drop of glue on the AFM cantilever. Generally, this preparation method can be applied to nearly all solid particles without restriction. [16, 17] However, its application to colloidal probes of soft materials, especially hydrogels, was not possible. Hydrogels incorporate a high water content in a cross-linked polymeric structure and are prone to alterations of their properties upon drying. [34] For this purpose, a novel method has been developed allowing for a complete *in situ* preparation of colloidal probes from hydrogels to overcome current limitations.

Alginate hydrogel beads are chosen as model systems for soft colloidal probes, because they are well-known to undergo irreversible changes upon rehydration. [34] Hydrogel beads were obtained by injection of an alginic acid solution into a precipitation bath containing multivalent ions, which cross-link the anionic polysaccharide molecules. The resulting spherical hydrogel beads had diameters larger than $30\ \mu\text{m}$ and their expected low elastic modulus ($\sim 300\ \text{kPa}$) has been confirmed by AFM indentation measurements.

The novel method for the *in situ* preparation of colloidal probes presented in this study is based on micropipette techniques well known from microbiology. [35, 36] The complete manipulation is performed in aqueous environment, thereby preventing the critical drying step *e.g.* for hydrogels. A small amount of a particle suspension and a

3.2 Content of the Individual Publications

micropipette were placed into a water-filled petri dish (*cf.* Figure 3.11 a). The positioning of the micropipette is controlled by means of a micro-manipulator comparable to the preparation of colloidal probes in air. The aspirated hydrogel bead is attached to a chemically modified AFM cantilever with an adhesive layer. In the last step, the hydrogel bead is softly pressed against the cantilever, and the bead is released by applying an overpressure pulse. Figure 3.11 b shows an *in situ* prepared alginate colloidal probe.

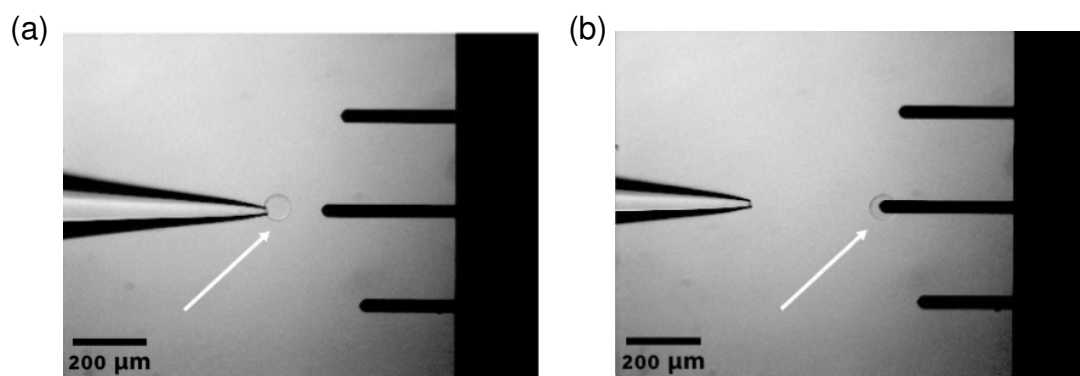


Figure 3.11: Representative optical microscopy images acquired during the *in situ* preparation of alginate hydrogel colloidal probes using micro-capillaries: (a) aspirated bead in the vicinity of an AFM cantilever and (b) final hydrogel colloidal probe with an attached bead to the middle cantilever. Adapted with permission from Helfricht *et al.*, *Soft Matter*, **2017**, 13, 578-589, © 2017 The Royal Society of Chemistry.

The applicability of the *in situ* prepared hydrogel probes was demonstrated in a first set of direct force measurements in the sphere-plane geometry *versus* a glass surface. Furthermore, the importance of the developed method for hydrogel materials was demonstrated by investigating the effect of drying, where the alginate probe was exposed to air with subsequent rehydration. These experiments revealed the alteration of the adhesive and mechanical properties, which are in line with a collapsed state of the network structure upon drying. Due to the low elastic modulus and the large particle size, several corrections for the data analysis had to be applied (*e.g.* determination of the *InvOLS* and introduction of an effective spring constant).

In situ prepared alginate hydrogel colloidal probes were used to probe the pull-off forces on various recombinant spider silk protein films with varying surface charge. In order to evaluate the adhesive behaviour in a semi-quantitative manner, similar

3 Synopsis

measurements were performed on self-assembled monolayers (SAMs) bearing a well-defined surface chemistry of specific functional groups (-CH₃, -OH, -COOH and -NH₂). It was found that the adhesive behaviour for these hydrogels is quite different compared to solid interfaces. Solvent exclusion is negligible due to the high water content incorporated in the network structure. The adhesion forces are mainly dominated by chemical interactions, namely hydrogen bonds and attractive electrostatic interactions. Therefore, the highest adhesion forces were evaluated on the NH₂-terminated SAMs, which even led to a partial disintegration of polysaccharide strands. The presented framework of the underlying adhesion process of alginate hydrogels allows to evaluate the measurements on complex protein films. Hence, these proteins are well-defined on the molecular level due to their amino acid sequence, despite the overall complexity of these biomaterials.

In conclusion, an *in situ* preparation method for colloidal probes from materials susceptible to drying was successfully developed. A further advantage of the presented method is that floating particles are aspirated from the solution preventing a contamination of the contact area compared to other methods, where particles were first immobilized on a surface.

3.3 Individual Contributions to Joint Publications

In this thesis, the results of seven scientific publications are compiled. Most of these publications were obtained within the framework of collaborative research projects. Hence, various co-authors participated in the research and writing of these publications. The individual contributions to each of the joint publications are specified in the following. The asterisks denote the corresponding authors.

A Direct Biocombinatorial Strategy towards Next Generation, Mussel-Glue Inspired Saltwater Adhesives (cf. Chapter 4)

*by Patrick Wilke, Nicolas Helfricht, Andreas Mark, Georg Papastavrou, Damien Faivre and Hans G. Börner**

Patrick Wilke developed the phage display biopanning, synthesized and characterised all polymer-peptide conjugates. Furthermore, he carried out and evaluated all QCM adsorption experiments. I implemented and improved the coupling strategy for the polymer-peptide conjugates. Moreover, I performed and evaluated all AFM single-molecule force spectroscopy experiments. Andreas Mark participated in programming the SMFS data evaluation routines. Prof. Dr. Georg Papastavrou, Dr. Damien Faivre and Prof. Dr. Hans Börner supervised the project and were involved in all scientific discussions. All authors contributed to writing the manuscript.

Surface properties of spider silk particles in solution (cf. Chapter 5)

Nicolas Helfricht, Maria Klug, Andreas Mark, Volodymyr Kuznetsov, Claudia Blüm, Thomas Scheibel and Georg Papastavrou**

I performed and evaluated most of the presented experiments, did the calculations according to the O'Brien and White theory and wrote the first draft of the manuscript. Moreover, I supervised Maria Klug within the framework of her bachelor thesis. She was involved in preliminary experiments, which include the determination of the electrophoretic mobility of the protein particles. Andreas Mark performed parts of the direct force measurements during a practical course under my supervision. Volodymyr Kuznetsov provided help with the first set of direct force measurements in the sphere-sphere geometry. Claudia Blüm prepared various batches of recombinant spider silk

3 Synopsis

protein particles. Prof. Dr. Thomas Scheibel and Prof. Dr. Georg Papastavrou supervised the project and were involved in scientific discussions. All authors revised the manuscript.

Colloidal Properties of Recombinant Spider Silk Protein Particles (*cf.* Chapter 6)

Nicolas Helfricht, Elena Doblhofer, Jérôme F. L. Duval, Thomas Scheibel and Georg Papastavrou**

I performed and evaluated all electrokinetic and AFM measurements. Furthermore, I wrote parts of the manuscript. Elena Doblhofer prepared different types of recombinant spider silk protein particles, including the multilayered spidroin particles. Dr. Jérôme F. L. Duval performed the calculations and simulations according to the electrokinetic theories of soft particles. He also wrote parts of the manuscript and was involved in scientific discussions. Prof. Dr. Thomas Scheibel participated in scientific discussions and corrected the publication. Prof. Dr. Georg Papastavrou supervised the project and wrote parts of the manuscript.

Extending the Limits of Direct Force Measurements: Colloidal Probes from Sub-Micron Particles (*cf.* Chapter 7)

*Nicolas Helfricht, Andreas Mark, Livie Dorwling-Carter, Tomaso Zambelli and Georg Papastavrou**

I performed all experiments using the FluidFM technique and evaluated the data. Andreas Mark wrote some of the algorithms used for the data conversion and evaluation. He also prepared the 'classical' colloidal probes and performed the corresponding direct force measurements. Livie Dorwling-Carter drilled small apertures into closed FluidFM cantilevers using the focussed ion beam under the supervision of Dr. Tomaso Zambelli. Prof. Dr. Georg Papastavrou supervised the project and wrote the first draft of the manuscript. All authors revised the manuscript.

Writing with Fluid: Structuring Hydrogels with Micrometer Precision by AFM in Combination with Nanofluidics (cf. Chapter 8)

Nicolas Helfricht¹, Andreas Mark¹, Marina Behr, Andreas Bernet, Hans-Werner Schmidt and Georg Papastavrou**

I performed all experiments using the FluidFM and characterized the structured hydrogel films via confocal laser scanning microscopy and prepared the samples for the SEM investigations. Furthermore, I evaluated the data and wrote parts of the manuscript. Andreas Mark implemented the electrogelation setup, optimized the parameters and prepared the hydrogel films. He also characterized the films by AFM and evaluated the resulting data. Marina Behr and Dr. Andreas Bernet provided the low-molecular weight gelator and gave advice concerning the hydrogel formation. Prof. Dr. Georg Papastavrou and I wrote the first draft of the manuscript. Prof. Dr. Hans-Werner Schmidt and Prof. Dr. Georg Papastavrou supervised the project and revised the manuscript.

Long-Range Interaction Forces between Melt-Electrospun 1,3,5-Cyclohexane-trisamide Fibers in Crossed-Cylinder Geometry (cf. Chapter 9)

Benedikt R. Neugirg, Nicolas Helfricht, Steffen Czich, Hans-Werner Schmidt, Georg Papastavrou and Andreas Fery**

Benedikt R. Neugirg carried out the direct force measurements, including the imaging of the fiber surfaces and the preparation of the fiber probes. He evaluated most of the data and wrote the first draft of the manuscript. I prepared the silica colloidal probes and evaluated parts of the data. Furthermore, I helped writing the manuscript and was involved in scientific discussions. Steffen Czich was in charge of the synthesis of the flourinated 1,3,5-cyclohexanetrissamides and the preparation of the fibers. The project was performed under the supervision of Prof. Dr. Hans-Werner Schmidt, Prof. Dr. Georg Papastavrou and Prof. Dr. Andreas Fery. They were also involved in scientific discussions and corrected the manuscript.

¹These authors contributed equally.

3 Synopsis

Probing the Adhesion of Alginate Hydrogel: A New Approach towards the Preparation of Soft Colloidal Probes for Direct Force Measurements (cf. Chapter 10)

*Nicolas Helfricht, Elena Doblhofer, Vera Bieber, Petra Lommes, Volker Sieber, Thomas Scheibel and Georg Papastavrou**

I developed the *in situ* preparation of soft colloidal probes, performed the AFM measurements, and evaluated the data. I wrote the first draft of the manuscript. Elena Doblhofer provided the recombinant spider silk protein films. Vera Bieber prepared some alginate colloidal probes during a lab course under my supervision. Petra Lommes prepared the polysaccharide solutions. Prof. Dr. Volker Sieber, Prof. Dr. Thomas Scheibel and Prof. Dr. Georg Papastavrou were involved in scientific discussions and revised the manuscript.

References

- [1] H-J Butt, B Cappella, and M Kappl. Force Measurements with the Atomic Force Microscope: Technique, Interpretation and Applications. *Surface Science Reports*, 59(1-6):1–152, 2005.
- [2] M I Giannotti and G J Vancso. Interrogation of Single Synthetic Polymer Chains and Polysaccharides by AFM-Based Force Spectroscopy. *The European Journal of Chemical Physics and Physical Chemistry*, 8(16):2290–2307, 2007.
- [3] N Helfrich, E Doblhofer, V Bieber, P Lommes, V Sieber, T Scheibel, and G Papatavrou. Probing the adhesion properties of alginate hydrogels: a new approach towards the preparation of soft colloidal probes for direct force measurements. *Soft Matter*, 13(3):578–589, 2017.
- [4] H Lee, B P Lee, and P B Messersmith. A reversible wet/dry adhesive inspired by mussels and geckos. *Nature*, 448:338–341, 2007.
- [5] B P Lee, P B Messersmith, J N Israelachvili, and J H Waite. Mussel-Inspired Adhesives and Coatings. *Annual Review of Materials Research*, 41(1):99–132, 2011.
- [6] H Lee, N F Scherer, and P B Messersmith. Single-molecule mechanics of mussel adhesion. *Proceedings of the National Academy of Sciences USA*, 103(35):12999–13003, 2006.
- [7] S Krysiak, Q Wei, K Rischka, A Hartwig, R Haag, and T Hugel. Adsorption mechanism and valency of catechol-functionalized hyperbranched polyglycerols. *Beilstein journal of organic chemistry*, 11:828–836, 2015.
- [8] E Doblhofer, A Heidebrecht, and T Scheibel. To spin or not to spin: spider silk fibers and more. *Appl Microbiol Biotechnol*, pages 1–22, 2015.
- [9] A S Lammel, X Hu, S-H Park, D L Kaplan, and T R Scheibel. Controlling silk fibroin particle features for drug delivery. *Biomaterials*, 31(16):4583–4591, 2010.
- [10] R W O'Brien and L R White. Electrophoretic mobility of a spherical colloidal particle. *J. Chem. Soc., Faraday Trans.*, 2:1607–1626, 1978.

3 Synopsis

- [11] M P Neubauer, C Blüm, E Agostini, J Engert, T Scheibel, and A Fery. Micromechanical characterization of spider silk particles. *Biomaterials Science*, 1:1160–1165, 2013.
- [12] A Meister, M Gabi, P Behr, P Studer, J Vörös, P Niedermann, J Bitterli, J Polesel-Maris, M Liley, H Heinzelmann, and T Zambelli. FluidFM: Combining Atomic Force Microscopy and Nanofluidics in a Universal Liquid Delivery System for Single Cell Applications and Beyond. *Nano Letters*, 9(6):2501–2507, 2009.
- [13] P Dörig, D Ossola, A M Truong, M Graf, F Stauffer, J Vörös, and T Zambelli. Exchangeable Colloidal AFM Probes for the Quantification of Irreversible and Long-Term Interactions. *Biophysical Journal*, 105(2):463–472, 2013.
- [14] E Doblhofer and T Scheibel. Engineering of recombinant spider silk proteins allows defined uptake and release of substances. *Journal of Pharmaceutical Sciences*, 104(3):988–994, 2015.
- [15] H Ohshima. Electrophoresis of soft particles. *Advances in Colloid and Interface Science*, 62(2):189 – 235, 1995.
- [16] Y Gan. Invited Review Article: A review of techniques for attaching micro- and nanoparticles to a probe’s tip for surface force and near-field optical measurements. *Review of Scientific Instruments*, 78(8):081101–9, 2007.
- [17] M Kappl and H J Butt. The colloidal probe technique and its application to adhesion force measurements. *Particle & Particle Systems Characterization*, 19(3):129–143, 2002.
- [18] F J Montes Ruiz-Cabello, M Moazzami-Gudarzi, M Elzbieciak-Wodka, P Maroni, C Labbez, M Borkovec, and G Trefalt. Long-ranged and soft interactions between charged colloidal particles induced by multivalent coions. *Soft matter*, 11(8):1562–1571, 2015.
- [19] F J Montes Ruiz-Cabello, G Trefalt, P Maroni, and M Borkovec. Electric double-layer potentials and surface regulation properties measured by colloidal-probe atomic force microscopy. *Physical Review E*, 90(1):012301–10, 2014.
- [20] H-J Butt. Measuring electrostatic, van der Waals, and hydration forces in electrolyte solutions with an atomic force microscope. *Biophysical Journal*, 60(6):1438–1444, 1991.

References

- [21] W A Ducker, T J Senden, and R M Pashley. Direct Measurement of Colloidal Forces Using an Atomic Force Microscope. *Nature*, 353(6341):239–241, 1991.
- [22] S Rentsch, R Pericet-Camara, G Papastavrou, and M Borkovec. Probing the validity of the Derjaguin approximation for heterogeneous colloidal particles. *Physical Chemistry Chemical Physics*, 8(21):2531–2538, 2006.
- [23] M Giesbers, J M Kleijn, and M Stuart. The Electrical Double Layer on Gold probed by Electrokinetic and Surface Force Measurements. *Journal of Colloid and Interface Science*, 248(1):88–95, 2002.
- [24] V Kuznetsov and G Papastavrou. Ion Adsorption on Modified Electrodes as Determined by Direct Force Measurements under Potentiostatic Control. *The Journal of Physical Chemistry C*, 118(5):2673–2685, 2014.
- [25] R R Grüter, J Vörös, and T Zambelli. FluidFM as a lithography tool in liquid: spatially controlled deposition of fluorescent nanoparticles. *Nanoscale*, 5(3):1097–1104, 2013.
- [26] L Hirt, S Ihle, Z Pan, L Dowling-Carter, A Reiser, J M Wheeler, R Spolenak, J Vörös, and T Zambelli. Template-Free 3D Microprinting of Metals Using a Force-Controlled Nanopipette for Layer-by-Layer Electrodeposition. *Advanced Materials*, 28(12):2311–2315, 2016.
- [27] L Hirt, A Reiser, R Spolenak, and T Zambelli. Additive Manufacturing of Metal Structures at the Micrometer Scale. *Advanced Materials*, 2017. DOI: 10.1002/adma.201604211.
- [28] A Bernet, R Q Albuquerque, M Behr, S T Hoffmann, and H-W Schmidt. Formation of a supramolecular chromophore: a spectroscopic and theoretical study. *Soft Matter*, 8(1):66–69, 2012.
- [29] J N Israelachvili. *Intermolecular and Surface Forces*. Elsevier, 3rd edition, 2011.
- [30] J N Israelachvili and G E Adams. Measurement of forces between two mica surfaces in aqueous electrolyte solutions in the range 0–100 nm. *Journal of the Chemical Society, Faraday Transactions 1: Physical Chemistry in Condensed Phases*, 74(0):975–1001, 1978.

3 Synopsis

- [31] L Meagher, G V Franks, M L Gee, and P J Scales. Interaction forces between α -alumina fibres in aqueous electrolyte measured with an atomic force microscope. *Colloids and Surfaces A: Physicochemical and Engineering Aspects*, 146(1–3):123 – 137, 1999.
- [32] I Muir, L Meagher, and M Gee. Interaction Forces between α -Alumina Fibers with Coadsorbed Polyelectrolyte and Surfactant. *Langmuir*, 17(16):4932–4939, 2001.
- [33] E Max, W Häfner, F W Bartels, A Sugiharto, C Wood, and A Fery. A novel AFM based method for force measurements between individual hair strands. *Ultramicroscopy*, 110(4):320–324, 2010.
- [34] R Vreeker, L Li, Y Fang, I Appelqvist, and E Mendes. Drying and rehydration of calcium alginate gels. *Food biophysics*, 3:361–369, 2008.
- [35] Y Zhang and L-C Yu. Microinjection as a tool of mechanical delivery. *Current Opinion in Biotechnology*, 19(5):506–510, 2008.
- [36] R M Hochmuth. Micropipette aspiration of living cells. *Journal of Biomechanics*, 33(1):15–22, 2000.

Scientific Publications

CHAPTER 4

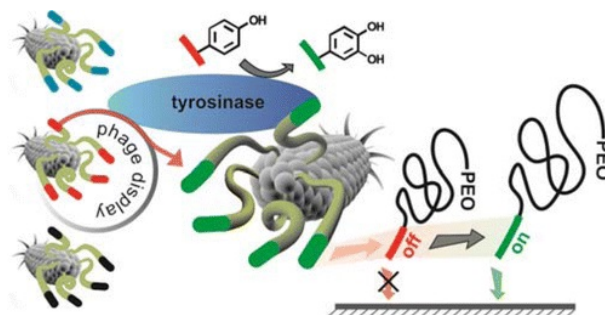
A Direct Biocombinatorial Strategy towards Next Generation, Mussel-Glue Inspired Saltwater Adhesives

Patrick Wilke,^a Nicolas Helfricht,^b Andreas Mark,^b
Georg Papastavrou,^b Damien Faivre,^c Hans Börner^{*a}

^a Department of Chemistry, Laboratory for Organic Synthesis of Functional Systems, Humboldt-Universität zu Berlin, 12490 Berlin, Germany. Email: h.boerner@hu-berlin.de

^b Physical Chemistry II, University of Bayreuth, Universitätsstr. 30, 95440 Bayreuth, Germany.

^c Department of Biomaterials, Max Planck Institute of Colloids and Interfaces, Science Park Golm, 14424 Potsdam, Germany.



Reprinted with permission from:

"A Direct Biocombinatorial Strategy toward Next Generation, Mussel-Glue Inspired Saltwater Adhesives", P. Wilke, N. Helfricht, A. Mark, G. Papastavrou, D. Faivre, H. Börner, *Journal of the American Chemical Society*, **2014**, 136(36), 12667-12674, DOI: 10.1021/ja505413e.

© 2014 American Chemical Society.

Abstract

Biological materials exhibit remarkable, purpose-adapted properties that provide a source of inspiration for designing new materials to meet the requirements of future applications. For instance, marine mussels are able to attach to a broad spectrum of hard surfaces under hostile conditions. Controlling wet-adhesion of synthetic macromolecules by analogue processes promises to strongly impact materials sciences by offering advanced coatings, adhesives, and glues. The *de novo* design of macromolecules to mimic complex aspects of mussel adhesion still constitutes a challenge. Phage display allows material scientists to design specifically interacting molecules with tailored affinity to material surfaces. Here, we report on the integration of enzymatic processing steps into phage display biopanning to expand the biocombinatorial procedure and enable the direct selection of enzymatically activable peptide adhesion domains. Adsorption isotherms and single molecule force spectroscopy show that those *de novo* peptides mimic complex aspects of bioadhesion, such as enzymatic activation (by tyrosinase), the switchability from weak to strong binders, and adsorption under hostile saltwater conditions. Furthermore, peptide-poly(ethylene oxide) conjugates are synthesized to generate protective coatings, which possess anti-fouling properties and suppress irreversible interactions with blood-plasma protein cocktails. The extended phage display procedure provides a generic way to non-natural peptide adhesion domains, which not only mimic nature but also improve biological sequence sections extractable from mussel-glue proteins. The *de novo* peptides manage to combine several tasks in a minimal 12-mer sequence and thus pave the way to overcome major challenges of technical wet glues.

4.1 Introduction

Marine mussels adhere rapidly in hostile environments onto practically any hard surface and in many aspects their adhesive properties still outperform state of the art wet glues. [1, 2] Tremendous efforts have been spent to understand and mimic the byssal adhesive system to realize bioinspired coatings or glues. [3, 4, 5, 6, 7] Waite *et al.* described the underlying biochemistry as a concerted process in which several purpose-adapted proteins are expressed, enzymatically processed, and excreted to form the adhesive byssus.[3, 8, 9, 10] Within those regulated processes the enzymatic oxidation of tyrosine residues in adhesive protein precursors has been identified as one of the key steps. [5, 11, 12] On the one hand, the generated L-3,4-dihydroxyphenylalanine (L-dopa) residues contribute to cohesion, building chemical cross-links between adhesive proteins. [10, 13] On the other hand, L-dopa plays a dominant role in adhesion, generating effective interfaces to various surfaces. [4, 7] Identification of the importance of L-dopa residues led to mussel-glue inspired polymers that mimic certain aspects

4.1 Introduction

of the mussel adhesives. The first segmented copolymers containing L-dopa were realized in a pioneering study by Yamamoto *et al.* in 1978. [14] Messersmith *et al.* significantly expanded the scope of applications and exploited L-dopa-containing polymers for materials and biomedical sciences. [1, 15, 16] For instance, poly(ethylene oxide)-*block*-(L-dopa)₁₋₃(PEO-(L-dopa)₁₋₃) led to anti-fouling coatings, and (PEO-L-dopa)₄ star polymers formed hydrogels with accurately adjustable mechanical properties. [17, 18] Deming *et al.* accessed poly(L-dopa-co-L-Lys) and demonstrated the utilization of chemical or enzymatic oxidation to remarkably improve cohesion in those adhesives. [12, 19] More recently, Börner *et al.* described the use of tyrosinase to activate adhesion properties of bioconjugates composed of PEO and a precursor segment of the mussel foot protein 1 of *Mytilus edulis* (mefp-1). [20]

However, mefp-1 serves in nature only as a protective coating of the mussel byssus. Hence, the enzyme activated mefp-1-*block*-PEO failed to adhere efficiently under seawater conditions. This failure imposed the need for finding more suitable sequences in order to improve bioinspired, enzyme-activated coatings and obtain synthetic sequence models to better understand and mimic bioadhesive processes.

Biocombinatorial approaches, such as phage display, represent a widely exploited strategy to select peptides or proteins that exhibit highly specific affinity to substrates. [21] The resulting methodology was applied to various biological entities, and more recently the exciting opportunities for materials sciences were explored. [22] Thereby, peptides have been selected, which discriminate between highly related semiconductor surfaces, [23] differentiate poly(methyl methacrylate)s with different tactility, [24] control biomimetic crystallization, [25, 26] or bind strongly to biomedical relevant material surfaces. [27, 28] However, these established biopanning methods are not applicable to directly screen for mussel inspired adhesives as the sequences of interest have to meet additional requirements apart from just specific interactions to a target surface (*cf.* Figure 4.1b).

Illustration of the advanced phage display cycle (a) consisting of a tyrosinase processing of the entire library (top) and biopanning under harsh conditions to select binding phages to be sequenced for bioconjugate synthesis (right) and the objective to select appropriate peptide sequences with desired property profiles from the sequential space spanned by the phage library (b).

Here, we describe an advanced biocombinatoric screening strategy that enables the selection of enzyme triggered adhesive peptides for construction aluminum. The common biopanning was expanded with a tyrosinase processing step leading to a generic procedure, which enables the direct selection of peptides having excellent substrate properties for the enzyme of interest

4 Mussel-Glue Inspired Saltwater Adhesives

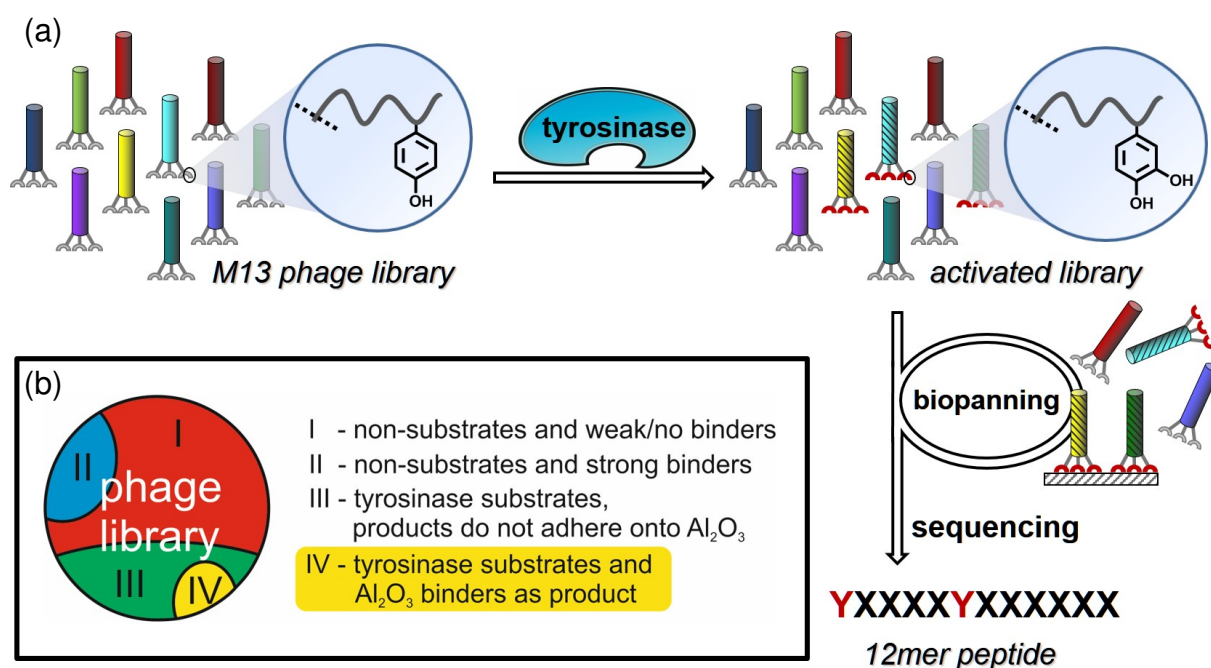


Figure 4.1: Illustration of the activated phage display cycle (a) consisting of a tyrosinase processing of the entire library (top) and biopanning under harsh conditions to select binding phages to be sequenced for bioconjugate synthesis (right) and the objective to select appropriate peptide sequences with desired property profiles from the sequential space spanned by the phage library (b).

(e.g., tyrosinase). Moreover, the peptides should in the non-activated state show weak or no binding to surfaces of interest. Activation of the peptide substrate by tyrosinase should significantly increase the adhesive properties leading to highly adhesive peptides, which even allow generating stable coatings under saltwater conditions.

4.2 Methods

Peptide/Conjugate Activation

Enzymatic activation kinetics of peptides and peptide-polymer conjugates were carried out using 100 units of tyrosinase and $0.29 \mu\text{mol}$ substrate in a final volume of 1 mL incubated at 25°C (protocol modified from procedures described by Waite *et al.*). [29] Peptide and conjugates ($0.29 \mu\text{mol}$) were dissolved in potassium phosphate buffer (17 mM, pH 6.5). Subsequently, the solution for activation of the peptides/conjugates was prepared by mixing $33 \mu\text{L}$ of 2.2 mM (for UV kinetics; activation to quinone) ascorbic acid or 220 mM (for QCM measurements, activation to L-dopa) sodium ascorbate and 100 units of tyrosinase in 50 mM potassium phosphate buffer (pH 6.5) with $10 \mu\text{L}$ of 0.2 mM L-dopa in a separate tube. To start the oxidation, this solution was

transferred to the peptide or conjugate. Kinetic plots were obtained for 15 h. Peptide conversion was evaluated *via* MALDI-TOF-MS.

UV-vis Kinetics

UV-vis spectroscopy was carried out on a Varian Cary 100 Bio UV-vis spectrophotometer (Agilent Technologies) with a Varian Cary temperature controller unit using quartz cuvettes (enzymatic assay). Peptide/Conjugate activation was monitored on a EonC Microplate Spectrophotometer (BioTec, Germany) using UV 96-well plates (Fisher Scientific, Germany). Kinetic plots were obtained at 25 °C reading at 280 nm.

Quartz Crystal Microbalance

Quartz crystal microbalance measurements were conducted on a Q-sense E1 single-sensor QCM-D module (Q-Sense, Sweden) with QE 401 electronic unit and equipped with a multi-channel pump (IPC Ismatec SA, Switzerland). Piezoelectric sensor crystals coated with 50 nm aluminum oxide (Q-Sense, Sweden) were cleaned in an ultrasonic bath with 2 % Helmanex in Milli-Q-water for 15 min and ethanol for 10 min prior to use. Subsequently, sensors were thoroughly washed Milli-Q-water and dried under compressed air flow. Finally, crystals were cleaned in a ZEPTO plasma cleaner (diener electronics, Germany) for 3 min at 75 W by air plasma. Immediately afterward, the sensors were mounted into the flow chamber and incubated with buffer using a flow rate of 100 μ L/min until the frequency signals were constant (1-3 h). Subsequently, samples with a concentration of 50 mg/mL in buffer were pumped into the flow chamber, and signals were again monitored until being constant. Following measurements were conducted with 0.8 mM potassium phosphate buffer (pH 6.5), 599 mM NaCl, 10 mg/mL bovine serum albumin (BSA) as well as fetal bovine serum and human serum. Experiments were performed at 22 °C (unless stated otherwise) and overtones 3, 5, 7, 9, 11, and 13 were recorded. If not stated otherwise, the third overtones of all experiments were used for evaluation of the frequency shift.

Single Molecule Force Spectroscopy

The single molecule force spectroscopy was performed with a MFP-Plus equipped with an ARC2-controller and a standalone base (Asylum Research, Santa Barbara, CA). The instrument was placed on an active vibration isolation and in an acoustic shielding. In order to detect the detachment of single peptides from the aluminum oxide surface the peptide has to be covalently coupled to the tip of an AFM cantilever by means of a PEO-spacer (*cf.* SI 4.7.3). Typically, the single molecule experiments have been performed with a ramp size of about 250 nm, which is significantly larger than the length of the PEO spacer. The single force curves were acquired

4 Mussel-Glue Inspired Saltwater Adhesives

at a cantilever velocity of about 100 nm/s and a data acquisition rate of 50000 kHz. In order to increase the probability of peptide binding, a dwell time of 4 s has been applied during which the probe remains in contact with the sample surface. For each peptide-PEO-modified cantilever at least 1000 curves at 5 different positions have been acquired. All measurements were performed in 0.8 mM potassium phosphate buffer (pH 6.5, without addition of ascorbic acid). The pH has been controlled directly before the measurements. As sample the same sensors as used for the QCM measurements have been used. The spring constant of the cantilevers has been determined by the thermal noise method. For the conversion of the raw data a program based on standard algorithms written in IGOR Pro (Wavemetrics) has been used (*cf.* SI 4.7.4).

4.3 Results and discussion

The selection of mussel inspired adhesion domains *via* phage display methodologies intends to find peptides that fulfill complex requirements, making the adaptation of biopanning protocols essential (*cf.* Figure 4.1). The selected sequences should be (i) effective enzyme substrates and (ii) possess in the non-activated state weak or no adhesive properties to the material surface of interest. From the sequential space of peptides that meet these requirements, the method has to furthermore discriminate sequence populations that (iii) will not adhere to the surface of interest after enzymatic processing.

Hence, a strategy was chosen that enables the selection of those sequences, for which adhesion will occur only after enzymatic activation (*cf.* Figure 4.1). A proof of principle was demonstrated by using mushroom tyrosinase as an inexpensive enzyme analogue of the oxidase from marine mussels, which process L-tyrosine residues into L-dopa. Aluminum (more accurately the alumina passivation layer of aluminum oxide) was chosen as one important lightweight construction material, where gluing and surface modification would be of interest.

The established protocols of biopanning had to be modified and accompanied by an enzymatic activation step. Figure 4.1 summarizes the adapted phage display and biopanning cycle. In contrast to common procedures, where phage-surface interactions are carefully equilibrated by long incubation times under mild conditions, the applied non-equilibrium biopanning uses comparatively harsh conditions (pH 4) and short contact times (1 s) to suppress the selection of non-activated strong binders. To select peptide sequences that exhibit strong adherence after being oxidized by tyrosinase, the entire phage library was enzymatically processed prior to the panning procedure. For that purpose, the phage pool was treated with tyrosinase (100 u/mL) and 0.1 mM ascorbic acid in potassium phosphate buffer (pH 6.5) for 3 h to oxidize the available tyrosine (Tyr) substrates. The reaction time was chosen as a compromise to activate the

4.3 Results and discussion

phage library most effectively but prevent activation of rather poor, slowly activable substrates. Noteworthy, short reaction times (1 h) did not result in significant enrichment of tyrosine in the selected binding domains (data not shown). After enzyme removal, the "activated" library was incubated with an Al_2O_3 surface in citrate buffer at pH 4 (10 repetitions of approximately 1 s). Rigorous washing steps at pH 2.2 with glycine hydrochloride buffer elute most of the non-activated phages from the Al_2O_3 surface as shown by reference experiments with the initial non-activated phage library (*cf.* SI). Final elution of residual strong binding phages was realized by trypsinization. The eluted subset of phages was isolated, amplified, and used for a second round, repeating the panning with increased selection pressure for a total of three rounds. Subsequently, a total of 44 phages were selected and sequenced. The resulting peptide sequences are summarized in Figure 4.2 (for the full sequence set *cf.* SI).

A successful selection procedure was suggested by the obvious increase of L-tyrosine residues in the selected set of peptides (*cf.* Figure 4.2). The total occurrence frequency for tyrosine over all found sequences was about 13 %, which comprises an accumulation with respect to 3.9 % in the initial library (*cf.* SI). Roughly 80 % of the analyzed peptides showed one or more tyrosine residues. From 44 sequenced phages, a total number of 30 sequences contained tyrosine, and only 8 peptides were tyrosine-free (6 phages did not show an insert). Furthermore, 5 different sequences contained 2-3 tyrosine residues. It has to be pointed out that phage display screening on aluminum substrates under standard conditions does not lead to an accumulation of tyrosine. [30] Generally, higher L-dopa content exhibits stronger adhesion. Nonetheless, mussel adhesive proteins contain up to approximately 30 mol% L-dopa. [2] It also has been shown that incorporation of L-dopa in for instance polystyrene polymers only showed stronger adhesion up to 33 mol%. [31] Therefore, a 12-mer peptide theoretically could contain up to 4 L-dopa moieties. For the present study, tyrosinase substrate characteristics of each tyrosine residue also are of high importance. Hence, 12-mer peptide sequences containing 2-3 tyrosine residues seem to constitute the best compromise out of activation and binding.

4 Mussel-Glue Inspired Saltwater Adhesives

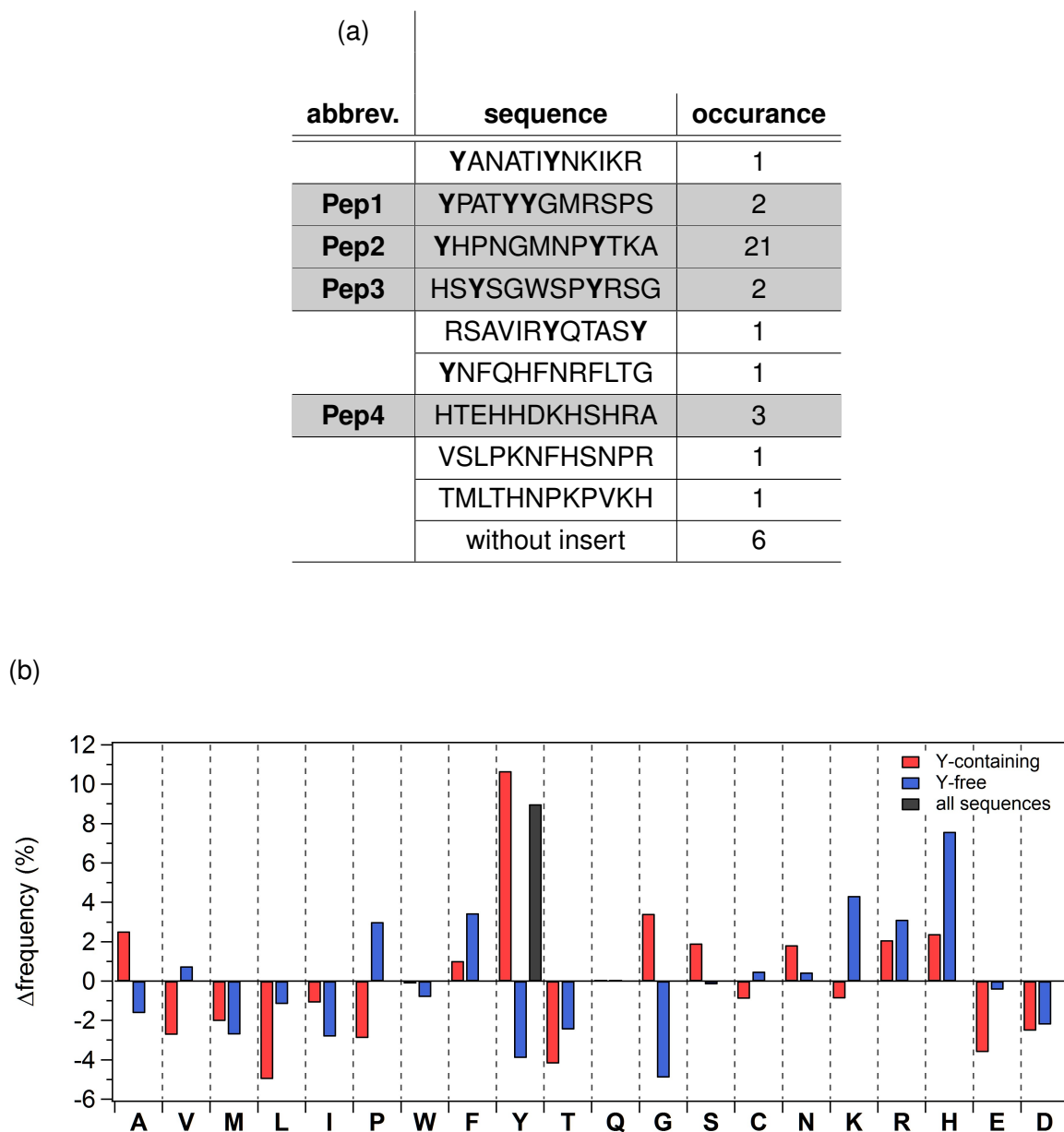


Figure 4.2: Excerpt from the 12-mer peptide adhesion domains selected from third round of enzyme activated phage display screening indicating an accumulation of tyrosine containing peptides (a) and in-depth analysis of the amino acid occurrence in the selected sequences showing the discrimination or enrichment of residues with respect to the occurrence in the initial phage library (b), statistics of tyrosine-containing peptides (red) and tyrosine-free peptides (blue) counted every sequence once and tyrosine content over all found sequences (black).

4.3 Results and discussion

Global sequence analysis of the tyrosine-containing peptides indicated a preference for N-terminal tyrosine residues. Out of the eight different enzymatically processable peptides, five show multiple tyrosine (Tyr) residues. Usually, polar amino acids populate the direct neighbor positions next to tyrosine, but further preferences of amino acids for certain sequence positions were not obvious. Figure 4.2 b summarizes the in-depth analysis of amino acid frequencies of residues that could be found in the selected sequences compared to the frequencies in the initial library. Counting every sequence only once and analyzing the subset of tyrosine-containing peptides, both acidic amino acids (E, D) and hydrophobic residues (V, M, L, P) obviously seem to be suppressed. Potentially the latter could be explained by lower substrate characteristics of tyrosine flanked by hydrophobic residues. Only minor deviation is shown for the majority of polar amino acids. Asparagine and serine are slightly enriched, whereas threonine is diminished. This was surprising, as previous reports of phage display on aluminum resulted in a dominance of hydroxyl group carrying amino acids, predominantly serine. [30] Nonetheless, besides tyrosine Pep₁ also contains two serine residues and one threonine, while Pep₃ bears even four serines. Basic amino acids with soft cations like arginine and histidine are slightly favored, reflecting the known interactions of cations with polar oxidic surfaces. [32] Moreover, a general enrichment of glycine and alanine in the tyrosine-containing sequences is evident. These residues generally offer increased conformational freedom to the peptide. It might be straightforward to speculate that this can contribute to the ease of enzymatic modification and/or optimized positioning of functionalities for surface contacts. Interestingly, the enriched types of amino acid residues are also more prominent in common motifs of mussel adhesive proteins. Sequences of mefp-3 and mefp-5 apart from L-dopa are dominated by very few amino acids such as glycine and basic amino acids. The mefp-5 protein additionally contains a high amount of serine residues, which are mostly phosphorylated in the active protein state. [33, 34, 35] Therefore, the biocombinatorial phage display approach obviously selects analogues of amino acid compositions, which are also relevant for the biological adhesive systems.

A different selection of amino acids was found, when peptide sequences that contain no tyrosine were analyzed, indicating alternative interaction modes of peptide binders without L-dopa. Most obviously, basic amino acids show a cumulative increase of ~11% if compared to the Tyr-bearing sequence set. This result was consistent with other biocombinatoric screenings on aluminum. [36] Proline and phenylalanine are slightly favored, whereas the other hydrophobic amino acids, including both glycine and alanine, are generally reduced.

From the pool of selected peptides, four different sequences have been chosen for further investigation (*cf.* Figure 4.2). Peptide-poly(ethylene oxide) conjugates (Pep-PEO) were synthesized to study enzyme substrate properties as well as adsorption/adhesion properties prior and after enzymatic processing. Two peptide sequences were chosen, which exhibit a seemingly

4 Mussel-Glue Inspired Saltwater Adhesives

important N-terminal tyrosine residue (Pep₁ and Pep₂). While Pep₁ was the only sequence containing three tyrosine residues and therefore might be the most promising adhesive, Pep₂ comprised the most abundant sequence found 21-times. Pep₃ was selected because it contains no N-terminal Tyr residue but one on sequence position 3. Moreover, Pep₃ shows on the one hand some sequence analogies to Pep₂ as Tyr⁹ shares related neighbors. On the other hand, similarities of tyrosine positions and their neighbors to the well-studied mefp-1 repetitive sequence are evident (AKPSY⁵PPTY⁹K; similar neighbors are underlined). [20] Furthermore, Pep₃ provides glycine, serine, histidine, and arginine. Hence, a relation to the composition of amino acids found in mussel adhesive protein mefp-5 is shown. [34, 35] Finally, Pep₄ represents the reference sequence for a non-tyrosine containing adhesion domain for aluminum oxide. The peptide-poly(ethylene oxide) conjugates with PEO blocks of $M_{n,PEO} = 3200$ were accessed *via* solid-phase supported synthesis by inverse conjugation strategies. [37] Prior work indicated that adhesion properties of peptide-PEO conjugates can be studied in comparison to non-conjugated peptides in a more accurate manner due to suppression of multilayer formation. [28]

UV-vis activation assays were carried out in order to investigate the substrate characteristics for each of the tyrosine containing conjugates. For this purpose, solutions of the different bioconjugates in pH 6.5 potassium phosphate buffer were oxidized by 100 u/mL tyrosinase in the presence of ascorbic acid (70 μ M). As the absorbance maximum of L-dopa is at 280 nm, enzymatic oxidation of tyrosine over time can be monitored at that wavelength (Figure 4.3). [29] Noteworthy, due to the UV absorbance of ascorbic acid, its applied concentration during UV kinetics cannot be sufficiently high to keep tyrosine oxidation in the L-dopa state over 8 h. Therefore, in the UV kinetics oxidation to the corresponding dopa-quinone-derivate is observed.

The kinetics indicate that all bioconjugates Pep₍₁₋₃₎-PEO have excellent tyrosinase substrate characteristics and oxidation levels off after approximately 2-4 h. MALDI-TOF-MS confirmed complete oxidation of both Pep₂-PEO and Pep₃-PEO (*cf.* SI, Figure S17 and S18). However, a quantitative oxidation of Pep₁-PEO under the applied conditions was not achieved. Mass spectrometry indicated a mixture of two and three oxidized tyrosines (*cf.* SI, Figure S16), which is consistent with the spectroscopic activity assay. Both Pep₂-PEO and Pep₃-PEO with two tyrosines result in a final absorbance of ~ 1.0 , whereas Pep₁-PEO containing three tyrosines reaches only ~ 1.2 . Noticeably, oxidation kinetics of non-conjugated Pep₃ showed a rather similar progression compared to Pep₃-PEO, suggesting that the PEO-block does not dramatically influence the enzyme-substrate recognition as previously also reported for congener bioconjugates. [20] Quantification of dopa-content of the PEO-peptide conjugates under the applied conditions is not trivial. Nonetheless, incubation of the synthetic di-dopa containing analogue Pep₃^{*-synth.}-PEO with tyrosinase under the same conditions as compared to the kinetic oxida-

4.3 Results and discussion

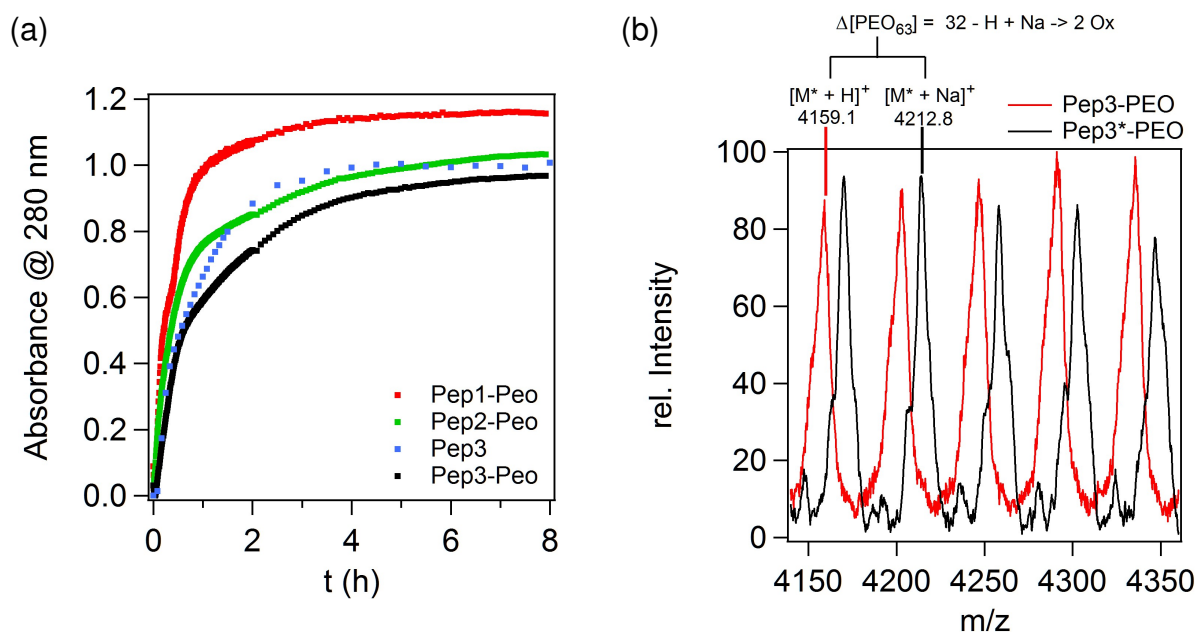


Figure 4.3: Enzymatic activation assays of Pep_3 and the $\text{Pep}_{(1-3)}$ -PEO conjugates revealing distinct differences in oxidation kinetics by UV spectroscopy (a) and MALDI-TOF-MS spectra of non-activated Pep_3 -PEO compared to L-dopa carrying activated Pep_3^* -PEO (b). Conditions: (a) and (b): 0.29 mM conjugates in potassium phosphate buffer (pH 6.5), 100 u/mL enzyme, 25 °C; (a) 70 μM ascorbic acid, (b) 7 mM ascorbate, 8 h.

tion experiments yielded a final absorbance of 0.99 ± 0.06 au at 280 nm (*cf.* SI). The absorption value meets the same absorption region reached by all activated bioconjugates, which contain 2 tyrosine residues. Hence, enzymatic activation of Pep_3 , Pep_2 -PEO, and Pep_3 -PEO can be considered as practically quantitative. Enzymatic oxidation of Pep_1 -PEO, which contained 3 Tyr residues, resulted obviously in a product mixture. To exclude that the tyrosinase oxidation of peptides was not leading to the formation a peptide exhibiting the dioxidation product L-trihydroxyphenylalanine (2,4,5 or 3,4,5 isomer, L-topa) instead of two L-dopa residues, MS/MS studies were performed (*cf.* SI, Figure S50). The fragmentation products of the oxidized Pep_3 sequence show two L-dopa moieties and exclude the L-topa formation pathway to occur under the given conditions.

To confirm the switchability of the bioconjugate adhesive-function, proof of an enzyme-induced transition of the peptide segments from weak to strong binders is required. For that purpose, quartz crystal microbalance (QCM) measurements have been conducted, investigating the enzymatically activable adhesion systems. The QCM experiments were carried out on aluminum oxide coated sensors, studying the adsorption and stability of the different non-activated $\text{Pep}_{(1-3)}$ -PEO precursors and the corresponding L-dopa carrying oxidation products. During bioconjugate activation for QCM adsorption studies, high amounts of ascorbate were used as-

4 Mussel-Glue Inspired Saltwater Adhesives

uring the immediate and quantitative reduction of L-dopaquinone residues as the immediate oxidation intermediate to L-dopa.

QCM experiments were performed at pH 6.5, where the oxidation mixture could be used directly without enzyme removal. At pH 4, which was required for high selection pressure-phage display, fast adsorption of tyrosinase to the QCM substrates was obvious (data not shown). This was not relevant during biopanning as the enzyme was carefully removed after phage library activation. Clearly, non-activated $\text{Pep}_{(1-3)}$ -PEO and activated $\text{Pep}_{(1-3)}^*$ -PEO bioconjugates were distinguishable in adsorption rates and reversibility (Figure 4.4). All precursor bioconjugates represent weak and reversible aluminum oxide binders as indicated by minor frequency shifts of the QCM sensor (7-8 Hz) and almost complete elution of the precursors from the surface upon rinsing with buffer (pH 6.5). After activation, however, the amounts of adhered materials significantly increased for all bioconjugates, proving the successful screening procedure to directly select peptides useful for enzyme activable coatings. The analysis of adsorption isotherms indicated distinct differences in the binding processes of the activated systems. Pep_3^* -PEO proved to be most efficient in terms of adsorption, reaching 85% of surface coating within 2 min. Application of the Voigt model [38] results in a calculated layer thickness of approximately 6 nm, suggesting an extended mushroom-like conformation of the conjugate. Pep_1^* -PEO and Pep_2^* -PEO also lead to efficient coatings, though reaching maximum surface coverage in a slower manner (*cf.* Figure 4.4 a). Interestingly, extensive washing steps with buffer lead only to minor removal of the bioconjugates, indicating a non-reversible coating under these conditions. More noteworthy, however, is the fact that all $\text{Pep}_{(1-3)}^*$ -PEO lead to a stable coating, even defying model seawater solutions such as high concentrations of NaCl (599 mM) and in case of Pep_3^* -PEO also nine salts solution (*cf.* SI, Figure S31). [39, 40] Control experiments exclude the interference of the enzyme with the coating process, as tyrosinase shows only minor, slow adsorption (*cf.* Figure 4.4). Furthermore, the comparison of enzyme activated Pep_3^* -PEO with directly synthesized, enzyme free $\text{Pep}_3^{\text{synth.}}$ -PEO shows equivalent adsorption isotherms and thus suggests enzyme co-adsorption to be negligible (*cf.* SI, Figure S28 and S29).

Adhesion under seawater conditions represents one of the major challenges for both technical wet glues and bioinspired coatings. [41, 42] Hence, experiments were carried out under saltwater conditions, investigating the binding, adsorption, and desorption properties of Pep_3^* -PEO as the most promising candidate. Figure 4.4 provides the QCM adsorption kinetics in 599 mM aqueous NaCl solution, which represents an established model electrolyte for seawater adhesion experiments. [39] Under these harsh, high-salt conditions, the activated bioconjugate Pep_3^* -PEO adhered effectively onto aluminum oxide surfaces, whereas both the nonactivated Pep_3 -PEO conjugate and the enzyme reference show very slow binding originating from a small

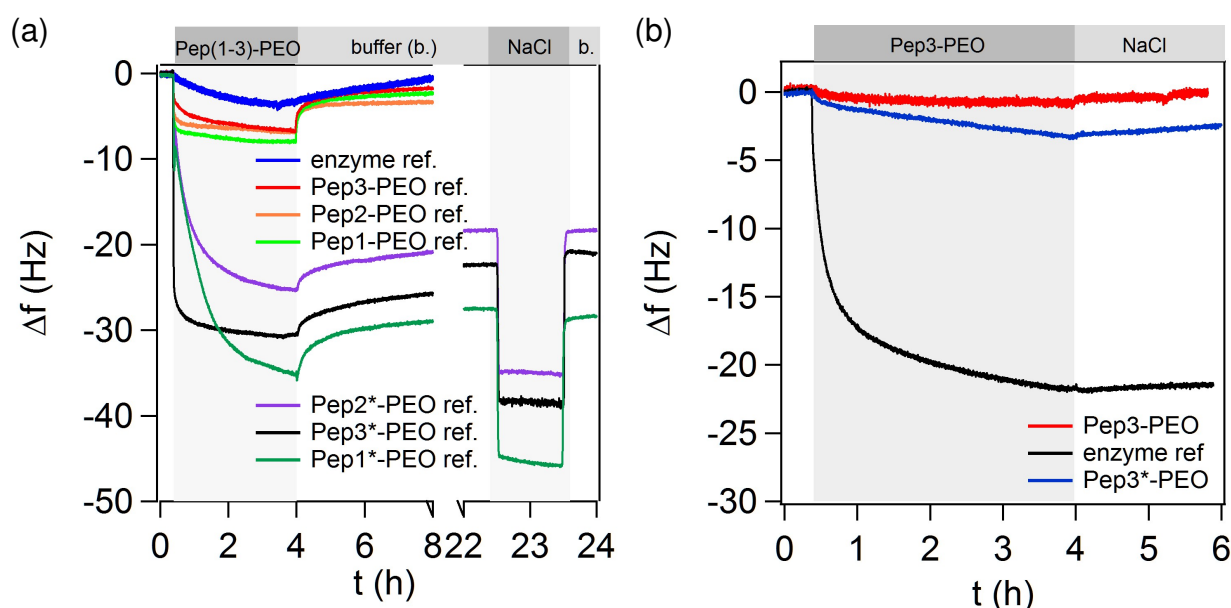


Figure 4.4: QCM adsorption and desorption kinetics of the set of bioconjugates in buffer (a) and under saltwater conditions (b). (a) Adsorption and desorption of non-activated conjugates $\text{Pep}_{(1-3)}\text{-PEO}$ compared to activated $\text{Pep}_{(1-3)}^*\text{-PEO}$ conjugates. (b) Adsorption and desorption kinetics of non-activated $\text{Pep}_3\text{-PEO}$ conjugate compared to the activated conjugate $\text{Pep}_3^*\text{-PEO}$ under saltwater conditions showing the effective generation of stable coatings in hostile environments. Conditions: (a) Buffer equilibrated aluminum oxide substrates were exposed to conjugate solutions and rinsed with 0.8 mM potassium phosphate buffer pH 6.5. The stability against saltwater was studied by rinsing the coatings with a solution of 599 mM NaCl, followed by buffer for end-point estimation and (b) solution of 599 mM NaCl.

sticking probability, which corresponds to low adhesion (*cf.* Figure 4.4 b).

Comparison of the adsorption isotherms of $\text{Pep}_3^*\text{-PEO}$ at high-salt conditions with those in buffer (Figure 4.4 b *versus* 4.4 a) revealed a slower adsorption in the presence of salt but the same final frequency shift of -21 Hz. Hence, for both electrolyte solutions (low- and high-salt), comparable amounts of $\text{Pep}_3^*\text{-PEO}$ have been adsorbed. Furthermore, reference experiments with the L-dopa-containing conjugate $\text{Y}^*\text{GY}^*\text{G-PEO}$ were carried out by QCM under comparable conditions (*cf.* SI, Figure S25). Noteworthy, only minor and reversible adsorption occurred in this case. This underlines the need for a more complex peptide sequence to compose multiple soft-interaction modes and mediate adhesion of binding L-dopa residues onto the target surface particularly under harsh conditions. Apparently, serine and arginine/histidine as common residues in adhesive domains significantly contribute to the Pep_3^* adhesion processes, particularly under high-salt conditions. To show the binding effects of amino acids apart from L-dopa, NMR techniques are currently used that might offer insights into molecular binding

4 Mussel-Glue Inspired Saltwater Adhesives

events (results will be reported elsewhere). Additionally, the frequency shifts for the plateaus in the Langmuir isotherms were used to determine the binding constants of Pep_3^* -PEO (*cf.* SI, Figure S46). [43] Under buffered conditions, an association saturation constant for Pep_3^* -PEO of $K_A = 1.63 \pm 0.32 \times 10^6 \text{ M}^{-1}$ has been determined, categorizing the L-dopa bearing bioconjugate as a very strong binder for aluminum oxide. [24] Even more important were binding constants for the activable system under saltwater conditions. Whereas non-activated Pep_3 -PEO did not show adsorption even at higher concentrations, for Pep_3^* -PEO a $K_{A,NaCl} = 4.00 \pm 0.70 \times 10^4 \text{ M}^{-1}$ could be calculated (*cf.* SI). As could be expected, the binding constant of the activated bioconjugate decreases in high ionic strength medium. However, the adhesive still shows remarkably high affinity toward aluminum oxide under these harsh conditions.

The adhesion of *de novo* 12-mer peptides can be probed by single molecule force spectroscopy (SMFS) based on the atomic force microscopy (AFM) in order to provide a more quantitative insight into the binding process on the molecular level. In the SMFS experiments the adhesion of the most promising candidate Pep_3 onto aluminum oxide was studied. For that purpose, Pep_3 and chemically (enzyme free) synthesized $\text{Pep}_3^{*synth.}$ were covalently coupled by Cys-maleimide ligation to a PEO-spacer that was attached on the other chain end to an amino-silane modified AFM-tip (Figure 4.5 a and SI Figure 4.7)). [44] The PEO-spacer and the peptide span a maximum length of approximately 110 nm in a fully extended, all-trans conformation. The SMFS measurements enable the comparison of the difference in adhesion for non-oxidized Pep_3 -PEO-Probes and $\text{Pep}_3^{*synth.}$ -PEO-Probes on aluminum oxide surfaces. A significant difference of binding strength between non-oxidized and oxidized peptide segments was observed and therefore confirmed the QCM findings. Exemplary, force-distance curves for Pep_3 -PEO-Probes and $\text{Pep}_3^{*synth.}$ -PEO-Probes are shown in Figure 4.5 (*cf.* c,d). Detachment events have been observed in about 35 % and 20 % of the force curves for $\text{Pep}_3^{*synth.}$ -PEO-Probe and Pep_3 -PEO-Probe, respectively. A scatter plot provides a summary of the detachment forces and related PEO-extension lengths for all unbinding events of peptides from the surface (*cf.* Figure 4.5 b). Clearly, the two peptides differ in the detachment forces and the corresponding extension lengths of the PEO-spacers. Whereas detachment of Pep_3 -PEO-Probes occurs generally at much lower forces and smaller separation lengths of 30-60 nm, $\text{Pep}_3^{*synth.}$ -PEO-Probe detachment occurs at larger forces and significantly longer distances of 60-100 nm. This difference was expected, as stronger surface binding of the activated peptide segment enables an extended stretching of the PEO-spacer before detachment occurs.

A quantitative evaluation provides insight into the forces acting on the molecular level. The unbinding forces for detachments are obtained for a selected set of PEO-peptide conjugates that have been identified by statistical means from a large number of force curves (*cf.* SI Figure 4.8). A bimodal distribution with remarkably high unbinding forces for $\text{Pep}_3^{*synth.}$ -PEO-Probes

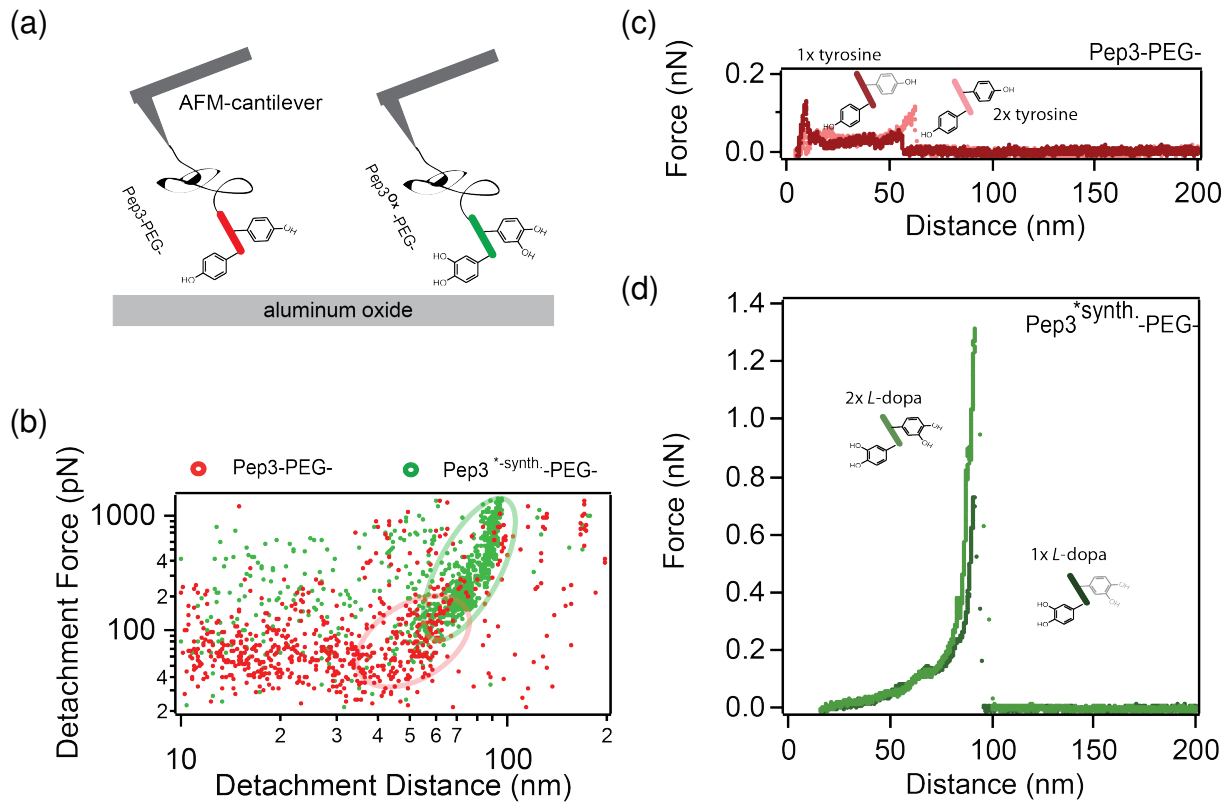


Figure 4.5: SMFS reveals differences in binding force between the activated (here synthesized, Pep₃^{*-synth.}) and the non-activated (Pep₃) domains on aluminum oxide surfaces and provides insights into interactions occurring on the molecular level. Schematic illustration of the measurement setup using a modified AFM-cantilever that bears a PEO-spacer with the non-activated (red) and activated peptides (green) Pep₃ and Pep₃^{*-synth.}, respectively (a). Scatter plots summarizing the forces required for the detachment of the adhesion domains from aluminum substrates in 0.8 mM potassium phosphate buffer (pH 6.7) together with the corresponding extension of the PEO-spacer (b). Exemplary force *versus* distance curves acquired with Pep₃-PEO-Probe and Pep₃^{*-synth.}-PEO-Probe (c, d). The large detachment forces for Pep₃^{*-synth.}-PEO-Probe can be attributed to one and two L-dopa moieties. By contrast, the forces for Pep₃-PEO-Probe correspond to interaction strengths expected for tyrosine.

4 Mussel-Glue Inspired Saltwater Adhesives

of 640 ± 140 and 1160 ± 390 pN, respectively, per activated peptide was observed. The latter detachment force is in the same order of magnitude as the force of 1.4 ± 0.3 nN necessary to rupture Au-S bonds, [45] but slightly too small to challenge a C-C bond with 2.6 nN. [46] On the other hand, non-activated Pep_3 -PEO-Probes show with about 55 ± 25 and 100 ± 25 pN a much weaker binding to the surface. Hence, Pep_3^* clearly leads to a very strong non-covalent binding. The interesting bimodality in the detachment forces for both peptides can be rationalized by the fact that the adhesive peptides exhibit two binding loci, e.g. $\text{Pep}_3^{*-synth.}$ -PEO-Probe bears two L-dopa residues enabling surface attachment *via* either both or only one L-dopa. Single molecule force spectroscopy enables tracing those binding events in the force curves (*cf.* Figure 4.5 c,d). These lower detachment forces for the peptides are in good agreement with the values reported by Messersmith *et al.* for L-tyrosine and L-dopa binders on oxidic surfaces. [47] Furthermore, the detachment of $\text{Pep}_3^{*-synth.}$ -PEO and Pep_3 -PEO as measured by SMFS is consistent with the binding behavior observed by QCM. Hence, the single molecule experiments suggest the origins of strong binding to be primarily mediated by L-dopa, confirming the importance of tyrosine for the activable adhesion systems.

The strong binding of Pep_3^* -PEO to aluminum oxide surfaces subsequently enables the preparation of "PEGylated" surfaces, which could suppress interactions with proteins and are of great interest for biomedical applications due to anti-fouling characteristics. QCM experiments were performed to study the adsorption of model proteins onto Pep_3^* -PEO coatings. Comparison of non-coated and coated aluminum oxide surfaces reveals significant reduction of protein adsorption. The latter coating results in an almost fully reversible protein adsorption. For instance, where bovine serum albumin (BSA) adsorbs strongly and irreversibly onto non-coated aluminum oxide leading to frequency shifts of about -35 Hz, Pep_3^* -PEO coated surfaces reduced the amount of adsorbed BSA by 72 % (Figure 4.6 a). A more effective coating was generated when adhesion of Pep_3^* -PEO was carried out closer to the PEO cloud point at 55 °C. [48] These more compact coatings completely defy BSA, leading to fully reversible adsorption (Figure 4.6 a). However, treatment of coatings with fetal bovine serum or human full blood serum seems to be more relevant for practical applications (*cf.* Figure 4.6 b and SI). Pep_3^* -PEO coated surfaces resist both protein cocktails, as sensor frequencies practically return to initial values upon buffer rinsing. Instead, non-coated Al_2O_3 surfaces show high and irreversible serum adsorption. Furthermore, on the non-coated surface adsorbed human serum proteins even precipitate upon rinsing with Millipore water, which can be suggested from the short frequency drop, while dissipation shows a fast formation of a rather rigid layer (*cf.* SI, Figure S37). In comparison, adsorption of serum proteins could be significantly reduced by 95 %. Thereby, anti-fouling properties of non-covalent Pep_3^* -PEO coatings show similar effects in the range of covalent aluminum coatings with comparable PEO layer thickness. [49] This low adsorption not only shows a sufficiently dense coating of PEO on the surface but also highlights the binding

strength of Pep₃*-PEO on aluminum oxide, as displacement by proteins is negligible.

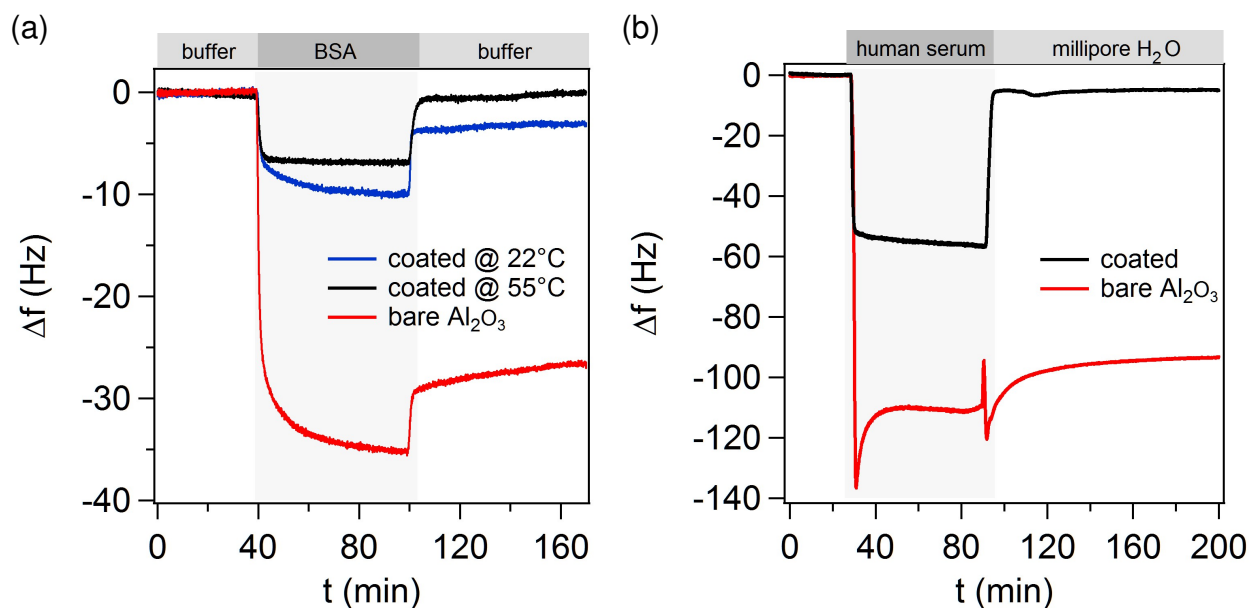


Figure 4.6: QCM experiments demonstrating the anti-fouling properties of Pep₃*-PEO coated aluminum compared to non-coated aluminum oxide surfaces. (a) Kinetics and reversibility of BSA adsorption onto Pep₃*-PEO coatings (coating @ 22 and 55 °C) revealing near cloud point coatings to be most efficient. (b) Adsorption isotherms demonstrating the reversibility of the adsorption of human serum protein cocktails on Pep₃*-PEO coated aluminum (coating @ 55 °C compared to non-coated aluminum).

4.4 Conclusion

In conclusion, the integration of an enzymatic processing step into phage display biopanning enabled the direct selection of 12-mer peptides, which serve as excellent *de novo* substrates for tyrosinase. As implemented by the screening conditions, the native non-oxidized peptides show weak binding properties to aluminum surfaces but switch toward high-strength binders after being oxidized by tyrosinase. Measurements of the adsorption kinetics for resulting peptide-*block*-poly(ethylene oxide) bioconjugates (Pep-PEO) in non-activated and activated state highlight dramatic changes in the adsorption rates, adsorption constants, and reversibility of adsorption upon rinsing. Noticeably, all coatings of the activated bioconjugates (Pep*-PEO) withstood intense washing with model seawater solutions. The most promising candidate was HSY*SGWSPY*RSG-*block*-PEO (Pep₃*-PEO, where Y* equals L-dopa) as adherence took place effectively even under high-salt conditions. SMFS quantified the dramatic differences in adhesion for Pep₃-PEO (nonactivated) and Pep₃*-*synth*-PEO (activated), revealing a maximum difference in binding forces per peptide molecule by a factor of approximately 10. Langmuir

4 Mussel-Glue Inspired Saltwater Adhesives

adsorption isotherms indicated for Pep₃*-PEO binding constants of $K_A = 1.63 \times 10^6 \text{ M}^{-1}$, categorizing the oxidized adhesion domain as a very strong binder. The resulting coatings exhibited anti-fouling properties, as adsorption of BSA proteins and full blood serum was strongly reduced and practically reversible upon washing. The directed selection of *de novo* adhesive peptides *via* extended phage display biopanning enabled one to realize tyrosinase activated adhesives showing a transition from weak to strong binders. Extended phage display screening offers direct access to enzymatically processable non-natural peptide domains. The study demonstrated the identification of activable adhesion domains and provides further insight into the concerted process of complex bioadhesion. However, the process is more generic and might pave the way toward the general screening for suitable substrates for a large variety of posttranslational modifications.

4.5 Associated content

Supporting Information Materials; methods; phage display data; NMR, IR, MALDI, and HPLC results for synthesized substances; MALDI of activated peptides/conjugates; QCM experiments under various conditions; SMFS data evaluation. This material is available free of charge *via* the Internet at <http://pubs.acs.org>.

4.6 Acknowledgments

The authors acknowledge Dr. S. Weidner (BAM-Berlin) for enabling access to the MALDI-TOF-MS instrument, Dr. E. Krause (FMP Berlin) for the NanoLC-MS/MS analytic, K. Linkert (HU Berlin) for synthesis of control peptides, and T. Schwemmer (HU Berlin) and J. Baumgartner (MPIKG, Potsdam) for introduction to phage display. H.G.B. and D.F. would like to acknowledge financial support by the German research council (DFG BEKs BO1762/5-1). Further support was granted for HGB by the European Research Council under the European Union' 7th Framework Program (FP07-13)/ERC starting grant "Specifically Interacting Polymer-SIP" (ERC 305064). This research was supported in DF's lab by the Max Planck Society and a starting Grant from the European Research Council (Project MB2, no. 256915). G.P. acknowledges support by the German research council (SFB 840).

4.7 Supporting Information¹

4.7.1 Materials

Single Molecule AFM Measurements

Malhex-NH-PEG-O-C₃H₆-CONHS ($M = 9256$ Da, $D = 1.03$, Rapp Polymere GmbH, Tübingen, Germany) and 3-aminopropyldiisopropylethoxysilane (ABCR, Karlsruhe, Germany) were used as received for the modification of the AFM-cantilevers (PPP-CONT, Nanosensors, Wetzlar, Germany). The heterofunctional PEO has been stored at -20 °C and was dissolved in dimethylsulfoxide (anhydrous, ≥ 99.9 %, Sigma-Aldrich). Sodium chloride (≥ 99 %, Aldrich) and formic acid (≥ 99 %, Grüssing, Germany) were used as received.

4.7.2 Instrumentation

The single molecule force spectroscopy was performed with a MFP-Plus equipped with an ARC2- controller and a standalone base (Asylum Research, Santa Barbara, CA). The instrument was placed on an active vibration isolation and an acoustic shielding.

4.7.3 Methods

Single Molecule AFM Measurements

In order to detect the detachment of single peptides from the aluminum oxide surface the peptide has to be covalently coupled to the tip of an AFM cantilever by means of a PEO-spacer. [50, 44] AFM contact mode cantilevers made from silicon (PPP-CONT without Al-coating and a nominal spring constant of about 0.2 N/m, Nanosensors) were cleaned with MilliQ-water and ethanol (p.a., VWR) before modification. In order to obtain a large number of OH-groups at the Si-surface the cantilevers were exposed to O₂-plasma (0.2 mbar, 100 % O₂) in a plasma cleaner (Plasma Technology) connected to an O₂-generator (DeVilbiss Healthcare). The silanization has been carried out in the gas phase. The freshly cleaned cantilevers were directly transferred into a petri dish containing 500 μ L 3-aminopropyldiisopropylethoxysilane. The dish has been placed in a desiccator to which vacuum has been applied for about 1 min by means of a membrane pump (Vacuubrand, Germany). The silanization has been carried out overnight for at least 12 h. After silanization, the cantilevers were thoroughly cleaned with ethanol in order to remove unreacted silane and rinsed with the buffer solution (50 mM potassium phosphate, pH 7.5 , 150 mM NaCl) used for the coupling of the PEO-spacer to the silanized cantilevers. For the

¹The Supporting Information is given here in condensed form and is restricted to the AFM related experiments. The entire Supporting Information is available in the Appendix 11.0.1

4 Mussel-Glue Inspired Saltwater Adhesives

coupling the cantilevers were placed in vessel containing the buffer solution. The malhex-PEO-NHS-spacer was dissolved in dry DMSO resulting in final concentration of 20 mM; 50 μ L of this solution were added for each mL of buffer solution. The reaction was performed for 1 h at room temperature in the dark. After the reaction the cantilever were first cleaned with the potassium phosphate buffer (pH 7.5) and afterwards with the buffer solution for peptide coupling (0.1 M potassium phosphate, pH 7.0). Coupling of the peptides was carried out simultaneously but in different reaction vessels. Each of the two peptides (Pep₃ and Pep₃^{*-synth.}) were both dissolved in MilliQ-water with a final concentration of 0.1 mM. For each of the peptides 0.8 mL of peptide solution was added to 3.2 mL potassium phosphate buffer (0.1 M, pH 7.0, 0.1 % formic acid) in a separate vessel. After 1 h reaction time, the cantilevers were rinsed first with the phosphate buffer (0.1 M potassium phosphate, pH 7.0) and then with the buffer solution (0.8 mM potassium phosphate, pH 6.5) used also for the AFM-measurements. The peptide-PEO-modified cantilevers were stored before the measurements in this buffer for not more than one week and ascorbic acid was added to avoid oxidation of the peptides during storage (0.7 mM, degassed solutions). Directly before use the cantilevers were rinsed with copious amounts of buffer solution containing no ascorbic acid.

Typically, the single molecule experiments have been performed with ramp-size of about 250 nm, which is significantly larger than the length of the PEO-spacer. The single force curves were acquired at a cantilever velocity of about 100 nm/s and data acquisition rate of 50000 kHz. In order to increase the probability of peptide binding, a dwell time of 4 seconds has been applied during which the probe remains in contact with the sample surface. For each peptide-PEO-modified cantilever at least 1000 curves at 5 different positions have been acquired. All measurements were performed in 0.8 mM potassium phosphate buffer (pH 6.5, without addition of ascorbic acid). The pH has been controlled directly before the measurements. As sample the same sensors as used for the QCM measurements have been used. The spring constant of the cantilevers has been determined by the thermal noise method. [51] For the conversion of the raw data program based on standard algorithms written in IGOR Pro (Wavemetrics) has been used.

4.7.4 Single molecule force spectroscopy: Data evaluation

AFM cantilever were prepared according to the procedure described above (section 4.7.3). Figure 4.7 shows the reaction of an amine functionalized cantilever with NHS-activated PEO. Subsequently, a cysteinyl-carrying peptide is introduced *via* maleimide-thiol coupling.

For the data evaluation only curves containing clearly identifiable detachments events have been taken into consideration. To reduce the signal-to-noise ratio, the raw data were smoothed by a boxcar average of 41 points and a reduction of the data points by a factor of 10 in anal-

4.7 Supporting Information

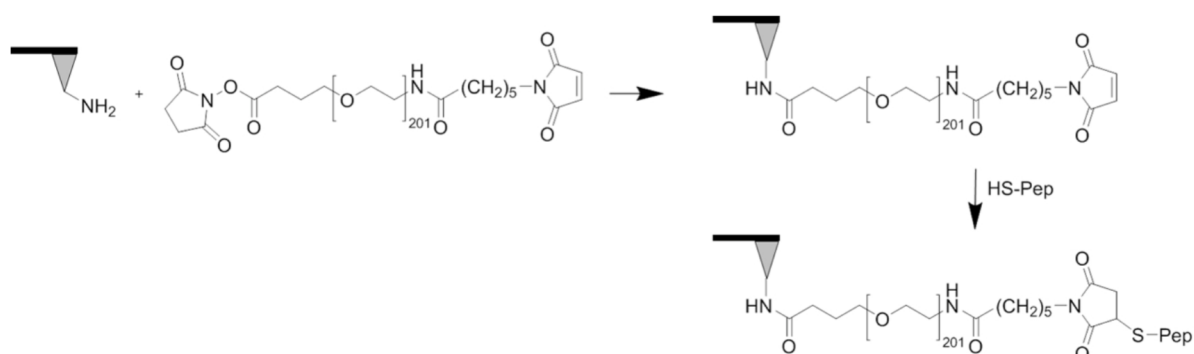


Figure 4.7: Preparation of functionalized AFM cantilever with Pep_3 and $\text{Pep}_3^{*synth.}$.

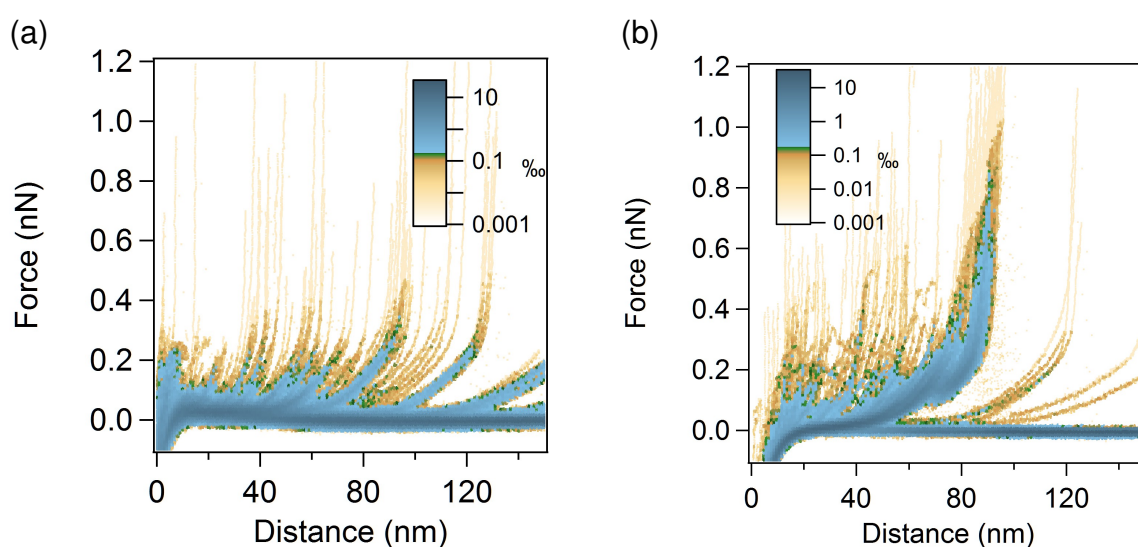


Figure 4.8: Superposition of single force curves obtained with a cantilever modified by a PEO-spacer and (a) Pep_3 and (b) $\text{Pep}_3^{*synth.}$, respectively. The colour scale is based on the percentage of data points falling in a two-dimensional data bin (10 pN and 1 nm, respectively).

ogy to recently reported single molecule force spectroscopy experiments [52]. The detachment events were detected by modified algorithm based on the work of Gergerly *et al.* [53] and implemented in custom written program in IGOR PRO. This algorithm has been used previously [54, 55]. The detachment events obtained by this automatic evaluation are summarized for both peptides in the scatter plots of Figure 4.5 (b). In order to demonstrate that always the same PEO-spacer is stretched and thus same peptides are detaching from the QCM-D sensor all force plots are superimposed, as proposed recently [56]. The force *versus* distance profiles in Figure 4.8 were obtained by binning the single data points in terms of force and distance intervals (10 pN and 1 nm, respectively).

A statistical evaluation of the detachment data results in the histograms shown in Figure 4.9

4 Mussel-Glue Inspired Saltwater Adhesives

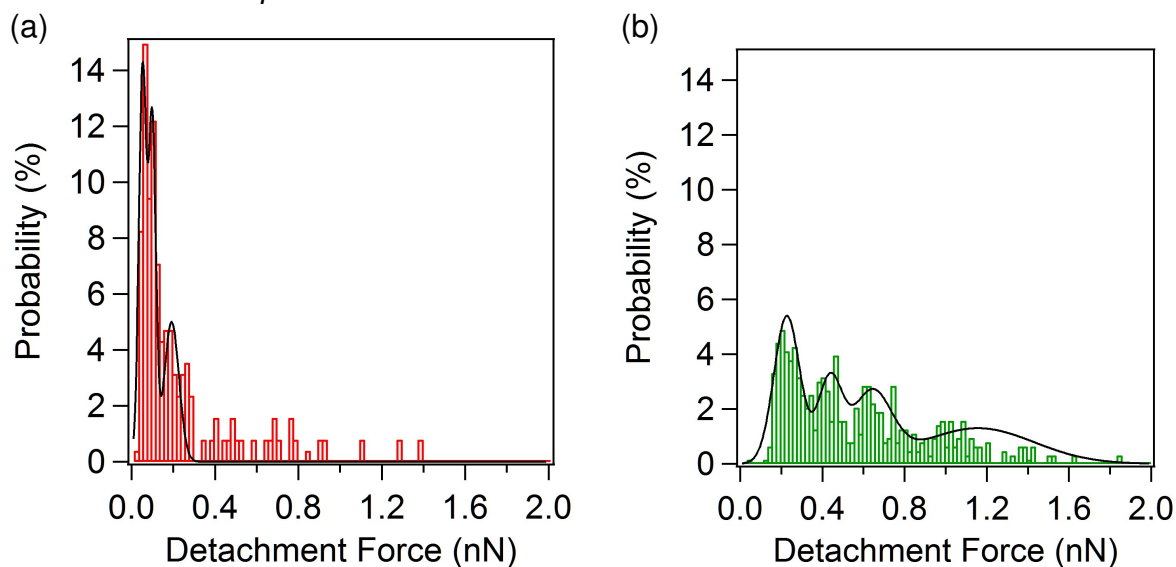


Figure 4.9: Histogram of the detachment forces for (a) Pep₃ and (b) Pep₃^{*}-synth., respectively.

where the detachment forces for the two different peptides can be identified. The solid lines are based on a multi-peak fits of Gaussians implemented in IGOR PRO and correspond to the forces stated in the text.

A detailed analysis of the detachment events revealed the occurrence of additional pull-off forces for Pep₃^{*}-synth.-PEO-Probe with around 225 ± 90 and 430 ± 90 pN. This set is probably attributed to the oxidative formation of dopa-quinone from L-dopa moieties as the forces are comparatively well in line with the values of dopa-quinone on titanium substrates reported by Messersmith and coworkers. [47]

References

- [1] H Lee, B P Lee, and P B Messersmith. A reversible wet/dry adhesive inspired by mussels and geckos. *Nature*, 448:338–341, 2007.
- [2] B P Lee, P B Messersmith, J N Israelachvili, and J H Waite. Mussel-Inspired Adhesives and Coatings. *Annual Review of Materials Research*, 41(1):99–132, 2011.
- [3] T H Waite and M L Tanzer. Polyphenolic Substance of *Mytilus edulis*: Novel Adhesive Containing L-Dopa and Hydroxyproline. *Science*, 212(4498):1038–1040, 1981.
- [4] H Lee, S M Dellatore, W M Miller, and P B Messersmith. Mussel-Inspired Surface Chemistry for Multifunctional Coatings. *Science*, 318(5849):426–430, 2007.
- [5] Q Lin, D Gourdon, C Sun, N Holten-Andersen, T H Anderson, J H Waite, and J N Israelachvili. Adhesion mechanisms of the mussel foot proteins mfp-1 and mfp-3. *Proceedings of the National Academy of Sciences*, 104(10):3782–3786, 2007.
- [6] T J Deming. Mussel byssus and biomolecular materials . *Current Opinion in Chemical Biology*, 3(1):100 – 105, 1999.
- [7] C E Brubaker and P B Messersmith. The Present and Future of Biologically Inspired Adhesive Interfaces and Materials. *Langmuir*, 28(4):2200–2205, 2012.
- [8] J H Waite, T J Housley, and M L Tanzer. Peptide repeats in a mussel glue protein: theme and variations. *Biochemistry*, 24(19):5010–5014, 1985.
- [9] D S Hwang, H Zeng, A Masic, M J Harrington, J N Israelachvili, and J H Waite. Protein- and Metal-dependent Interactions of a Prominent Protein in Mussel Adhesive Plaques. *Journal of Biological Chemistry*, 285(33):25850–25858, 2010.
- [10] L A Burzio and J H Waite. Cross-Linking in Adhesive Quinoproteins: Studies with Model Decapeptides. *Biochemistry*, 39(36):11147–11153, 2000.
- [11] P B Messersmith. Multitasking in Tissues and Materials. *Science*, 319(5871):1767–1768, 2008.
- [12] M Yu, J Hwang, and T J Deming. Role of L-3,4-Dihydroxyphenylalanine in Mussel Adhesive Proteins. *Journal of the American Chemical Society*, 121(24):5825–5826, 1999.
- [13] M J Harrington, A Masic, N Holten-Andersen, J H Waite, and P Fratzl. Iron-Clad Fibers: A Metal-Based Biological Strategy for Hard Flexible Coatings. *Science*, 328(5975):216–220, 2010.

4 Mussel-Glue Inspired Saltwater Adhesives

- [14] H Yamamoto and T Hayakawa. Improved synthetic method and conformation studies of polymers and copolymers of L- β -3,4-dihydroxyphenyl- α -alanine with L-glutamic acid. *Polymer*, 19(10):1115 – 1117, 1978.
- [15] J Su, F Chen, V L Cryns, and P B Messersmith. Catechol Polymers for pH-Responsive, Targeted Drug Delivery to Cancer Cells. *Journal of the American Chemical Society*, 133(31):11850–11853, 2011.
- [16] K C L Black, J Yi, J G Rivera, D C Zeladko-Leon, and P B Messersmith. Polydopamine-enabled surface functionalization of gold nanorods for cancer cell-targeted imaging and photothermal therapy. *Nanomedicine*, 8(1):17–28, 2013.
- [17] J L Dalsin, B-H Hu, B P Lee, and P B Messersmith. Mussel Adhesive Protein Mimetic Polymers for the Preparation of Nonfouling Surfaces. *Journal of the American Chemical Society*, 125(14):4253–4258, 2003.
- [18] N Holten-Andersen, M J Harrington, H Birkedal, B P Lee, P B Messersmith, K Y C Lee, and J H Waite. pH-induced metal-ligand cross-links inspired by mussel yield self-healing polymer networks with near-covalent elastic moduli. *Proceedings of the National Academy of Sciences*, 108(7):2651–2655, 2011.
- [19] M Yu and T J Deming. Synthetic Polypeptide Mimics of Marine Adhesives. *Macromolecules*, 31(15):4739–4745, 1998.
- [20] P Wilke and H G Börner. Mussel-Glue Derived Peptide-Polymer Conjugates to Realize Enzyme-Activated Antifouling Coatings. *ACS Macro Letters*, 1(7):871–875, 2012.
- [21] J F Smothers, S Henikoff, and P Carter. Affinity Selection from Biological Libraries. *Science*, 298(5593):621–622, 2002.
- [22] T Douglas and M Young. Viruses: Making Friends with Old Foes. *Science*, 312(5775):873–875, 2006.
- [23] S R Whaley, D S English, E L Hu, P F Barbara, and A M Belcher. Selection of peptides with semiconductor binding specificity for directed nanocrystal assembly. *Nature*, 405:665–668, 200.
- [24] T Serizawa, H Matsuno, and T Sawada. Specific interfaces between synthetic polymers and biologically identified peptides. *Journal of Materials Chemistry*, 21:10252–10260, 2011.
- [25] J Baumgartner, M A Carillo, K M Eckes, P Werner, and D Faivre. Biomimetic Magnetite Formation: From Biocombinatorial Approaches to Mineralization Effects. *Langmuir*, 30(8):2129–2136, 2014.

References

- [26] D Gebauer, A Verch, H G Börner, and H Cölfen. Influence of Selected Artificial Peptides on Calcium Carbonate Precipitation - A Quantitative Study. *Crystal Growth Design*, 9(5):2398–2403, 2009.
- [27] M Sarikaya, C Tamerler, A K-Y Jen, K Schulten, and F Baneyx. Molecular biomimetics: nanotechnology through biology. *Nature Materials*, 2:557–585, 2003.
- [28] T Schwemmer, J Baumgartner, D Faivre, and H G Börner. Peptide-Mediated Nanoengineering of Inorganic Particle Surfaces: A General Route toward Surface Functionalization via Peptide Adhesion Domains. *Journal of the American Chemical Society*, 134(4):2385–2391, 2012.
- [29] K Marumo and J H Waite. Optimization of hydroxylation of tyrosine and tyrosine-containing peptides by mushroom tyrosinase. *Biochimica et Biophysica Acta (BBA) - Protein Structure and Molecular Enzymology*, 872(1-2):98 – 103, 1986.
- [30] R Zuo, D Örnek, and T K Wood. Aluminum- and mild steel-binding peptides from phage display. *Applied Microbiology and Biotechnology*, 68(4):505–509, 2005.
- [31] C R Matos-Perez, J D White, and J J Wilker. Polymer Composition and Substrate Influences on the Adhesive Bonding of a Biomimetic, Cross-Linking Polymer. *Journal of the American Chemical Society*, 134(22):9498–9505, 2012.
- [32] A Vallee, V Humblot, and C-M Pradier. Peptide Interactions with Metal and Oxide Surfaces. *Accounts of Chemical Research*, 43(10):1297–1306, 2010.
- [33] V V Papov, T V Diamond, K Biemann, and J H Waite. Hydroxyarginine-containing Polyphenolic Proteins in the Adhesive Plaques of the Marine Mussel *Mytilus edulis*. *Journal of Biological Chemistry*, 270(34):20183–20192, 1995.
- [34] D S Hwang, H J Yoo, J H Jun, W K Moon, and H J Cha. Expression of Functional Recombinant Mussel Adhesive Protein Mgfp-5 in *Escherichia coli*. *Applied and Environmental Microbiology*, 70(6):3352–3359, 2004.
- [35] J H Waite and X Qin. Polyphosphoprotein from the Adhesive Pads of *Mytilus edulis*. *Biochemistry*, 40(9):2887–2893, 2001.
- [36] B L Adams, A S Finch, M M Hurley, D A Sarkes, and D N Stratis-Cullum. Genetically Engineered Peptides for Inorganics: Study of an Unconstrained Bacterial Display Technology and Bulk Aluminum Alloy. *Advanced Materials*, 25(33):4585–4591, 2013.
- [37] J-F Lutz and H G Börner. Modern trends in polymer bioconjugates design. *Progress in Polymer Science*, 33(1):1 – 39, 2008.

4 Mussel-Glue Inspired Saltwater Adhesives

- [38] F Höök, B Kasemo, T Nylander, C Fant, K Sott, and H Elwing. Variations in Coupled Water, Viscoelastic Properties, and Film Thickness of a Mefp-1 Protein Film during Adsorption and Cross-Linking: A Quartz Crystal Microbalance with Dissipation Monitoring, Ellipsometry, and Surface Plasmon Resonance Study. *Analytical Chemistry*, 73(24):5796–5804, 2001.
- [39] M F Sharqawy, J H Lienhard, and S M Zubair. Erratum to Thermophysical properties of seawater: A review of existing correlations and data. *Desalination and Water Treatment*, 29(1-3):355–355, 2011.
- [40] P Marden, A Tunlid, K Malmcrona-Friberg, O Göran, and S Kjelleberg. Physiological and morphological changes during short term starvation of marine bacterial isolates. *Archives of Microbiology*, 142:326–332, 1985.
- [41] R J Stewart, T C Ransom, and V Hlady. Natural underwater adhesives. *Journal of Polymer Science Part B: Polymer Physics*, 49(11):757–771, 2011.
- [42] M M Rahman, I Lee, H-H Chun, H D Kim, and H Park. Properties of waterborne polyurethane-fluorinated marine coatings: The effect of different types of diisocyanates and tetrafluorobutanediol chain extender content. *Journal of Applied Polymer Science*, 131(4):39905.1–39905.7, 2014.
- [43] T Wangchareansak, C Sangma, P Ngermmeesri, A Thitithanyanont, and P A Lieberzeit. Self-assembled glucosamine monolayers as biomimetic receptors for detecting WGA lectin and influenza virus with a quartz crystal microbalance. *Analytical and Bioanalytical Chemistry*, 405(20):6471–6478, 2013.
- [44] A Ebner, L Wildling, R Zhu, C Rankl, T Haselgrübler, P Hinterdorfer, and H J Gruber. Functionalization of Probe Tips and Supports for Single-Molecule Recognition Force Microscopy. In P Samori, editor, *STM and AFM Studies on (Bio)molecular Systems: Unravelling the Nanoworld*, pages 29–76. Springer-Verlag, Berlin, 2008.
- [45] M Grandbois, M Beyer, M Rief, H Clausen-Schaumann, and H E Gaub. How Strong Is a Covalent Bond? *Science*, 283(5408):1727–1730, 1999.
- [46] S S Sheiko, F C Sun, A Randall, D Shirvanyants, M Rubinstein, H-I Lee, and K Matyjaszewski. Adsorption-induced scission of carbon-carbon bonds. *Nature*, 440:191–194, 2006.
- [47] H Lee, N F Scherer, and P B Messersmith. Single-molecule mechanics of mussel adhesion. *Proceedings of the National Academy of Sciences*, 103(35):12999–13003, 2006.

References

- [48] P Kingshott, H Thissen, and H J Griesser. Effects of cloud-point grafting, chain length, and density of PEG layers on competitive adsorption of ocular proteins. *Biomaterials*, 23(9):2043 – 2056, 2002.
- [49] T Weber, M Bechthold, T Winkler, J Dauselt, and A Terfort. Direct grafting of anti-fouling polyglycerol layers to steel and other technically relevant materials. *Colloids and Surfaces B: Biointerfaces*, 111(0):360 – 366, 2013.
- [50] I Popa, R Berkovich, J Alegre-Cebollada, C L Badilla, J A Rivas-Pardo, Y Taniguchi, M Kawakami, and J M Fernandez. Nanomechanics of HaloTag Tethers. *Journal of the American Chemical Society*, 135(34):12762–12771, 2013.
- [51] J L Hutter and J Bechhoefer. Calibration of atomic-force microscope tips. *Review of Scientific Instruments*, 64(7):1868–1873, 1993.
- [52] J P Junker and M Rief. Single-molecule force spectroscopy distinguishes target binding modes of calmodulin. *Proc Natl Acad Sci USA*, 106(34):14361–14366, 2009.
- [53] C Gergely, B Senger, J-C Voegel, J K H Hörber, P Schaaf, and J Hemmerle. Semi-automatized processing of AFM force-spectroscopy data. *Ultramicroscopy*, 87(1-2):67 – 78, 2001.
- [54] G Papastavrou, L J Kirwan, and M Borkovec. Decomposing Bridging Adhesion between Polyelectrolyte Layers into Single Molecule Contributions. *Langmuir*, 22(26):10880–10884, 2006.
- [55] Ö Kaftan, S Tumbiolo, F Dubreuil, R Auzély-Velty, A Fery, and G Papastavrou. Probing Multivalent Host–Guest Interactions between Modified Polymer Layers by Direct Force Measurement. *The Journal of Physical Chemistry B*, 115(24):7726–7735, 2011.
- [56] M Zocher, C Zhang, S G F Rasmussen, B K Kobilka, and D J Müller. Cholesterol increases kinetic, energetic, and mechanical stability of the human β 2-adrenergic receptor. *Proceedings of the National Academy of Sciences*, 109(50):E3463–E3472, 2012.

CHAPTER 5

Surface Properties of Spider Silk Particles in Solution

Nicolas Helfricht,^a Maria Klug,^a Andreas Mark,^a Volodymyr Kuznetsov,^a Claudia Blüm,^b
Thomas Scheibel,^{*b} Georg Papastavrou^{*a}

^a Physical Chemistry II, University of Bayreuth, Universitätsstr. 30, 95440 Bayreuth, Germany. Email:
Georg.Papastavrou@uni-bayreuth.de

^b Lehrstuhl Biomaterialien, University of Bayreuth, Universitätsstr. 30, 95440 Bayreuth, Germany.
Email: Thomas.Scheibel@uni-bayreuth.de



Reprinted with permission from:

"Surface properties of spider silk particles in solution", N. Helfricht, M. Klug, A. Mark, V. Kuznetsov, C. Blüm, T. Scheibel and G. Papastavrou, *Biomaterials Science*, **2013**, 1, 1166, DOI: 10.1039/C3BM60109A.

© 2013 Royal Society of Chemistry.

Abstract

Recombinant spider silk proteins, such as eADF4(C16), can be used for various applications. Colloidal particles of eADF4(C16) show potential as drug delivery systems. Tuning the colloidal properties of suspensions of eADF4(C16) particles represents a major prerequisite for their use in pharmaceutical formulations. In this study we determined the surface properties concerning inter-particle interactions by means of electrophoretic mobility and direct force measurements. The surface charge of eADF4(C16) spider silk particles was determined as a function of ionic strength and pH, respectively. The resulting electrophoretic mobility can be described using the O'Brien and White theory and is directly related to the amino acid sequence of the protein. We determined the extension of a fuzzy protein layer protruding into the solution by direct force measurements using a colloidal probe technique. This soft layer leads to deviations in the electrophoretic mobility and is responsible for additional repulsive forces at small separation distances. These steric forces lead to a stabilization of the particle suspension at high ionic strength.

5.1 Introduction

Spider silk is known to combine properties such as biocompatibility and mechanical strength. [1, 2, 3] Recombinant spider silk production provides spider silk proteins in large quantities and enables the development of silk-based materials for a large number of applications. [4, 5] In addition to the naturally occurring spider silk fibers, recombinant spider silk proteins can be assembled into various other shapes, such as films and particles, being particularly useful for distinct drug delivery applications. [5, 6, 7, 8] One prerequisite for applying spider silk particles in pharmaceutical formulations is the stability of the colloidal suspensions, *e.g.* over a wide range of electrolyte concentrations. [6] A rational approach to tune the properties of spider silk particles for specific applications is based on the control of the resulting inter-particle forces and colloidal properties such as surface charge, roughness or mechanical properties. Here, we resolved the surface properties of spider silk particles made of the recombinant spider silk protein eADF4(C16) by their electrophoretic mobility as well as by direct force measurements. We further demonstrate that the colloidal properties of the spider silk particles are directly related to the amino-acid sequence of the underlying eADF4(C16).

5.2 Results and discussion

5.2.1 Amino acid composition and surface properties of spider silk particles

eADF4(C16) spider silk particles (Fig. 5.1a) were obtained by salting out the protein using potassium phosphate as described previously. [7] As shown in Scheme 5.2, one eADF4(C16) molecule contains 16 glutamic acid residues (one per C-module), which represent the only functional groups dissociated at a moderate pH value, as their pK_a is around 4.3. The termini of eADF4(C16) provide one amino- and carboxyl-group, respectively. However, these contribute to a much smaller extent to the charging behaviour due to their highly acidic / basic pK_a values and their low occurrence. The methionine residue at the amino-terminus is most likely post-translationally removed in *E. coli*, resulting in a terminal alanine residue that has a similar pK_a value. [9] Each C-module also contains two tyrosine residues (32 in total per eADF4(C16)), with a relatively high pK_a , and thus tyrosine residues are only of importance at very basic pH values. Furthermore, the T7-Tag contains one arginine residue with an extremely high pK_a , which has been neglected in the following as it is not in the examined pH-range.

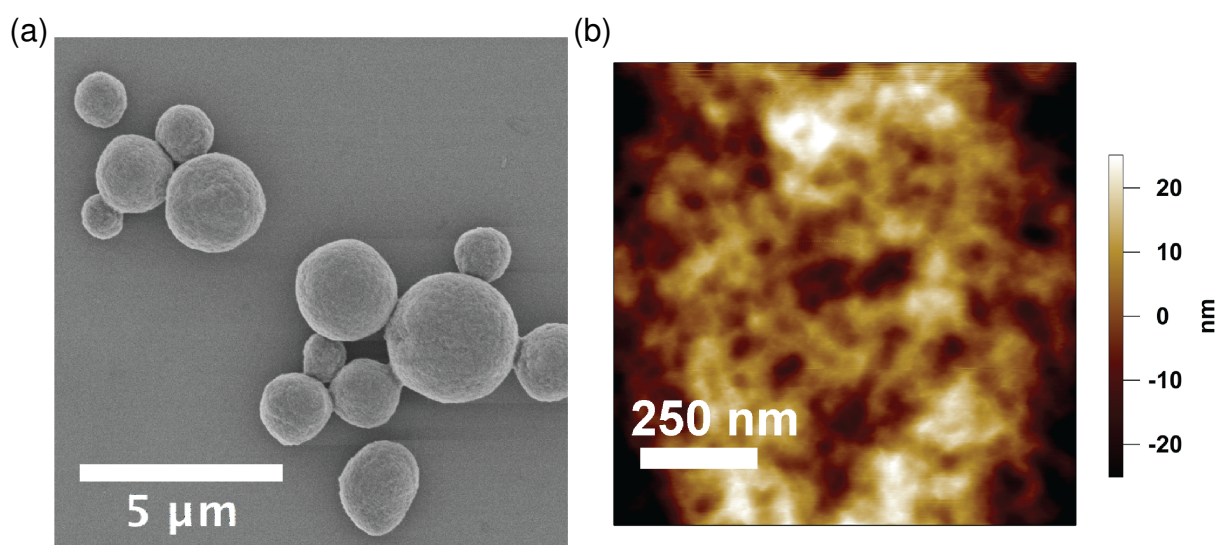


Figure 5.1: (a) SEM-image of eADF4(C16) particles in the dehydrated state. (b) Surface topography acquired at the apex of an eADF4(C16) particle in solution by AFM in Tapping Mode.

Table 5.1 compiles the ionizable entities in eADF4(C16) with their relative occurrence per module and the corresponding pK_a . The pK_a of the surface can be approximated by the pK_a for the isolated amino acids [10] due to their low occurrence per molecule, which results in a large

5 Surface Properties of Spider Silk Particles in Solution

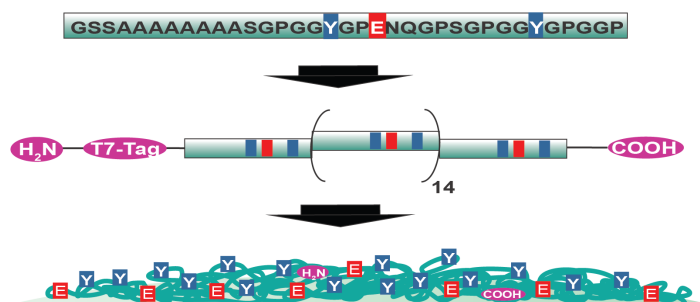


Figure 5.2: Schematic representation of the consensus sequence of ADF4, the engineered recombinant eADF4(C16) and the particle surface distribution of the amino acids.

separation between ionizable groups. From their occurrence per protein one can directly infer in a first order approximation the surface coverage Γ (in groups per area) of the spider silk particle. This approximation assumes that the surface composition of the spider silk particles does not deviate significantly from the composition per molecule and that the amino acids occupy comparable volumes. Its validity is experimentally directly accessible by determining the electrophoretic mobility of the particles.

Dehydrated particles (Fig. 5.1a) have an average diameter of $2.1 \pm 0.8 \mu\text{m}$, which increases upon hydration with a volume-swelling factor of 2.3. [11] The resulting particle diameter of $2.8 \mu\text{m}$ is used in the following. The particle morphology remains relatively constant over one batch and is shown in detail for the dried state in the ESI Section 5.6.1. The particle surface retains its smooth topography in solution with a root mean square (rms) roughness of $17.3 \pm 4.3 \text{ nm}$ as obtained by Tapping Mode AFM in liquid (Fig. 5.1b).

5.2.2 Electrophoretic mobility

Fig. 5.3a shows the electrophoretic mobility at two different ionic strengths (*i.e.* 1 mM and 10 mM, respectively) as a function of pH. As expected from the amino acid composition and the pK_a , the negative value of the electrophoretic mobility increases with increasing pH yielding a plateau above pH 8. At neutral pH no mobilities could be determined due to the ill-defined pH-values on the time scale of the mobility measurements in this regime. The experimental data can be readily compared to calculations based on the theory of O'Brien and White [12] and a surface composition as given by Γ_{mob} in Table 5.1. In contrast to the Debye-Hückel and Helmholtz-Smoluchowski equations, normally used to relate ζ -potential and electrophoretic mobility, the O'Brien and White theory takes the relaxation effect of the surrounding ion cloud into account. [12, 13] Therefore, we varied Γ_{mob} by about $\pm 30\%$, as indicated by the coloured area

5.2 Results and discussion

in Fig. 5.3, to allow calculations for a variation of the surface composition of eADF4(C16) particles in respect to the properties of single eADF4(C16) molecules. Furthermore, the surface coverage of the tyrosine residues could be significantly lower at the surface due to steric contributions and a more positive hydrophathy index, which has been taken into consideration by the values in brackets in Table 5.1. The experimental data are in very good agreement with the theoretical calculations, especially at acidic pH. The observed charge reversal is in agreement with the theoretical isoelectric point of 3.48 for single eADF4(C16) molecules. [4] The plane of shear, determining when hydrodynamic drag acts on the ion layer, has been chosen as 0.25 nm in agreement with comparable studies. [14, 15]

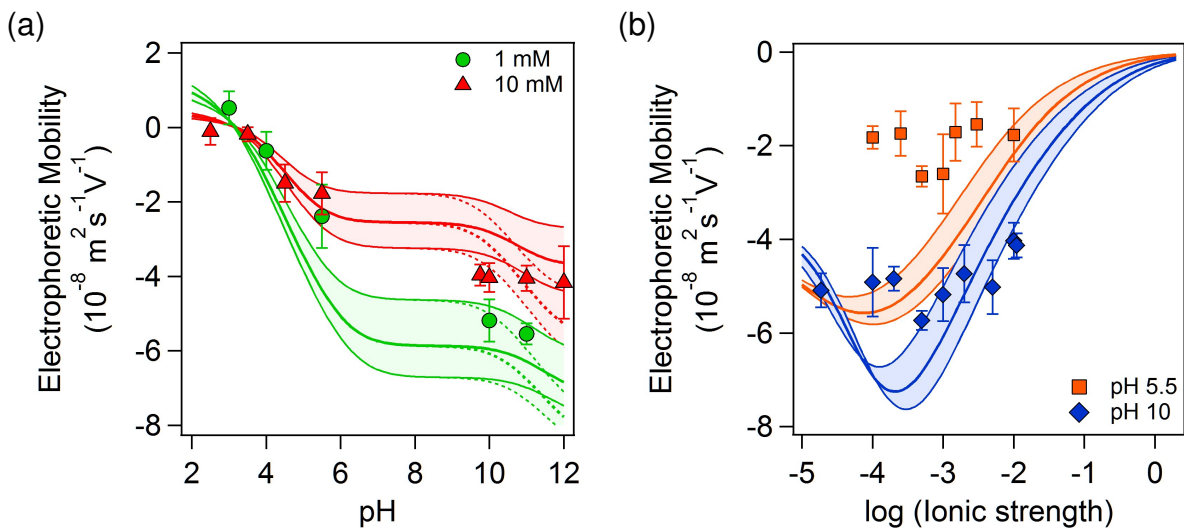


Figure 5.3: Electrophoretic mobility measured as a function of (a) pH and (b) ionic strength. The lines represent the calculation according to the O'Brien and White theory with a constant eADF4(C16) particle radius of $2.8 \mu\text{m}$ and a surface composition according to Γ_{mob} in Table 5.1, where the colored areas include the upper and lower limits for Γ_{mob} , respectively. The gray data point has been reported by Hofer *et al.* and represents the electrophoretic mobility in an electrolyte solution resembling physiological conditions in terms of ionic strength and pH. [8]

In order to validate the applicability of the O'Brien and White theory to describe the electrophoretic mobility, we next varied the ionic strength at constant pH (Fig. 5.3 b). The minima in the electrophoretic mobility disagree with the Smoluchowsky equation predicting a monotonic decrease of the absolute values for the electrophoretic mobility with increasing ionic strength (at constant pH). The existence of such minima in mobility as a function of ionic strength has been reported previously, albeit for hard colloidal particles made of latex or silica. [14, 15, 16] For spider silk particles the minima in mobility occur at ionic strengths as predicted by the calculations according to the O'Brien and Whites theory [12] and the values in Table 5.1. However,

Table 5.1 : Ionizable groups of eADF4(C16)

	C-module	C-terminus	N-terminus	T7-Tag	
Amino acid	Glutamic acid E	Tyrosine Y	Glycine G	Methionine M	Arginine R
pK_a	4.25	10.07	2.34	9.21	12.48
Groups/ molecule	16	32	1	1	1
Hydropathy index	-3.5	-1.3	-0.4	1.9	-4.5
Γ_{theo} [nm^{-1}]	0.0625	0.125	0.0039	0.0039	0.0039
Γ_{mob} [nm^{-1}]	0.06 ± 0.02	0.12 ± 0.04 &	0.004 ± 0.001	0.004 ± 0.001	
	(0.03 \pm 0.01)				

the absolute value of the mobilities is somewhat lower than calculated. As this effect is more pronounced at low pH, we assume this deviation to result from a diffuse protein layer, *i.e.* a soft interface on the spider silk particles, which leads to the diffuse plane of shear and lower mobility as pointed out by Ohshima and others. [17, 18] Analogous effects can be observed for other macromolecules. [19] For applications in drug delivery the mobility under physiological conditions is relevant. Corresponding measurements of electrophoretic mobility for analogous spider particles have been reported previously. [8] The resulting electrophoretic mobilities can be described as well in the framework of the here-presented model (*cf.* Fig. 5.3 b and ESI Section 5.6.2).

5.2.3 Direct force measurements

In order to experimentally corroborate the presence of such a diffuse protein layer on the surface of eADF4(C16) spider silk particles, we determined their interfacial properties by direct force measurements using a colloidal probe. Spider silk particles were immobilized on a silane-modified glass surface together with colloidal silica particles from the same batch as used for the colloidal probe (Fig. 5.4 a). The silica particles served as 'internal standards' for an incompressible surface and allowed to additionally determine the diffuse layer properties of the colloidal probe during the measurements on a well-known surface *in situ*. [20]

Fig. 5.4 b shows the interaction force profile between a colloidal silica probe and a silica particle (immobilized on the substrate) at pH 5.5 and an ionic strength of $I = 1$ mM. The interaction forces have been normalized to the effective radius of the sphere-sphere geometry (*cf.* eqn 5.1 in the experimental methods). [21, 22] The interaction force profile is based on the overlap of diffuse layers originating from the silica particles. The interaction is quantitatively evaluated by fits using the full solutions of the Poisson-Boltzmann equation including the classical boundary conditions of constant charge (CC) and constant potential (CP), as well as charge regulation in the constant regulation approximation (CR). [23] The latter accurately describes experimental data over nearly the whole interaction range. The resulting decay length at large separation distances is $\kappa^{-1} = 10.6$ nm and corresponds to the Debye-length calculated from the nominal ionic strength I within reasonable accuracy. Assuming two identical silica particles, one obtains a diffuse layer potential of $\Psi_{SiO_2} = -46.5$ mV in agreement with the values reported in the literature. [21, 22, 24] Nevertheless, heat treatment of silica particles is known to have an influence on their surface chemistry, resulting in higher diffuse layer potentials. [25] We attribute the additional repulsive forces at small separation distances (*i.e.* < 5 nm) to soluble protein originating from the eADF4(C16) particles deposited on the sample. The interaction profile between the colloidal probe and eADF4(C16) particles is more complex than the one between

5 Surface Properties of Spider Silk Particles in Solution

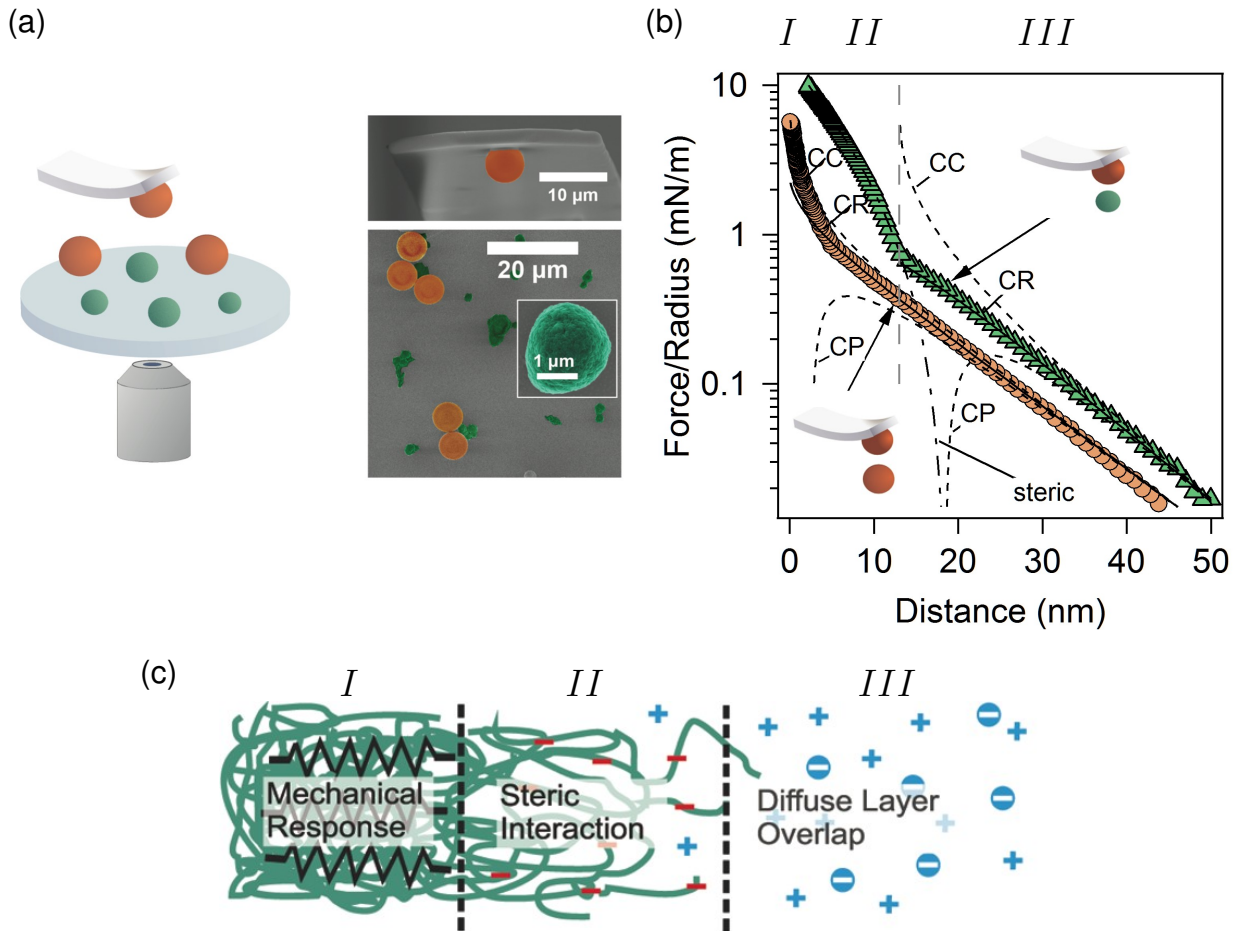


Figure 5.4: (a) Schematic representation of direct force measurements (left side). A colloidal silica probe and the sample with immobilized silica (orange) and eADF4(C16) particles (green) are additionally shown in SEM-images (right panel). (b) Representative force profiles for the interaction between silica (orange) and eADF4(C16) (green) particles, respectively. The diffuse layer overlap has been fitted according to the full solutions of the Poisson-Boltzmann equation with classical boundary conditions of constant charge (CC) and constant potential (CP), as well as the constant regulation approximation (CR). (c) Different contributions to the force profiles in dependence of the separation for the colloidal probe *versus* the eADF4(C16) particles.

the silica particles, since different interactions occur as a function of separation distance. At large separations the interaction forces result primarily from diffuse layer overlaps and are due to charges present on the surface of the eADF4(C16) particles. In this regime (*i.e.* separations > 10-15 nm and region III as indicated in Fig. 5.4 c) the decay length is identical to the one for the silica-silica interaction, leading to parallel force profiles. Due to the intrinsic surface roughness of the eADF4(C16) particles (*cf.* Fig. 5.1 b) the charge distribution is more compli-

5.3 Conclusion

cated, and one obtains generally smaller diffuse layer potentials. [26, 27] Here, we obtained a diffuse layer potential of $\Psi = -23.8$ mV for the eADF4(C16) particles, which is compatible with the electrophoretic mobility at pH 5.5 and 1 mM ionic strength. However, this potential is based on defining a plane of charge located at a separation of 13 nm (*cf.* the dashed vertical line in Fig. 5.4 b), coinciding with the onset of an additional repulsive force attributed to primarily steric interactions. These steric forces result from the complex and fuzzy surface structure of the particles. However, they can be described in an approximate manner by an Alexander-deGennes type of interaction between polymer brushes (*cf.* the dash-point line in Fig. 5.4 b and region II in Fig. 5.4 c). [28] Based on our fits, an extension of 30-50 nm was obtained from the force profile, which is approximately in the same regime as the measured rms-roughness using Tapping Mode in liquid. A further increase in force leads to an elastic deformation of the entire particle and results from the overall elasticity of the soft particles, which is examined in more detail elsewhere. [11] The onset for this regime of elastic compression (*cf.* region I in Fig. 5.4 b and 5.4 c) occurs at contact in the force profile. No variation of the elastic behaviour could be observed by varying the idle time (*i.e.* dwell time away from the surface) between different force cycles. The interfacial spring constant of the eADF4(C16) particles in solution was 2.7 N m^{-1} obtained by comparing the cantilever response on the hard silica particle and the soft eADF4(C16) particles (*cf.* eqn 5.2 in the Experimental section). This interfacial spring constant is in agreement with the elastic modulus of approximately 3.0 MPa determined by compression experiments over a significantly larger force regime. [11]

5.3 Conclusion

Both electrophoretic mobility and direct force measurements allow us to propose a model for eADF4(C16) particles as schematically depicted in 5.4 c: a fuzzy, interfacial layer of protruding eADF4(C16) strands has an extension of about 30-50 nm and varies within a batch, being most likely responsible for the decrease in magnitude of electrophoretic mobilities upon longer storage times (several months) accompanied by the disappearance of the local minimum in Fig. 5.3 b. The variability of this interfacial layer allows a transition of a primarily hard particle (with a thin layer) to an increasingly soft particle permeable for ions, whose electrophoretic mobility would have to be described in the framework of the Ohshima-theory. [17, 18] This interpretation is in agreement with the identified increase in size of eADF4(C16) particles upon prolonged storage. [8] The steric forces caused by this layer would explain the detected colloidal stability of spider silk particles at high ionic strength or under physiological conditions. [6, 8] Spider silk particles have a great potential for drug delivery applications. However, their surface properties have to be tunable in a defined manner to adapt to different administration and stability of the colloidal suspensions. We could demonstrate that the overall inter-particle long-range interaction forces are based on two contributions, namely electrostatic and steric

5 Surface Properties of Spider Silk Particles in Solution

forces. The long-range electrostatic interaction results from the overlap of diffuse layers and is, thus, directly related to the protein sequence. In order to influence this parameter, the protein sequence can be tuned. The large diffuse layer potentials determined for eADF4(C16) particles indicate one charged group per C-module to be efficient to provide sufficiently strong inter-particle forces for electrostatic stabilization in solution in combination with the steric interaction forces.

5.4 Materials and methods

Formation of eADF4(C16) particles

The recombinant spider silk protein eADF4(C16) was produced and purified as described previously. [4] For protein precipitation, eADF4(C16) in 10 mM Tris (hydroxy-methyl)-amino-methane-HCl (Tris-buffer), pH 8 at a concentration of 6 mg mL⁻¹ was dialyzed against 1 M potassium phosphate (pH 8) for 45 min at room temperature using a dialysis membrane with a molecular weight cut-off of 6000-8000 Da (Spectra/Por, Rancho Dominguez, CA, USA). After particle formation, the suspension was centrifuged for 15 min at 17 000 g followed by three washing steps with Milli-Q water.

Particle immobilization

Circular glass slides for the AFM-cell (Borofloat, Irlbacher Blickpunkt Glas GmbH, Schönsee, Germany) were cleaned by sonication in a 2% Hellmanex III (Hellma, Müllheim, Germany) solution at 40 °C, followed by sonication in a mixture of isopropanol and water (v/v = 3:1) at room temperature. Afterwards they were treated with a modified RCA-cleaning procedure consisting of a mixture of Milli-Q water, hydrogen peroxide and ammonia (v/v/v = 5:1:1) at 80 °C for 20 min. [29] The substrates were then thoroughly rinsed with Milli-Q water and dried in a nitrogen stream. Directly before silanization with 3-aminopropyl-diisopropylethoxysilane (ABCR, Karlsruhe, Germany) the glass substrates were treated with O₂-plasma. Silanization was carried out from the gas phase in a desiccator for at least 8 h. After silanization, the substrates were rinsed with ethanol and tempered at 80 °C for 2 h. Suspensions of silica particles ($d = 6.8 \mu\text{m}$, Bangs Laboratories Inc., Fishers, IN, USA) and eADF4(C16) were drop-cast on these amino-functionalized glass slides and dried. Then, the samples were allowed to equilibrate in the electrolyte solution before the direct force measurements for 2 h.

AFM imaging of eADF4(C16) particles

The surface topography of the silk particles was determined by Tapping Mode in liquid on an AFM MFP-3D (Asylum Research, CA). Double-beam silicon nitride cantilevers (SNL-10, Bruker) with a nominal resonance frequency of 56 kHz and a nominal spring constant of 0.24 N m^{-1} were used for imaging in Tapping Mode.

Scanning electron microscopy (SEM)

The particle suspension was placed on cleaned silicon wafers and air-dried. The samples were sputtered with 1.3-2.6 nm thick layers of platinum (Sputter coater 208 HR, Cressington). The SEM-measurements (Leo 1530 VP Gemini, Zeiss) were performed at 3.00 kV.

Electrophoretic mobility

The electrophoretic mobility was determined by video microscopy on the single particle level. The measurements were carried out using a ZetaView PMX 100 (ParticleMetrix GmbH, Meerbusch, Germany) equipped with a laser scattering microscope allowing direct observation of the migrating particles. The electrophoretic mobilities have been calculated according to the theory of O'Brien and White based on the algorithm by Hunter. [15, 30]

Preparation of colloidal probes

For the preparation of colloidal probes tipless AFM-cantilevers from silicon were used (NSC12 with no coating, Mikromasch), which had a nominal spring constant of 0.3 N m^{-1} . A recently reported procedure for the sintering of colloidal silica particles has been used in a modified form. [31] The AFM-cantilevers were cleaned by rinsing with Milli-Q water and ethanol. After drying, they were treated with oxygen plasma. A diluted suspension of Ludox silica particles (Ludox AM 30, Sigma-Aldrich) was mixed with an UV-curable glue (Norland Optical Adhesives No. 63, Norland Products, Cranbury, NJ, USA). A μm -sized drop of this mixture was placed on the end of a tipless cantilever using a micromanipulator (Märzhäuser, DC-3 KS, Wetzlar, Germany) and an etched tungsten wire. Afterwards μm -sized colloidal particles from the same batch as used for sample preparation were placed on top of this glue-drop by means of another etched wire. Finally, the cantilever with the immobilized colloidal particle was treated in a muffle furnace at 1250°C for 2 h.

Direct force measurements

Interaction forces were measured by the colloidal probe technique on a closed-loop AFM (MFP-3D, Asylum Research, CA). These measurements were carried out in sphere-sphere geometry

5 Surface Properties of Spider Silk Particles in Solution

in a semi-closed fluid cell. [21] The particles were coarsely aligned by optical microscopy. Then, force maps were used to determine the apex of the immobilized particle with a resolution of less than 50 nm. For each particle combination about 50 force distance curves were acquired with a velocity of 800 nm s^{-1} and loading forces of approximately 15-20 nN. The spring constant of the cantilevers was determined by the thermal noise method. [32] The raw data were converted according to previously described procedures. [21] In particular, the data sets for each particle combination were averaged and normalized by the effective radius

$$R_{eff} = \frac{R_1 \times R_2}{(R_1 + R_2)} \quad (5.1)$$

Here, R_1 (*i.e.* colloidal probe) was determined by optical microscopy and R_2 (*i.e.* immobilized particles) from height data acquired in the force maps and optical micrographs, respectively. The diffuse layer potentials were fitted using the Poisson-Boltzmann equation according to the constant regulation approximation. [23] The stiffness of the spider silk particles was calculated according to the following equation:

$$k_{eADF4} = \frac{k_c}{\left(\frac{c_{eADF4}}{c_{SiO_x}} - 1\right)} \quad (5.2)$$

where c_{eADF4} and c_{SiO_x} are force responses (*i.e.* force vs. piezo displacement) of the cantilever in contact with the eADF4(C16) and silica particles, respectively. [33] The cantilever force constant is k_c .

5.5 Acknowledgements

The authors thank C. Kunert for help with the scanning electron microscopy. The authors further thank A. Fery and M. Neubauer for valuable discussions and M. Hofer as well as J. Engert for generously providing their original data for the electrophoretic mobility at high ionic strength (*cf.* ref. [8]). This work was supported in parts by the Deutsche Forschungsgemeinschaft (SFB 840) as well as Bundesministerium für Bildung und Forschung (BMBF, grant number 13N11340) and by the Deutsche Forschungsgemeinschaft (DFG, grant number SCHE 603/9-1).

5.6 Supporting Information

5.6.1 Surface structure of dried eADF4(C16) particles

The surface structure of dried spider silk protein particles has been examined by scanning electron microscopy. Figure 5.5 shows the surface structure of an exemplary particle at higher magnification in addition to the overview image in Figure 5.1 a.

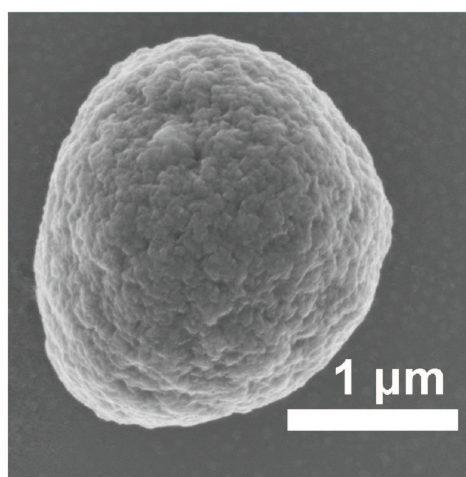


Figure 5.5: Scanning electron microscopy image of an eADF4(C16) particle in the dehydrated state.

5.6.2 Calculation of ζ -potentials and electrophoretic mobilities

Electrophoretic Mobility in the Framework of the O'Brien and White Theory

The surface charge density of the spider silk particles is described by a simple model for their surface chemistry. This model is based on the number density of ionizable groups and their corresponding pK_a -values. [34, 35] The resulting surface charge density is then used to calculate the diffuse layer potential. [23] The electrophoretic mobility is finally obtained from the diffuse layer potential in the framework of the theory of O'Brien and White. [12] It can be determined by interpolation of tabulated values as given for example in the book of Hunter. [30] Additional parameters necessary for the interpolation are particle radius and limiting conductance of the electrolyte solutions. Analogous calculations are available in the literature where surface chemistry and electrophoretic mobility have been related. [36, 37, 15, 38, 16, 39] More general algorithms than used here are available in the literature.

5 Surface Properties of Spider Silk Particles in Solution

Electrophoretic mobilities of spider silk particles at high ionic strength as reported by Hofer *et al.*

Hofer *et al.* reported the electrophoretic mobility of spider silk protein particles comparable to ones used here, albeit at significantly higher ionic strength. [8] At high ionic strength, the deviations between the equation of Smoluchowsky and the theory of O'Brien and White are becoming significantly smaller. According to the Smoluchowsky equation the ζ -potential and the electrophoretic mobility are related by: [30]

$$\mu = \frac{\epsilon_r \epsilon_0}{\eta} \zeta \quad (5.3)$$

Where η is the viscosity, while ϵ_r and ϵ_0 are the relative permittivity of the electrolyte and of vacuum, respectively. It should be pointed out that in the framework of the Smoluchowski equation no local minima are expected in the electrophoretic mobility, contrary to the ones observed in Figure 5.3).

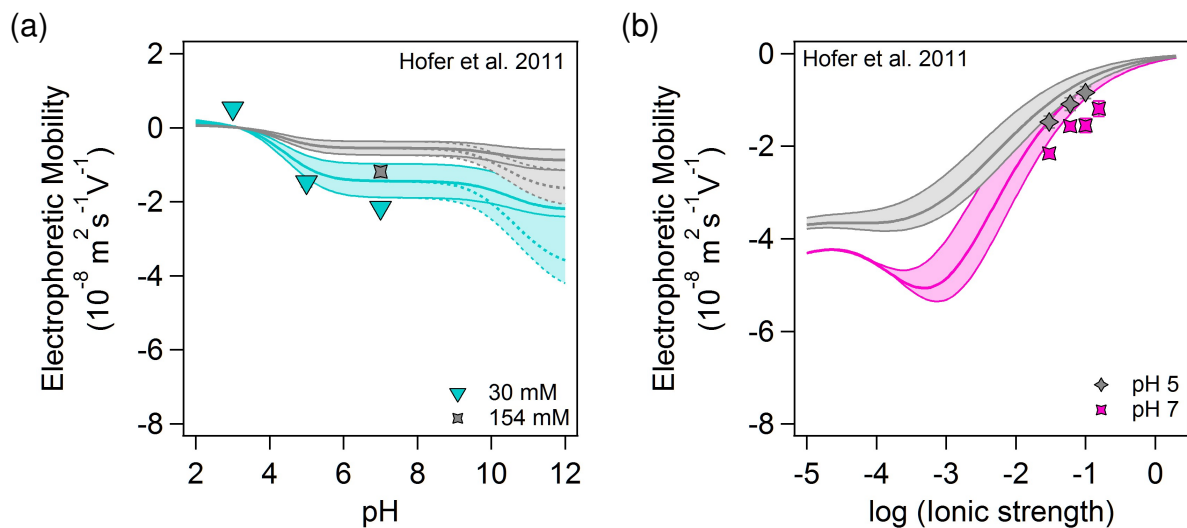


Figure 5.6: Electrophoretic mobility as a function of a) pH and b) ionic strength. The data points are from Hofer *et al.* [8], while the lines represent calculations based on the theory of O'Brien and White with the parameters summarized in Table 5.1 except a different average particle radius of 260.5 nm.

Figure 5.6 compares the experimental data reported by Hofer *et al.* with our model. Again, the theoretical mobilities have been calculated with the parameters given in Table 5.1. A conversion by equation 5.3 of the ζ -potentials reported in ref. [8] gains the same results, although particle radii of 260.5 nm have been used for the calculations, as reported in Ref. [8].

5.6 Supporting Information

Figure 5.6 demonstrates that the model and parameters summarized in Table 5.1 also provide an accurate description of the electrophoretic mobilities of spider silk particles at high ionic strength, in particular for electrolyte solutions that resemble physiological conditions.

References

- [1] J M Gosline, P A Guerette, C S Ortlepp, and K N Savage. The mechanical design of spider silks: From fibroin sequence to mechanical function. *Journal of Experimental Biology*, 202(23):3295–3303, 1999.
- [2] L Römer and T Scheibel. The elaborate structure of spider silk. *Prion*, 2(4):154–161, 2008.
- [3] M Humenik, A M Smith, and T Scheibel. Recombinant Spider Silks—Biopolymers with Potential for Future Applications. *Polymers*, 3(4):640–661, 2011.
- [4] D Huemmerich, C W Helsen, S Quedzuweit, J Oschmann, R Rudolph, and T Scheibel. Primary Structure Elements of Spider Dragline Silks and Their Contribution to Protein Solubility. *Biochemistry*, 43(42):13604–13612, 2004.
- [5] K Spiess, A Lammel, and T Scheibel. Recombinant Spider Silk Proteins for Applications in Biomaterials. *Macromolecular Bioscience*, 10(9):998–1007, 2010.
- [6] A Lammel, M Schwab, M Hofer, G Winter, and T Scheibel. Recombinant spider silk particles as drug delivery vehicles. *Biomaterials*, 32(8):2233 – 2240, 2011.
- [7] C Blüm and T Scheibel. Control of drug loading and release properties of spider silk sub-microparticles. *BioNanoScience*, 2(2):67–74, 2012.
- [8] M Hofer, G Winter, and J Myschik. Recombinant spider silk particles for controlled delivery of protein drugs. *Biomaterials*, 33(5):1554 – 1562, 2012.
- [9] P H Hirel, M J Schmitter, P Dessen, G Fayat, and S Blanquet. Extent of N-terminal methionine excision from Escherichia coli proteins is governed by the side-chain length of the penultimate amino acid. *Proceedings of the National Academy of Sciences*, 86(21):8247–8251, 1989.
- [10] D L Nelson and M M Cox. *Lehninger: Principles of Biochemistry*. Palgrave Macmillan, 2012.
- [11] M P Neubauer, C Blüm, E Agostini, J Engert, T Scheibel, and A Fery. Micromechanical characterization of spider silk particles. *Biomaterials Science*, 1:1160–1165, 2013.
- [12] R. W. O'Brien and L. R. White. Electrophoretic mobility of a spherical colloidal particle. *J. Chem. Soc., Faraday Trans.*, 2:1607–1626, 1978.

References

- [13] A V Delgado, F Gonzalez-Caballero, R J Hunter, L K Koopal, and J Lyklema. Measurement and interpretation of electrokinetic phenomena. *Journal of Colloid and Interface Science*, 309(2):194 – 224, 2007.
- [14] M Antonietti and L Vorwerk. Examination of the atypical electrophoretic mobility behavior of charged colloids in the low salt region using the O’Brian-White theory. *Colloid and Polymer Science*, 275(9):883–887, 1997.
- [15] M Borkovec, S H. Behrens, and M Semmler. Observation of the Mobility Maximum Predicted by the Standard Electrokinetic Model for Highly Charged Amidine Latex Particles. *Langmuir*, 16(11):5209–5212, 2000.
- [16] M Kobayashi. Electrophoretic mobility of latex spheres in the presence of divalent ions: experiments and modeling. *Colloid and Polymer Science*, 286(8-9):935–940, 2008.
- [17] H Ohshima. Electrophoretic Mobility of Soft Particles. *Journal of Colloid and Interface Science*, 163:474–483, 1994.
- [18] J F L Duval and H P van Leeuwen. Electrophoretics of Diffuse Soft Interfaces. 1. Limit of Low Donnan Potentials. *Langmuir*, 20:10324–10336, 2004.
- [19] E Rotureau, F Thomas, and J F L Duval. Relationship between Swelling and the Electrohydrodynamic Properties of Functionalized Carboxymethyl-dextran Macromolecules. *Langmuir*, 23(16):8460–8473, 2007.
- [20] I Popa, P Sinha, M Finessi, P Maroni, G Papastavrou, and M Borkovec. Importance of Charge Regulation in Attractive Double-Layer Forces between Dissimilar Surfaces. *Physical Review Letters*, 104:228301–1–228301–4, 2010.
- [21] S Rentsch, R Pericet-Camara, G Papastavrou, and M Borkovec. Probing the validity of the Derjaguin approximation for heterogeneous colloidal particles. *Physical Chemistry Chemical Physics*, 8(21):2531–2538, 2006.
- [22] V Kuznetsov and G Papastavrou. Adhesion of Colloidal Particles on Modified Electrodes. *Langmuir*, 28(48):16567–16579, 2012.
- [23] R Pericet-Camara, G Papastavrou, S H Behrens, and M Borkovec. Interaction between Charged Surfaces on the Poisson–Boltzmann Level: The Constant Regulation Approximation. *The Journal of Physical Chemistry B*, 108(50):19467–19475, 2004.
- [24] P G Hartley, I Larson, and P J Scales. Electrokinetic and Direct Force Measurements between Silica and Mica Surfaces in Dilute Electrolyte Solutions. *Langmuir*, 13(8):2207–2214, 1997.

5 Surface Properties of Spider Silk Particles in Solution

- [25] M Kobayashi, M Skarba, P Galletto, D Cakara, and M Borkovec. Effects of heat treatment on the aggregation and charging of Stöber-type silica. *Journal of Colloid and Interface Science*, 292(1):139 – 147, 2005.
- [26] S Bhattacharjee, C-H Ko, and M Elimelech. DLVO Interaction between Rough Surfaces. *Langmuir*, 14(12):3365–3375, 1998.
- [27] L Suresh and J Y Walz. Direct Measurement of the Effect of Surface Roughness on the Colloidal Forces between a Particle and Flat Plate. *Journal of Colloid and Interface Science*, 196(2):177 – 190, 1997.
- [28] H-J Butt, M Kappl, H Mueller, R Raiteri, W Meyer, and J Rühle. Steric Forces Measured with the Atomic Force Microscope at Various Temperatures. *Langmuir*, 15(7):2559–2565, 1999.
- [29] W Kern and D A Poutinen. Cleaning solution based on hydrogen peroxide for use in silicon semiconductor technology. *RCA Rev.*, 31:187–206, 1970.
- [30] J L Hunter. *Zeta-Potential in Colloid Science*. Academic Press, 1989.
- [31] V Kuznetsov and G Papastavrou. Note: Mechanically and chemically stable colloidal probes from silica particles for atomic force microscopy. *Review of Scientific Instruments*, 83(11):116103–116103, 2012.
- [32] J L Hutter and J Bechhoefer. Calibration of atomic-force microscope tips. *Review of Scientific Instruments*, 64(7):1868–1873, 1993.
- [33] W A Ducker, Z Xu, and J N Israelachvili. Measurements of Hydrophobic and DLVO Forces in Bubble-Surface Interactions in Aqueous Solutions. *Langmuir*, 10(9):3279–3289, 1994.
- [34] T W Healy and L R White. Ionizable surface group models of aqueous interfaces. *Advances in Colloid and Interface Science*, 9:303–345, 1978.
- [35] S H Behrens and M Borkovec. Electrostatic Interaction of Colloidal Surfaces with Variable Charge. *Journal of Physical Chemistry B*, 103(15):2918–2928, 1999.
- [36] S H Behrens, M Borkovec, and P Schurtenberger. Aggregation in Charge-Stabilized Colloidal Suspensions Revisited. *Langmuir*, 14(8):1951–1954, 1998.
- [37] S H Behrens, D I Christl, R Emmerzael, P Schurtenberger, and M Borkovec. Charging and Aggregation Properties of Carboxyl Latex Particles: Experiments versus DLVO Theory. *Langmuir*, 16(6):2566–2575, 2000.

References

- [38] W Lin, M Kobayashi, M Skarba, C Mu, P Galletto, and M Borkovec. Heteroaggregation in Binary Mixtures of Oppositely Charged Colloidal Particles. *Langmuir*, 22(3):1038–1047, 2006.
- [39] I Popa, G Papastavrou, and M Borkovec. Charge regulation effects on electrostatic patch-charge attraction induced by adsorbed dendrimers. *Physical Chemistry Chemical Physics*, 12(18):4863, 2010.

CHAPTER 6

Colloidal Properties of Recombinant Spider Silk Protein Particles

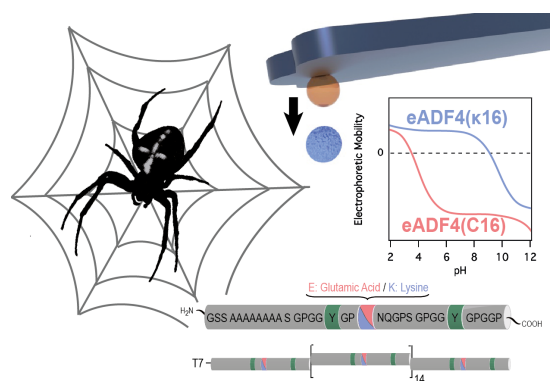
Nicolas Helfricht,^a Elena Doblhofer,^b Jérôme F. L. Duval,^{*c,d}
Thomas Scheibel,^b Georg Papastavrou^{*a}

^a Physical Chemistry II, University of Bayreuth, Universitätsstr. 30, 95440 Bayreuth, Germany.
Email: Georg.Papastavrou@uni-bayreuth.de

^b Biomaterials, Fakultät für Ingenieurwissenschaften, Universität Bayreuth, Universitätsstr. 30,
95440 Bayreuth, Germany.

^c Université de Lorraine, Laboratoire Interdisciplinaire des Environnements Continentaux (LIEC), UMR
7360, Vandœuvre-lès-Nancy, F-54501, France. Email: jerome.duval@univ-lorraine.fr

^d CNRS, Laboratoire Interdisciplinaire des Environnements Continentaux (LIEC), UMR 7360,
Vandœuvre-lès-Nancy, F-54501, France. Email: jerome.duval@univ-lorraine.fr



Reprinted with permission from:

"Colloidal Properties of Recombinant Spider Silk Protein Particles", N. Helfricht, E. Doblhofer, J. F. L. Duval, T. Scheibel, G. Papastavrou, *Journal of Physical Chemistry C*, **2016**, 130(32), 18015, DOI: 10.1021/acs.jpcc.6b03957.

© 2016 American Chemical Society.

Abstract

Colloidal particles have been prepared from polyanionic and polycationic recombinant spider silk protein. The amino acid sequences of these spider silk proteins are identical except for 16 residues bearing either a cationic or an anionic ionizable group. Electrophoretic titration showed that protonation of the acidic and basic amino acids had significant impact on the electrophoretic mobility of the protein particles and, in particular, on their point of zero mobility (PZM). The experimentally determined PZMs are in good agreement with the theoretical values evaluated on the basis of the relevant amino acid sequences. A comprehensive description of the electrokinetic properties of the recombinant spider silk protein particles as a function of pH and solution ionic strength was provided from adequate application of electrokinetic theory for soft particles. Within the framework of this formalism, spider silk protein particles are viewed as porous colloids penetrable for ions and characterized by a finite penetration length for the electroosmotic flow. The differentiated electrokinetic properties of the particles were shown to be solely governed by the electrohydrodynamic features of their poorly charged outer peripheral layer with a thickness of about 10-20 nm. This finding was further corroborated experimentally by demonstrating that electrokinetics of particles bearing an additional outer layer consisting of oppositely charged spider silk proteins is entirely dominated thereby. The presence of a fuzzy, ion-permeable particle interface with an extension of several tenths of a nanometer was confirmed by direct measurement of the resulting steric forces using the colloidal probe atomic force microscopy (AFM) technique.

6.1 Introduction

Structural proteins play an increasing role in the development of biomaterials for drug delivery systems or drug depots. [1] The recombinant production of such structural proteins in combination with genetic engineering allows establishing tailor-made materials. [1, 2, 3] Such engineered proteinaceous materials offer both predictable biofunctionality and precise tenability, a combination lacking in most synthetic polymer materials. [4] Like synthetic polymers, structural proteins can be assembled into morphologies with no counterpart in nature, such as films, membranes, coatings, or particles. [5, 6]

Spider silk proteins, called spidroins, represent a prominent and well-known example [7] of such structural proteins and consist of highly repetitive core sequences. One well-established recombinant spidroin is based on the sequence of one of the proteins of the dragline silk of the European garden spider *Araneus diadematus*, which is referred to as eADF4(C16). It can be processed into a variety of morphologies such as foams, [8] fibers, [9] nonwoven meshes, [10]

hydrogels, [11] films, and colloidal particles. [12, 13, 14] By varying the amino acid sequences and substituting all glutamic acid (E) residues of eADF4(C16) with lysine (K) ones, the negative net-charge at neutral pH is converted into a positive one. For the modified protein, which is denoted hereafter as eADF4(κ 16), the processing properties are indistinguishable to that of eADF4(C16). [14]

Particles made of recombinant spidroins are of special interest for the encapsulation of pharmaceutically active substances as they combine a unique set of properties, including biocompatibility and stability. [14, 15, 16, 17] Surface chemistry of such colloids is in some aspects fundamentally different to that of "classical" solid colloids. For protein-based colloids the chemical composition should expectedly remain constant throughout the whole particle. Moreover, the density of ionizable groups is determined by the amino acid composition of the constituting structural proteins. Electrophoretic methods are, in this respect, valuable techniques commonly used for the analytical characterization of spidroin particles. [7, 13, 14]

A basic theory for electrophoresis of so-called hard particles, *i.e.*, particles impermeable to ions and solvent, has been developed about a century ago and refined over the years to, *e.g.*, account for surface ion-conduction processes and electric double layer polarization. [18] The numerical treatment of the standard electrokinetic model by O'Brien and White [19] is pivotal for analyzing situations where simplified analytical equations derived within the framework of the Debye-Hückel approximation are not applicable. In comparison, only recently precise modeling has been established for describing the electrokinetics of soft particles. [20, 21] Following the definition by Ohshima, [22] soft particles consist partly or entirely of ion- and solvent-permeable materials with electrophoretic properties significantly different to those of their hard counterparts. Examples of such particles include bacteria, viruses, and dendrimers. [20, 23] The presence of a charged permeable layer is manifested prominently by the existence of a nonzero mobility plateau value reached at large electrolyte concentrations at which particle charges are completely screened by ions from a background electrolyte. [20, 22] This feature originates from intralayer electroosmotic flow and has been confirmed experimentally for various systems. [20, 23]

Since the pioneering work by Hermans and Fujita, [24] Levine *et al.*, [25] and Ohshima, [22] on electrophoresis of soft particles there has been a rich body of theoretical and experimental studies on electrohydrodynamics of core-shell or porous (nano)particles. For these systems the concept of ζ -potential, only strictly applicable to hard particles, is not playing any role. [20] In particular, Hill *et al.* [26] and Duval and Ohshima [27] established a formalism to account for heterogeneous (or diffuse) distribution of charged polymer segments across a particle's shell. While in the literature a large number of models exist to describe the electrokinetic properties

6 Colloidal Properties of Recombinant Spider Silk Protein Particles

of soft colloidal particles, [20, 28, 29, 30] these models have never been applied for protein particles prepared by salting-out procedures.

Here, the properties of colloidal spidroin particles were determined by electrophoretic mobility and direct force measurements. Two different types of spidroin particles were evaluated, which have been prepared from spidroins with nearly identical amino acid sequences, namely, eADF4(C16) and eADF4(κ 16). A number of electrokinetic measurements have been reported for spidroin particles so far, and determination of their ζ -potential is an important, generally used analytical tool. [14, 31, 32] However, a recent study combining electrophoretic mobility with direct force measurements demonstrated that for such recombinant spidroin particles a pronounced diffuse interface with protruding protein segments exists, limiting the application of the classical O'Brien-White theory [19] (valid only for hard colloidal particles) to provide a comprehensive interpretation of the electrophoretic mobility as a function of pH and solution ionic strength. [13] Since the features of the spidroin particle surface depend critically on the production processing by salting-out, [33] a large number of parameters has to be taken into account. [12] Here, we address how far electrokinetic methods can be employed to characterize protein particles and to predict their overall colloidal stability.

6.2 Methods and Materials

Protein Production and Particle Preparation

The spider silk proteins eADF4(C16) with the amino acid sequence **T7**-(GSSAAAAAAAAASGGPGGYGPENQGPGSPGGYGPGGPG)₁₆ and eADF4(κ 16) with the sequence **T7**-(GSSAAAAAASGGPGGYGPKNQGPGSPGGYGPGGPG)₁₆, have been produced and purified as described elsewhere. [14, 34] The T7-tag has the following sequence: MAS-MTGGQQM. For particle preparation, lyophilized eADF4(κ 16) and eADF4(C16) were dissolved in 6 M guanidinium thiocyanate (GdmSCN, Carl Roth GmbH & Co. KG, Karlsruhe, Germany) and dialyzed against 25 mM Tris/HCl (Carl Roth GmbH & Co. KG, Karlsruhe, Germany), pH 7.5 (Tris buffer). The dialysis continued for 16 h with three buffer changes at 25 °C using a dialysis membrane with a molecular weight cutoff of 6000-8000 Da (SpectrumR Laboratories, Irving, Texas). The resulting spider silk protein solutions were diluted to a concentration of 3 mg/mL using Tris buffer. Aliquots of 2 mL of the diluted solutions were dialyzed against 1 M potassium phosphate (Carl Roth GmbH & Co. KG, Karlsruhe, Germany), pH 7.0, over a period of 1 h at room temperature. Then, the occurring particle suspension was centrifuged at 17 000 g for 2 min to obtain a pellet consisting of the precipitated protein particles. The particles were washed three times with Millipore water (MQ-H₂O).

6.2 Methods and Materials

Layer-by-layer coatings of the particles were produced by diluting the particle suspension to a concentration of 1 mg/mL, centrifugation of the particle suspension at 17 000 g for 2 min, and resuspending the particle pellet in a protein solution containing 0.5 mg/mL of the oppositely charged protein in the same volume of Tris buffer (*i.e.*, eADF4(C16) for eADF4(κ 16) particles and eADF4(κ 16) for eADF4(C16) particles). This mixture was incubated under continuous mixing conditions (1000 rpm) for 1 h at room temperature. The particles were finally washed with MQ-H₂O.

Particle suspensions were systematically sonicated for 5 min at room temperature prior to use.

Particle Immobilization

The recombinant spider silk protein particles were immobilized on a substrate for the direct force measurements by atomic force microscopy (AFM). For that purpose, WillCo dishes (series GWSB-5040 with a glass bottom and a diameter of 47.0 mm, WillCo Wells, Amsterdam, Netherlands) were cleaned with Millipore water and pure ethanol (VWR). Afterward, the dishes were exposed to air plasma for 10 min (Zepto, Diener electronic GmbH & Co. KG, Ebhausen, Germany). Half of the glass dish was modified with polyethylenimine (branched PEI, 1 g/L, $M_w \approx 25\,000$ g/mol, Aldrich) serving as adhesion promoter for negatively charged particles. After 15 min, the PEI solution was removed, and the Petri dish was cleaned thoroughly with Millipore water.

Optical Microscopy

Modified glass dishes (see above) were filled with potassium chloride solution (1 mM, pH 5.5; BioUltra, $\geq 99.5\%$, Sigma). A diluted suspension of both types of protein particles was added to separate dishes that were transferred to an inverted optical microscope (Axio Observer.Z1, Carl Zeiss Microscopy GmbH, Jena, Germany). The particles were allowed to sediment, and afterward the particle diameter was determined based on optical micrographs using ImageJ software.

Scanning Electron Microscopy (SEM)

Silicon wafers were cut into pieces of 10 mm x 10 mm and cleaned with a CO₂ Snow Jet (tectra, Frankfurt, Germany). Afterward, the substrates were rinsed with 100% ethanol (VWR) and dried in a nitrogen stream. Diluted particle suspensions were placed on the cleaned substrates, allowing the liquid to evaporate. After complete drying, the samples were rinsed twice with Millipore water. The prepared samples were sputtered with a 1.3 nm layer of platinum and then examined with a scanning electron microscope (Leo 1530 VP Gemini, Zeiss).

6 Colloidal Properties of Recombinant Spider Silk Protein Particles

Electrokinetic Measurements

The electrophoretic mobility of recombinant spidroin particles was measured using a Zetasizer Nano-ZS (Malvern Instruments Ltd., Worcestershire, U.K.). This instrument is based on laser-Doppler-microelectrophoresis and uses M3-PALS (phase analysis light scattering). Disposable capillary cells (DTS1060, Malvern Instruments Ltd., Worcestershire, U.K.) were used for the measurements, and their performance/quality was evaluated using a Malvern transfer standard particle suspension. The electro-phoretic mobility was investigated as a function of pH at different ionic strengths (0.1, 1, and 10 mM, respectively). The pH value of the electrolyte solutions was adjusted with HCl and KOH (1 M, Titrisol, Merck). The total ionic strength of each solution (0.1, 1, and 10 mM, respectively) was obtained by addition of KCl (BioUltra, $\geq 99.5\%$, Sigma). The pH value was controlled after each measurement.

Direct Force Measurements

Interaction forces between individual pairs of particles were measured with a FluidFM setup mounted on an inverse optical microscope (Axio Observer.Z1, Carl Zeiss Microscopy GmbH, Jena, Germany). The FluidFM is a combination of an atomic force microscope (FlexAFM V5 head equipped with a C3000 controller, Nanosurf AG, Liestal, Switzerland) and a pressure control unit (Cytosurge AG, Glattbrugg, Switzerland). This microfluidic controller is connected to special hollow cantilevers, so-called FluidFM micropipettes (Cytosurge AG, Glattbrugg, Switzerland), premounted on a Cytoclip with a spherical aperture at the free end of the lever arm with an opening diameter of $2\ \mu\text{m}$. The used FluidFM cantilevers had a nominal spring constant of $0.2\ \text{N/m}$. The actual spring constant was determined by the added mass method after the measurements to avoid any contaminations of the lever arm. [35] To that end, small tungsten spheres were picked up from a glass surface, and the corresponding shifts in resonant frequency were monitored and evaluated.

Prior to direct force measurements, the FluidFM cantilevers were treated with air plasma for 10 min (Zepto, Diener electronic GmbH & Co. KG, Ebhausen, Germany). All solutions were degassed and filtered through PES syringe filters (pore size = $0.2\ \mu\text{m}$; Carl Roth GmbH & Co. KG, Karlsruhe, Germany). A liquid reservoir at the end of the Cytoclip was filled with $50\ \mu\text{L}$ of the measurement solution (ionic strength 1 mM, pH 3). Beside both types of spidroin particles, silica particles (average diameter $6.8\ \mu\text{m}$, Bangs Laboratories Inc., Fishers, IN, U.S.A.) were immobilized on the functionalized dishes as "hard" internal standard. [13]

The FluidFM setup enables the use of exchangeable colloidal probes. [36] First, the cantilever was approached near a silica particle, and an aspiration pressure of $-800\ \text{mbar}$ was applied. After aspirating a single particle to the aperture, the pressure was reduced to $-300\ \text{mbar}$ to

retain the captured bead during the measurements. The silica particles were used as probe particles to determine the inverse optical lever sensitivity (*InvOLS*) in a symmetric system involving two silica particles being aligned using an optical microscope. Interaction forces were hence measured in the sphere-sphere geometry. Force *versus* distance curves were recorded with a piezo travel velocity of 500 nm s⁻¹. For each pair of particle combinations, around 30 force profiles were acquired. After completing the experiment, the aspirated particle was finally released with an overpressure pulse (+1000 mbar).

The recorded raw data were converted into force *versus* distance curves and evaluated using a custom-written procedure programmed in FORTRAN and IgorPro (Wavemetrics). [13, 37] The *InvOLS*, as determined in a symmetric system between two silica particles, was used as a constant to convert the raw data due to the soft and deformable behavior of the spider silk particles. [38]

For the interaction of a hard colloidal probe with a polymer brush, measured interaction forces were fitted by the asymmetric Alexander-de Gennes (AdG) model according to [39, 40]

$$\frac{F(D)}{R_{eff}} = 2\pi \frac{2kTL}{35s^2} \left(7 \left(\frac{L}{D} \right)^{5/4} + 5 \left(\frac{D}{L} \right)^{7/4} - 12 \right) \quad (6.1)$$

where $F(D)/R_{eff}$ is the normalized interaction force at separation D , L is the brush thickness, and s is the anchor distance between the polymer brushes.

6.3 Theory Section

6.3.1 Electrokinetic Theory of Soft Porous Particles

The fundamental equations governing the mobility of soft particles in an externally applied (static) electrical field have been previously described in detail. [22, 26, 27] Briefly, the mobility of soft particles is evaluated from the numerical solution of highly coupled electrostatic and hydrodynamic flow equations including (i) the nonlinear Poisson-Boltzmann equation taking into account the three-dimensional distribution of the structural charges in the particle shell, (ii) the Navier-Brinkman equation that comprises the friction force exerted by the particle on the electroosmotic flow, taking into account that this friction term depends on the distribution of polymer segments, [41] and (iii) the continuity equations for all mobile ions present in the system and for the steady incompressible flow. For situations where the density of charges and polymer segments within the soft component of the particle do not depend on position, evaluation of particle electrophoretic mobility only requires the adjustment of two basic parameters (in case

6 Colloidal Properties of Recombinant Spider Silk Protein Particles

particle core size and shell thickness are known): the net density ρ_0 of charges throughout the homogeneous peripheral surface structure of the soft particle and the characteristic penetration length $1/\lambda_0$ of the electroosmotic flow within this structure (*cf.* Figure 6.1 a). [22] In cases where the density of charges carried by the polymer segments constituting the soft particle is not homogeneous, the density distributions of charges and polymer segments need to be further specified. [27] The strategy to do so is recalled below for the specific example of spidroin particles.

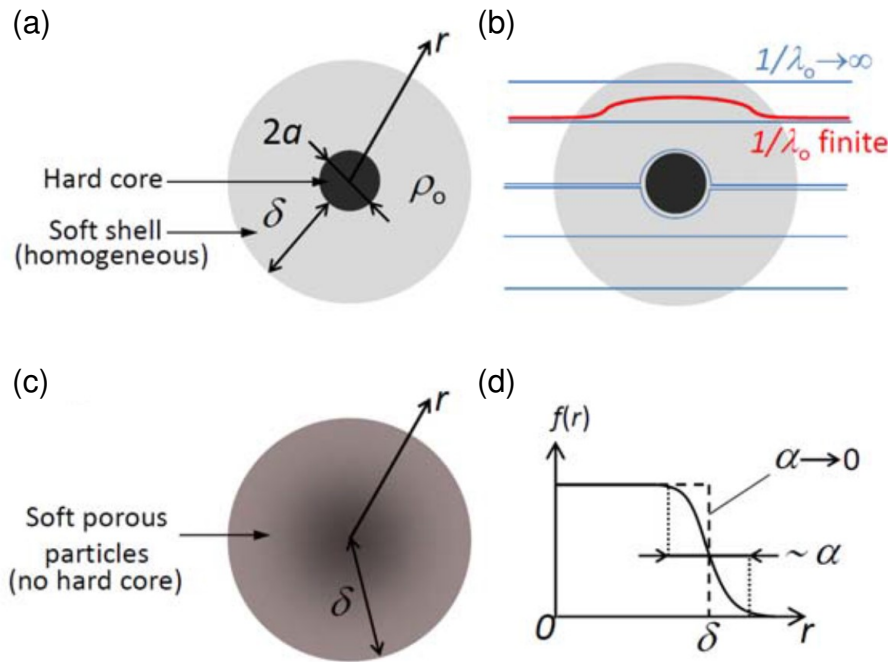


Figure 6.1: Illustration of various parameters introduced in the text for core-shell particles (a) and soft porous particles (b) devoid of a core component. (c) Schematic representation of the flow streamlines under electrophoretic conditions in the extreme of a free-draining particle shell ($1/\lambda_0 \rightarrow \infty$) and for a finite value of $1/\lambda_0$. (d) The radial function $f(r)$ from eqs 6.4 and 6.6 and its dependence on the parameter α .

6.3.2 Electrohydrodynamics of Spidroin Particles

The spidroin particles are *stricto sensu* devoid of an ion-impermeable core and carry both negative as well as positive charges (*cf.* Figure 6.1 a). The negative charges are originating from the deprotonation of acid (*e.g.*, carboxylic) groups, and the positive charges originate from the protonation of basic (*e.g.*, amine) groups:



6.3 Theory Section



where $\equiv R_a H$ and $\equiv R_c$ refer to the functional acid or basic groups in the particles whose total (effective) volume densities are hereafter denoted as ρ_a/F and ρ_c/F respectively, with F being the Faraday constant. Following the strategy by Duval and Ohshima, [27] the local charge density within the particles depends on pH according to

$$\rho(r) = f(r) \left\{ \frac{\rho_c}{1 + 10^{pH - pK_c} \exp[y(r)]} - \frac{\rho_a}{1 + 10^{pK_a - pH} \exp[-y(r)]} \right\} \quad (6.4)$$

where $y(r) = zF\Psi(r)/RT$ is the local dimensionless electrostatic potential at the radial position r (origin set at the particle center, *cf.* Figure 6.1) with R being the gas constant, T the temperature, z the valence of the z/z electrolyte, and $\Psi(r)$ the local electrostatic potential derived from the nonlinear Poisson-Boltzmann equation. pK_a and pK_c depict the negative logarithms of the dissociation constants pertaining to reactions 6.2 and 6.3, respectively. Obviously, in view of the intrinsic heterogeneous chemical composition of the spidroin particles, pK_a and pK_c have to be seen as mean dissociation constants. Equation 6.4 includes the radial function f that pertains to the radial density distribution of proteins bearing the ionizable residues $\equiv R_a H$ and $\equiv R_c$ in the particle (*cf.* Figure 6.1 b). Sufficiently far from the particles interface, f necessarily satisfies the condition $f(r \gg \delta) = 0$, where δ is the particle radius. This condition expresses the required vanishing of the polymer interphase at sufficiently large r . As previously reported, [20, 27] the following form for $f(r)$ may be adopted

$$f(r) = \chi \{1 - \tanh[(r - \delta)/\alpha]\} / 2 \quad (6.5)$$

where α is the length scale defining the gradual transition of segment density distribution from the bulk particle to the outer electrolyte solution (Figure 6.1 b). The limit $\alpha \rightarrow 0$ corresponds to the situation of a homogeneous distribution of polymer segments in the porous particles, and the scalar χ in eq 6.5 further ensures that the total amount of polymer segments across the interphase is conserved upon modification of the spatial profiles $f(r)$ via changes in α as a result of, *e.g.*, swelling processes.

On the basis of eqs 6.4 and 6.5, the friction coefficient $k(r)$ describing the resistance at position r of the polymer chains to flow is [20, 27]

$$k(r) = \chi \eta \lambda_0^2 f(r) \quad (6.6)$$

where η is the dynamic viscosity of water and $1/\lambda_0$ is the flow penetration length scale introduced in the preceding section. In the limit $1/\lambda_0 \rightarrow 0$, there is no flow penetration within the particle and the hard particle case is retrieved, while the limit of free-draining particle is

6 Colloidal Properties of Recombinant Spider Silk Protein Particles

reached at $1/\lambda_0 \rightarrow \infty$ (cf. Figure 6.1). For a given set of $\rho_{a,c}$, $pK_{a,c}$, and $1/\lambda_0$ parameters, the dependence of the particle electrophoretic mobility μ on solution pH and solution ionic strength can be evaluated from numerically solving the governing electrostatic and electrohydrodynamic equations using the COLSYS package, [42] as described in previous studies. [20, 23, 27]

6.4 Results and Discussion

In this study, we determined the electrophoretic mobility and interfacial properties of spidroin particles. Their properties depend on the underlying amino acid sequences, depicted as κ - and C-module (Figure 6.2 a), which are repeated 16 times in the individual proteins. The glutamic acid (E) residues present in eADF4(C16) are replaced by lysine (K) ones in the κ -module of eADF4(κ 16). Glutamic acid is an acidic amino acid, while lysine is a basic amino acid. Both repetitive modules contain additionally two tyrosine (Y) residues also bearing ionizable groups. However, these groups contribute only to the charging behavior under very basic pH conditions due to their high pK_a value. In addition, both proteins comprise an aminoterminal T7-tag, which shows a pH-dependent ionization behavior. However, the termini constitute only about 4 % of the total number of ionizable groups (cf. Table 6.2 in the Supporting Information). Therefore, the termini have only a minor influence on the overall particle charging state.

6.4.1 Particle Morphology

Colloidal particles were prepared by a salting-out process schematically depicted in Figure 6.2 b. The preparation of protein-based particles by salting-out in potassium phosphate buffer represents a standard preparation method and has been reported previously for eADF4(C16) [13, 14] and for eADF4(κ 16). [14] The particle radius was selected in the micrometer range, e.g., to allow for direct force measurements by AFM. The size of the particles was adjusted by controlling the mixing conditions, in particular the mixing speed. [17]

Parts c and d of Figure 6.2 show SEM images of eADF4(κ 16) and eADF4(C16) particles in dried state, respectively. The spidroin particles' diameters were determined by *in situ* optical microscopy (electrolyte solution with KCl 1 mM, pH 5.5). Parts e and f of Figure 6.2 show the corresponding size distributions in the hydrated state for both types of protein particles. The hydrated eADF4(κ 16) particles are in average about 20 % larger in diameter compared to eADF4(C16) particles. The size distributions are highly polydisperse, which is typical for colloids prepared by a salting-out process. [12]

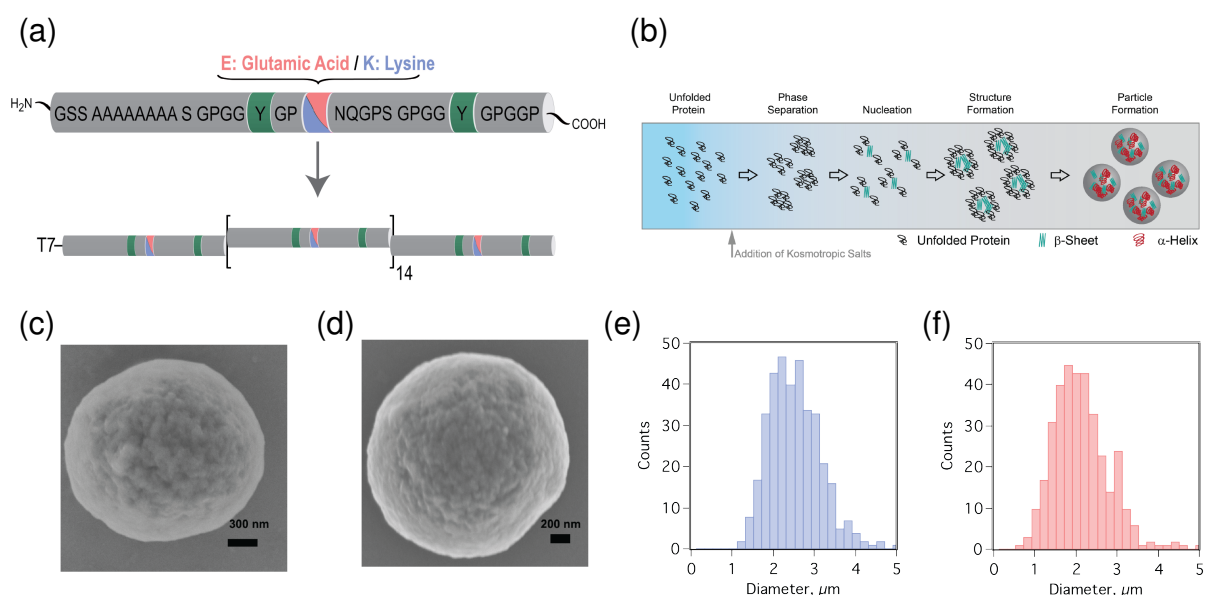


Figure 6.2: (a) Schematic representation of the modular structure of the two recombinant spider silk proteins eADF4(κ 16) and eADF4(C16), which differ only by one amino acid per module, which is repeated 16 times. (b) Outline of the particle preparation by salting-out of the protein using a kosmotropic salt. (c and d) Representative SEM images of dried spider silk particles prepared from (c) eADF4(κ 16) and (d) eADF4(C16), respectively. (e and f) Particle size distributions in the hydrated state as determined at an ionic strength of 1 mM and pH 5.5 by optical microscopy for (e) eADF4(κ 16) and (f) eADF4(C16), respectively.

6.4.2 Electrophoretic Mobility of Spidroin Particles

Figure 6.3 shows the electrophoretic mobility μ of eADF4(κ 16) and eADF4(C16) particles, respectively, at three solution ionic strengths $I = 10$ mM (Figure 6.3, parts a and d), 1 mM (Figure 6.3, parts b and e), and 0.1 mM (Figure 6.3, parts c and f) as a function of pH. Qualitatively, μ of eADF4(κ 16) particles was positive and approximately constant for $4 \leq \text{pH} \leq 8$, regardless of the ionic strength. At $\text{pH} \approx 9.3-9.7$, the mobility switched sign, indicating the point of zero mobility (PZM). The PZM nearly coincided with the theoretical $pI = 9.7$ estimated for eADF4(κ 16) by ExPASy ProtParam. [43] With increasing pH above the PZM, μ increased by approximately 1 order of magnitude. Only for $I = 1$ mM an increase of μ with decreasing pH ($\text{pH } 4 \rightarrow \text{pH } 3$) could be observed. However, this increase was not detected under the two other ionic strength conditions. Basically, the obtained data are consistent with previous electrokinetic data reported for particles prepared from eADF4(κ 16) but measured at a single pH and ionic strength. [14]

Due to the relatively small fraction of residual groups in the proteins that can be ionized in the investigated pH range, the amino acid replacement from lysine to glutamic acid leads to

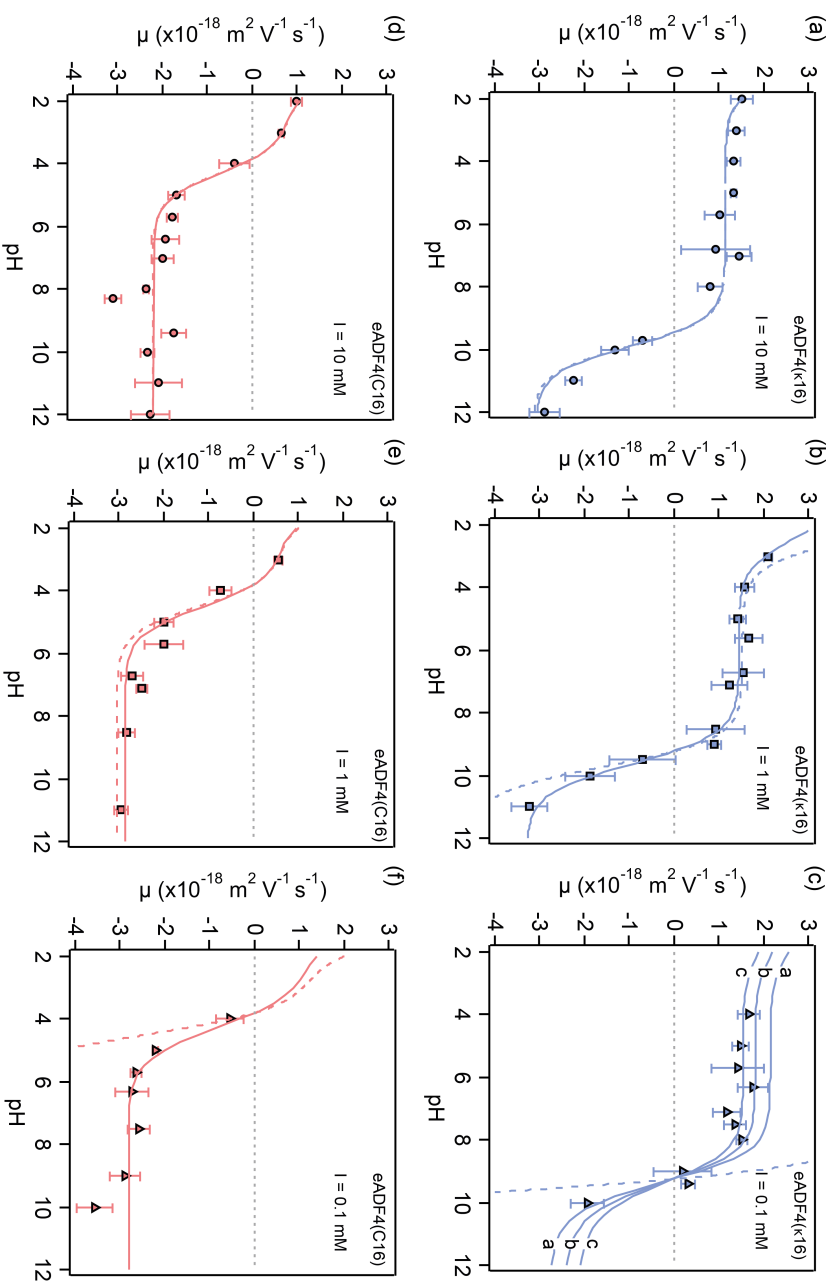


Figure 6.3: Electrophoretic mobility of eADF4(κ 16) and eADF4(C16) particles at an ionic strength of 10 mM (a and d), 1 mM (b and e), and 0.1 mM (c and f) as a function of pH. Symbols correspond to the experimental data. The dashed lines correspond to eq 6.9, and the solid lines are computations performed on the basis of Duva-Ohshima's theory (ref [44] in the limit of homogeneous polymer segment density distribution in the porous eADF4(κ 16) and eADF4(C16) particles (*i.e.*, $\alpha \rightarrow 0$). Model parameter values for ρ_c/F^+ , ρ_a/F^+ , pK_c , pK_a , and $1/\lambda_0$ are summarized in Table 6.1. Calculations were performed with $\delta = 1.5 \mu\text{m}$ (eADF4(κ 16) particles) and $\delta = 1.0 \mu\text{m}$ (eADF4(C16) particles). Lines a, b, and c in panel c refer to $1/\lambda_0 = 1, 7$, and 3 nm , respectively. See text for further details.

pronounced differences concerning the dependence of eADF4(C16) electrophoretic mobility on pH (Figure 6.3 d-f) as compared to that of eADF4(κ 16) (*cf.* Figure 6.3 a-c). In particular, the PZM was reached at lower pH values (ca. pH 3.5-4) for eADF4(C16) particles. Again, the PZM correlated well with the theoretical value $pI = 3.5$ calculated using ExpASy ProtParam. [43] The electrophoretic mobility of eADF4(C16) particles depended more significantly on the solution ionic strength compared to that of eADF4(κ 16) particles. These differences between electrokinetic response of eADF4(κ 16) and eADF4(C16) particles may originate from a different particle structure, and therewith from changes in flow permeability (parameter $1/\lambda_0$) as further discussed below upon quantitative modeling of the electrokinetic data (solid and dashed lines in Figure 6.3).

6.4.3 Electrophoretic Mobility of eADF4(κ 16) Particles

For eADF4(κ 16) particles, the mobility plateau values reached in the pH range of 4-8 at $I = 10$ mM and $I = 1-0.1$ mM depended only weakly on electrolyte concentration, with mean values of $\mu \sim 1.2 \times 10^{-8} \text{ m}^2 \text{ V}^{-1} \text{ s}^{-1}$ and $\mu \sim 1.4-1.5 \times 10^{-8} \text{ m}^2 \text{ V}^{-1} \text{ s}^{-1}$, respectively. Such a weak dependence of μ on I is classically observed for soft particles even at much higher electrolyte concentrations ($I \geq 100$ mM) when particle charges are completely screened by ions. [20, 22, 27] For this limit of an infinitely thin electrical double layer ($\kappa\delta \gg 1$), μ is defined by $\mu \sim \rho_0/(\lambda_0^2)$, [22] with $\lambda_0 \delta \gg 1$. Here, κ^{-1} is the Debye length, and ρ_0 and $1/\lambda_0$ have been defined in the theoretical section. The finding that μ is practically independent of the ionic strength at a low range of 0.1-10 mM strongly suggests that eADF4(κ 16) particles are poorly charged (*i.e.*, their dimensionless radial potential satisfies $y(r) \ll 1$) and that their electrophoretic mobility is essentially determined by a strong penetration of the electroosmotic flow within the particle, which corresponds to large values of $1/\lambda_0$. These anticipations are confirmed below by the quantitative interpretation of the data upon application of the electrokinetic theory for soft particles.

The key electrohydrodynamic parameters $\rho_{a,c}$, $pK_{a,c}$, and $1/\lambda_0$ of eADF4(κ 16) particles were determined as follows: In the pH range of 4-8, μ does not depend on solution pH, indicating that the inequalities $\text{pH} \gg pK_a$ and $\text{pH} \ll pK_c$ are essentially satisfied in this pH range, *i.e.*, the dissociation of acid groups and the protonation of basic groups in the protein particles are complete. Consequently, in this pH range the following relationship is valid

$$\rho(r) = f(r)\rho_0 \quad (6.7)$$

with $\rho_0 = \rho_c - \rho_a$. This expression is derived from eq 6.4 in the limits of $\text{pH} \gg pK_a$ and $\text{pH} \ll pK_c$. In addition, a homogeneous distribution of charged polymer segments within the particle

6 Colloidal Properties of Recombinant Spider Silk Protein Particles

(i.e., $\alpha \rightarrow 0$) can be legitimately assumed in a first approach. This assumption is valid either at sufficiently high salt concentrations and/or for poorly charged porous particles for which repulsive interactions between ionizable groups are least significant. [20, 27] Under these conditions $\rho_0 \sim \rho(0 \leq r \leq \delta)$ can be approximated, which is the case for pH 4-8. As a result, only two unknown parameters have to be determined, ρ_0 and $1/\lambda_0$, in order to rationalize the particle mobility values μ as measured in the pH range from pH 4 to 8 at $I = 10, 1, \text{ and } 0.1 \text{ mM}$.

The parameters ρ_0 and $1/\lambda_0$ cannot be fitted independently but have to be determined simultaneously. Figure 6.4 summarizes the ensemble of $(\rho_0; 1/\lambda_0)$ pairs obtained by numerically solving the set of governing electrohydrodynamic equations in order to reproduce the measured μ value for pH 4-8 at the three different ionic strengths. Within the range of particle sizes (*cf.* Figure 6.2 e) it is emphasized that particle mobility does not depend on δ (*cf.* Supporting Information, Figure 6.9). Basically, this independence of μ on δ results from the fact that the particle size largely exceeds the key length scales pertaining to the distribution of the electrostatic ($\kappa^{-1} = 3\text{-}30 \text{ nm}$ under the investigated electrolyte conditions) and hydrodynamic flow fields ($1/\lambda_0 \sim$ tens of nanometers at most). Ohshima demonstrated an analogous independence of μ on δ by deriving analytically his well-known soft particle mobility expression in ref [22] valid in the limit of "large" core sizes and "large" shell thickness.

Figure 6.4 highlights that the value of ρ_0 is required to decrease with increasing $1/\lambda_0$ in order to match the measured mobility μ at a fixed ionic strength I . This trend is the direct consequence of the relationship $\mu \sim \rho_0/(\eta\lambda_0^2)$ as stated before. Interestingly, the analysis showed that there is a unique pair of $(\rho_0; 1/\lambda_0)$ values leading to a consistent recovery of the measured mobility values at $I = 10 \text{ mM}$ and $I = 1 \text{ mM}$ at low pH. This pair corresponded to the coordinates of the intersection point of the curves depicted in Figure 6.4 for $I = 10 \text{ mM}$ and $I = 1 \text{ mM}$. The obtained values $\rho_0/F = 0.84 \pm 0.05 \text{ mM}$, expressed as equivalent concentration of elementary charges, and $1/\lambda_0 = 11 \pm 0.5 \text{ nm}$ (Figure 6.4 a) allowed us to reconstruct the dependence of μ on pH over the entire range of tested pH values (*cf.* Figure 6.3, parts a and b). For that purpose, additional adjustments of $pK_{a,c}$ and either ρ_a or ρ_c are necessary, with the constraint that the difference $\rho_c - \rho_a$ must correspond to the value of ρ_0 evaluated from Figure 6.4. It has to be emphasized that pK_a , pK_c , and ρ_c primarily control (i) the range of pH where μ is constant, (ii) the pH value where mobility changes sign, and (iii) the mobility level at high pH. The analysis lead to $\rho_c/F = 3.24 \pm 0.1 \text{ mM}$, $\rho_a/F = 2.4 \pm 0.1 \text{ mM}$, $pK_c = 9.8 \pm 0.1$, and $pK_a = 1.2\text{-}2.5$. The uncertainty on pK_a is rather large as this parameter essentially determines the rate of variation of μ at low pH where the experimental value of μ is practically constant. Taken in the limit $\alpha \rightarrow 0$ and $y(r) \rightarrow 0$, from eq 6.4 followed the definition of the point of zero mobility defined by the pH value where $\mu = 0$, by

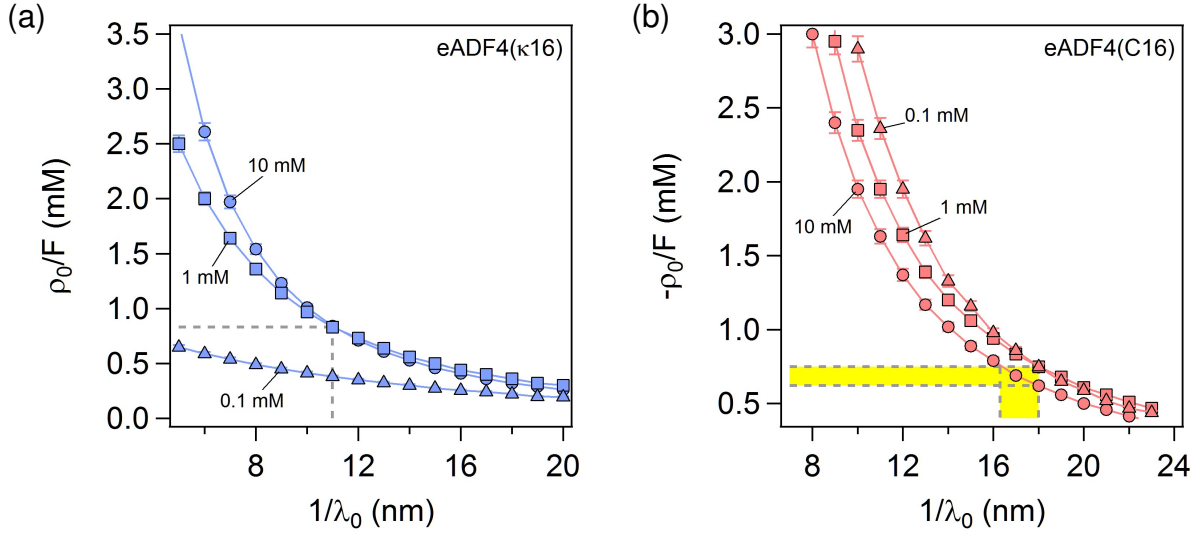


Figure 6.4: Sets of $(\rho_0/F; 1/\lambda_0)$ pairs adopted for retrieving the experimentally determined mobility plateau values reached at low pH (eADF4(κ 16), panel a) or high pH (eADF4(C16), panel b) (see Figure 6.3) employing the Duval-Ohshima theory (ref [44]). The parameter $1/\lambda_0$ pertains to the characteristic electroosmotic flow penetration length scale in the particle, and ρ_0/F is the net (volume) particle charge density (expressed in equivalent molar concentration of elementary charges). Computations were carried out assuming a homogeneous distribution of polymer segment density ($\alpha \rightarrow 0$). Standard deviations were evaluated from the uncertainty of the experimental mobility values. In panel a, the dotted lines illustrate the way the $(\rho_0/F; 1/\lambda_0)$ couple was determined leading to a fit of mobility data at large ionic strengths (10, 1 mM) in the pH range of 4-8. In panel b, the dotted lines and shadow areas illustrate the way the $(-\rho_0/F; 1/\lambda_0)$ couple was determined leading to a fit of mobility data at 10, 1, and 0.1 mM ionic strengths for pH ≥ 6 .

$$PZM = \log \left\{ \left[\frac{\rho_c/\rho_a - 1}{K_c} + \left[\left(\frac{\rho_c/\rho_a - 1}{K_c} \right)^2 + 4 \frac{\rho_c/\rho_a}{K_a K_c} \right]^{1/2} \right] / 2 \right\} \quad (6.8)$$

Based thereon, eq 6.8 reduces to the well-known result $PZM = (pK_a + pK_c)/2$ in the specific case of $\rho_c/\rho_a = 1$. For eADF4(κ 16) particles eq 6.8 leads to $PZM = 9.4 \pm 0.1$, which is in excellent agreement with the theoretical isoelectric point of 9.7 estimated by ExPASy ProtParam. [43] It was verified that the PZM for eADF4(κ 16) is independent of pK_a and is solely defined by the quantities pK_c and $\rho_{a,c}$.

6.4.4 Electrophoretic Mobility of eADF4(κ 16) Particles at Low Ionic Strength

At the lowest ionic strength of $I = 0.1$ mM, the mobility of eADF4(κ 16) particles could not be modeled within the framework outlined in the previous paragraph. Figure 6.3 c shows the comparison between pH-dependent mobility measured at $I = 0.1$ mM and predictions from theory using the electrohydrodynamic parameters $pK_{a,c}$, $\rho_{a,c}$, and $1/\lambda_0$ determined according to the aforementioned procedure. While mobility for $\text{pH} \geq 8$ was correctly reproduced, the experimental data at $\text{pH} \leq 8$ (cf. curve a in Figure 6.3 c) were overestimated. This deviation suggested that the $(\rho_0; 1/\lambda_0)$ pair determined by analyzing the electrokinetic data collected at $I = 10$ mM and $I = 1$ mM was not appropriate for interpreting electrokinetic behavior of eADF4(κ 16) particles at 0.1 mM in the pH range where μ was constant. The absence of a common intersection point between the curves pertaining to $I = 0.1$ mM and $I = 10$ mM or $I = 1$ mM (cf. Figure 6.4 a) confirmed this result. Figure 6.4 a shows that a successful description of the experimental mobility values measured at $\text{pH} \leq 8$ and $I = 0.1$ mM required a lower ρ_0 and/or a lower $1/\lambda_0$ compared to that used for $I = 10$ mM or $I = 1$ mM. Decreasing $1/\lambda_0$ from 11 nm (cf. curve a in Figure 6.3 c) to ca. 3 nm (cf. curve c, Figure 6.3 c) indeed provided a satisfactory fit of the electrokinetic data measured at $I = 0.1$ mM, while leaving the other parameters unaffected. A decrease in $1/\lambda_0$ with decreasing ionic strength is in line with a particle swelling process. The peripheral charged chains that mostly determine the electrokinetic flow structure [20, 21] extend due to enhanced repulsion between their charged groups, increasing the overall resistance to flow (or particle drag), which contributes in fine to a lowered particle mobility. [27, 45] As revealed by X-ray/neutron diffusion and reflectivity studies of numerous soft polyelectrolyte interfaces, [20, 27, 44] interfacial swelling is generally heterogeneous and leads to enhanced decay lengths of the segment density distribution from the bulk particle to the outer electrolyte solution, as illustrated in Figure 6.1 b (eq 6.5). [45] In line with this representation, the mobility values measured at $I = 0.1$ mM could also be correctly reproduced upon adjustment of α from 0 (no significant swelling) at $\text{pH} = 12$ to about 35 nm (maximum swelling) at $\text{pH} \leq 8$ (Figure 6.5) using values of $pK_{a,c}$, $\rho_{a,c}$, and $1/\lambda_0$ as estimated at higher ionic strengths. Additional spatially resolved data would obviously be required to determine whether the particle swelling process at 0.1 mM significantly affects the interfacial homogeneous segment density distribution at larger ionic strengths, or not. This would help determining whether the reconstruction of the electrokinetic data upon variation of $1/\lambda_0$ at constant $\alpha \sim 0$ (Figure 6.3 c) or variation of α at constant $1/\lambda_0$ (Figure 6.5) is eligible. Regardless of this uncertainty, interpretation reveals in all cases an increase of the overall hydrodynamic particle drag with decreasing salt concentration as a result of a particle surface structure that further protrudes toward the outer electrolyte solution due to osmotic swelling.

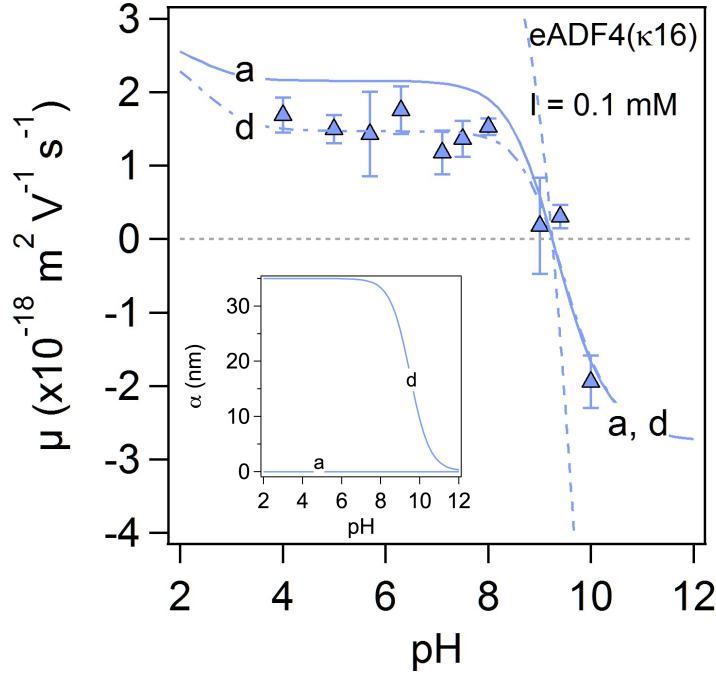


Figure 6.5: Influence of diffuse segment density distribution on the electrophoretic mobility and comparison to experimental values. The solid line (a) corresponds to $\alpha \sim 0$, and the dotted line (d) corresponds to Duval-Ohshima's theory (ref 40) evaluations with diffuse segment density distribution at the eADF4(κ 16)/solution interface as described by the pH-dependent parameter α (see inset). Other model parameter values: $\delta = 1.5 \mu\text{m}$, $1/\lambda_0 = 11 \pm 0.5 \text{ nm}$, $\rho_c/F = 3.24 \pm 0.1 \text{ mM}$, $\rho_a/F = 2.4 \pm 0.1 \text{ mM}$, $pK_c = 9.8 \pm 0.1$, $pK_a = 1.2\text{-}2.5$.

6.4.5 Validity of the Debye-Hückel Limit for Porous Particles

To compare our results with results obtained from rigorous numerical treatment of the governing electrokinetic equations, we consider below the (approximate) theoretical mobility μ_{HF} to be based on the Hermans-Fujita's expression and derived in the Debye-Hückel limit for homogeneous porous particles satisfying $\kappa \delta \gg 1$ and $\lambda_0 \delta \gg 1$: [22, 24]

$$\mu_{HF} = \frac{1}{\eta \lambda_0^2} \left[\frac{\rho_c}{1 + 10^{pH - pK_c}} - \frac{\rho_a}{1 + 10^{pK_a - pH}} \right] \left[1 - \left(\frac{\lambda_0}{\kappa} \right)^2 \frac{1 + \lambda_0/2\kappa}{1 + \lambda_0/\kappa} \right] \quad (6.9)$$

Using the electrohydrodynamic parameters reported in Table 6.1, results indicated that eq 6.9 was satisfactorily applicable at $I = 10 \text{ mM}$ (*cf.* Figure 6.3 a), since only insignificant deviations

6 Colloidal Properties of Recombinant Spider Silk Protein Particles

were observed upon comparison with rigorous numerical treatment of the electrokinetics of porous particles. However, with decreasing I (*cf.* Figure 6.3, parts b and c), eq 6.9 became increasingly inadequate as (i) potentials in the bulk particle and at the interface with the outer electrolyte solution significantly exceeded justification by the Debye-Hückel approximation and the corresponding linearization of Poisson-Boltzmann equation and (ii) electrical double layer polarization, ignored in eq 6.9, became significant. Under the conditions $\kappa \delta \gg 1$, the potential reached in the bulk particle corresponded to the Donnan potential Ψ_D , which is defined by $\Psi_D = \frac{RT}{F} \sinh^{-1} \frac{\rho_c - \rho_a}{2FI}$ at $4 \leq \text{pH} \leq 8$. [22] Using the data summarized in Table 6.1, $\Psi_D \sim 1, 11,$ and 55 mV for $I = 10, 1,$ and 0.1 mM were obtained at $4 \leq \text{pH} \leq 8$, respectively.

Table 6.1: Summary of the electrohydrodynamic parameters estimated for the spider silk particles prepared from eADF4(κ 16) and eADF4(C16).

	ρ_a / F (mM)	ρ_c / F (mM)	$\text{p}K_a$	$\text{p}K_c$	$1/\lambda_0$ (nm)
eADF4(κ 16)	2.4 ± 0.1	3.24 ± 0.1	1.2 - 2.5	9.8 ± 0.1	11 ± 0.5
eADF4(C16)	0.69 ± 0.07	0.87 ± 0.03	1.2 ± 0.1	4.4 ± 0.1	17.3 ± 0.7

6.4.6 Electrophoretic Mobility of eADF4(C16) Particles

The mobility μ of eADF4(C16) particles depended weakly on the ionic strength with $\mu \sim -2.2 \times 10^{-8} \text{ m}^2 \text{ V}^{-1} \text{ s}^{-1}$ for $I = 10$ mM and $\mu \sim -2.9 \pm 0.1 \times 10^{-8} \text{ m}^2 \text{ V}^{-1} \text{ s}^{-1}$ for $I = 1-0.1$ mM at $\text{pH} \geq 6$ (*cf.* Figure 6.3 d-f). In order to evaluate the parameters $\text{p}K_{a,c}$, $\rho_{a,c}$, and $1/\lambda_0$ for eADF4(C16) particles, the approach was used as described previously for eADF4(κ 16) particles. However, the mobility values measured at $\text{pH} \geq 6$ for $I = 10, 1,$ and 0.1 mM were now considered to identify the set of $(\rho_0 = \rho_a; 1/\lambda_0)$ pairs describing the electrokinetic behavior of eADF4(C16) at high pH. The corresponding results are shown in Figure 6.4 b. Unlike eADF4(κ 16) particles, eADF4(C16) particles showed a common intersection point for the curves at $I = 10, 1,$ and 0.1 mM within the experimental errors, with $-\rho_0/F = \rho_a/F = 0.69 \pm 0.07$ mM and $1/\lambda_0 = 17.3 \pm 0.7$ nm. Adopting these parameters, full dependence of μ on pH was reproduced by further setting $\rho_c/F = 0.87 \pm 0.03$ mM, $\text{p}K_c = 4.4 \pm 0.1$, and $\text{p}K_a = 1.2 \pm 0.1$, as indicated by the solid lines in Figure 6.3 d-f.

The PZM of eADF4(C16) particles was about 3.8 ± 0.1 as evaluated from eq 6.8 using the determined $\text{p}K_{a,c}$ and $\rho_{a,c}$, which is again in good agreement with the theoretical isoelectric point

of 3.5 calculated by ExPASy ProtParam. [43] Analogously to eADF4(κ 16) particles, eq 6.9 was of limited use to accurately reproduce the pH-dependent electrokinetic features of eADF4(C16) particles at low ionic strength (*cf.* dashed lines in Figure 6.3). The Donnan potential for bulk eADF4(C16) particles was $\Psi_D \sim -0.9, -9, \text{ and } -50 \text{ mV}$ for $I = 10, 1, \text{ and } 0.1 \text{ mM}$, respectively, at $\text{pH} \geq 6$. Table 6.1 summarizes the set of electrohydrodynamic parameters determined for eADF4(κ 16) and eADF4(C16) particles.

6.4.7 Multilayered Spidroin Particles

Preparation of multilayer systems is well established for oppositely charged macromolecules in interface and colloid science. [46, 47, 48, 49] The corresponding process is also often referred to as layer-by-layer (LbL) preparation. While this concept has been mostly exploited for combinations of polyelectrolytes, LbL films and capsules can also be prepared from polyelectrolyte/protein or protein/protein combinations. [6] Due to the opposite charge of eADF4(C16) and eADF4(κ 16) (*cf.* Figure 6.3), LbL systems with alternating layers of these spidroins were obtained as reported previously. [14]

LbL particles with one additional layer of oppositely charged protein type (*i.e.* eADF4 (C16) particles with a layer of eADF4(κ 16) and eADF4(κ 16) particles with a layer of eADF4(C16), respectively) were examined in terms of their respective electrophoretic mobility. The outer layer allowed deciphering its role in the overall electrokinetic properties of the spidroin particles. In Figure 6.6 the electrophoretic mobility of the particles prepared from a single protein type is compared with the mobility of particles having an additional outer layer. Each graph displays the electrophoretic mobility as a function of pH for particles terminated with the same type of protein. All measurements have been performed at a constant ionic strength of 10 mM.

Figure 6.6 a shows that within the accuracy of the measurements the mobility of eADF4(κ 16) particles and eADF4(C16) particles coated with a layer of eADF4(κ 16) was practically identical over the entire pH range examined in this work, and likewise the mobility of eADF4(C16) particles and eADF4(κ 16) particles coated by a layer of eADF4(C16) (*cf.* Figure 6.6 b). In both cases, the largest differences between "bare" and coated particles were observed near the PZM. At the respective PZM values of the coatings, the outermost particle region is uncharged with the charge of the underlying particle component, consisting of a different protein (with distinct electrostatic features) impacting the particle mobility. However, as reported for polyelectrolyte multilayers, [49] despite intercalation of the layers the overall charge was primarily dominated by the outermost layer.

6 Colloidal Properties of Recombinant Spider Silk Protein Particles

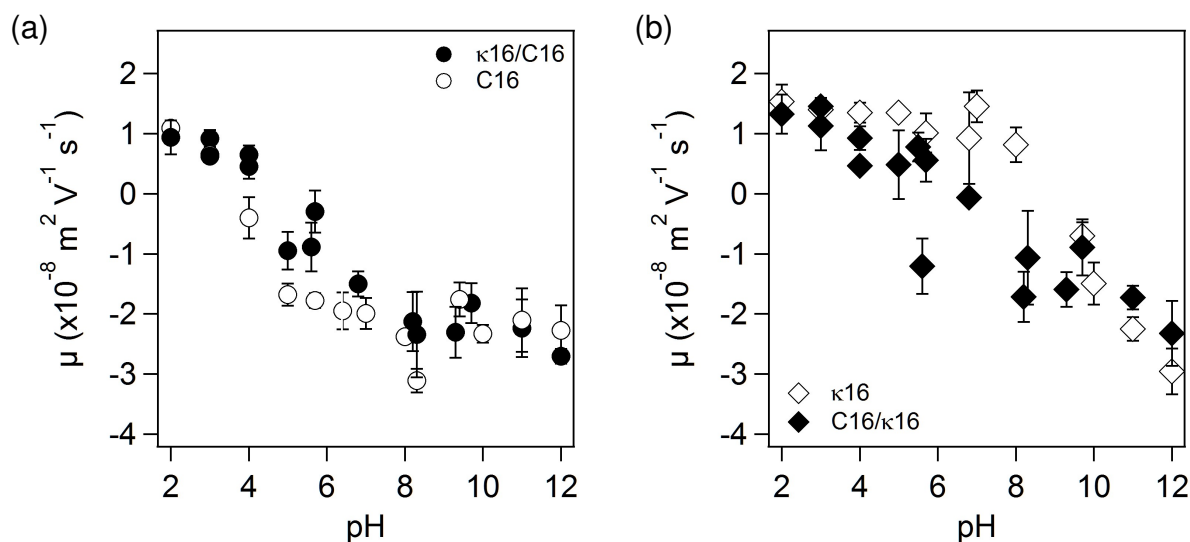


Figure 6.6: Electrophoretic mobility of layer-by-layer spider silk protein particles compared to that of homogeneous particles (*i.e.*, without additional protein layer). (a) eADF4(C16) particles (open symbols) and eADF4(κ 16) particles coated with a layer of eADF4(C16) (filled symbols). (b) eADF4(κ 16) particles (open symbols) and eADF4(C16) particles coated with a layer of eADF4(κ 16) (closed symbols).

6.4.8 Direct Force Measurements of Spidroin Particles

Direct force measurements were performed using the colloidal probe AFM technique in sphere-sphere geometry, [50, 51] as recently reported. [13] The spidroin particles, either eADF4(C16) or eADF4(κ 16), were coadsorbed on a solid substrate together with silica particles. The interaction force profiles were determined with a silica colloidal probe. The FluidFM technique allows for attaching silica particles in a temporary manner and exchanging them in case of contamination. [36] The silica particles immobilized on the substrate served as "internal standards" as they are incompressible and have well-known diffuse layer properties. [52, 53] The direct force measurements were performed at pH 3 in a 1 mM solution ionic strength, the condition at which the mobility of both types of spidroins was similar in terms of magnitude and sign (*cf.* Figure 6.3, parts b and e).

Figure 6.7 a shows the force profile obtained between a silica colloidal probe and an immobilized silica particle. The measured forces were systematically normalized to the effective radius R_{eff} given by $1/R_{eff} = 1/\delta + 1/\delta_{SiOx}$ with δ_{SiOx} being the radius of the probe particle and δ that of the immobilized particle (*i.e.*, either silica or spidroin particle). The lines represent fits of the measured force *versus* distance profiles using theoretical predictions based on the full solutions of the Poisson-Boltzmann equation under standard boundary conditions of constant

6.4 Results and Discussion

charge (CC), constant potential (CP), or charge regulation. The latter corresponds to the solid line and provides a superior description of experimental data collected at small separation distances, *i.e.*, below approximately one Debye length. [54] The Debye length of $\kappa^{-1} = 9.3$ nm has been calculated on the basis of the nominal ionic strength of 1 mM adopted in these experiments. The decay of the interaction forces coincided with this theoretical Debye length value at larger separation distances, indicating that the interaction forces resulted from diffuse layer overlap, thus being of pure electrostatic origin. The obtained diffuse layer potential $\Psi = -25$ mV is in good agreement with that expected for the well-documented ionization behavior of silica. [54, 55, 56]

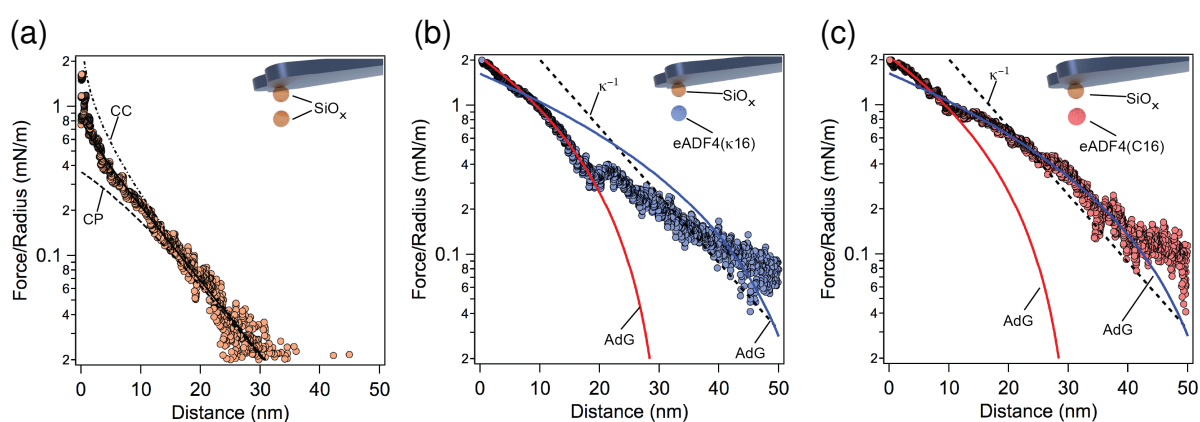


Figure 6.7: (a) Interaction forces between two silica particles. The lines indicate fits based on the full solutions of the Poisson-Boltzmann equation under constant potential (CP) or constant charge (CC) boundary conditions (see labels) as well as including charge regulation (solid line). The interaction between the silica particles is dominated by diffuse layer overlap, and the decay length corresponds to the theoretical Debye length. (b and c) Interaction forces between a silica particle and eADF4(κ 16) and eADF4(C16) particles (indicated). Steric interactions dominate the force profiles, which were measured at an ionic strength of 1 mM at pH 3. In panels b and c, red and blue solid lines are fits of force *versus* distance profiles collected for eADF4(κ 16) and eADF4(C16) particles, according to the Alexander-de Gennes (AdG) model. For the sake of comparison, these curves are reported both in panels b and c.

Parts b and c of Figure 6.7 show representative examples of the interaction force profiles measured between colloidal silica probes and eADF4(κ 16) or eADF4(C16) particles, respectively. The spidroin particles were relatively soft and could be easily compressed. [13, 38] Due to the softness of these particles, the relative distance between the AFM colloidal probe and the spider silk protein particle could not be determined in an unambiguous manner. Since eADF4(C16) and eADF4(κ 16) particles showed comparable elastic moduli, the separation distance between

6 Colloidal Properties of Recombinant Spider Silk Protein Particles

the colloidal probe and the protein particles was set to zero for an applied force of $F_m = 2$ mN/m, below which the force acting on the cantilever resulted only from the mechanical compression of the particle.

The dashed lines in Figure 6.7, parts b and c, indicate the interaction decay length expected for a scenario where diffuse layers overlap (*i.e.*, the same κ^{-1} as that obtained for the interaction between two silica particles, see Figure 6.7 a). Obviously, the interaction force profiles for both types of spidroin particles were not compatible with such a diffuse layer overlap scenario, since the slope of the force profiles was not constant (plotted in a semilogarithmic representation) with distance even at large separations. More than 75% of the force profiles showed also secondary minima measured for both types of spidroin particles. In addition, the silica probes were only slightly negatively charged at pH 3, [54] while both protein particles were positively charged (Figure 6.3). The absence of long-ranged attractive forces, as expected for interacting oppositely charged particles, provided evidence that other forces than electrostatics, *e.g.*, steric forces, govern the interparticular interactions. Steric repulsive forces can be described by means of the AdG model due to the compression of the flexible protein structures by the silica particle (*cf.* eq 6.1). [57, 58, 59, 60, 61, 62] While this model was established for the interaction of uncharged polymer brushes, it can be also applied for describing interaction forces between physisorbed polyelectrolyte layers. [39, 40] Over a significant range of separation distances D ($0.1 L < D < 0.9 L$), the interaction profile could be described with sufficient accuracy in terms of a purely exponential decay (albeit with a characteristic decay length that differed from the theoretical κ^{-1}). [59] If additional electrostatic contributions are taken into account the resulting electrosteric interaction profiles follow as well an approximately exponential force law. [63]

The solid lines in Figure 6.7, parts b and c, resulted from fits of force *versus* distance profiles according to the AdG model at separation distances in the range of 10-20 nm for eADF4(κ 16) (blue curve) and of 20-40 nm for eADF4(C16) (red curve), respectively. For both particles, comparable average anchor densities were obtained with $s = 4.8 \pm 1$ nm for eADF4(κ 16) and 6.7 ± 3.7 nm for eADF4(C16), respectively. However, the obtained brush lengths were significantly different with $L = 192 \pm 47$ nm and $L = 321 \pm 87$ nm for eADF4(κ 16) and eADF4(C16) particles, respectively. It is premature and speculative at this stage to quantitatively relate protein segment density distributions, interaction force profiles (Figure 6.7), and electrokinetics, in particular friction forces under lateral flow conditions (Figure 6.3), due to the lack of a sufficiently detailed description of the actual protein distribution within the particles prepared by salting-out. [44] Despite this difficulty, AFM and electrokinetics showed some key colloidal features of eADF4(κ 16) and eADF4(C16) particles that are further discussed below.

6.5 Summary and Discussion

The electrophoretic mobility of spidroin particles is determined by the electrohydrodynamic properties of their outer surface layer, a feature that has been reported for other soft micrometer-sized particles and films. [20] The relevant protolytic, electrostatic, and flow penetration length parameters are summarized in Table 6.1. The electrophoretic mobility was basically independent of particle size and was governed by the volume charge density and the friction characteristics of the electrokinetically active particle region located at the outer particle periphery. The thickness of this region is controlled by the hydrodynamic penetration depth $1/\lambda_0$ and the Debye length κ^{-1} (*i.e.*, few tens of nanometers). [20, 21, 23] The existence of this electrokinetically active layer of limited thickness at the particle's outer region was further confirmed by the electrokinetic response of multilayered particles. The measured electrophoretic mobility was shown to be primarily governed by the electrohydrodynamic features only of the outer protein layer (*cf.* Figure 6.6). In addition, direct force measurements confirmed that the protein particles are poorly charged and they exhibit a fuzzy, peripheral porous structure leading to significant steric forces at large separation distances when interacting with hard silica spheres. The existence of such a peripheral porous structure was supported by the significant electroosmotic flow penetration lengths as derived from analysis of electrokinetics. Compilation and analysis of electrohydrodynamic data collected for various Gram-positive and Gram-negative bacteria, also displaying soft proteinaceous and/or polysaccharidic surface structures, revealed charge densities and flow penetration lengths in the range of 1-200 mM and 0.5-7 nm, respectively. [20] In the framework of the AdG model, assuming a brushlike structure, the steric forces were comparable for both types of protein particles and the brushlike structure extended to several tenths of nanometers. In order to model the interaction force with more realistic interaction potentials including electrosteric and mechanical particle deformation contributions, [29] a more refined density profile of the protein segments at the particle/solution interface would be required. The larger brush length of eADF4(C16) particles in comparison to that of eADF4(κ 16) ones could be indicative for a larger solvent uptake, and thus for a larger flow penetration length scale under electrokinetic conditions, agreeing with the larger $1/\lambda_0$ value obtained for eADF4(C16) particles (Table 6.1).

AFM force profiles and measured electrophoretic mobilities for spidroin particles can significantly differ depending on the particle batches investigated. These variations are probably connected to differences in the segment density profiles resulting from preparation conditions and to slight changes thereof, a result that is well-known for particles produced by salting-out. [12] In line with this, previous work demonstrated that the electrophoretic mobility of silkworm silk fibroin particles strongly depends on tiny changes in particle preparation conditions. [12, 64]

6 Colloidal Properties of Recombinant Spider Silk Protein Particles

The derived electrohydrodynamic parameters are in agreement with the chemical composition of the constitutive amino acid sequence of the spidroins. The obtained effective dissociation constants $pK_{a,c}$ and charge densities $\rho_{a,c}/F$ lead to points of zero mobility being in very good agreement with the theoretical isoelectric points calculated by ExPASy ProtParam. Using this algorithm, the complete amino acid sequence (including every single pK_a value of each amino acid involved) is taken into account to calculate a theoretical pI . The consistency of the results provided by the ExPASy tool was addressed in several other studies and compared within a good accuracy to experimental data obtained from isoelectric focusing. [65, 66] Due to the simple structure of the spider silk proteins studied here, one can assume a good prediction of the pI by ExPASy ProtParam, which has been confirmed here by isoelectric focusing, thus making a separate analysis of the single proteins (electrokinetic/potentiometric titration) not mandatory. The ionization behavior of the amino acids in the side chains of the two spider silk proteins (*i.e.*, lysine and glutamic acid, respectively) coincide largely with the pK_a found experimentally (*cf.* Table 6.1 and Table 6.2 in the Supporting Information). The experimentally determined ionization constants pK_a most likely include contributions from ion adsorption to the hydrophobic parts of the proteins, as reported for poly(ethylene glycol) (PEG) or hydrophobic self-assembled monolayers. [53] The influence of such counterion binding could be addressed by measuring the electrophoretic mobility of single proteins as demonstrated for lysozyme. [67] However, the recombinant spider silk proteins are intrinsically unfolded as shown by circular dichroism spectroscopy. [34] Hence, electrophoretic measurements will be not as conclusive as for the compact lysozymes. The volume charge densities $\rho_{a,c}/F$ obtained from the fits of electrokinetic measurements fall in the range of 3.2-0.7 mM for both particle types (*cf.* Table 6.1). In order to verify if these values for $\rho_{a,c}/F$ are reasonable, we estimated in the following the number of ionizable groups per volume in the eADF4(C16) spidroin particles: For the particles a density of 1.35 g/cm^3 can be assumed in the hydrated state. [68] The spidroin eADF4(C16) has a molecular mass of $M_w = 47\,698.3 \text{ g/mol}$, and we obtained $(1.35 \text{ g/cm}^3 - 1 \text{ g/cm}^3) / M_w$ for the concentration of one protein molecule per unit volume neglecting the volume occupied by the protein. Assuming that the charge primarily originates from lysine or glutamic acid residues (*i.e.*, one ionized group per protein module) an upper limit of 0.46 mM is found for $\rho_{a,c}/F$. Despite the inherent heterogeneities in particle structure/size and the difficulties to relate electrokinetic and titrable charge densities, [22] the above estimate compares remarkable well with values for $\rho_{a,c}/F$ reported in Table 6.1 and derived here from electrokinetic analysis. It should be pointed out that, for practical applications, the eq 6.9 is a good approximation for the relationship between electrophoretic mobility and volume charge density at sufficiently high ionic strengths.

6.6 Conclusions

Changing the amino acid composition of spidroins induces profound changes in electrokinetics of colloidal particles made thereof. However, the influence of the preparation method is experimentally more difficult to control than the amino acid composition. Salting-out processes influence the interfacial/bulk particle structure (*e.g.*, in terms of arrangement of constitutive proteins) that may change even after small variations of the preparation conditions (stirring speed, local electrolyte concentrations, local pH gradient, etc.). The resulting charge density profile of the outer layer of the protein particle predominantly affects the particle's electrophoretic mobility. Direct force measurements by AFM support conclusions drawn from the electrokinetic analysis, *i.e.*, eADF4(κ 16) and eADF4(C16) particles are poorly charged colloidal systems, displaying a fuzzy (soft) polymer-like structure, and their stability *versus* aggregation is primarily ensured via repulsive steric forces. The measurement of the electrophoretic mobility of the particles as a function of pH and salt concentration provided a direct analytical approach to efficiently probe their interface and, thus, characterize their electrohydrodynamic features.

6.7 Acknowledgments

The authors thank C. Kunert for her help with scanning electron microscopy measurements. We further thank Christian Bippes, Patrick Frederix (Nanosurf AG), and Pablo Dörig (Cytosurge AG) for technical support. This work has been supported by the Deutsche Forschungsgesellschaft (German research council) in the framework of the SFB 840 (TP C4 and TP A8).

6.8 Supporting Information

6.8.1 SEM images of spidroin particles

6 Colloidal Properties of Recombinant Spider Silk Protein Particles

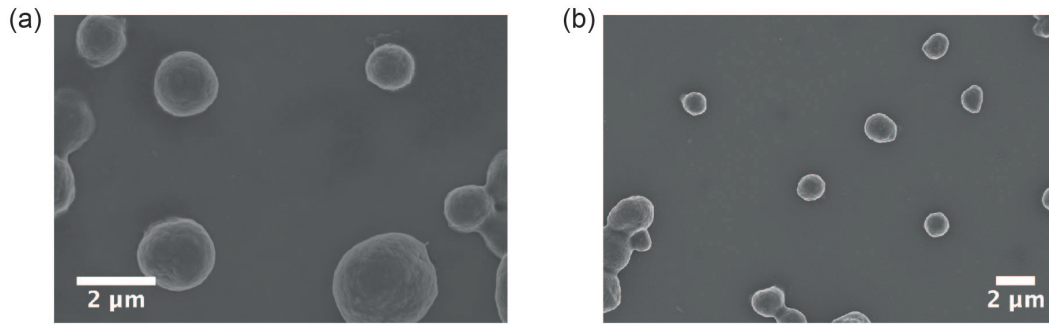


Figure 6.8: SEM images of several particles of each protein type (a) eADF4(κ 16) and (b) eADF4(C16).

6.8.2 Independence of particle mobility with respect to changes in particle size

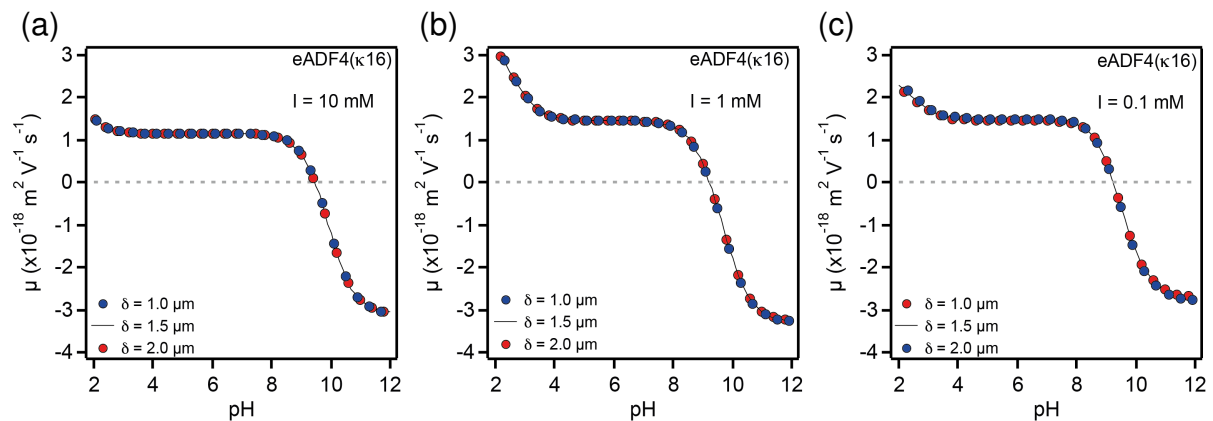


Figure 6.9: Evidence of the size-independence of eADF4(κ 16) electrophoretic mobility in the radius range 1-2 μm at 10 mM (a), 1 mM (b) and 0.1 mM (c) under the conditions as used for the studies shown in Figure 6.3 a, 6.3 b, 6.3 c (line (a) therein), respectively, using the Duval-Oshima's theory. [27] Meaning of symbols and line are specified in the figure with δ the porous particle radius.

The polydispersity of the here presented protein particles is rather large. However, the derived electrokinetic parameters from our analysis are basically independent of the protein particles size over a wide range of radii as shown in Figure 6.9 for various ionic strengths.

6.8.3 Summary of ionizable groups of the recombinant spider silk proteins eADF4(C16) and eADF4(κ 16)

Table 6.2: Ionizable groups of recombinant spider silk proteins eADF4(κ 16) and eADF4(C16).

	κ - module	C- module	both modules	C- terminus	N- terminus	T7-Tag
Amino acid	Lysine L	Glutamic acid E	Tyrosine Y	Glycine G	Methionine M	Arginine R
pK_{sidechain}	10.53 [69]	4.25 [69]	10.07 [69]	-	- 12.28 [69]	
pK_{carboxyl-term.}	-	-	-	2.34	-	-
pK_{amino-term.}	-	-	-	-	9.21	-
Groups / molecule	16	16	32	1	1	1
Hydropathy index	-3.9	-3.5	-1.3	-0.4	1.9	-4.5

References

- [1] M S Desai and S-W Lee. Protein-based functional nanomaterial design for bioengineering applications. *Wiley Interdisciplinary Reviews: Nanomedicine and Nanobiotechnology*, 7(1):69–97, 2015.
- [2] R L DiMarco and S C Heilshorn. Multifunctional Materials through Modular Protein Engineering. *Advanced Materials*, 24(29):3923–3940, 2012.
- [3] D L Nettles, A Chilkoti, and L A Setton. Applications of elastin-like polypeptides in tissue engineering. *Advanced Drug Delivery Reviews*, 62(15):1479 – 1485, 2010.
- [4] N H Romano, D Sengupta, C Chung, and S C Heilshorn. Protein-engineered biomaterials: Nanoscale mimics of the extracellular matrix. *Biochimica et Biophysica Acta (BBA) - General Subjects*, 1810(3):339 – 349, 2011.
- [5] K Schacht and T Scheibel. Processing of recombinant spider silk proteins into tailor-made materials for biomaterials applications. *Current Opinion in Biotechnology*, 29:62 – 69, 2014.
- [6] X Wang, H J Kim, P Xu, A Matsumoto, and D L Kaplan. Biomaterial Coatings by Stepwise Deposition of Silk Fibroin. *Langmuir*, 21(24):11335–11341, 2005.
- [7] E Doblhofer, A Heidebrecht, and T Scheibel. To spin or not to spin: spider silk fibers and more. *Applied Microbiology and Biotechnology*, 99(22):9361–9380, 2015.
- [8] K Schacht, J Vogt, and T Scheibel. Foams Made of Engineered Recombinant Spider Silk Proteins as 3D Scaffolds for Cell Growth. *ACS Biomaterials Science & Engineering*, 2(4):517–525, 2016.
- [9] A Heidebrecht, L Eisoldt, J Diehl, A Schmidt, M Geffers, G Lang, and T Scheibel. Biomimetic Fibers Made of Recombinant Spidroins with the Same Toughness as Natural Spider Silk. *Advanced Materials*, 27(13):2189–2194, 2015.
- [10] G Lang, S Jokisch, and T Scheibel. Air Filter Devices Including Nonwoven Meshes of Electrospun Recombinant Spider Silk Proteins. *Journal of Visualized Experiments*, 75:50492, 2015.
- [11] K Schacht and T Scheibel. Controlled Hydrogel Formation of a Recombinant Spider Silk Protein. *Biomacromolecules*, 12(7):2488–2495, 2011.
- [12] A Lammel, M Schwab, U Slotta, G Winter, and T Scheibel. Processing Conditions for the Formation of Spider Silk Microspheres. *ChemSusChem*, 1(5):413–416, 2008.

6 Colloidal Properties of Recombinant Spider Silk Protein Particles

- [13] N Helfricht, M Klug, A Mark, V Kuznetsov, C Blüm, T Scheibel, and G Papastavrou. Surface properties of spider silk particles in solution. *Biomaterials Science*, 1:1166–1171, 2013.
- [14] E Doblhofer and T Scheibel. Engineering of Recombinant Spider Silk Proteins Allows Defined Uptake and Release of Substances. *Journal of Pharmaceutical Sciences*, 104(3):988 – 994, 2015.
- [15] A Florczak, A Mackiewicz, and H Dams-Kozłowska. Functionalized Spider Silk Spheres As Drug Carriers for Targeted Cancer Therapy. *Biomacromolecules*, 15(8):2971–2981, 2014.
- [16] M Hofer, G Winter, and J Myschik. Recombinant spider silk particles for controlled delivery of protein drugs. *Biomaterials*, 33(5):1554 – 1562, 2012.
- [17] A Lammel, M Schwab, M Hofer, G Winter, and T Scheibel. Recombinant spider silk particles as drug delivery vehicles. *Biomaterials*, 32(8):2233 – 2240, 2011.
- [18] F Leermakers, J C Eriksson, and H Lyklema. *Fundamentals of Interface and Colloid Science*, volume 1, chapter Chapter 4 - Association Colloids and their Equilibrium Modelling, pages 4.1–4.123. Academic Press: New York, 1995.
- [19] R W O'Brien and L R White. Electrophoretic mobility of a spherical colloidal particle. *Journal of the Chemical Society, Faraday Transactions 2*, 74:1607–1626, 1978.
- [20] J F L Duval and F Gaboriaud. Progress in electrohydrodynamics of soft microbial particle interphases. *Current Opinion in Colloid Interface Science*, 15(3):184 – 195, 2010.
- [21] R Zimmermann, S S Dukhin, C Werner, and J F L Duval. On the use of electrokinetics for unraveling charging and structure of soft planar polymer films. *Current Opinion in Colloid Interface Science*, 18(2):83 – 92, 2013.
- [22] H Ohshima. Electrophoresis of soft particles. *Advances in Colloid and Interface Science*, 62(2):189 – 235, 1995.
- [23] M Moussa, C Caillet, R M Town, and J F L Duval. Remarkable Electrokinetic Features of Charge-Stratified Soft Nanoparticles: Mobility Reversal in Monovalent Aqueous Electrolyte. *Langmuir*, 31(20):5656–5666, 2015.
- [24] J J Hermans and H Fujita. Electrophoresis of charged polymer molecules with partial free drainage. *Proc. K. Ned. Akad. Wet, Ser. B: Phys. Sci*, B58:182–187, 1955.
- [25] S Levine, M Levine, K A Sharp, and D E Brooks. Theory of the electrokinetic behavior of human erythrocytes. *Biophysical Journal*, 42(2):127 – 135, 1983.

References

- [26] R J Hill, D A Saville, and W B Russel. Electrophoresis of spherical polymer-coated colloidal particles. *Journal of Colloid and Interface Science*, 258(1):56 – 74, 2003.
- [27] J F L Duval and H Ohshima. Electrophoresis of Diffuse Soft Particles. *Langmuir*, 22(8):3533–3546, 2006.
- [28] H Ohshima. Electrophoretic Mobility of Soft Particles. *Journal of Colloid and Interface Science*, 163(2):474 – 483, 1994.
- [29] J F L Duval, J Merlin, and P A L Narayana. Electrostatic interactions between diffuse soft multi-layered (bio)particles: beyond Debye-Huckel approximation and Deryagin formulation. *Physical Chemistry Chemical Physics*, 13:1037–1053, 2011.
- [30] H Ohshima. Electrokinetic phenomena of soft particles. *Current Opinion in Colloid Interface Science*, 18(2):73 – 82, 2013.
- [31] M Hofer, G Winter, and J Myschik. Recombinant spider silk particles for controlled delivery of protein drugs. *Biomaterials*, 33(5):1554 – 1562, 2012.
- [32] C Blüm and T Scheibel. Control of Drug Loading and Release Properties of Spider Silk Sub-Microparticles. *BioNanoScience*, 2(2):67–74, 2012.
- [33] E M Pritchard, P B Dennis, F Omenetto, R R Naik, and D L Kaplan. Physical and chemical aspects of stabilization of compounds in silk. *Biopolymers*, 97(6):479–498, 2012.
- [34] D Huemmerich, C W Helsen, S Quedzuweit, J Oschmann, R Rudolph, and T Scheibel. Primary Structure Elements of Spider Dragline Silks and Their Contribution to Protein Solubility. *Biochemistry*, 43(42):13604–13612, 2004.
- [35] J P Cleveland, S Manne, D Bocek, and P K Hansma. A nondestructive method for determining the spring constant of cantilevers for scanning force microscopy. *Review of Scientific Instruments*, 64(2):403–405, 1993.
- [36] P Dörig, D Ossola, A M Truong, M Graf, F Stauffer, J Vörös, and T Zambelli. Exchangeable Colloidal AFM Probes for the Quantification of Irreversible and Long-Term Interactions. *Biophysical Journal*, 105(2):463 – 472, 2013.
- [37] V Kuznetsov and G Papastavrou. Adhesion of colloidal particles on modified electrodes. *Langmuir*, 28(48):16567–16579, 2012.
- [38] M P Neubauer, C Blüm, E Agostini, J Engert, T Scheibel, and A Fery. Micromechanical characterization of spider silk particles. *Biomaterials Science*, 1(11):1160, 2013.

6 Colloidal Properties of Recombinant Spider Silk Protein Particles

- [39] S Block and C A Helm. Measurement of long-ranged steric forces between polyelectrolyte layers physisorbed from 1 M NaCl. *Physical Review E*, 76:030801, Sep 2007.
- [40] S Block and C A Helm. Conformation of Poly(styrene sulfonate) Layers Physisorbed from High Salt Solution Studied by Force Measurements on Two Different Length Scales. *The Journal of Physical Chemistry B*, 112(31):9318, 2008.
- [41] S S Dukhin, R Zimmermann, J F L Duval, and C Werner. On the applicability of the Brinkman equation in soft surface electrokinetics. *Journal of Colloid and Interface Science*, 350(1):1 – 4, 2010.
- [42] U Ascher, J Christiansen, and R D Russell. Collocation Software for Boundary-Value ODEs. *ACM Transactions on Mathematical Software*, 7(2):209–222, June 1981.
- [43] E Gasteiger, C Hoogland, A Gattiker, S Duvaud, M R Wilkins, R D Appel, and A Bairoch. *Protein Identification and Analysis Tools on the ExPASy Server*, pages 571–607. Humana Press, Totowa, NJ, 2005.
- [44] R Zimmermann, D Romeis, I Bihannic, M Cohen Stuart, J-U Sommer, C Werner, and J F. L. Duval. Electrokinetics as an alternative to neutron reflectivity for evaluation of segment density distribution in peo brushes. *Soft Matter*, 10:7804–7809, 2014.
- [45] J R S Martin, I Bihannic, C Santos, J P S Farinha, B Demé, F A M Leermakers, J P Pinheiro, E Rotureau, and J F L Duval. Structure of Multiresponsive Brush-Decorated Nanoparticles: A Combined Electrokinetic, DLS, and SANS Study. *Langmuir*, 31(16):4779–4790, 2015.
- [46] G Decher. Fuzzy Nanoassemblies: Toward Layered Polymeric Multicomposites. *Science*, 277(5330):1232–1237, 1997.
- [47] G B Sukhorukov, H Möhwald, G Decher, and Y M Lvov. Assembly of polyelectrolyte multilayer films by consecutively alternating adsorption of polynucleotides and polycations. *Thin Solid Films*, 284-285:220–230, 1996.
- [48] M Schönhoff. Layered polyelectrolyte complexes: physics of formation and molecular properties. *Journal of Physics: Condensed Matter*, 15(49):R1781–R1808, 2003.
- [49] R v. Klitzing. Internal structure of polyelectrolyte multilayer assemblies. *Physical Chemistry Chemical Physics*, 8:5012–5033, 2006.
- [50] S Rentsch, R Pericet-Camara, G Papastavrou, and M Borkovec. Probing the validity of the Derjaguin approximation for heterogeneous colloidal particles. *Physical Chemistry Chemical Physics*, 8(21):2531–2538, 2006.

References

- [51] M Borkovec, I Szilagyi, I Popa, M Finessi, P Sinha, P Maroni, and G Papastavrou. Investigating forces between charged particles in the presence of oppositely charged polyelectrolytes with the multi-particle colloidal probe technique. *Advances in Colloid and Interface Science*, 179-182:85–98, 2012.
- [52] P G Hartley, I Larson, and P J Scales. Electrokinetic and direct force measurements between silica and mica surfaces in dilute electrolyte solutions. *Langmuir*, 13(8):2207–2214, 1997.
- [53] V Kuznetsov and G Papastavrou. Ion Adsorption on Modified Electrodes as Determined by Direct Force Measurements under Potentiostatic Control. *The Journal of Physical Chemistry C*, 118(5):2673–2685, 2014.
- [54] R Pericet-Camara, G Papastavrou, S H Behrens, and M Borkovec. Interaction between Charged Surfaces on the Poisson-Boltzmann Level: The Constant Regulation Approximation. *The Journal of Physical Chemistry B*, 108(50):19467–19475, 2004.
- [55] M Kobayashi, F Juillerat, P Galletto, P Bowen, and M Borkovec. Aggregation and Charging of Colloidal Silica Particles: Effect of Particle Size. *Langmuir*, 21(13):5761–5769, 2005.
- [56] M Porus, P Maroni, and M Borkovec. Highly-sensitive reflectometry setup capable of probing the electrical double layer on silica. *Sensors and Actuators B: Chemical*, 151(1):250–255, 2010.
- [57] J Klein. Forces between mica surfaces bearing layers of adsorbed polystyrene in cyclohexane. *Nature*, 288:248–250, 1980.
- [58] P G de Gennes. Polymers at an interface; a simplified view. *Advances in Colloid and Interface Science*, 27:189–209, 1987.
- [59] J N Israelachvili. *Intermolecular and Surface Forces*. Academic Press: London, 2nd edition, 1992.
- [60] H-J Butt, M Kappl, H Mueller, R Raiteri, W Meyer, and J R uhe. Steric Forces Measured with the Atomic Force Microscope at Various Temperatures. *Langmuir*, 15(7):2559–2565, 1999.
- [61] D Kleshchanok, R Tuinier, and P R Lang. Direct measurements of polymer-induced forces. *Journal of Physics: Condensed Matter*, 20(7):073101, 2008.
- [62] S Kaufmann, G Papastavrou, K Kumar, M Textor, and E Reimhult. A detailed investigation of the formation kinetics and layer structure of poly(ethylene glycol) tether supported lipid bilayers. *Soft matter*, 5(14):2804–2814, 2009.

6 Colloidal Properties of Recombinant Spider Silk Protein Particles

- [63] T Abraham, D Christendat, Z Xu, J Masliyah, J F Gohy, and R J r me. Role of poly-electrolyte charge density in tuning colloidal forces. *AIChE Journal*, 50(10):2613–2626, 2004.
- [64] A S Lammel, X Hu, S-H Park, D L Kaplan, and T R Scheibel. Controlling silk fibroin particle features for drug delivery. *Biomaterials*, 31(16):4583–4591, 2010.
- [65] B Bjellqvist, G J Hughes, C Pasquali, N Paquet, F Ravier, J-C Sanchez, S Frutiger, and D Hochstrasser. The focusing positions of polypeptides in immobilized pH gradients can be predicted from their amino acid sequences. *Electrophoresis*, 14(1):1023–1031, 1993.
- [66] B Bjellqvist, B Basse, E Olsen, and J E Celis. Reference points for comparisons of two-dimensional maps of proteins from different human cell types defined in a pH scale where isoelectric points correlate with polypeptide compositions. *Electrophoresis*, 15(1):529–539, 1994.
- [67] A Yamaguchi and M Kobayashi. Quantitative evaluation of shift of slipping plane and counterion binding to lysozyme by electrophoresis method. *Colloid and Polymer Science*, 294:1019–1026, 2016.
- [68] Y Termonia. Molecular Modeling of Spider Silk Elasticity. *Macromolecules*, 27(25):7378–7381, 1994.
- [69] D L Nelson and M M Cox. *Lehninger: Principles of Biochemistry*. Palgrave Macmillan, 2012.

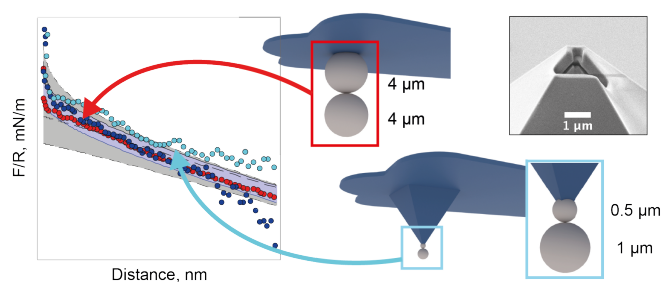
CHAPTER 7

Extending the Limits of Direct Force Measurements: Colloidal Probes from Sub-Micron Particles

Nicolas Helfricht^a, Andreas Mark^a, Livie Dorwling-Carter^b,
Tomaso Zambelli^b, Georg Papastavrou^a

^a Physical Chemistry / Physics of Polymers, Bavarian Polymer Institute, University of Bayreuth, Universitätsstr. 30, 95440 Bayreuth, Germany. Email: Georg.Papastavrou@uni-bayreuth.de

^b Laboratory of Biosensors and Bioelectronics, Institute for Biomedical Engineering, ETH Zurich, CH-8092 Zurich, Switzerland.



Reprinted with permission from:

"Extending the limits of direct force measurements: colloidal probes from sub-micron particles", N. Helfricht, A. Mark, L. Dorwling-Carter, T. Zambelli and G. Papastavrou, *Nanoscale*, **2017**, 9, 9491-9501, DOI: 10.1039/C7NR02226C.

© 2017 Royal Society of Chemistry.

Abstract

Direct force measurements by atomic force microscopy (AFM) in combination with the colloidal probe technique are widely used to determine interaction forces in colloidal systems. However, a number of limitations are still preventing a more universal applicability of this technique. Currently, one of the most significant limitations is that only particles with diameters of several micrometers can be used as probe particles. Here, we present a novel approach, based on the combination of nanofluidics and AFM (also referred to as FluidFM-technique), that allows to overcome this size limit and to extend the size of suitable probe particles below diameters of 500 nanometers. Moreover, by aspiration of colloidal particles with a hollow AFM-cantilever, the immobilization process is independent of the particle's surface chemistry. Furthermore, the probe particles can be exchanged *in situ*. The applicability of the FluidFM-technique is demonstrated with silica particles, which are also the types of particles most often used for the preparation of colloidal probes. By comparing 'classical' colloidal probes, *i.e.* probes from particles irreversibly attached with glue, and various particle sizes aspirated by the FluidFM-technique, we can quantitatively evaluate the instrumental limits. Evaluation of the force profiles demonstrate that even for 500 nm silica particles the diffuse layer properties can be evaluated quantitatively. Therefore, direct force measurements on the level of particle sizes used in industrial formulations will become available in the future.

7.1 Introduction

Direct force measurements have become an indispensable analytical tool to determine surface-dominated interactions in colloid and interface science in recent years. [1, 2, 3, 4, 5] Initially, most measurements were carried out with the surface force apparatus (SFA), whereby the interaction forces were measured between two crossed mica cylinders. [1] With the development of the atomic force microscope (AFM) and the colloidal probe technique direct force measurements at the level of single particles became possible for the first time. [6, 7] The colloidal probe technique is based on attaching a spherical colloidal particle to the end of an AFM-cantilever. This technique allows for determining the interaction of particles with flat surfaces in the sphere/plane geometry as well as between two particles in the sphere/sphere geometry, respectively. [8] Despite the fact that the colloidal probe technique was presented 25 years

ago, [6, 7] the preparation of colloidal probes has not changed fundamentally with time: in most cases a μm -sized colloidal particle is picked up with the end of a thin wire by means of capillary forces and is placed with the help of a micromanipulator and an optical microscope on a tipless AFM-cantilever to which the colloidal particle is permanently attached by adhesives or sintering techniques. [9, 10] Commonly, the diameters of the particles used as colloidal probes fall in the range of few μm up to several tenths of μm . [8, 9, 10, 11, 12, 13, 14]

Two fundamental limits prevent a more general use of the colloidal probe technique: first, the irreversible immobilization of the colloidal particles by gluing or sintering to the AFM-cantilever prevents or significantly complicates the acquisition of large data sets, as the cantilever has to be exchanged several times. The 'multiple colloidal probe' technique allows to overcome these limitations by a reversible chemical immobilization of the colloidal particle. [15, 16] The 'multiple colloidal probe' technique is carried out in a liquid cell, which contains a large number of colloidal particles, *e.g.* after injecting a colloidal suspension in the cell and allowing the colloids to sediment. [15] By contrast to the 'classical' colloidal probes, these colloids are immobilized *in situ* temporarily and it is necessary to chemically modify the surface of the cantilever. Hence, the 'multiple colloidal probe' technique is not applicable for all types of colloidal particles, as a corresponding surface modification of the cantilever must be available to allow for sufficiently strong adhesion.

The second and more significant restriction is that currently nanoparticles cannot be used as colloidal probes for direct force measurements. The manipulation steps for the attachment of particles require the control by optical microscopy. Hence, particle dimensions are limited by the optical resolution, which can be significantly lower than the theoretical limit of about $\lambda/2$. Only, in very few cases direct force measurements or the preparation of colloidal probes with particles of diameters below $2\mu\text{m}$ have been reported. [13, 17, 18] The preparation of colloidal probes from sub- μm particles has been reported only in very few, selected cases, where the preparation is based on picking-up the particles by the cantilever by chance and having little control over the particle position on the cantilever. [17, 18] Hence, post-measurement analysis by electron microscopy is mandatory in order to characterize the colloidal probe. In consequence, the preparation of such sub- μm colloidal probes has never been implemented widely, as the possibility to acquire statistically significant data sets is lacking and only a few types of colloidal particles are suitable.

7 Extending the Limits of Direct Force Measurements

Here, we present a novel approach for direct force measurements with colloidal probes that overcomes the aforementioned limitations of the colloidal probe technique. It is based on a combination of nanofluidics with AFM, often referred to as fluidic force microscopy or shortly FluidFM. [19] The essential components for FluidFM are special, hollow AFM-cantilevers, which are connected to a nanofluidic controller. By an open aperture at the end of the cantilever, liquid can be ejected or colloidal objects can be aspirated. Originally, the FluidFM-technique was developed with the intention to aspirate and manipulate single cells. [20, 21] Recently, it has been shown that the FluidFM-technology is also suitable to aspirate colloidal particles with diameters of several μm , which then can be used as temporary and exchangeable colloidal probes. [22, 23]

We will demonstrate in the following that by FluidFM, sub-micron particles with diameters $\leq 500\text{ nm}$ can be immobilized at the aperture of the FluidFM cantilever. The possibility to use such small particles as colloidal probes opens for the first time a door to determine the interaction potentials between sub- μm sized colloids as used in industrial formulations. However, here we used silica particles for the first *proof-of-principle*. This choice is motivated by several factors: firstly, silica particles are among the best-studied colloidal suspensions. [24, 25, 26] Secondly, silica particles are by far the most frequently used particles as colloidal probes, in particular for direct force measurements. [6, 7, 12, 14, 27, 28, 29, 30, 31, 32, 33, 34] Thirdly, their surface chemistry has prevented so far their use in the 'multiple colloidal probe' technique.

7.2 Experimental Section

Materials

Batches of silica particles with different nominal diameters ($0.5\ \mu\text{m}$, $\sim 1.0\ \mu\text{m}$, and $4.3\ \mu\text{m}$ respectively) have been purchased from MicroParticles (Berlin, Germany). FluidFM-cantilevers of two different types have been purchased from Cytosurge (Glattbrugg, Switzerland): tipless micropipettes (*regular*, nominal spring constant $k_n = 2\ \text{N m}^{-1}$ and *soft*, $k_n = 0.3\ \text{N m}^{-1}$, respectively) with nominal apertures of $2\ \mu\text{m}$ and pyramidal Nanopipettes (*soft*, $k_n = 0.6\ \text{N m}^{-1}$) with nominal apertures of $300\ \text{nm}$. 'Classical' colloidal probes have been prepared with tipless cantilevers from MicroMasch (CSC 37 with a nominal spring constant $k_n = 0.6\ \text{N m}^{-1}$, MicroMasch, Sofia, Bulgaria).

Surface Preparation and Particle Immobilization

Circular glass slides with a diameter of 35 mm (Menzel Gläser, thickness 2, Thermo Scientific,) were cleaned by a modified RCA procedure: [35] First, the glass slides were sonicated in a 2 % Hellmanex II (Hellma GmbH Co. KG, Müllenheim, Germany) solution at 40 °C for 20 min and then thoroughly rinsed with water of Millipore-quality (MQ-water). Second, the substrates were sonicated in a 3:1 (v/v) mixture of isopropanol (p.a., Bernd Kraft GmbH, Duisburg, Germany) and MQ-water for 20 min at room temperature. Afterwards, the slides were rinsed again with MQ-water. Finally, the glass slides were immersed in a 5:1:1 (v/v/v) MQ-water, ammonia (25 %, Normapur, VWR) and hydrogen peroxide (30 %, VWR) at 70 °C for 10 min and then rinsed with MQ-water. The cleaned glass slides were stored in MQ-water for less than one week and were dried under a nitrogen stream directly before use.

The cleaned glass slides were mounted in a fluid cell of a commercial AFM (Asylum Research, Oxford Instruments, Santa Barbara, CA) and a diluted particle suspension was placed in the cell, allowing the aqueous medium to evaporate overnight. The substrates were cleaned with fresh MQ-water, which was exchanged 4 times with the electrolyte solution afterwards used for the direct force measurements. The procedure resembles the one used in the 'multiple colloidal probe' technique but omits the surface modification of the substrate and the AFM cantilever. [15, 36]

Direct Force Measurements

Direct force measurements have been performed on a FluidFM (Flex-FPM V5 equipped with a C3000-controller, Nanosurf AG, Liestal, Switzerland and a Cytosurge nanofluidic control system) and on a MFP-3D (Asylum Research, Santa Barbara), respectively. Both AFMs were mounted on inverted optical microscopes (Axio Observer Z1, Carl Zeiss). The direct force measurements were performed in aqueous electrolyte solutions at pH 10 and different total ionic strength (0.1, 0.3 and 1.0 mM, respectively). The aqueous solutions were prepared from KCl (potassium chloride, Bio Ultra, Sigma) and the pH was adjusted by addition of potassium hydroxide solution (1 M, Titrisol, Merck).

The FluidFM-cantilevers were cleaned for 5 min in air plasma (Zepto, Diener Electronics, Ebhausen, Germany). The reservoir of the FluidFM-cantilevers was filled with ~ 50 μ L MQ-water, which had been degassed and filtered beforehand (Rotilabo-syringe PES filters with pore diameter 0.2 μ m, Carl Roth GmbH, Karlsruhe, Germany). The

7 Extending the Limits of Direct Force Measurements

FluidFM-cantilevers were mounted on the AFM head (Flex-FPM V5) with a suitable cantilever holder. Their resonant frequency was monitored before and after complete filling of the microchannel. The large μm -sized silica particles were aspirated floating near the surface by placing the FluidFM-cantilever in the vicinity of the particle without touching the particles. Success of this procedure was always verified by optical microscopy. By contrast for the particles $< 1 \mu\text{m}$, the particles were randomly floating in the solution and were aspirated by applying a continuous aspiration pressure and running subsequent forces *versus* distance cycles. For continuous immobilization of the particles the holding pressure was reduced to -100 or -300 mbar. The interaction forces were measured either in the sphere/sphere geometry against a second particle immobilized on the surface and in the sphere/plane geometry against the planar surface of the glass slide. The force *vs.* distance cycles were conducted with a ramping velocity of 500 nm s^{-1} for the z-piezo. For each combination of colloidal probe and sample (*i.e.* particle or position on the glass surface) around 50 force profiles were acquired. The raw data were converted into force *versus* distance curves with standard algorithms [5, 37] by a set of custom build routines implemented in IgorPro (Wavemetrics). [8, 23, 38] The spring constants of the FluidFM cantilevers have been determined by the so-called added-mass method. [39, 40] The calibration procedure has been performed after the measurements in aqueous solutions in order to avoid any contaminations during the calibration procedure. The FluidFM cantilevers were dried and the internal cantilever's channel was filled as well by air. Spherical tungsten particles ($n > 5$) were picked up from a glass surface due to capillary forces and the resulting shift in resonant frequency has been determined. The actual particle diameter and the position on the FluidFM-cantilever were evaluated using ImageJ. [41]

'Classical' colloidal probes have been prepared with the help of a UV-curable glue as described previously. [8, 42] First, tipless cantilevers (CSC 37, MicroMasch) were subsequently cleaned with various solvents (ethanol, water, acetone) and air plasma (5 min, Zepto, Diener Electronics, Ebhausen, Germany) before modification. A single silica particle with an average diameter of around $4.1 \mu\text{m}$ was attached to the free end of a tipless AFM cantilever by means of a micromanipulator (DC-3 KS, Märzhäuser, Wetzlar, Germany) and a UV-curable glue (Norland Optical Adhesive 63, Norland Products, Cranbury, NJ). The preparation of the colloidal probes was conducted on a fixed stage-microscope (Axio Examiner D1, Carl Zeiss). Moreover, a suspension of silica particles was dried overnight on a RCA-cleaned glass substrate installed in a liquid cell. Force measurements with these colloidal probes were performed with a MFP-

3D atomic force microscope (Asylum Research Oxford Scientific Instruments, Santa Barbara, CA). The spring constant of each cantilever was calibrated before the immobilization of the colloidal particle according to the thermal noise method [43] and the obtained results were compared with values calculated using the so-called Sader method. [41]

Also for the experiments with 'classical' colloidal probes, for each particle/particle and particle/substrate combination at least 50 force curves were recorded. The force curves were performed with a scanning velocity of 500 nm s^{-1} comparable to the FluidFM experiments and a maximum loading force of around 7 nN has been applied. The data evaluation was performed analogous to the one acquired by the FluidFM.

After conversion of the raw data, the force profiles were normalized to the effective radius for the μm -sized particles. As the actual diameter of probe particles $< 1 \mu\text{m}$ could not be determined by optical microscopy with sufficient accuracy, the effective radius for those interaction geometries has been calculated from the average radii (*cf.* Figure 7.1 b). The force profiles were fitted to the full solutions of the Poisson-Boltzmann equation in the constant regulation approximation [44] for separation distances D with $0.5 \kappa^{-1} < D < 2 \kappa^{-1}$. Contributions by the van der Waal forces can be neglected at these separation distances, in particular due to the surface roughness of not heat-treated silica particles. [8, 34] The obtained average surface potentials, regulation parameter and the fitted solution ionic strength are summarized in the ESI.

Scanning Electron Microscopy (SEM)

To image the silica particles by SEM, particle suspensions were drop cast onto silicon wafers. Beforehand, silicon diced wafer pieces (11 x 11 mm) were cleaned with MQ-water, pure ethanol (p.a. grade, VWR) and treated with a SnowJet (tectra, Frankfurt, Germany). FluidFM-cantilevers were mounted directly on sample holders with conductive adhesives (Plano, Marburg, Germany). All samples were sputtered with a thin layer of platinum of $\sim 1.2 \text{ nm}$ and measured with a Leo 1530 VP Gemini (Zeiss, Germany).

7.3 Results and Discussion

Figure 7.1 a shows an SEM image of the different types of colloidal silica particles used in this study. Besides large silica particles with an average diameter of $4.07 \pm$

7 Extending the Limits of Direct Force Measurements

0.20 μm , two types of smaller silica particles with diameters below 1 μm have been used throughout this study. These particles have an average diameter of 983 ± 30 nm and 496 ± 16 nm, respectively. For all types of silica particles their corresponding size distributions, as determined by SEM, are summarized in Figure 7.1 b. All silica particles have comparable surface chemistry, as we used silica particles prepared by the same process and from the same supplier.

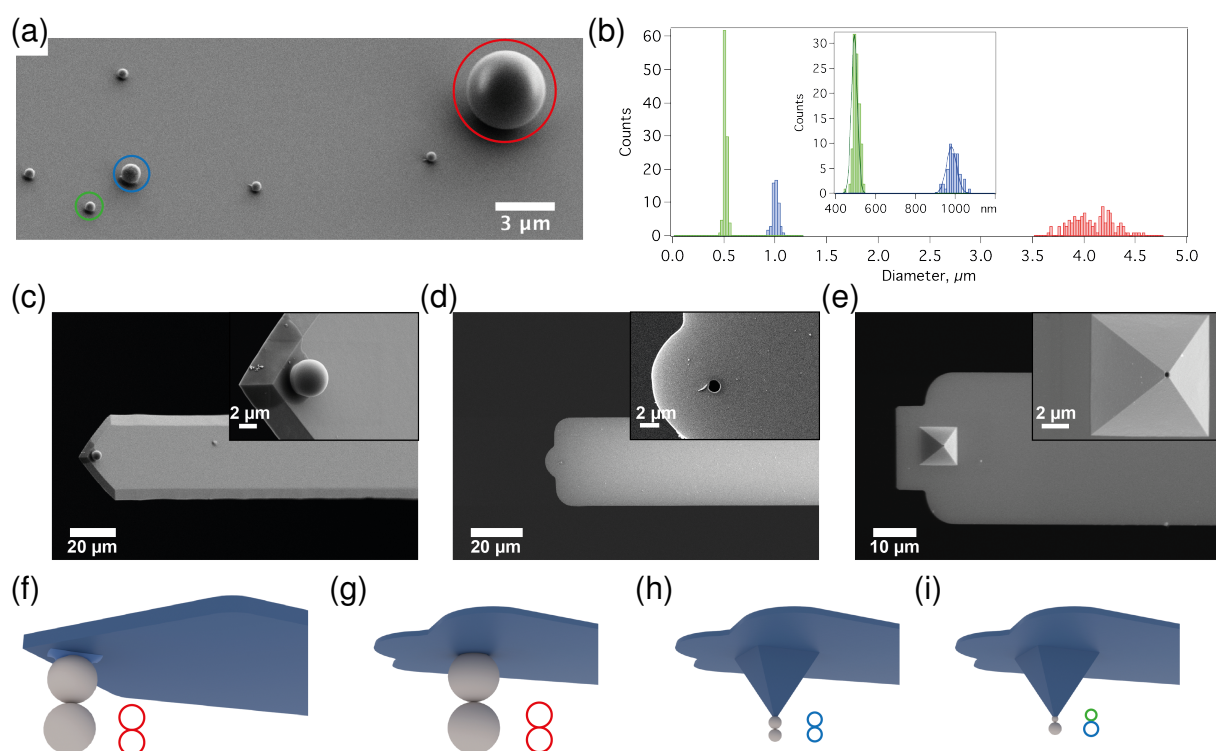


Figure 7.1: (a) SEM image comparing the different types of silica particles used in this study. (b) Size distributions for the three different types of silica particles. The inset shows the distributions for two smaller particle types. (c) 'Classical' colloidal probe with a $\sim 4 \mu\text{m}$ -sized silica particle, which has been glued to the cantilever. (d) Tipless FluidFM-cantilever with an aperture of around $2 \mu\text{m}$ in diameter used for aspirating the large colloidal particles of $\sim 4 \mu\text{m}$ diameter. (e) FluidFM-cantilever with a pyramidal tip and an aperture of around 300 nm in diameter. (f-i) Different combinations of particles and cantilever types by which the direct force measurements in the sphere/sphere geometry have been carried out in this study.

The large particles serve as reference particles for the smaller particles and have been either used as 'classical' colloidal probes (*cf.* Figure 7.1 c) or they were temporarily immobilized to a FluidFM-cantilever by underpressure to a FluidFM cantilever with an

aperture of around $2\ \mu\text{m}$ (*cf.* inset in Figure 7.1 d). In order to immobilize the smaller (*i.e.* sub- μm) particles a different type of FluidFM-cantilever is later required (*cf.* Figure 7.1 e). These cantilevers have a 300 nm aperture (in diameter), which is situated at the apex of a pyramidal shape with a height of $\sim 7\ \mu\text{m}$ is important in order to exclude long-range force contributions due to the lever arm.

Fig. 7.1 f-i illustrate the different combinations of silica particles (*cf.* Figure 7.1 a-b) and cantilevers (*cf.* Figure 7.1 c-e) that have been used in this study for determining the interaction forces between silica particles in the sphere/sphere geometry. According to the Derjaguin approximation the interaction force $F(D)$ at a separation D between the two particles is given by: [1, 5]

$$F(D) = 2\pi R_{eff}W(D) \quad (7.1)$$

where $W(D)$ is the free interaction energy at separation D . $W(D)$ depends on the silica surface chemistry as well as the solution conditions. Therefore, $W(D)$ does not change with the particle diameter. The effective radius R_{eff} is defined as $1/R_{eff} = 1/R_1 + 1/R_2$, where R_1 and R_2 are the radii of the colloidal probe and the particle immobilized on the surface, respectively. Based on eqn 7.1, we expect that the transition from μm -sized particles to the smallest particles leads to a decrease of the interaction forces by nearly one order of magnitude as $R_{eff} \sim 1.06\ \mu\text{m}$ (*cf.* Figure 7.1 f, g) is decreased to $R_{eff} = 0.165\ \mu\text{m}$ (*cf.* Figure 7.1 i), respectively. For the largest particles, we utilized both, the 'classical' colloidal probe technique as well as the FluidFM technique (*cf.* Figure 7.1 f, g). Thereby, it was possible to compare the results for the same types of particles and to estimate also the influence of instrumental parameters on the acquired force profiles. All measurements presented have been carried out under the same pH-value (pH 10) at which the silica particles are highly charged.

Additionally, we determined for each type of colloidal probe the interaction forces with the bare glass substrate in the sphere/plane geometry to which the 'lower' particles in the sphere/sphere geometry are immobilized on a glass slide. This flat glass surface can be considered as an additional surface against which the interaction forces can be determined. As the surface chemistry of glass is different compared to the silica particles [46] it can be utilized as an additional 'internal reference'.

Colloidal Interactions between μm -Sized Silica Particles

Figure 7.2 a shows some exemplary force profiles for the interaction between two $4\ \mu\text{m}$ -sized silica particles at pH 10 and three different ionic strengths I ($I = 0.1\ \text{mM}$, $0.3\ \text{mM}$, and $1\ \text{mM}$). These measurements have been performed with a 'classical' colloidal probe, *i.e.* a silica particle that is glued permanently with an UV-curable adhesive to a tipless AFM-cantilever. The lower particle adheres to the glass surface during the measurements to the glass surface. Both particles have been centered towards each other by optical microscopy comparable to the procedure as used for the 'multiple colloidal probe' technique and for other measurements in the sphere/sphere geometry. [15, 34] R_1 and R_2 have been determined by optical microscopy during the measurements and the interaction forces were normalized by the effective radius for the sphere/sphere geometry (*cf.* eqn 7.1). [8, 15]

As the force profiles in Figure 7.2 a have been acquired for a completely symmetric combination of surfaces, the diffuse layer potentials can be determined unambiguously from fits to the full solutions of the Poisson-Boltzmann equation. The dashed lines indicate the fits taking into account the classical boundary conditions of constant charge (CC) and constant potential (CP), respectively. However, at small separations D , *i.e.* for $D < 1-2\ \kappa^{-1}$ with κ^{-1} the Debye length, the charge regulation (CR) between the surfaces has to be taken into account. [44] The Debye length is given by:

$$\kappa^{-1} = \sqrt{\frac{\epsilon\epsilon_0 k_B T}{2N_A e^2 I}} \quad (7.2)$$

where $\epsilon\epsilon_0$ is the total permittivity, $k_B T$ is the thermal energy, N_A is the Avogadro's number, e is the elementary charge and I is the total ionic strength of the aqueous solution. The regulation behavior of the silica surfaces has been accounted for by the so-called constant regulation approximation with a regulation parameter p . [44] Commonly, one expects $0 < p < 1$, where 0 corresponds to constant potential and 1 to constant charge boundary conditions. [44] Based on the 1-pK model of the silica surface, [46] a value of $p = 0.4-0.6$ is expected for pH 10 and $I = 0.1\ \text{mM}$. [44] Due to the surface roughness of the silica particles without any pre-treatment, which is in the order of $1\ \text{nm RMS}$, [8] the influence of van-der-Waals (vdW) interactions is negligible. [34] Prolonged immersion in aqueous solution leads to the formation of a gel-like layer that also contributes to the suppression of vdW-forces. [24] Only for silica particles that have been exposed to temperatures $> 1000\ ^\circ\text{C}$ the vdW-forces can be traced in the force profiles. [25, 34]

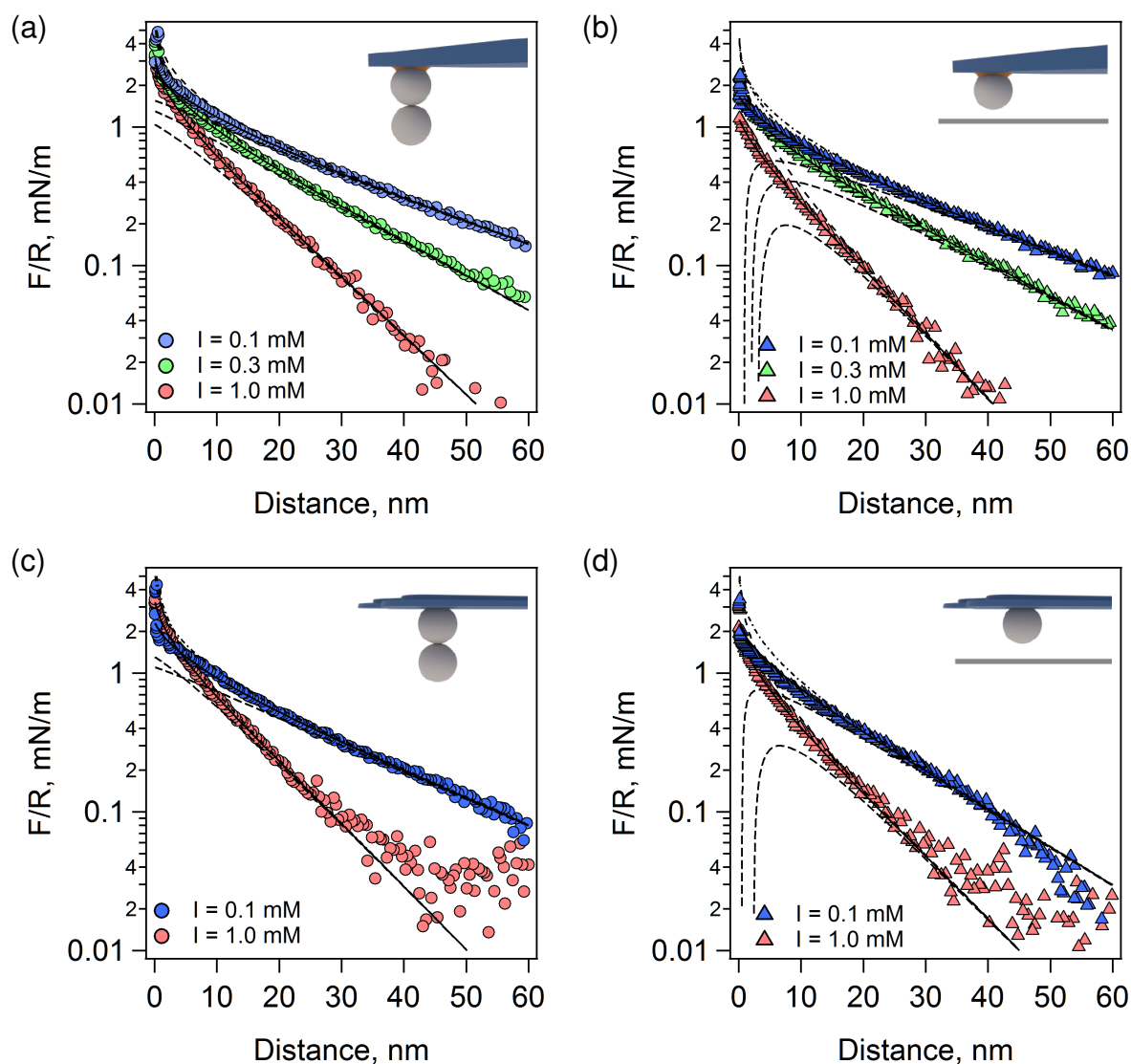


Figure 7.2: Direct force measurements with $\sim 4\ \mu\text{m}$ -sized colloidal silica particles in sphere/sphere (a, c) geometry between two silica particles and in sphere/plane (b, d) geometry between a silica particle and the glass surfaces. The measurements have been performed either with a 'classical' colloidal probe (a, b) or silica particles immobilized to a FluidFM-cantilever by temporary aspiration (c, d). The fits to the full solutions of the Poisson-Boltzmann equation are indicated for the boundary conditions of constant potential (dashed line), constant charge (dotted lines) and charge regulation (solid lines), respectively.

Diffuse layer potentials of $\Psi^d \approx -71\ \text{mV}$ for $I=0.1\ \text{mM}$ and $\Psi^d \approx -50\ \text{mV}$ for $I=1\ \text{mM}$, respectively, were obtained from the fits with charge regulation. These values are compatible with potentials reported previously for untreated silica surfaces. [28, 29,

7 Extending the Limits of Direct Force Measurements

30, 31, 32, 33] However, the range of values reported for silica diffuse layer potentials is rather broad and depends critically on preparation protocol and sample history. [24, 25, 26, 34] In particular, heat treatment as well as ozone or plasma cleaning lead to differences in the diffuse layer potentials. The here-determined regulation parameters, fall in the range calculated ($p = 0.5-0.6$, *cf.* ref. [44]) or experimentally determined ($p = 0.58$, *cf.* ref. [14]) for silica surfaces (*cf.* ESI).

Figure 7.2 b shows representative force profiles for the interaction of the same probe particles as in Figure 7.2 a, but this time the interaction against the bare glass surface was determined in sphere/plane geometry. These force profiles have been evaluated quantitatively as well. However, in this case the asymmetric combination of surfaces has to be taken into account for the full-fits to the Poisson-Boltzmann equation: the diffuse layer potential Ψ^d and the regulation parameter p for the colloidal probe have been set constant to the values previously determined for the silica surfaces in the symmetric combination and only the corresponding parameters for the glass surface have been determined from the fits (*cf.* Table 7.2 in ESI). This procedure is analogous to the one pursued for obtaining the diffuse layer potential of latex particles bearing different functional groups at their surface. [15] The resulting diffuse layer potentials for the glass surface are significantly lower compared to the silica surfaces ($\Psi^d(\text{glass}) \approx -56 \text{ mV}$ vs. $\Psi^d(\text{SiOx}) \approx -71 \text{ mV}$ for $I=0.1 \text{ mM}$). This finding is in line with previously reported results and is also observed consistently for the diffuse layer potentials of quartz and borosilicate glass. [46]

Reversible Colloidal Probes by FluidFM

The FluidFM -technique allows to immobilize particles at the aperture by applying an underpressure. Hence, these particles can be used as temporary probes for direct force measurements. [22, 23] Figures 7.3 a-c illustrate in a schematic manner the steps followed to perform direct force measurements with the FluidFM. It should be noted that these steps are mostly analogous to those executed for the 'multiple colloidal probe' technique. However, for the latter a chemical modification of the cantilever is mandatory. [16] Both techniques (*i.e.* 'multiple colloidal probe' and FluidFM, respectively) are carried out in a measurement cell containing a large amount of particles and temporary colloidal probes are formed. For silica particles with an average diameter of $\sim 4 \mu\text{m}$ the manipulation sequence can be directly observed by optical light-microscopy

(cf. Figures 7.3 d-f). First, an underpressure is applied to the FluidFM-cantilever via the nanofluidic controller. This underpressure leads to the aspiration of a single colloidal particle to the aperture (cf. Figures 7.3 a, b and Figures 7.3 d, e). Second, by applying a continuous underpressure, the so-called holding pressure, the particle is immobilized at the aperture. The immobilized particle is used in the following as colloidal probe and a series of force *versus* distance cycles are acquired (cf. Figures 7.3 c, f). The sphere/sphere geometry requires a coarse alignment of the colloidal probe and another particle immobilized on the substrate, as reported previously for μm -sized particles. [23] Finally, after finishing the force measurements, the particle is removed from the aperture by applying a large overpressure (here about +1000 mbar for several seconds) and the process can be repeated with a new particle as colloidal probe.

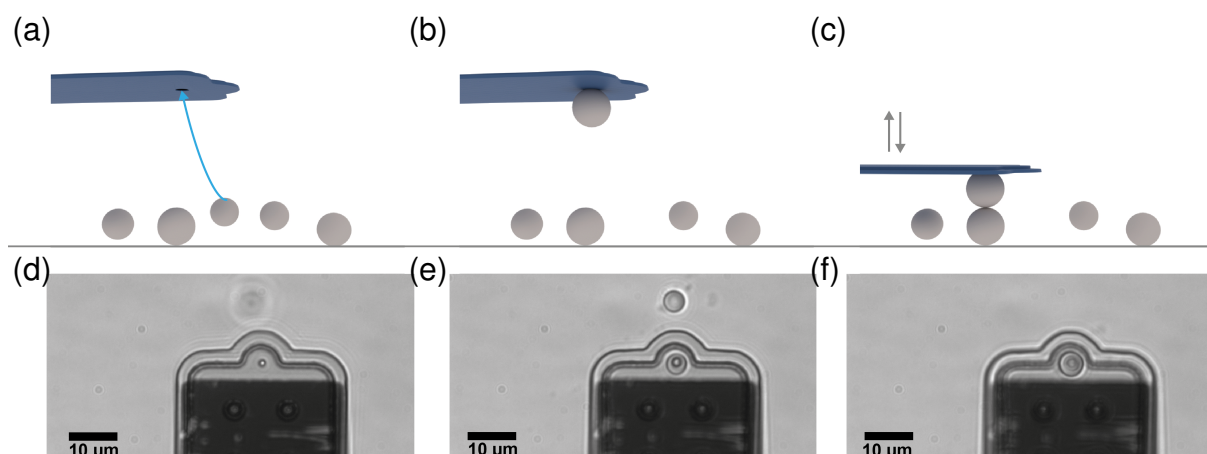


Figure 7.3: Schematic illustrations (a-c) and corresponding optical microscopy images (d-f) of the essential steps for direct force measurements based on the FluidFM-technique. First (a, d), an underpressure is applied in order to aspirate a single particle (b, e). Second, the colloidal probe is aligned with respect to a second particle, which is immobilized on the glass surface (c, f). Finally, the interaction forces are determined in the sphere/sphere geometry (cf. arrows in c). The measurements in the sphere/plane geometry are performed analogously (cf. movie in the ESI).

Direct Force Measurements with the FluidFM for μm -sized particles

The interaction force profiles upon approach between two $4\ \mu\text{m}$ -sized silica particles is shown in Figure 7.2 c as acquired with the FluidFM. The force profiles are practically identical to those obtained with 'classical' colloidal probes (cf. Fig 7.2 a). However,

7 Extending the Limits of Direct Force Measurements

the force resolution for the data acquired by the FluidFM-technique is lower. We attribute this lower resolution to several factors: first, due to the sandwich-structure of the FluidFM-cantilevers, the reflection of the laser beam from the cantilever leads to more interferences. Moreover, due to the internal structure of the FluidFM-cantilevers, the resulting interference patterns are also more complex. These effects are discussed more in detail in the ESI and have been observed before. [47, 48] Second, the interaction force profiles have been measured on different commercial AFMs, which have different intrinsic noise levels. Nevertheless, these optical artefacts have only a significant influence at large separation distances where small forces are acting.

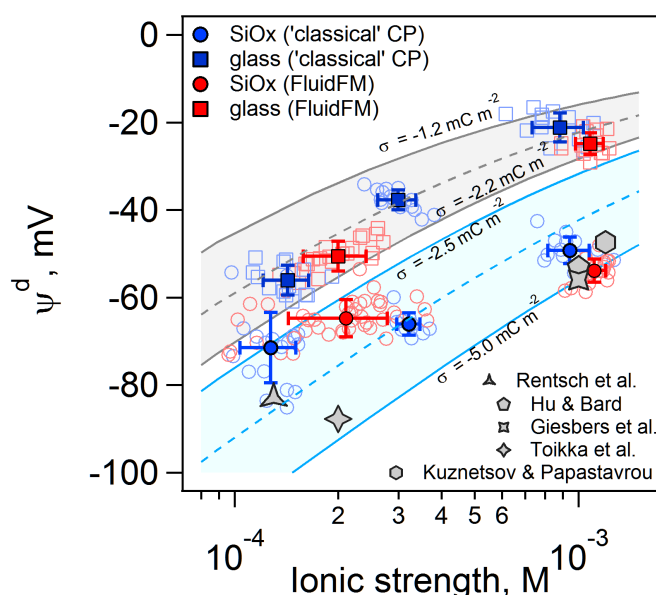


Figure 7.4: Diffuse layer potential as a function of the ionic strength for large silica particles ($\sim 4 \mu\text{m}$ in diameter, circles) and glass surfaces (squares). The measurements have been performed with 'classical' colloidal probes (blue) and the FluidFM (red), respectively. The solid symbols are averages of the data sets represented by the open symbols. The filled grey symbols represent data compiled from the literature under comparable conditions. [8, 49, 50, 51, 52] The shaded areas are based on the Grahame-equation for a constant surface charge.

Figure 7.4 summarizes the diffuse layer potentials for the large, μm -sized silica particles as obtained by both techniques (*i.e.* 'classical' colloidal probe and FluidFM, respectively). The diffuse layer potentials are plotted as a function of the total solution ionic strength. The latter has been determined from the fits to the long-range interaction forces and coincide within the measurement errors for silica as well as for the

glass surface. The slight shift of the determined ionic strengths (as obtained from the fits) compared to the nominal values results most likely from dissolved CO₂ (*cf.* ref. [38]) and to a lower extent to the aforementioned interference patterns for the FluidFM-cantilevers. The blue and grey regions in Figure 7.4 show the intervals given by upper and lower limits for the surface charge densities of silica and glass, respectively. These boundary curves for diffuse layer Ψ^d vs. ionic strength I have been calculated for the boundary surface charges σ by eqn 7.3 in such a manner that the experimental data points fall in these limits. The surface charge density σ is related to the diffuse layer potential Ψ^d by the Grahame equation: [1]

$$\sigma = \frac{2\epsilon\epsilon_0\kappa k_B T}{e} \sinh\left(\frac{e\Psi^d}{2k_B T}\right) \quad (7.3)$$

The values found in our experiments are slightly lower than for some reported elsewhere for the same conditions (pH 10). [14, 34, 46] This discrepancy can be attributed to the absence of heat treatment for the silica particles. [53] The difference in charge density between the glass and the silica falls in the previously reported ratio. [46] Moreover, some matching literature values for the diffuse layer potentials of silica that have been determined at the same pH-value (pH 10) are indicated in Figure 7.4. [8, 49, 50, 51, 52] Moreover, as we find no difference in the diffuse layer potentials obtained by 'classical' colloidal probes and aspirated particles (*e.g.* FluidFM), we can safely assume that drying the particles, as required for the colloidal probes, does not lead to different surface properties. Hence, the particles immobilized on the substrate and the aspirated particles have comparable surface properties.

In conclusion, the temporary immobilization of the probe particle by underpressure does in principle allow for data of equivalent quality as for 'classical' colloidal probes but with the advantage that statistically relevant data is acquired more efficiently. In the following, we demonstrate how the FluidFM-technique can be extended to obtain comparable data for probe particles significantly smaller than 1 μm .

Detection of Sub-micron Particles Aspirated to FluidFM-Cantilevers

FluidFM-cantilevers with pyramidal tips having apertures of 200-350 nm allow to aspirate sub-micron particles with diameters below 1 μm . While these apertures are sufficiently small to allow for the aspiration and immobilization of sub-micron particles, the particles cannot be resolved by optical light microscopy anymore. Hence, the aspira-

7 Extending the Limits of Direct Force Measurements

tion process cannot be followed directly anymore as in the case of large particles and a different procedure had to be developed, which is summarized in Figure 7.5. As all size fractions of silica particles have the same surface chemistry, we can compare datasets from different sizes after normalization to the effective radii.

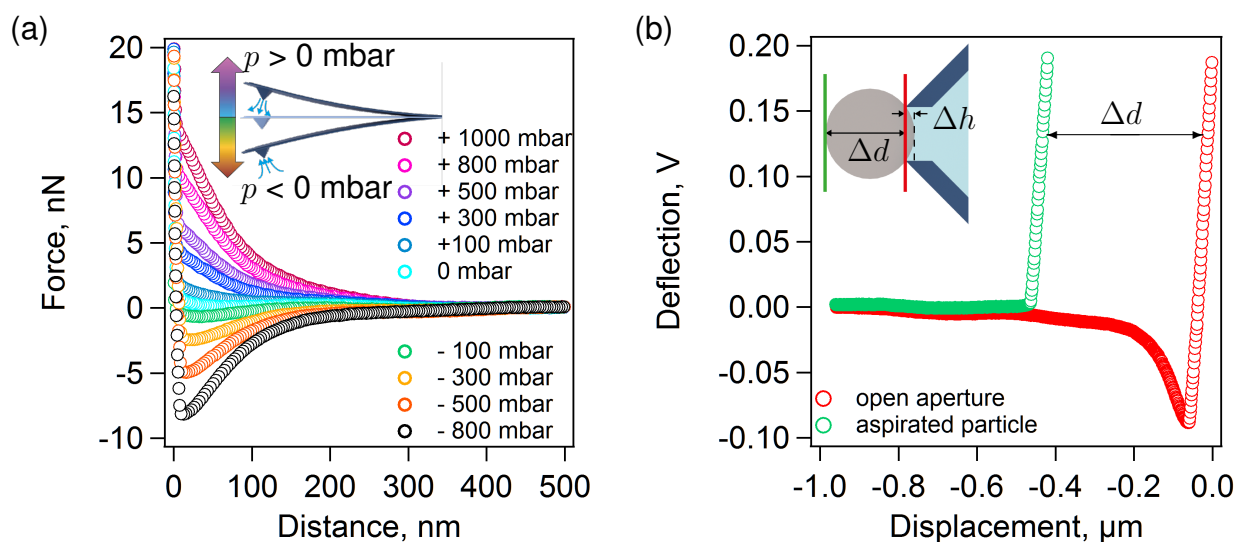


Figure 7.5: (a) Hydrodynamic forces acting on a pyramidal FluidFM-cantilever near the glass substrate as function of distance and externally applied pressure ($I=0.1$ mM and pH 10). (b) Deflection *versus* displacement curves (*i.e.* raw data format) These curves were acquired continuously while applying a constant underpressure of -800 mbar. Upon aspiration of a ~ 490 nm particle, the force profiles change instantaneously from long-range attraction due to hydrodynamics to repulsion due to diffuse layer overlap. The shift in the displacement scale upon aspiration of a particle corresponds approximately to the particle diameter (*cf.* schematic insert).

Figure 7.5 a shows the force profiles for a FluidFM-cantilever with a free aperture opening near a glass surface for various pressures applied by nanofluidic controller. The cantilever has a pyramidal tip with an opening of ~ 300 nm at its apex. For each pressure p applied, a separate force *versus* distance curve has been acquired. Overpressures (*i.e.* $p > 0$ mbar) lead to long-ranged repulsive forces that are caused by the liquid jet impinging on the surface (*cf.* Figure 7.5 a, top). By contrast, underpressures (*i.e.* $p < 0$ mbar) lead to long-ranged attractive forces due to a suction effect in the vicinity of the surface (*cf.* Figure 7.5 a, bottom). In both cases, the resulting force is of hydrodynamic origin and its magnitude depends on the magnitude of the externally applied pressure. Moreover, the range is much longer than one would expect for the forces due to the overlap of diffuse layers.

These hydrodynamic forces exerted on the cantilever can be exploited to detect the blocking of the aperture: the aspiration of small particles floating in the solution takes place while a constant underpressure is applied. During the acquisition of continuous force *versus* distance curves, the abrupt transition from long-ranged attraction to rather short-ranged repulsion indicates the blocking of the aperture by the absence of hydrodynamic forces. Figure 7.5 b shows an example for this transition, which is taking place between two consecutive force *versus* displacement curves (*i.e.* in a time frame of < 2 s). A constant underpressure of $p = -800$ mbar is applied, when particles with an average diameter of 496 ± 16 nm were in the solution. The shift of the contact region to shorter piezo-displacements by $\Delta d \approx 420$ nm provides an important additional indicator for the aspiration of a single sub-micron particle. This value for Δd corresponds to about 90% of the particle diameter, which results from the immobilization of the particle inside the aperture (*cf.* ESI) and the size distribution of the colloids, respectively. We found that the immobilization of smaller silica particles (*i.e.* those with ~ 496 nm) is more stable than for the larger ones (*i.e.* those with ~ 983 nm). Smaller particles are obviously better fitting into the ~ 300 nm-sized apertures of the FluidFM cantilevers and are thus less susceptible to shear forces during the direct force measurements.

Determining Interaction Forces between Sub-micron Particles

Figure 7.6 a shows some exemplary force *versus* distance curves that have been acquired with silica particles of 983 ± 30 nm (blue curve) and 496 ± 16 nm (light blue curve) as colloidal probes, respectively. During these measurements, the particles were immobilized in 300 nm-sized apertures of FluidFM cantilevers (*cf.* Figure 7.1 e) by application of holding pressures (underpressure of ~ -300 mbar). The measurements were conducted at pH 10 and $I = 0.1$ mM in the sphere/sphere geometry, as well as in the sphere/plane geometry against the glass surfaces. We measured the following combinations of sub-micron particles: 983 nm vs. 983 nm particles (*cf.* Figure 7.1 h, which nominal to $R_{eff} = 0.25 \mu\text{m}$), and 983 nm vs. 496 nm particles (*cf.* Figure 7.1 i, nominal to $R_{eff} = 0.17 \mu\text{m}$), respectively. For comparison, the interaction force between two $4 \mu\text{m}$ sized particles (*cf.* Figure 7.1 g, $R_{eff} = 1.06 \mu\text{m}$ as determined by optical microscopy) has been added to the graph. Measurements in the sphere/sphere geometry between two 496 nm particles were not possible as these particles do not adhere sufficiently strongly to the glass substrate in order to prevent detachment during

7 Extending the Limits of Direct Force Measurements

the measurements in the sphere/sphere geometry. This reduction of particle adhesion with decreasing diameter can be rationalized on the basis of the JKR and DMT theory, which both postulate that the adhesion force decreases linearly with particle radius. [1]

The diameters of the small silica particles ($\leq 1 \mu\text{m}$) cannot be determined with sufficient accuracy *in situ* by optical microscopy. Therefore, the force profiles in Figure 7.6 a have not been normalized to the effective radius. According to the Derjaguin approximation (*cf.* eqn 7.1), the overall interaction forces become smaller leading to decreased R_{eff} , while the electrostatic decay length remains identical. However, at large separation distances $> 30 \text{ nm}$, optical artefacts lead to pseudo-forces. Unfortunately, the shape and position of the interference pattern varies between consecutive measurements, limiting the lower force regime detectable by FluidFM-cantilevers to about $\sim 200 \text{ pN}$ in some cases.

Figure 7.6 b is derived from the same experimental data as shown in Figure 7.6 a but the interaction forces have been normalized to nominal effective radii as given by the average values for the particle size distributions (*cf.* Figure 7.1 b). Only for the μm -sized particles, the radii were determined by optical microscopy. These normalized data can be compared to the force profiles calculated on the basis of the average diffuse layer potentials obtained from the measurements with the large particles (*cf.* Figure 7.4). The shaded areas in Fig. 7.6 b indicate the range for these calculated data if the standard deviation for Ψ^d is taken into account (*cf.* Table 7.1 in the ESI). The blue area results from the boundary condition of constant charge regulation, while the grey area is based on the upper and lower limits of CC and CP boundary conditions, respectively. The experimental force profiles for the sub-micron particles fall to a good degree of accuracy within these calculated limits and we attribute the observed deviations mostly to the interference patterns. This finding is corroborated by the data in the sphere/plane geometry. Fig. 7.6 c shows the direct force measurements with the same colloidal probes as in Fig. 7.6 a and b but this time against the planar glass surface. The interaction forces has been normalized analogously to Fig. 7.6 b. The R_{eff} have been adapted to the sphere/plane geometry. Again, the shaded areas indicate the theoretically expected range for the asymmetric combination of silica and glass surface based on average values obtained from the data in Fig. 7.4 (*cf.* Table 7.1 in the ESI).

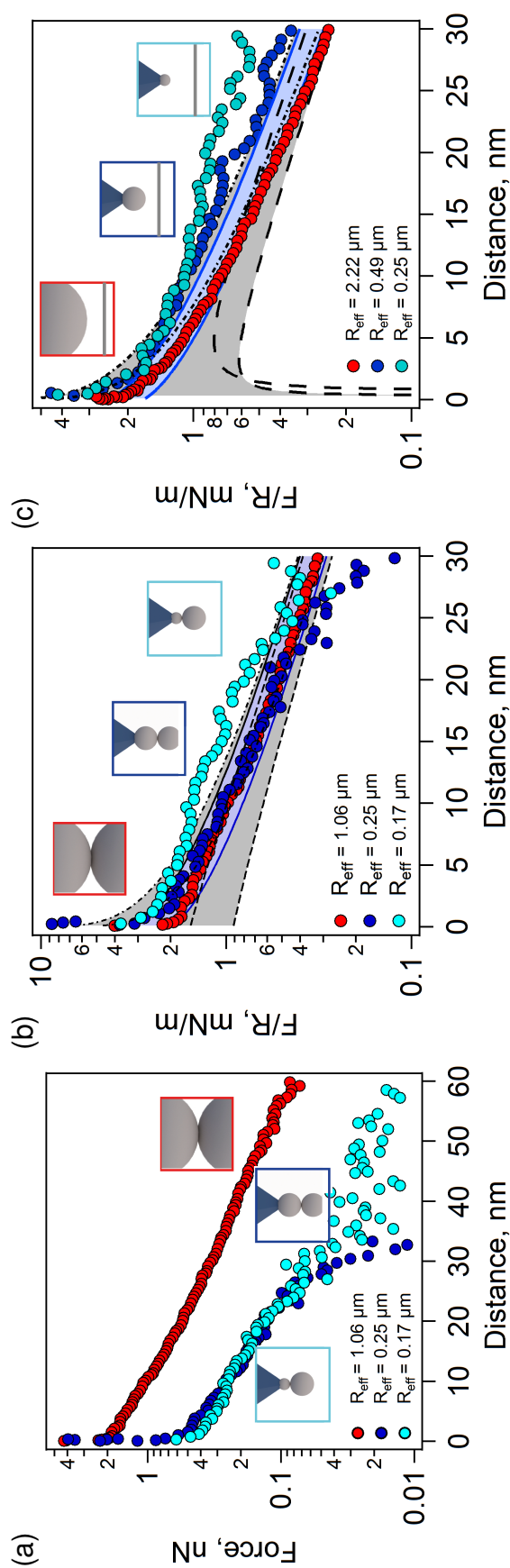


Figure 7.6: Direct force measurements with sub-micron particles as colloidal probes at pH 10 and $I = 0.1$ mM. The sub-micron particles had a nominal average diameter of 983 ± 30 nm (dark blue) and 496 ± 16 nm (light blue), respectively. For comparison, supplementary force profiles measured with large (*i.e.* $\sim 4 \mu\text{m}$, red) colloidal particles, are shown. The effective radii indicated originate from the different combination of particles involved (*cf.* Figure 7.1 g-i) Force versus distance curves between silica particles in the sphere/sphere interaction geometry. The force data are not normalized to the effective radii. (b) Identical set of force versus distance data as above but normalized to effective radii on the basis of nominal particle diameters for the sub-micron particles (blue data points). The shaded areas are based on calculations for $\Psi^d(\text{SiO}_x)$ and p , as determined for the large particles (see the text and Table 7.1 in the SI). (c) Normalized interaction force profiles for the same colloidal probes as above but against a flat glass surfaces. The shaded areas are based again on theoretical calculations.

7.4 Conclusions

The here-presented *proof-of-concept* allows for determining the interaction forces between individual silica sub-micron particles. Silica particles have been extensively used as colloidal probes in the past. But to the best of our knowledge, silica particles have been neither used before as temporary colloidal probes in the framework of the 'multiple colloidal probe' technique nor for the routine preparation of colloidal probes with dimensions $< 2 \mu\text{m}$. Utilizing the FluidFM-technique, we were able to overcome these restrictions and push the lower limit of the colloidal probe technique by nearly one order of magnitude. At the same time, it was possible to conserve the advantages of the 'multiple colloidal probe' approach.

In the future, we aim to push the limit of minimal particle size to the regime of 'true' nanoparticles with diameters of less than 300 nm. The current lower limit for the fabrication of apertures by a focused ion beam is in the order of 150-250 nm. [54] At even smaller particle diameters, a number of additional limits of hydrodynamic origin (external pressure difference required for aspiration) as well as dominance of surface forces (*e.g.* van der Waals) over aspiration pressure would become important and would have to be taken into account.

A great advantage of the approach is that no chemical modification of the cantilever surface is required. Hence, a wide range of particles with different surface chemistries can be aspirated and used as colloidal probes. In particular, particles with soft interfaces, such as core-shell particles, would become accessible as colloidal probes. Therefore, a large fraction of particles currently utilized in industrial formulations could be characterized for the first time by direct force measurements. Such direct force measurements will allow to bridge the gap between bulk techniques, such as electrokinetic methods or light scattering, as true interaction potentials would become accessible even for these complex systems.

7.5 Acknowledgements

The authors thank Christian Bippes (Nanosurf AG) for support. Carmen Kunert provided help with the SEM measurements. The presented study has been supported

7.5 Acknowledgements

by the DFG within the framework of the SFB840 (G.P.), and by the Swiss Innovation Promotion Agency CTI-KTI (18511.1 PFNM-NM, T.Z.).

7.6 Supporting Information

Silica Particle Dimensions

Monodisperse silica particles were purchased from MicroParticles GmbH (Berlin, Germany) in three different sizes. The nominal diameters, as specified by the manufacturer, are compared in Table 7.1 to the particle diameter determined by scanning electron microscopy (SEM). The values in Table 7.1 were obtained from the histograms shown in Figure 7.1 of the manuscript.

Table 7.1: Diameters of silica particles used in this study.

Material	Nominal diameter ^a	Average diameter ^b
SiO _x	4.28 ± 0.14 μm	4.07 ± 0.20 μm
SiO _x	977 ± 26 nm	983 ± 30 nm
SiO _x	500 ± 13 nm	496 ± 16 nm

^a as provided by the manufacturer (MicroParticles, Berlin, Germany)

^b as determined from SEM images

Summary of Diffuse Double Layer Properties used for Theoretical Calculations

The diffuse double layer potentials and the regulation parameters for the silica particles were determined by the 'classical' colloidal probe method in the sphere/sphere geometry. The fits according to the full-solutions of the Poisson-Boltzmann equation with the constant regulation approximation assume two identical surface chemistries. [44] Based on the data for the silica surfaces, the diffuse layer properties of glass surface have been determined by 'classical' colloidal probe *versus* a glass surface (sphere/plane geometry). The obtained values are compiled in Table 7.2. These data were used to calculate the theoretical interaction force profiles shown in Figure 7.6 in the manuscript.

Table 7.2: Compilation of the diffuse layer potential and the regulation parameter for silica colloidal and glass surfaces as determined by 'classical' colloidal probes

	Nominal ionic strength	Diffuse layer potential	Regulation parameter
	I	Ψ^d	p
silica	0.1 mM	-71.4 ± 8.1 mV	0.60 ± 0.23
	0.3 mM	-66.1 ± 2.5 mV	0.65 ± 0.16
	1.0 mM	-49.2 ± 3.0 mV	0.66 ± 0.20
glass	0.1 mM	-56.1 ± 3.4 mV	0.61 ± 0.25
	0.3 mM	-37.7 ± 2.3 mV	0.66 ± 0.16
	1.0 mM	-21.2 ± 3.3 mV	0.67 ± 0.15

Regulation parameter for silica and glass surfaces

The regulation parameter for silica and glass surfaces as a function of the ionic strength was determined at pH 10 from measurements with 'classical' colloidal probe technique. The values obtained from the fits are compiled in Table 7.2 and are plotted in Figure 7.7 against the fitted ionic strength. For comparison, the values reported by Pericet-Camara *et al.* were added, which were obtained from theoretical calculations assuming a 1-pK model for the surface chemistry of silica. [44]

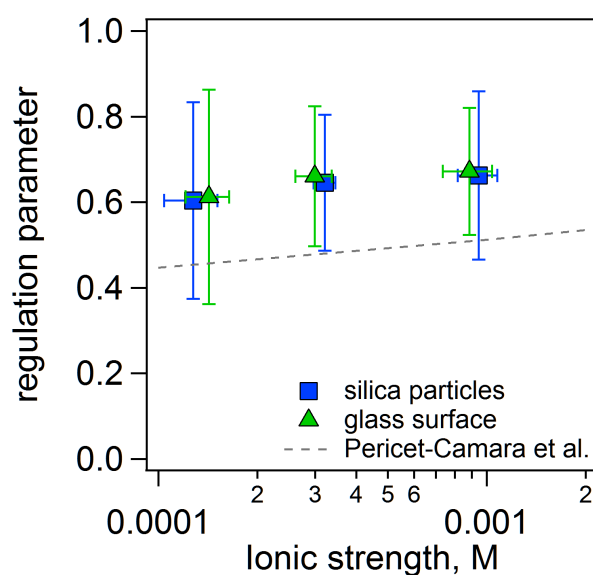
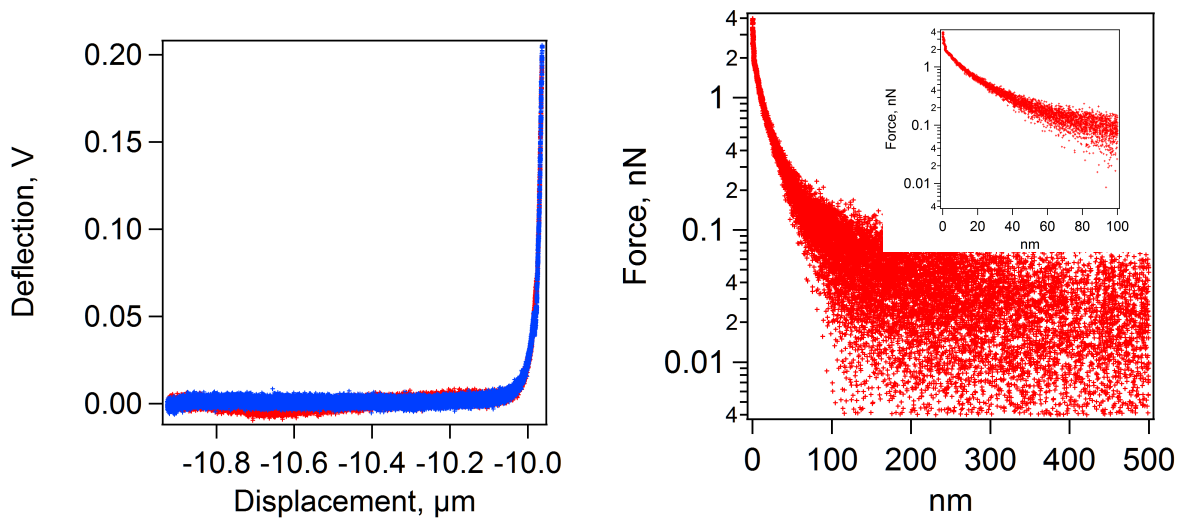


Figure 7.7: Determined regulation parameter as a function of the fitted total ionic strength for silica (blue squares) and glass surfaces (green triangles). The dashed line are the theoretical calculations by Pericet-Camara *et al.* [44]

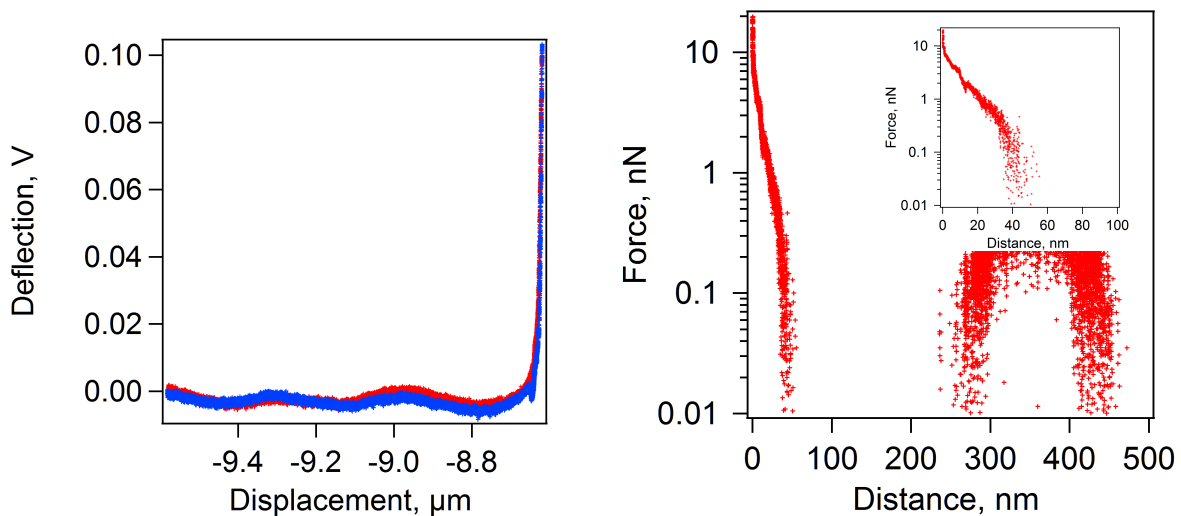
Influence of Optical Interferences on the Force Profiles Acquired by FluidFM

The following raw data demonstrate the influence of optical interferences at FluidFM-cantilever on the quality of converted interaction force profiles. All interaction force profiles were acquired under the same conditions ($I = 0.1$ mM and pH 10) but with different FluidFM-cantilevers. Two different types of FluidFM-cantilevers have been used termed as MicroPipettes ($2\ \mu\text{m}$ aperture) and NanoPipettes (300 nm aperture at apex of pyramidal tip).

MicroPipette showing few interference fringes

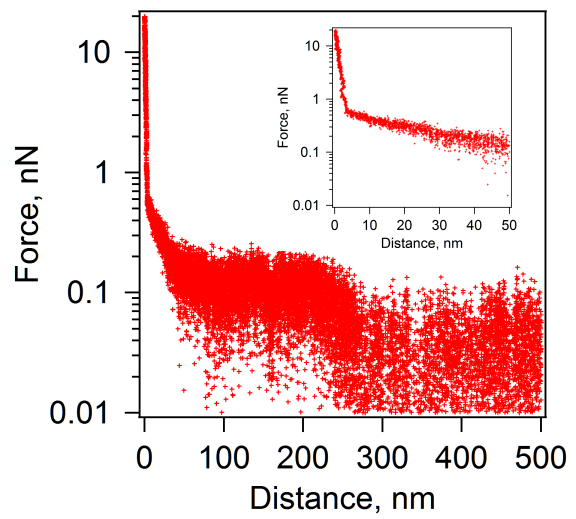
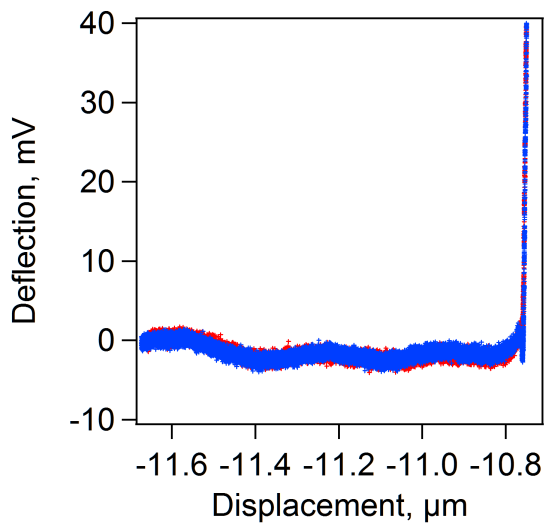
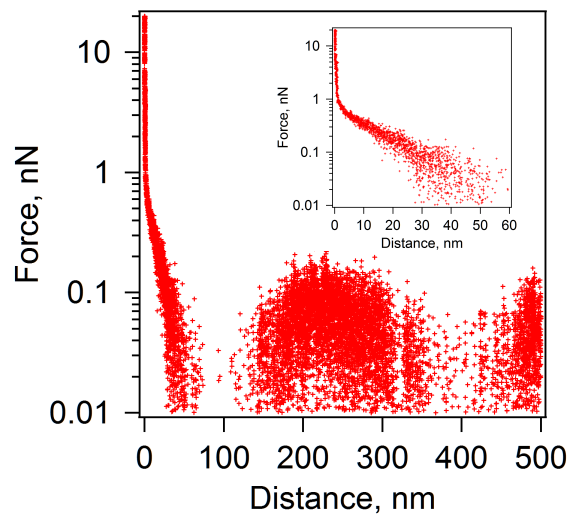
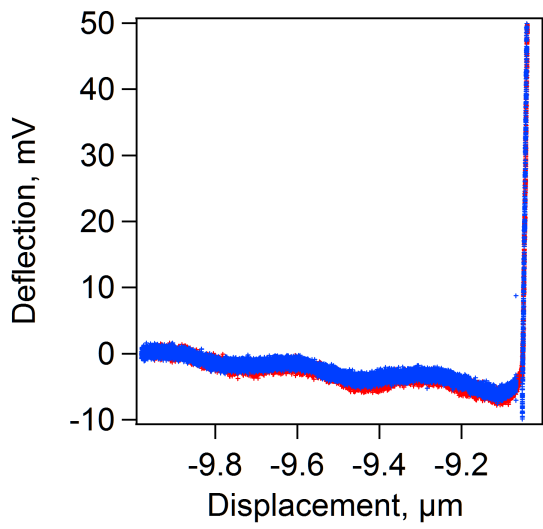


MicroPipette with pronounced interference fringes



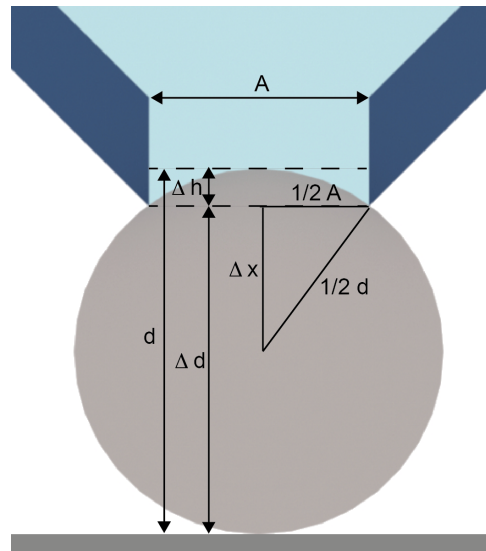
7 Extending the Limits of Direct Force Measurements

NanoPipette



Aspiration of Nanoparticles to the Aperture - Geometrical Effects

Upon aspiration of colloidal particles to the aperture of a FluidFM-cantilever, the total particle diameter is reduced by Δh . Hence, in the deflection vs. displacement data a shift of Δd is detected, with $d - \Delta h$. One finds by the theorem of Pythagoras:



$$\Delta h = d - \Delta d = 1/2d - \Delta x = 1/2 \left(d^2 - \sqrt{(d^2 - A^2)} \right) \quad (7.4)$$

With the nominal values for the aperture diameter and particle diameter ($A = 300$ nm and $d = 496$ nm) one obtains $\Delta h \approx 50$ nm, which is approximately the double of the standard deviation found for the diameter of the smallest silica particles (*cf.* Table 7.1).

Real-time movie of direct force measurements using the FluidFM technology

The enclosed real-time movie illustrates the temporary aspiration of a single silica particle to the aperture of a FluidFM-cantilever and shows a single force *versus* distance cycle with this temporary colloidal probe against the glass surface (sphere/plane geometry).

References

- [1] J Israelachvili. *Intermolecular and Surface Forces*. American Press: London, New York, 2nd edition, 1992.
- [2] B A Derjaguin. A Theory of Interaction of Particles in Presence of Electric Double-Layers and the Stability of Lyophobic Colloids and Disperse Systems. *Progress in Surface Science*, 43:1–14, 1993.
- [3] H J Butt, R Berger, E Bonaccorso, Y Chen, and J Wang. Impact of atomic force microscopy on interface and colloid science. *Advances in Colloid and Interface Science*, 133(2):91–104, 2007.
- [4] M Kappl and H J Butt. The colloidal probe technique and its application to adhesion force measurements. *Particle & Particle Systems Characterization*, 19(3):129–143, 2002.
- [5] H-J Butt, B Cappella, and M Kappl. Force measurements with the atomic force microscope: Technique, interpretation and applications. *Surface Science Reports*, 59(1-6):1–152, 2005.
- [6] W A Ducker, T J Senden, and R M Pashley. Direct Measurement of Colloidal Forces Using an Atomic Force Microscope. *Nature*, 353(6341):239–241, 1991.
- [7] H-J Butt. Measuring electrostatic, van der Waals, and hydration forces in electrolyte solutions with an atomic force microscope. *Biophysical Journal*, 60(6):1438–1444, 1991.
- [8] S Rentsch, R Pericet-Camara, G Papastavrou, and M Borkovec. Probing the validity of the Derjaguin approximation for heterogeneous colloidal particles. *Physical Chemistry Chemical Physics*, 8(21):2531–2538, 2006.
- [9] Y Gan. Invited Review Article: A review of techniques for attaching micro- and nanoparticles to a probe's tip for surface force and near-field optical measurements. *Review of Scientific Instruments*, 78(8):081101–8, 2007.
- [10] V Kuznetsov and G Papastavrou. Note: mechanically and chemically stable colloidal probes from silica particles for atomic force microscopy. *Review of Scientific Instruments*, 83(11):116103, 2012.

References

- [11] C E McNamee, M Matsumoto, P G Hartley, and P Mulvaney. Interaction forces and zeta potentials of cationic polyelectrolyte coated silica surfaces in water and in ethanol: Effects of chain length and concentration of Perfluorinated Anionic Surfactants on Their Binding to Surface. *Langmuir*, 17(20):6220–6227, 2001.
- [12] E Greenfield and U Sivan. Measuring changes in surface potential as two charged bodies approach in electrolyte solution. *Physical Review Letters*, 102(10):106101, 2009.
- [13] M Moazzami-Gudarzi, G Trefalt, I Szilagyi, P Maroni, and M Borkovec. Nanometer-ranged attraction induced by multivalent ions between similar and dissimilar surfaces probed using an atomic force microscope (AFM). *Physical Chemistry Chemical Physics*, 18:8739–8751, 2016.
- [14] V Valmacco, M Elzbieciak-Wodka, D Herman, G Trefalt, P Maroni, and M Borkovec. Forces between silica particles in the presence of multivalent cations. *Journal of Colloid and Interface Science*, 472:108–115, 2016.
- [15] I Popa, P Sinha, M Finessi, P Maroni, G Papastavrou, and M Borkovec. Importance of charge regulation in attractive double-layer forces between dissimilar surfaces. *Physical Review Letters*, 104(22):228301, 2010.
- [16] M Borkovec, I Szilagyi, I Popa, M Finessi, P Sinha, P Maroni, and G Papastavrou. Investigating forces between charged particles in the presence of oppositely charged polyelectrolytes with the multi-particle colloidal probe technique. *Advances in Colloid and Interface Science*, 179-182:85–98, 2012.
- [17] I U Vakarelski and K Higashitani. Single-Nanoparticle-Terminated Tips for Scanning Probe Microscopy. *Langmuir*, 22(7):2931–2934, 2006.
- [18] D J D'Sa, H-K Chan, and W Chrzanowski. Attachment of micro- and nanoparticles on tipless cantilevers for colloidal probe microscopy. *Journal of Colloid and Interface Science*, 426(C):190–198, 2014.
- [19] A Meister, M Gabi, P Behr, P Studer, J Vörös, P Niedermann, J Bitterli, J Polesel-Maris, M Liley, H Heinzelmann, and T Zambelli. FluidFM: Combining Atomic Force Microscopy and Nanofluidics in a Universal Liquid Delivery System for Single Cell Applications and Beyond. *Nano Letters*, 9(6):2501–2507, 2009.

7 Extending the Limits of Direct Force Measurements

- [20] P Dörig, P Stiefel, P Behr, E Sarajlic, D Bijl, M Gabi, J Vörös, J A Vorholt, and T Zambelli. Force-Controlled Spatial Manipulation of Viable Mammalian Cells and Micro-Organisms by means of FluidFM Technology. *Applied Physics Letters*, 97(2):023701, 2010.
- [21] O Guillaume-Gentil, E Potthoff, D Ossola, C M Franz, T Zambelli, and J A Vorholt. Force-controlled manipulation of single cells: from AFM to FluidFM. *Trends in Biotechnology*, 32(7):381–388, 2014.
- [22] P Dörig, D Ossola, A M Truong, M Graf, F Stauffer, and T Vörös, Jand Zambelli. Exchangeable Colloidal AFM Probes for the Quantification of Irreversible and Long-Term Interactions. *Biophysical Journal*, 105(2):463–472, 2013.
- [23] N Helfricht, E Doblhofer, JFL Duval, Thomas Scheibel, and Georg Papastavrou. Colloidal Properties of Recombinant Spider Silk Protein Particles. *The Journal of Physical Chemistry C*, 120(32):18015–18027, 2016.
- [24] G Vigil, Z Xu, S Steinberg, and J Israelachvili. Interactions of silica surfaces. *Journal of Colloid and Interface Science*, 165:67–385, 1994.
- [25] M Kobayashi, M Skarba, P Galletto, D Cakara, and M Borkovec. Effects of heat treatment on the aggregation and charging of Stöber-type silica. *Journal of Colloid and Interface Science*, 292(1):139–147, 2005.
- [26] B C Donose, E Taran, I U Vakarelski, H Shinto, and K Higashitani. Effects of cleaning procedures of silica wafers on their friction characteristics. *Journal of Colloid and Interface Science*, 299(1):233–237, 2006.
- [27] P G Hartley, I Larson, and P J Scales. Electrokinetic and Direct Force Measurements between Silica and Mica Surfaces in Dilute Electrolyte Solutions. *Langmuir*, 13(8):2207–2214, 1997.
- [28] J J Valle-Delgado, J A Molina-Bolivar, F Galisteo-Gonzalez, M J Galvez-Ruiz, A Feiler, and M W Rutland. Hydration Forces between Silica Surfaces: Experimental Data and Predictions from different Theories. *The Journal of Chemical Physics*, 123(3):034708–13, 2005.
- [29] E Taran, B C Donose, I U Vakarelski, and K Higashitani. pH dependence of friction forces between silica surfaces in solutions. *Journal of Colloid and Interface Science*, 297(1):199–203, 2006.

- [30] S M Acuña and P G Toledo. Short-Range Forces between Glass Surfaces in Aqueous Solutions. *Langmuir*, 24(9):4881–4887, 2008.
- [31] N C Christov, K D Danov, Y Zeng, P A Kralchevsky, and R von Klitzing. Oscillatory Structural Forces Due to Nonionic Surfactant Micelles: Data by ColloidalProbe AFM vs Theory. *Langmuir*, 26(2):915–923, 2010.
- [32] J Morag, M Dishon, and U Sivan. The Governing Role of Surface Hydration in Ion Specific Adsorption to Silica: An AFM-Based Account of the Hofmeister Universality and Its Reversal. *Langmuir*, 29(21):6317–6322, 2013.
- [33] J L Bitter, G A Duncan, D J Beltran-Villegas, D H Fairbrother, and M A Bevan. Anomalous Silica Colloid Stability and Gel Layer Mediated Interactions. *Langmuir*, 29(28):8835–8844, 2013.
- [34] V Valmacco, M Elzbieciak-Wodka, C Besnard, P Maroni, G Trefalt, and M Borkovec. Dispersion Forces Acting between Silica Particles across Water: Influence of Nanoscale Roughness. *Nanoscale Horizons*, 1:325–330, 2016.
- [35] W Kern and D A Poutinen. Cleaning solution based on hydrogen peroxide for use in silicon semiconductor technology. *RCA Rev.*, 31:187–206, 1970.
- [36] I Popa, G Gillies, G Papastavrou, and M Borkovec. Attractive Electrostatic Forces between Identical Colloidal Particles Induced by Adsorbed Polyelectrolytes. *The Journal of Physical Chemistry B*, 113(25):8458–8461, 2009.
- [37] T J Senden. Force Microscopy and Surface Interactions. *Current Opinion in Colloid & Interface Science*, 6(2):95–101, 2001.
- [38] L J Kirwan, P Maroni, S H Behrens, G Papastavrou, and M Borkovec. Interaction and Structure of Surfaces Coated by Poly(vinyl amines) of Different Line Charge Densities †. *The Journal of Physical Chemistry B*, 112(46):14609–14619, 2008.
- [39] J P Cleveland, S Manne, D Bocek, and P K Hansma. A nondestructive method for determining the spring constant of cantilevers for scanning force microscopy. *Review of Scientific Instruments*, 64(2):403–405, 1993.
- [40] D Ossola, P Dörig, J Vörös, T Zambelli, and M Vassalli. Serial weighting of micro-objects with resonant microchanneled cantilevers. *Nanotechnology*, 27(41):415502, 2016.

7 Extending the Limits of Direct Force Measurements

- [41] J E Sader, I Larson, P Mulvaney, and L R White. Method for the calibration of atomic force microscope cantilevers. *Review of Scientific Instruments*, 66(7):3789–3798, 1995.
- [42] C Stelling, A Mark, G Papastavrou, and M Retsch. Showing Particles their Place: Deterministic Colloid Immobilization by Gold Nanomeshes. *Nanoscale*, 8(30):14556–14564, 2016.
- [43] J L Hutter and J Bechhoefer. Calibration of atomic–force microscope tips. *Review of Scientific Instruments*, 64(7):1868–1873, 1993.
- [44] R Pericet-Camara, G Papastavrou, S H Behrens, and M Borkovec. Interaction between Charged Surfaces on the PoissonBoltzmann Level: The Constant Regulation Approximation. *The Journal of Physical Chemistry B*, 108(50):19467–19475, 2004.
- [45] S Guriyanova, D S Golovko, and Elmar Bonaccorso. Cantilever contribution to the total electrostatic force measured with the atomic force microscope. *Measurement Science and Technology*, 21(2):025502, 2009.
- [46] S H Behrens and D G Grier. The Charge of Glass and Silica Surfaces. *The Journal of Chemical Physics*, 115:6716–6721, 2001.
- [47] E Potthoff, D Ossola, T Zambelli, and J A Vorholt. Bacterial Adhesion Force Quantification by Fluidic Force Microscopy. *Nanoscale*, 7(9):4070–4079, 2015.
- [48] O Guillaume-Gentil, E Potthoff, D Ossola, P Dörig, T Zambelli, and J A Vorholt. Force-Controlled Fluidic Injection into Single Cell Nuclei. *Small*, 9(11):1904–1907, 2012.
- [49] K Hu, F-R F Fan, A J Bard, and A C Hillier. Direct Measurement of Diffuse Double-Layer Forces at the Semiconductor/Electrolyte Interface Using an Atomic Force Microscope. *The Journal of Physical Chemistry B*, 101(41):8298–8303, 1997.
- [50] G Toikka and R A Hayes. Direct Measurement of Colloidal Forces between Mica and Silica in Aqueous Electrolyte. *Journal of Colloid and Interface Science*, 191(1):102–109, 1997.
- [51] M Giesbers, J M Kleijn, and M Stuart. The Electrical Double Layer on Gold probed by Electrokinetic and Surface Force Measurements. *Journal of Colloid and Interface Science*, 248(1):88–95, 2002.

References

- [52] V Kuznetsov and G Papastavrou. Ion Adsorption on Modified Electrodes as Determined by Direct Force Measurements under Potentiostatic Control. *The Journal of Physical Chemistry C*, 118(5):2673–2685, 2014.
- [53] M Kobayashi, F Juillerat, P Galletto, P Bowen, and M Borkovec. Aggregation and Charging of Colloidal Silica Particles: Effect of Particle Size. *Langmuir*, 21(13):5761–5769, 2005.
- [54] D Ossola. *FluidFM for Force-Controlled Electrophysiology*. Phd-dissertation, ETH Zürich, 2014.

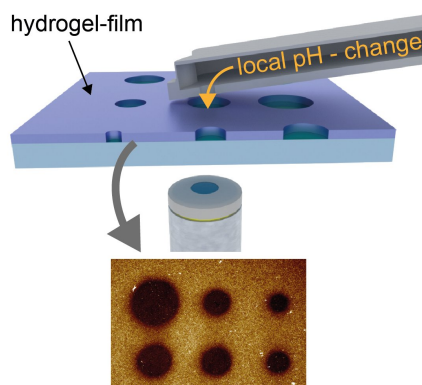
CHAPTER 8

Writing with Fluid: Structuring Hydrogels with Micrometer Precision by AFM in Combination with Nanofluidics

Nicolas Helfricht^a, Andreas Mark^a, Marina Behr^b, Andreas Bernet^b, Hans-Werner Schmidt^b, Georg Papastavrou^a

^a Physical Chemistry / Physics of Polymers, Bavarian Polymer Institute, University of Bayreuth, Universitätsstr. 30, 95440 Bayreuth, Germany. Email: Georg.Papastavrou@uni-bayreuth.de

^b Macromolecular Chemistry I, Bavarian Polymer Institute, University of Bayreuth, Universitätsstr. 30, 95440 Bayreuth, Germany. Email: Hans-Werner.Schmidt@uni-bayreuth.de



Reprinted with permission from:

"Writing with Fluid: Structuring Hydrogels with Micrometer Precision by AFM in Combination with Nanofluidics", N. Helfricht, A. Mark, M. Behr, A. Bernet, H.-W. Schmidt, G. Papastavrou, *Small*, **2017**, 13(31), 1700962, DOI: 10.1002/smll.201700962.

© 2017 WILEY-VCH Verlag GmbH & Co. KGaA, Weinheim.

8 Writing with Fluid: Structuring Hydrogels with Micrometer Precision

Hydrogels have many applications in biomedical surface modification and tissue engineering. However, structuring hydrogels after their formation represents still a major challenge, in particular due to their softness. Here, a novel approach is presented that is based on the combination of atomic force microscopy (AFM) and nanofluidics, also referred to as FluidFM technology. Its applicability is demonstrated for supramolecular hydrogel films that are prepared from low-molecular weight hydrogelators, such as derivatives of 1,3,5-benzene tricarboxamides (BTAs). BTA films can be dissolved selectively by ejecting alkaline solution through the aperture of a hollow AFM-cantilever connected to a nanofluidic controller. The AFM-based force control is essential in preventing mechanical destruction of the hydrogels. The resulting 'chemical writing' process is studied in detail and the influence of various parameters, such as applied pressure and time, is validated. It is demonstrated that the achievable structuring precision is primarily limited by diffusion and the aperture dimensions. Recently, various additive techniques have been presented to pattern hydrogels. The here-presented subtractive approach can not only be applied to structure hydrogels from the large class of reversibly formed gels with superior resolution but would also allow for the selective loading of the hydrogels with active substances or nanoparticles.

One of the fundamental requirements in macroscopic engineering is the ability to machine materials into predesigned shapes. One distinguishes between additive and subtractive techniques, depending if material is selectively added or removed. A typical technique for the former is 3D printing, while the latter includes techniques such as milling or cutting with water and plasma. The transfer of macroscopic techniques down to the micrometer- and to the nanometer-scale has been pursued actively in recent years. [1] Many of these new approaches are based on scanning probe techniques, in particular when dealing with nanometer-sized structures. [2, 3] However, for soft materials, such as hydrogels, only a limited number of techniques are available, in particular techniques that would allow for a rapid and versatile prototyping process. Due to the great importance of hydrogels in modern biotechnology (e.g., for tissue engineering) [4, 5], it is hardly surprising that the development of structuring techniques for this class of materials has been intensively pursued in recent years. Currently, most approaches to structure hydrogels are based on additive manufacturing [6, 7, 8, 9, 10, 11], photochemistry, [12, 13, 14] or molding [15] to control bulk hydrogel formation. However, for many applications, especially in cell culture or tissue engineering, it would be important to structure hydrogels with high precision, ideally in the sub-micrometer regime. Due to their softness, [16] hydrogels are not accessible to conventional subtractive processing techniques, such as milling.

Many hydrogels, in particular supramolecular ones, are responsive to external stimuli, such as changes in temperature or pH, leading to reversible gel formation. Supramolecular hydrogels can be prepared from low molecular weight (lmw) gelators. [17, 18] An interesting class of lmw

8.0 Writing with Fluid: Structuring Hydrogels with μm Precision

gelators are derivatives of 1,3,5-benzene tricarboxamides (BTAs). [19, 20, 21, 22] One particular BTA derivative, which is bearing terminal carboxyl groups, is shown in Figure 8.1 a. Under basic pH, these gelator molecules are water soluble due to the deprotonated terminal carboxylate groups. In acidic milieu, the carboxylate moieties are protonated, thus the intermolecular electrostatic repulsion is reduced. Only under these conditions supramolecular nanofibers are formed. [23] The necessary change in pH can be induced electrochemically by applying a sufficiently high overpotential (larger than +1.2 V *versus* Ag/AgCl). [24, 25] Thereby, the local pH in the vicinity of the electrode is reduced due to the electrolysis of water and the generation of H⁺-ions. This process is often referred to as electrogelation, [24, 25] which allows for a controlled hydrogel film growth. The film thickness can be adjusted by the gelation time, *i.e.* the time the potential is applied. BTA-hydrogels formed on electrodes can be dissolved in an analogous manner as bulk BTA-hydrogels. [19]

Based on the reversible formation/dissolution of BTA-hydrogels upon pH-change, we propose a completely novel approach to structure hydrogel films. This approach is based on a combination of atomic force microscopy (AFM) with nanofluidics and is known as FluidFM-technology. [26] A special hollow AFM-cantilever with an aperture at its end is connected to a nanofluidic pressure controller. The latter allows for the application of a defined underpressure at the aperture, in order to aspirate particles or cells. [27, 28] So far the FluidFM technique has been used only for additive manufacturing, specifically for the deposition of nanoparticles or the electrochemical printing of 3D-metal structures. [29, 30, 31] We will demonstrate that the FluidFM technology, especially due to its combination of force and pressure control provides a versatile platform for subtractive manufacturing of soft materials, such as hydrogels.

Thin BTA-hydrogel films were prepared by electrogelation in a three-electrode electrochemical cell (*cf.* schematic in Figure 8.1 b), which comprised an indium tin oxide (ITO)-coated glass slide as working electrode, a coiled Pt-wire as counter electrode, and Ag/AgCl-wire as reference electrode. By applying a constant potential of +1.6 V (*versus* Ag/AgCl) with a potentiostat, the pH-value at the electrode is locally altered by the electrolysis of water according to: $2\text{H}_2\text{O}(l) \rightarrow \text{O}_2(g) + 4\text{H}^+(aq) + 4e^-$. The reduced pH-value leads to the protonation of the BTA sodium salt, which forms in consequence a hydrogel on the electrode (*cf.* Figure 8.1 b). For gelation times of about 30 s, we find an average film thickness of $\approx 1.1 \mu\text{m}$, as measured by determining *in situ* the depth of a scratch with Peak Force Tapping Mode AFM (*cf.* Figure 8.7). Topography AFM images and SEM images reveal the fibrillar structure of BTA hydrogel films (*cf.* Figure 8.1 d,e). Further details about the film characterization are given in the supporting information (*cf.* Figures 8.5, 8.6 and 8.7).

The scheme in Figure 8.2 a illustrates the basic approach to structure electrogelated BTA films

8 Writing with Fluid: Structuring Hydrogels with Micrometer Precision

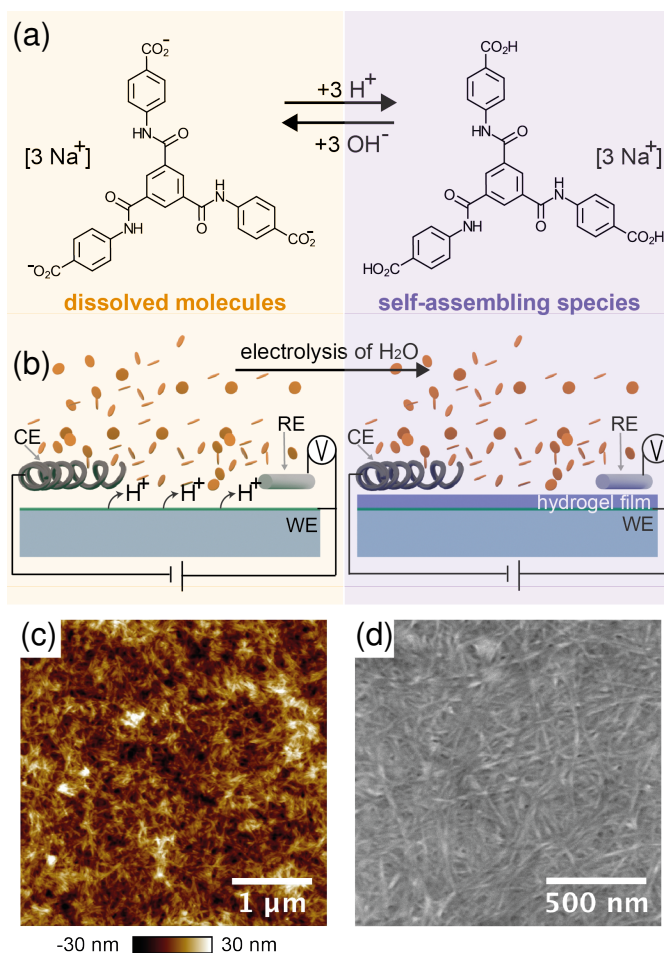


Figure 8.1: (a) Sodium salt of N, N', N''-tris(4-carboxyphenylene)-1,3,5-benzenetricarboxamide (BTA) in the deprotonated state (orange) remains dissolved, while it forms supramolecular hydrogels in the protonated (blue) state. (b) Schematic illustration of the electrogelation setup of BTA films by local generation of H^+ -ions on an ITO-working-electrode in a three-electrode electrochemical cell. (c) The AFM image and the (d) SEM-image show a dried electrogelated BTA hydrogel film with fibrillar morphology.

by FluidFM: By filling the microchanneled FluidFM-cantilever and the corresponding reservoir with an alkaline solution of pH 12, a defined liquid stream can be dispensed locally on the hydrogel film. Bulk hydrogels of this BTA-derivate dissolve for $\text{pH} > 6.2$. [19] To accomplish locally-defined dissolution of hydrogel films by FluidFM, the cantilever is approached in z-direction to the hydrogel surface as for standard AFM-experiments. During approach, the deflection of the cantilever is monitored. If the deflection overcomes a predefined threshold (*i.e.* the maximum loading force), the movement of the piezo is stopped and the cantilever rests with a defined loading force on the hydrogel film. Afterward, an overpressure pulse of defined length Δt and

8.0 Writing with Fluid: Structuring Hydrogels with μm Precision

pressure Δp is applied. By contrast, during the approach to the surface only a constant idle pressure of 10-30 mbar is applied in order to prevent diffusion of the bulk solution into the cantilever channel. A sequence of the cantilever movements in z-direction and the corresponding pressure pulses is shown schematically in Figures 8.2 b,c. After performing the steps (1) - (3), to which we refer to as 'ramp and write' cycle, the lateral position on the film (4) is changed by means of the xy-scanner of the AFM and a novel 'ramp & write' cycle can be conducted on a different position with different parameters.

Figures 8.2 d and 8.2 e demonstrates that the release of alkaline solution by defined pressure pulses leads to the local removal of hydrogel from a BTA-film. Each of the circular areas of removed hydrogel corresponds to a single 'ramp and write' cycle with systematic changes of pressure and pulse duration. The grid-like structure results from the variation of pulse duration in horizontal direction (100 - 300 ms, right to left) and of overpressure in vertical direction (100 - 500 mbar, bottom to top), respectively (*cf.* arrows in Figure 8.2 d). BTA hydrogels are auto-fluorescent with an absorption band at 330-360 nm and an emission band centered at 450 nm. [19] Hydrogels on ITO-electrodes can be directly imaged by optical microscopy. Figure 8.2 d has been acquired on a confocal laser scanning microscope (CLSM) equipped with a laser for an excitation wavelength of 405 nm directly after structuring the BTA film by FluidFM. The parts of the film in which the BTA has been removed are represented as bright areas. Optical transmission microscopy is possible during the FluidFM experiments (*cf.* Figure 8.2 a), albeit with lower resolution. A movie illustrating the *in situ* creation of structures analogous to the ones presented in Figure 8.2 d,e is available in the Supporting Information.

Figure 8.2 e shows the surface topography of structured and subsequently dried BTA-hydrogel film as determined by AFM. Dark regions correspond to areas with reduced height. Complete removal of the hydrogel leads to bare areas of the substrate. Their presence can be confirmed by imaging the large difference in the elastic moduli between the hard ITO-substrate and the soft hydrogel film with peak force tapping (*cf.* Figure 8.5 in the Supporting Information). In order to confirm that the selective removal of the BTA-hydrogel is entirely based on dissolution by alkaline solutions and not on the applied pressure, a control experiment has been performed with a FluidFM cantilever, where Millipore water at pH 5.5 has been ejected while the cantilever was in contact with the BTA-film. Even for the application of large overpressures of > 1000 mbar and prolonged time intervals (*i.e.* minutes instead of milliseconds), we have not been able to detect removal of the hydrogel (*cf.* Supporting Information and accompanying Movies S1 and S2 in the Supporting Information).

Figure 8.2 f illustrates in a quantitative manner how the removal of hydrogel depends on the duration t and applied overpressure p . The volume V_{rem} of hydrogel removed by a pressure pulse

8 Writing with Fluid: Structuring Hydrogels with Micrometer Precision

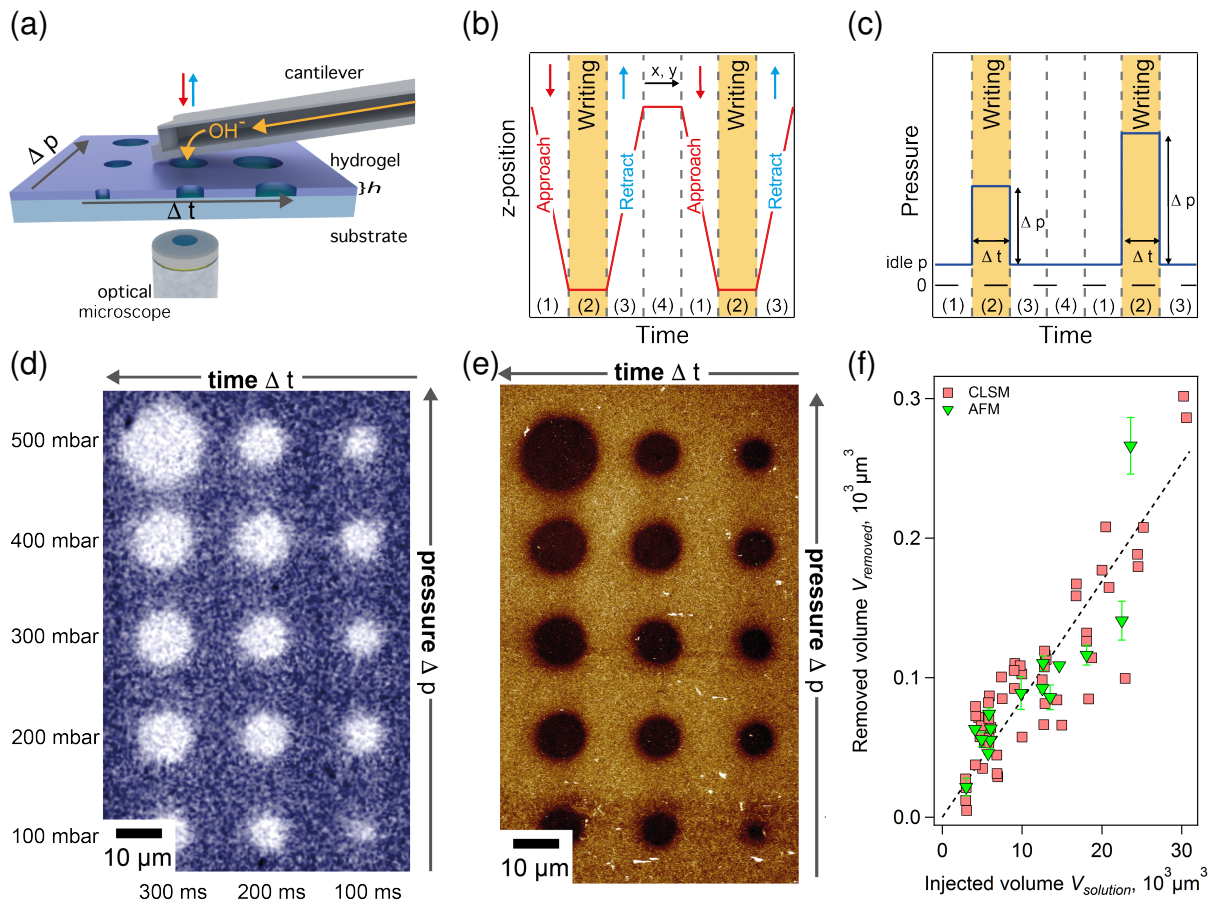


Figure 8.2: (a) Schematic representation of the setup used to structure hydrogel films by the local release of alkaline solution from a FluidFM cantilever. The 'writing' procedure is illustrated in (b) for the AFM movement and (c) for the applied pressure: (1) A FluidFM-cantilever filled with alkaline solution is approached to the surface while a low idle-pressure is applied. (2) When the cantilever touches the surface an overpressure pulse is applied for a defined time interval. (3) Subsequently, the pressure is reduced to an idle pressure and the AFM cantilever is retracted from the surface. After completion of such a 'ramp and write'-cycle the lateral position is changed and a new cycle is initiated. (d) Confocal laser scanning microscope (CLSM) image of an electrogelated BTA-hydrogel film, which has been structured by different 'ramp and write'-cycles. For each cycle the time interval Δt (100-300 ms; x-direction) and the applied pressure Δp (100-500 mbar; y-direction) have been varied. (e) Surface topography AFM image for the 'ramp and write'-cycles corresponding to the CLSM-image. (f) Quantitative dependence of the dissolved hydrogel volume V_{rem} as a function of dispensed volume of alkaline solution V_{sol} as obtained from CLSM and AFM data.

8.0 Writing with Fluid: Structuring Hydrogels with μm Precision

can be estimated from the hydrogel-free volume in the BTA-film as determined by CLSM and AFM images, respectively. Besides the areas, the thickness of the films has been determined by imaging the structures *in situ* (cf. Supporting Information). The total volume V_{sol} of alkaline solution released through the aperture of the cantilever (cf. Figure 8.4 in the Supporting Information) during a pressure pulse can be estimated by $V_{sol} = pt/R_{tot}$, where R_{tot} is the total hydrodynamic resistance of a hollow cantilever. For the FluidFM cantilevers used here, one finds a hydrodynamic resistance of $R_{tot} \approx 5 \times 10^{17}$ (cf. calculation in section 8.3.4 in the Supporting Information). [32] The volumetric flow rate Q through the aperture is $Q = p/R_{tot} = V_{sol}/t$. As the pressure is not building up instantaneously, the accurate ejected volume has been determined for each pressure pulse by integrating over the pressure as recorded by the internal pressure sensor. Hence, one obtains for the total volume ejected during a pulse of length: (cf. SI for an example of $\Delta p(t)$). The experimental data are in a first order approximation compatible with and $k \approx 0.01$ as shown in Figure 8.2 f. A similar, linear dependency of the ejected volume on the flow rate has been reported for the deposition of nanoparticles by FluidFM. [29] However, the low value for k indicates that dissolution is rate determining in a process resembling the one for the dissolution of a polymeric material. [33]

The smallest spot in the lower right corner of Figure 8.2 e has a diameter of $\sim 2.5 \mu\text{m}$ at the height of the substrate, which is comparable with the diameter of the aperture ($\sim 1.8 \mu\text{m}$) for the FluidFM cantilever used in our experiments (cf. Figure 8.4, Supporting Information). The boundaries between substrate and hydrogel are very well defined, even below the micrometer-level as traceable by the elasticity difference in peak force tapping imaging (cf. Figure 8.5 in the Supporting Information). However, at the surface of the hydrogel film the structures are less well defined and a diameter of $\sim 6 \mu\text{m}$ has been measured by CLSM (cf. Figure 8.2 d). Besides the diameter of the aperture, the applied idle-pressure, and diffusion lead to a nonhomogeneous dissolution of the hydrogel as a function of the distance to the solid substrate.

The preparation of more complex patterns requires the lateral movement of FluidFM-cantilevers during the structuring process. A simple example for such processes is depicted schematically in Figure 8.3 a: The cantilever is moved laterally perpendicular to its fast scan axis over surface of an electrogelated hydrogel film with different velocities. Simultaneously, alkaline solution is ejected through the aperture. Figure 8.3 b shows *in situ* AFM images of line patterns generated in a BTA-hydrogel film at different writing velocities but a constant loading force of $\approx 35 \text{ nN}$. All structures have been created by the same FluidFM-cantilever but imaging had to be carried out in peak force tapping mode with a cantilever to which a colloidal particle has been attached in order to reduce the pressure exerted on the soft hydrogel. [34] Figure 8.3 c summarizes the corresponding cross-sections as determined by peak force tapping AFM in liquid. The *in situ* AFM data reveal that the line width Δw , here reported as full width at half maximum, depends

8 Writing with Fluid: Structuring Hydrogels with Micrometer Precision

critically on the velocity v with which the aperture is moved over the hydrogel film. In the case of a resting cantilever (*cf.* Figure 8.2 d, e), one finds $V_{sol} \propto \Delta t$, which leads to $\Delta w \propto v^{-1}$ during lateral movement according to $v = s/t$ and $V_{sol} = h\Delta s \Delta w$ with h as thickness of the hydrogel film. Figure 8.3 d confirms the approximate proportionality $\Delta w \propto v^{-1}$ for the AFM- as well as for the CLSM-data. A similar dependency between the obtained line width and the scanning velocity has been reported previously by Zambelli and co-workers for the deposition of nanoparticles on flat substrates. [29] However, here we find no indication that the liquid stream through the aperture leads to a repulsive deflection of the cantilever near the surface. This difference is attributed to the softness and permeability of the BTA-hydrogel film due to its large water content. In particular, we could not observe any dependence of the line width on the applied loading force in the range of 17-180 nN, *cf.* Figure 8.3 e). For fast writing speeds with $v > 6 \mu\text{m/s}$, the aperture moves so fast over the film that the removal of hydrogel is incomplete at the bottom and the substrate is still covered by a residual layer of hydrogel. The quantitative dependence of trench depth on the writing velocity for films in the hydrated and dried state is summarized in the Supporting Information (*cf.* Figure 8.9 in the Supporting Information).

Defined removal of hydrogel during lateral movement of the FluidFM-cantilever is a prerequisite for producing larger and more complex structures. Figure 8.3 f shows a first proof of principle for a well-like structure in a BTA-film. By gelation times > 10 min thicker hydrogel films have been obtained that allow to demonstrate that structures can be written in the film without exposing the solid substrate. The single square well shown in Figure 8.3 f comprised an approximately rectangular area of about $30 \times 30 \mu\text{m}$. An ensemble of similar wells, arranged in chessboard-like structures, is presented in Figure 8.13 (Supporting Information). Such structures can be used for example in cell culture in order to separate single cells during growth at well-defined distances. [35] More complex, but nevertheless directly implementable patterns would comprise the construction of substrates with interconnecting channels between the wells, for example to control neuronal growth. [36, 37]

The here-presented approach for structuring hydrogels is by no means restricted to BTA-based hydrogels. Many hydrogels, in particular those formed from lmw gelators, can dissolve upon change of the environmental conditions. [17] The combination of nanofluidics and AFM allows for a laterally and axially defined dissolution of such hydrogel films on a highly local scale. The achievable resolution is presently in the range of few micrometers but can be optimized by utilizing smaller apertures in the nanometer range. The time required for structuring hydrogels in this manner is rather short: The patterns shown in Figures 8.2 d,e have been produced in less than 100 s and a movie demonstrating the process in real time is available in the Supporting Information. The AFM-based force control is essential in preventing a mechanical destruction of the hydrogels while utilizing chemical techniques to structure the gel-layer via controlled nanoflu-

8.0 Writing with Fluid: Structuring Hydrogels with μm Precision

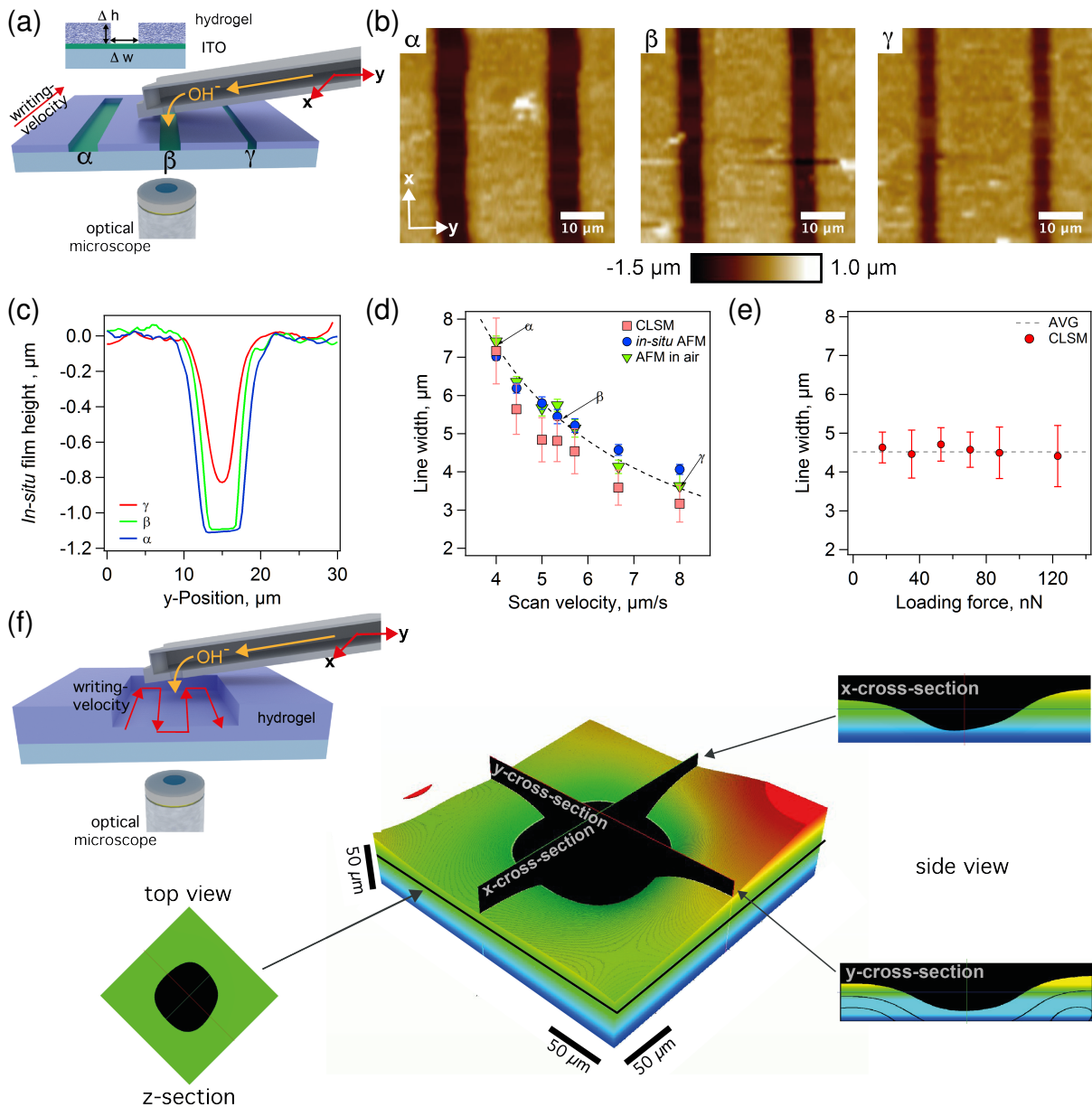


Figure 8.3: (a) Schematic representation of 'writing' line structures by FluidFM into BTA-films. (b) Topography of line patterns as determined by in-situ AFM in the hydrated state for different writing velocities (α : 4 $\mu\text{m/s}$; β : 5.5 $\mu\text{m/s}$; γ : 8 $\mu\text{m/s}$). (c) Corresponding cross sections from the previous images. (d) Evaluation of the line width as a function of the writing velocity for CLSM and AFM data. (e) Independence of line width from the cantilever loading force for constant writing velocity and applied pressure. (f) Schematic representation of the creation of more complex structures by means of the FluidFM. CLSM image of a single square well in a hydrogel film with a thickness $\gg 1 \mu\text{m}$. The square has been written by moving the FluidFM cantilever laterally in a square pattern, while ejecting alkaline solution. The insets show the cross-sections and a top view, respectively.

8 Writing with Fluid: Structuring Hydrogels with Micrometer Precision

idics. It should be pointed out that the structuring of hydrogel films by mechanical 'scratching' with an AFM-tip is possible but leads to deposition of debris as no chemical dissolution is taking place (*cf.* Supporting Information for an example). Moreover, the partial removal of hydrogel in thick films as shown in Figure 8.3 f would be also not possible by a simple mechanical approach.

The processing of hydrogels for special purposes, *e.g.* rapid prototyping of complex cell compartments for tissue engineering, [36, 38, 39, 40] can be readily implemented with the here-presented approach. In the future, FluidFM-based nanofluidic techniques might find further applications for hydrogel films, such as loading the structured hydrogel locally, for example with active substances for cell culture or nanoparticles.

8.1 Experimental Section

The sodium salt of N, N', N''-tris(4-carboxyphenylene)-1,3,5-benzenetricarboxamide (*cf.* Figure 1 a) has been synthesized and characterized as reported previously. [19] BTA hydrogel films were prepared by electrogelation on ITO coated glass slides (Merck; Darmstadt, Germany) cell from a 1 g/L solution of the BTA salt, containing 10 mM NaCl (Aldrich) as background electrolyte. A potential of +1.6 V *versus* Ag/AgCl has been applied for 30 s to the ITO-working electrode. The FluidFM system is based on a commercial system (Flex-FluidFM, Nanosurf AG, Liestal, Switzerland and Cytosurge AG, Glattbrugg, Switzerland) on an inverted optical microscope (Examiner.D1, Zeiss, Germany). Tipless FluidFM cantilevers (Micropipettes, Cytosurge AG, Glattbrugg, Switzerland) with a nominal spring constant of 2 N/m and 2 μm apertures have been used throughout the experiments. These cantilevers were used to locally release an alkaline solution (pH 12, KOH, Titrisol, Merck). All manipulations were performed in Milli-Q water. Hydrogel films were characterized after patterning by CLSM and AFM. Further details are given in the Supporting Information.

8.2 Acknowledgements

N. H. and A. M. contributed equally to this work. The authors thank Yannick Jännsch, Daniel Keim, and Andreas Rösch for their help with the initial experiments leading to this study. Mathias Schlenk provided help with confocal laser scanning microscopy imaging, Carmen Kunert with SEM measurements, and Volodymyr Kuznetsov with electrogelation. This work was supported by the DFG in the framework of the SFB840.

8.3 Supporting Information

8.3.1 Extended Experimental Section

Electrogelation

The sodium salt of N, N', N"-tris(4-Carboxyphenylene)-1,3,5-benzenetricarboxamide has been synthesized and characterized as reported previously. [19] The hydrogel films were prepared by electrogelation on indium tin oxide (ITO) coated glass slides (Merck; Darmstadt, Germany). Prior to the gelation, the substrates were subsequently cleaned with pure 2-propanol (Bernd Kraft, Duisburg, Germany), 1 M KOH (Titrisol, Merck, Germany) and water of MQ grade. A custom-made three-electrode set-up has been used for the electrogelation. A coiled platinum wire counter electrode was arranged in a circular manner around the ITO working electrode. A silver wire, which has been chlorinated beforehand in a 1 M KCl solution (Sigma-Aldrich) with an ACI-01 Automatic Chlorider (npi electronic GmbH, Tamm, Germany), was used as Ag/AgCl reference electrode. The electrodes were immersed in a 1 g/L solution of the BTA salt, containing 10 mM NaCl (Aldrich) as background electrolyte. A scanning potentiostat (Model 362, EG&G Princeton Applied Research, UK) was used to apply a controlled potential of +1.6 V vs Ag/AgCl for 30 s (if not stated otherwise). After finishing the electrogelation, the solution was exchanged 5 times with MQ-water to remove the residual BTA. The BTA-hydrogel films were always prepared directly before transfer to the FluidFM setup ensuring that the hydrogel did not dry.

FluidFM

The experimental FluidFM setup is based on a commercial system (Flex-FluidFM, Nanosurf AG, Liestal, Switzerland & Cytosurge AG, Glattbrugg, Switzerland). The AFM head is installed on an inverted optical microscope (Axio Observer.Z1, Carl Zeiss, Jena, Germany) equipped with fluorescence filter cubes to detect the photoluminescence of the BTA-film during the FluidFM-manipulations of the hydrogel film. Tipless FluidFM cantilevers (Micropipettes, Cytosurge AG, Glattbrugg, Switzerland) with a nominal spring constant of 2 N/m and an aperture of 2 μm in diameter were used. These cantilevers were used to locally release an alkaline solution (pH 12, KOH, Titrisol, Merck). All manipulations were performed in pure MQ-water. Prior to every FluidFM experiment, all used solutions were degassed and filtrated through PES syringe filters (pore diameter of 0.2 μm ; Carl Roth GmbH & Co. KG, Karlsruhe, Germany).

Figure 8.4 shows a scanning electron microscopy SEM image of an exemplary FluidFM can-

8 Writing with Fluid: Structuring Hydrogels with Micrometer Precision

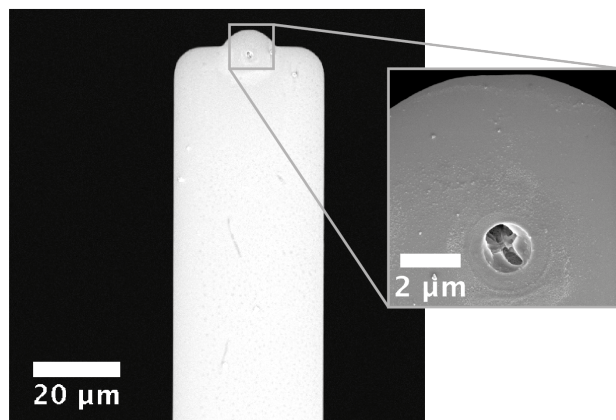


Figure 8.4: SEM image of a FluidFM cantilever used in the present study and imaged after finishing the structuring experiments.

tiler as used in the experiments. The aperture, through which the liquid is ejected, is shown in the inset.

Characterization of Hydrogel Films

Hydrogel films were characterized after structuring by CLSM and AFM. The CLSM (TCS SP8, Leica GmbH, Germany) was equipped with an excitation laser of 405 nm wavelength. AFM characterization was performed by either tapping mode or peak force tapping Mode AFM on a Dimension ICON equipped with a Nanoscope V controller (Bruker, Camarillo, CA).

Peak Force Imaging

All images in peak force tapping mode were acquired with a Dimension ICON AFM equipped with a Nanoscope V controller (Bruker, Camarillo, CA). Samples of dried hydrogel films were imaged with a RTESPA-150-cantilever (Bruker, Camarillo, CA) bearing a sharp tip and a nominal spring constant of 5 N/m. Imaging *in situ*, *i.e.* in Milli-Q water, of freshly prepared hydrogels was carried out using a cantilever with a colloidal particle attached to its end, analogous to a colloidal probe used in direct force measurements. [34] The preparation was carried out as follows: A soft cantilever (ScanAsyst-Fluid, Bruker, Camarillo, CA) with a nominal spring constant of 0.7 N/m was cleaned subsequently with ethanol and water. By means of a micromanipulator (Märzhäuser DC-3KS, Wezlar, Germany) and UV-curable glue (Norland Optical Adhesive 63, Norland Products, Cranbury, NJ) colloidal silica particles (Bangs Laboratories, Fischers, IN) with an average diameter of 4.63 μm were attached to the cantilever. The glue was then cured

by UV-light.

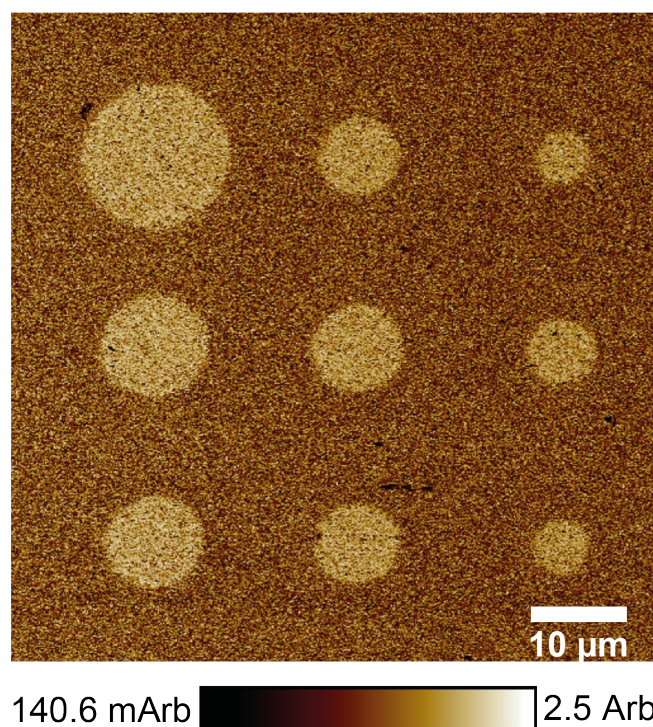


Figure 8.5: Peak force tapping image showing a qualitative elasticity contrast in the structured hydrogel film.

The evaluation of the line arrays written by FluidFM is based on $80 \times 80 \mu\text{m}$ topography images, which show each three lines prepared by FluidFM with identical parameters (*i.e.* scan speed and pressure) of the 'writing'-process. From each image a cross-section over three parallel trenches was averaged over a $10 \mu\text{m}$ wide section. These cross-sections were then used to calculate the full width at half maximum (FWHM) value of the line structures created by FluidFM. This analysis procedure has been performed in the same way for the freshly prepared and the dried hydrogel films, respectively.

AFM peak force tapping allowed to differentiate between local variations of the sample elasticity. Figure 8.5 shows the qualitative elasticity data corresponding to the upper half of the topography AFM image in Figure 8.2 e in the manuscript. This elasticity image allowed to clearly distinguish between the soft BTA hydrogel ($\sim 10 \text{ kPa}$) and the hard ITO substrate ($\sim 92 \text{ GPa}$). [41] Furthermore, a complete dissolution of the hydrogel down to the ITO electrode was revealed.

Confocal Laser Scanning Microscopy

Confocal laser scanning microscopy (CLSM) provides an alternative method to determine the film structure after writing by FluidFM. CLSM was carried out with a laser with an excitation wavelength of 405 nm. The absorption band of the photoluminescence of the BTA hydrogel films in the solid state has a maximum at 330-360 nm but extends to wavelengths > 500 nm while the emission maximum is at about 450 nm. [19] Figure 8.8 shows an example for the reconstruction of the film structure from the z-stacks obtained by detecting the auto-fluorescence of the BTA-film. CLSM has been utilized to analyze the different 'ramp & write' cycles (*cf.* Figure 8.6 a) as well as the line patterns (*cf.* Figure 8.6 b). The dark blue areas correspond to the emission of the BTA hydrogels, whereby the bright spots correspond to reduced fluorescence emission due to the removed film.

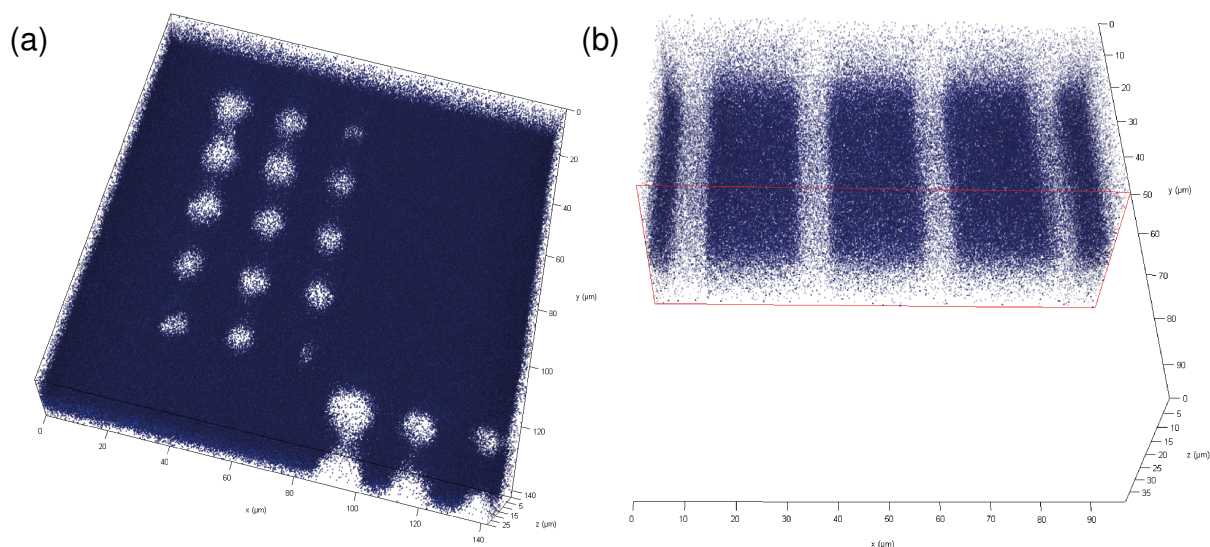


Figure 8.6: CLSM reconstruction of the film structure for 'ramp & write' patterns (a) and line patterns (b).

8.3.2 *In-situ* Determination of the Film Thickness

The thickness of electrogelated BTA-films has been determined *in situ* by peak force tapping Mode AFM with colloidal probe cantilevers (*cf.* section 8.3.1) on the boundary between an artificial scratch in the freshly prepared film. The former has been obtained with a very thin metal piece to which enough force has been applied to expose the substrate. Figure 8.7 a shows a representative *in situ* image of the boundary film/scratch. An approximate film height of 1150 nm has been determined from an averaged cross-section (*cf.* fig. 8.7 b).

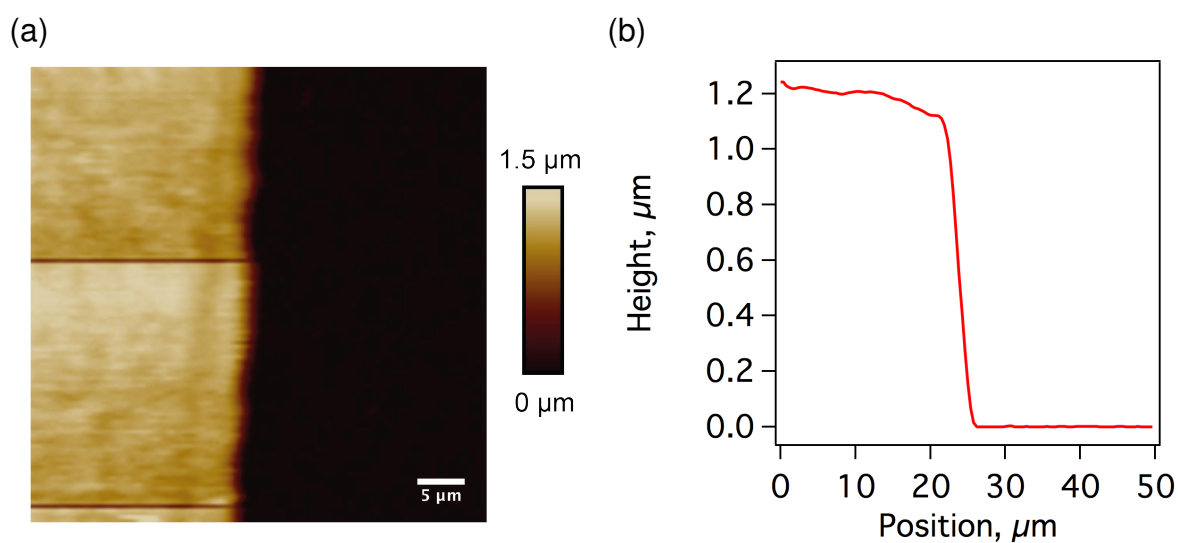


Figure 8.7: (a) Topography image of a freshly prepared BTA-film with a corresponding scratch imaged by *in situ* Peak Force Tapping AFM using a cantilever bearing a colloidal probe instead of a sharp tip. (b) Averaged cross-section that allows to determine the film thickness.

8.3.3 Characterization of Patterns Written by FluidFM

AFM-characterization of Structures obtained by 'Ramp & Write' Cycles with FluidFM

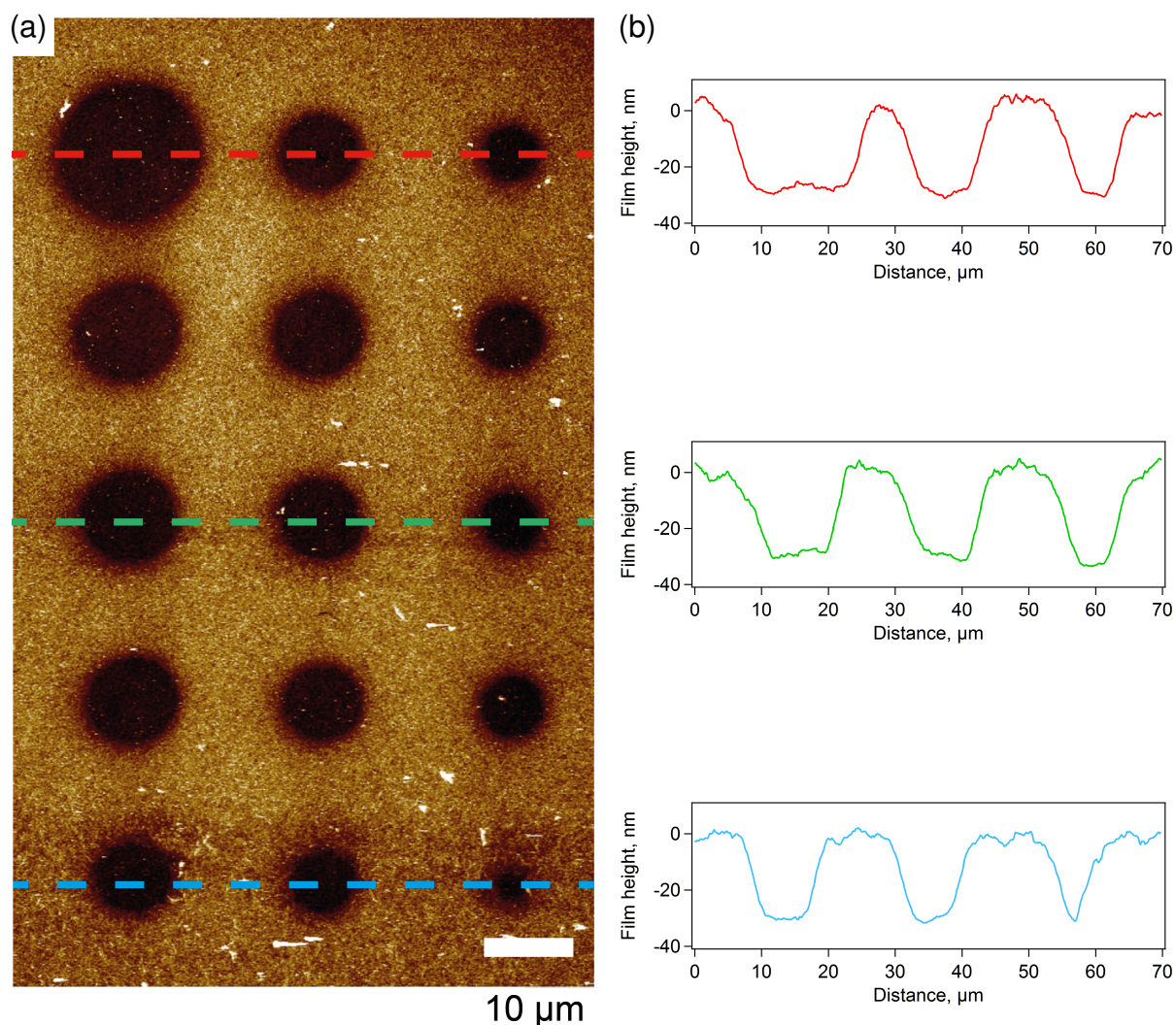


Figure 8.8: (a) Topography of a BTA-hydrogel film after 'ramp & write' patterns using several pressure pulses and duration times. (b) Corresponding cross-sections, which were used to evaluate the dissolved area of the hydrogel film.

The structures obtained by 'ramp & write' cycles (*cf.* Figure 8.2 e) were imaged by Peak Force Tapping AFM in dried state. Figure 8.8 a shows the result of a 'ramp & write' cycle, where time and pressure have been varied. The size of the dissolved spots in the hydrogel film were evaluated by analysing cross-sections as the ones shown in Figure 8.8 b. These cross-sections were smoothed by a boxcar averaging over 20 data points.

Comparison of Line Width and Trench Depth for Dried and Hydrated Hydrogel Films

Figure 8.3 b shows some line patterns obtained by FluidFM. In order to determine the influence of the writing velocity on the trench depth, we analyzed cross-sections obtained by AFM (*cf.* 8.3 b) in liquid environment (*i.e. in situ*) and in the dried state, respectively. The data summarized in Figure 8.9 were calculated from several cross-sections comprising three trenches for each writing velocity.

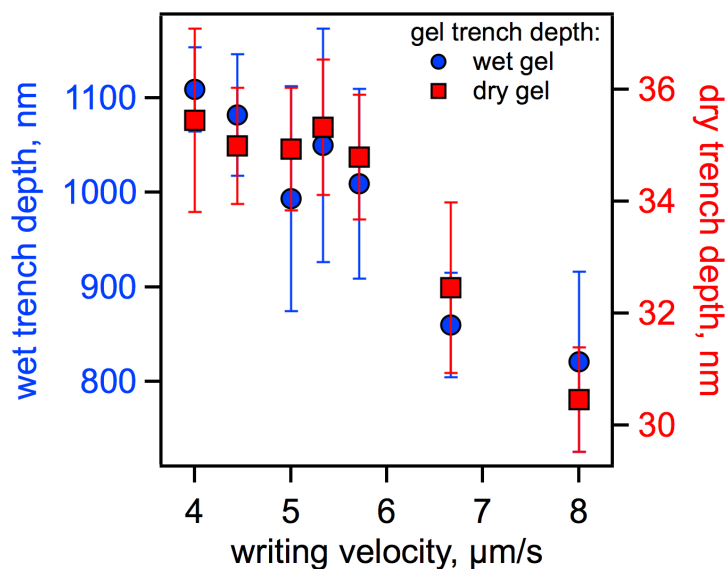


Figure 8.9: Evaluated trench depth for the wet/hydrated state (blue) and for the dried (red) state as a function of the writing velocity as determined from the creation of line patterns

8.3.4 Estimation of Hydrodynamic Parameters during Writing by FluidFM

Calculation of the Hydrodynamic Resistance of FluidFM Cantilevers

The total hydrodynamic resistance R_{h-tot} of a FluidFM cantilever is the main parameter determining how much liquid can be ejected during writing with FluidFM. [42, 32] is given by the sum of the hydrodynamic resistances of the aperture at the end of the FluidFM cantilever $R_{h-aperture}$ and of the channel $R_{h-channel}$.

$$R_{h-tot} = R_{h-aperture} + R_{h-channel} \quad (8.1)$$

For the tipless FluidFM-cantilevers used here, the hydrodynamic resistance of the aperture can be approximated for an aperture diameter D_h ($2 \mu\text{m}$) as [42]

$$R_{h-aperture} = \frac{128\mu L_c}{\pi D_h^4} \quad (8.2)$$

where L_c is the wall thickness of the cantilever (600 nm) and μ is the dynamic viscosity of water ($\mu = 0.001 \text{ Pa s}$). One finds for the hydrodynamic resistance of the aperture a value of $1.5 \times 10^{15} \text{ Pa s m}^{-3}$. For aperture diameters larger than $1 \mu\text{m}$, the total hydrodynamic resistance is primarily limited by the hydrodynamic resistance of the channel, which is given by:

$$R_{h-channel} = \frac{12\mu L}{wh^3(1 - 0.63\frac{h}{w})} \quad (8.3)$$

where L is the length of the channel (here given by the length of the cantilever of $\sim 200 \mu\text{m}$ and the channel inside the carrier chip, in total $L \sim 1.4 \text{ mm}$), w the channel width ($36 \mu\text{m}$), and h the channel height ($1 \mu\text{m}$), respectively. The influence of the internal pillars can be neglected as those are contributing only about additional 10 % hydrodynamic resistance to the hydrodynamic resistance of the channel of $\sim 4.75 \times 10^{17} \text{ Pa s m}^{-3}$.

Reconstruction of the Time Dependence for the Pressure Pulses

Upon application of a pressure pulse in order to eject liquid from the FluidFM cantilever, one has to take into account that there is a finite response time from the nanofluidic controller. Hence, the pressure as function of time was recorded by the internal pressure sensor in the nanofluidic controller in order to correct for the 'true' volume of liquid ejected during the pressure pulses. The recorded time series was evaluated with a set of custom-written routines implemented in IGOR Pro (Wavemetrics).

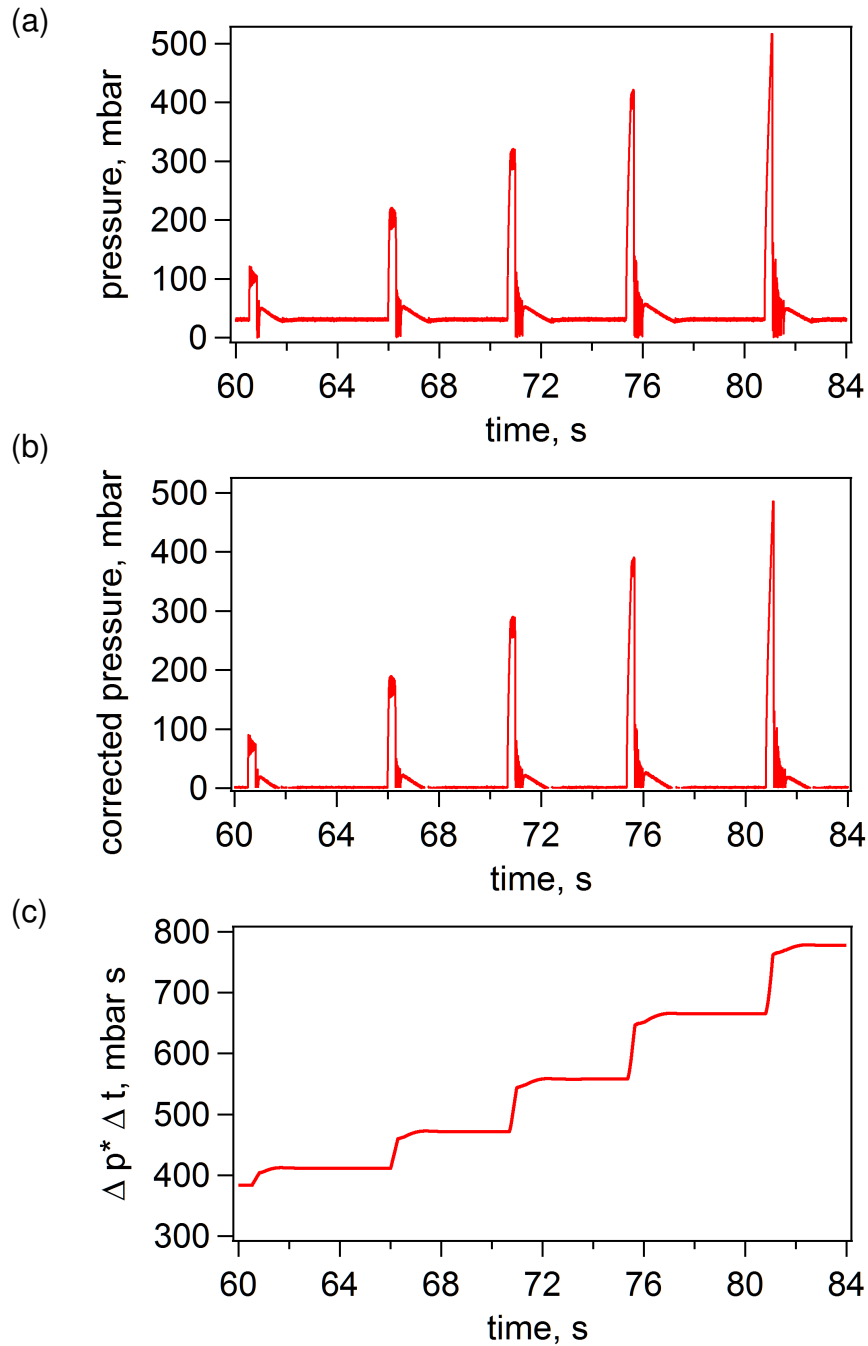


Figure 8.10: (a) Exemplary pressure sequence during a 'ramp & write' sequence. (b) The data were corrected for the applied idle pressure. (c) $\Delta p \times \Delta t$ is obtained from the step height of the integrated pressure data.

Figure 8.10 a shows an example for a sequence of pressure pulses. The pressure has been recorded as a function of time. Between the pulses an idle-pressure is applied, which is kept constant during the experiments. First, the idle pressure was fitted over a time interval before

8 Writing with Fluid: Structuring Hydrogels with Micrometer Precision

starting a 'ramp & write' cycle, in order to correct the pressure pulses later by subtracting the idle-pressure (*cf.* Figure 8.10 b). Finally, $\Delta p \times \Delta t$ was determined from the step heights of the integrated pressure pulses (*cf.* Figure 8.10 c).

8.3.5 *In-Situ* Determination of the *InvOLS* for FluidFM Cantilevers

The spring constant of the FluidFM-cantilevers was calibrated in air by the so-called Sader method, [43] which is implemented in the software of the AFM used (FlexAFM with C3000-controller, Nanosurf AG, Liestal, Switzerland). Due to the softness of the hydrogel film, the inverse optical lever sensitivity (*InvOLS*) could not be obtained from force versus distance curves on the films. Therefore, we pursued another approach in order to determine the *InvOLS in situ*. [44] Shortly, the thermal noise spectrum of the FluidFM cantilever was acquired in aqueous solution before each series of measurements and the *InvOLS* was determined by the equipartition theorem [45] from these thermal power spectra on base of the beforehand determined spring constant.

8.3.6 Control Experiments Demonstrating the Chemical Dissolution of BTA-Hydrogels at pH 12 as primary process

In order to demonstrate that the removal of hydrogel in the vicinity of the FluidFM-aperture has to be attributed solely to a chemical dissolution processes, the reservoir of a FluidFM cantilever has been filled with MQ-water (*i.e.* pH 5.5). Not even for very high overpressures (> 1000 mbar) and prolonged times of > 9 min any removal of hydrogel could be observed by optical microscopy (*cf.* Figure 8.11). By contrast, a basic electrolyte solution of pH 12 leads under the same pressure to an immediate removal of the BTA-hydrogel in an area with a diameter $> 100 \mu\text{m}$ after 1 s as shown in Figure 8.12.

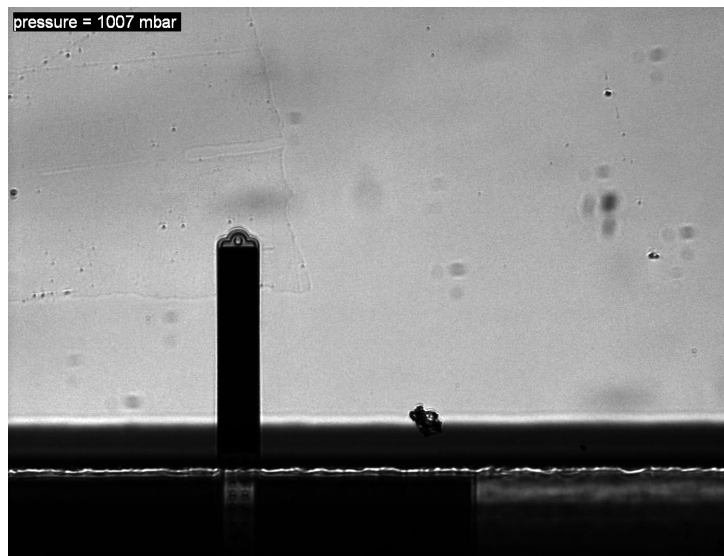


Figure 8.11: No removal of BTA-hydrogel film after 9 min and 1 bar for MilliQ-water (pH ≈ 5.5)

8 Writing with Fluid: Structuring Hydrogels with Micrometer Precision

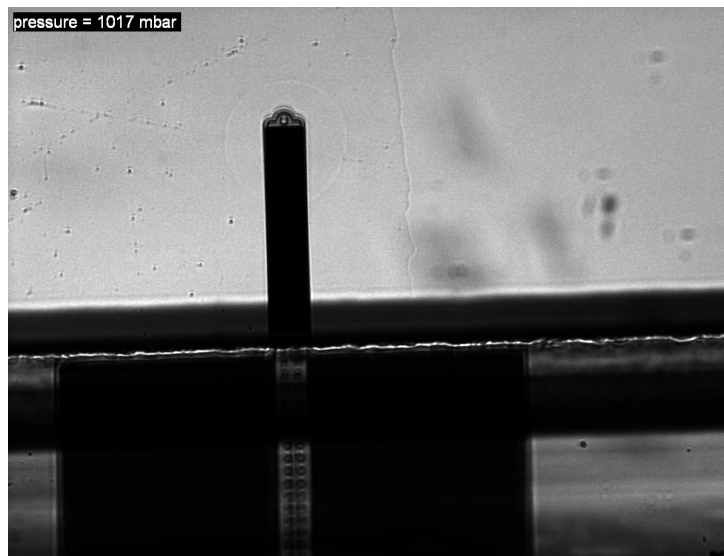


Figure 8.12: Removal of BTA-hydrogel film after 1 s and 1 bar for pH 12.

8.3.7 Example for Large Scale Patterns in Hydrogel Films

Figure 8.13 shows an example for a periodic structure in a very thick hydrogel film prepared by electrogelation. The pattern is composed from several well-like structures as shown in Figure 8.3 f. The image has been acquired by CLSM. The single wells have a depth of about $10\ \mu\text{m}$ and a diameter of about $50\ \mu\text{m}$.

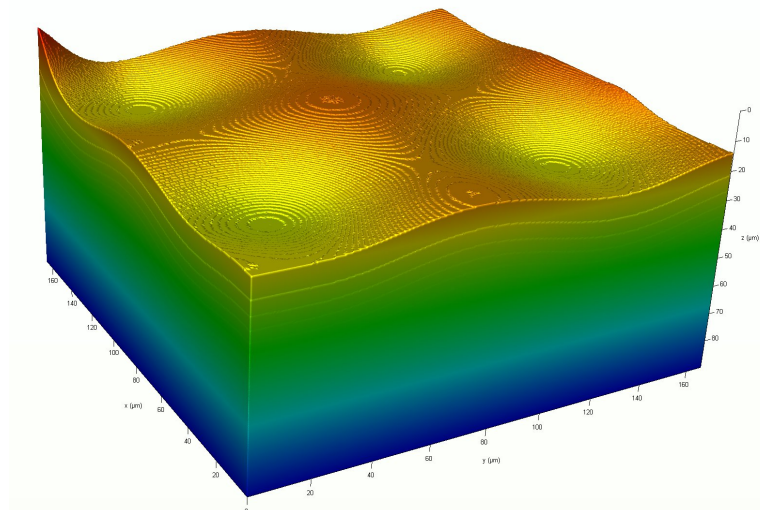


Figure 8.13: CLSM-image of a pattern prepared by the FluidFM-technique in a BTA-hydrogel film.

8.3.8 Mechanical Removal of Hydrogel Films by Scratching with an AFM-Tip

The mechanical removal of thin, soft films represents a standard technique in AFM that is often used to determine the thickness of polymer films. [46] However, this process leads to the deposition of debris outside the area where the film has been removed. Figure 8.14 shows an example for this technique for an electrogelated BTA-film (30 s at 1.6 V vs. Ag/AgCl).

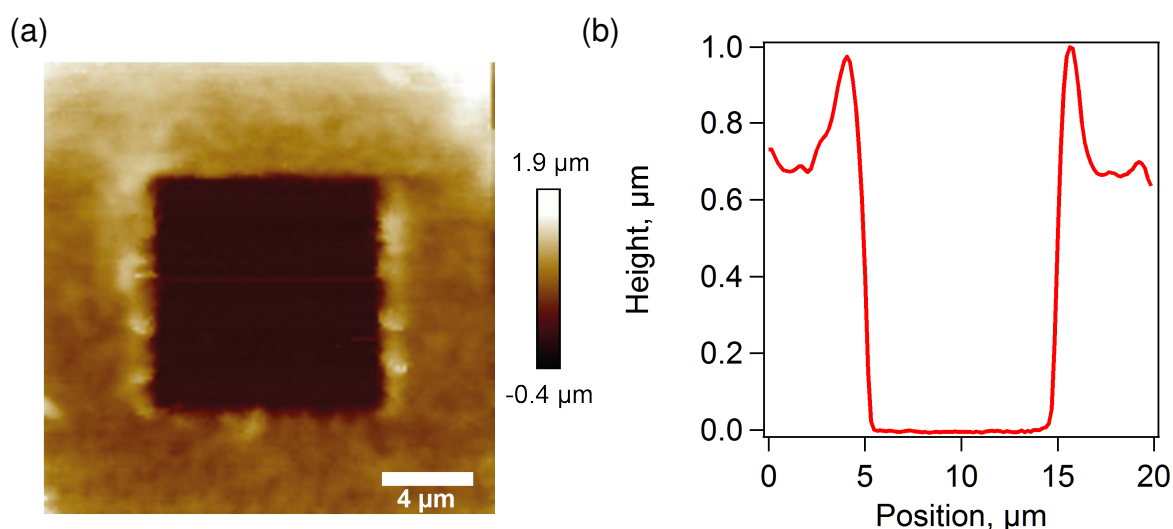


Figure 8.14: (a) AFM image of a hydrated BTA-film after mechanical removal by 'scratching' with an AFM-tip in a $10 \times 10 \mu\text{m}$ area. (b) Corresponding cross-section.

The square pattern ($10 \times 10 \mu\text{m}$) in Figure 8.14 a was obtained by contact mode imaging with a Scanasyst Fluid cantilever (Burker) with a nominal spring constant of 0.7 N/m at a scan velocity of $8 \mu\text{m/s}$. Directly afterwards, the obtained structure was characterized by force volume mapping (128×128 points) for an area of $20 \times 20 \mu\text{m}$. The experiment has been performed in liquid (Milli-Q water). Figure 8.14 b represents a cross-section, demonstrating the debris around the original scan area.

8.3.9 Movie

A real-time movie showing a representative sequence of different 'ramp & write' cycle is provided in the electronic supporting information, entitled: "Writing with Fluids.m4v".

Two additional movies are available, illustrating a control experiment with Milli-Q water in direct comparison to the 'positive' experiment with a solution of pH 12 (*cf.* section 8.3.6 are available.)

References

- [1] E B Brousseau, S S Dimov, and D T Pham. Some recent advances in multi-material micro- and nano-manufacturing. *The International Journal of Advanced Manufacturing Technology*, 47(1-4):161–180, 2009.
- [2] J Zhao, L A Swartz, W-F Lin, P S Schlenoff, J Frommer, J B Schlenoff, and G-Y Liu. Three-Dimensional Nanoprinting via Scanning Probe Lithography-Delivered Layer-by-Layer Deposition. *ACS Nano*, 10(6):5656–5662, 2016.
- [3] L Hirt, A Reiser, R Spolenak, and T Zambelli. Additive Manufacturing of Metal Structures at the Micrometer Scale. *Advanced Materials*, 2017. DOI: 10.1002/adma.201604211.
- [4] M W Tibbitt and K S Anseth. Hydrogels as extracellular matrix mimics for 3D cell culture. *Biotechnology and Bioengineering*, 103(4):655–663, 2009.
- [5] N A Peppas, J Z Hilt, A Khademhosseini, and R Langer. Hydrogels in Biology and Medicine: From Molecular Principles to Bionanotechnology. *Advanced Materials*, 18(11):1345–1360, 2006.
- [6] M P Lutolf and J A Hubbell. Synthetic biomaterials as instructive extracellular microenvironments for morphogenesis in tissue engineering. *Nature Biotechnology*, 23(1):47–55, 2005.
- [7] K Pataky, T Braschler, A Negro, P Renaud, M P Lutolf, and J Brugger. Microdrop printing of hydrogel bioinks into 3D tissue-like geometries. *Advanced materials (Deerfield Beach, Fla.)*, 24(3):391–396, 2012.
- [8] P Galliker, J Schneider, H Eghlidi, S Kress, V Sandoghdar, and D Poulikakos. Direct printing of nanostructures by electrostatic autofocussing of ink nanodroplets. *Nature Communications*, 3:890, 2012.
- [9] R Suntivich, I Drachuk, R Calabrese, D L Kaplan, and V V Tsukruk. Inkjet Printing of Silk Nest Arrays for Cell Hosting. *Biomacromolecules*, 15(4):1428–1435, 2014.
- [10] T J Hinton, Q Jallerat, R N Palchesko, J H Park, M S Grodzicki, H-J Shue, M H Ramadan, A R Hudson, and A W Feinberg. Three-dimensional printing of complex biological structures by freeform reversible embedding of suspended hydrogels. *Science advances*, 1(9):e1500758, 2015.
- [11] H Kang, S Hwang, and J Kwak. A hydrogel pen for electrochemical reaction and its applications for 3D printing. *Nanoscale*, 7(3):994–1001, 2015.

References

- [12] A M Kloxin, A M Kasko, C N Salinas, and K S Anseth. Photodegradable hydrogels for dynamic tuning of physical and chemical properties. *Science*, 324(5923):59–63, 2009.
- [13] C Jungnickel, M V Tsurkan, K Wogan, C Werner, and M Schlierf. Bottom-Up Structuring and Site-Selective Modification of Hydrogels Using a Two-Photon [2+2] Cycloaddition of Maleimide. *Advanced materials (Deerfield Beach, Fla.)*, 29(2):1603327, 2017.
- [14] T E Brown, I A Marozas, and K S Anseth. Amplified Photodegradation of Cell-Laden Hydrogels via an Addition-Fragmentation Chain Transfer Reaction. *Advanced Materials*, 29(11):1605001–6, 2017.
- [15] M Diez, P Mela, V Seshan, M Möller, and M C Lensen. Nanomolding of PEG-based hydrogels with sub-10-nm resolution. *Small*, 5(23):2756–2760, 2009.
- [16] C D Markert, X Guo, A Skardal, Z Wang, S Bharadwaj, Y Zhang, K Bonin, and M Guthold. Characterizing the micro-scale elastic modulus of hydrogels for use in regenerative medicine. *Journal of the Mechanical Behavior of Biomedical Materials*, 27:115 –127, 2013.
- [17] M de Loos, B L Feringa, and J H van Esch. Design and Application of Self-Assembled Low Molecular Weight Hydrogels. *European Journal of Organic Chemistry*, 2005(17):3615–3631, 2005.
- [18] X-Q Dou and C-L Feng. Amino Acids and Peptide-Based Supramolecular Hydrogels for Three-Dimensional Cell Culture. *Advanced materials (Deerfield Beach, Fla.)*, 2017. DOI: 10.1002/adma.201604062.
- [19] A Bernet, R Q Albuquerque, M Behr, S T Hoffmann, and H-W Schmidt. Formation of a supramolecular chromophore: a spectroscopic and theoretical study. *Soft matter*, 8(1):66–69, 2012.
- [20] Y Zhang, Q Wang, Y J Xiao, J Han, and X L Zhao. Structure diversity of a series of new coordination polymers based on a C₃-symmetric tridentate ligand with rosette architecture. *Polyhedron*, 33(1):127–136, 2012.
- [21] R C T Howe, A P Smalley, A P M Guttenplan, M W R Doggett, M D Eddleston, J C Tan, and G O Lloyd. A family of simple benzene 1,3,5-tricarboxamide (BTA) aromatic carboxylic acid hydrogels. *Chemical Communications*, 49(39):4268–4270, 2013.
- [22] C M A Leenders, T Mes, M B Baker, M M E Koenigs, P Besenius, A R A Palmans, and E W Meijer. From supramolecular polymers to hydrogel materials. *Materials Horizons*, 1(1):116–120, 2014.

8 Writing with Fluid: Structuring Hydrogels with Micrometer Precision

- [23] I U Vakarelski and K Higashitani. Single-Nanoparticle-Terminated Tips for Scanning Probe Microscopy. *Langmuir*, 22(7):2931–2934, 2006.
- [24] E K Johnson, D J Adams, and P J Cameron. Directed self-assembly of dipeptides to form ultrathin hydrogel membranes. *Journal of the American Society*, 132, 2010.
- [25] G G Leisk, T J Lo, T Yucel, Q Lu, and D L Kaplan. Electrogelation for Protein Adhesives. *Advanced Materials*, 22(6):711–715, 2010.
- [26] A Meister, M Gabi, P Behr, P Studer, J Vörös, P Niedermann, J Bitterli, J Polesel-Maris, M Liley, H Heinzelmann, and T Zambelli. FluidFM: Combining Atomic Force Microscopy and Nanofluidics in a Universal Liquid Delivery System for Single Cell Applications and Beyond. *Nano Letters*, 9(6):2501–2507, 2009.
- [27] O Guillaume-Gentil, E Potthoff, D Ossola, C M Franz, T Zambelli, and J A Vorholt. Force-controlled manipulation of single cells: from AFM to FluidFM. *Trends in biotechnology*, 32(7):381–388, 2014.
- [28] N Helfricht, E Doblhofer, J F L Duval, T Scheibel, and G Papastavrou. Colloidal Properties of Recombinant Spider Silk Protein Particles. *The Journal of . . .*, 120(32):18015–18027, 2016.
- [29] R R Grüter, J Vörös, and T Zambelli. FluidFM as a lithography tool in liquid: spatially controlled deposition of fluorescent nanoparticles. *Nanoscale*, 5(3):1097–1104, 2013.
- [30] L Hirt, R R Grüter, T Berthelot, R Cornut, J Vörös, and T Zambelli. Local surface modification via confined electrochemical deposition with FluidFM. *RSC Advances*, 5:84517–84522, 2015.
- [31] L Hirt, S Ihle, Z Pan, L Dowling-Carter, A Reiser, J M Wheeler, R Spolenak, J Vörös, and T Zambelli. Template-Free 3D Microprinting of Metals Using a Force-Controlled Nanopipette for Layer-by-Layer Electrodeposition. *Advanced Materials*, 28(12):2311–2315, 2016.
- [32] P Dörig, D Ossola, A M Truong, M Graf, F Stauffer, J Vörös, and T Zambelli. Exchangeable Colloidal AFM Probes for the Quantification of Irreversible and Long-Term Interactions. *Biophysical Journal*, 105(2):463–472, 2013.
- [33] J Siepmann and A Göpferich. Mathematical modeling of bioerodible, polymeric drug delivery systems. *Advanced drug delivery reviews*, 48:229–247, 2001.
- [34] S Block and C A Helm. Measurement of long-ranged steric forces between polyelectrolyte layers physisorbed from 1MNaCl. *Physical Review E*, 76(3):030801–4, 2007.

References

- [35] S Khetan and J A Burdick. Patterning hydrogels in three dimensions towards controlling cellular interactions. *Soft Matter*, 7(3):830–838, 2011.
- [36] S Wüst, R Müller, and S Hofmann. Controlled Positioning of Cells in Biomaterials-Approaches Towards 3D Tissue Printing. *Journal of functional biomaterials*, 2(3):119–154, 2011.
- [37] H Dermutz, R R Grüter, A M Truong, L Demkó, J Vörös, and T Zambelli. Local polymer replacement for neuron patterning and in situ neurite guidance. *Langmuir*, 30(23):7037–7046, 2014.
- [38] B Duan, L A Hockaday, K H Kang, and J T Butcher. 3D Bioprinting of heterogeneous aortic valve conduits with alginate/gelatin hydrogels. *Journal of Biomedical Materials Research Part B: Applied Biomaterials*, 101A(5):1255–1264, 2012.
- [39] A P Wong, R Perez-Castillejos, J Christopher Love, and G M Whitesides. Partitioning microfluidic channels with hydrogel to construct tunable 3-D cellular microenvironments. *Biomaterials*, 29(12):1853–1861, 2008.
- [40] D Falconnet, G Csucs, H M Grandin, and M Textor. Surface engineering approaches to micropattern surfaces for cell-based assays. *Biomaterials*, 27(16):3044–3063, 2006.
- [41] T Wittkowski, J Jorzick, H Seitz, B Schröder, and K Jung. Elastic properties of indium tin oxide films. *Thin Solid Films*, 398-399:465–470, 2001.
- [42] S P Dörig. *Manipulating cells and colloids with FluidFM*. Phd-dissertation, ETH Zürich, 2013.
- [43] J E Sader. Frequency response of cantilever beams immersed in viscous fluids with applications to the atomic force microscope. *Journal of Applied Physics*, 84(1):64–76, 1998.
- [44] N Helfricht, E Doblhofer, V Bieber, P Lommès, V Sieber, T Scheibel, and G Papastavrou. Probing the adhesion properties of alginate hydrogels: a new approach towards the preparation of soft colloidal probes for direct force measurements. *Soft matter*, 13(3):578–589, 2017.
- [45] J L Hutter and J Bechhoefer. Calibration of atomic-force microscope tips. *Review of Scientific Instruments*, 64(7):1868–1873, 1993.
- [46] M Morga, Z Adamczyk, S Gödrich, M Oćwieja, and G Papastavrou. Monolayers of poly-L-lysine on mica - Electrokinetic characteristics. *Journal of Colloid and Interface Science*, 456(C):116–124, 2015.

CHAPTER 9

Long-range interaction forces between 1,3,5-cyclohexanetrissamide fibers in crossed-cylinder geometry

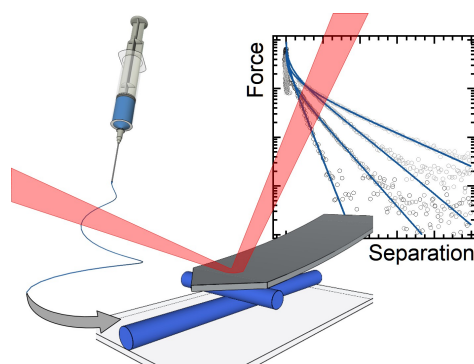
Benedikt R. Neugirg,^a Nicolas Helfricht,^a Steffen Czich,^b
Hans-Werner Schmidt,^{b,c} Georg Papastavrou^{*a}, Andreas Fery^{*a,d}

^a Physical Chemistry II, University of Bayreuth, Universitätsstr. 30, 95440 Bayreuth, Germany. Email: Georg.Papastavrou@uni-bayreuth.de

^b Macromolecular Chemistry I, University of Bayreuth, Universitätsstr. 30, 95440 Bayreuth, Germany.

^c Bayreuth Institute of Macromolecular Research (BIMF) and Bayreuth Center for Colloids and Interfaces (BZKG), University of Bayreuth, Universitätsstr. 30, 95440 Bayreuth, Germany.

^d Leibniz-Institut für Polymerforschung Dresden e. V., Institute of Physical Chemistry and Polymer Physics, Dresden 01069, Germany. Email: Fery@ipfdd.de



Reprinted with permission from:

"Long-range interaction forces between 1,3,5-cyclohexanetrissamide fibers in crossed-cylinder geometry", B. R. Neugirg, N. Helfricht, S. Czich, H.-W. Schmidt, G. Papastavrou, A. Fery, *Polymer*, **2016**, *102*, 363-371, DOI: 10.1016/j.polymer.2016.03.068.

© 2016 Elsevier Ltd.

Abstract

We report on direct force measurements between single melt-electrospun 1,3,5-cyclo-hexane-trisamide (CTA) fibers in crossed-cylinder geometry. The two CTA compounds selected for this study differ in their peripheral substituents: aliphatic ($-\text{C}_{10}\text{H}_{21}$) and fluorinated chains ($-\text{CH}_2\text{C}_6\text{F}_{13}$), respectively. Melt-electrospinning of the CTAs results in smooth and circular fibers with diameters of about $5\ \mu\text{m}$. Individual segments of these fibers were attached to tipless atomic force microscope (AFM) cantilevers and used to measure long-range interaction forces *versus* a second fiber from the same compound in crossed-cylinder geometry. This geometry is well-known from the surface force apparatus and allows for the normalization of forces according to the Derjaguin approximation. From symmetrical measurements, *i. e.* measurements between fibers from the same type of CTA, we quantify the diffuse layer properties in aqueous electrolyte solutions within the framework of the Derjaguin, Landau, Verwey and Overbeek (DLVO) theory. Apparent diffuse layer potentials resulting from the fits to the full solutions of the Poisson-Boltzmann equation show that the fiber surfaces bear a negative surface charge. Most likely, the origin of charging is the adsorption of hydroxyl ions as residual charges from the electrospinning process would be compensated upon the immersion in the electrolyte solutions. Such ion adsorption processes are well-known for other hydrophobic surfaces such as aliphatic and fluorinated self-assembled monolayers (SAMs) (terminating with $-\text{CH}_3$ and $-\text{CF}_3$ groups). The apparent diffuse layer potentials for CTA fibers are comparable to the values reported for these SAMs.

9.1 Introduction

The invention of the atomic force microscope (AFM) fundamentally changed the way how colloidal and soft matter systems can be studied *in situ* [1]. In addition to the possibility of imaging a surface, one can also probe the interaction of an AFM tip with the sample by direct force measurements [2]. To overcome the problem of ill-defined contact, the colloidal probe (CP) technique was invented [3]. Typically, the CP-technique utilizes a spherical, μm -sized colloidal particle that replaces the sharp tip at the end of an AFM cantilever. The particle's dimensions can be determined with reasonable accuracy by optical or scanning electron microscopy (SEM). A CP allows for a well-defined interaction geometry, which on the one hand enables the determination of mechanical properties. In contact mechanics, one relates the force exerted by the CP on the sample and the resulting deformation in the contact area. Thus, material properties such as Young's modulus and the work of adhesion per unit area can be obtained [2, 4, 5] and [6]. On the other hand, a well-defined interaction geometry is the prerequisite to

9.1 Introduction

investigate long-range forces in colloidal suspensions in a quantitative manner [7] and [8]. The Derjaguin approximation relates experimentally determined forces to free interaction energies per unit area [9]. Prior to the advent of CP, the only possibility to accomplish such direct force measurements was the surface force apparatus (SFA) which is based on the measurements of interaction forces between two smooth macroscopic mica surfaces of cylindrical shape in crossed-cylinder geometry [10] and [11]. This particular interaction geometry was first adapted to the AFM in 1998 by Meagher *et al.* and permitted to determine the interaction forces between α -alumina fibers in electrolyte solutions [12] and [13].

Utilizing fiber fragments as CPs represents an important experimental approach as fibrillar (cylindrical) systems are ubiquitous in nature. For instance in case of hair, the contact interactions, *i. e.* adhesive and frictional properties, dominate the haptics and are thus of great interest in the formulation of hair care products. To study these interactions, researchers attached hair fragments to tipless AFM cantilevers. Force *versus* distance (F-D) curves and lateral friction loops acquired in sliding contact with a second hair enabled the direct investigation of adhesion and friction on the level of single hairs for the first time [14, 15] and [16]. Adhesion and friction also play an important role in many non-woven fabrics made from polymer fibers. A crucial factor for the stability and integrity in many networks is the junction strength of two fibers touching each other. Polyester [17] and pulp [18] microfibers as well as Nylon [19] nanofibers were studied in terms of their adhesive and frictional behavior.

Self-assembly processes provide the possibility to form micro- and nanofibers by a bottom-up approach *via* secondary interactions. Among the multitude of suitable supra-molecular motifs, a well-known example are 1,3,5-benzenetrisamides (BTAs), which are capable of forming nanofibers. Typically, the formation of supramolecular nanofibers by these small molecules is driven by three uniaxially directed hydrogen bonds. AFM investigations on individual supramolecular objects unraveled a pronounced mechanical stability of these BTA-based micro- and nanofibers [20] and [21]. Recently, we have reported on the *in situ* formation of supramolecular nanofibers in a polymer nonwoven scaffold resulting in a remarkably stable microfiber-nanofiber composite. These composites, which exhibit a dense nanofiber network, are highly suitable to remove particulate matter from air and are thus promising to be used in air filtration applications [22]. However, a fundamental understanding of the interaction forces between individual fibers in these composites is still missing.

Besides fiber formation *via* self-assembly processes, BTAs can also be melt-electro-spun into supramolecular micro- and nano-fibers [23]. Electrospinning is a technique commonly used for fiber fabrication from viscous polymer solutions [24]. Under the influence of a strong electrical field, a thin jet is ejected from the so-called Taylor cone (see Fig. 9.1) [25]. Electrospinning

9 Interaction forces between fibers in crossed-cylinder geometry

of BTAs to homogenous [26] and mechanically stable [27] fibers with circular cross-section and smooth surfaces depends on various parameters such as molecular structure, temperature and viscosity of the melt, and the applied electric field. In this context, electrospinning of supramolecular fibers and avoiding the formation of solid spheres during the electrospinning process (*i. e.* electrospraying) is facilitated by using 1,3,5-cyclohexanetrissamides (CTAs) compared to BTAs [26] and [28].

Here, we investigate the interaction forces between individual melt-electrospun supra-molecular fibers. We selected two CTAs that differ significantly in the terminating functional groups at their periphery (Fig. 9.1). In the alkyl CTA (Fig. 9.1 left side), each amide group is linked to a decyl chain. In the fluorinated CTA (Fig. 9.1 right side) the amide substituent consists of a methylene group followed by a perfluorinated C₆ chain. Due to the length of these pending chains, the outmost layer of the compounds can be considered as aliphatic or perfluorinated, respectively. By attaching CTA fiber fragments to AFM cantilevers and immobilizing a second fiber of the same compound on the substrate, we adapted the classical crossed-cylinder geometry from the SFA. Direct F-D measurements in these symmetric systems immersed in aqueous electrolyte solution of various concentrations allow for unambiguous identification of the fiber surface's interaction forces, including apparent diffuse layer potentials [29].

9.2 Results and discussion

9.2.1 Melt-electrospun cyclohexanetrissamide fibers

Both CTAs have been obtained by the reaction of the cyclohexane-1,3,5-tricarboxylic acid chloride with the corresponding amines in THF in the presence of pyridine. Details of the synthesis for the alkyl CTA (Fig. 9.1 left side) have been reported previously [30] and [31]. The ones for the fluorinated CTA (Fig. 9.1 right side) are given in the experimental section.

For melt-electrospinning, we utilized the same custom-made setup as described in detail by Singer *et al.* [28]. Electrospinning of CTAs results in a jet that is sufficiently stable to obtain continuous fibers and thereby illustrates their strong inter-molecular cohesion [26]. Important for the successful melt-electrospinning to fibers is the knowledge of the thermal stability and the phase behavior of the CTAs (see Fig. SI 9.7). Typically, electrospinning of BTAs from the isotropic phase results in the formation of solid droplets (electrospraying), whereas highly ordered mesophases are too viscous to perform electrospinning. However, CTAs feature columnar nematic phases readily allowing for fiber formation by melt-electrospinning. Both CTAs could be spun employing identical electrospinning parameters. The CTAs were placed into a

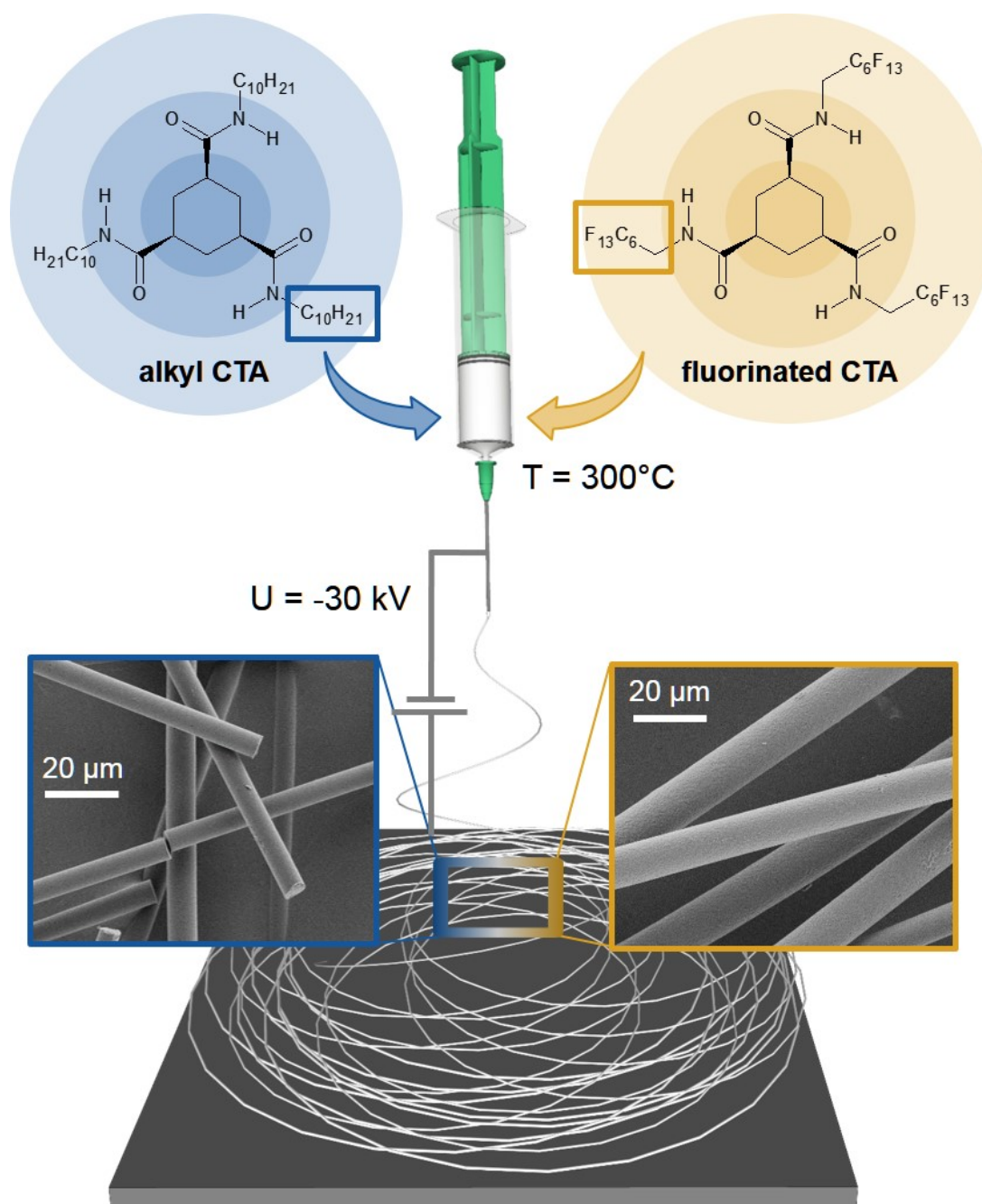


Figure 9.1: Schematic fabrication of 1,3,5-cyclohexanetrissamide (CTA) fibers by melt-electrospinning. The chemical structures of both CTAs consist of a cyclohexane core surrounded by three amide groups and peripheral aliphatic single bond $\text{-C}_{10}\text{H}_{21}$ (left side) and fluorinated single bond $\text{-CH}_2\text{C}_6\text{F}_{13}$ (right side) substituents, respectively. For both compounds, electrospinning from a melt at $T = 300^\circ\text{C}$ at a voltage of -30 kV yields in continuous and homogeneous fibers with diameters in the range of $5\ \mu\text{m}$ as verified by SEM.

9 Interaction forces between fibers in crossed-cylinder geometry

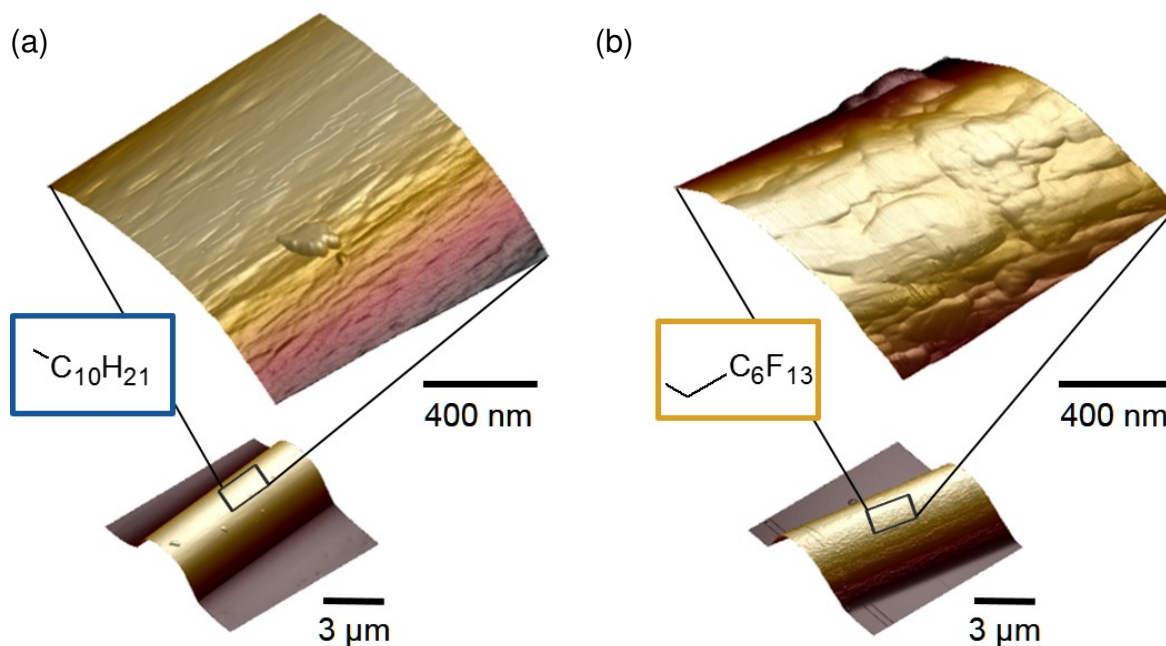


Figure 9.2: AFM tapping-mode images acquired in air depicting a fiber segment of the alkyl CTA (a) and the fluorinated CTA (b). The magnified sections show the morphology of the fiber surfaces. The RMS roughness of the topography is 4.1 ± 1.6 nm for the alkyl CTA and 16.4 ± 2.4 nm for the fluorinated CTA, respectively.

glass syringe and equilibrated in the heating unit at 300 °C for 3 min. After this step a voltage of $U = -30$ kV was applied to spin fibers which were collected on top of an aluminum foil. Under these conditions, we obtained homogeneous and smooth fibers with a diameter in the range of 5 μm (Fig. 9.1 bottom), which are well-suited for fiber manipulation and direct force measurements.

Melt-electrospun fiber segments can be immobilized on solid substrates by means of a UV-curable glue. Fig. 9.2 compares tapping-mode AFM images in air of fibers from both compounds. Despite a pronounced convolution effect of the cylindrical fiber and the sharp AFM tip, there are no indications for the fiber cross-section to deviate from a circular shape. These observations are in perfect agreement with the SEM images (*cf.* Fig. 9.1 bottom).

The surfaces of both fiber types are smooth and defect-free. However, on the nm-level a pronounced ultrastructure can be observed: the topography of the alkyl CTA consists of elongated features with an overall root mean square (RMS) roughness of 4.1 ± 1.6 nm and an average peak-to-peak distance of 34.9 ± 11.7 nm (Fig. 9.2 a). The drop-like ultrastructure in the case of the fluorinated CTA, leads to a significantly larger roughness (RMS: 16.4 ± 2.4 nm and peak-

to-peak distance: 112 ± 29 nm) (Fig. 9.2 b). These values for the roughnesses were derived from the residuals after a 3rd-order plane fit to remove the surface curvature from the $2 \times 2 \mu\text{m}$ images. The roughnesses determined for the fibers here are slightly larger than the one reported for Al-fibers in the study of Meagher *et al.* [12] and [13] Nevertheless, the overall circular cross-section and relative smoothness of melt-electrospun CTA fibers still allows for the determination of apparent diffuse layer potentials. The latter is the potential, as determined from fits to the full Poisson-Boltzmann equation at large separation distances, without any corrections for the surface roughness.

9.2.2 Direct interaction force measurements in crossed-cylinder geometry

We probed the long-range interaction forces between a symmetrical pair of CTA fibers by direct force measurements in crossed-cylinder geometry. This geometry follows the one used in the surface force apparatus (SFA) [10] and [11]. The bottom fiber is immobilized in the same manner as in the previous paragraph. For the probe, we prepared fiber segments attached to tipless AFM cantilevers by means of a micromanipulator. Here again, it is essential that the glue does not contaminate the future contact area of the fibers. Hence, a very thin film of the glue which can be observed under an optical microscope was deposited on the cantilever. As indicated by the iridescence color due to interference effects, the film thickness can be assumed to be below $1 \mu\text{m}$ (Fig. 9.3 a and b). During the preparation process, special diligence is necessary to avoid any rotation of the fiber segment about its long axis as this would inevitably contaminate the fiber surface. We verified additionally for a separate set of cantilevers by SEM that only the part of the fiber in contact with the cantilever is wetted by glue (as highlighted by the yellow color in Fig. 9.3 c and d). We found also by SEM no indication for any glue residues on the lower surface of the fiber fragments for which we report the interaction forces. This set of cantilevers were not used for any interaction measurements due to the metal coating necessary for SEM imaging.

We determined the interaction forces only for symmetric combinations of two aliphatic or two fluorinated CTA fibers, respectively. The measurements were carried out in aqueous electrolyte solutions of pH 5.5 and varying ionic strength (nominal NaCl concentrations 0.1, 0.5, 1 and 5 mM). The crossed-cylinder geometry applied for these measurements is schematically illustrated in Fig. 9.4 a. In our setup, the AFM is combined with an inverted optical microscope, which we used to align the fibers perpendicular to each other (Fig. 9.4 b). Furthermore, we determined the fiber radii optically and found them to be in the range of 4 - $8 \mu\text{m}$. Diameters of about $5 \mu\text{m}$ are best suited for CP preparation and force measurements. The crossed-cylinder geometry has the advantage that it is self-adjusting, therefore, possible tilts of the cantilever

9 Interaction forces between fibers in crossed-cylinder geometry

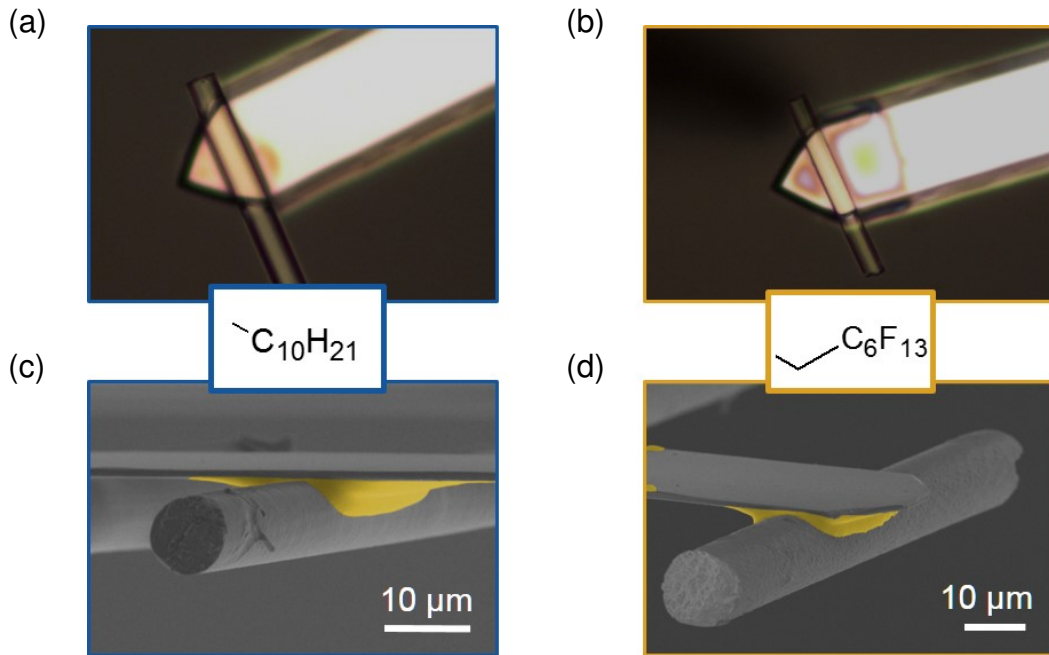


Figure 9.3: Fragments of the alkyl (a and c) and the fluorinated CTA (b and d) fibers attached to tipless AFM cantilevers. a and b show optical bottom view micrographs acquired during the micromanipulation process. The area of the cantilever covered in glue can be recognized by its darker shade and the iridescence color. c and d show SEM images for a different set of cantilevers prepared by an identical procedure. SEM confirms that no glue residues are present on the lower surface of the fiber fragments (c and d). The glue is highlighted by the yellow color.

would not influence the interaction geometry of two fibers. Due to the high lateral spring constant of the cantilever, torsional motion can be neglected in the examined force regime.

Our aim is to relate the forces measured between two fibers at perpendicular contact to their diffuse layer properties. In this quantitative analysis, a well-defined interaction geometry is essential: the Derjaguin approximation allows to relate the measured interaction force F at a separation distance D with the free interaction energy $W(D)$ at the same separation [9]. Analytical expressions for the normalization of several interaction geometries exist, *e.g.* sphere/plane, sphere/sphere and two crossed cylinders [11]. Eq. 9.1) gives the corresponding approximation for two crossed cylinders of radii R_1 and R_2 and the effective radius R_{eff} .

$$F_{cylinder}(D) = 2\pi\sqrt{R_1R_2}W(D) = 2\pi R_{eff}W(D) \quad (9.1)$$

Fig. 9.4 c and d show representative force *versus* distance profiles acquired during approach in crossed-cylinder geometry. The interaction forces have been normalized to the effective

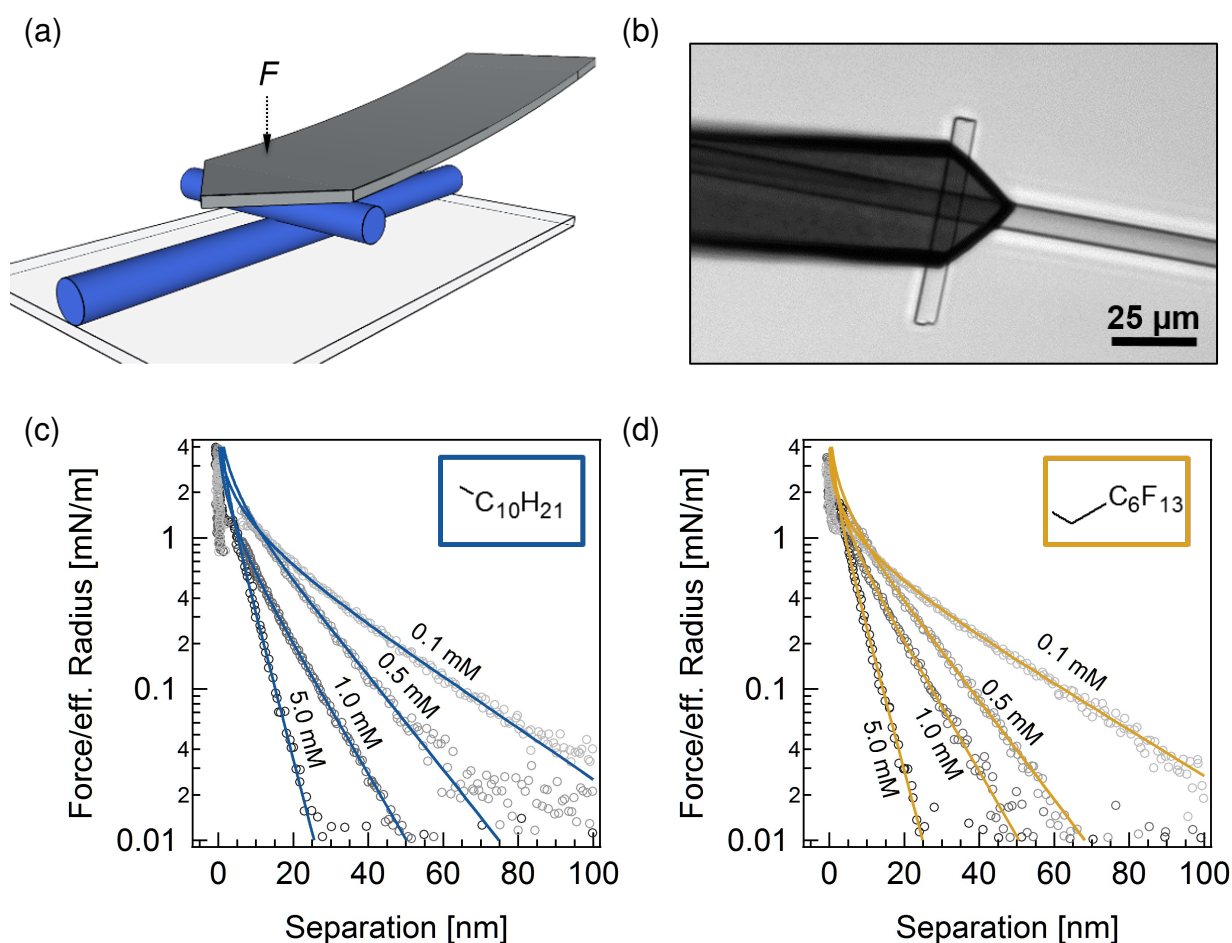


Figure 9.4: Schematic representation of the crossed-cylinder measurement configuration (a) and optical bottom view micrograph during the experiment (b). Representative approach F-D curves normalized to the crossed-cylinder geometry for the alkyl (c) and the fluorinated CTA (d) show a decrease of electrostatic interaction with increasing nominal electrolyte (NaCl) concentration.

radius for the crossed-cylinder geometry (according to Eq. 9.1) and are represented in semi-logarithmic graphs. The retract part of the curves is omitted as we want to focus on long-range electrostatic interactions in the following.

In an AFM experiment, conversion of the photo-diode signal to forces requires the inverse optical lever sensitivity (*InvOLS*) and the effective cantilever spring constant k_{eff} . In the case of the fiber-CP, the determination of these two parameters is non-trivial. To account for possible thermal drifts during a measurement session, we determined the *InvOLS* for each fiber-fiber approach curve individually from the constant compliance regime. The exclusion of any mechanical deformations in the applied force regime has been verified by reference measurements

9 Interaction forces between fibers in crossed-cylinder geometry

with a hard spherical silica colloidal probe (see Fig. SI 9.9 for details). The cantilever spring constant k was calibrated by the thermal noise method [32]. It has to be corrected due to off-end loading as the fiber is attached a certain distance ΔL away from the cantilever's free end at L (see scheme in Fig. SI 9.10). The effective spring constant k_{eff} accounting for the apparent cantilever stiffening due to the shift in the contact point is given by [33].

$$k_{eff} = k \left(\frac{L}{L - \Delta L} \right)^3 \quad (9.2)$$

All measurements were performed in electrolyte solutions with a total ionic strength of 0.1, 0.5, 1 and 5 mM adjusted by addition of NaCl. The Debye length κ^{-1} for an ionic strength of c_0 is given by Eq. 9.3 [11].

$$\kappa = \sqrt{\frac{2e^2 c_0}{\epsilon \epsilon_0 k_B T}} \quad (9.3)$$

where $\epsilon \epsilon_0$ is the total permittivity of the medium, $k_B T$ the thermal energy and e the elementary charge. At large separation distances the interaction force decays exponentially with κ^{-1} as decay constant. In the semi-logarithmic representation of Fig. 9.4 c and d such a decay results in a linear dependency.

For a symmetric system of two identical materials, the total interaction energy $W(D)$ is given by two contributions: the diffuse layer overlap W_{DL} and the van-der-Waals W_{vdW} force according to Derjaguin, Landau, Verwey and Overbeek (DLVO) theory. However, this assumes ideal, smooth surfaces. At large separation distances W_{DL} dominates the interaction and the diffuse layer potential Ψ_0 can be obtained from fits to the Poisson-Boltzmann theory. The van-der-Waals forces are generally much shorter ranged. Thus, for rough surfaces, a general expression for the interaction energy as function of separation is extremely difficult to determine, in particular when the decay length of the interaction is of the same order as the surface roughness. Despite different studies [34, 35] and [36], no consistent theory has been established to date as standard approach in order to account for the effects of surface roughness in direct force measurements, especially regarding non-contact forces.

The CTA fibers that we study here have a RMS surface roughness of several nm (*cf.* Fig. 9.2), which is of the order of the Debye length. Due to the special interaction geometry of crossed cylinders, we do not apply any corrections for surface roughness. Instead, we state the apparent diffuse layer potential $\Psi_{0,app}$ that results from the fits at large separation distances D (with $D > 10$ nm). An additional advantage is that thereby charge regulation can be neglected and, moreover, also the van-der-Waals forces are reduced due to the surface roughness. We did not take these forces into account for data fitting. The interaction force profiles were fitted at large

9.2 Results and discussion

separation distances ($D > 10$ nm) and the Hamaker constants of hydro- and fluorocarbons in water are relatively small. Hence, we found very similar surface potentials when theoretical Hamaker constants for both fibers have been considered (data not shown).

The solid lines in Fig. 9.4 c and d represent fits to full solutions of the Poisson-Boltzmann equation under the boundary condition of constant charge [29]. The Debye length resulting from these fits is in good agreement with the one calculated based on the nominal ionic strength (*cf.* Eq. 9.3 and Fig. SI 9.8). However, deviations at low ionic strength are expected due to dissolution of CO_2 as reported previously [37].

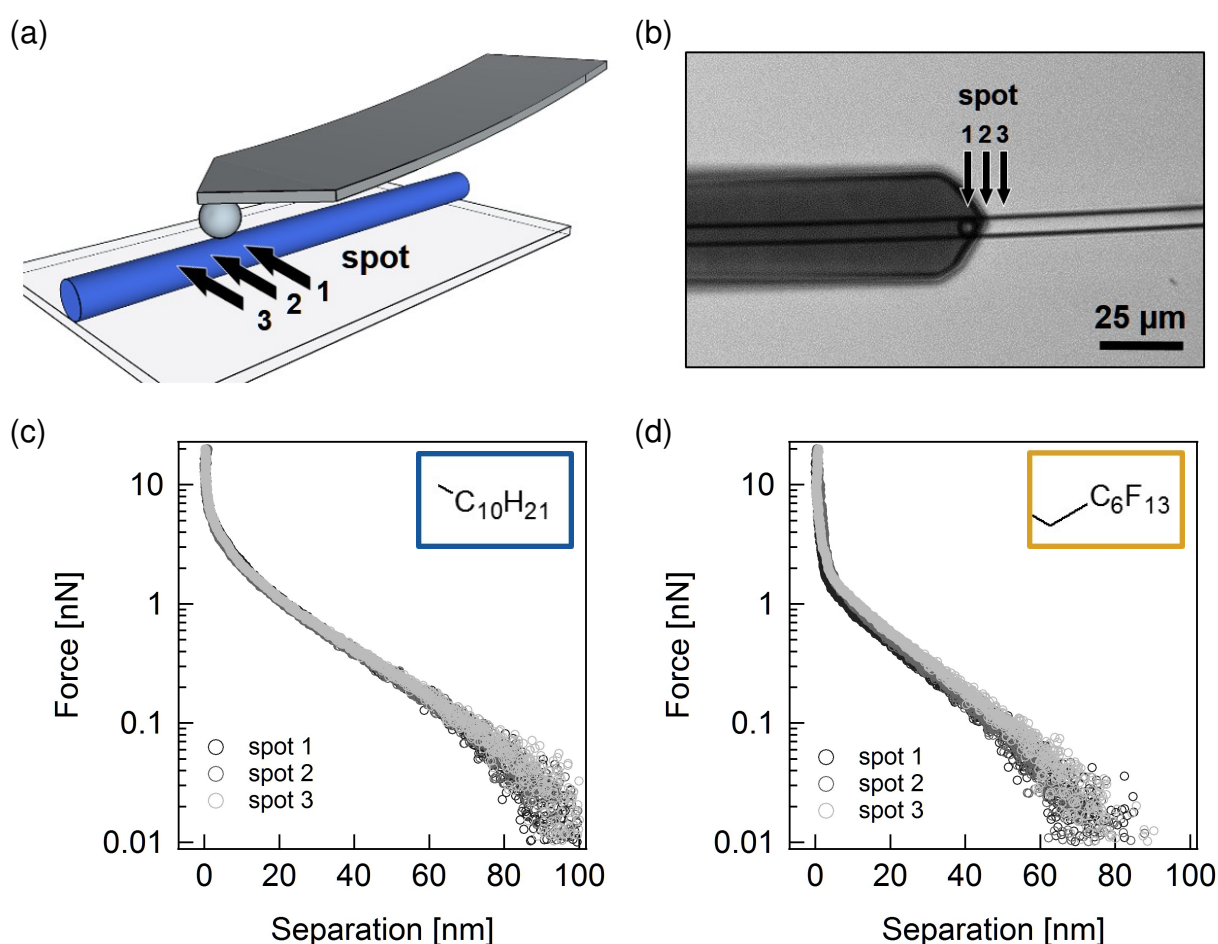


Figure 9.5: Schematic representation of the sphere-cylinder measurement configuration (a) and optical micrograph during the experiment (b). Representative approach F-D curves for the alkyl (c) and the fluorinated CTA (d) show purely repulsive forces irrespective of the fiber type and position on the fiber.

From symmetric F-D measurements, two positively or two negatively charged surfaces are

9 Interaction forces between fibers in crossed-cylinder geometry

indistinguishable as they would give the same repulsive W_{DL} . Due to the symmetric combination of fibers investigated here, the sign of the apparent diffuse layer potential $\Psi_{0,app}$ has to be verified in a separate set of measurements. Hence, we utilized the CP technique with a spherical silica particle that is well-known to be negatively charged in aqueous media [3] and [38]. A schematic representation of the measurement with the silica colloidal probe and a fiber segment is shown in Fig. 9.5 a. A corresponding optical micrograph is given in Fig. 9.5 b. In the fiber-fiber experiments described above, the interaction forces were normalized to the effective radius for two crossed cylinders, which is well known from the Derjaguin approximation. However, in the case of a sphere-cylinder geometry no analytical expression is available and interaction potentials would have to be calculated numerically [39, 40] and [41]. Therefore, the force profiles in Fig. 9.5 c and d are only given as force *versus* separation and not normalized with respect to the interaction geometry. Fig. 9.5 c and d show interaction force profiles at three consecutive spots ($2\ \mu\text{m}$ apart) for the silica colloidal probe measured against an alkyl-terminated and a fluorinated CTA fiber, respectively. We repeated these measurements in several regions along the bottom fibers. In every case, the resulting interaction forces are completely repulsive, which confirms that both fiber types are negatively charged. Several previous studies reported negative potentials for hydrophobic surfaces in aqueous solutions [42, 43] and [44]. We found the force profiles to be highly reproducible showing almost no deviations from spot to spot indicating an absence of charge heterogeneities on the scale of the resolution achievable by a μm -sized probe (Fig. 9.5 c and d).

Fig. 9.6 summarizes the results for $\Psi_{0,app}$ as obtained from fits to the full Poisson-Boltzmann equation. In this graph $\Psi_{0,app}$ is plotted against the ionic strength as determined from the same set of fits (derived from fitted κ^{-1} values). In order to account for the variations in the measurement, the following representation has been chosen: each lightly colored data point corresponds to the average from fitting of 30 F-D curves of a fiber CP-probe at three spots on a bottom fiber. The average of one top-bottom fiber combination is shown as the intermediate color shade. The overall average of all fiber-fiber pairs for one ionic strength is presented in the darkest shade. Fig. 9.6 a is based on measurements of 10 different alkyl fiber-fiber pairs (2 independent fiber probes *versus* 5 independent bottom fibers) and Fig. 9.6 b on the results of 8 different fluorinated fiber-fiber pairs (2 independent fiber probes *versus* 4 independent bottom fibers) at 4 different electrolyte concentrations (0.1, 0.5, 1 and 5 mM), respectively.

We found apparent diffuse layer potentials of the alkyl CTA in the range of -50 to -120 mV and for fluorinated CTA between -20 and -50 mV. Hence, the charge of fibers with alkyl periphery exceeds the one of the fluorinated CTA over the whole investigated range of ionic strengths. The decline of the absolute potential with increasing ionic strength is in accordance with the Gouy-Chapman theory. The Grahame equation relates the previously determined diffuse layer

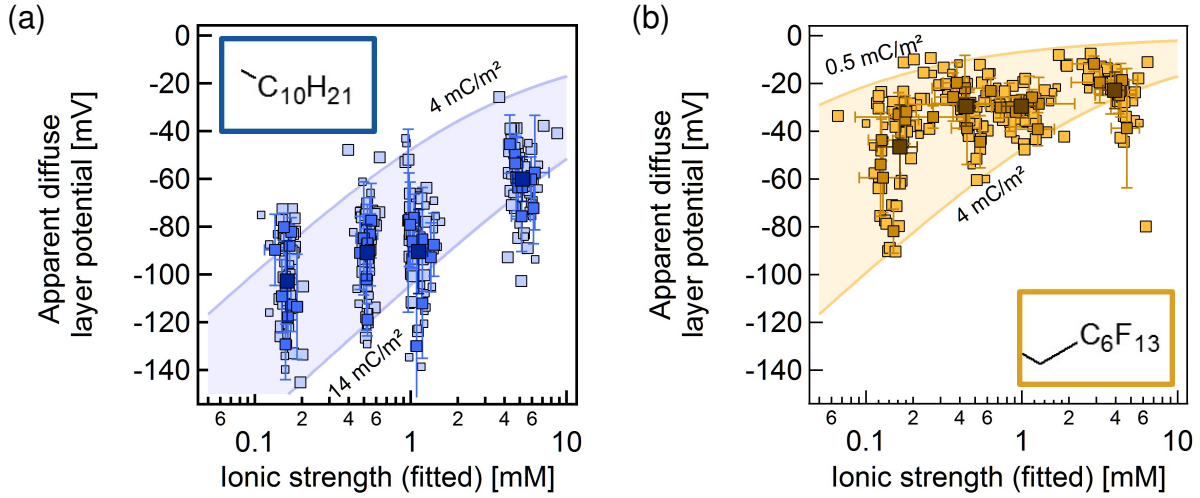


Figure 9.6: Fitted apparent diffuse layer potentials as a function of the fitted ionic strength for the alkyl (a) and the fluorinated CTA (b). The limits for the resulting surface charge density as calculated by the Grahame equation are indicated by the solid lines.

potential $\Psi_{0,app}$ and the surface charge density σ_{app} (Eq. (9.4)), where the index "app" indicates again that the resulting charge density is not necessarily the true surface charge density of the rough surface.

$$\sigma_{app} = \sqrt{8c_0\epsilon\epsilon_0RT} \sinh\left(\frac{ze\Psi_{0,app}}{2k_B T}\right) \quad (9.4)$$

where R denotes the universal gas constant and z is the charge number.

The solid lines in Fig. 9.6 indicate an approximate range for σ_{app} of the CTA fibers. We found σ_{app} roughly between 4 and 14 mC/m² for aliphatic and between 0.5 and 4 mC/m² for fluorinated fibers. It should be pointed out additionally that even at large ionic strength and thus small Debye lengths smaller values for the fluorinated fibers have been found. Under these conditions surface roughness should influence $\Psi_{0,app}$ and thus σ_{app} to a much smaller degree.

Electrospun fibers lose their residual charges from the electrospinning process upon immersion in electrolyte solutions. Hence, these residual charges are not responsible for the observed surface charge. As both CTA fiber types are lacking ionizable groups on their surface, the proposed mechanism for charge generation on these hydrophobic surfaces is the asymmetric adsorption of water ions. Especially hydroxide ions have been shown to adsorb preferentially onto hydrophobic surfaces [45]. Studies on undecanethiol self-assembled monolayers (SAMs) as well as Teflon AF thin films showed an isoelectric point at about pH 4 [42]. The pH range in

9 Interaction forces between fibers in crossed-cylinder geometry

our measurements is 5.5-5.8 and is thus compatible with a negative surface charge. For SAMs from undecanethiol zeta potentials between -30 and -50 mV have been reported [42]. Also for alkyl SAMs negative diffuse layer potentials have been found in this pH-range, albeit lower than the apparent ones determined here for the alkyl CTA fibers [43, 46]. The potentials for Teflon surfaces were generally lower and range from -20 to -30 mV (at 1 mM and pH 5) [42]. In another study based on direct force measurements between a silica colloidal probe (RMS roughness: 10-15 nm) against Teflon AF, diffuse layer potentials have been reported with $\Psi_0 = -50$ to -40 mV for 0.1 mM and around -15 mV for 1 mM of aqueous KCl solutions at approximately the same pH. These agree reasonably well with the apparent diffuse layer potentials obtained here [44].

A model by Lützenkirchen *et al.* based on sum frequency vibrational spectroscopy and molecular dynamics simulations reasonably reproduces the results of reference [47] and states that the surface charge density at the location of the first water layer for Teflon is 1.497 mC/m² [48]. This result is in very good agreement with the results for fibers from the fluorinated CTA reported here.

9.3 Conclusions

Direct force measurements between electrospun fibers from two different types of 1,3,5-cyclohexanetrissamides (CTA) allowed to determine the diffuse layer properties of these fibers in electrolyte solutions. We selected two CTAs featuring either alkyl or fluorinated substituents on their periphery. Despite the absence of ionizable groups we found a negative surface charge, which originates most likely from the hydrophobic character of both CTAs, leading to the adsorption of hydroxide ions in aqueous media. The direct force measurements reveal lower apparent surface charge densities for fibers from the fluorinated CTA (approx. 0.5 - 4 mC/m²) as compared to fibers from its aliphatic counterpart (approx. 4 - 14 mC/m²). A comparable difference has also been observed for fluorinated and alkyl SAMs in previous studies.

This study demonstrates that the adsorption of ions is also highly relevant for the effective surface charge of fibers. While this effect has been known and studied for flat surfaces (*e.g.* Refs. [42, 43, 46]) it has to the best of our knowledge not been studied so far for fibers. By measuring interaction forces between fibers in the crossed-cylinder geometry and symmetrical fiber combinations many uncertainties of streaming potential measurements, especially for fibrous systems can be avoided. As many fibrous materials are exposed to electrolyte solutions we believe that determining surface charge properties by direct force measurements of single fibers should be especially useful in understanding adsorption phenomena. This issue

might be for example of fundamental interest concerning the adsorption of water contaminants to microplastics on fibers. Direct force measurements between fibers might not only provide important insights in the underlying interaction forces for fiber systems, as it has been the case for colloidal interactions but provide also the basis for an optimization of fibers towards specific applications.

9.4 Materials and methods

9.4.1 Synthesis of 1,3,5-cyclohexanetricarboxamides

NMR data were recorded on a Bruker Avance 300 spectrometer at 300.1 MHz at room temperature. Mass spectrometry was conducted on a Finnigan MAT 8500 GC/MS. Thermogravimetric analysis was performed with a Mettler SDTA 851 TGA at 10 K min⁻¹. Phase-transition temperatures were determined using a Perkin-Elmer Diamond DSC with a heating rate of 10 K min⁻¹ under N₂. XRD measurements were carried out in the range $\theta = 0.5\text{-}15^\circ$ from room temperature to 250 °C on a Huber Guinier diffractometer 600 equipped with a Huber germanium monochromator 611 to get CuK α 1 radiation ($\lambda = 154.05$ pm).

The synthesis and characterization of N,N',N''-tris(decyl)-cis,cis-1,3,5-cyclohexanetri-carboxamide (alkyl CTA) is described in detail elsewhere [31].

N,N',N''-tris(tridecafluoroheptyl)-cis,cis-1,3,5-cyclohexanetricarboxamide was prepared in a two-step synthesis. In a first step, cis,cis-1,3,5-cyclohexanetricarboxylic acid chloride were obtained by adding 2.66 g of oxalyl chloride dropwise at 0 °C under nitrogen to a suspension consisting of 20 mL of anhydrous dichloromethane, 1 mL of dimethylformamide, and 0.73 g of cis,cis-1,3,5-cyclohexanetricarboxylic acid. The reaction mixture was stirred for 12 h at room temperature and 1 h at 50 °C. After cooling to room temperature the remaining oxalyl chloride and the solvents were evaporated. The obtained solid was used without further purification. In a second step, 3.9 g of tridecafluoro-heptane-1-amine was added at 0 °C under inert gas to a mixture consisting of 40 mL of anhydrous tetrahydrofuran (THF), 0.9 mL of pyridine, and 0.91 g of cyclohexane-1,3,5-tricarboxylic acid chloride. The reaction mixture was allowed to warm to room temperature and was subsequently stirred for 24 h at 60 °C. After cooling to room temperature the solution was precipitated in ice water. The precipitate was filtered off, dried under vacuum and purified by recrystallization several times from an isopropanol/THF mixture and THF, respectively. 2.6 g (66 %) of the fluorinated CTA was obtained as white solid. ¹H NMR (CF₃COOD/CDCl₃ 5:1): $\delta = 1.72\text{-}1.84$ (m, 3H), 2.23-2.27 (m, 3H), 2.63 (t, 3H), 4.04 (t, 6H)

9 Interaction forces between fibers in crossed-cylinder geometry

ppm. MS: 1209 (M+ 11); 1191 (45); 863 (55); 836 (100); 485 (38); 457 (70); 447 (19); 432 (34); 411 (12); 377 (12); 110 (30); 81 (39) m/z (%).

9.4.2 Melt-electrospinning

For electrospinning, a custom-made setup was used as described previously in detail [23] and [26]. The corresponding CTAs were placed into a glass syringe and heated at 300 °C for 3 min. After the annealing step, a voltage of $U = -30$ kV over the distance of 6 cm and a flow rate of 500 $\mu\text{L/h}$ was applied. The fibers were collected with an aluminum foil. SEM samples were carbon-coated utilizing a MED 010 coating machine from Baltzer. SEM imaging of freshly electrospun CTA fibers was performed with a Zeiss LEO 1530 FESEM instrument (Zeiss, Jena, Germany) at 3 kV.

9.4.3 Cantilever and substrate preparation

Using an AFM (MFP-3D, Asylum Research, Santa Barbara, California), uncoated and tipless cantilevers (CSC37, μmasch , Sofia, Bulgaria) were calibrated in air according to the thermal noise method [32]. Cantilevers with spring constants ranging from 0.262 to 0.317 N/m were treated with oxygen plasma and transferred to a micromanipulation setup (DC-3 KS, Märzhäuser, Wetzlar, Germany). A μm -sized droplet of a UV-curable glue (Norland Optical Adhesives No. 63, Norland Products, Cranbury, New Jersey) was placed at the free end of each cantilever using an etched tungsten wire and under optical control (Axio Examiner.D1, Zeiss, Jena, Germany). Due to the glue's limited spread (below 10% of the cantilever length) and its significantly smaller Young's modulus (<2 GPa) compared to the silicon cantilever material (169 GPa), we assumed the shift in the cantilever spring constant negligible. Employing a different tungsten wire, fragments of fractured melt-electrospun CTA fibers with diameters from 4.4 to 8 μm were positioned in the spreaded glue droplet. Thereby special care was taken to prevent any fiber rotation that could contaminate the fiber surface. The silica CP cantilever was prepared as reported previously [49]. The flawlessness of the preparation procedure was verified by SEM imaging (Zeiss LEO 1530 FESEM, Zeiss, Jena, Germany). Accordingly, we glued fibers of both CTAs to the surface of a glass disk that is forming the bottom of the fluid cell in the force measurements.

9.4.4 AFM imaging

The surface morphology of immobilized fiber segments was investigated by AFM imaging (Dimension Icon, Bruker, Billerica, Massachusetts) utilizing an OTESPA-R3 (Bruker, Billerica, Massachusetts).

9.4.5 Force measurements

For the measurements, we equipped the combined setup of the AFM (MFP-3D, Asylum Research, Santa Barbara, California) and an inverted optical microscope (Axio Observer Z1, Zeiss, Jena, Germany) with a fiber probe cantilever and optically aligned the fiber probe ("top fiber") and the fiber immobilized on the substrate ("bottom fiber") in crossed-cylinder geometry perpendicular to each other. All measurements were performed in solutions (0.1, 0.5, 1 and 5 mM) of NaCl (Bernd Kraft GmbH, Duisburg, Germany) in Milli-Q water of pH 5.5-5.8. For every symmetric combination of top and bottom fibers we recorded 30 force-distance (F-D) curves at 6 different spots along the long axis of the bottom fiber. In each F-D curve, the cantilever velocity was 500 nm/s and the force setpoints were between 10 and 25 nN. In this force regime, torsional cantilever movements upon fiber-fiber contact can be excluded. We interpreted the constant compliance regime as the fibers in contact defining the point of zero separation. In total, we analyzed the combinations of 2 top and 5 bottom fibers for the aliphatic compound (>7000 F-D curves) and 2 top and 4 bottom fibers for the fluorinated compound (>5000 F-D curves).

The data was evaluated using a custom-written program in FORTRAN and IGOR Pro (WaveMetrics, Inc., Lake Oswego, Oregon) [29]. Fitting each F-D curve to the DLVO-theory yielded the apparent surface potential and, additionally, the Debye length as internal reference.

9.5 Acknowledgment

This work received financial support from the German Research Foundation (Deutsche Forschungsgemeinschaft) within the SFB 840 (projects B8 and C4, respectively). BRN acknowledges the support of the Elite Network of Bavaria. The authors thank Carmen Kunert for her support with the SEM images and Dr. Klaus Kreger for his help with the manuscript.

9.6 Supporting Information

9.6.1 CTA Phase Behavior

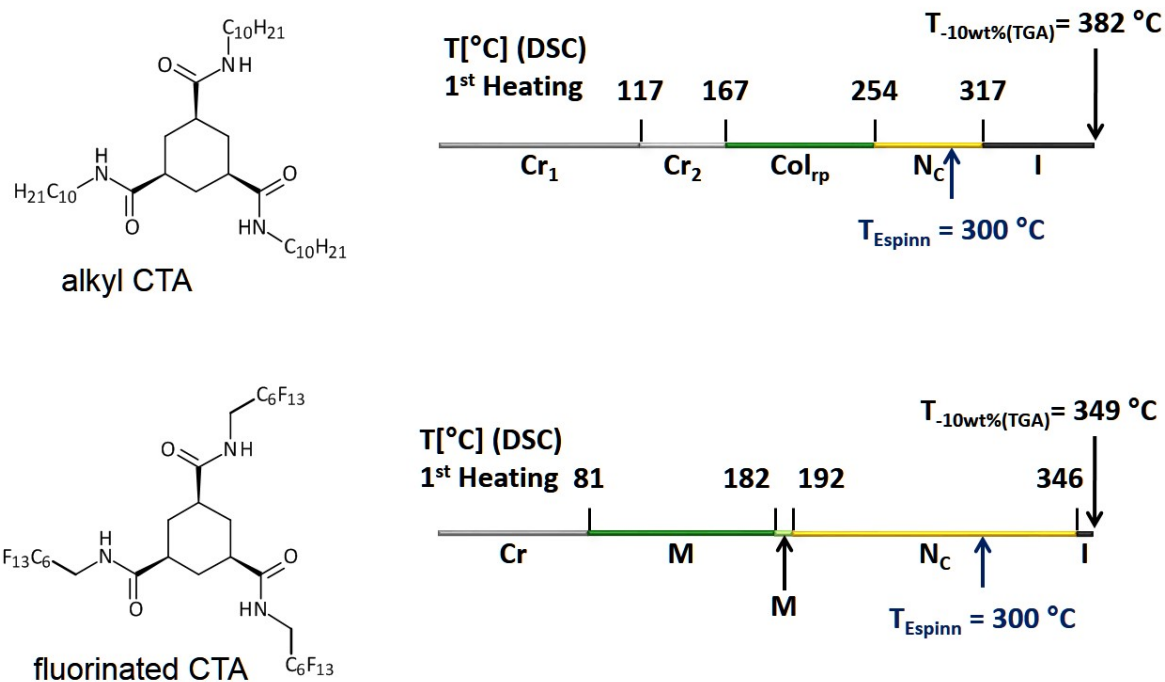


Figure 9.7: Schematic illustration of the phase behavior of the alkyl CTA and the fluorinated CTA as determined by differential scanning calorimetry (1st heating scan, 10 K/min, under N₂). A combination of DSC, X-ray powder diffraction and polarization microscopy were employed to assign the type of phase. The temperature at which a 10 wt% weight loss of the compounds were detected by means of thermogravimetric analysis and at which electrospinning was performed is indicated (Cr: crystalline, Col_{rp}: columnar rectangular plastic, N_c, columnar nematic, I: isotropic, M: unidentified mesophase, N: nematic).

9.6.2 Salt Concentration

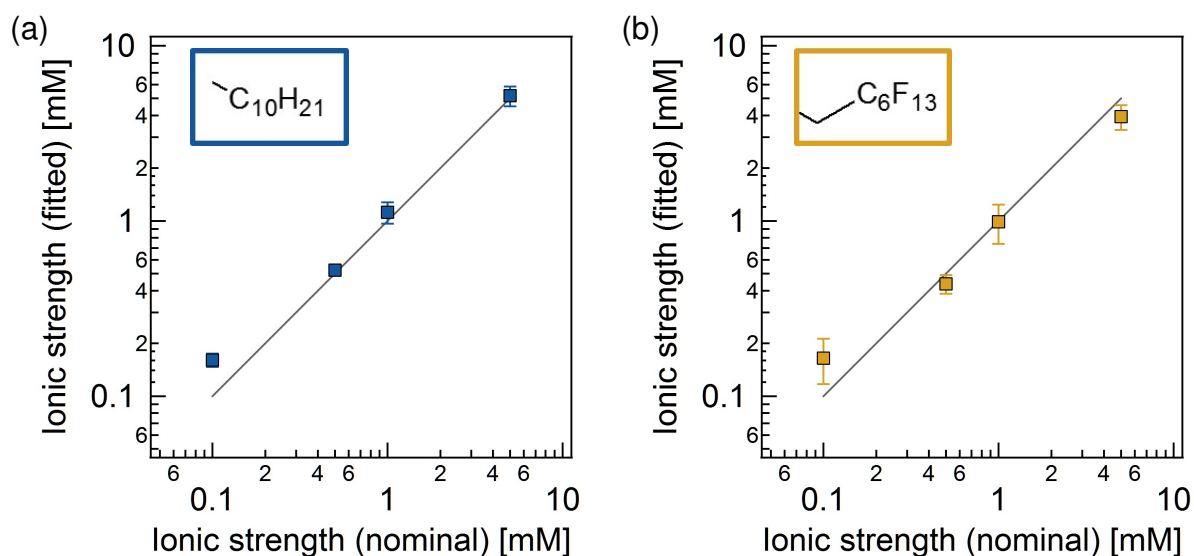


Figure 9.8: Fitted ionic strength as a function of the nominal ionic strength for the alkyl (a) and the fluorinated CTA (b). The gray line's slope is 1.

Figure 9.8 relates the nominal electrolyte concentrations to the ones derived from the Debye length as fitting parameter. The accordance is very good for both fiber types. The deviations at 0.1 mM ionic strength can be attributed to residual ions, *e.g.* from the dissolution of CO_2 . [37]

9.6.3 Determination of the *InvOLS*

We verified the absence of mechanical deformations in the applied force regime by the experiments depicted in Figure 9.9. Approaching a hard silica colloidal probe (SiCP) to the ("undeformable") glass substrate yields the pure cantilever deformation upon piezo extension in the constant compliance regime. From such an experiment, the *InvOLS* is typically derived. Repeating the same experiment on a fluorinated or aliphatic CTA fiber, respectively, yields identical values for the *InvOLS* within experimental errors. This consensus confirms the lack of mechanical deformation of the fibers in the applied force regime, *i.e.* in that range, the fibers can be assumed infinitely hard. Therefore, one can use the constant compliance regime in a fiber-fiber experiment to unambiguously deduce the *InvOLS*.

9 Interaction forces between fibers in crossed-cylinder geometry

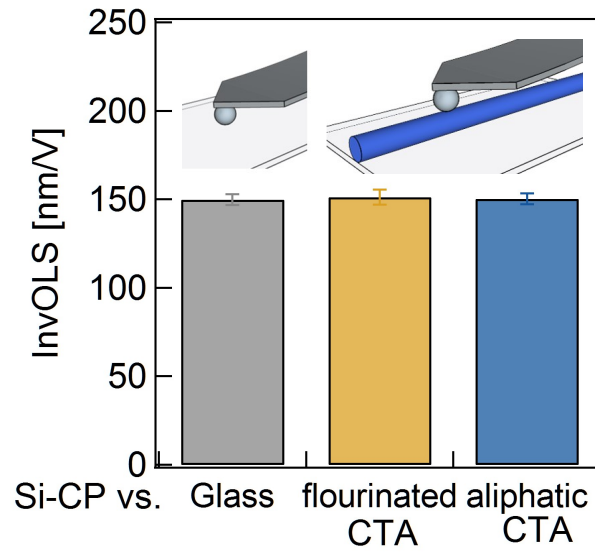


Figure 9.9: Inverse optical lever sensitivity (*InvOLS*) as determined for a cantilever decorated with a silica colloidal probe (SiCP) from three different approaches: SiCP vs glass substrate (gray), SiCP vs fluorinated CTA fiber (yellow) and SiCP vs aliphatic CTA fiber (blue). All three approaches give identical results for the *InvOLS* within experimental errors in the applied force regime.

9.6.4 Effective Spring Constant k_{eff}

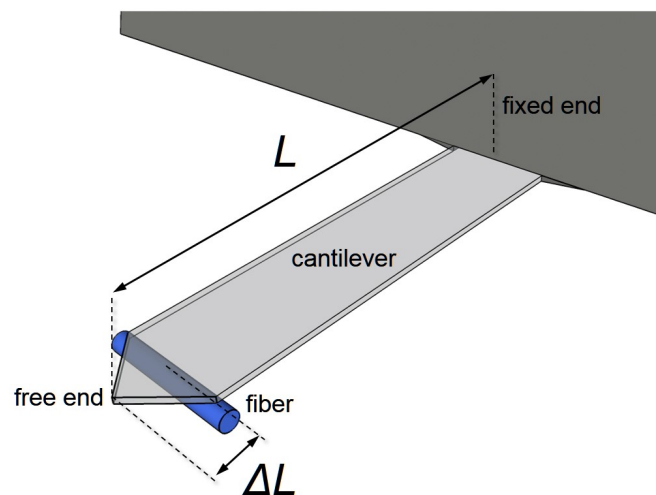


Figure 9.10: Scheme of a cantilever with a fiber attached. The total length L of the cantilever and the difference between the free end and the position where the fiber segment is situated ΔL illustrate Eq. 9.2 which is used to calculate the effective spring constant k_{eff} .

References

- [1] G. Binnig, C. F. Quate, and C. Gerber. Atomic force microscope. *Physical Review Letters*, 56(9):930–933, 1986.
- [2] H-J Butt, B Cappella, and M Kappl. Force measurements with the atomic force microscope: Technique, interpretation and applications. *Surface Science Reports*, 59(1-6):1–152, 2005.
- [3] W A Ducker, T J Senden, and R M Pashley. Measurement of Forces in Liquids Using a Force Microscope. *Langmuir*, 8(7):1831–1836, 1992.
- [4] J Erath, S Schmidt, and A Fery. Characterization of adhesion phenomena and contact of surfaces by soft colloidal probe AFM. *Soft Matter*, 6(7):1432–1437, 2010.
- [5] M P Neubauer, M Poehlmann, and A Fery. Microcapsule mechanics: from stability to function. *Advances in Colloid and Interface Science*, 207:65–80, 2014.
- [6] H J Butt, R Berger, E Bonaccorso, Y Chen, and J Wang. Impact of atomic force microscopy on interface and colloid science. *Advances in Colloid and Interface Science*, 133(2):91–104, 2007.
- [7] W A Ducker, T J Senden, and R M Pashley. Direct Measurement of Colloidal Forces Using an Atomic Force Microscope. *Nature*, 353(6341):239–241, 1991.
- [8] H J Butt. Measuring electrostatic, van der Waals, and hydration forces in electrolyte solutions with an atomic force microscope. *Biophysical Journal*, 60(6):1438–1444, 1991.
- [9] B Derjaguin. Untersuchung über die Reibung und Adhäsion IV. *Kolloid-Zeitschrift*, 69(2):155–164, 1934.
- [10] J N Israelachvili and G E Adams. Measurement of forces between two mica surfaces in aqueous electrolyte solutions in the range 0–100 nm. *Journal of the Chemical Society, Faraday Transactions 1: Physical Chemistry in Condensed Phases*, 74(0):975–1001, 1978.
- [11] J N Israelachvili. *Intermolecular and Surface Forces [Online]*. Elsevier, 3 edition, 2011.
- [12] L Meagher, G V Franks, M L Gee, and P J Scales. Interaction forces between α -alumina fibres in aqueous electrolyte measured with an atomic force microscope. *Colloids and Surfaces A: Physicochemical and Engineering Aspects*, 146(1–3):123 – 137, 1999.
- [13] I Muir, L Meagher, and M Gee. Interaction Forces between α -Alumina Fibers with Coadsorbed Polyelectrolyte and Surfactant. *Langmuir*, 17(16):4932–4939, 2001.

9 Interaction forces between fibers in crossed-cylinder geometry

- [14] E Max, W Häfner, F W Bartels, A Sugiharto, C Wood, and A Fery. A novel AFM based method for force measurements between individual hair strands. *Ultramicroscopy*, 110(4):320–324, 2010.
- [15] H Mizuno, G S Luengo, and M W Rutland. Interactions between crossed hair fibers at the nanoscale. *Langmuir*, 26(24):18909–18915, 2010.
- [16] H Mizuno, G S Luengo, and M W Rutland. New insight on the friction of natural fibers. Effect of sliding angle and anisotropic surface topography. *Langmuir*, 29(19):5857–5862, 2013.
- [17] H Mizuno, N Kjellin, T Pettersson, V Wallqvist, M Fielden, and M W Rutland. Friction measurement between polyester fibres using the fibre probe SPM. *Australian Journal of Chemistry*, 59(6):390–393, 2006.
- [18] F Huang, K Li, and A Kulachenko. Measurement of interfiber friction force for pulp fibers by atomic force microscopy. *Journal of Materials Science*, 44(14):3770–3776, 2009.
- [19] U Stachewicz, F Hang, and A H Barber. Adhesion Anisotropy between Contacting Electrospun Fibers. *Langmuir*, 30(23):6819–6825, 2014.
- [20] D Kluge, F Abraham, S Schmidt, H-W Schmidt, and A Fery. Nanomechanical Properties of Supramolecular Self-Assembled Whiskers Determined by AFM Force Mapping. *Langmuir*, 26(5):3020–3023, 2010.
- [21] D Kluge, J C Singer, J W Neubauer, F Abraham, H-W Schmidt, and A Fery. Influence of the Molecular Structure and Morphology of Self-Assembled 1,3,5-Benzenetrisamide Nanofibers on their Mechanical Properties. *Small*, 8(16):2563–2570, 2012.
- [22] H Misslitz, K Kreger, and H-W Schmidt. Supramolecular Nanofiber Webs in Nonwoven Scaffolds as Potential Filter Media. *Small*, 9(12):2053–2058, 2013.
- [23] J C Singer, R Giesa, and H-W Schmidt. Shaping self-assembling small molecules into fibres by melt electrospinning. *Soft Matter*, 8:9972–9976, 2012.
- [24] A Greiner and J H Wendorff. Electrospinning: A Fascinating Method for the Preparation of Ultrathin Fibers. *Angewandte Chemie International Edition*, 46(30):5670–5703, 2007.
- [25] S Agarwal, A Greiner, and J H Wendorff. Functional materials by electrospinning of polymers. *Progress in Polymer Science*, 38(6):963 – 991, 2013.
- [26] J C Singer, A Ringk, R Giesa, and H-W Schmidt. Melt electrospinning of small molecules. *Macromolecular Materials and Engineering*, 300(3):259–276, 2015.

References

- [27] D Kluge, J C Singer, B R Neugirg, J W Neubauer, H-W Schmidt, and A Fery. Top-down meets bottom-up: A comparison of the mechanical properties of melt electrospun and self-assembled 1,3,5-benzenetrisamide fibers. *Polymer*, 53(25):5754–5759, 2012.
- [28] J C Singer, R Giesa, and H-W Schmidt. Shaping self-assembling small molecules into fibres by melt electrospinning. *Soft Matter*, 8:9972–9976, 2012.
- [29] R Pericet-Camara, G Papastavrou, S H Behrens, and M Borkovec. Interaction between Charged Surfaces on the PoissonBoltzmann Level: The Constant Regulation Approximation. *The Journal of Physical Chemistry B*, 108(50):19467–19475, 2004.
- [30] I Tomatsu, C F C Fitie, D Byelov, W H de Jeu, P C M M Magusin, M Wubbenhorst, and R P Sijbesma. Thermotropic Phase Behavior of Trialkyl Cyclohexanetriamides. *The Journal of Physical Chemistry B*, 113(43):14158–14164, 2009.
- [31] A Timme, R Kress, R Q Albuquerque, and H-W Schmidt. Phase Behavior and Mesophase Structures of 1,3,5-Benzene- and 1,3,5-Cyclohexanetricarboxamides: Towards an Understanding of the Losing Order at the Transition into the Isotropic Phase. *Chemistry - A European Journal*, 18(27):8329–8339, 2012.
- [32] J L Hutter and J Bechhoefer. Calibration of atomic-force microscope tips. *Review of Scientific Instruments*, 64(7):1868–1873, 1993.
- [33] J E Sader, I Larson, P Mulvaney, and L R White. Method for the calibration of atomic force microscope cantilevers. *Review of Scientific Instruments*, 66(7):3789–3798, 1995.
- [34] D Barten, J M Kleijn, J Duval, J Lyklema, and M A Cohen Stuart. Double Layer of a Gold Electrode Probed by AFM Force Measurements. *Langmuir*, 19(4):1133–1139, 2003.
- [35] S Rentsch, R Pericet-Camara, G Papastavrou, and M Borkovec. Probing the validity of the Derjaguin approximation for heterogeneous colloidal particles. *Physical Chemistry Chemical Physics*, 8(21):2531–2538, 2006.
- [36] M Valtiner, X Banquy, K Kristiansen, G W Greene, and J N Israelachvili. The Electrochemical Surface Forces Apparatus: The Effect of Surface Roughness, Electrostatic Surface Potentials, and Anodic Oxide Growth on Interaction Forces, and Friction between Dissimilar Surfaces in Aqueous Solutions. *Langmuir*, 28(36):13080–13093, 2012.
- [37] L J Kirwan, P Maroni, S H Behrens, G Papastavrou, and M Borkovec. Interaction and Structure of Surfaces Coated by Poly(vinyl amines) of Different Line Charge Densities. *The Journal of Physical Chemistry B*, 112(46):14609–14619, 2008.

9 Interaction forces between fibers in crossed-cylinder geometry

- [38] V Kuznetsov and G Papastavrou. Ion Adsorption on Modified Electrodes as Determined by Direct Force Measurements under Potentiostatic Control. *The Journal of Physical Chemistry C*, 118(5):2673–2685, 2014.
- [39] Y Gu. The Electrical Double-Layer Interaction between a Spherical Particle and a Cylinder. *Journal of Colloid and Interface Science*, 231(1):199–203, 2000.
- [40] K Li and Y Chen. Evaluation of DLVO interactions between a sphere and a cylinder. *Colloids and Surfaces A: Physicochemical and Engineering Aspects*, 415:218–229, 2012.
- [41] S W Montgomery, M A Franchek, and V W Goldschmidt. Analytical Dispersion Force Calculations for Nontraditional Geometries. *Journal of Colloid and Interface Science*, 227(2):567–584, 2000.
- [42] R Zimmermann, U Freudenberg, R Schweiß, D Küttner, and C Werner. Hydroxide and hydronium ion adsorption — A survey. *Current Opinion in Colloid & Interface Science*, 15(3):196–202, 2010.
- [43] P Maroni, F J Montes Ruiz-Cabello, and A Tiraferri. Studying the role of surface chemistry on polyelectrolyte adsorption using gold–thiol self-assembled monolayer with optical reflectivity. *Soft Matter*, 10(46):9220–9225, 2014.
- [44] A Drechsler, N Petong, J Zhang, D Y Kwok, and K Grundke. Force measurements between Teflon AF and colloidal silica particles in electrolyte solutions. *Colloids and Surfaces A: Physicochemical and Engineering Aspects*, 250(1-3):357 – 366, 2004.
- [45] K N Kudin and R Car. Why are water - hydrophobic interfaces charged? *Journal of the American Chemical Society*, 130(12):3915–3919, 2008.
- [46] S Rentsch, H Siegenthaler, and G Papastavrou. Diffuse Layer Properties of Thiol-Modified Gold Electrodes Probed by Direct Force Measurements. *Langmuir*, 23(17):9083–9091, 2007.
- [47] R Zimmermann, S Dukhin, and C Werner. Electrokinetic Measurements Reveal Interfacial Charge at Polymer Films Caused by Simple Electrolyte Ions. *The Journal of Physical Chemistry B*, 105(36):8544–8549, 2001.
- [48] J Lützenkirchen, T Preočanin, and N Kallay. A macroscopic water structure based model for describing charging phenomena at inert hydrophobic surfaces in aqueous electrolyte solutions. *Physical Chemistry Chemical Physics*, 10(32):4946–4955, 2008.
- [49] N Helfricht, M Klug, A Mark, V Kuznetsov, C Blüm, T Scheibel, and G Papastavrou. Surface properties of spider silk particles in solution. *Biomaterials Science*, 1(11):1166–1171, 2013.

CHAPTER 10

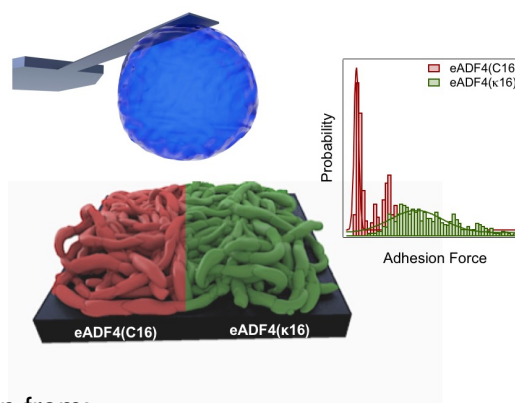
Probing the Adhesion Properties of Alginate Hydrogels: A New Approach towards the Preparation of Soft Colloidal Probes for Direct Force Measurements

Nicolas Helfricht^a, Elena Doblhofer^b, Vera Bieber^a, Petra Lommes^c, Volker Sieber^b, Thomas Scheibel^c, Georg Papastavrou^a

^a Physical Chemistry II, University of Bayreuth, Universitätsstr. 30, 95440 Bayreuth, Germany.
Email: Georg.Papastavrou@uni-bayreuth.de

^b Chemistry of Biogenic Resources, Technical University Munich, 94315 Staubing, Germany.

^c Biomaterials, Fakultät für Ingenieurwissenschaften, Universität Bayreuth, Universitätsstr. 30, 95440 Bayreuth, Germany.



Reprinted with permission from:

”Probing the adhesion properties of alginate hydrogels: a new approach towards the preparation of soft colloidal probes for direct force measurements”, N. Helfricht, E. Doblhofer, V. Bieber, P. Lommes, V. Sieber, T. Scheibel, G. Papastavrou, *Soft Matter*, **2017**, *13*, 578-589, DOI: 10.1039/C6SM02326F.

© 2017 Royal Society of Chemistry.

Abstract

The adhesion of alginate hydrogels to solid surfaces was probed by atomic force microscopy (AFM) in the sphere/plane geometry. For this purpose a novel approach has been developed for the immobilization of soft colloidal probes onto AFM-cantilevers, which is inspired by techniques originating from cell biology. The aspiration and consecutive manipulation of hydrogel beads by micropipettes allows the entire manipulation sequence to be carried-out *in situ*. Hence, any alteration of the hydrogel beads upon drying can be excluded. The adhesive behaviour of alginate hydrogels was first evaluated by determining the distribution of pull-off forces on self-assembled monolayers (SAMs) terminating in different functional groups (-CH₃, -OH, -NH₂, -COOH). It was demonstrated that solvent exclusion plays practically no role in the adhesion process, in clear difference to solid colloidal probes. The adhesion of alginate beads is dominated by chemical interactions rather than solvent exclusion, in particular in the case of amino-terminated SAMs. The data set acquired on the SAMs provided the framework to relate the adhesion of alginate beads on recombinant spider silk protein films to specific functional groups. The preparation of soft colloidal probes and the presented approach in analysing the adhesive behaviour is not limited to alginate hydrogel beads but can be generally applied for probing and understanding the adhesion behaviour of hydrogels on a wide range of substrates, which would be relevant for various applications such as biomedical surface modification or tissue engineering.

10.1 Introduction

Hydrogels comprise hydrophilic, network-like structures with high water content. [1, 2, 3] Their elastic modulus is in the kPa-range. [4] Hydrogels have many applications in materials science, biology, medicine and adjacent disciplines. In particular, hydrogels are often used as scaffolds for tissue engineering, [5, 6] drug delivery, [3, 5] wound dressings, [3, 7] or contact lenses. [8]

Hydrogels can be prepared from various substances, ranging from small gelator molecules [9] to large macromolecules, such as polysaccharides or synthetic polymers. [10, 11, 12]

Alginate hydrogels are based on an anionic polysaccharide, composed of building blocks bearing D-mannuronic and L-guluronic acid. [2, 5] It is naturally occurring in macroalgae. [13] Alginate hydrogels can be prepared either in the form of scaffolds [6] or beads. [14] The preparation of alginate beads in the upper μm -range is relatively straightforward: drops of an alginic acid sodium salt solution are dispensed into a buffer solution containing divalent cations such as Ca²⁺ or Ba²⁺. [15] The process parameters, such as stirring speed, salt concentration, or nozzle have a strong influence on the structure and polydispersity of the alginate beads.

[16, 17, 18, 19] Alginate hydrogels have been used as matrix for various composite materials. [6, 20] Moreover, these hydrogels have also been studied extensively in terms of their response to external stimuli (*e.g.* pH or ionic composition) and in respect to their mechanical properties. [2, 18]

When hydrogels are used as substitutes for tissue or for surface modification, their interaction with proteins and cells defines their function. [10] The adhesive properties of hydrogels represent a crucial parameter for their interaction with other materials, *e.g.* in composite materials. [21] Due to the highly hydrated state of hydrogels only a limited number of analytical techniques are available for determining their adhesive properties *in situ*. So far, AFM has been primarily used to characterize the mechanical properties of hydrogel materials on a microscopic level. [22] Despite the fact that the prevalent approach for determining the adhesion on the microscopic level is atomic force microscopy (AFM), [23, 24, 25, 26] only a limited number of direct force measurements by AFM are reported on the adhesive properties of hydrogels, [21, 27, 28] whereby a hydrogel bead is used as probe particle.

In order to obtain a defined interaction geometry for direct force measurements, a colloidal particle can be immobilized at the end of an AFM cantilever. This approach is known as colloidal probe technique. [29, 30] One advantage is the extensive choice of materials for the probes. Nonetheless, colloidal probes have been prepared since more than two decades mostly by 'hard' materials, such as silica or latex particles. [24] In contrast, 'soft' colloidal probes, *i.e.* colloidal probes prepared from highly deformable materials, are considerably less popular, and only few applications for such probes have been reported so far. [27, 31, 32, 33, 34] The preparation of soft colloidal probes has been reported initially for polyethylene (PE) and polydimethylsiloxane (PDMS). [27, 31, 32, 33, 34] Hydrogels and in particular alginate beads have been utilized only very sparsely for the preparation of soft colloidal probes. [21, 28, 35]

A critical step in the preparation of soft colloidal probes is their attachment to the AFM cantilever, in particular for hydrogel beads. The structure of hydrogels is susceptible to dehydration and irreversible conformational changes taking place upon drying. Hence, an *in situ* preparation of the corresponding probes is practically mandatory. Moreover, contamination of the interaction area of the hydrogel bead or by dissolution of the adhesive must be avoided. Here, we present a novel approach that is based on micromanipulation of single hydrogel particles by means of micropipettes allowing to overcome the above mentioned obstacles. Our approach is inspired by methods used in cell biology since many years [36, 37] but also applied in soft matter science, for example for the manipulation of giant vesicles. [38] Upon attaching hydrogel beads onto a chemically-modified AFM cantilever in liquid instead of gluing them, the cross-contamination with water-soluble low molecular weight compounds can be avoided completely.

10 Probing the Adhesion Properties of Alginate Hydrogels

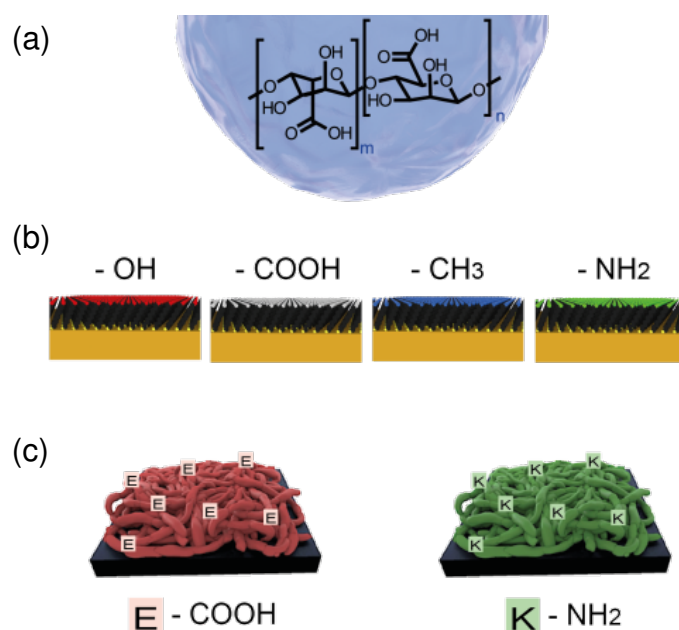


Figure 10.1: (a) Chemical structure of alginate, which is used to prepare the hydrogel beads. (b) Schematic representation of the self-assembled monolayers (SAMs) with different terminating functional groups (-OH, -COOH, -CH₃, -NH₂). (c) Schematic representation of the two drop-cast recombinant spider silk protein films, eADF4(C16) and eADF4(κ 16), respectively.

In order to reveal the adhesion mechanisms for alginate hydrogels on a molecular level, first adhesion measurements were performed on chemically well-defined self-assembled monolayers (SAMs) terminating in different functional groups (*cf.* Scheme 10.1). [39] The data set acquired on the SAMs provides the framework to relate the adhesion of alginate beads on unknown and more complex samples. Here, we concentrate on the interaction of alginate with films of different recombinant spider silk proteins, whereby the exchange of one amino acid leads to the inversion of the overall surface charge. [40, 41]

10.2 Experimental Section

Alginate hydrogel bead preparation

Low viscosity alginic acid sodium salt from brown algae (Sigma-Aldrich) was slowly dissolved in fully deionized water of Millipore-quality at a concentration of 1% (w/v). The solution was stirred for at least 24 h and afterwards vacuum filtrated through a cascade of eight filters with decreasing pore sizes. The first four filters were ranging from 25 μ m down to 2 μ m in pore size (MN 640 we: 12-25 μ m, MN 640 w: 7-12 μ m, MN 640 md: 4-7 μ m, and MN 640 d: 2-4 μ m, all

10.2 Experimental Section

purchased from Machery-Nagel GmbH & Co. KG (Düren, Germany)). The second set of filters was ranging from 1.2-0.2 μm and was made from cellulose nitrate (1.2 μm , 0.8 μm , 0.45 μm , and 0.2 μm , all purchased from Sartorius Stedim Biotech GmbH, Göttingen, Germany).

The precipitation solution of 1% (w/v) barium chloride dihydrate (Sigma Aldrich) in 10 mM MOPS (3-(N-morpholino)-propane sulfonic acid obtained from Carl Roth GmbH & Co. KG, Karlsruhe, Germany) was adjusted to pH 7.4 by addition of 1 M NaOH (Carl Roth GmbH & Co. KG, Karlsruhe, Germany). To this solution absolute ethanol (VWR) with a concentration of 5% v/v was added in order to reduce the surface tension.

For the preparation of the hydrogel beads, the filtrated alginate solution was filled into pre-pulled glass capillaries with an opening diameter of 30 μm (μ -Tip, World Precision Instruments Inc., Sarasota, FL). The filled micropipettes were placed 15 cm above the precipitation solution, which was constantly stirred during the preparation. By applying short pressure pulses (pneumatic pico-pump PV830, World Precision Instruments Inc., Sarasota, FL), drops were formed at the end of the micropipette, which precipitated in the barium chloride solution into hydrogel beads. The obtained suspension was stirred for additional 15 min after finishing the preparation. The size distribution of the alginate beads was highly polydisperse, ranging from 30 μm up to 1 mm. For the alginate beads immobilized on an AFM cantilever, the actual diameter was always determined by optical microscopy.

Preparation of flat gold substrates

Silicon wafers (CrysTec GmbH, Berlin, Germany) and glass slides were cleaned first by a modified RCA procedure, [42] which consists of the following steps: first, the substrates were sonicated in 2% (v/v) Hellmanex III-solution (Hellma, Müllheim, Germany) at 40 °C for 20 min and afterwards in a 3:1 isopropanol/water mixture (v/v) for additional 20 min. The substrates were then immersed in a mixture of Milli-Q water, hydrogen peroxide (30%, VWR), and ammonia (25%, VWR) (v/v/v = 5:1:1), which was heated to 80 °C for 15 min. After each cleaning step, the substrates were thoroughly rinsed with Milli-Q water. The substrates were stored in pure ethanol (VWR) for not longer than one week. Directly before usage, the substrates were again rinsed with pure ethanol and dried afterwards by a nitrogen stream.

Ultra-flat gold substrates were prepared by the template stripped method. [43, 44] RCA-cleaned silicon wafers (see above) were coated with a 150 nm thick gold layer by thermal evaporation (Minicoater, tectra, Germany). Afterwards, RCA-cleaned glass pieces (1 x 1 cm, 1 mm thickness) were glued onto the gold-coated side of the silicon wafer with an epoxy adhesive (Epo-Tek 377, Epoxy Technology, Inc., Billerica). The adhesive was cured for 1 h at 150 °C. The ultra-flat

10 Probing the Adhesion Properties of Alginate Hydrogels

gold surfaces were modified by a self-assembled monolayer (SAM). Directly before thiol adsorption the glass slides were freshly cleaved from the silicon wafer and directly immersed in a 1 mM ethanolic solution of alkane thiols for at least 12 h. The following thiols were used for the preparation of SAMs: 16-mercaptohexadecan-1-ol (Frontier Scientific), 16-mercaptohexadecanoic acid (Frontier Scientific), hexadecanethiol (Aldrich), and 11-amino-1-undecanethiol (Aldrich). The samples were removed directly before use from their respective solutions and were rinsed thoroughly with ethanol, Milli-Q water and finally with the electrolyte solution before mounting in the sample holder.

Preparation of protein films

Recombinant spider silk proteins eADF4(C16) and eADF4(κ 16) were produced and purified as described previously. [40] Both proteins were separately dissolved in formic acid at a concentration of 20 mg mL⁻¹. Finally, these protein solutions were drop casted onto RCA-cleaned glass slides (see Preparation of ultraflat gold substrates). The volume for the drop casting was chosen to obtain a protein surface concentration of about 1 μ g cm⁻².

Contact angle measurements

Static contact angles were measured by placing a drop of fresh Milli-Q water (about 25 μ L) on the samples, and the measurements were carried out with a commercial setup (OCA-15 from Data Physics, Filderstadt, Germany). An image of the static drop was acquired with a CCD-camera after 5 s. The contact angle was obtained by evaluation of the drop profiles with the accompanying image analysis software (SCA-20, DataPhysics, Filderstadt, Germany). At least 3 drops were measured on different positions for each substrate. The average and standard deviation over several substrates is reported (*cf.* Table 10.1).

In situ preparation of alginate hydrogel colloidal probes

Tipless silicon AFM cantilevers (NSC 12 and CSC 37, no-AI, μ -Masch, Bulgaria) were rinsed with Milli-Q water and absolute ethanol before O₂-plasma treatment at 0.2 mbar for 5 min (Mini-Flecto, Plasma Technology, Herrenberg, Germany). Directly after plasma treatment the cantilever surfaces were rendered adhesive by adsorption of a cationic polyelectrolyte layer of hyper-branched poly(ethyleneimine) (PEI). The adsorption was performed by immersion of the cantilever in a 1 g L⁻¹ solution of PEI (avg. M_w 25000 Da, Aldrich) for 15 min and successive rinsing with Milli-Q water. It is important that the preparation of the alginate hydrogel beads (as previously described) and the modification of cantilever were performed directly before the fixation of the alginate beads to the AFM cantilever.

Table 10.1: Compilation of data on surface properties of alginate beads, self-assembled monolayers, and recombinant spider silk protein films.

Surface	Functional group	$\gamma_{sur,face/H_2O}$, [mN/m]	pK_i	Contact angle (exp.) [°]	Contact angle (Lit.) [°]	F_{adh}/R_i , [$\mu\text{N/m}$]
Alginate	- OH	70.0 ^a	-	-	-	-
	- COOH	-	5.4 ^c	-	-	-
SAM	- OH	1.6 ^b	-	24 ± 4	< 10 ^g	25
	- COOH	6.0 ^b	5.5 ^d	15 ± 6	28 ± 10 ^g	37
	- CH ₃	46.0 ^b	-	107 ± 3	109 ± 2 ^g	56
	- NH ₂	< 1	-	28 ± 7	42 ± 2 ^g	339
eADF4(C16)	- COOH	1.6 ^b	-	64 ± 7	-	6
eADF4(κ :16)	- NH ₂	1.6 ^b	-	72 ± 7	-	37

^a see Chan *et al.* [45]; ^b see Warszynski *et al.* [46], ^c see Draget *et al.* [47], ^d see Noy *et al.* [48], ^e see Glinski *et al.* [49], ^f see Zhang *et al.* [50], ^g see Maroni *et al.* [51], ^b as calculated by ProtParam by Helfricht *et al.* [41]

10 Probing the Adhesion Properties of Alginate Hydrogels

The immobilization of the alginate beads to the modified cantilevers was performed on a fixed-stage microscope (Examiner.D1, Carl Zeiss Microscopy GmbH, Jena, Germany) equipped with a motorized micromanipulator (DC-3KS, Märzhäuser, Wetzlar GmbH Co. KG, Wetzlar, Germany). A capillary holder (World Precision Instruments Inc., Sarasota, FL) was attached to the micromanipulator and the micropipettes were connected to a manual micro-injector (CellTram vario, Eppendorf AG, Hamburg, Germany). As micropipettes, borosilicate glass capillaries with an opening diameter of 10 or 30 μm (μ -Tip, World Precision Instruments Inc., Sarasota, FL) were used. This *in situ* preparation of alginate soft colloidal probes allowed to select alginate beads with suitable diameter and perfect spherical geometry. Further details concerning the micromanipulation setup, including a movie illustrating the preparation sequence, are given in the ESI, Sections 10.6.1 and 10.6.2.

Scanning electron microscopy

In situ prepared alginate hydrogel colloidal probes were prepared as described above and were dried for several days. The colloidal probes were sputtered with a thin layer of platinum (1.1-1.3 nm, Sputter coater 208 HR, Cressington). Afterwards, SEM-measurements (Leo 1530 VP Gemini, Carl Zeiss) were performed at an accelerating voltage of 3.0 kV.

Indentation measurements

Direct force measurements were performed using a MFP-3D (Asylum Research, Santa Barbara) mounted on an inverted optical microscope (Axio Observer.Z1, Carl Zeiss, Göttingen, Germany).

The mechanical properties of alginate hydrogel beads were determined by a series of indentation measurements with non-deformable colloidal probes prepared from silica particles with a nominal diameter of 6.8 μm (Bangs Laboratories Inc., Fishers, IN, USA). These silica colloidal probes were attached to tipless silicon AFM cantilevers (NSC 12, μ -Masch, Bulgaria) by means of a sintering process. The preparation protocol has been described in detail elsewhere. [52] Indentation measurements were performed at the same conditions as the adhesion measurements using alginate probes (*i.e.* 1 mM KCl and pH 5.5). In order to immobilize the alginate beads onto flat substrates for these indentation measurements, a suspension of alginate beads was transferred into a surface-modified Petri dish (PEI-modification, see below) containing the electrolyte solution, allowing the particles to sediment onto the surface. Afterwards the solution was exchanged twice with the measurement solution. The surface of the Petri dishes was coated previously with a 1 g L⁻¹ solution of PEI, as for the modification of the AFM cantilever surfaces.

The inverse optical lever sensitivity (*InvOLS*) for the indentation measurements was determined by evaluation of the slope in the constant compliance region of the acquired force vs. distance curves, which were obtained by ramping against the bottom of the glass Petri dish. The raw data was converted into force vs. indentation curves and evaluated within the framework of the Hertz theory using the software provided with the AFM (Asylum Research, Santa Barbara). Hertzian contact mechanics is summarized by eqn 10.1 - 10.3 and describes the indentation of alginate beads by a spherical indenter (*i.e.* silica particle). The externally applied loading force F_L leads to an indentation depth δ . For the Hertzian contact mechanics in sphere-sphere geometry one expects an exponent of $n \approx 3/2$. E_C is the total elastic modulus of the system comprising alginate bead and silica probe (*cf.* eqn 10.2), with elastic moduli E_{bead} and Poisson ratio ν_{bead} (alginate bead) and E_{SiOx} , ν_{SiOx} (colloidal probe), respectively. [53, 54]

$$F_L = \frac{4}{3} E_C R^{1/2} \delta^n \quad (10.1)$$

$$E_{bead} = \left(-\frac{1 - \nu_{SiOx}^2}{E_{SiOx}} + \frac{1}{E_C} \right)^{-1} (1 - \nu_{bead}^2) \quad (10.2)$$

$$\frac{1}{R_{eff}} = \frac{1}{R_{SiOx}} + \frac{1}{R_{bead}} \quad (10.3)$$

The effective radius R_{eff} is defined by eqn (3) where R_{SiOx} and R_{bead} are the radii of the silica colloidal probe and the immobilized alginate bead, respectively.

10.2.1 Direct force measurements using soft colloidal probes

All direct force measurements using soft colloidal probes were conducted on the same AFM-setup as used for the indentation experiments. The measurements were performed with alginate colloidal probes against thiol-modified gold-coated glass slides and drop casted protein films on solid substrates. If not otherwise stated, the aqueous phase was pH 5.5 and 1 mM KCl. The spring constants of unmodified cantilevers were determined by the thermal noise method in air. [55] Moreover, these spring constants were verified by the so-called 'Sader-method'. [56] Cantilevers were excluded when a discrepancy of more than 15% between both methods was exceeded. The spring constants were always determined for the bare cantilevers before the chemical modification and attachment of alginate beads. All direct force measurements were performed at ramping velocities smaller than $0.8 \mu\text{m s}^{-1}$ in order to avoid significant hydrodynamic drag on the lever and the attached alginate bead. The raw data were evaluated by a set of custom-written routines under IGOR PRO (Wavemetrics) implementing standard procedures for the conversion of force *versus* displacement curves to force *versus* distance curves [23, 57] as well as averaging routines. [44] The contact point between alginate probe and sample sur-

10 Probing the Adhesion Properties of Alginate Hydrogels

face has been determined as the intersection point between the non-contact baseline and the last part of the contact line, where a nearly linear force response is found. [23, 57] This procedure has been already applied for measurements on soft polymeric materials or biological cells. [58]

However, the here-presented alginate colloidal probes required some additional steps for the data evaluation, as the hydrogel probe beads had a low elastic modulus and their diameter significantly exceeds the top-view width of the cantilever. The first point required some further steps in determining the *InvOLS*. The second point had to be taken into account when analyzing the force profiles, as the apparent spring constant of the AFM cantilever will be altered due to the lever laws from mechanics and the reduced length of the lever (*cf.* ESI 10.6.3).

Soft alginate probe particles are easily compressed even under slight loading forces. Therefore, an independent determination of the *InvOLS* was required. The standard approach was not possible due to the deformation of the beads upon external load forces. Hence, determining the *InvOLS* from the slope of the contact regime in the photodiode voltage vs. displacement curves is not possible for such soft colloidal probes. [23] A common alternative is the acquisition of force *versus* displacement curves on the edge of a step structure, instead of a flat surface. [31] However, due to the large dimensions of the alginate beads, this procedure could not be applied here. Instead, the *InvOLS* has been determined in an indirect manner on base of the power spectral density (PSD) of the cantilever's thermal noise. The PSD was recorded directly before the force measurement by acquiring the thermal noise of each alginate probe in the electrolyte solution. As the spring constant k_c of the cantilever is independent from the medium in which the cantilever vibrates, we used the following relation from the equipartition theorem to determine the *InvOLS*: [55, 59]

$$\frac{1}{2}k_B T = \frac{1}{2}k_c c_{corr} (\text{InvOLS})^2 \langle \Delta z^2 \rangle \quad (10.4)$$

here, k_B is the Boltzmann constant, T the temperature, and $\langle \Delta z^2 \rangle$ is the area under the power spectral density of the first vibrational mode. The correction factor c_{corr} results from the finite spot size and the restriction to the first vibrational mode. [60] The cantilever's spring constant k_C was determined in air for each cantilever before attaching the alginate beads. Hence, the only free parameter in eqn 10.4 is the *InvOLS*, which can be determined thereby.

The used alginate beads had diameters in the range of 60-140 μm . The effective length of the lever arm is reduced since the alginate beads could not be attached to the very end of the cantilever of length L_c , but instead at L_{bead} with $L_c > L_{bead}$. In consequence the apparent spring

constant k_{app} is given for an alginate probe by

$$k_{app} = \left(\frac{L_c}{L_{bead}} \right)^3 k_c \quad (10.5)$$

as reported by Buzio *et al.* and Sader *et al.* for colloidal probes with large probe particles. [31, 56]

10.3 Results and discussion

The soft colloidal probes used in this study were prepared *in situ* from alginate hydrogel beads using a novel micropipette-based technique. Alginate beads have a significantly lower elastic modulus than most materials previously used as soft colloidal probes, such as polydimethylsiloxane (PDMS). [27, 31, 32] The elastic modulus of the here-prepared alginate beads has been obtained from an independent set of experiments in which the immobilized beads have been indented by silica colloidal probes. In order to provide a quantitative analysis of the adhesion behaviour of alginate hydrogels, the adhesion was determined on well-defined model surfaces, namely thiol-based self-assembled monolayers (SAMs) and on films from recombinant spider silk proteins.

10.3.1 *In situ* preparation of alginate colloidal probes

The entire preparation process of the soft colloidal probes has been carried out in aqueous environment and can either be conducted in a simple Petri dish or in a closed AFM fluid cell (further experimental details are given in the ESI, Section 10.6.2). First, the AFM cantilevers have been modified by adsorption of a monolayer of polyethyleneimine (PEI). PEI is known to be an excellent adhesion promoter and is used for example as precursor film for preparing polyelectrolyte multilayer films. [61, 62] The chemical modification of the AFM cantilevers allows the omission of commercial adhesives that might leak low-molecular weight compounds into the aqueous solution while curing.

Fig. 10.2 summarizes the different steps for the *in situ* preparation of soft colloidal probes from alginate hydrogel beads. First, the chemically modified cantilever is placed in the preparation vessel mounted on an upright, fixed-stage optical microscope. Then, a small amount of alginate hydrogel particles is deposited on the bottom of the vessel (*cf.* Fig. 10.2 a). The alginate beads prepared in this study have a rather broad size distribution due to the preparation procedure with diameters ranging from 30 μm to 1 mm. However, perfectly spherical particles with suitable diameters can be easily selected under the optical microscope. Alginate beads with a diameter

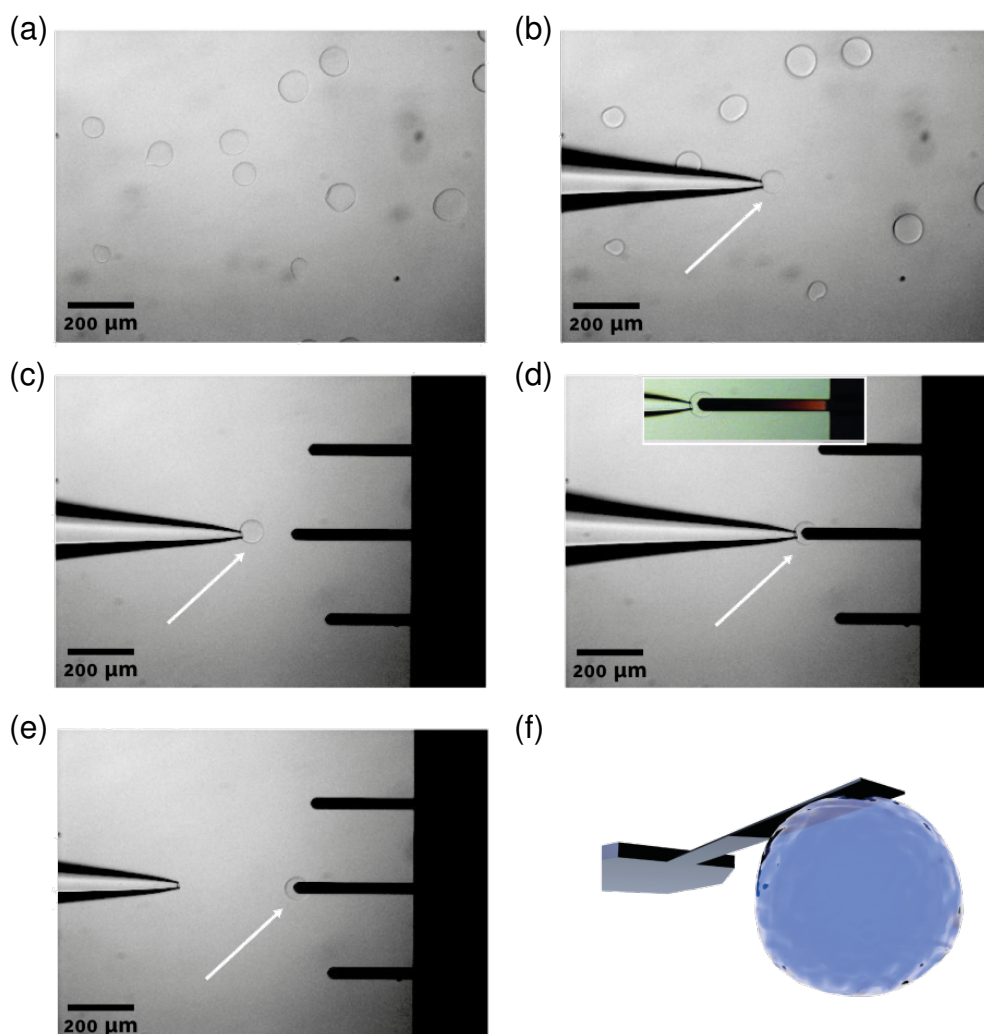


Figure 10.2: Optical micrographs, representing the sequence of the *in situ* preparation of alginate hydrogel colloidal probes. All steps are performed in aqueous environment. The position of the bead is indicated by the arrow. (a) The suspension with the alginate beads is injected in a Petri-dish. (b) An alginate bead is aspirated by a glass micropipette by means of a small underpressure. (c) The bead is in the following transferred to a chemically modified AFM cantilever without tip. (d) The hydrogel bead is approached and pressed against the cantilever until a deflection of the lever is visible (*cf.* inset). (e) Finally, the micropipette is lifted up, and the particle is released by a short overpressure pulse. (f) Schematic representation of a hydrogel colloidal probe.

10.3 Results and discussion

of 60-140 μm were used for the preparation of the colloidal probes. These were picked up by approaching a micropipette with an opening diameter of about 10-30 μm near to a desired bead (*cf.* Fig. 10.2 b) and applying a small suction pressure p_s . An estimated suction pressure of about $p_s \approx -50$ mbar was sufficient for the aspiration of a single particle. The aspirated alginate bead was then transferred to the end of a tipless AFM cantilever previously coated with PEI (*cf.* Fig. 10.2 c). By vertically pressing the aspirated hydrogel bead onto the modified cantilever the bead was immobilized on its surface. The force applied by the micromanipulator is limited due to the resulting cantilever deflection (*cf.* inset in Fig. 10.2 d). This force was kept for several seconds to ensure the formation of the contact area. Finally, the micromanipulator was lifted up, and a small overpressure $p_o \approx +20-50$ mbar was applied to release the bead from the micropipette. A video of a complete preparation procedure is provided in the ESI, Section 10.6.1. In Fig. 10.2 f a schematic representation is given of the used alginate probes. The outlined sequence of manipulation steps resembles the 'classical' preparation of colloidal probes in air, where an etched tungsten wire is used instead of a micropipette. [52] In difference, to other approaches for the preparation of soft colloidal probes in the aqueous phase [28] the future contact area of the soft colloidal particle remains unaffected by the preparation and potential contaminations can be excluded.

10.3.2 Effect of drying on alginate colloidal probes

The structure of alginate hydrogels is highly susceptible to air drying as the contact zones formed during drying remain stable in water and counteract swelling. [63] Upon drying so-called "egg-box" multimer structures are formed that can only be broken under certain conditions. [63] Hence, subsequent re-hydration of previously dried or partially dried alginate colloidal probes did not lead to a recovery of the original mechanical properties. Fig. 10.3 a shows an image of an alginate probe prepared *in situ* (*cf.* procedure in Fig. 10.1) and in the fully hydrated state. Fig. 10.3 b shows the same alginate probe after drying followed by immediate re-hydration. The spherical shape was not conserved, and the contact area between alginate bead and cantilever restricts the overall shape of the re-hydrated bead.

The structural changes in the hydrogel resulting from drying could be also demonstrated by direct force measurements. Fig. 10.3 c and d show the interaction force profiles before and after drying/re-hydration of the alginate probe shown in Fig. 10.3 a and b, respectively. The force profiles were obtained by averaging about 100 single force profiles acquired at pH 5.5 and an ionic strength $I = 1$ mM. The measurements were performed in the sphere/plane geometry between the alginate probe and a bare glass surface. Upon approach (*cf.* red data) of the alginate probe, considerable repulsive forces were observed. For the native alginate bead, *i.e.* without

10 Probing the Adhesion Properties of Alginate Hydrogels

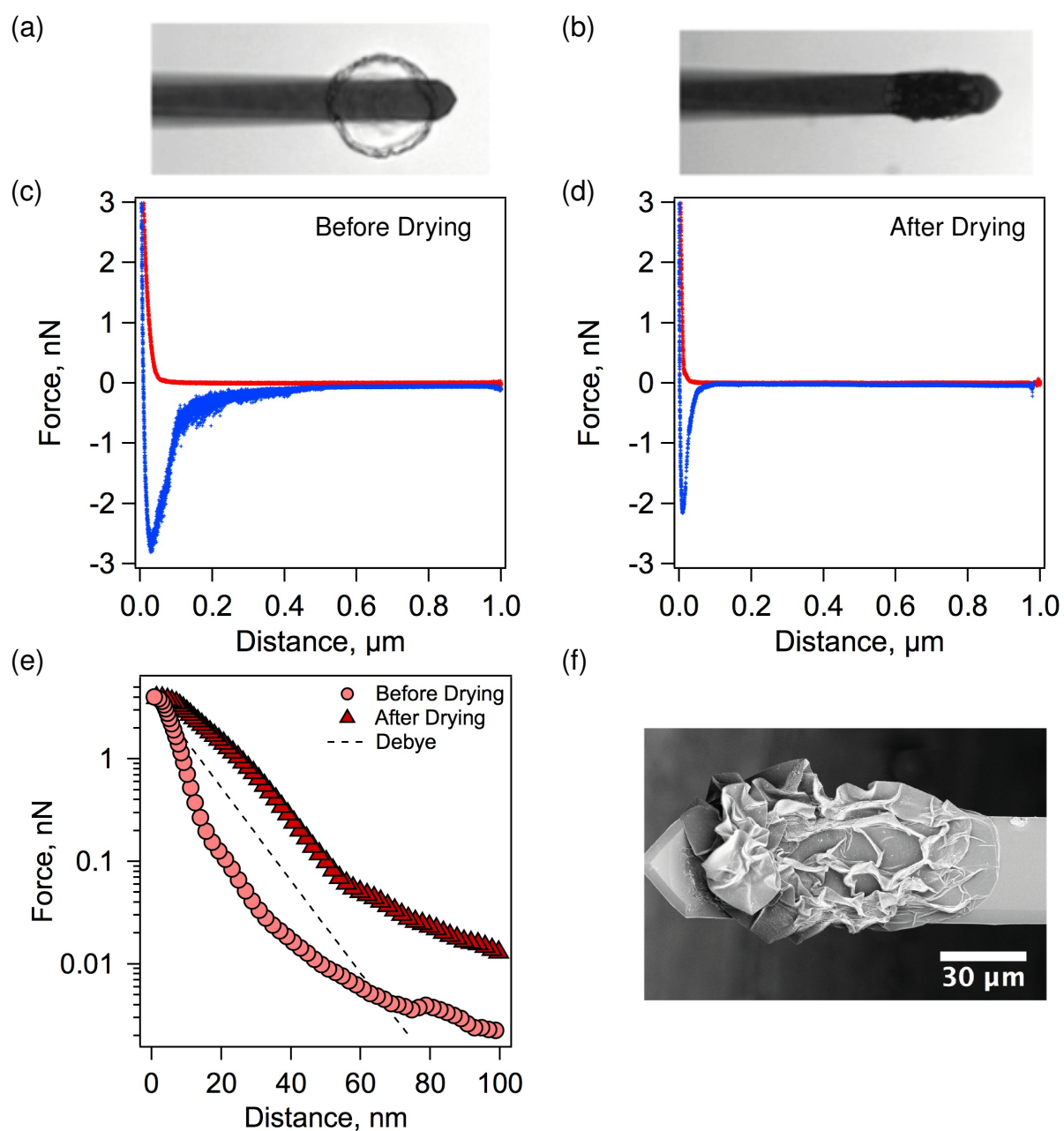


Figure 10.3: (a and b) *In situ* prepared alginate probe in aqueous solution before and after drying. (c) Force versus distance curves obtained by averaging about 100 single curves acquired with an *in situ* prepared alginate probe vs. clean glass slide. (d) Force vs. distance curves obtained under the same conditions but after drying/re-hydration. (e) Interaction forces in semi-logarithmic representation before (triangles) and after drying (circles). The dashed line indicates the theoretical Debye length for a pure diffuse layer overlap. (f) SEM image of a dried alginate probe.

any drying step, the repulsion started at larger separation distances of about 50 nm, compared to 20-25 nm for dried/re-hydrated probe. The approach curves are also compiled in the semi-logarithmic plot in Fig. 10.3 e. The dashed line in Fig. 10.3 e indicates the decay expected on base of the theoretical Debye-length for an ionic strength of 1 mM. The incompatibility of the data with pure diffuse layer repulsion is attributed to steric forces, reported previously for comparable systems. [41] Moreover, the linear slope changed in the contact regime of alginate bead and glass substrates before and after drying. This region of the force distance curve is indicative for the bulk elastic properties of the material. Differences in the contact region's slope indicated different effective spring constants and different elastic moduli for the bead. The reduced steric forces and the higher elastic modulus are indicative for a more 'compact' alginate bead after the drying/re-hydration step.

The adhesion forces between the alginate probe and the glass surface changed as well (*cf.* blue part of the interaction force profile in Fig. 10.3 c and d). Alginate beads in their native state, *i.e.* beads that have never been dried, detached from the glass surface in two steps: firstly, a jump-out of contact with a corresponding force of approximately 3 nN has been observed. Secondly, at larger separation distances various segments of the alginate particle were stretched and successively detached from the glass surface. The latter process is comparable to the removal of bacteria from solid substrates. [64, 65] Both processes lead to the total work of adhesion, which can be obtained in an approximate manner integrating the retraction part of the force curve.

The work of adhesion is practically completely dominated from the first jump-out of contact for the beads that have been dried and re-hydrated before the measurements (*cf.* Fig. 10.3 d, blue data). "Egg-box" multimer structures are in-line with the collapsed state of the alginate bead observed from the data upon approach, since a more compact bead will have a more defined contact area with less binding of hydrogel segments outside this area.

10.3.3 Elastic properties of alginate beads

In order to determine the 'softness' of the alginate beads, indentation experiments were carried out (*cf.* Fig. 10.4) The mechanical properties of alginate hydrogels, either in the form of films or beads, have been studied extensively. Elastic moduli reported fall in the range of 2-550 kPa, depending on the preparation conditions. [66, 67, 47] This large scattering of values suggests a profound influence of the molecular composition of the alginate as well as the preparation conditions. [68]

Here, the elastic moduli of the alginate beads were determined by AFM indentation measure-

10 Probing the Adhesion Properties of Alginate Hydrogels

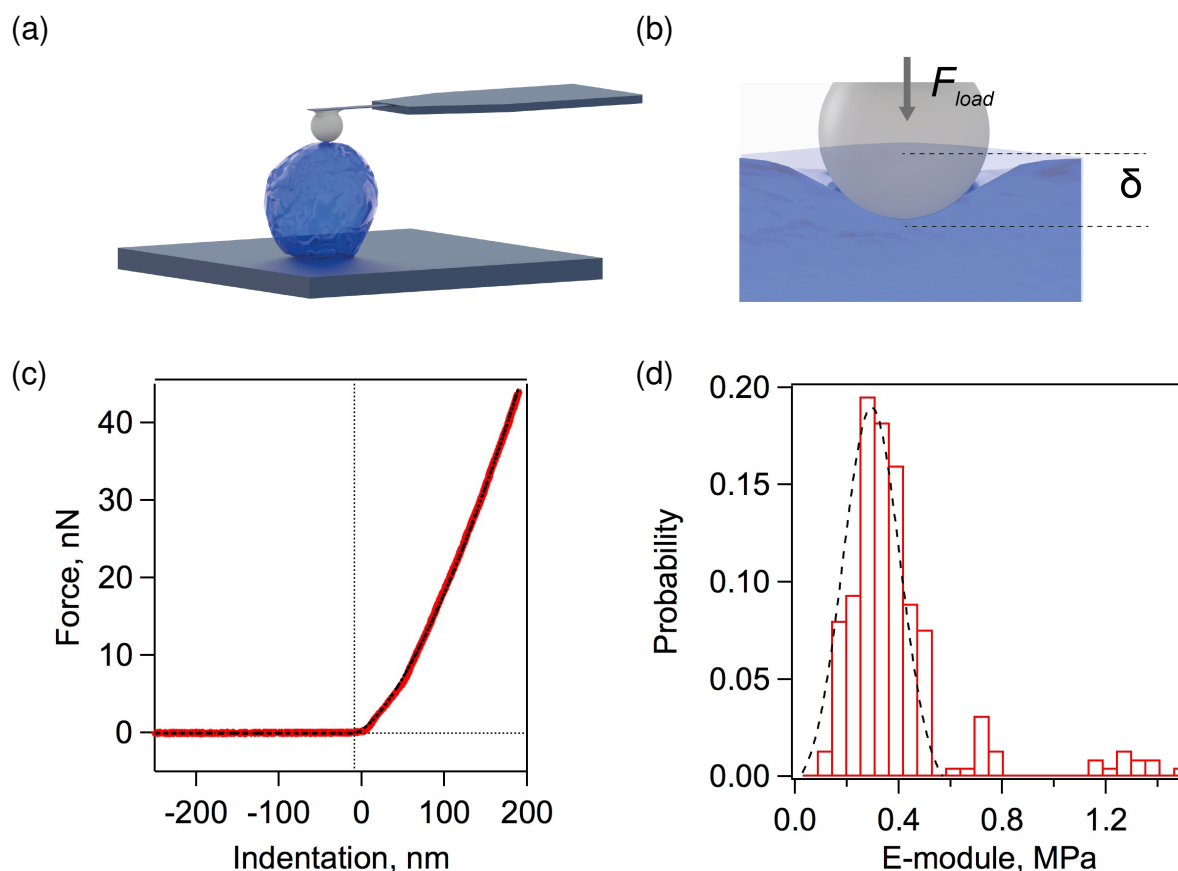


Figure 10.4: (a) Schematic illustration of indentation measurements on the alginate beads with 'hard' colloidal probes. A spherical silica particle is attached to a tipless AFM cantilever and used as indenter to determine the mechanical properties of immobilized alginate hydrogel beads. (b) The applied loading force F_{load} leads to an indentation depth δ in the hydrogel bead. (c) Representative force *versus* indentation curve acquired on an alginate hydrogel bead. (d) Distribution of the elastic moduli for >50 alginate beads. The same beads have been used as soft colloidal probes.

ments using 'hard' colloidal probes prepared from silica particles. [52] Fig. 10.4 a schematically illustrates the experimental setup: the diameter of the used hydrogel beads were 30-160 μm . The silica particles of the colloidal probes (*i.e.* the indenter) had a diameter of about 6.8 μm . The silica particles can be considered as practically non-deformable in comparison to the hydrogel beads. Any external force exerted by the silica colloidal probe leads to an indentation depth δ in the alginate bead as indicated in Fig. 10.4 b. Only deformations with $\delta < 250$ nm, *i.e.* very small deformations in comparison to the overall bead diameter of >30 μm , were considered for quantitative evaluation. Therefore, any influence of the substrate could be neglected. [69] The force *versus* distance curves were converted to force *versus* indentation curves. An example for an indentation profile is shown in Fig. 10.4 c. The indentation profiles were evalu-

10.3 Results and discussion

ated quantitatively by the Hertz-model outlined by eqn 10.1 - 10.3. The dashed line in Fig. 10.4 c represents the resulting fit to the indentation curve. The following parameters were used to obtain the elastic modulus E_{bead} from the fits: $E_{SiOx} \approx 74.9$ GPa, $\nu_{SiOx} \approx 0.17$. Furthermore, we assumed $\nu_{bead} \approx 0.5$, which is a common approximation for alginate hydrogels. [66, 67, 47] Indentation measurements are summarized for more than 50 different alginate beads by the histogram in Fig. 10.4 d. The distribution of the elastic moduli followed in good approximation a Gaussian (dashed line) with $E_{bead} = 297 \pm 155$ kPa. This value falls in the middle of the reported elastic moduli (*i.e.* 2-550 kPa) [66, 67, 47, 46] and is in good agreement with 330 kPa reported for micro-compression tests. [46]

10.3.4 Direct force measurements using alginate hydrogel probes

The adhesion between alginate hydrogel beads and various SAMs were determined in order to attribute the adhesion behaviour to different functional groups present on solid interfaces with a well-defined surface chemistry. SAMs have been used extensively in quantitative adhesion measurements, in particular in the framework of chemical force microscopy, where also the AFM-tip is modified by such a SAM. [70, 48, 71]

In contrast to 'classical' adhesion measurements, hydrogel colloidal probes are very soft, and various parts of the experimental procedure have to be adapted accordingly for quantitative measurements: firstly, the inverse optical lever sensitivity (*InvOLS*) for cantilevers with soft probes has to be determined independently in a separate set of measurements. An accurate determination of the *InvOLS* is an important prerequisite for the conversion of the measured photo-diode signal to cantilever deflection. Secondly, due to the well-known mechanics of levers, an apparent spring constant for the cantilever has to be considered as the accurate position of the attachment of the colloidal probe has to be taken into account with increasing size of the bead. [31, 56]

Alginate beads deform significantly even under small loading forces due to their low elastic modulus. Hence, the standard procedure can be not applied, in which the *InvOLS* is directly determined by pressing the colloidal probe onto a hard, non-deform-able surface and comparing the deflection signal with the piezo displacement. Therefore, we determined the *InvOLS* by an indirect method based on the equipartition theorem, which is normally used to determine the cantilever spring constant. [72] The spring constant of the cantilever has been determined in air before attaching the alginate beads to the cantilever. The *InvOLS* is calculated according to eqn 10.4 from the thermal noise spectrum of the cantilever with attached bead in aqueous solution. This procedure leads to consistent values of the *InvOLS* with an estimated error in

10 Probing the Adhesion Properties of Alginate Hydrogels

the order of about 20-30 %.

Alginate beads with diameters of 60-140 μm have been used for the preparation of soft colloidal probes. Hence, the beads were large in comparison to the top view dimensions of 35 μm (width) and 400 μm (length) of the cantilevers (*cf.* Fig. 10.1 e or Fig. 10.3 a). According to the mechanical lever law, the attachment point did not correspond to the free end of the cantilever, which leads to an apparent stiffening of the cantilever. The resulting effective spring constant for alginate probes were calculated by eqn 10.5 by determining the diameter and attachment point for each alginate bead from optical microscopy images. [31, 56]

10.3.5 Adhesion forces on self-assembled monolayers

Fig. 10.5 a-d show representative force profiles measured with alginate hydrogel probes on SAMs terminating in four different functional groups, namely -OH, -COOH, -CH₃ and -NH₂. Thus, the adhesion of alginate was probed with SAMs terminating in non-ionizable groups of hydrophilic and hydrophobic character (*i.e.* -OH and -CH₃), respectively, as well as in ionizable groups of anionic or cationic character (*i.e.* -COOH and -NH₂), respectively. The pH of 5.5 was chosen to ensure that both of the latter SAMs are at least partly ionized. Thiol-SAMs have been studied extensively and Table 10.1 compiles parameters such as interfacial energy, surface pK and wettability.

In general, the adhesion behaviour of alginate hydrogel beads is rather complex on the SAMs and it resembles the one observed for cells [73, 74] or polymeric systems with multivalent bonds. [75] This finding is not surprising due the network-like structure of hydrogels. The force profiles upon retraction can be separated into two distinct parts: in the first part, near to the surface, a dominant jump-out of contact has been observed for most adhesion events. This jump-out of contact coincides with the maximum pull-off force applied (*i.e.* the absolute minimum in the retraction part of the force profiles). However, the jump-out of contact is mostly not as sharp as observed between two hard, non-deformable surfaces (*e.g.* two SAMs). Instead, some alginate segments remain attached to the SAM, leading to a 'flattened' minimum of the pull-off force (*cf.* Fig. 10.10 in the ESI). In the second part of the retraction curve these segments are stretched and desorb subsequently. The latter events were most pronounced for the CH₃- and NH₂-terminated SAMs, which showed the strongest adhesion (*cf.* Fig. 10.10 in the ESI). It has been proposed that for such systems the total work of adhesion \tilde{W}_{adh} , can be approximated by the area under the retraction curve in the force profile. [64, 45] However, in order to normalize \tilde{W}_{adh} to the radius of the alginate bead of the true contact area has to be determined by optical microscopy, which is here not possible due the non-transparency of the Au-layers for the SAMs. The best estimate in this case is the well-defined pull-off force

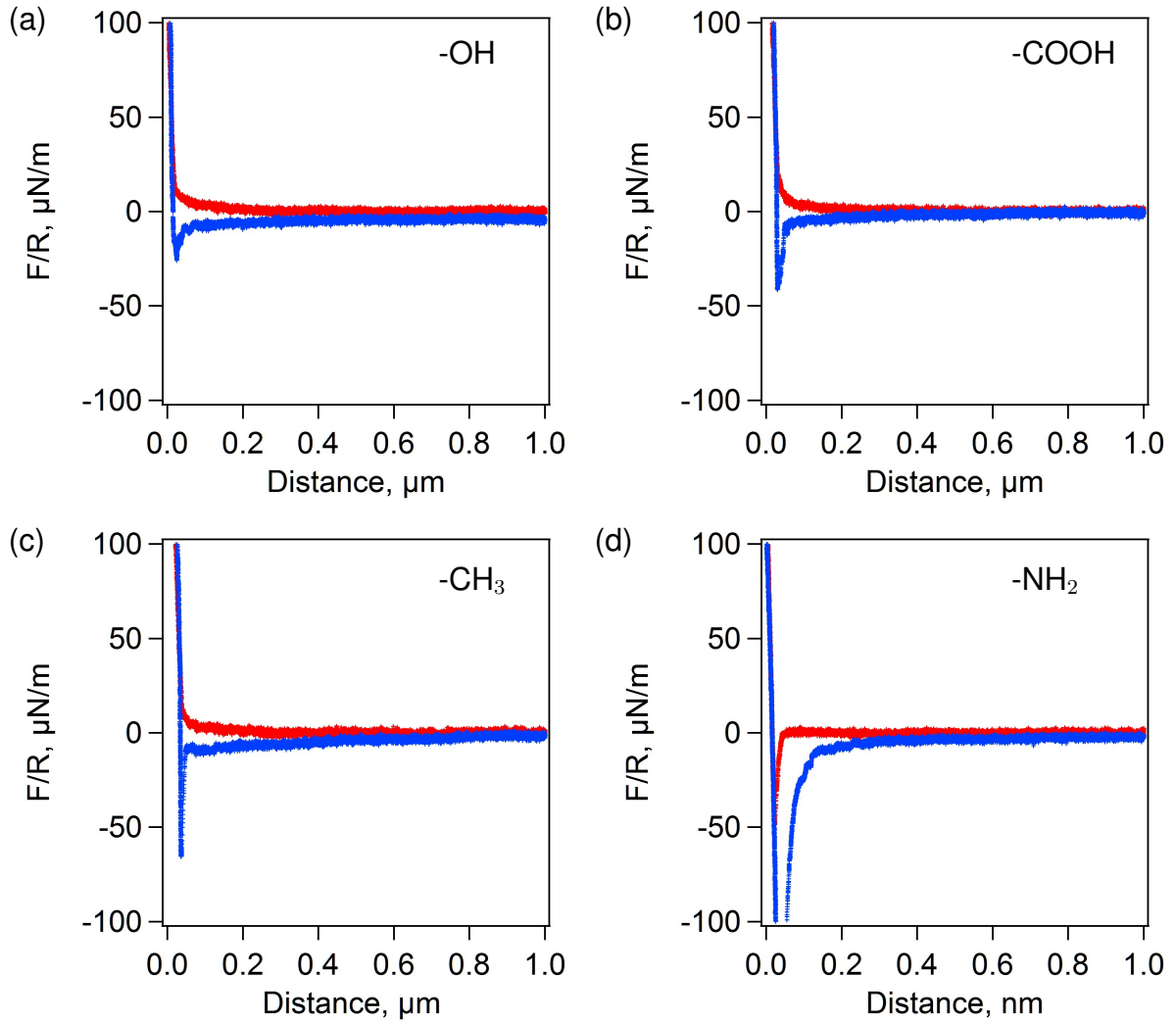


Figure 10.5: Representative force *versus* distance curves acquired with alginate colloidal probes on different self-assembled monolayers (SAMs). These SAMs terminate in different functional groups: (a) hydroxyl (-OH), (b) carboxyl (-COOH), (c) methyl (-CH₃), and (d) amino (-NH₂).

F_{adh} , which corresponds to the minimum in the retraction part of force profiles. Studies based on soft colloidal probes in combination with optical microscopy demonstrate that pull-off forces according to the Johnson-Kendall-Roberts (JKR) theory provide a good estimate for \tilde{W}_{adh} as determined for the area under the force profiles. [28] This F_{adh} can be described within the framework of the JKR theory in the sphere/plane geometry as [70, 48, 71]

$$F_{adh} = \frac{3}{2}\pi R_{bead}W_{adh} \quad (10.6)$$

where R_{bead} is the radius of the probe bead and W_{adh} is the work of adhesion per unit area. The latter is given by

10 Probing the Adhesion Properties of Alginate Hydrogels

$$W_{adh} = \gamma_{bead/H_2O} + \gamma_{SAM/H_2O} - \gamma_{bead/SAM} \quad (10.7)$$

with γ_{bead/H_2O} as interfacial energy between alginate bead and solution, γ_{SAM/H_2O} as interfacial energy between SAM and solution, and $\gamma_{bead/SAM}$ as interfacial energy between alginate bead and SAM, respectively. [70, 48] The JKR-theory according to eqn 10.6 and 10.7 has been successfully utilized for the quantitative description of adhesion forces in chemical force microscopy, which is based on the defined surface modification of an AFM-tip. [70, 48]

The adhesion of the alginate beads on the SAMs is dominated in most cases by the pull-off force at 'apparent zero-separation' (*cf.* Fig. 10.5 and Fig. 10.10 and 10.12 in the ESI), which corresponds to the minimum in the force profiles upon separation. Due to the elasticity of the alginate beads, the beads are slightly elongated when they are removed from the sample. Hence, the separation distance at which the pull-off occurs does not coincide with the zero-separation as determined for the initial contact of two surface. Only for non-compressible, hard surface the zero-separation upon approach and separation correspond to each other.

In the following, the focus is on the pull-off forces, which can be used to a good degree of accuracy as indicator for the overall adhesive behaviour of soft probes. [28] A clear trend in the adhesion forces can be identified on base of the pull-off forces (at 'quasi-zero separation') as summarized in Table 10.1 and Fig. 10.6. To allow for a comparison between measurements with different alginate probes (*i.e.* varying radii of the alginate beads), the pull-off forces were normalized to the probe radius according to eqn 10.3 and 10.6.

Fig. 10.6 a and b shows the distributions of pull-off forces necessary to remove an alginate probe from the different SAMs. At least three independent pairs of alginate probes and SAM substrates were used for each type of SAM to compile these distributions. The average pull-off forces increase in the following order for the terminating functional groups: $F_{adh}(-OH) < F_{adh}(-COOH) < F_{adh}(-CH_3) < F_{adh}(-NH_2)$. The solid lines in Fig. 10.6 indicate associated fits assuming a Gaussian distribution for the pull-off forces. Moreover, the average pull-off forces and their standard deviations are compiled in Table 10.1. Students T-test and a cumulative plot of the adhesion forces $F_{adh}(-OH)$, $F_{adh}(-COOH)$, and $F_{adh}(-CH_3)$ confirm that the differences are statistically significant (*cf.* ESI 10.6.5).

The following interaction mechanisms can contribute to the pull-off forces: van der Waals forces, long-ranged electrostatic forces (*i.e.* due to diffuse double layer overlap), chemical bonds, and solvent exclusion. The latter results from the creation and destruction of interfaces with the

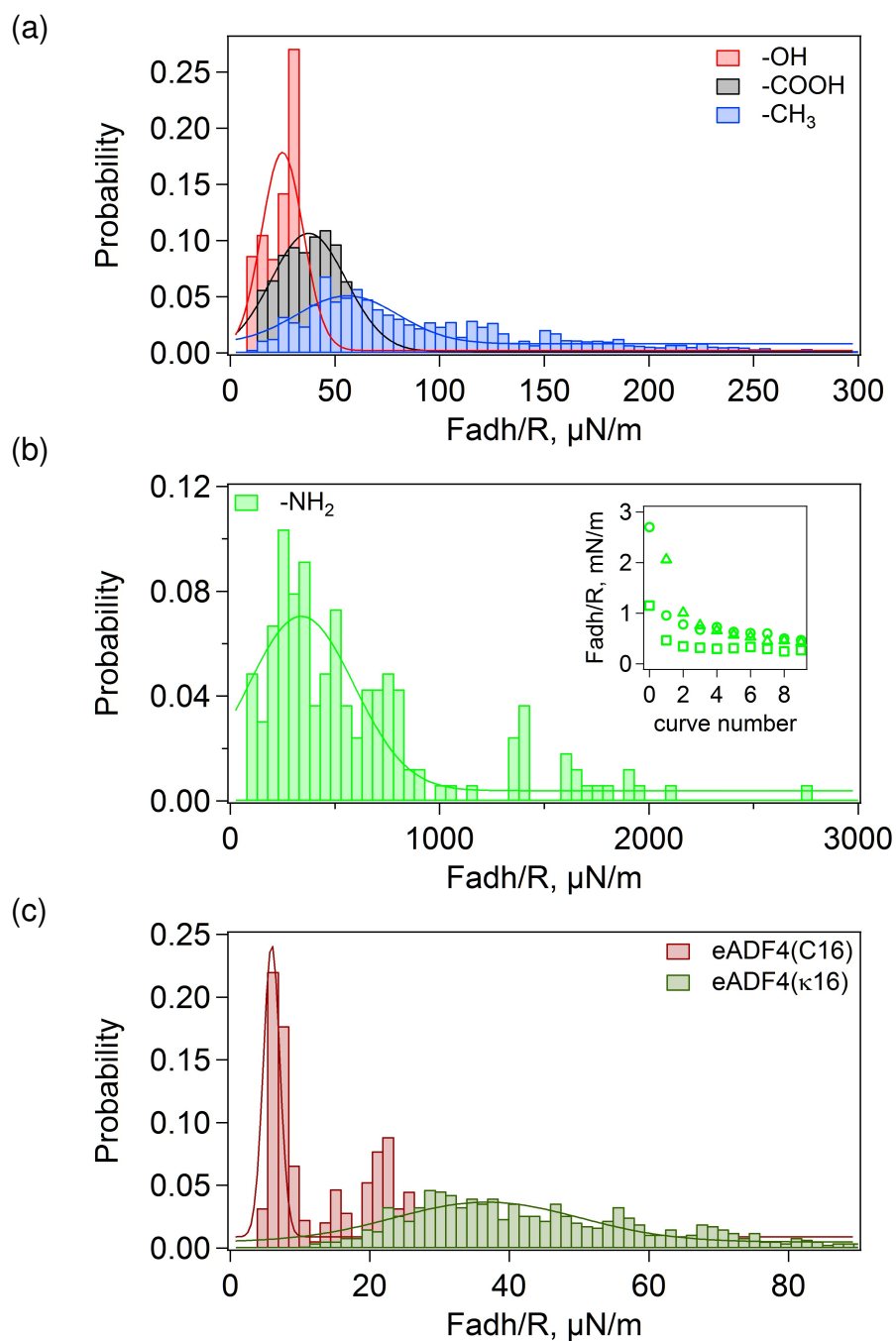


Figure 10.6: Distributions of the pull-off forces for the different surfaces. The solid lines indicate fits to a Gaussian-distribution. (a) Pull-off forces acquired by at least three different probes on OH-, CH₃-, and COOH- terminated SAMs. (b) Pull-off forces acquired on NH₂-terminated SAMs. The inset illustrates the decrease of the pull-off forces with increasing number of measurements on different positions as represented by the different symbols in the graph. (c) Pull-off forces as measured on drop-casted spider silk protein films.

10 Probing the Adhesion Properties of Alginate Hydrogels

aqueous phase according to eqn 10.7 and can be described in terms of the interfacial energies $\gamma_{surface/H_2O}$ as compiled in Table 10.1. [70, 48, 71, 51] The base of a semi-quantitative understanding of the pull-off forces on the different SAMs is provided by Table 10.1.

These interfacial energies are strongly related to the measured contact angles (*cf.* Table 10.1). The lowest pull-off forces were measured for the hydrophilic SAMs (-OH, -COOH), but the difference to the highly hydrophobic CH₃-terminated SAM is quite small. By contrast, much higher adhesion forces could be observed for NH₂-terminated SAM with contact angles significantly lower than for the CH₃-terminated SAMs. Hence, solvent exclusion does not play a major role for this strong adhesion. Hydrogel beads have thus a very different adhesion behaviour compared to the one observed for solid probes as the ones prepared from hard *e.g.* silica particles (Fig. 10.7). [44] This finding is not surprising as hydrogels are composed primarily by water (> 95 %).

Contributions by van der Waals forces can be neglected in the following comparison, as these forces are small due to the high water content of the hydrogel and are of comparable magnitude for all SAMs. Hence, electrostatic forces and chemical interactions in the contact area remain as primary contributions to the observed variations in adhesion.

Alginate is an anionic polysaccharide composed of mannuronic acid and guluronic acid blocks. [2, 5] Hence, the interface of alginate beads contains hydroxyl- (-OH) as well as carboxyl- (-COOH) groups. The isoelectric point of alginate is between 3.4 and 5.4, depending on the specific composition of mannuronic and guluronic acid monomer units. [68] Therefore, a significant number of carboxyl-groups of the alginate hydrogel is deprotonated at pH 5.5, which is the pH-value used throughout the experiments. At this pH all SAMs are negatively charged with the exception of the NH₂-terminated SAM. In case of the COOH-SAM with $pK \approx 5.7$, the charge results from the deprotonation of the surface groups. For the OH- and CH₃-terminated SAMs, which contain no ionizable groups and ion adsorption leads to the surface charge. [72, 50] In the case of the NH₂-SAM the overall surface charge is positive (*cf.* Table 10.1). [49] The approach parts of the force curves (*cf.* Fig. 10.5 a-d) are compatible with these different signs for the surface charge of the SAMs. All approach interactions are repulsive with the exception of NH₂-SAM. However, one finds that also for the NH₂-terminated SAM the interaction forces upon approach of the alginate bead can turn increasingly repulsive with increasing number of measurements at one position. The adhesion forces decrease during this process (*cf.* Fig. 10.6 b, inset), but remain much larger than the ones found for the other SAMs. In all cases the adhesion forces for the NH₂-SAM are much higher than one would expect on the forces observed upon approach. Hence, another process must attribute during contact of the bead with the SAM to the adhesion.

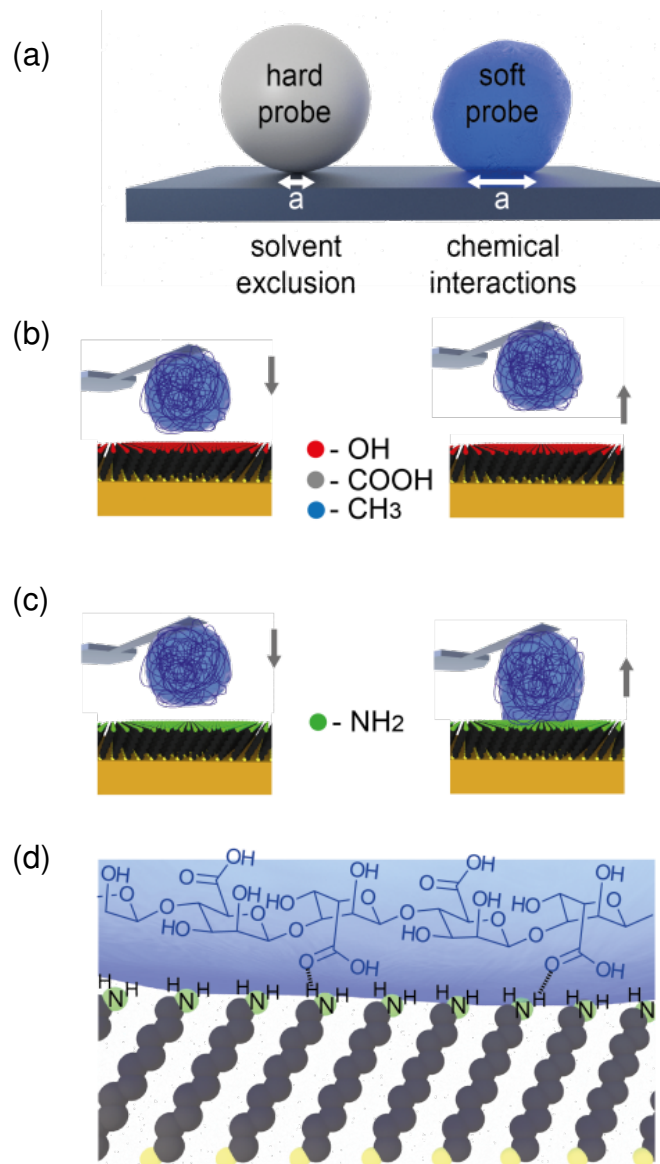


Figure 10.7: Schematic representation of the adhesion process on different surfaces and the differences in the adhesion behaviour between solid and soft colloidal probes. (a) Due to the high water content of the hydrogel only a small fraction of the probe is interacting with the surface (right). Hence, solvent exclusion does not play an important role in the adhesion process in contrast to solid colloidal probes (left), where solvent exclusion is especially important for hydrophobic surfaces. (b) For weak binding between the alginate and the surface a practically reversible deformation takes place, and the probe keeps its structural integrity. (c) Upon strong binding between the hydrogel and the surface parts of the bead remain on the surface after removing the probe. (d) Schematic representation for the single hydrogen bonds between parts of the alginate hydrogel bead and the SAM as indicated in black.

10 Probing the Adhesion Properties of Alginate Hydrogels

Solvent exclusion and formation of chemical bonds can only take place in the contact area between alginate bead and SAM.

The pull-off forces for alginate beads from NH_2 -terminated SAMs are nearly one order of magnitude larger than the determined for the hydrophobic SAM (*cf.* Fig. 10.6 a and b), although the interfacial energy with water is lower for this SAM. [76] Therefore, the strong adhesion can be attributed to chemical interactions between the amino groups of the SAM and the carboxyl groups from the alginate, namely the formation of hydrogen bonds and local attractive electrostatic interactions. [77] This mechanism is compatible with other studies: an enthalpy of 23 kcal mol^{-1} for the reaction of a primary amine with a solution of carboxylic acid has been reported based calorimetric measurements. [78] Moreover, adhesion measurements between NH_2 - and COOH -terminated SAMs in vacuum give enthalpic energies in the range of 16 kcal mol^{-1} compared to 5 kcal mol^{-1} for the interaction between two COOH -terminated SAMs. [79] The latter can also form hydrogen bonds, albeit of much reduced strength. [80] For the OH - and COOH -terminated SAMs the formation of very weak hydrogen bonds, *e.g.* COO^- - COOH or COOH/OH , has been reported previously by chemical force microscopy between SAMs. [79, 81] However, due to the presence of like charges on alginate and SAMs the resulting pull-off forces are much lower than in the case of NH_2 -terminated SAMs.

Additional features observed for the adhesion on NH_2 -terminated SAMs are compatible with stronger molecular interactions: firstly, a successive reduction of the pull-off force is observed (*cf.* inset in Fig. 10.6 b and Fig. 10.12 in the ESI). This reduction results from the partial disintegration of the alginate probe. The breaking of C-C bonds occurs at forces larger than about 2.6 nN. [82] Hence, the adhesion forces are large enough to allow for the breakage of single chelate Ca^{2+} -complexes, which would lead in consequence to the disintegration/removal of several polysaccharide molecules from the hydrogel network and thus the deposition of alginate segments on the SAM. The thereby deposited debris blocks the surface of the SAM and leads after several force-distance cycles to a change of the originally attractive forces upon approach to increasingly repulsive interactions. Secondly, a large number of stretching events occur in some force curves that can extend to rather large separation distances (*cf.* ESI). A similar behaviour was observed sometimes for CH_3 -terminated SAMs but much less pronounced.

10.3.6 Adhesion between alginate probes and recombinant spider silk protein films

Alginate probes have been utilized for probing the adhesion between alginate and films prepared from two different recombinant spider silk proteins. [40, 41, 83] These proteins have a highly repetitive structure in which one module is repeated 16 times. [84] Each of these mod-

10.4 Conclusions

ules contains only one charged amino acid, namely glutamic acid (E) in eADF4(C16) with a carboxyl group and lysine (K) in eADF4(κ 16) with an amino group. [40, 85] The other ionizable groups are located in the terminal regions of the proteins and the T7-tag and can be neglected due to their low occurrence at the surface of the protein films and thus have only a minor influence on the surface chemistry. [41, 42]

In general, the pull-off forces on eADF4(C16) and eADF4(κ 16) films were much smaller than the ones determined for the SAMs. This reduction can be attributed to two factors: (i) firstly, the protein films have a significantly higher surface roughness than the SAMs on ultra-flat gold. Surface roughness can have a significant influence on pull-off forces due to the strongly reduced overall contact area. [86] (ii) Secondly, the number of charged functional groups, *i.e.* amino- and carboxyl-groups, is much smaller than the one in the densely packed SAMs. The former have about 4.6 groups per nm², [44, 87] while the latter have about 0.0625 groups per nm². [42]

The observed difference in the pull-off forces between the two spider silk protein films is in very good agreement with the results obtained on the COOH- and NH₂-SAMs, respectively. The pull-off forces on eADF4(C16)-films are three times lower than on eADF4(κ 16)-films, which is the film with NH₂-groups. The at least 70x lower number of COOH- and NH₂-groups on the surface for eADF4(C16) and eADF4(κ 16) films leads to a significant reduction of the pull-off forces. Nevertheless, the more hydrophobic character of the spider silk protein films (*cf.* contact angles in Table 10.1 in comparison the SAMs) has not a strong influence on the interactions on the molecular level: the presence of NH₂-groups in the protein films leads to a clear increase of the alginate adhesion.

10.4 Conclusions

A new method is presented for an *in situ* preparation of soft colloidal probes by aspiration and manipulation with micropipettes being adaptable for all kinds of colloidal particles, especially for those colloids that should not be exposed to certain ambient conditions, such as air, in order to avoid structural alterations or contaminations. The contact takes place between micropipette and an area of the colloidal particle that will be later not used for measuring the interaction forces; in contrast to methods in which particles are collected directly with the cantilever from a solid substrate. Hence, the *in situ* preparation is less prone to contaminations. The micropipette method is especially useful for the preparation of soft colloidal probes, which have a much lower elastic modulus than the 300 kPa of the alginate beads utilized here.

10 Probing the Adhesion Properties of Alginate Hydrogels

The influence of different functional groups can be determined in an unambiguous manner by determining the adhesion behaviour of alginate hydrogel beads on highly defined SAMs terminating in various functional groups. Comparing the adhesion behaviour of alginate on the SAMs with the one on recombinant spider silk protein films allowed for the identification of the mainly involved functional groups in these more complex biomaterials. For recombinant spider silk protein films, adhesion is primarily mediated by one functional group, while the interfacial energy is not of great significance for the adhesion as determined by the pull-off forces. The adhesive behaviour of hydrogels is fundamentally different to that observed for solid particles. While for the latter solvent exclusion, especially for hydrophobic surfaces, is always of importance, the former incorporates so much water in their internal structure that the adhesion is practically exclusively dominated by chemical and electrostatic interactions. This strong dependence of bead adhesion on the formation of bonds supports the high sensitivity found by microscopy-based measurements with large soft colloidal probes. [88]

10.5 Acknowledgements

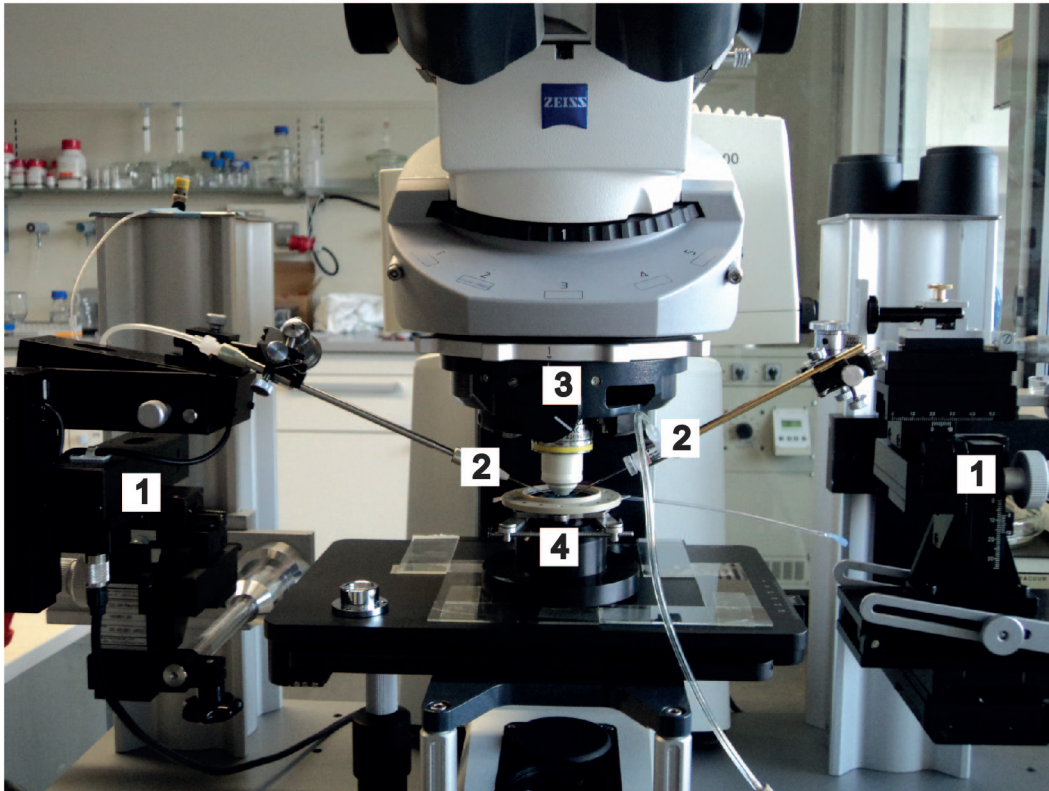
The authors thank J. Flemke for the preparation of the first batch of alginate beads and M. Neubauer for helpful discussions about indentation measurements on soft colloids. Furthermore, the authors thank C. Kunert the SEM images. G. P. and T. S. thank the German research council (DFG) for financial support in the framework of the SFB 840 (projects C4 and A8, respectively).

10.6 Supporting Information

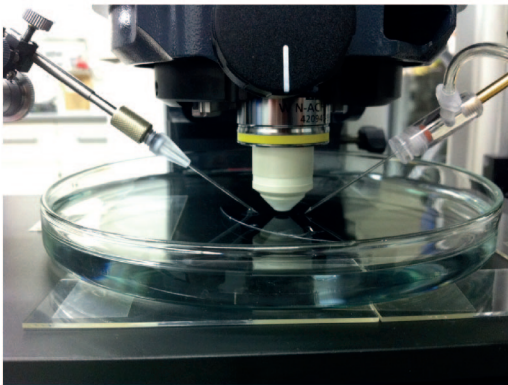
10.6.1 *In situ* preparation of colloidal probes from alginate beads by micromanipulation (movie)

The provided movie (*In situ Preparation of Soft Colloidal Probes.m4v*) shows an exemplary and complete sequence for the *in situ* preparation of a soft alginate hydrogel colloidal probe in real-time.

(a)



(b)



(c)

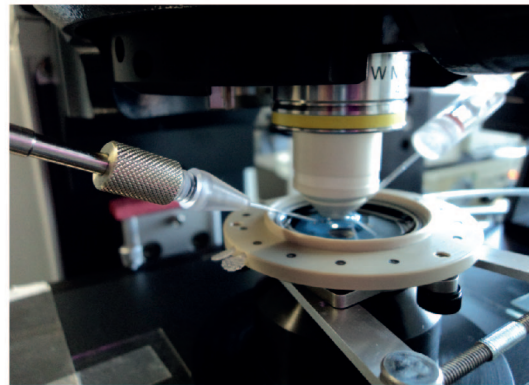


Figure 10.8: (a) Experimental setup for the *in situ* preparation of soft hydrogel colloidal probes with: (1) two micromanipulators, (2) glass micropipettes, (3) a fixed stage microscope and (4) a preparation vessel. The latter is either a petri-dish (b) or an AFM fluid cell (c) with a previously mounted tipless AFM-cantilever. The cell shown in (c) can be sealed completely after preparing the soft colloidal probe.

10.6.2 Micromanipulation setup for *in situ* preparation of alginate probes

Figure 10.8 (a) shows the experimental setup used for the *in situ* preparation of soft hydrogel colloidal probes. Micromanipulators **(1)** allow for a precise positioning and movement of glass micropipettes **(2)** during the preparation procedure. A first micropipettes of various opening diameters has been used for injecting a small amount of a particle suspension. The opening diameter was always much larger than the particle diameter. A second micropipette has been used to aspirate a single particle and transfer it to the AFM cantilever. The opening diameter of this second micropipette was significantly smaller compared to the diameter of the alginate beads. The complete procedure can be directly monitored *via* a fixed stage microscope **(3)** (*cf.* movie in S1). The presented method allows preparing the probes completely *in situ*, *i.e.* in aqueous medium. The preparation can be performed in a simple petri dish (*cf.* Figure 10.8 b) or directly in an AFM fluid cell (*cf.* **(4)** and Figure 10.8 c). In the case, that the preparation is performed in a petri dish, it has to be ensured that the prepared soft colloidal probe is transferred rapidly onto a previously wetted cantilever holder.

10.6.3 Apparent spring constant k_{app}

Immobilization of alginate hydrogel beads corresponds to a new effective spring constant for the cantilever as the length of the AFM cantilever L_c is reduced to L_{bead} . According to the lever law this reduction in lever length leads to an apparent stiffening of the used force sensor according to eq. 10.5. [56, 31, 89]

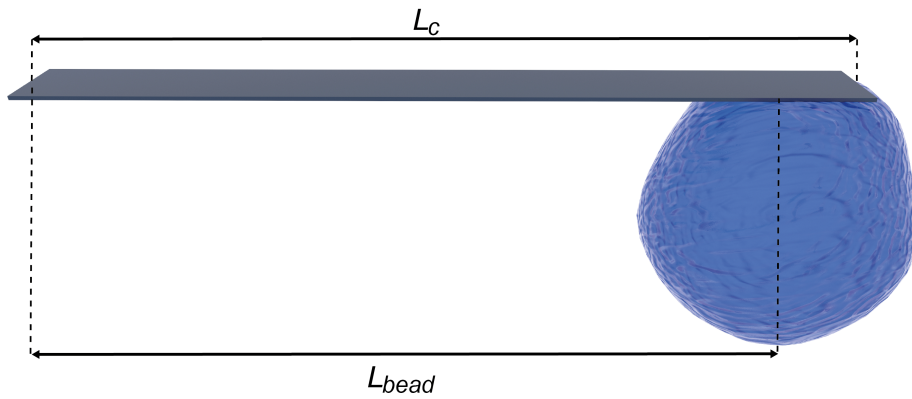


Figure 10.9: Schematic representation of the apparent stiffening of a cantilever with an alginate bead attached due to the reduced effective lever length.

10.6.4 Examples of force vs. distance curves on self-assembled monolayers (Zoom-In)

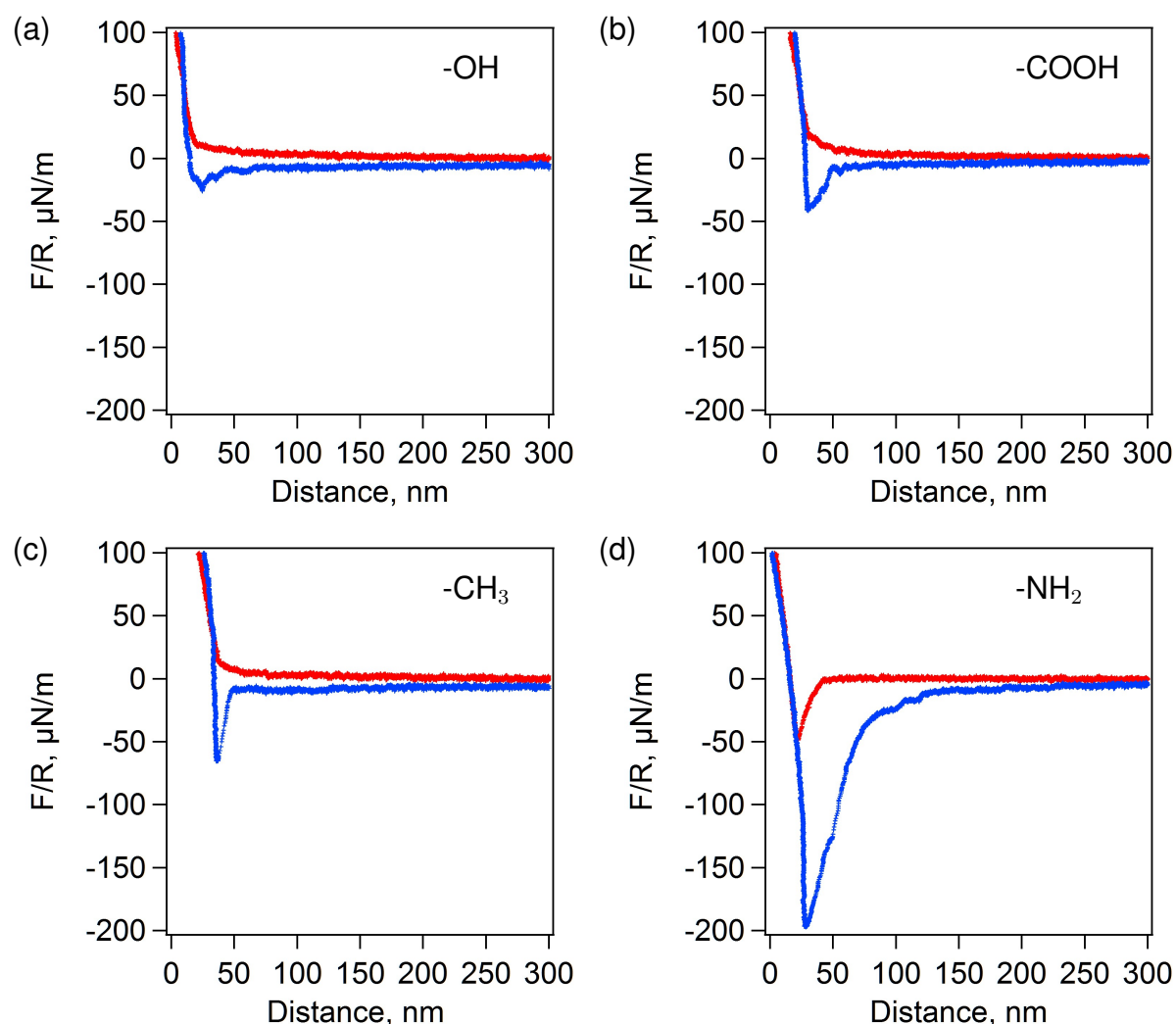


Figure 10.10: Different axis scales for the force profiles as shown in Figure 10.5. The scaling shows that the adhesion is dominated by the pull-off force for the alginate bead. This force corresponds to the minimum in the retraction part (*i.e.* blue data) of the force profiles. However, the pull-off is not a sharp transition as for two hard surfaces, as some segments of the alginate bead still adhere to the SAM and are stretched subsequently.

10.6.5 Statistical analysis of the determined adhesion forces

The pull-off forces obtained for an alginate hydrogel colloidal probe were determined as the minimum in the retraction part of the force profile (*cf.* Figure 10.10). The resulting Gaussian distributions are shown in Figure 10.6 and the average values and the evaluated standard deviations are given in Table 10.1. A Student T-test confirms by the differences in the pull-off force forces are significant (p -value < 0.05) for the different SAMs (-OH, -COOH and -CH₃). The difference in adhesion behaviour on those SAMs can be additionally visualized by a cumulative distribution plot shown in Figure 10.11.

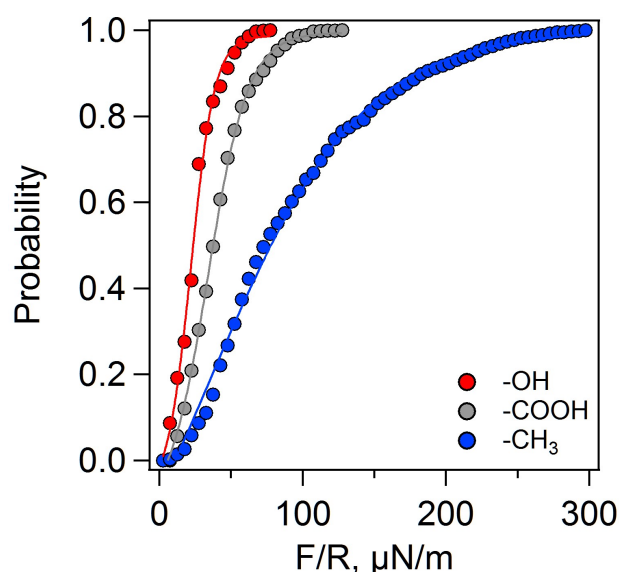


Figure 10.11: Cumulative distribution plot of the pull-off forces between an alginate hydrogel colloidal probe and various SAMs surfaces terminating in different functional groups: -OH (red), -COOH (grey) and -CH₃ (blue), respectively.

10.6.6 Force vs. distance curves acquired on NH₂-terminated SAMs

The adhesion behaviour of alginate beads as probed on NH₂-terminated SAMs is more complex than the one observed on the other SAMs as the adhesion is much stronger. We observed that with an increasing number of force vs. distance cycles the adhesion was reduced. This reduction was observed for the pull-off forces as well as for the stretching of alginate segments at larger separation distances. Figure 10.12 shows examples for the same alginate bead at two different lateral positions on a NH₂-terminated SAM.

10 Probing the Adhesion Properties of Alginate Hydrogels

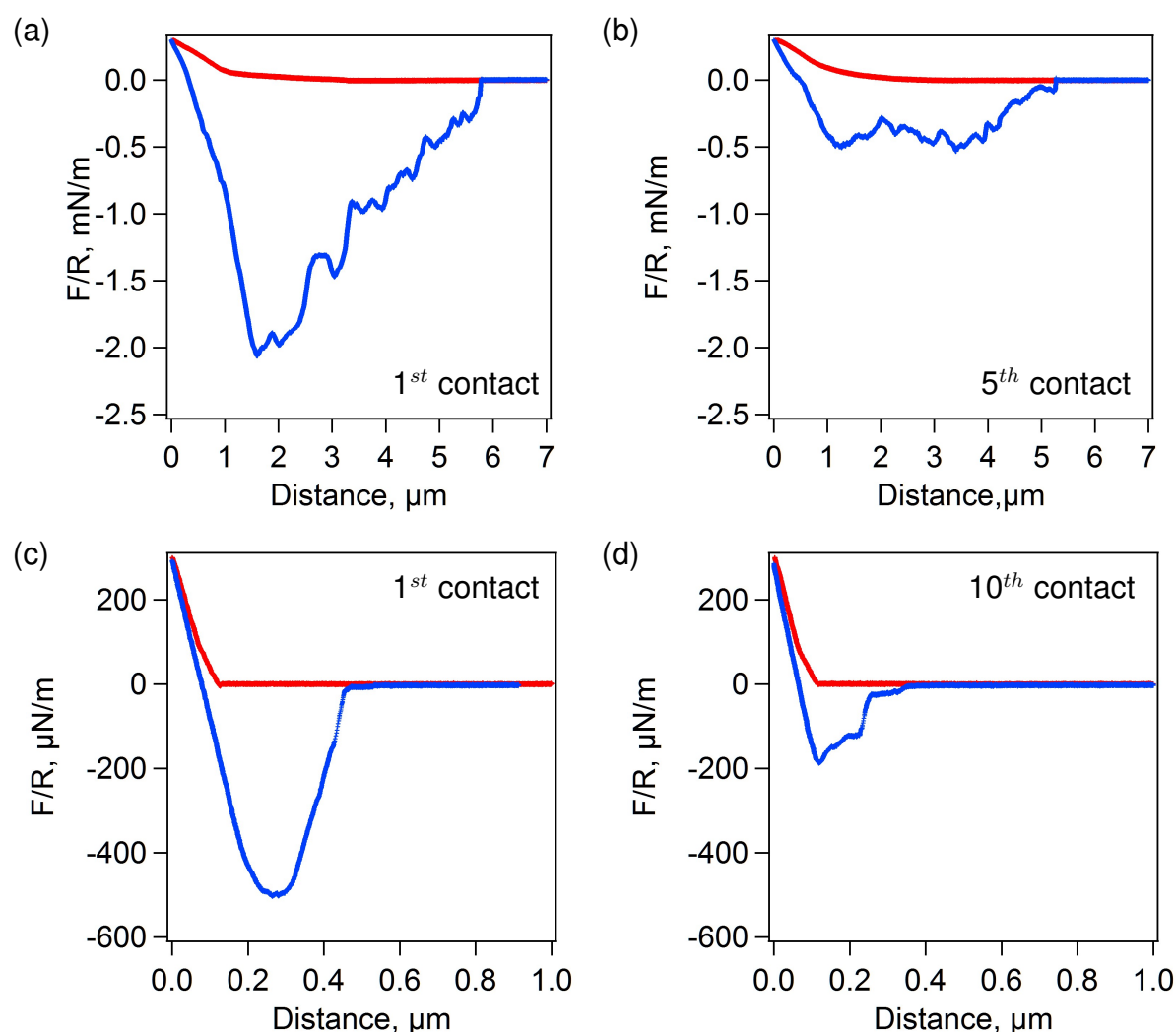


Figure 10.12: Force *versus* distance curves acquired with an alginate colloidal probe on a NH_2 -terminated SAM. (a) and (c) show the normalized force profiles for the initial contact with a "fresh" area of the SAM. The decrease in the adhesion forces after several force *versus* distance cycles is shown in (b) and (d), respectively. (b) has been acquired after 5 previous force *versus* distance cycles and (d) after 10 cycles but always at the same positions as for (a) and (c), respectively.

10.6.7 Adhesion forces on recombinant spider silk protein films

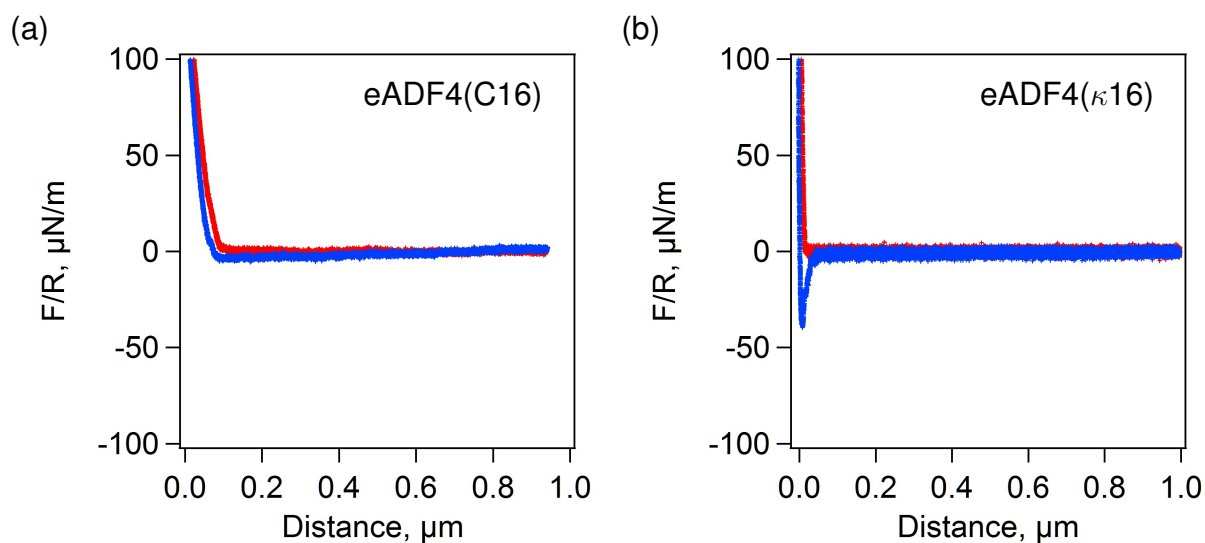


Figure 10.13: Representative force *versus* distance curves acquired with an alginate hydrogel colloidal probe on two different recombinant spider silk protein films: (a) eADF4(C16) and (b) eADF4(κ 16), respectively. The measurements were performed for at least two probe - protein film combinations.

References

- [1] J A Rowley, G Madlambayan, and D J Mooney. Alginate hydrogels as synthetic extracellular matrix materials. *Biomaterials*, 20(1):45–53, 1999.
- [2] J-Y Sun, X Zhao, W R K Illeperuma, O Chaudhuri, K H Oh, D J Mooney, J J Vlassak, and Z Suo. Highly stretchable and tough hydrogels. *Nature*, 489:133–136, 2012.
- [3] N A Peppas, J Z Hilt, A Khademhosseini, and R Langer. Hydrogels in Biology and Medicine. *Advanced Materials*, 18:1345–1360, 2006.
- [4] A J Engler, S Sen, H L Sweeney, and D E Discher. Matrix elasticity directs stem cell lineage specification. *Cell*, 126(4):677–689, 2006.
- [5] K Y Lee and D J Mooney. Alginate: Properties and biomedical applications. *Progress in Polymer Science*, 37(1):106, 2012.
- [6] K Ziv, H Nuhn, Y Ben-Haim, L S Sasportas, P J Kempen, T P Niedringhaus, M Hrynyk, R Sinclair, A E Barron, and S S Gambhir. A tunable silk-alginate hydrogel scaffold for stem cell culture and transplantation. *Biomaterials*, 35(12):3736–3743, 2014.
- [7] B Balakrishnan, M Mohanty, P R Umashankar, and A Jayakrishnan. Evaluation of an in situ forming hydrogel wound dressing based on oxidized alginate and gelatin. *Biomaterials*, 26(32):6335 – 6342, 2005.

10 Probing the Adhesion Properties of Alginate Hydrogels

- [8] B J Tighe. The design of polymers for contact lens applications. *British Polymer Journal*, 8:71–77, 1976.
- [9] R C T Howe, A P Smalley, A P M Guttenplan, M W R Doggett, M D Eddleston, J C Tan, and G O Lloyd. A family of simple benzene 1,3,5-tricarboxamide (BTA) aromatic carboxylic acid hydrogels. *Chemical Communications*, 49(39):4268, 2013.
- [10] J Thiele, Y Ma, S M C Bruekers, S Ma, and W T S Huck. 25th Anniversary Article: Designer Hydrogels for Cell Cultures: A Materials Selection Guide. *Advanced Materials*, 26(1):125–148, 2013.
- [11] E Caló and V V Khutoryanskiy. Biomedical applications of hydrogels: A review of patents and commercial products. *European Polymer Journal*, 65:252–267, 2015.
- [12] D Pasqui, M De Cagna, and R Barbucci. Polysaccharide-Based Hydrogels: The Key Role of Water in Affecting Mechanical Properties. *Polymers*, 4(4):1517–1534, 2012.
- [13] S N Pawar and K J Edgar. Alginate derivatization: A review of chemistry, properties and applications. *Biomaterials*, 33(11):3279–3305, 2012.
- [14] J P Paques, E van der Linden, C J M van Rijn, and L M C Sagis. Preparation methods of alginate nanoparticles. *Advances in Colloid and Interface Science*, 209:163–171, 2014.
- [15] Y A Mørch, I Donati, B L Strand, and G Skjåk-Bræk. Effect of Ca²⁺, Ba²⁺, and Sr²⁺ on Alginate Microbeads. *Biomacromolecules*, 7(5):1471–1480, 2006.
- [16] A Martinsen, G Skjåk-Bræk, and O Smidsrod. Alginate as immobilization material: I. Correlation between chemical and physical properties of alginate gel beads. *Biotechnology and Bioengineering*, 33(1):79–89, 1989.
- [17] D B Seifert and J A Phillips. Production of Small, Monodispersed Alginate Beads for Cell Immobilization. *Biotechnology Progress*, 13(5):562–568, 1997.
- [18] M George and T E Abraham. Polyionic hydrocolloids for the intestinal delivery of protein drugs: Alginate and chitosan - a review. *Journal of Controlled Release*, 114(1):1 – 14, 2006.
- [19] H B Eral, E R Safai, B Keshavarz, J J Kim, J Lee, and P S Doyle. Governing Principles of Alginate Microparticle Synthesis with Centrifugal Forces. *Langmuir*, 32(28):7198–7209, 2016.
- [20] J G Hardy and T R Scheibel. Composite materials based on silk proteins. *Progress in Polymer Science*, 35(9):1093–1115, 2010.

References

- [21] B Benli, J Nalaskowski, S Assemi, M S Celik, and J D Miller. Evaluation of Adhesion Forces in Alginate–Filler System Using an AFM Colloidal Probe Technique. *Journal of Adhesion Science and Technology*, 25(11):1159–1173, 2012.
- [22] J P Best, M P Neubauer, S Javed, H H Dam, A Fery, and F Caruso. Mechanics of pH-responsive hydrogel capsules. *Langmuir*, 29(31):9814–9823, 2013.
- [23] H-J Butt, B Cappella, and M Kappl. Force measurements with the atomic force microscope: Technique, interpretation and applications. *Surface Science Reports*, 59(1-6):1–152, 2005.
- [24] M Kappl and H J Butt. The colloidal probe technique and its application to adhesion force measurements. *Particle & Particle Systems Characterization*, 19(3):129–143, 2002.
- [25] T Hugel and M Seitz. The study of molecular interactions by AFM force spectroscopy. *Macromolecular Rapid Communications*, 22(13):989–1016, 2001.
- [26] M E McConney, S Singamaneni, and V V Tsukruk. Probing Soft Matter with the Atomic Force Microscopies: Imaging and Force Spectroscopy. *Polymer Reviews*, 50(3):235–286, 2010.
- [27] J Erath, S Schmidt, and A Fery. Characterization of adhesion phenomena and contact of surfaces by soft colloidal probe AFM. *Soft Matter*, 6(7):1432, 2010.
- [28] D Pussak, D Ponader, S Mosca, T Pompe, L Hartmann, and S Schmidt. Specific Adhesion of Carbohydrate Hydrogel Particles in Competition with Multivalent Inhibitors Evaluated by AFM. *Langmuir*, 30(21):6142, 2014.
- [29] W A Ducker, T J Senden, and R M Pashley. Direct Measurement of Colloidal Forces Using an Atomic Force Microscope. *Nature*, 353(6341):239–241, 1991.
- [30] H-J Butt. Measuring electrostatic, van der Waals, and hydration forces in electrolyte solutions with an atomic force microscope. *Biophysical Journal*, 60(6):1438–1444, 1991.
- [31] R Buzio, A Bosca, S Krol, D Marchetto, S Valeri, and U Valbusa. Deformation and Adhesion of Elastomer Poly(dimethylsiloxane) Colloidal AFM Probes. *Langmuir*, 23(18):9293–9302, 2007.
- [32] R Buzio and U Valbusa. Interfacial stiffness and adhesion of randomly rough contacts probed by elastomer colloidal AFM probes. *Journal of Physics: Condensed Matter*, 20(35):354014, 2008.

10 Probing the Adhesion Properties of Alginate Hydrogels

- [33] M Reitsma, V Craig, and S Biggs. Elasto-plastic and visco-elastic deformations of a polymer sphere measured using colloid probe and scanning electron microscopy. *International Journal of Adhesion and Adhesives*, 20(6):445–448, 2000.
- [34] G W Tormoen and J Drelich. Deformation of soft colloidal probes during AFM pull-off force measurements: elimination of nano-roughness effects. *Journal of Adhesion Science and Technology*, 19(3-5):181–198, 2005.
- [35] C Carrick, S A Pendergraph, and L Wågberg. Nanometer Smooth, Macroscopic Spherical Cellulose Probes for Contact Adhesion Measurements. *ACS Applied Materials & Interfaces*, 6(23):20928–20935, 2014.
- [36] Y Zhang and L-C Yu. Microinjection as a tool of mechanical delivery. *Current Opinion in Biotechnology*, 19(5):506–510, 2008.
- [37] R M Hochmuth. Micropipette aspiration of living cells. *Journal of Biomechanics*, 33(1):15–22, 2000.
- [38] E Mabrouk, D Cuvelier, L-L Pontani, B Xu, D Lévy, P Keller, F Brochard-Wyart, P Nassoy, and M-H Li. Formation and material properties of giant liquid crystal polymersomes. *Soft Matter*, 5(9):1870–1878, 2009.
- [39] J C Love, L A Estroff, J K Kriebel, R G Nuzzo, and G M Whitesides. Self-assembled monolayers of thiolates on metals as a form of nanotechnology. *Chemical Reviews*, 105(4):1103–1169, 2005.
- [40] E Doblhofer and T Scheibel. Engineering of recombinant spider silk proteins allows defined uptake and release of substances. *Journal of pharmaceutical sciences*, 104(3):988–994, 2015.
- [41] N Helfricht, E Doblhofer, J F L Duval, T Scheibel, and G Papastavrou. Colloidal Properties of Recombinant Spider Silk Protein Particles. *The Journal of Physical Chemistry C*, 120(32):18015–18027, 2016.
- [42] N Helfricht, M Klug, A Mark, V Kuznetsov, C Blüm, T Scheibel, and G Papastavrou. Surface properties of spider silk particles in solution. *Biomaterials Science*, 1(11):1166, 2013.
- [43] D Stamou, D Gourdon, M Liley, N A Burnham, A Kulik, H Vogel, and C Duschl. Uniformly flat gold surfaces: Imaging the domain structure of organic monolayers using scanning force microscopy. *Langmuir*, 13(9):2425–2428, 1997.
- [44] V Kuznetsov and G Papastavrou. Adhesion of colloidal particles on modified electrodes. *Langmuir*, 28(48):16567–16579, 2012.

References

- [45] S Martin, H Wang, L Hartmann, T Pompe, and S Schmidt. Quantification of protein–materials interaction by soft colloidal probe spectroscopy. *Physical Chemistry Chemical Physics*, 17(5):3014, 2015.
- [46] C X Wang, C Cowen, Z Zhang, and C R Thomas. High-speed compression of single alginate microspheres. *Chemical Engineering Science*, 60(23):6649–6657, 2005.
- [47] G Kaklamani, D Cheneler, L M Grover, M J Adams, and J Bowen. Mechanical properties of alginate hydrogels manufactured using external gelation. *Journal of the Mechanical Behavior of Biomedical Materials*, 36:135–142, 2014.
- [48] D V Vezenov, A Noy, L F Rozsnyai, and C M Lieber. Force Titrations and Ionization State Sensitive Imaging of Functional Groups in Aqueous Solutions by Chemical Force Microscopy. *Journal of the American Chemical Society*, 119(8):2006–2015, 1997.
- [49] H Zhang, H X He, T Mu, and Z F Liu. Force titration of amino group-terminated self-assembled monolayers of 4-aminothiophenol on gold using chemical force microscopy. *Thin Solid Films*, 327-329:778–780, 1998.
- [50] V Kuznetsov and G Papastavrou. Ion Adsorption on Modified Electrodes as Determined by Direct Force Measurements under Potentiostatic Control. *The Journal of Physical Chemistry C*, 118(5):2673–2685, 2014.
- [51] E-S Chan, B-B Lee, P Ravindra, and D Poncelet. Prediction models for shape and size of ca-alginate macrobeads produced through extrusion–dripping method. *Journal of Colloid and Interface Science*, 338(1):63–72, 2009.
- [52] V Kuznetsov and G Papastavrou. Note: mechanically and chemically stable colloidal probes from silica particles for atomic force microscopy. *Review of Scientific Instruments*, 83(11):116103, 2012.
- [53] K Trenkenschuh, J Erath, V Kuznetsov, J Gensel, F Boulmedais, P Schaaf, G Papastavrou, and A Fery. Tuning of the Elastic Modulus of Polyelectrolyte Multilayer Films built up from Polyanions Mixture. *Macromolecules*, 44(22):8954–8961, 2011.
- [54] M P Neubauer, C Blüm, E Agostini, J Engert, T Scheibel, and A Fery. Micromechanical characterization of spider silk particles. *Biomaterials Science*, 1(11):1160, 2013.
- [55] J L Hutter and J Bechhoefer. Calibration of atomic-force microscope tips. *Review of Scientific Instruments*, 64(7):1868–1873, 1993.
- [56] J E Sader, I Larson, P Mulvaney, and L R White. Method for the calibration of atomic force microscope cantilevers. *Review of Scientific Instruments*, 66(7):3789–3798, 1995.

10 Probing the Adhesion Properties of Alginate Hydrogels

- [57] T J Senden. Force microscopy and surface interactions. *Current Opinion in Colloid & Interface Science*, 6(2):95–101, 2001.
- [58] K A Melzak, S Moreno-Flores, K Yu, J Kizhakkedathu, and J L Toca-Herrera. Rationalized approach to the determination of contact point in force-distance curves: Application to polymer brushes in salt solutions and in water. *Microscopy Research and Technique*, 73:959–964, 2010.
- [59] H J Butt and M Jaschke. Calculation of thermal noise in atomic force microscopy. *Nanotechnology*, 6(1):1–70, 1995.
- [60] T E Schäffer. Calculation of thermal noise in an atomic force microscope with a finite optical spot size. *Nanotechnology*, 16(6):664–670, 2005.
- [61] R Pericet-Camara, G Papastavrou, and M Borkovec. Atomic Force Microscopy Study of the Adsorption and Electrostatic Self-Organization of Poly(amidoamine) Dendrimers on Mica. *Langmuir*, 20(8):3264, 2004.
- [62] R von Klitzing. Internal structure of polyelectrolyte multilayer assemblies. *Physical Chemistry Chemical Physics*, 8:5012–5033, 2006.
- [63] R Vreeker, L Li, Y Fang, I Appelqvist, and E Mendes. Drying and rehydration of calcium alginate gels. *Food biophysics*, 3:361–369, 2008.
- [64] Ö Kaftan, S Tumbiolo, F Dubreuil, R Auzély-Velty, A Fery, and G Papastavrou. Probing Multivalent Host–Guest Interactions between Modified Polymer Layers by Direct Force Measurement. *The Journal of Physical Chemistry B*, 115(24):7726–7735, 2011.
- [65] E Potthoff, D Ossola, T Zambelli, and J A Vorholt. Bacterial adhesion force quantification by fluidic force microscopy. *Nanoscale*, 7(9):4070–4079, 2015.
- [66] N Raz, J K Li, L K Fiddes, E Tumarkin, and G C Walker. Microgels with an interpenetrating network structure as a model system for cell studies. *Macromolecules*, 43:7277–7281, 2010.
- [67] M Ø Olderøy, M Xie, J-P Andreassen, B L Strand, Z Zhang, and P Sikorski. Viscoelastic properties of mineralized alginate hydrogel beads. *Journal of Materials Science: Materials in Medicine*, 23(7):1619–1627, 2012.
- [68] K I Draget, G S Braek, and O Smidsrod. Alginic Acid Gels - the Effect of Alginate Chemical-Composition and Molecular-Weight. *Carbohydrate Polymers*, 25(1):31–38, 1994.
- [69] R Long, M S Hall, M Wu, and C-Y H. Effects of Gel Thickness on Microscopic Indentation Measurements of Gel Modulus. *Biophysical Journal*, 101:643–650, 2011.

References

- [70] P Warszyński, G Papastavrou, K D Wantke, and H Möhwald. Interpretation of adhesion force between self-assembled monolayers measured by chemical force microscopy. *Colloids and Surfaces A: Physicochemical and Engineering Aspects*, 214(1-3):61, 2003.
- [71] A Noy, D V Vezenov, and C M Lieber. Chemical force microscopy. *Annual Review of Materials Science*, 27:381–421, 1997.
- [72] P Maroni, F J M Ruiz-Cabello, and A Tiraferri. Studying the role of surface chemistry on polyelectrolyte adsorption using gold–thiol self-assembled monolayer with optical reflectivity. *Soft Matter*, 10:9220–9225, 2014.
- [73] G Weder, O Guillaume-Gentil, N Matthey, F Montagne, H Heinzemann, J Vörös, and M Liley. The quantification of single cell adhesion on functionalized surfaces for cell sheet engineering. *Biomaterials*, 31(25):6436–6443, 2010.
- [74] J Friedrichs, K R Legate, R Schubert, M Bharadwaj, C Werner, D J Müller, and M Benoit. A practical guide to quantify cell adhesion using single-cell force spectroscopy. *Methods*, 60(2):169 – 178, 2013. Nanoimaging Methods for Biomedicine.
- [75] L J Kirwan, P Maroni, S H Behrens, G Papastavrou, and M Borkovec. Interaction and Structure of Surfaces Coated by Poly(vinyl amines) of Different Line Charge Densities. *The Journal of Physical Chemistry B*, 112(46):14609–14619, 2008.
- [76] J Glinski, G Chavepeyer, and J K Platten. Phase diagrams and interfacial properties of water-hexylamine, water-heptylamine, and water-octylamine systems. *Journal of Colloid and Interface Science*, 162(1):129–134, 1994.
- [77] H Ebeltoft, J Sjöblom, J O Saeten, and G Olofsson. Fatty Acid/Base Interactions in Model Systems. A Langmuir Film, Surface Tension, and Calorimetric Study. *Langmuir*, 10(7):2262–2266, 1994.
- [78] L Sun, R M Crooks, and A J Ricco. Molecular interactions between organized, surface-confined monolayers and vapor-phase probe molecules. 5. Acid-base interactions. *Langmuir*, 9(7):1775–1780, 1993.
- [79] R C Thomas, J E Houston, R M Crooks, T Kim, and T A Michalske. Probing Adhesion Forces at the Molecular Scale. *Journal of the American Chemical Society*, 117(13):3830–3834, 1995.
- [80] G A Jeffrey and W Saenger. *Hydrogen Bonding in Biological Structures*. Springer, 1 edition, 1991.

10 Probing the Adhesion Properties of Alginate Hydrogels

- [81] D V Vezenov, A Noy, and P Ashby. Chemical force microscopy: probing chemical origin of interfacial forces and adhesion. *Journal of Adhesion Science and Technology*, 19(3-5):313, 2005.
- [82] M Grandbois. How Strong Is a Covalent Bond? *Science*, 283(5408):1727–1730, 1999.
- [83] S Wohlrab, K Spieß, and T Scheibel. Varying surface hydrophobicities of coatings made of recombinant spider silk proteins. *Journal of Materials Chemistry*, 22(41):22050, 2012.
- [84] M Humenik, A M Smith, and T Scheibel. Recombinant Spider Silks—Biopolymers with Potential for Future Applications. *Polymers*, 3(4):640–661, 2011.
- [85] D Huemmerich, C W Helsen, S Quedzuweit, J Oschmann, R Rudolph, and T Scheibel. Primary structure elements of spider dragline silks and their contribution to protein solubility. *Biochemistry*, 43(42):13604–13612, 2004.
- [86] Y I Rabinovich, J J Adler, A Ata, R K Singh, and B M Moudgil. Adhesion between Nanoscale Rough Surfaces. *Journal of Colloid and Interface Science*, 232(1):10–16, 2000.
- [87] M D Porter, T B Bright, D L Allara, and C E D Chidsey. Spontaneously organized molecular assemblies. 4. Structural characterization of n-alkyl thiol monolayers on gold by optical ellipsometry, infrared spectroscopy, and electrochemistry. *Journal of the American Chemical Society*, 109(12):3559–3568, 1987.
- [88] D Pussak, M Behra, S Schmidt, and L Hartmann. Synthesis and functionalization of poly(ethylene glycol) microparticles as soft colloidal probes for adhesion energy measurements. *Soft Matter*, 8(5):1664, 2012.
- [89] B R Neugirg, N Helfricht, S Czich, H-W Schmidt, G Papastavrou, and A Fery. Long-range interaction forces between 1,3,5-cyclohexanetrissamide fibers in crossed-cylinder geometry. *Polymer*, 102:363–371, 2016.

CHAPTER 11

Appendix

11.0.1 Complete Supporting Information for Chapter 4

Supporting Information

A direct biocombinatorial strategy towards next generation, mussel-glue inspired saltwater adhesives.

Journal: Journal of the American Chemical Society

Corresponding Author: Hans G. Börner

Other Authors: Patrick Wilke, Nicolas Helfricht, Andreas Mark, Georg Papastavrou, Damien Faivre

*to whom correspondence is to be addressed

Prof. Dr. Hans G. Börner: Humboldt-Universität zu Berlin, Brook-Taylor-Str. 2, 12489 Berlin, Germany

E-Mail: h.boerner@hu-berlin.de

Phone: +49 (0)30-2093 7348

Fax: +49 (0)30 2093-7500

Contents

Materials.....	4
Phage Display.....	4
Peptide/Conjugate Synthesis.....	4
Peptide/Conjugate activation.....	5
Quartz crystal microbalance.....	5
Single Molecule AFM measurements.....	5
Instrumentation.....	5
Methods.....	7
Peptide and bioconjugate activation.....	7
UV/Vis kinetics.....	7
Quartz Crystal Microbalance.....	7
Single Molecule AFM Measurements.....	7
Phage Display Procedure.....	9
Preparation of aluminum oxide samples.....	9
Enzymatic processing of phage library.....	9
Panning procedure.....	9
Phage Amplification.....	10
Phage Titering.....	10
Sequence determination.....	10
Reference experiments.....	10
Synthesis of peptides and peptide-poly(ethylene oxide) conjugates.....	13
Analysis of synthesized peptides/conjugates.....	14
Analysis of HSYSGWSPYRSG (Pep ₃).....	14
Analysis of HSYSGWSPYRSGGGGC (Pep _{3Y}).....	15
Analysis of HS-Dopa-SGWSP-Dopa-RSGGGGC (Pep ₃ ^{*synth.}).....	17
Analysis of YPATYYGMRS- <i>block</i> -PEO ₇₂ (Pep ₁ -PEO).....	18
Analysis of YHPNGMNPYTKA- <i>block</i> -PEO ₇₂ (Pep ₂ -PEO).....	19
Analysis of HSYSGWSPYRSG- <i>block</i> -PEO ₇₂ (Pep ₃ -PEO).....	20
Analysis of HS-Dopa-SGWSP-Dopa-RSG- <i>block</i> -PEO ₇₂ (Pep ₃ ^{*synth.} -PEO).....	21
Analysis of HTEHHDKSHRA- <i>block</i> -PEO ₇₂ (Pep ₄ -PEO).....	22
Analysis of Dopa-G-Dopa-G- <i>block</i> -PEO ₇₂ (Pep ₅ -PEO).....	23
Enzyme activity assay.....	24
Enzymatic activation of peptide and peptide-polymer conjugate.....	25
MALDI-TOF-MS of activated products.....	25
Analysis of HSY*SGWSPY*RSG (Pep ₃ [*]) [activation to quinone].....	25
Analysis of Y/Y*PATY*Y*GMRS- <i>block</i> -PEO ₇₂ (Pep ₁ [*] -PEO) [activation to catechol].....	26
Analysis of Y*HPNGMNPY*TKA- <i>block</i> -PEO ₇₂ (Pep ₂ [*] -PEO) [activation to catechol].....	27
Analysis of HSY*SGWSPY*RSG- <i>block</i> -PEO ₇₂ (Pep ₃ [*] -PEO) [activation to catechol].....	28
QCM measurements.....	29
Control experiments.....	29
Sodium ascorbate reference experiment (regular buffered).....	29
Tyrosinase reference experiment (regular buffered).....	29

11 Appendix

Adsorption and Desorption Experiments	31
QCM experiment: Pep ₁ -PEO adsorption prior to the activation.....	31
QCM experiment: Pep ₂ -PEO control (adsorption prior to the activation).....	31
QCM experiment: Pep ₃ -PEO control (adsorption prior to the activation).....	32
QCM experiment: Pep ₃ -PEO adsorption of a tyrosine-free sequence from phage display	33
QCM experiment: Pep ₃ -PEO (adsorption of synthesized dopa reference).....	34
QCM experiment: Pep ₁ [*] -PEO (adsorption after activation).....	34
QCM experiment: Pep ₂ [*] -PEO (adsorption after activation).....	35
QCM experiment: Pep ₃ [*] -PEO (adsorption after activation).....	37
QCM experiment: Pep ₃ ^{*synth} -PEO (adsorption of synthesized “active” conjugate).....	38
QCM experiment: Pep ₃ ^{*synth} -PEO at 55 °C (adsorption of synthesized “active” conjugate).....	39
QCM experiment: NSS wash of Pep ₃ ^{*synth} -PEO coated surface (coated at 55°C).....	40
Anti-fouling experiments: BSA control experiment.....	41
Anti-fouling experiments: BSA on 22 °C Pep ₃ [*] -PEO coated surface at 22 °C	42
Anti-fouling experiments: BSA on 55 °C Pep ₃ [*] -PEO coated surface at 22 °C	43
Anti-fouling experiments: Fetal bovine serum control experiment.....	44
Anti-fouling experiments: Fetal bovine serum on 55 °C Pep ₃ [*] -PEO coated surface at 22 °C.....	45
Anti-fouling experiments: Human serum control experiment.....	46
Anti-fouling experiments: Human serum on 55 °C Pep ₃ [*] -PEO coated surface at 22 °C.....	47
Measurements under saltwater conditions.....	48
Tyrosinase control experiment (in 599 mM NaCl).....	48
QCM experiment: Pep ₃ -PEO control in 599 mM NaCl (adsorption prior to the activation).....	49
QCM experiment: Pep ₃ [*] -PEO in 599 mM NaCl (adsorption after activation)	50
QCM experiment: Pep ₃ ^{*synth} -PEO in 599 mM NaCl (adsorption of synthesized “active” conjugate).....	51
Langmuir kinetics:.....	52
QCM experiment: Pep ₃ [*] -PEO (Langmuir kinetics).....	52
QCM experiment: Pep ₃ -PEO in 599 mM NaCl (Langmuir kinetics)	53
QCM experiment: Pep ₃ [*] -PEO in 599 mM NaCl (Langmuir kinetics).....	53
Langmuir Isotherms: Data evaluation	55
Single molecule force spectroscopy: Data evaluation.....	56
Sequence analysis of Pep ₃ [*] -PEO	58
UV-kinetics of Pep ₃ ^{*synth} -PEO.....	59
References.....	60

Materials

Phage Display

M13 phage display library and E.coli ER2738 host strain (F' *proA*⁺*B*⁺*lacI*^f Δ (*lacZ*)M15 *zzf*: *Tn10*(*Tet*^R)/*fhuA2 glnV* Δ (*lac-proAB thi-1* Δ (*hsdS-mcrB*)5) were purchased from New England BioLabs Inc. (Frankfurt am Main, Germany) with a tyrosine content of 3.9 %. Yeast extract, Tween20 and tris(hydroxymethyl) aminomethane (Tris base) were obtained from Fisher BioReagents. Glycine (>99%), 3-(*N*-Morpholino)propanesulfonic acid (MOPS) and poly(ethyleneglycol) (PEG8000) were purchased from Acros organics. Tryptone (enzymatic digest from casein, Fluka), sodium chloride (J.T. Baker), agarose (Serva) and *N,N*-dimethylformamide (DMF, Biosolve) were used as received. Furthermore, magnesium chloride hexahydrate (MgCl₂·H₂O, >99%) as well as isopropyl β -D-thiogalactoside (IPTG, >99%) and 5-bromo-4-chloro-3-indolyl- β -D-galactoside (Xgal, >99%) were obtained from Roth. Sodium azide (NaN₃) and tetracycline were purchased from Sigma-Aldrich. Trypsin solution (0.25% w/v in BPS w/ Ca²⁺) was obtained from Biochrom AG (Berlin, Germany).

Peptide/Conjugate Synthesis

N- α -Fmoc protected amino acids Fmoc-Ala-OH, Fmoc-Arg(Pbf)-OH, Fmoc-Asp(*t*Bu)-OH, Fmoc-Asn(Trt)-OH, Fmoc-Glu(*t*Bu)-OH, Fmoc-Gly-OH, Fmoc-His(Boc)-OH, Fmoc-Lys(Boc)-OH, Fmoc-Met-OH, Fmoc-Pro-OH, Fmoc-Ser(*t*Bu)-OH, Fmoc-Thr(*t*Bu)-OH, Fmoc-Trp(Boc)-OH, Fmoc-Tyr(Boc)-OH, scavenger tri-methyl silylbromide (TMSBr) as well as coupling reagents 2-(1H-benzotriazole-1-yl)-1,1,3,3-tertamethyluronium-hexafluorophosphate (HBTU), (benzotriazol-1-yloxy)tripyrrolidino-phosphoniumhexa-fluorophosphate (PyBOP), and *N*-methyl-2-pyrrolidone (NMP, 99.9%, peptide synthesis grade) were used as received from IRIS Biotech GmbH (Marktredwitz, Germany). Fmoc-DOPA(acetonid)-OH was purchased from Novabiochem (Merck group, Darmstadt, Germany). TentaGel PAP resin (PEG attached peptide resin, loading: 0.27 mmol/g; Mw = 3200, PDI = 1.04) and TentaGel S RAM resin (loading: 0.24 mmol/g) were obtained from Rapp Polymere GmbH (Tübingen, Germany). *N,N*-diisopropyl ethylamine (DIPEA; peptide grade), piperidine (peptide grade), 2,5-Dihydroxybenzoic acid (99%) were purchased from Acros Organics and used without further purification. Triethylsilane (TES; Alfa Aesar, Karlsruhe, Germany, 98+ %), α -Cyano-4-hydroxy-cinnamic acid (99%, Sigma Aldrich) and guanidine hydrochloride (99.5%, Roth, Karlsruhe, Germany) were used as received. Trifluoroacetic acid (TFA; Acros Organics, peptide grade) was distilled prior to use. Dichloromethane (DCM, IRIS Biotech GmbH, peptide grade) was distilled from CaH₂ prior to use.

Peptide/Conjugate activation

Tyrosinase (\approx 4300 units/mg) from mushroom, *L*-tyrosine, potassium phosphate monobasic (\geq 98%) and potassium phosphate dibasic (\geq 98%) were purchased from Sigma-Aldrich and used as received. Tyrosinase was stored at -20°C . *L*-3-(3,4-Dihydroxyphenyl)alanine (99%) (Acros Organics), *L*(+)-ascorbic acid (\geq 99%, Roth, Karlsruhe, Germany) and *L*(+)-ascorbic acid sodium salt (\geq 99%, Fluka) were used without further purification.

Quartz crystal microbalance

Human serum and Helmanex were purchased from Sigma-Aldrich. Serum was filtered prior to use via Rotalibo syringe filter (Roth, KY62.1, pvdf, pore size $0.2\mu\text{m}$, $\text{Ø}33$ mm). Sodium sulfate (Roth), sodium hydrogen carbonate (Roth), potassium chloride (Fluka), potassium bromide (Acros), calcium chloride dihydrate (Fluka), strontium chloride hexahydrate (Roth) and boric acid (Roth) were used as received.

Single Molecule AFM measurements

Malhex-NH-PEG-O-C₃H₆-CONHS ($M = 9256$ Da, $D = 1.03$, Rapp Polymere GmbH, Tübingen, Germany) and 3-aminopropyl-diisopropylethoxysilane (ABCR, Karlsruhe, Germany) were used as received for the modification of the AFM-cantilevers (PPP-CONT, Nanosensors, Wetzlar, Germany). The heterofunctional PEO has been stored at -20°C and was dissolved in dimethylsulfoxide (anhydrous, \geq 99.9%, Sigma-Aldrich). Sodium chloride (\geq 99%, Aldrich) and formic acid (\geq 99%, Grüssing, Germany) were used as received.

Instrumentation

^1H nuclear magnetic resonance spectra ($^1\text{H-NMR}$) were recorded on a Bruker AV 500 spectrometer at 500 MHz in TFA-*d*1 at room temperature.

Fourier Transform Infrared FTIR-Spectroscopy was conducted on a JASCO FT/IR-4200 Spectrometer in a range of $600 - 4000\text{ cm}^{-1}$. Samples were measured in solid form at 24°C .

Mass spectrometry (MALDI-TOF MS) was performed on a Bruker autoflex III smartbeam with matrix assisted laser desorption/ionization and time of flight detector. On the sample plate, $2\mu\text{L}$ of peptide or peptide-polymer conjugate (dissolved in potassium phosphate buffer [17 mM, pH 6.5]) were mixed with $1\mu\text{L}$ matrix solution, consisting of 10 mg/mL 2,5-dihydroxybenzoic acid or 7 mg/mL α -Cyano-4-hydroxy-cinnamic acid in MQ-water-acetonitrile (1:1, v/v) with 0.1 % TFA. Samples were air-dried at ambient temperature. Measurements were performed in linear positive mode.

Peptides were purified via preparative HPLC at 6 mL/min on an Agilent 1100 series using a Polaris C18 (Varian, 5 μ m, 250x10, 220Å) column and Solvent A/Solvent B-mixtures (Solvent A: 98.9 % MilliQ H₂O: 1.0 % Acetonitrile:0.1 % TFA; Solvent B: 98.9 % Acetonitrile:1.0 % MilliQ H₂O:0.1 % TFA) as solvents.

Analytical HPLC-MS was performed on a Shimadzu (Germany) system using a SLC-10A vp system controller, a SPD-10A vp UV-VIS detector and a LC-10AD vp liquid chromatograph pump unit. Chromatographic separation was conducted on a EC 150/2 NUCLEODUR Polar Tec (Machery Nagel) reversed phase column using Solvent A/Solvent B-mixtures (Solvent A: 99.9 % MilliQ H₂O:0.1 % TFA; Solvent B: 99.9 % Acetonitrile: 0.1 % TFA) as solvents. Finally, mass spectrometry detection (ESI-MS) was performed on a high performance liquid chromatograph electron spray ionization mass spectrometer (LC-ESIMS) (Shimadzu, qp8000, Germany) in positive acceleration mode.

LC-MS/MS measurements were performed on a LTQ-Orbitrap XL mass spectrometer (Thermo Scientific) with nano LC system (Ultimate 3000, Dionex) using a PepMap RSLC Viper (75 μ m · 15 cm; Dionex) capillary column and a PepMap C18 nano trap column (75 μ m · 2 cm; Dionex). As mobile phases, solvent A (0.1 % (v/v) formic acid in MilliQ-water) and solvent B (0.1 % (v/v) formic acid in acetonitrile) were applied.

Quartz crystal microbalance measurements were conducted on a Q-sense E1 single-sensor QCM-D module as well as on a Q-sense E4 module (Q-Sense, Sweden) with QE 401 Electronic Unit and equipped with a multichannel pump (IPC Ismatec SA, Switzerland).

UV/vis spectroscopy (enzymatic assay) was carried out on a Varian Cary 100 Bio UV-visible Spectrophotometer (Agilent Technologies) with a Varian Cary Temperature Controller unit using quartz cuvettes (enzymatic assay). Peptide/Conjugate activation was monitored on a EonC Microplate Spectralphotometer (BioTek, Bad Friedrichshall, Germany) using UV 96 well plates (Fisher Scientific, Schwerte, Germany). Kinetic plots were obtained at 25 °C reading at 280 nm and 325 nm, respectively.

The single molecule force spectroscopy was performed with a MFP-Plus equipped with an ARC2-controller and a standalone base (Asylum Research, Santa Barbara, CA). The instrument was placed on an active vibration isolation and an acoustic shielding.

Methods

Peptide and bioconjugate activation

Enzymatic activation kinetics of peptides and peptide-polymer conjugates were carried out using 100 units of tyrosinase and 0.29 μmol substrate in a final volume of 1 mL incubated at 25 °C. Peptide and conjugates (0.29 $\mu\text{mol/mL}$) were dissolved in potassium phosphate buffer (17 mM, pH 6.5). Subsequently, the “activation” solution was prepared by mixing 33 μL of 2.2 mM (for UV kinetics; activation to quinone) ascorbic acid or 220 mM (for qcm measurements, activation to dopa) sodium ascorbate and 100 units of tyrosinase in 50 mM potassium phosphate buffer (pH 6.5) with 10 μL of 0.2 mM DOPA in a separate tube. To start the oxidation, this solution was transferred to the peptide or conjugate. Kinetic plots were obtained for 15 h. Peptide conversion was evaluated via MALDI-TOF-MS.

UV/Vis kinetics

UV-Vis spectroscopy was carried out on a Varian Cary 100 Bio UV-visible Spectrophotometer (Agilent Technologies) with a Varian Cary Temperature Controller unit using quartz cuvettes (enzymatic assay). Peptide/Conjugate activation was monitored on a EonC Microplate Spectrophotometer (BioTec, Germany) using UV 96 well plates (Fisher Scientific, Germany). Kinetic plots were obtained at 25 °C reading at 280 nm.

Quartz Crystal Microbalance

Piezoelectric sensor crystals coated with 50 nm aluminum oxide (Q-Sense, Sweden) were cleaned in an ultrasonic bath with 2% Helmanex in MilliQ-water for 15 minutes and ethanol for 10 minutes prior to use. Subsequently, the sensors were thoroughly washed by MilliQ-water and dried under compressed air flow. Finally, crystals were cleaned in a ZEPTO plasma cleaner (diener electronics, Germany) for 3 min at 75 W by air plasma. Immediately afterwards, the sensors were mounted into the flow chamber and incubated until the frequency signals were constant (1-3 h) with buffer using a flow rate of 100 $\mu\text{L/min}$. Subsequently, samples with a concentration of 50 mg/mL in buffer were pumped into the flow chamber and signals were again monitored until being constant. Following washing steps were conducted with 0.8 mM potassium phosphate buffer (pH 6.5), 599 mM NaCl, 10 mg/mL bovine serum albumin (BSA) as well as fetal bovine serum and human serum. Experiments were performed at 22° C (unless stated otherwise) in a stop-flow mode, and overtones 3, 5, 7, 9, 11 and 13 were recorded. If not stated otherwise, the third overtones of all experiments were used for evaluation of the frequency shift.

Single Molecule AFM Measurements

In order to detect the detachment of single peptides from the aluminum oxide surface the peptide has to be covalently coupled to the tip of an AFM cantilever by means of a PEO-spacer.[1,2] AFM contact mode cantilevers made from silicon (PPP-CONT without Al-coating and a nominal spring constant of about 0.2

N/m, Nanosensors) were cleaned with MilliQ-water and ethanol (p.a., VWR) before modification. In order to obtain a large number of OH-groups at the Si-surface the cantilevers were exposed to O₂-plasma (0.2 mbar, 100% O₂) in a plasma cleaner (Plasma Technology) connected to an O₂-generator (DeVilbiss Healthcare). The silanization has been carried out in the gas phase. The freshly cleaned cantilevers were directly transferred into a petri dish containing 500 µL 3-aminopropyltriethoxysilane. The dish has been placed in a desiccator to which vacuum has been applied for about 1 min by means of a membrane pump (Vacuubrand, Germany). The silanization has been carried out overnight for at least 12 h. After silanization, the cantilevers were thoroughly cleaned with ethanol in order to remove unreacted silane and rinsed with the buffer solution (50 mM potassium phosphate, pH 7.5, 150 mM NaCl) used for the coupling of the PEO-spacer to the silanized cantilevers. For the coupling the cantilevers were placed in vessel containing the buffer solution. The malhex-PEO-NHS-spacer was dissolved in dry DMSO resulting in final concentration of 20 mM; 50 µL of this solution were added for each mL of buffer solution. The reaction was performed for 1 h at room temperature in the dark. After the reaction the cantilever were first cleaned with the potassium phosphate buffer (pH 7.5) and afterwards with the buffer solution for peptide coupling (0.1 M potassium phosphate, pH 7.0). Coupling of the peptides was carried out simultaneously but in different reaction vessels. Each of the two peptides (Pep₃ and Pep₃^{*-synth}) were both dissolved in MilliQ-water with a final concentration of 0.1 mM. For each of the peptides 0.8 mL of peptide solution was added to 3.2 mL potassium phosphate buffer (0.1 M, pH 7.0, 0.1 % formic acid) in a separate vessel. After 1 h reaction time, the cantilevers were rinsed first with the phosphate buffer (0.1 M potassium phosphate, pH 7.0) and then with the buffer solution (0.8 mM potassium phosphate, pH 6.5) used also for the AFM-measurements. The peptide-PEO-modified cantilevers were stored before the measurements in this buffer for not more than one week and ascorbic acid was added to avoid oxidation of the peptides during storage (0.7 mM, degassed solutions). Directly before use the cantilevers were rinsed with copious amounts of buffer solution containing no ascorbic acid.

Typically, the single molecule experiments have been performed with ramp-size of about 250 nm, which is significantly larger than the length of the PEO-spacer. The single force curves were acquired at a cantilever velocity of about 100 nm/s and data acquisition rate of 50000 kHz. In order to increase the probability of peptide binding, a dwell time of 4 seconds has been applied during which the probe remains in contact with the sample surface. For each peptide-PEO-modified cantilever at least 1000 curves at 5 different positions have been acquired. All measurements were performed in 0.8 mM potassium phosphate buffer (pH 6.5, without addition of ascorbic acid). The pH has been controlled directly before the measurements. As sample the same sensors as used for the QCM measurements have been used. The spring constant of the cantilevers has been determined by the thermal noise method.[3] For the conversion of the raw data program based on standard algorithms written in IGOR Pro (Wavemetrics) has been used.

Phage Display Procedure

Preparation of aluminum oxide samples

Prior to panning procedure, aluminum oxide samples (1×1×0.1 cm) were cleaned in an ultrasonic bath using cyclohexane (3 min), ethanol (3 min) and ultrapure water (5 min). Subsequently, plates were immobilized on a petri dish (Ø = 5.2 cm) under sterile conditions. Directly before treatment with activated phage library, the surface was incubated with TBST for 5 minutes and washed with 1 mL TBS.

Enzymatic processing of phage library

Enzymatic processing was performed with tyrosinase (20 u) and 10µL of the phage library or amplified phages from previous rounds ($c > 10^9$ pfu·mL⁻¹) including co-factors ascorbic acid (0.1 mM) and L-dopa (50 nM) in a total volume of 200 µL potassium phosphate (17 mM; pH 6.5) buffered solution. This mixture was incubated at 25 °C for 3 h in the dark. Subsequently, phages were precipitated with 34 µL of PEG/NaCl solution (20% w/v PEG-8000, 2.5 M NaCl) on ice for 30 minutes. Isolation of the modified library and removal of enzyme was achieved by centrifugation at 4 °C and 8500 rpm for 15 minutes. Afterwards, the supernatant was discarded followed by resuspension of phages with 1 mL citrate buffer (50 mM; pH 4.0). Noteworthy, an acidic pH was chosen as biopanning at neutral pH resulted in nonspecific binding of phages exclusively leading to phage sequences without insert.

Panning procedure

Activated phage library was added to the petri dish containing the aluminum oxide substrate. Subsequently, the petri dish was shaken in a nutating mixer (Labnet International, Inc.) in order to allow contact of phages with the substrate 10 times. Immediately afterwards, the substrate was washed 3 times with 1 mL TBST (50 mM Tris-HCl [pH 7.5], 150 mM NaCl, 0.5 % v/v Tween 20) and transferred into a centrifuge tube. The substrate was washed 10 times by repetitive treatment with 2 mL glycine/HCl (0.2 mM, pH 2.2) by vortexing for 1 min, decantation of the supernatant and rinsing with 1 mL TBST followed by transferring into a new tube after 5 steps. Finally, the aluminum oxide substrate was washed with 1 mL TBS (50 mM Tris-HCl [pH 7.5], 150 mM NaCl). Subsequent elution of strong binding phages was achieved by incubation with 2 mL Trypsin solution (0.25% w/v in BPS w/ Ca²⁺) for 30 min by shaking at 25 °C and 500 rpm. Afterwards, the digestion was stopped by addition of 6.8 mL SB-medium (10g·L⁻¹ MOPS, 20g·L⁻¹ yeast extract, 30 g·L⁻¹ tryptone, adjusted to pH 7.0). For rounds two and three, 15 and 20 washing steps were applied to increase selection pressure.

Phage Amplification

Pre-cultures of E.coli (ER2738) were grown overnight in LB-medium (6 g·L⁻¹ yeast extract, 10 g·L⁻¹ tryptone, 5 g·L⁻¹ NaCl) containing 20 µg·mL⁻¹ tetracycline at 37 °C and 220 rpm agitation. For amplification of eluted phages, a total of 40 mL containing phage solution (approx. 8 mL) and 32 mL LB-medium was inoculated with 400 µL of the pre-culture in a sterile flask and incubated at 37 °C for 4.5 h and 220 rpm. Subsequent removal of E.coli cells was achieved by centrifugation at 4 °C and 4000 rpm for 20 minutes. Phage precipitation occurred at 4 °C overnight by addition of 6.6 mL PEG/NaCl solution. Phages were isolated by centrifugation at 4 °C and 4500 rpm for 45 min, discarding the supernatant and re-suspension in 1 mL TBS. The obtained supernatant was transferred into a new tube and centrifuged at 4 °C and 8500 rpm for 10 min. This was repeated a second time for complete removal of E.coli cells. Phages were then precipitated by addition of 170 µL PEG/NaCl and incubation on ice for 30 min. After centrifugation, phages were re-suspended in 100 µL TBS + 0.02 % NaN₃ and stored at 4 °C. Obtained phages were used for consecutive panning rounds.

Phage Titering

For quantification of eluted and amplified phages an E.coli (ER2738) culture was incubated in LB-medium at 37 °C and 220 rpm until mid-log phase was reached (OD₆₀₀ ~ 0.5). Subsequently, 200 µL of this culture were infected with a phage dilution series (1:10¹ - 1:10⁻² for eluted phages; 1:10⁻⁸ - 1:10⁻¹¹ for amplified phages) incubating for 5 min. Then, infected cultures were transferred to tubes containing 45 °C Top Agar (LB-medium containing 7 g·L⁻¹ agarose and 1 g·L⁻¹ MgCl₂·H₂O) and briefly vortexed. Immediately afterwards, the culture was poured onto a pre-warmed (~37 °C) LB/IPTG/Xgal plate (LB-medium containing 15 g·L⁻¹ agar, 50 mg·L⁻¹ IPTG and 40 mg·L⁻¹ Xgal) and gently spread evenly. Plates were allowed to cool for 5 min, inverted and incubated at 37 °C overnight. Phages were counted on plates with ~100 plaques.

Sequence determination

Single plaques were picked and phages amplified as described above. Phage-DNA was extracted via QUIAGEN QIAprepSpin M13 Kit (50). DNA sequencing was performed by StarSEQ GmbH (Mainz, Germany).

Reference experiments

For third round reference experiments, panning procedures were performed as described above, excluding tyrosinase treatment. After phage titering, cultures for dilutions of 1:10¹ typically yielded 0-40 phages, whereas enzyme activated libraries reached 10-40 on 1:10⁻² dilutions.

11 Appendix

Phage sequences selected after 3rd of biopanning including enzymatic activation of phage library:

1. YANATIYNKIKR (1×)
2. YPATYYGMRSPTS (2×)
3. YHPNGMNPYTKA (21×)
4. HSYSGWSPYRSG (2×)
5. RSAVIRYQTASY (1×)
6. YNFQHFNRFLTG (1×)
7. DGLVNWQYGLSH (1×)
8. DAHHYSARNHGQ (1×)
9. HTEHHDKSHSRA (3×)
10. VSLPKNFHSNPR (1×)
11. TMLTHNPKPVKH (1×)
12. ARCDPTQNRTLW (1×)
13. DILPVSQRHFVKR (1×)
14. FPLQSSFPVKAN (1×)
15. Without insert (6×)

Reference experiment: Third round of phage display without enzymatic activation:

1. without insert (1×)
2. AGNNPAGTTMQM (1×)
3. DILPVSQRHFVKR (1×)
4. HYSKPDQSFYKV (1×)
5. ISLHRKTRLQRK (1×)
6. YHPNGMNPYTKA (1×)
7. IGPBKLTTLAMQ (1×)
8. HEVPGRLAYHAS (1×)
9. VSHAAAGRAAEM (1×)
10. FPLQSSFPVKAN (1×)

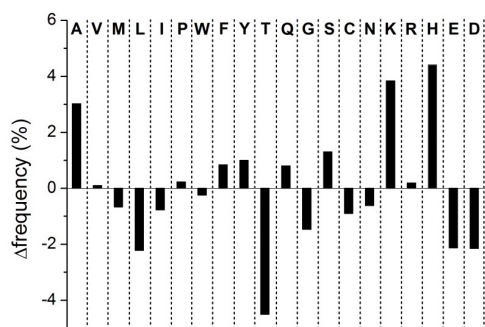


Figure S1. Frequency changes of amino acids found in phage display reference compared to the frequencies of the original library.

Direct biopanning of the phage library from the second round leads only to few bound phages on titer plates (0-40 without dilution). Analyzed sequences generally show a similar result compared to the enzymatically processes library, as one might expect. The important exception is the only minor enriched tyrosine residues, highlighting the phage processing to generate strongly adhesive dopa.

Synthesis of peptides and peptide-poly(ethylene oxide) conjugates

Standard Fmoc-amino acid derivatives were coupled on peptide synthesis resin supports with an Applied Biosystems ABI 433a peptide synthesizer. For peptides, a TentaGel S RAM resin (loading 0.24 mmol/g, 0.1 mmol) was applied. Peptide-polymer conjugates were synthesized on TentaGel PAP resin (loading: 0.27 mmol/g; $M_n = 3200$, $M_w/M_n = 1.06$ (GPC), 0.1 mmol). Peptide synthesis was performed in NMP and the standard ABI-Fastmoc protocols (single coupling, no capping) were applied. Fmoc-amino acid coupling was facilitated by HBTU/DIPEA. After final Fmoc removal the resin was transferred to a 10 mL syringe reactor and subsequently washed with dichloromethane. Liberation of the peptide or the bioconjugates was conducted with 95:4:1 vol.% TFA/H₂O/TES for 2.5 h and resulted in fully deprotected peptide or peptide-polymer conjugates. Products were isolated by precipitation with diethyl ether and subsequent centrifugation. Purified conjugates were obtained by dialysis with 0.1% w/v guanidine HCl against MQ-water at pH 6-7 followed by lyophilization from water.

In total, peptides HSYSGWSPYRSG (Pep₃), HS-Dopa-SGWSP-Dopa-RSGGGGC (Pep₃^{*-synth.}, for SMFS) as well as peptide-polymer conjugates YPATYYGMRSPPS-*block*-PEO₇₂ (Pep₁-PEO), YHPNGMNPYTKA-*block*-PEO₇₂ (Pep₂-PEO), HSYSGWSPYRSG-*block*-PEO₇₂ (Pep₃-PEO), HS-Dopa-SGWSP-Dopa-RSG-*block*-PEO₇₂ (Pep₃^{*-synth.}-PEO) and HTEHHDKSHRA -*block*-PEO₇₂ (Pep₄-PEO) were obtained by this method.

Analysis of synthesized peptides/conjugates

Analysis of HSYSGWSPYRSG (Pep₃)

HPLC

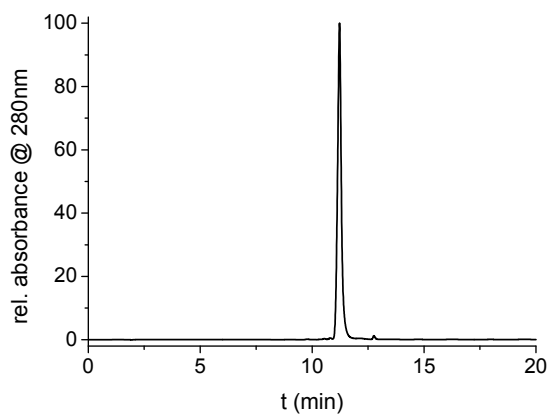


Figure S2. HPLC of HSYSGWSPYRSG (Pep₃) using a gradient of 0 % - 30 % Acetonitrile in ultrapure water within 20 min (rt = 11.2 min).

MALDI

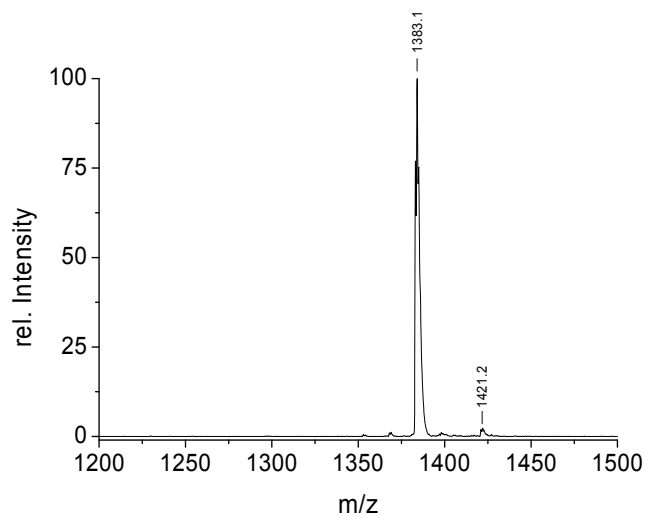
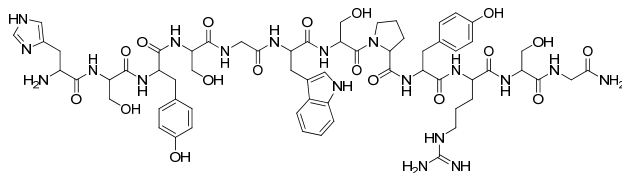


Figure S3. Maldi-TOF-MS of HSYSGWSPYRSG (Pep₃).

S14



$M[\text{Th}] = 1382.5 \text{ Da}$

$M[\text{peak}] = 1383.1 [\text{M}+\text{H}]^+, 1421.2 [\text{M}+\text{K}]^+$

The signals can be assigned within $\pm 1 \text{ Da}$ accuracy.

$^1\text{H-NMR}$ (500 MHz, TFA-d, δ in ppm): 8.55-8.51 (m, 1 H, $\text{CH}_{\text{Ar,H}}$), 7.50-7.46 (m, 1 H, $\text{CH}_{\text{Ar,H}}$), 7.44-7.27 (m, 1 H, $\text{CH}_{\text{Ar,W}}$), 7.13-7.07 (m, 2 H, $2\times\text{CH}_{\text{Ar,Y}}$), 7.04-6.98 (m, 2 H, $2\times\text{CH}_{\text{Ar,Y}}$), 6.87-6.77 (m, 4 H, $4\times\text{CH}_{\text{Ar,Y}}$), 5.07-4.99 (m, 1 H, CH_Y), 4.95-4.88 (m, 1 H, CH_Y), 4.86-4.74 (m, 5 H, CH_W , $4\times\text{CH}_S$), 4.70-4.55 (m, 2 H, CH_R , CH_P), 4.50-4.42 (m, 1 H, CH_H), 4.29-4.05 (m, 10 H, $4\times\text{CH}_{2,S}$, $\text{CH}_{2,G}$), 4.03-3.79 (m, 2 H, $\text{CH}_{2,G}$), 3.33-3.16 (m, 4 H, $2\times\text{CH}_{2,Y}$), 3.12-2.89 (m, 4 H, $\text{CH}_{2,W}$, $\text{CH}_{2,H}$), 2.30-2.21 (m, 2 H, $\text{CH}_{2,R}$), 2.08-1.81 (m, 4 H, $\text{CH}_{2,P,R}$), 1.77-1.56 (m, 4 H, $\text{CH}_{2,P,R}$), 1.38-1.22 (m, 2 H, $\text{CH}_{2,P}$)

Analysis of HSYSGWSPYRSGGGGC (Pep_{3Y})

HPLC

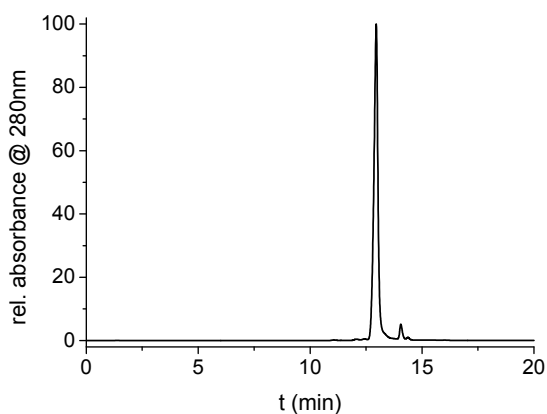


Figure S4. HPLC of HSYSGWSPYRSGGGGC (Pep_{3Y}) using a gradient of 0 % - 30 % Acetonitrile in ultrapure water within 20 min (rt = 12.9 min).

Analysis of HS-Dopa-SGWSP-Dopa-RSGGGGC (Pep₃^{*-synth.})

HPLC

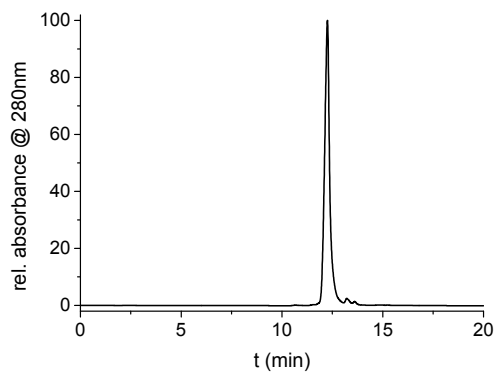


Figure S6. HPLC of HS-Dopa-SGWSP-Dopa-RSGGGGC (Pep₃^{*-synth.}) using a gradient of 0 % - 30 % Acetonitrile in ultrapure water within 20 min (rt = 12.2 min).

ESI-MS

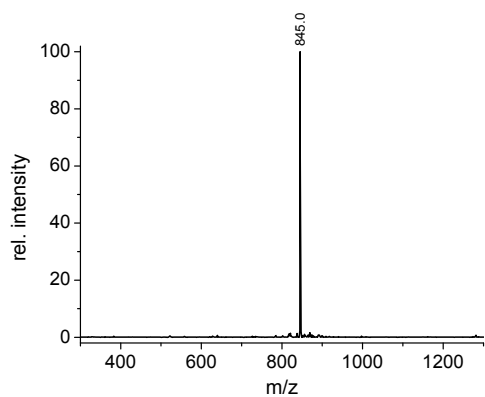
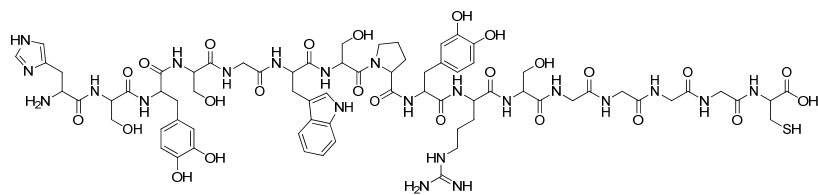


Figure S7. ESI-MS of HS-Dopa-SGWSP-Dopa-RSGGGGC (Pep₃^{*-synth.}).



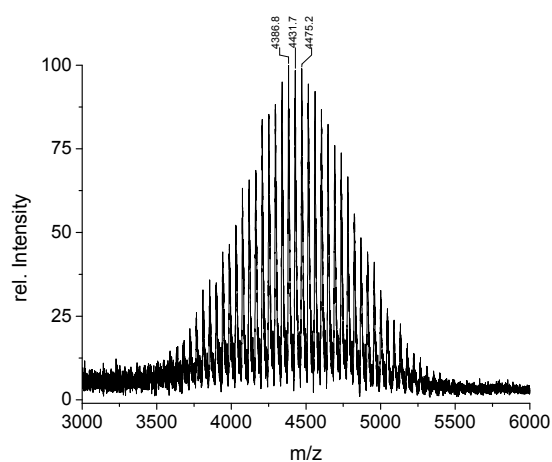
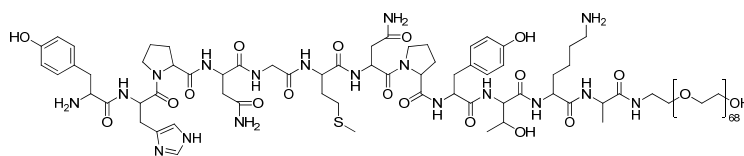
m/z (%) in g/mol: $M_{Th} = 1688.8$ g/mol:

$M_{peak} = 845.0$ (100) $[M+H]^{2+}$

The signals can be assigned within ± 1 Da accuracy.

Analysis of YHPNGMNPYTKA-*block*-PEO₇₂ (Pep₂-PEO)

MALDI-TOF-MS

**Figure S9.** Maldi-TOF-MS of YHPNGMNPYTKA-*block*-PEO₇₂ (Pep₂-PEO).

$\Delta m = 44$ Da, characteristic of the EO repeat units.

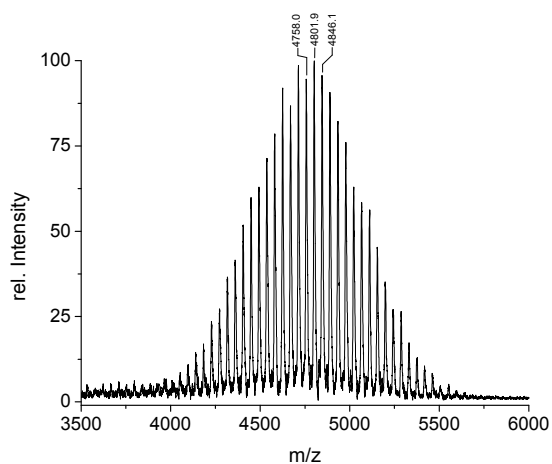
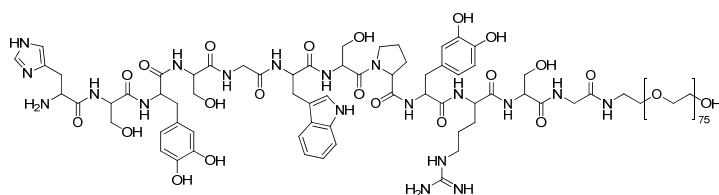
$M[\text{peak}] = m/z$ 4431.7 assignable to $[M(\text{Pep}_2\text{-PEO}_{69}) + \text{H}]^+ = 4432.1$ Da within ± 1 Da accuracy.

¹H-NMR (500 MHz, TFA-d, δ in ppm): 8.56 (s, 1 H, CH_{Ar,H}), 7.40 (s, 1 H, CH_{Ar,H}), 7.16-7.03 (m, 4 H, 4×CH_{Ar,Y}), 6.93-6.81 (m, 4 H, 4×CH_{Ar,Y}), 5.31-5.24 (m, 3 H, CH_{Y,H,M}), 4.97-4.82 (m, 2 H, 2×CH_N), 4.70-4.55 (m, 5 H, CH_K, 2×CH_{T,P}), 4.52-4.43 (m, 3 H, CH_{2,G}, CH_A), 4.36-4.17 (m, 1 H, CH_Y), 4.04-3.55 (m, 332 H, 166×CH_{2,PEO}), 3.76-3.51 (m, 4 H, CH_{2,H}, CH_{2,Y}), 3.40-3.28 (m, 2 H, CH_{2,Y}), 3.23-2.79 (m, 8 H, 2×CH_{2,N}, CH_{2,K,M}), 2.68-2.29 (m, 4 H, 2×CH_{2,P}), 2.18-1.93 (m, 10 H, 4×CH_{2,P}, CH_{2,K}), 1.88-1.76 (m, 2 H, CH_{2,M}), 1.58-1.45 (m, 5 H, CH_{2,K}, CH_{3,M}), 1.39-1.26 (m, 8 H, CH_{3,T,A}, CH_{2,K}).

FT-IR ($\nu(\text{cm}^{-1})$): 3311 (w), 2880 (m), 1650 (m), 1536 (w), 1518 (w), 1465 (m), 1359 (w), 1342 (m), 1279 (m), 1240 (m), 1145 (m), 1101 (vs), 1060 (s), 960 (s), 841 (s).

Analysis of HS-Dopa-SGWSP-Dopa-RSG-*block*-PEO₇₂ (Pep₃^{*-synth.}-PEO)

MALDI-TOF-MS

**Figure S11.** Maldi-TOF-MS of HS-Dopa-SGWSP-Dopa-RSG-*block*-PEO₇₂ (Pep₃^{*-synth.}-PEO).

$\Delta m = 44$ Da, characteristic of the EO repeat units.

$M[\text{peak}] = m/z$ 4801.9 assignable to $[M(\text{Pep}_3^{\text{*synth.}}\text{-PEO}_{76}) + K]^+$ = 4801.4 Da within ± 1 Da accuracy.

¹H-NMR (500 MHz, TFA-d, δ in ppm): 8.61 (s, 1 H, CH_{Ar,H}), 7.54 (s, 1 H, CH_{Ar,H}), 6.94-6.68 (m, 4 H, 4xCH_{Ar,Dopa}) 5.19-5.02(m, 3 H, 2xCH_Y, CH_W), 4.94-4.82 (m, 4 H, 4xCH_S), 4.74-4.59 (m, 8 H, CH_{R,P}, CH_{2,G}, 2xCH_{2,S}), 4.29-4.15 (m, 4 H, 2xCH_{2,S}), 4.06-4.00 (m, 5 H, CH_{Ar,H}, 1.5xCH_{2,G,PEO}), 3.95-3.77 (m, 349 H, 174.5xCH_{2,PEO}), 3.72-3.45 (m, 6 H, 2xCH_{2,Dopa}, CH_{2,W}), 3.36-3.18(m, 3 H, CH_{2,H}), 3.11-2.92 (m, 3 H, CH_{2,R}), 2.41-2.16 (m, 2 H, CH_{2,P}), 2.10-1.87 (m, 4 H, CH_{2,P,R}), 1.77-1.59 (m, 4 H, CH_{2,P,R})

FT-IR ($\nu(\text{cm}^{-1})$): 3309 (w), 2878 (m), 1657 (m), 1528 (w), 1466 (w), 1342 (m), 1279 (m), 1240 (w), 1200 (w), 1145 (m), 1101 (vs), 1060 (vs), 959 (s), 841 (s).

Analysis of HTEHHDKSHRA-block-PEO₇₂ (Pep₄-PEO)

MALDI-TOF-MS

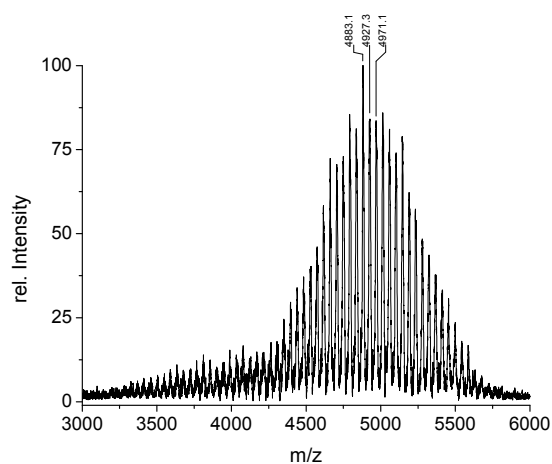
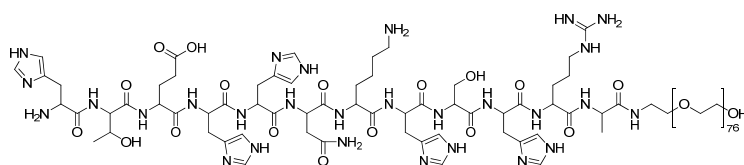


Figure S12. Maldi-TOF-MS of HTEHHDKSHRA-block-PEO₇₂ (Pep₄-PEO).



$\Delta m = 44$ Da, characteristic of the EO repeat units.

$M[\text{peak}] = m/z 4883.1$ assignable to $[M(\text{Pep}_4\text{-PEO}_{77}) + \text{H}]^+ = 4883.5$ Da within ± 1 Da accuracy.

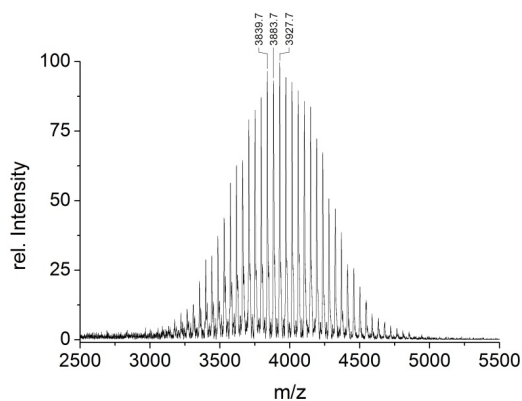
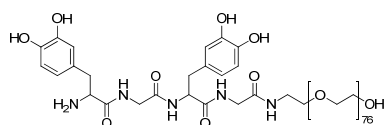
¹H-NMR (500 MHz, TFA-d, δ in ppm): 8.64 (s, 1 H, CH_{Ar,H}(terminal)), 8.58 (s, 4 H, 4xCH_{Ar,H}), 7.53 (s, 1 H, CH_{Ar,H}(terminal)), 7.40 (s, 4 H, 4xCH_{Ar,H}), 5.09-5.02 (m, 6 H, 4xCH_H, CH_{D,E}), 4.80-4.71 (m, 3 H, CH_{R,K,H}(terminal)), 4.64-4.53 (m, 4 H, 2xCH_T, CH_{A,S}), 4.04-3.98 (m, 4 H, CH_{2,S,PEO}), 3.95-3.78 (m, 318 H, 159xCH_{2,PEO}), 3.73-3.44 (m, 12 H, 4xCH_{2,PEO}, 2xCH_{2,H}), 3.32-3.22 (m, 8 H, 3xCH_{2,H}, CH_{2,E}), 3.14-3.00 (m, 2 H, CH_{2,D}), 2.63-2.54 (m, 2 H, CH_{2,R}), 2.33-2.18 (m, 2 H, CH_{2,K}), 2.09-1.61 (m, 10 H, CH_{2,E}, 2xCH_{2,K,R}), 1.50-1.36 (m, 8 H, CH_{2,K}, CH_{3,T,A})

FT-IR ($\nu(\text{cm}^{-1})$): 3287 (w), 2877 (m), 1663 (s), 1536 (w), 1466 (w), 1343 (m), 1280 (w), 1241 (w), 1199 (m), 1141 (s), 1103 (vs), 1062 (s), 960 (s), 840 (s).

S22

Analysis of Dopa-G-Dopa-G-block-PEO₇₂ (Pep₅-PEO)

MALDI-TOF-MS

**Figure S13.** Maldi-TOF-MS of Dopa-G-Dopa-G-block-PEO₇₂ (Pep₅-PEO).

$\Delta m = 44$ Da, characteristic of the EO repeat units.

$M[\text{peak}] = m/z$ 3883.7 assignable to $[M(\text{Pep}_5\text{-PEO}_{77}) + \text{H}]^+ = 3882.4$ Da within ± 1.5 Da accuracy.

¹H-NMR (500 MHz, TFA-d, δ in ppm): 6.90-6.85 (m, 3 H, CH_{Ar,Dopa}), 6.79 (s, 1 H, CH_{Ar,Dopa}), 6.71-6.67 (m, 2 H, CH_{Ar,Dopa}), 4.91 (t, $J = 6.73$ Hz, 1 H, CH_{H,Dopa}), 4.57-4.55 (m, 2 H, CH_{2,G}), 4.52-4.42 (m, 1 H, CH_{H,Dopa}), 4.26-4.01 (m, 4 H, CH_{2,G}, CH_{2,PEO}), 3.98-3.51 (m, 376 H, 188 \times CH_{2,PEO}), 3.26-2.93 (m, 4 H, 2 \times CH_{2,Dopa}).

Enzyme activity assay

Before oxidation of peptide or conjugate, enzymatic activity of tyrosinase was determined by standard activity assay according to supplier (Sigma-Aldrich) using UV-vis spectroscopy. Briefly, the absorption (reading at 280 nm) of 0.7 mM tyrosine in 3 mL potassium phosphate (17 mM, pH 6.5) buffered solution containing 0.1 mL of approximately 100 units of tyrosinase in potassium phosphate buffer (50 mM, pH 6.5) was recorded for 20 min. Subsequently, the maximal slope was determined for an interval of 3 min (Fig. S5) and used for activity calculation according to equation 1. Due to the sensitivity of the enzyme, activity assays were carried out before every reaction.

$$\text{activity (units)} = \frac{m_{\max(3 \text{ min})}}{0.001} \quad (1)$$

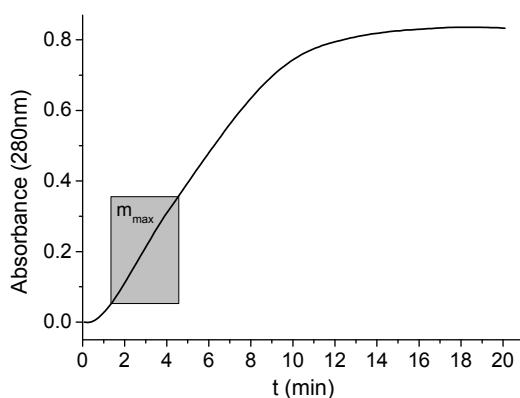


Figure S14. Typical enzymatic activity assay trace.

Enzymatic activation of peptide and peptide-polymer conjugate

Enzymatic activation kinetics of peptides and peptide-polymer conjugates were carried out according to procedure described above (Page S7). Oxidation was monitored by UV-vis measurement at 280 nm. Final products were analyzed with MALDI-TOF-MS, Y* indicating processed tyrosine (quinone/catechol – as stated).

MALDI-TOF-MS of activated products

Analysis of HSY*SGWSPY*RSG (Pep₃^{*}) [activation to quinone]

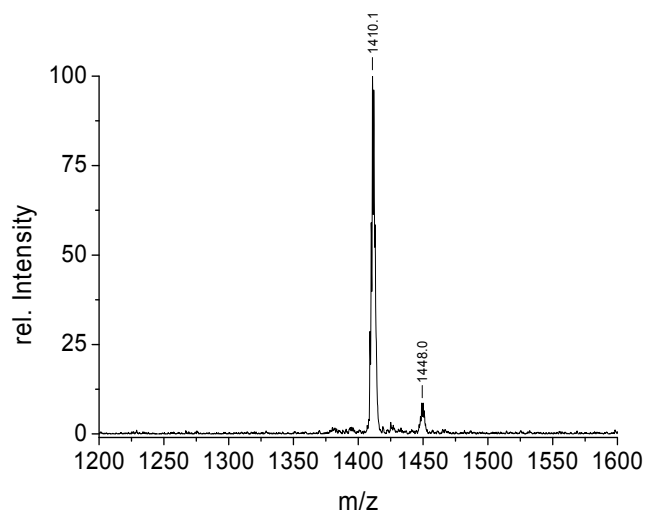
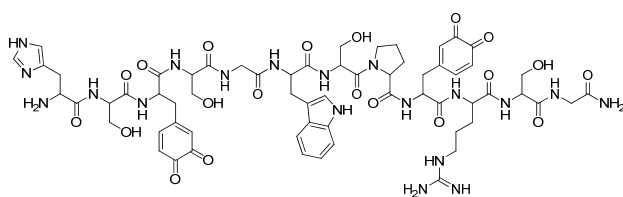


Figure S15. Maldi-TOF-MS of HSY*SGWSPY*RSG (Pep₃^{*}).



$$M[\text{peak}] = 1410.1 [M(\text{Pep}_3^*) + \text{H}]^+, 1448.0 [(Pep_3^*) + \text{K}]^+$$

$$M[\text{Th}] = 1410.5 \text{ Da}$$

The signals can be assigned to the corresponding quinone-activated peptide with an accuracy of ± 1 Da.

Analysis of Y/Y*PATY*Y*GMRSPS-block-PEO₇₂ (Pep₁*-PEO) [activation to catechol]

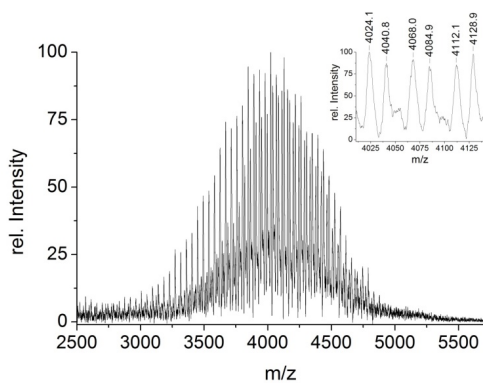
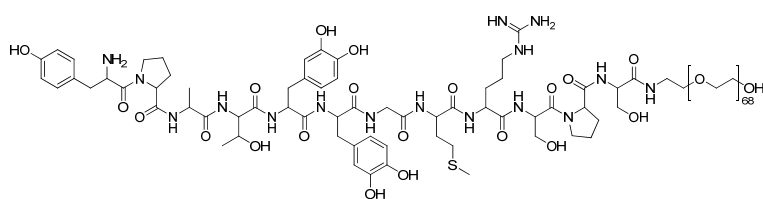


Figure S16. Maldi-TOF-MS of Y/Y*PATY*Y*GMRSPS-block-PEO₇₂ (Pep₁*-PEO).

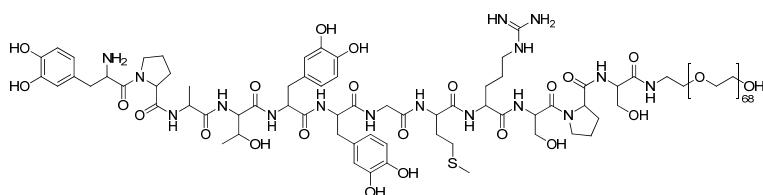
2x activation to catechol:



$\Delta m = 44$ Da, characteristic of the EO repeat units.

$M[\text{peak}] = m/z$ 4068.0 assignable to $[M(\text{Pep}_1^{*\text{di-dopa}}\text{-PEO}_{60}) + \text{H}]^+ = 4067.7$ Da within ± 1 Da accuracy.

3x activation to catechol:



$\Delta m = 44$ Da, characteristic of the EO repeat units.

$M[\text{peak}] = m/z$ 4084.9 assignable to $[M(\text{Pep}_1^{*\text{tri-dopa}}\text{-PEO}_{60}) + \text{H}]^+ = 4083.7$ Da within ± 2 Da accuracy.

Analysis of Y*HPNGMNPY*TKA-block-PEO₇₂ (Pep₂*-PEO) [activation to catechol]

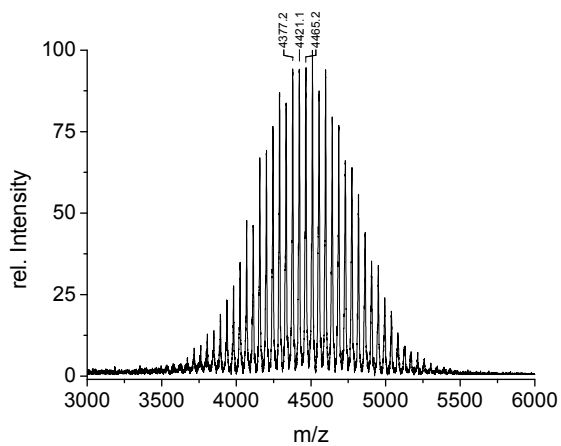
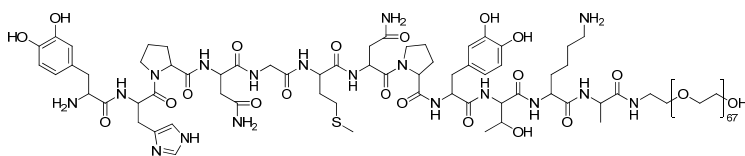


Figure S17. Maldi-TOF-MS of Y*HPNGMNPY*TKA-block-PEO₇₂ (Pep₂*-PEO).



$\Delta m = 44$ Da, characteristic of the EO repeat units.

$M[\text{peak}] = m/z 4421.1$ assignable to $[M(\text{Pep}_2^*-\text{PEO}_{68}) + \text{H}]^+ = 4420.1$ Da within ± 1 Da accuracy.

Analysis of HSY*SGWSPY*RSG-block-PEO₇₂ (Pep₃*-PEO) [activation to catecholl]

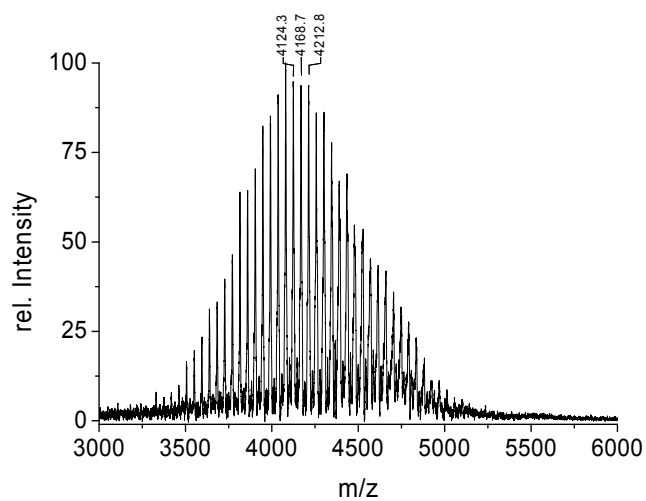
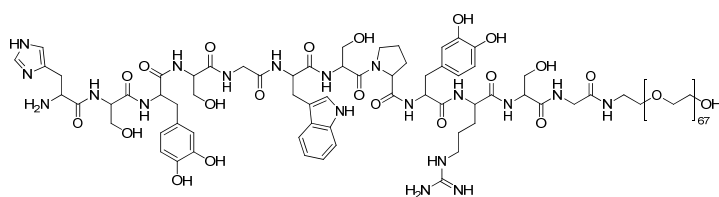


Figure S18. Maldi-TOF-MS of HSY*SGWSPY*RSG-block-PEO₇₂ (Pep₃*-PEO).



$\Delta m = 44$ Da, characteristic of the EO repeat units.

$M[\text{peak}] = m/z$ 4168.7 assignable to $[M(\text{Pep}_3^*-\text{PEO}_{62}) + \text{Na}]^+ = 4168.6$ Da within ± 1 Da accuracy.

QCM measurements

All adsorption measurements were performed at pH 6.5 opposing to pH 4 during the phage display panning procedure, as we intended to apply the enzyme containing adhesive product without further purification steps needed. Under acidic conditions, tyrosinase adsorption can be neglected. Therefore, the pH of the oxidation mixture (pH 6.5) was applied, where only minor adsorption of tyrosinase to the surfaces occurs (cf. Fig. S20).

Control experiments

Sodium ascorbate reference experiment (regular buffered)

In order to investigate the adsorption of ascorbate onto the aluminum oxide surface, sodium ascorbate was dissolved in 0.8 mM potassium phosphate buffer (pH 6.5) in a concentration of 0.33 μM . Measurements on aluminum oxide sensors were carried out as described above (Page S7). No adsorption of ascorbate could be observed.

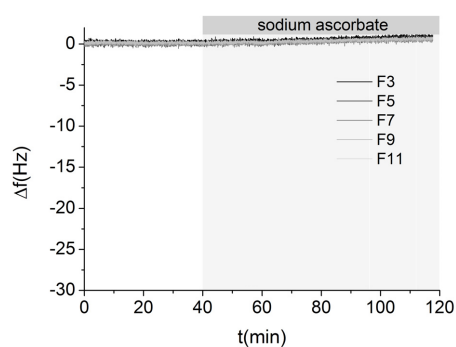


Figure S19. QCM measurement of sodium ascorbate adsorption showing frequency overtones F3 – F11.

0–40 min.: rinse with buffer

40–117 min.: sodium ascorbate control solution

Tyrosinase reference experiment (regular buffered)

A tyrosinase control experiment was carried out at 25 °C using 100 units of tyrosinase and 0.29 μmol PEG₃₀₀₀ in a final volume of 1 mL. The polymer was dissolved in potassium phosphate buffer (17 mM,

pH 6.5). Subsequently, the “activation” solution was prepared by mixing 33 μ L of 220 mM sodium ascorbate and 100 units of tyrosinase in 50 mM potassium phosphate buffer (pH 6.5) with 10 μ L of 0.2 mM DOPA in a separate tube. This solution was then transferred to the polymer. After incubation for 15 h, the solution was diluted with 21 mL of MQ water resulting in a final buffer concentration of 0.8 mM potassium phosphate (pH 6.5). Subsequent QCM measurements on aluminum oxide sensors were carried out according to the protocol described above (Page S7).

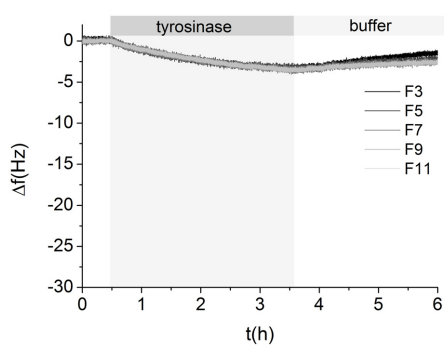


Figure S20. QCM measurement of tyrosinase adsorption/desorption showing frequency overtones F3 – F11.

Conditions:

0-0.5 h: rinse with buffer

0.5-3.5 h: tyrosinase control solution

3.5-6h: rinse with buffer

Adsorption and Desorption Experiments

QCM experiment: Pep₁-PEO adsorption prior to the activation

Bioconjugate Pep₁-PEO was dissolved in 0.8 mM potassium phosphate buffer (pH 6.5) at a concentration of 60 µg/mL. Subsequent QCM measurements on aluminum oxide were carried out according to the protocol described above (Page S7).

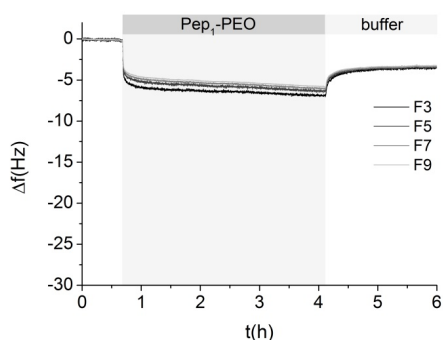


Figure S21. QCM adsorption and desorption kinetics of non-activated conjugate Pep₁-PEO showing frequency overtones F3 – F9.

Conditions:

0-0.7 h: rinse with buffer

0.7-4.2 h: Pep₁-PEO solution

4.2-6h: rinse with buffer

QCM experiment: Pep₂-PEO control (adsorption prior to the activation)

Bioconjugate Pep₂-PEO was dissolved in 0.8 mM potassium phosphate buffer (pH 6.5) at a concentration of 60 µg/mL. Subsequent QCM measurements on aluminum oxide were carried out according to the protocol described above (Page S7).

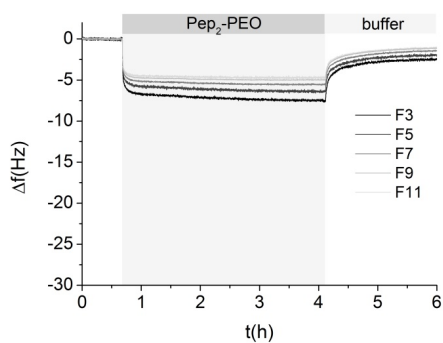


Figure S22. QCM adsorption and desorption kinetics of non-activated conjugate Pep₂-PEO showing frequency overtones F3 – F11.

Conditions:

0-0.7 h: rinse with buffer

0.7-4.2 h: Pep₂-PEO solution

4.2-6h: rinse with buffer

QCM experiment: Pep₃-PEO control (adsorption prior to the activation)

Bioconjugate Pep₃-PEO was dissolved in 0.8 mM potassium phosphate buffer (pH 6.5) at a concentration of 60 μg/mL. Subsequent QCM measurements on aluminum oxide were carried out according to the protocol described above (Page S7).

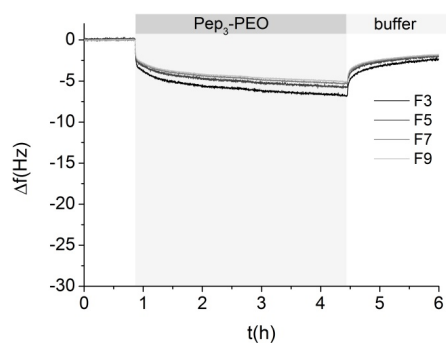


Figure S23. QCM adsorption and desorption kinetics of non-activated conjugate Pep₃-PEO showing frequency overtones F3 – F9.

11 Appendix

Conditions:

0-0.9 h: rinse with buffer

0.9-4.4 h: Pep₃-PEO solution

4.4-6h: rinse with buffer

QCM experiment: Pep₄-PEO adsorption of a tyrosine-free sequence from phage display

Bioconjugate Pep₄-PEO was dissolved in 0.8 mM potassium phosphate buffer (pH 6.5) at a concentration of 60 µg/mL. Subsequent QCM measurements on aluminum oxide were carried out according to the protocol described above (Page S7). Although incubation leads to an efficient adsorption onto the aluminum oxide surface, the coating slowly washes off upon rinsing. Therefore, an effective and stable coating is not achieved, underlining the excellent adhesive properties of dopa-containing peptides.

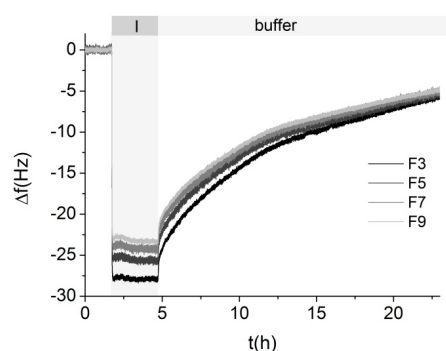


Figure S24. QCM adsorption and desorption kinetics of conjugate Pep₄-PEO showing frequency overtones F3 – F9.

Conditions:

0-1.7 h: rinse with buffer

1.7-4.7 h: Pep₄-PEO solution (I)

4.7-23h: rinse with buffer

QCM experiment: Pep₅-PEO (adsorption of synthesized dopa reference)

Bioconjugate Pep₅-PEO was dissolved in 0.8 mM potassium phosphate buffer (pH 6.5) containing 599 mM NaCl and 0.33 μ M sodium ascorbate at a concentration of 13.2 μ M. Subsequent QCM measurements on aluminum oxide were carried out according to the protocol described above (Page S7). Upon incubation, frequencies only drop to approx. -5 Hz indicating only minor interactions with the aluminum oxide substrate. Furthermore, rinsing with 599 mM NaCl leads to an almost quantitative wash off. Therefore, it is straight forward to postulate, that dopa-residues need a specific peptide backbone in order to adhere efficiently under the applied harsh conditions.

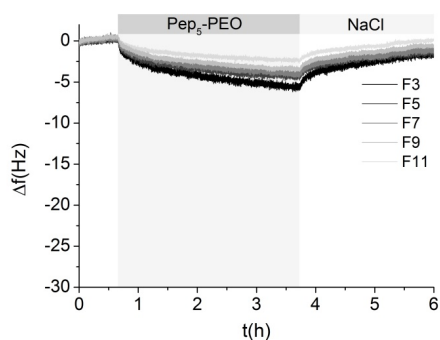


Figure S25. QCM adsorption and desorption kinetics of dopa reference conjugate Pep₅-PEO showing frequency overtones F3 – F11.

Conditions:

0-7 h: rinse with buffer (0.8 mM potassium phosphate, 599 mM NaCl, pH 6.5)

0.7-3.7 h: conjugate Pep₅-PEO solution

3.7-6 h: rinse with buffer (0.8 mM potassium phosphate, 599 mM NaCl, pH 6.5)

QCM experiment: Pep₁^{}-PEO (adsorption after activation)*

Conjugate Pep₁-PEO was activated according to protocol described above (Page S7). After incubation for 15 h, the reaction mixture was diluted with 21 mL of MQ water resulting in a final buffer concentration of 0.8 mM potassium phosphate (pH 6.5). Subsequent QCM measurements on aluminum oxide sensors were carried out according to the protocol described above (Page S7).

11 Appendix

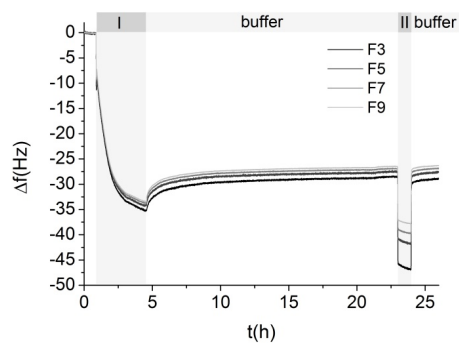


Figure S26. QCM adsorption and desorption kinetics of activated conjugate Pep_1^* -PEO showing frequency overtones F3 – F9.

Conditions:

0-1h: rinse with buffer

1-4.5 h: conjugate Pep_1^* -PEO solution (I)

4.5-23 h: rinse with buffer

23-24 h: rinse with 599 mM NaCl (II)

24-26 h: rinse with buffer

QCM experiment: Pep_2^ -PEO (adsorption after activation)*

Conjugate Pep_2 -PEO was activated according to protocol described above (Page S7). After incubation for 15 h, the reaction mixture was diluted with 21 mL of MQ water resulting in a final buffer concentration of 0.8 mM potassium phosphate (pH 6.5). Subsequent QCM measurements on aluminum oxide sensors were carried out according to the protocol described above (Page S7).

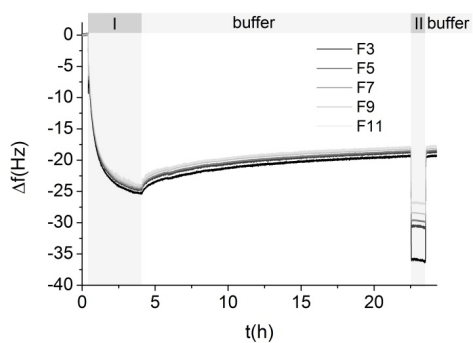


Figure S27. QCM adsorption and desorption kinetics of activated conjugate Pep_2^* -PEO showing frequency overtones F3 – F11.

Conditions:

0-0.5 h: rinse with buffer

0.5-4 h: conjugate Pep_2^* -PEO solution (I)

4-22.5 h: rinse with buffer

22.5-23.5 h: rinse with 599 mM NaCl (II)

23.5-24.5 h: rinse with buffer

11 Appendix

QCM experiment: Pep₃^{}-PEO (adsorption after activation)*

Conjugate Pep₃-PEO was activated according to protocol described above (Page S7). After incubation for 15 h, the reaction mixture was diluted with 21 mL of MQ water resulting in a final buffer concentration of 0.8 mM potassium phosphate (pH 6.5). Subsequent QCM measurements on aluminum oxide sensors were carried out according to the protocol described above (Page S7).

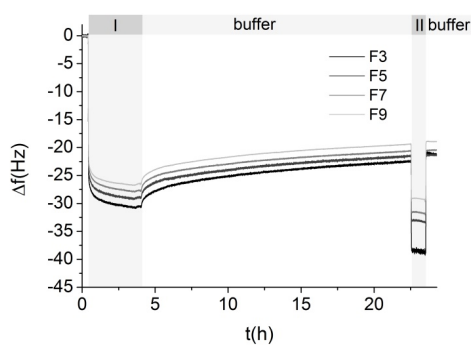


Figure S28. QCM adsorption and desorption kinetics of activated conjugate Pep₃^{*}-PEO showing frequency overtones F3 – F9.

Conditions:

0-0.5 h: rinse with buffer

0.5-4 h: conjugate Pep₃^{*}-PEO solution (I)

4-22.5 h: rinse with buffer

22.5-23.5 h: rinse with 599 mM NaCl (II)

23.5-24.5 h: rinse with buffer

*QCM experiment: Pep₃^{*synth.}-PEO (adsorption of synthesized “active” conjugate)*

Bioconjugate Pep₃^{*synth.}-PEO was dissolved in 0.8 mM potassium phosphate buffer (pH 6.5) containing 0.33 μM sodium ascorbate at a concentration of 60 μg/mL. Subsequent QCM measurements on aluminum oxide were carried out according to the protocol described above (Page S7).

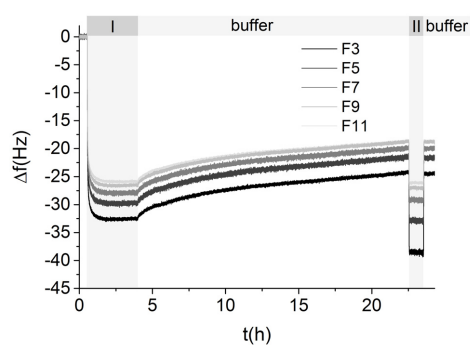


Figure S29. QCM adsorption and desorption kinetics of activated conjugate Pep₃^{*synth.}-PEO showing frequency overtones F3 – F11.

Conditions:

0-0.5 h: rinse with buffer

0.5-4 h: conjugate Pep₃^{*synth.}-PEO solution (I)

4-22.5 h: rinse with buffer

22.5-23.5 h: rinse with 599 mM NaCl (II)

23.5-24.5 h: rinse with buffer

11 Appendix

QCM experiment: Pep₃^{-synth.}-PEO at 55 °C (adsorption of synthesized “active” conjugate)*

Bioconjugate Pep₃^{*-synth.}-PEO was dissolved in 0.8 mM potassium phosphate buffer (pH 6.5) containing 0.33 μM sodium ascorbate at a concentration of 60 μg/mL and pre-heated to 65 °C. Subsequent QCM measurements on aluminum oxide were carried out according to the protocol described above (Page S7) under oxygen-free environment. Observed signal instability at 55 °C may be explained by formation slight expansion of the material, as signal stability increases with higher overtones. Nonetheless, overtones 5, 7 and 9 only show a minor noise upon increasing temperature leading to sufficient experiment.

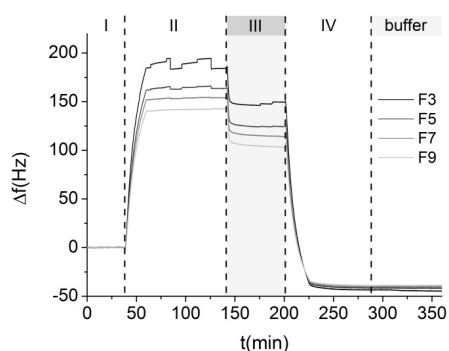


Figure S30. QCM adsorption and desorption kinetics of activated conjugate Pep₃^{*-synth.}-PEO at 55 °C showing frequency overtones F3 – F9.

Conditions:

0-38 min: rinse with buffer (I)

38-141 min: set temperature to 55 °C (II)

141-201 min: conjugate Pep₃^{*-synth.}-PEO solution (III)

201-288 min: stop chamber flow and set temperature to 22 °C (IV)

288-360 min: start chamber flow and rinse with buffer

QCM experiment: NSS wash of Pep₃^{-synth}-PEO coated surface (coated at 55°C)*

Aluminum oxide surface was coated with Pep₃^{*-synth}-PEO according to procedure above at 55°C (Page S38). Nine salts solution (17.6 g NaCl, 1.47g Na₂SO₄, 0.08 g NaHCO₃, 0.25 g KCl, 0.04 g KBr, 1.87 g MgCl₂·6 H₂O, 0.41 g CaCl₂·2 H₂O, 0.01 g SrCl₂·6 H₂O, 0.01 g H₃BO₃, 1 L bidest. H₂O) was filtered prior to use. Subsequent QCM measurements on aluminum oxide were carried out according to the protocol described above (Page S7).

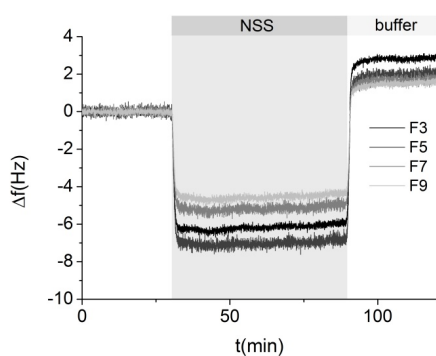


Figure S31. QCM adsorption and desorption kinetics of NSS wash of Pep₃^{*-synth}-PEO coated surface showing frequency overtones F3 – F9.

Conditions:

0-30 min: rinse coating with buffer

30-90 min: rinse with NSS

90-120 min: rinse with buffer

11 Appendix

Anti-fouling experiments: BSA control experiment

BSA was dissolved in 0.8 mM potassium phosphate buffer (pH 6.5) at a concentration of 10 mg/mL. Subsequent QCM measurements on aluminum oxide sensors were carried out according to the protocol described above (Page S7).

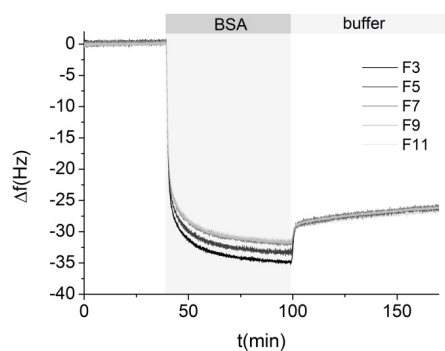


Figure S32. QCM frequency plot of BSA adsorption/desorption onto aluminum oxide showing frequency overtones F3 – F9.

Conditions:

0-40 min.: rinse with buffer

40-100 min.: BSA (10 mg/mL)

100-170 min.: rinse with buffer

Anti-fouling experiments: BSA on 22 °C Pep₃-PEO coated surface at 22 °C*

BSA was dissolved in 0.8 mM potassium phosphate buffer (pH 6.5) at a concentration of 10 mg/mL. Subsequent QCM measurements on Pep₃*-PEO coated aluminum oxide sensors were carried out according to the protocol described above (Page S7).

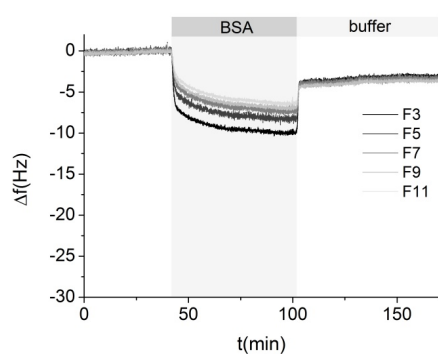


Figure S33. QCM frequency plot of BSA adsorption/desorption at 22 °C onto aluminum oxide surface coated at 55 °C with Pep₃*-PEO showing frequency overtones F3 – F11.

Conditions:

0-40 min.: rinse with buffer

40-100 min.: BSA (10 mg/mL)

100-170 min.: rinse with buffer

11 Appendix

Anti-fouling experiments: BSA on 55 °C Pep₃-PEO coated surface at 22 °C*

BSA was dissolved in 0.8 mM potassium phosphate buffer (pH 6.5) at a concentration of 10 mg/mL. Subsequent QCM measurements on Pep₃*-PEO coated aluminum oxide sensors were carried out according to the protocol described above (Page S7).

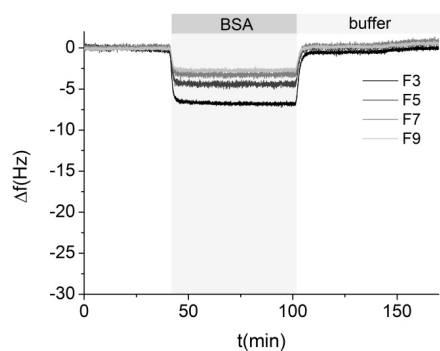


Figure S34. QCM frequency plot of BSA adsorption/desorption at 55 °C onto aluminum oxide surface coated at 55 °C with Pep₃*-PEO showing frequency overtones F3 – F9.

Conditions:

0-40 min.: rinse with buffer

40-100 min.: BSA (10 mg/mL)

100-170 min.: rinse with buffer

Anti-fouling experiments: Fetal bovine serum control experiment

Fetal bovine serum was filtered prior to use. Subsequent QCM measurements on aluminum oxide sensors were carried out according to the protocol described above (Page S7). Final adsorption of the serum is rather comparable with BSA adsorption, as frequencies equilibrate to approx. -30 Hz.

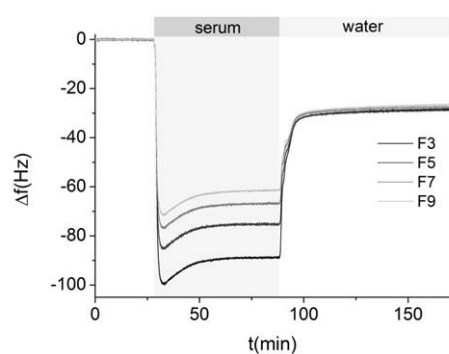


Figure S35. QCM frequency plot of the adsorption/desorption of fetal bovine serum onto aluminum oxide showing frequency overtones F3 – F9.

Conditions:

0-30 min.: rinse with MilliQ H₂O

30-90 min.: serum

90-170 min.: rinse with MilliQ H₂O

11 Appendix

Anti-fouling experiments: Fetal bovine serum on 55 °C Pep₃-PEO coated surface at 22 °C*

Fetal bovine serum was filtered prior to use. Subsequent QCM measurements on Pep₃*-PEO coated aluminum oxide sensors were carried out according to the protocol described above (Page S7). The coated surface completely defies the serum, as frequencies return to the originally incubated values.

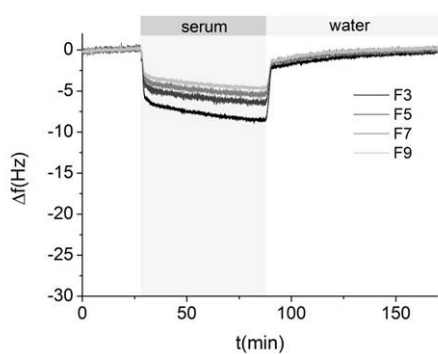


Figure S36. QCM frequency plot of the serum adsorption/desorption at 55 °C onto aluminum oxide surface coated at 55 °C with Pep₃*-PEO showing frequency overtones F3 – F9.

Conditions:

0-30 min.: rinse with MilliQ H₂O

30-90 min.: serum

90-170 min.: rinse with MilliQ H₂O

Anti-fouling experiments: Human serum control experiment

Human serum was filtered prior to use. Subsequent QCM measurements on aluminum oxide sensors were carried out according to the protocol described above (Page S7). Upon rinsing serum coated surfaces with MilliQ H₂O, frequency overtones initially rise for approx. 1 min followed by rapid decrease for 1.5 min. On the other hand, the dissipation solemnly drops in the same time interval, indicating the formation of a rather rigid surface. Therefore, it is straight forward to postulate enzyme precipitation on the aluminum oxide surface.

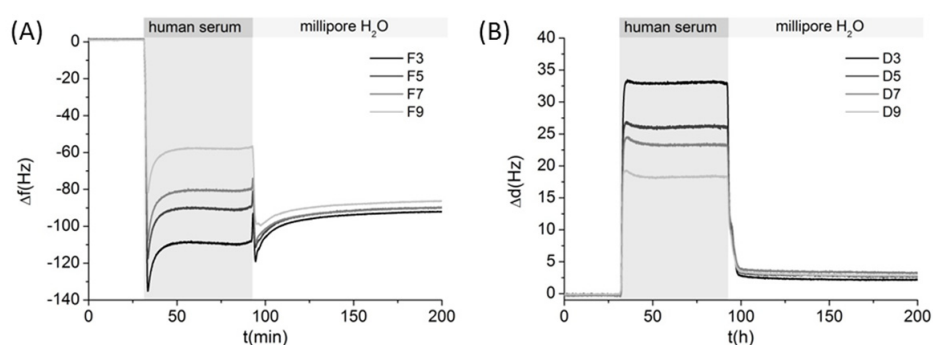


Figure S37. QCM control experiment for human serum adsorption /desorption. A – frequency shifts; B – dissipation shifts.

Conditions:

0-30 min.: rinse with MilliQ H₂O

30-90 min.: human serum

90-200 min.: rinse with MilliQ H₂O

11 Appendix

Anti-fouling experiments: Human serum on 55 °C Pep₃-PEO coated surface at 22 °C*

Human serum was filtered prior to use. Subsequent QCM measurements on Pep₃*-PEO coated aluminum oxide sensors were carried out according to the protocol described above (Page S7). Unlike in the reference experiment, serum does not directly interact with the aluminum oxide surface indicated by an almost complete return of the frequencies to the initial incubated values.

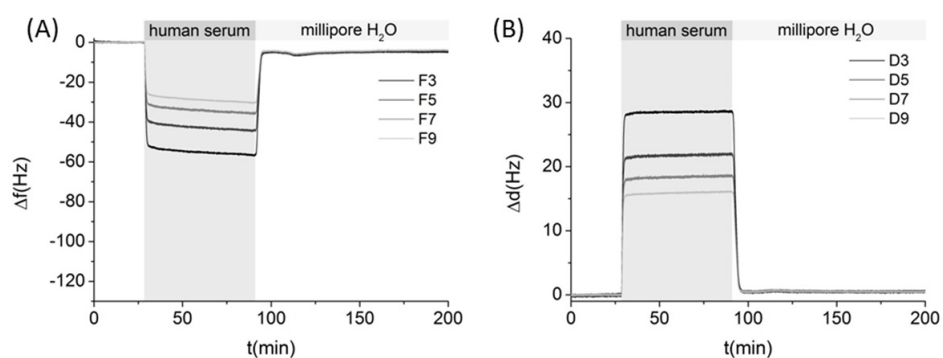


Figure S38. QCM measurement of human serum adsorption/desorption at 25 °C onto aluminum oxide surface coated at 55 °C with Pep₃*-PEO. A – frequency shifts; B – dissipation shifts.

Conditions:

0-30 min.: rinse with MilliQ H₂O

30-90 min.: human serum

90-200 min.: rinse with MilliQ H₂O

Measurements under saltwater conditions

Tyrosinase control experiment (in 599 mM NaCl)

A tyrosinase control experiment was carried out at 25 °C using 100 units of tyrosinase and 0.29 μmol PEG₃₀₀₀ in a final volume of 1 mL. The polymer was dissolved in potassium phosphate buffer (17 mM, pH 6.5). Subsequently, the “activation” solution was prepared by mixing 33 μL of 220 mM sodium ascorbate and 100 units of tyrosinase in 50 mM potassium phosphate buffer (pH 6.5) with 10 μL of 0.2 mM DOPA in a separate tube. This solution was then transferred to the polymer. After incubation for 15 h, the solution was diluted with 21 mL of 627 mM NaCl resulting in a final buffer concentration of 0.8 mM potassium phosphate/599 mM NaCl (pH 6.5). Subsequent QCM measurements on aluminum oxide sensors were carried out according to the protocol described above (Page S7).

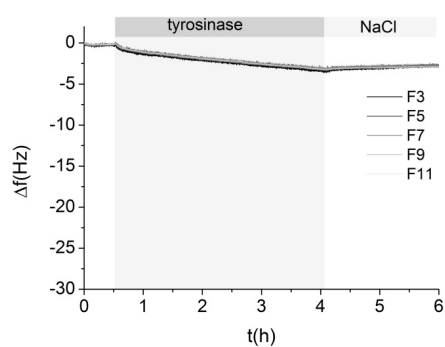


Figure S39. QCM measurement of tyrosinase adsorption/desorption under saltwater conditions (599 mM NaCl) showing frequency overtones F3 – F11.

Conditions:

0-0.5 h: rinse with buffer (0.8 mM potassium phosphate, 599 mM NaCl, pH 6.5)

0.5-4 h: tyrosinase control solution in 599 mM NaCl

4-6h: rinse with buffer (0.8 mM potassium phosphate, 599 mM NaCl, pH 6.5)

11 Appendix

QCM experiment: Pep₃-PEO control in 599 mM NaCl (adsorption prior to the activation)

Bioconjugate Pep₃-PEO was dissolved in 0.8 mM potassium phosphate buffer (pH 6.5) containing 599 mM NaCl and 0.33 μ M sodium ascorbate at a concentration of 60 μ g/mL. Subsequent QCM measurements on aluminum oxide were carried out according to the protocol described above (Page S7).

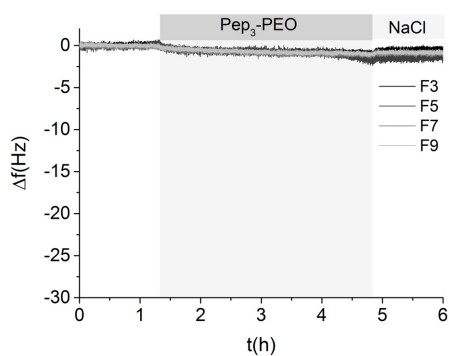


Figure S40. QCM adsorption and desorption kinetics of non-activated conjugate Pep₃-PEO in 599 mM NaCl showing frequency overtones F3 – F9.

Conditions:

0-1.3 h: rinse with buffer (0.8 mM potassium phosphate, 599 mM NaCl, pH 6.5)

1.3-4.8 h: Pep₃-PEO solution in 599 mM NaCl

4.8-6 h: rinse with buffer (0.8 mM potassium phosphate, 599 mM NaCl, pH 6.5)

QCM experiment: Pep₃^{}-PEO in 599 mM NaCl (adsorption after activation)*

Conjugate Pep₃-PEO was activated according to protocol described above (Page S7). After incubation for 15 h, the reaction mixture was diluted with 21 mL of 627 mM NaCl resulting in a final buffer concentration of 0.8 mM potassium phosphate/599 mM NaCl (pH 6.5). Subsequent QCM measurements on steel sensors were carried out according to the protocol described above (Page S7).

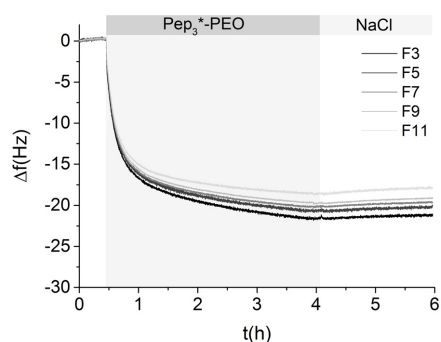


Figure S41. QCM adsorption and desorption kinetics of activated conjugate Pep₃^{*}-PEO in 599 mM NaCl showing frequency overtones F3 – F11.

Conditions:

0-0.5 h: rinse with buffer (0.8 mM potassium phosphate, 599 mM NaCl, pH 6.5)

0.5-4 h: Pep₃^{*}-PEO solution in 599 mM NaCl

4-6h: rinse with buffer (0.8 mM potassium phosphate, 599 mM NaCl, pH 6.5)

11 Appendix

QCM experiment: Pep₃^{-synth.}-PEO in 599 mM NaCl (adsorption of synthesized “active” conjugate)*

Bioconjugate Pep₃^{*-synth.}-PEO was dissolved in 0.8 mM potassium phosphate buffer (pH 6.5) containing 0.33 μM sodium ascorbate and 599 mM NaCl at a concentration of 60 μg/mL. Subsequent QCM measurements on aluminum oxide were carried out according to the protocol described above (Page S7).

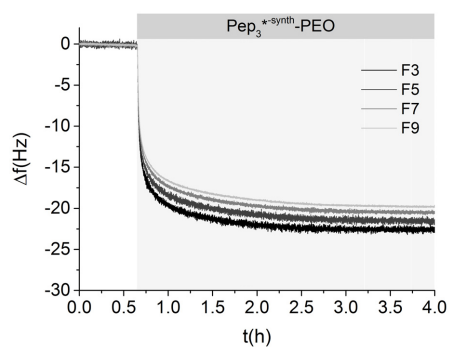


Figure S42. QCM adsorption and desorption kinetics of conjugate Pep₃^{*-synth.}-PEO in 599 mM NaCl showing frequency overtones F3 – F9.

Conditions:

0-0.6 h: rinse with buffer (0.8 mM potassium phosphate, 599 mM NaCl, pH 6.5)

0.6-4 h: Pep₃^{*-synth.}-PEO solution in 599 mM NaCl

Langmuir kinetics:

QCM experiment: Pep₃^{}-PEO (Langmuir kinetics)*

General procedure: Conjugate Pep₃-PEO was activated according to protocol described above (Page S7). After incubation for 15 h, different product concentrations (0.5 nmol, 4.9 nmol, 49.0 nmol, 147.0 nmol) were taken and diluted with buffer and 21 mL MQ water resulting in a final buffer concentration of 0.8 mM potassium phosphate (pH 6.5) and activated conjugate concentrations 0.02 μM, 0.22 μM, 2.20 μM and 6.70 μM, respectively. Subsequent QCM measurements on aluminum oxide sensors were carried out according to the protocol described above (Page S7).

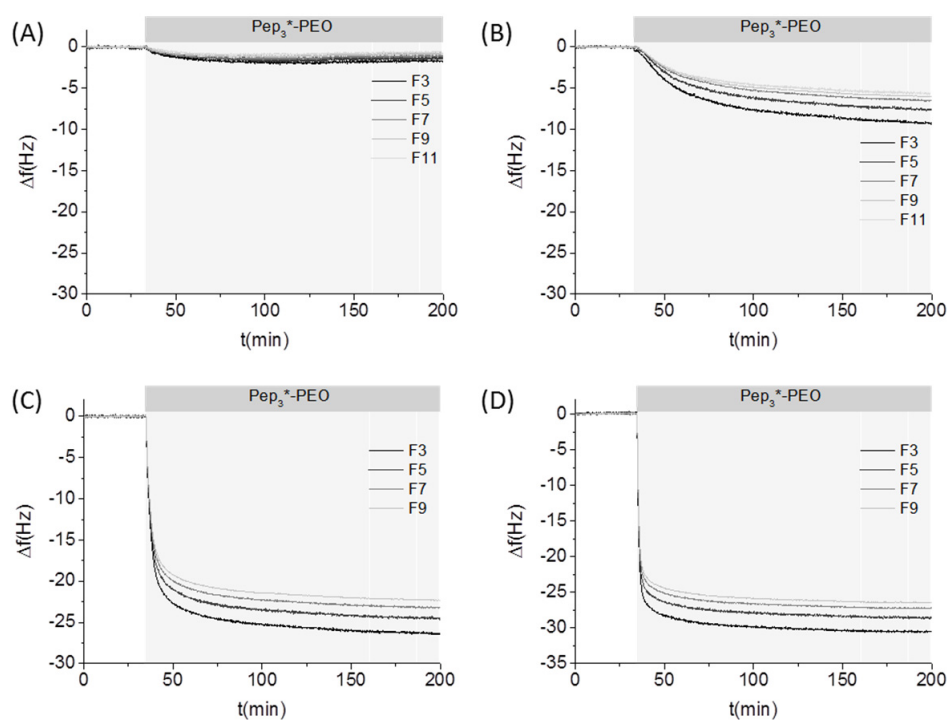


Figure S43. QCM adsorption kinetics of activated conjugate Pep₃^{*}-PEO. A – 0.02 μM; B – 0.22 μM, C – 2.20 μM, D – 6.70 μM.

Conditions:

0-30 min: rinse with buffer

30-200 min: conjugate Pep₃^{*}-PEO solution

11 Appendix

QCM experiment: Pep₃-PEO in 599 mM NaCl (Langmuir kinetics)

Bioconjugate Pep₃-PEO was dissolved in 0.8 mM potassium phosphate buffer (pH 6.5) containing 599 mM NaCl and 0.33 μ M sodium ascorbate at concentrations of 120 μ g/mL (26.6 μ M) and 240 μ g/mL (53.2 μ M). Subsequent QCM measurements on aluminum oxide were carried out according to the protocol described above (Page S7). No adsorption could be observed in both experiments.

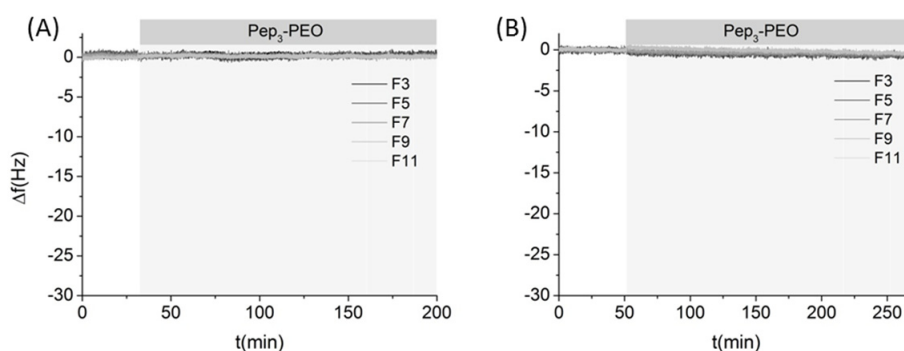


Figure S44. QCM adsorption kinetics of non-activated conjugate Pep₃-PEO in 599 mM NaCl. A – 26.6 μ M; B – 53.2 μ M.

Conditions:

0-30 min: rinse with buffer (0.8 mM potassium phosphate, 599 mM NaCl, pH 6.5)

30-200 min: Pep₃-PEO solution in 599 mM NaCl

QCM experiment: Pep₃^{}-PEO in 599 mM NaCl (Langmuir kinetics)*

General procedure: Conjugate Pep₃-PEO was activated according to protocol described above (Page S7). After incubation for 15 h, different product concentrations (4.9 nmol, 49.0 nmol, 143.0 nmol) were taken and diluted with buffer and 21 mL 627 mM NaCl (final buffer concentration 0.8 mM potassium phosphate, 599 mM NaCl) resulting in final activated conjugate concentrations 0.22 μ M, 2.20 μ M and 6.50 μ M, respectively. For a concentration of 19.5 μ M, Pep₃^{*-synth.}-PEO was taken and measured under comparable conditions only without enzyme. Subsequent QCM measurements on aluminum oxide sensors were carried out according to the protocol described above (Page S7).

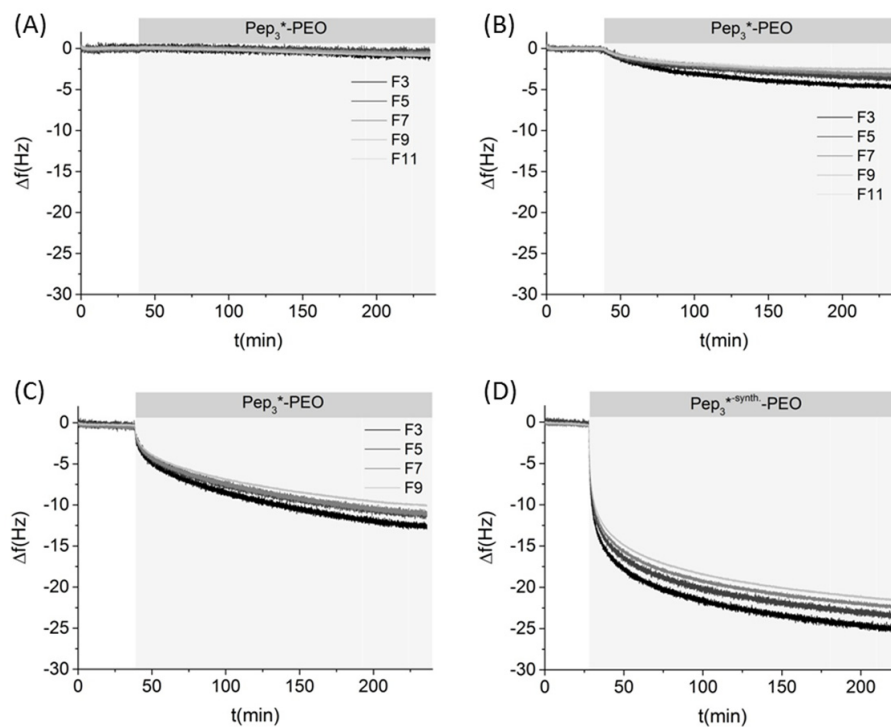


Figure S45. QCM adsorption kinetics of activated conjugate Pep_3^* -PEO and $\text{Pep}_3^{*\text{-synth}}$ -PEO, respectively, in 599 mM NaCl. A – 0.22 μM ; B – 2.20 μM , C – 6.50 μM , D – 19.50 μM .

Conditions:

0-45 min: rinse with buffer (0.8 mM potassium phosphate, 599 mM NaCl, pH 6.5)

45-235 min: Pep_3^* -PEO solution in 599 mM NaCl

Langmuir Isotherms: Data evaluation

Association saturation constants (K_a) could be obtained taking the maximal frequency changes for each measurement, as has been reported.[4] Subsequently, K_a was calculated from the ratio of slope and intercept according to the plot of $c \cdot \Delta f_{\text{eq}}^{-1}$ versus c . Measurements for each concentration were repeated 3 times.

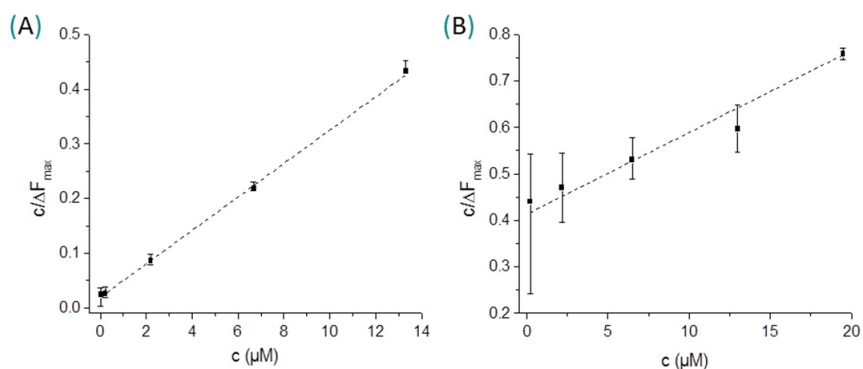


Figure S46. Langmuir adsorption isotherms of Pep_3^* -PEO under buffered (A, 0.8 mM potassium phosphate buffer, pH 6.5) and high ionic strength (B, 0.8 mM potassium phosphate buffer containing 599 mM NaCl, pH 6.5) conditions.

Single molecule force spectroscopy: Data evaluation

AFM cantilever were prepared according to the procedure described above (P. S8-9). Figure S47 shows the reaction of an amine functionalized cantilever with NHS-activated PEO. Subsequently, a cysteinyl-carrying peptide is introduced via maleimide-thiol coupling.

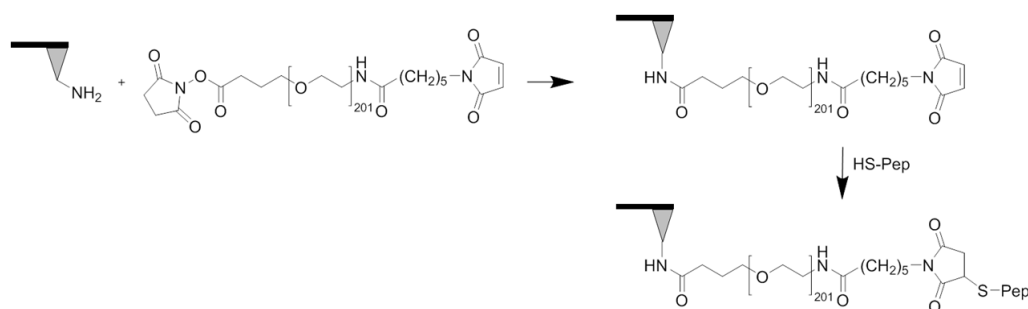


Figure 47. Preparation of functionalized AFM cantilever with Pep₃ and Pep₃^{*synth.}.

For the data evaluation only curves containing clearly identifiable detachments events have been taken into consideration. To reduce the signal-to-noise ratio, the raw data were smoothed by a boxcar average of 41 points and a reduction of the data points by a factor of 10 in analogy to recently reported single molecule force spectroscopy experiments [5]. The detachment events were detected by modified algorithm based on the work of Gergerly et al. [6] and implemented in custom written program in IGOR PRO. This algorithm has been used previously [7,8]. The detachment events obtained by this automatic evaluation are summarized for both peptides in the scatter plots of Figure 5 B. In order to demonstrate that always the same PEO-spacer is stretched and thus same peptides are detaching from the QCM-D sensor all force plots are superimposed, as proposed recently [9]. The force versus distance profiles in Figure S48 were obtained by binning the single data points in terms of force and distance intervals (10 pN and 1 nm, respectively).

A statistical evaluation of the detachment data results in the histograms shown in Figure S49 where the detachment forces for the two different peptides can be identified. The solid lines are based on a multi-peak fits of Gaussians implemented in IGOR PRO and correspond to the forces stated in the text.

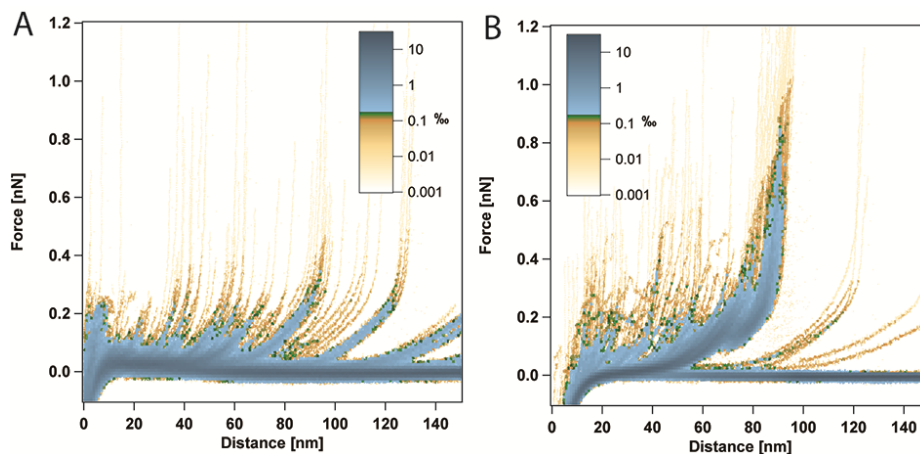


Figure 48. Superposition of single force curves obtained with a cantilever modified by a PEO-spacer and (A) Pep_3 and (B) $\text{Pep}_3^{*\text{-synth}}$, respectively. The colour scale is based on the percentage of data points falling in a two-dimensional data bin (10 pN and 1 nm, respectively).

A detailed analysis of the detachment events revealed the occurrence of additional pull-off forces for $\text{Pep}_3^{*\text{-synth}}$ -PEO-Probe with around 225 ± 90 and 430 ± 90 pN. This set is probably attributed to the oxidative formation of dopa-quinone from L-dopa moieties as the forces are comparatively well in line with the values of dopa-quinone on titanium substrates reported by Messersmith and coworkers.[10]

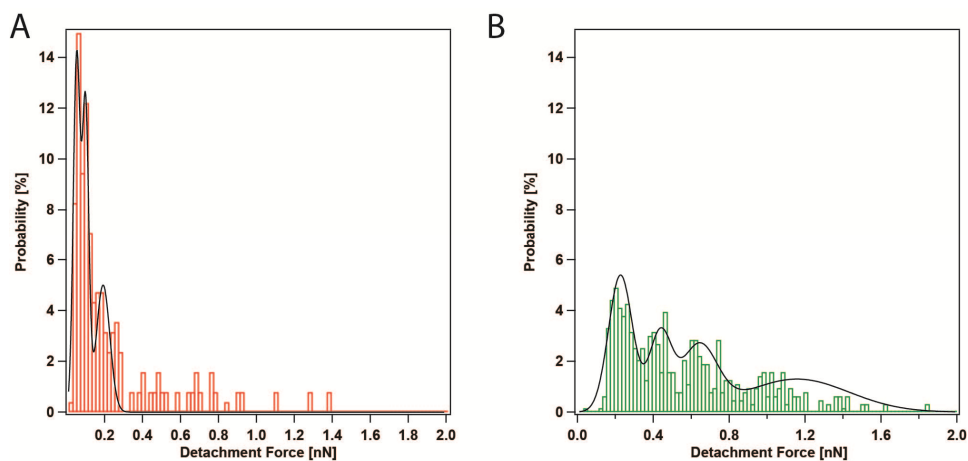
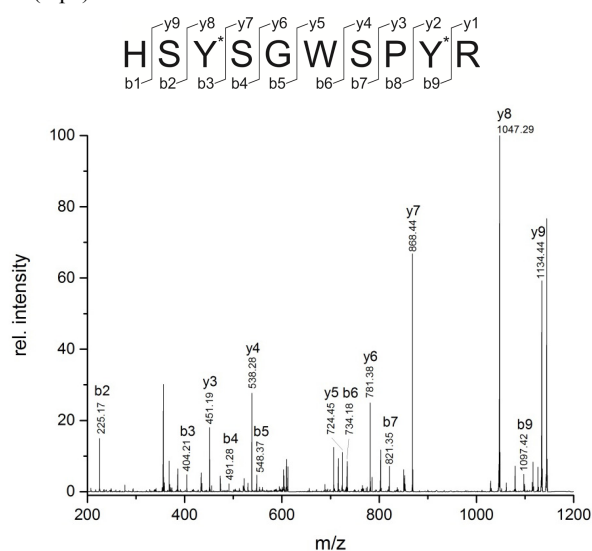


Figure S49. Histogram of the detachment forces for (A) Pep_3 and (B) $\text{Pep}_3^{*\text{-synth}}$, respectively.

Sequence analysis of Pep₃*-PEO

Activation of Pep₃-PEO was carried out according to the protocol described above (P. S7). In order to prove the oxidation of both tyrosine residues within the Pep₃ domain, LC-ms/ms measurements were performed. Due to the polymer block which does not enable direct ms/ms measurements, trypsinization had to be carried out at first. Briefly, 20 μ L (5.8 nmol) of activated conjugate solution were diluted with 380 μ L of Ammonium bicarbonate (ABC) buffer (50 mM). Trypsinization was carried out over night at room temperature by adding 30 μ L trypsin solution (1 μ g/30 μ L in 42 mM ABC buffer containing 0.2 mM HCl). Subsequently, the solution was acidified with 1 % TFA.

Digestion of Pep₃* yielded the 10mer sequence HSY*SGWSPY*R. Analysis with LC-ms/ms clearly identified the Pep₃ domain with two dopa moieties, dopa(3) and dopa(9), as both y and b fragments could be assigned (cf. Fig. S50). No evidence of multiple oxidation of tyrosine to quinone or trihydroxyphenylalanine (topa) was found.



fragment	expected	found	fragment	expected	found
y2	354.18	-	b2	225.10	225.17
y3	451.24	451.19	b3	404.16	404.21
y4	538.27	538.28	b4	491.19	491.28
y5	724.35	724.45	b5	548.22	548.37
y6	781.37	781.38	b6	734.29	734.18
y7	868.40	868.44	b7	821.33	821.35
y8	1047.46	1047.29	b8	918.38	-
y9	1134.50	1134.44	b9	1097.44	1097.42

Figure S50. LC-ms/ms fragmentation of trypsinized Pep₃*-PEO conjugate. Corresponding y and b fragmentation ions are found. Signals can be assigned within 0.35 Da accuracy.

11 Appendix

UV-kinetics of Pep₃^{*-synth.}-PEO

Enzymatic activation kinetics of Pep₃^{*-synth.}-PEO was carried out according to procedures described above (cf. page S7). Oxidation was monitored by UV-vis measurement at 280 nm using the same reference as for Pep³-PEO activation. A final absorbance of 0.99 ± 0.06 a.u. was observed from 3 repetitive measurements.

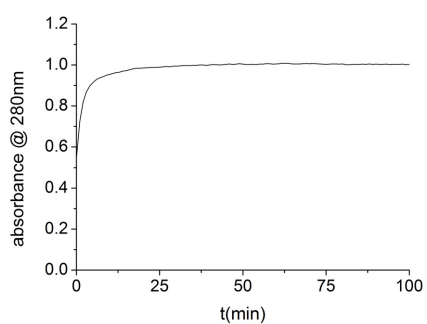


Figure S51. UV-kinetics of Pep₃^{*-synth.}-PEO activation at 280 nm.

References

- [1] Popa, I., Berkovich, R., Alegre-Cebollada, J., Badilla, C. L., Rivas-Pardo, J. A., Taniguchi, Y., Kawakami M., Fernandez, J. M.; Nano-mechanics of HaloTag Tethers., *J. Am. Chem. Soc.*, **2013**, *135*, 12762.
- [2] Ebner, A., Wildling, L., Zhu, R., Rankl, C., Haselgrübler, T., Hinterdorfer, P., Gruber, H. J.; Functionalization of Probe Tips and Supports for Single-Molecule Recognition Force Microscopy. In *Topics in Curr. Chem.*; Springer: Berlin **2008**, 285, pp. 29.
- [3] Hutter, J. L., Bechhoefer, J.; Calibration of Atomic Force Microscopy Tips. *Rev. Sci. Inst.*, **1993**, *64*, 1868.
- [4] Wangchareansak, T., Sangma, C., Ngermmeesri, P., Thitithanyanont, A. & Lieberzeit, P. A.; Self-assembled glucosamine monolayers as biomimetic receptors for detecting WGA lectin and influenza virus with a quartz crystal microbalance. *Anal. Bioanal. Chem.* **2013**, *405*, 6471.
- [5] Junker, J. P., & Rief, M.; Single-molecule force spectroscopy distinguishes target binding modes of calmodulin. *Proc. Natl. Acad. Sci. USA*, **2009**, *106*, 14361.
- [6] Gergely, C., Senger, B., Voegel, J., Horber, J., Schaaf, P., & Hemmerle, J. Semi-automatized processing of AFM force-spectroscopy data. *Ultramicroscopy*, **2001**, *87*, 67.
- [7] Papastavrou, G., Kirwan, L. J., & Borkovec, M.; Decomposing bridging adhesion between polyelectrolyte layers into single molecule contributions. *Langmuir*, **2006**, *22*, 10880.
- [8] Kaftan, O., Tumbiolo, S., Dubreuil, F., Auzély-Velty, R., Fery, A., & Papastavrou, G.; Probing multivalent host-guest interactions between modified polymer layers by direct force measurement. *J. Phys. Chem. B*, **2012**, *115*, 7726.
- [9] Zocher, M., Zhang, C., Rasmussen, S. G. F., Kobilka, B. K., & Muller, D. J.; Cholesterol increases kinetic, energetic, and mechanical stability of the human β_2 -adrenergic receptor. *Proc. Natl. Acad. Sci. USA*, **2012**, *109*, 20186.
- [10] Lee, H., Scherer, N. F., & Messersmith, P. B.; Single-molecule mechanics of mussel adhesion. *Proc. Natl. Acad. Sci. USA*, **2006**, *103*, 12999.

Danksagung

An dieser Stelle möchte ich allen Danken, die in irgendeiner Form zur Entstehung dieser Arbeit beigetragen haben!

Zuallererst möchte ich mich bei meinem Betreuer Prof. Dr. Georg Papastavrou herzlichst bedanken. Vielen Dank für das aufgebrachte Vertrauen in den letzten Jahren, die lehrreiche Betreuung und die vielen wissenschaftlichen Diskussionen. Herzlichsten Dank für alles!

Des Weiteren möchte ich meinen Kooperationspartnern für die sehr erfolgreiche Zusammenarbeit danken. Ich möchte mich aus diesem Grund besonders bei Prof. Dr. Thomas Scheibel, Prof. Dr. Hans-Werner Schmidt, Prof. Dr. Hans Börner, Prof. Dr. Andreas Fery, Dr. Jérôme F. L. Duval, Dr. Tomaso Zambelli and Prof. Dr. Volker Sieber für die vielseitigen Projekte und wissenschaftlichen Diskussionen bedanken. Des Weiteren möchte ich mich bei Dr. Claudia Blüm, Dr. Elena Doblhofer, Dr. Patrick Wilke, Dr. Marina Behr, Dr. Andreas Bernet, Dr. Klaus Kreger, Livie Dorwling-Carter und Petra Lommes für das Bereitstellen von zahlreichen Materialien bedanken. Ihr hattet es oft nicht leicht mit unserem Anspruch an 'saubere' Proben.

Vor allem möchte ich mich bei Dr. Volodymyr Kuznetsov und Dr. Öznur Kaftan bedanken. Ihr habt mich bereits während meines Studiums in die Geheimnisse der Kraftspektroskopie eingeweiht, was einen entscheidenden Beitrag zu dieser Arbeit darstellt. Besonderer Dank gilt Andreas 'Christian' Mark, der sich stets bereit erklärt hat und zahlreiche Igor-Prozeduren auf meine jeweiligen Problemstellungen angepasst hat. Ich möchte mich aber auch bei Carmen Kunert, Gustav Sauer, Markus Hund, Dr. Wolfgang Häfner, und Petra Zippelius bedanken. Ihr habt mir wirklich sehr geholfen, egal ob es sich um verschiedenste Messungen, Hilfestellungen oder Reinigungs- und Umzugsangelegenheiten diverser Geräte gehandelt hat.

Des Weiteren möchte ich mich bei der PC II: Sebastian, Dr. Inna, Ben 'Benjamin', Thomas, Paul, Yannick, Anna und Nadine für die entspannte Laboratmosphäre und diverse Kaffeepausen bedanken. Ich möchte aber auch den Ehemaligen der 'Force Group' danken, die stets gute Tipps für die Durchführung meiner Experimente beigesteuert haben. Ein beson-

11 Appendix

derer Dank gilt aber auch den zahlreichen Studenten, die mich und meine Projekte im Rahmen eines Praktikums oder einer Abschlussarbeit unterstützt haben. Vielen Dank an Maria Klug, Carsten Tschense, Martin Pretscher, Andreas Rösch, Sarah Jessel, Vera Bieber und Thomas Schmitt. Liebe Sybille, dir danke ich einfach für alles was du jeden Tag für uns am Lehrstuhl leistest.

Die FluidFM Publikationen wären ohne die anfängliche Hilfe und vor allem den stetigen Support von Dr. Christian Bippes und Dr. Patrick Frederix (Nanosurf AG), sowie Dr. Pablo Dörig (Cytosurge AG) nicht möglich gewesen. Des Weiteren muss ich mich an dieser Stelle auch einem Paket-Dienstleister gedankt werden, der uns einige 'spannende' Stunden beschert hat.

Besonders hervorheben möchte ich an dieser Stelle noch einmal Dr. Inna, Andreas, Sebastian, Jens und Yannick, die sich freundlicherweise bereit erklärt haben, Teile der Arbeit Korrektur zu lesen.

Zum Schluss möchte ich mich bei meiner Familie für die stetige Unterstützung während meiner Zeit in Bayreuth danken! Mein herzlichster Dank gilt allerdings Lena für deine Unterstützung. Du hast mir vor allem in den letzten beiden Jahren immer wieder den Rücken frei gehalten hat, damit ich die finalen Publikation und vor allem auch diese Arbeit fertigstellen konnte. Zu guter Letzt natürlich mein Lukas, vielen Dank für alle besonderen Momente.

Danke!

(Eidesstattliche) Versicherungen und Erklärungen

(§5 Nr. 4 PromO)

Hiermit erkläre ich, dass keine Tatsachen vorliegen, die mich nach den gesetzlichen Bestimmungen über die Führung akademischer Grade zur Führung eines Doktorgrades unwürdig erscheinen lassen.

(§8 S. 2 Nr. 5 PromO)

Hiermit erkläre ich mich damit einverstanden, dass die elektronische Fassung meiner Dissertation unter Wahrung meiner Urheberrechte und des Datenschutzes einer gesonderten Überprüfung hinsichtlich der eigenständigen Anfertigung der Dissertation unterzogen werden kann.

(§8 S. 2 Nr. 7 PromO)

Hiermit erkläre ich eidesstattlich, dass ich die Dissertation selbständig verfasst und keine anderen als die von mir angegebenen Quellen und Hilfsmittel benutzt habe.

(§8 S. 2 Nr. 8 PromO)

Ich habe die Dissertation nicht bereits zur Erlangung eines akademischen Grades anderweitig eingereicht und habe auch nicht bereits diese oder eine gleichartige Doktorprüfung endgültig nicht bestanden.

(§8 S. 2 Nr. 9 PromO)

Hiermit erkläre ich, dass ich keine Hilfe von gewerblichen Promotionsberatern bzw. -vermittlern in Anspruch genommen habe und auch künftig nicht nehmen.

.....

Ort, Datum, Unterschrift